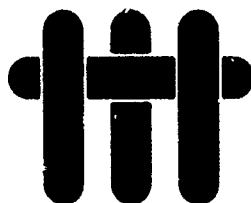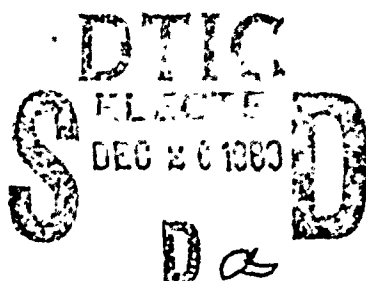AD-A216 142

ANNUAL REPORT
University Research Initiative
Contract No.: N00014-86-K-0753
September 15, 1988-September 14, 1989

The Processing and Mechanical Properties of High Temperature/ High Performance Composites

by

A. G. Evans & R. Mehrabian
University of California,
Santa Barbara

Arizona State University
Cambridge University
Harvard University
Stanford University
Washington State University
University of Wisconsin-Madison
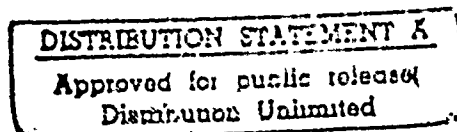
Book 2 of 6
Section 2: STRENGTH and FRACTURE RESISTANCE
Part 1 of 2

89 12 21 033

SUMMARY

of

TABLE OF CONTENTS

BOOK 2

SECTION 2: STRENGTH AND FRACTURE RESISTANCE

Part 1 of 2

Fiber Reinforcement

EXECUTIVE SUMMARY

The third annual report of the University Research Initiative project at UCSB on High-Temperature, High-Performance Composites consists of sections compiled in a total of six books. The first section in Book 1 is concerned with the properties and structure of bimaterial *interfaces* and the related problem of *coating* decohesion and cracking. The second section describes research on the *strengths and fracture resistance* of brittle matrix composites manufactured with fibers, whiskers and ductile phases. This information is presented in Books 2 and 3. The third section addresses the *flow and creep strength* of reinforced systems, with emphasis on effects of aspect ratio and the incidence of damage, and is offered in Book 4. The fourth section, Books 5 and 6, describes work on processing of intermetallic and ceramic matrices and composites, as well as numerical modelling of the melt-spinning process.

SECTION 2: STRENGTH AND FRACTURE RESISTANCE

FIBER REINFORCEMENT

The axial tensile properties of a range of fiber reinforced ceramics have been rigorously evaluated and shown to be consistent with models previously developed in the program. In particular, the matrix cracking stresses and the ultimate strength have been predicted through the models based on independent measurements of the elastic properties, the interface sliding stress, the interface debond energy, the residual strain and the *in situ* strengths of the fibers. The basic models applicable to tensile properties, as well as the methods for measuring the important microstructural properties, are thus concluded to capture the essential features of composite behavior.

1

Mode I resistance curve measurements have been made on composites heat treated to produce fiber interfaces having sufficient sliding resistance that delamination cracking is suppressed (Sbaizero). The materials and test specimens lead to large scale bridging and the measured data require correction for this, as elaborated below. The crack growth behavior has also been numerically simulated (Hom and McMeeking) based on bridging and sliding traction laws derived in previous research within the program. Good agreement between the simulation and experimental data is demonstrated for an interface sliding stress consistent with the measured fiber pull-out lengths. The results also reveal that frictional dissipation during pull-out provides the main contribution to the toughness ($K_c \approx 20\,\text{MPa}\sqrt{m}$ at steady-state) and that large scale bridging effects lead to substantial overestimates of actual toughness levels when conventional linear elastic fracture mechanics formulae are used.

Delamination cracking has been investigated in a laminated composite (Sbaizero et al.) and the data have been interpreted based on solutions for mixed mode cracking in anisotropic media (Suo). Delamination crack growth resistances have been deduced and shown to be governed primarily by the matrix fracture energy, with some contribution from distributed fibers that bridge the crack surfaces. The crack is also found to progress into a steady-state trajectory along a laminate interface; furthermore, the initial crack path rotates toward that interface in a sense governed by the sign of K_{II}.

To further understand these effects, a new method for fabricating ceramic composites has been invented (Folsom et al.). The method involves bonding together thin ceramic sheets and thin layers of fibers to form a multiple sandwich composite comprising of alternate layers of ceramic and fibers. The thin, strong ceramic sheets are formed by a method used to make ceramic substrates for electronic packaging. The fiber layers can be in the form of either aligned fibers or

cloth, which are penetrated with an appropriate bonding agent, e.g., an epoxy resin, metal or ceramic powder. The composite is formed by sandwiching the ceramic sheets with fiber layers and then bonding the ceramic sheets to the fiber layers with an applied pressure at the appropriate temperature. Current work emphasizes composites formed with epoxy resin, carbon fiber prepregs laminated between ceramic sheets comprised of either alumina, transformation toughened zirconia, or glass by hot-pressing. Because processing is simple and carried out at low temperatures, large numbers of composite modifications are being explored.

Fracture resistance caused through bridging by fiber and/or by ductile reinforcements has been addressed in the large scale bridging regime (Zok and Hom), by experiments conducted on metal reinforced ceramics (Velamakanni et al.), on fiber reinforced ceramics (Sbaizero et al.) and on a metal fiber reinforced polymer. The results establish a strong influence of large scale bridging on the apparent fracture resistance, consistent with numerical simulations of crack growth in such materials. An approximate analytical solution has also been developed that correlates well with the data and may be used for interpretation purposes and, furthermore, generates actual material resistances from the experimental results. Additionally, *this work clearly indicates that nominal fracture toughness results can substantially overestimate actual properties and must be used with caution.*

DUCTILE REINFORCEMENT

Following the results of the previous year which highlighted the importance of interface debonding and of the reinforcement ductility (Ashby et al.) on the toughness, a systematic study has been completed on the effects of those variables (Cao et al.; Dève et al.). For this purpose, experiments have been conducted on composite cylinders and on laminated systems consisting of TiAl and Nb/Ti alloys (thickness, 2R), with various thin oxide coatings and/or reaction product layers

between the matrix and reinforcements. The results reveal that Y_2O_3 coatings inhibit reactions and also allow extensive debonding (debond length d $\approx$ 20R), consistent with its relatively low fracture energy ($\Gamma_i \approx$ 25 Jm^{-2}). For high ductility reinforcements, such as high purity Nb, debonding leads to a large work of rupture ($\chi \rightarrow$ 6–7). In the absence of a coating, more limited debonding occurs (d $\approx$ 5–6R) along a σ-phase reaction product layer, resulting in a smaller work of rupture ($\chi \approx$ 2.5). Furthermore, for the latter, χ is found to be similar for composite cylinders, for laminates and for actual composites. High strength, low ductility reinforcements, such as Ti-33% Nb, indicate different characteristics. In this case, extensive debonding (induced by Y_2O_3 coatings) results in abrupt reinforcement rupture and small χ (1–1.5). However, when debonding is suppressed by averting the formation of a brittle reaction products layer, inhomogeneous deformation in the Ti/Nb apparently suppresses necking and allows a moderately large work of rupture ($\chi \approx$ 2–3 in laminates and $\chi \approx$ 4–5 in composites). The approach needed to achieve optimum toughening thus depends sensitively on the flow and fracture behavior of the reinforcement. An important effect of matrix crack offset on χ has also been found (Ashby) in the sense that χ increases as the offset angle increases. It remains to ascertain how this benefit can be encouraged in actual composites.

An essential, related aspect of this study concerns diffusion-couple annealing experiments which have been used to explore interactions between γ-TiAl matrices and ductile-phase reinforcements based on β-(Ti,Nb) alloys. The nature and rate of evolution of the interfacial layers have been characterized and the interdiffusion coefficients of Nb and Al in the β-(Ti,Nb) phase have been calculated for the 900-100°C temperature range using a Matano-Boltzmann analysis. While the interdiffusion coefficients are dependent on alloy composition, the activation energies were found to be quite similar in all cases, about 250 ± 40 kJ/mole (Jewett et al.).

A process for producing ceramics with an interpenetrating network of a metallic alloy has been invented (Velakammani et al.). In this process, ceramic powder is packed within a pyrolyzable preform, e.g., an organic fiber felt, by pressure filtration. The preform is then pyrolyzed at low temperature of produce a powder compact containing pore channels remnant of the preform. The ceramic powder is densified at higher temperatures without eliminating the pore channels which at infiltrated with a molten metal. A systematic study of the fracture toughness based on the above variables, which can be changed with this new processing method, is in progress. Initial studies have emphasized Al_2O_3 and transformation toughened ZrO_2 matrices containing 20 μm fibers of a Al-Mg alloy with an architecture remnant of a needled felt used to create the channels within the ceramic. Squeeze casting is used to intrude the molten metal into the pore channels. Preliminary fracture mechanics testing to determine crack growth resistance as a function of crack length has shown that the ductile bridging ligaments increase fracture toughness.

Studies of the deformation behavior of the reinforcements have provided additional insight. Deformation of TiNb involves rafted dislocation pile-ups in narrow, coarsely distributed slip bands that extend large distances away from the crack surfaces. Fracture occurs at the intersection of these bands. In the Nb system, twinning and slip occur in the γ matrix around the interface and near the crack plane. Furthermore, debonds along the σ phase reaction product layers appear to initiate at sites where the twins intersect this layer:

MATRIX TOUGHENING

An investigation of ceramics toughened with whiskers (Campbell et al.) has established both the prevalent contributions to toughness, as well as the realistic toughening potential. The two principal toughening contributions derive from the extra surface energy associated with debonding along the amorphous phase at the interface and the energy dissipated as acoustic waves when the whiskers fail in the crack wake. These contributions can lead to toughness of order $K_c \approx 10$ MPa$\sqrt{m}$. Much larger toughness could be induced by encouraging frictional dissipation by sliding and pull-out along debonded interfaces. Direct measurements of these effects (Ashby) produce an opportunity to understand how this contribution can be understood and emphasized.

Fracture resistance effects have also been explored for process zone toughening mechanisms (Stump and Budiansky; Hom and McMeeking). These results show that the resistance curves exhibit a peak preceding steady-state and that the peak height is related to the gradient in volume fraction of transformed material in the process zone, $f(y)$, in the sense that uniform transformation in the zone leads to the maximum peak height. A comparison of simulated fracture resistance curves with experimental results (Hom and McMeeking) reveals good agreement when independent measurements of $f(y)$ and of the process zone size and shape are used to set the magnitudes of the parameters used in the simulation.

The overall toughness of a reinforced system may involve multiplicative effects between matrix toughening and reinforcement toughening. Matrix toughening behaviors include the transformation and whisker mechanisms noted above, as well as twin toughening. Multiplicative effects with reinforcement toughening occurs primarily with process zone mechanisms (twinning, transformation, etc.). Analysis of the coupled toughening (Stump and Budiansky, Hom and McMeeking) have demonstrated conditions that provide the extremes of

6

multiplicative and additive behavior. Also, resistance curves applicable when multiple mechanisms operate have been simulated. These calculations provide the insight needed to select matrix microstructures consistent with that reinforcement scheme of choice.

MATERIALS

THE EFFECT OF INTERFACES ON THE MECHANICAL PERFORMANCE OF FIBER REINFORCED BRITTLE MATERIALS

by

H. C. Cao, E. Bischoff, O. Sbaizero, M. Rühle and A. G. Evans
Materials Department
College of Engineering
University of California
Santa Barbara, California 93106

D. B. Marshall
Rockwell Science Center
Camino Dos Rios
Thousand Oaks, California 91360

and

J. J. Brennan
UTRC
East Hartford, Connecticut 06108

ABSTRACT

The mechanical properties of a series of six fiber-reinforced ceramics and glasses has been evaluated with the objective of critically assessing present understanding. A major parallel theme has been the characterization of the interface and an assessment of the thermomechanical properties of the interfaces as they relate to composite behavior. The results establish that the available mechanical property models correlate well with experiments, provided that independent measurements are made of the residual stress, the interface sliding stress and the *in-situ* strength properties of the fibers. In addition, trends in the sliding stress are found to be qualitatively consistent with those expected for sliding along debonded surfaces.

1. INTRODUCTION

A variety of glasses, ceramics and glass ceramics have now been successfully reinforced with continuous graphite and Nicalon fibers.[1-5] In all cases, a desirable tensile performance for such composites, manifest as a large "work of fracture" (Fig. 1), has required a thin interfacial layer between the fiber and the matrix, introduced either by fiber coating[5] or in-situ by chemical reaction during processing/heat treating.[6,7] This layer has typically been either C or BN, often in an amorphous state. Alternative coatings have yet to be identified

Models that describe the salient features of the stress-strain curves and the mechanical role of the interfacial layer have also been developed (Fig. 2).[5-11] These models include such variables as the fracture energy of the coating, Γ_i, compared with that of the fiber, Γ_f,[12,13] the sliding resistance τ of a debonded fiber within the matrix and the mismatch strain ε between fiber and matrix caused by thermal expansion misfit, crystallization and by phase transformation. In addition, the elastic properties, the fiber strength and volume fraction and the matrix fracture toughness are involved.[8-11] The intent of the present study is to examine the applicability of these models by conducting an experimental investigation of the macroscopic tensile mechanical properties and of the interface thermomechanical properties of a series of composites, all reinforced with Nicalon fibers.

The knowledge generated by the models has resulted in the identification of three basic thermomechanical requirements for a desirable composite[12]: $\Gamma_i/\Gamma_f \lesssim 1/4$, $2 \lesssim \tau \lesssim 40$ MPa, $\varepsilon \lesssim 3 \times 10^{-3}$. The first of these criteria ensures that debonding occurs in preference to fiber failure during matrix cracking (Fig. 2b).[13] The second condition encourages fiber failure at a substantial distance from the matrix crack plane and thus allows a substantial pull-out contribution to "toughness"[14] through frictional dissipation, when the fibers are strong. The third criterion prevents

thermal cracking of either the fibers or the matrix.[10] In addition to these fundamental criteria, systematic mechanical property enhancement is predicted to occur with increase in the fiber bundle strength, S_b, the matrix fracture energy, Γ_m, and the fiber volume fraction, f.[12] There are also effects of elastic properties and fiber radius, R. The present study emphasizes the explicit effects of Γ_i/Γ_f, τ and ϵ.

The three important features of the stress-strain curves exhibited by "tough" ceramic/glass matrix composites are (Fig. 1): the matrix cracking stress σ_o, the ultimate strength, σ_u and the pull-out "tail." *Matrix cracking* is predicted to have a lower bound steady-state value[8-11]

$$\sigma_o = \sigma_* - q E/E_m \tag{1}$$

with

$$\sigma_* = \left[\frac{6\tau \Gamma_m f^2 E_f E^2}{(1-f) E_m^2 R} \right]^{1/3}$$

where E is Young's modulus of the composite, q is the axial residual stress in the matrix as governed by the misfit strain (positive q being tension) and the subscripts f and m refer to the fiber and matrix, respectively. Steady-state matrix cracking conditions exist when $\sigma_o < S_b/f$, whereupon most fibers remain intact during matrix cracking and when the initial matrix crack size a_o satisfies[9,11]

$$a_o > a_c$$

where

$$a_c = \left[\pi/4(2/3)^{4/3}\right]\left[\Gamma_m^{1/2}\frac{E_m^{3/2}(1-f)^2 R(1+\xi)}{\tau f^2 E_f(1-v^2)}\right]^{2/3} \tag{2}$$

with $\xi = E_f f/E_m(1-f)$. When a_o does not satisfy the above inequality, matrix cracking occurs at stresses $> \sigma_o$.

Upon increasing the stress above σ_o, matrix cracking continues, resulting in a periodic crack array.[8,15] The crack spacing reaches a *saturation value*, d, when the stress everywhere in the "matrix blocks" becomes smaller than that stress associated with the applied load capable of being supported by the uncracked matrix.[8] The average value of the saturation crack spacing is governed by the sliding stress, τ, such that τ and d are related by,

$$\tau = \lambda\left[(1-f)^2\Gamma_m E_f E_m R^2/fEd^3\right]^{1/2} \tag{3}$$

where λ is a quantity‡ equal to 1.34.[16] Consequently, the matrix cracking stresses can be expressed in terms of the crack spacing as;

$$\sigma_o = (6\lambda)^{1/3}\left[f\frac{\Gamma_m E_f E}{E_m d}\right]^{1/2} - q\frac{E}{E_m} \tag{4}$$

The trend in σ_o with fiber volume fraction for one of the composites used in the present study (material C, see Table I) is plotted on Fig. 3 to indicate that, typically, σ_o increases almost linearly as f increases.

---

‡ Note that $\lambda = 1.3\ldots^{3/2}\cdot(3/4)^{1/2} = 1.34\ldots$.

The *ultimate strength* coincides with fiber bundle failure.[12] A simple estimate of this strength, based on weakest link statistics,‡ gives;

$$\sigma_u = f\hat{S} \exp\left[-\frac{\left\{1 - (1 - \tau d/R\hat{S})^{m+1}\right\}}{(m+1)\left\{1 - (1 - \tau d/R\hat{S})^m\right\}}\right] \tag{5}$$

with

$$(R\hat{S}/\tau d)^{m+1} = \left(A_o/2\pi RL\right)(RS_o/\tau d)^m \left\{1 - (1 - \tau d/R\hat{S})^m\right\}^{-1}$$

S_o is the stress scale parameter, m the shape parameter, A_o is another scale parameter (usually set equal to $1m^2$) and L the specimen gauge length. The effect of the sliding stress on σ_u appears directly, as well as through its effect on the crack spacing d, while the effect of residual stress is present through its effect on τ.

A comparison of the above trends in composite behavior with experimental data requires independent measurement of τ, ε, Γ_i/Γ_f and Γ_m and knowledge of R, f, E_f and E_m. Estimates of τ can be obtained from the saturation crack spacing (Eqn. 3), as well as by using a nanoindenter[17,18] and from load/crack opening hysteresis.[15] The crack spacing is emphasized in the present study. The other methods are examined in a companion study. Values of Γ_f have previously been obtained for Nicalon fibers using fracture mirrors [19] ($\Gamma_f \approx 5\,Jm^{-2}$), while Γ_m and E_m are known for each material (Table I). Values of ε are extracted from thermal expansion data (Table I).

---

‡ This estimate neglects interaction effects between failed fibers and ignores the stress supported by fractured fibers by stress transfer from the matrix through interface friction.

Overall rationalization of the mechanical behavior in terms of the thermomechanical characteristic of the interface resides in characterization of the interfacial zone. This is achieved in the present study by a combination of conventional and analytical transmission electron microscopy with scanning Auger microscopy.

2. MATERIALS

Six different composite materials are investigated, having the characteristics summarized in Table I. Each material contained Nicalon fibers at a volume fraction f = 0.5. The systems have been selected to encompass a range of interface properties and of mismatch strain. The elastic properties of the matrix (Young's modulus and Poisson's ratio) remain essentially constant, while the fracture energy varies by a factor of 2. Previous studies have indicated that two of the materials have a well-delineated carbon coating between the fibers and the matrix (materials A and B). Two materials have no obvious debond layer (materials D and E). The fifth material (C) gives indications of a very thin carbon layer, using Auger spectroscopy.[6] Furthermore, A and B represent a material pair in which the fiber and fiber coating are expected to be essentially the same, but the misfit stress and the matrix fracture energy are different. In addition, composites B and C constitute a very interesting contrast in that the matrices in both materials have very similar thermomechanical properties, but the interfaces appear to have different composition and thus different debonding and sliding behavior.

3. MECHANICAL CHARACTERISTICS

3.1 TEST PROCEDURES

Uniaxial tensile stress-strain curves are measured using test specimen configurations described in previous studies.[15,20] The specimens consist of a rectangular cross section bar (2 x 3mm) with fibers oriented parallel to the tensile axis. One face of the specimen is polished to facilitate microstructure examination during and after testing. Reduced gauge sections of length ~ 12mm are used to prevent pull-out from the grips, which are attached to the specimen using an epoxy bond with a 8mm transfer length at each end. Tensile tests are conducted on a servohydraulic machine[#] at a constant strain-rate of 2×10^{-5} s^{-1}, using an aligning apparatus developed in previous studies.[20] Stresses are obtained from the imposed loads, while strains are determined from displacements measured within the gauge length using an axial extensometer.

Several experiments are conducted in four-point flexure and load/deflection curves measured by monitoring the displacement of the mid-point of the tensile surface.

3.2 MEASUREMENTS

The tensile stress-strain curves obtained for each material are summarized in Fig. 4. Fully brittle behavior is observed in material E with a strength sensitive to the flaw population in the material. The other four materials exhibit nonlinearity, characteristic of "tough" composites, having an initial matrix cracking stress, followed by "hardening" and then an ultimate strength at which an abrupt load

---

[#] MTS 810, MTS Systems Corporation, Minnesota

drop occurs. The trends in initial matrix cracking stress and in ultimate strength are summarized in Table II. The only material among the four which which does not have a distinct deviation from linearity is material D.

3.3 OBSERVATIONS

The four "tough" materials A→D all exhibit matrix cracking (Fig. 5). However, the cracks are not easily observable in all cases. It has been found that the matrix cracks can be highlighted by tensile testing, followed by notching and retesting in tension in order to propagate a delamination crack along the tensile axis. The interaction of the delamination crack with the previously formed matrix cracks results in strong height contrast (Fig. 6). In materials A and B for which the matrix cracks are readily observable (Fig. 5), the above method yields crack spacings identical to those measured using more conventional methods. Matrix crack measurements performed on materials A, B and C using these methods indicate that the first cracks coincide with the initial deviation from linearity σ_0. However, the number of cracks tends to accumulate with increase in stress, such that a saturation crack spacing d develops prior to failure, having the values listed in Table II. Material D, however, contains matrix cracks before testing (Fig. 7), although additional cracks are formed upon loading, causing the average crack spacing to reduce. Furthermore, it is noted that, in materials A and B, the matrix cracks are well-defined and propagate across specific planes, demonstrating no effect of the fibers on the crack path. However, matrix cracks are discontinuous in materials C and D, suggesting some interaction with the fibers.

Saturation matrix cracking is observed in composites A and B within a relatively narrow stress range, resulting in "bi-linear hardening." However, in material C, the number of matrix cracks accumulates slowly with increase in stress,

leading to nonlinear hardening. Material D also exhibits nonlinear behavior, but the nonlinearity is believed to be associated with failure of weak fibers and the propagation of delamination cracks.

Studies of fractured specimens indicate that those fibers which pull out from the matrix are typically smooth. Material D is an exception, wherein debris is attached to the fiber surfaces leading to roughness and suggesting that debonding occurred within an interphase layer (Fig. 8). Also, in this material, some radial cracking of the matrix is observed. Furthermore, the failure of small bundles of fibers is apparent, probably associated with processing damage (Fig. 9).

Finally, examinations of material E have revealed that fracture involves the unstable propagation of a single dominant processing flaw, resulting in a relatively flat fracture surface (Fig. 10).

4. INTERFACE CHARACTERIZATION

Thin sections normal to the fiber axis have been prepared by mechanical dimpling and by ion beam thinning, as described elsewhere[7] and examined by transmission electron microscopy. The three tough materials (A, B and C) all possessed amorphous carbon layers between the fiber and matrix (Fig. 11, 12). The LAS ceramic matrix system (A) also exhibited circumferential debonds in the carbon layer, as previously noted[7] (Fig. 11a), caused by expansion mismatch between the fiber and matrix. However, no debonds could be detected in the LAS glass matrix (B) system (Fig. 11b), which has a closer expansion match between the fiber and matrix (Table I). In the aluminosilicate matrix system (C) a carbon layer could not be identified by energy loss spectroscopy (EELS). However, a thin interface layer, ~ 0.01μm thick, which appeared brighter than either the matrix or the fiber was

evident (Fig. 12a), indicating the presence of material having low atomic number. This layer is probably the carbon layer detected by Auger electron spectroscopy.[6] Furthermore, matrix cracks mechanically induced into the material prior to thinning cause circumferential debonding at the interface between the above thin layer and the fiber (Fig. 12b). Consequently, whatever the composition of this layer, it evidently satisfies debonding requirements.

In the silica matrix material (E), neither chemical nor contrast difference could be detected near the fiber/matrix interface. Furthermore, matrix cracks generated within the foils remain within the matrix (Fig. 13) rather than causing interface debonding. Such cracks are typical of matrix cracks in a composite system with good interface bonding, subject to residual radial tension in the matrix.

Finally, the soda lime glass matrix material (D) exhibited some interface contrast (Fig. 14a) within a layer ~0.1μm thick. Some residual porosity exists within this layer. Moreover, matrix cracks that intersect the interface cause debonding *within* this layer, as evident from the image shown in Fig. 14b. Consequently, while this interface is capable of debonding, the debond does not occur at the fiber/interphase interface. These observations are consistent with the above SEM studies (Fig. 8) which indicate interface material attached to the fibers in composite D.

5.   RESIDUAL STRESSES

The residual stress has significant effects on both the interface sliding stress and matrix cracking stress,[10] as well as the ultimate strength. The residual stress arises from thermal contraction mismatch upon cooling, as well as from crystallization and phase changes (in the case of glass-ceramic matrices). In this

section, the stresses are estimated either from thermal expansion information or from experimental measurements.

In material A, the ceramed LAS matrix and silicon carbide fiber have appreciably different thermal expansion coefficients. However, the crystallization also involves a volume change. It is surmised that these changes tend to counteract, because the residual stress estimated from the matrix crack closure load is small[15]: $q < -50$ MPa, $p < 20$ MPa, where q is the stress in the matrix parallel to the fiber axis and p the stress normal to the interface.

Residual stresses in the other materials are more likely to be governed by the differential thermal shrinkage because a crystallization step is not involved. The following expressions are used[10] to obtain p and q from the thermal expansions,

$$\frac{q}{E_m} = \frac{\lambda_2}{\lambda_1} \left[\frac{E_f}{E} \right] \left(\frac{f}{1-v_m} \right) \varepsilon$$

$$\frac{p}{E_m} = \frac{1}{2\lambda_1} \left(\frac{1-f}{1-v_m} \right) \varepsilon \tag{6}$$

where λ_1 and λ_2 are functions of fiber volume fraction f, and elastic properties, E_f/E_m, v_f and v_m:

$$\lambda_1 = \frac{1-(1-E/E_f)(1-v_f)/2+(1-f)(v_m-v_f)/2-(E/E_f)[v_f+(v_m-v_f)fE_f/E]^2}{(1-v_m)[1+v_f+(v_m-v_f)fE_f/E]}$$

$$\lambda_2 = \frac{1-(1-E/E_f)/2(1+v_f)+(1+f)(v_m-v_f)/2}{[1+v_f+(v_m-v_f)fE_f/E]}$$

and $\varepsilon = (\alpha_f - \alpha_m)\Delta T$, with ΔT regarded as the difference between ambient and the glass transition temperature.

Using the information provided in Table I, the residual stress calculated using Eqn. (5) are listed in Table III. It is apparent that large residual stresses arise in material D. The large tensile axial stresses in the matrix are the source of matrix cracking during cooling. Furthermore, for this material, it is noted that large tensile hoop stresses also occur in the matrix. These stresses seemingly cause axial matrix cracks between the fibers (Fig. 8), which probably reduce the residual stress p to values lower than indicated by Table III.

6. FIBER STRENGTHS

Information concerning the in-situ fiber strengths can be obtained by measuring fracture mirror radii (see Fig. 8) and using the formula[19]

$$S = K_f / 3.5\sqrt{a_m} \qquad (7)$$

where S is the stress on the fiber at the fracture site, a_m is the mirror radius and K_f is the fracture toughness of the fiber ($1 MPa\sqrt{m}$ for Nicalon fiber). The cumulative distribution of fiber strengths obtained in this manner for the composite systems C and D is plotted on Fig. 15. The results conform with the function

$$G(S) = 1 - \exp\left[-\left(S/S^*\right)^\omega\right] \qquad (8)$$

where G is the cumulative probability, S^* is the scale parameter and ω the shape parameter. The values of S^* and ω for the fibers in materials C and D are indicated in Fig. 15. In particular, it is noted that the median fiber strength in composite D is substantially less than that for composite C, indicating significant fiber degradation

upon processing of the former. Similar measurements performed on materials A and B reveal a strength distribution essentially the same as that shown for material C.

7. INTERFACE MECHANICAL PROPERTIES

7.1 DEBONDING

The above experiments indicate that *debonding* requirements are satisfied in all materials *except* E. This lack of debonding in material E is consistent with previous observations[7,19] that silica coatings on Nicalon fibers inhibit debonding, because SiO_2 and Nicalon have similar fracture energies. It is also well-established that carbon layers satisfy debonding requirements on Nicalon fibers.[7] However, the fracture energy of the carbon found at the interface is not available. It is presumed to be much less than that of either glassy carbon[21] or polycrystalline graphite[22], because known values for these materials exceed the fracture energy of Nicalon fibers and thus, would seemingly contradict debonding requirements.[13] Indeed, upper bound estimates of Γ_i from nanoindenter measurements on material A,[17,18] confirm very small values ($< 1Jm^{-2}$) for the carbon layer in this material. An important additional feature to emphasize is that the very thin ($\sim 0.01\mu m$) carbon layer in material C is still sufficient to allow debonding.

Debonding in material D has substantial significance, because all other coatings that have demonstrated debonding are either carbon or boron nitride, as already noted. It is surmised that the reaction between the fiber and matrix generates an intermediate layer having a low fracture energy. One possible explanation is that local cation diffusion results in the formation of a low-density amorphous coating.

7.2 THE INTERFACE SLIDING STRESS

The interface sliding stresses estimated from the measured matrix crack spacing, using Eqn. (3) are summarized in Table III. The increased sliding stress for material D compared with A is broadly consistent with the residual stress normal to the interface changing from tension in A to compression in D, as might be expected for a Coulomb friction law in the presence on a nonplanar debonded interface. However, the larger τ for material C than material B is anomalous, but may reflect the observation (Figs. 11, 12) that the carbon debond layer in the former is very thin compared with that in either material B or in material A.

The sliding stress inferred for material D is surprisingly small, given that there is no carbon layer at the interface and that the debond surface is rough (Fig. 8). A possible explanation involves the incidence of radial matrix cracks (Fig. 8), which would reduce the matrix constraint upon fiber sliding, as already noted.

Additional study is clearly needed before trends in the sliding stress can be fully understood in terms of the properties of the coating, the surface roughness, etc.

8. STRESS/STRAIN CURVES

The matrix cracking stresses can be predicted using Eqn. (1) with the values of the sliding stresses and residual stresses indicated in Table III. The results are summarized in Table IV.

The predicted results are sensitive to the choice of the matrix toughness Γ_m. The values of this parameter listed in Table I represent a best attempt to obtain good values from the references listed in that table. It is notable, however, that other papers have used different values of Γ_m, especially for LAS. The specific predictions

listed in Table IV use the range of Γ_m given in Table I. Similar concerns exist regarding the accuracy of the residual stresses, as elaborated below.

For the first two materials (A and B) with "thick" carbon coatings, the agreement between theory and experiment is excellent. Furthermore, for material D, the matrix cracking stress is predicted to be negative at room temperature, indicating that cracking should have occurred on cooling. This prediction is again consistent with the experimental observations. The brittle behavior of material E is also consistent with the known debonding requirements. The only material for which significant deviation between theory and experiment is apparent is material C. This material also differs from the others in terms of its work hardening behavior, as elaborated below. The source of this discrepancy is not clear, but two possibilities are noted. This material has a more heterogeneous spatial distribution of fibers than t . others, resulting is local regions having small f. Reference to Fig. 2 indicates that such regions have a reduced matrix cracking stress. Alternatively, better agreement with theory would exist if the residual stress were zero: the predicted σ_0 would then be about 250MPa compared with a measured value of 240MPa. The present estimate of the residual stress could thus be in error. Some additional evidence in support of this contention has been obtained from nanoindenter tests.[21]

The ultimate strength of the composite can, in principle, be deduced from Eqn. (5). However, there is no direct connection between the statistical parameters for the fibers required to evaluate σ_u and the strength parameters measured from the fracture mirror radii, because the fracture locations in the fibers, vis-à-vis the matrix crack planes, are not readily assessed. Nevertheless, the fracture mirror measurements provide information that allows *scaling* between the different composite systems. Consequently, based on the prescribed ultimate strength of composite A, the ultimate strengths of the other composites is determined, using

16

Eqn. (5) in conjunction with the fiber strength results presented in Fig. 15 and the independently measured values of τ and d.[‡] The results, indicated in Table IV, accord well with experiment, establishing that fracture mirror measurements provide a useful means of scaling trends in the ultimate strength, as governed by fiber degradation effects.

The "hardening" region between σ_o and σ_u also merits discussion. When the composite has many matrix flaws that exceed the critical level, a_c, needed to allow steady-state cracki..$\acute{g}$ (Eqn. 3), satu.....on cracking occurs at stresses *just above* σ_o. Such materials should be essentially linear between σ_o and σ_u. This is the behavior that seemingly governs the bilinear stress/strain characteristics of materials A and B. Conversely, when the composite has few matrix flaws larger than a_c, matrix cracking at σ_o is unsaturated and further cracking occurs between σ_o and σ_u. Then the material should exhibit non-linear hardening. Such characteristics are consistent with the behavior of material C.

9.   CONCLU   ' G REMARKS

The models of matrix cracking seem to correlate well with experiment when critically evaluated for a range of different materials. Furthermore, the results emphasize that the residual stress and the interface sliding stress both have a major influence on the matrix cracking strength. It is also apparent that a matrix with relatively high thermal expansion coefficients can crack thermally: this occurs at useful fiber concentrations (f ~ 0.4) when the mismatch in thermal expansion coefficient with the fiber exceeds about 3×10^{-6} C^{-1}.

[‡] The effects of τ and d are relatively small compared with S_o and m.

The ultimate strength of the composite seemingly scales with the values expected using simple bundle statistics modified to take account of stress reduction in the fiber induced by friction at the sliding interfaces. Trends in ultimate strength thereby correlate with fiber strength estimated *in-situ* from fracture mirror determinations. Such measurements establish that fiber degradation can occur upon matrix consolidation in some cases, leading to a diminished ultimate strength. The bundle statistics approach is clearly simplified and neglects many details of fiber interactions, etc. Further analysis that couples micromechanics solutions of fiber cracking with stochastic simulation is needed to provide another level of insight into this phenomenon.

Some of the important interface observations revealed in this study concern both the seeming ability for carbon layers to allow debonding even at thicknesses of only 0.01μm (material C) and the viability of debonding without either a carbon or a boron nitride coating (material D). This latter observation encourages debonding research aimed at using either porous ceramic or refractory metal coatings.

The sliding stress at the debonded interfaces is a parameter of major importance. Yet, there is little understanding of how this parameter relates to the thermochemical and thermomechanical properties of the fiber/matrix interfacial zone. The development of a understanding of frictional sliding is a topic requiring future emphasis.

TABLE I

Nicalon Fiber Reinforced Composite Materials

Designation	Matrix	Thermal Expansion Mismatch $\alpha_f - \alpha_m$ (10^6 C^{-1})	Matrix Toughness Γ_m (Jm^{-2})	Matrix Modulus E_m(GPa)
A	LAS III glass-ceramic (ceramed)	3	20 – 30[a]	85
A´	LAS III glass-ceramic (ceramed, 0/90 laminate)	3	20 – 30[a]	85
B	LAS III glass (as pressed)	0	10 – 15[a]	80
C	Aluminosilicate Glass	1	7 – 9[b]	70
D	Soda Lime Glass	– 5	7 – 9[b]	70
E	Silica	4	7 – 9[b]	70

(a) T. J. Clark and J. S. Reed, Am. Ceram. Soc. Bull. 65 1506–12 (1986).

(b) S. W. Freiman, T. L. Baker and J. B. Wachtman, Jr., NBS Tech. Note No. 1212 (1985).

TABLE II

Measured Composite Mechanical Properties

Material	Saturation Crack Spacing, (µm)	Matrix Cracking Stress, (MPa)	Ultimate Strength (MPa)	Initial Modulus, (GPa)
A	400	290 ± 20	530 ± 18	120
A´	—	145 ± 10	276 ± 12	110
B	120	238 ± 16	557 ± 16	129
C	90	240 ± 20	555 ± 15	138
D	70	< 0	348 ± 30	120
E	—	—	66 ± 20	110

TABLE III

Composite Parameters

Material	Sliding Stress τ (MPa)	Residual Stresses (MPa)	
		p	q
A	2.0	20*	− 50*
B	7.0	0	0
C	9.0	12	− 30
D	12.0	− 70	180

* obtained from Reference 15

TABLE IV

Comparison between measurements and theory

Material	Matrix Cracking Stress, (MPa)		Ultimate Strength, (MPa)	
	Measurements	Theory	Measurements	Theory
A	290 ± 20	270 – 310	530 ± 18	530
A´	145 ± 10	135 – 165*	276 ± 12	265*
B	238 ± 16	240 – 300	557 ± 16	550
C	240 ± 20	300 – 320	555 ± 15	560
D	< 0	–30 to –70	348 ± 30	350

* These values are 1/2 the uniaxial composite values obtained ƒ · composite A because the net volume fracture of fiber f is reduced by a fact

REFERENCES

[1] R. Sambell, A. Briggs, D. C. Phillips and D. H. Bowen, J. Mat. Sci. 7 [6] (1972) 676–681.

[2] K. Prewo and J. J. Brennan, J. Mat. Sci. 15 [2] (1980) 463–468.

[3] R. L. Stewart, K. Chyung, M. P. Taylor and R. F. Cooper, *Fracture Mechanics of Ceramics* (Ed. R. C. Brandt, A. G. Evans, D. P. M. Hasselman and F. F. Lange) Vol. 7, pp. 33–51, Plenum NY (1986).

[4] K. Prewo and J. J. Brennan, J. Mat. Sci. 17 [4] (1982) 1201–1206.

[5] C. A. Anderson, private communication.

[6] J. J. Brennan and K. M. Prewo, J. Mat. Sci. 17[8] 2371–83 (1982).

[7] E. Bischoff, O. Sbaizero, M. Rühle and A. G. Evans, Jnl. Amer. Ceram. Soc., in press.

[8] J. Aveston, G. A. Cooper and A. Kelly, Properties of Fiber Composites, Conference Proceedings of the National Physical Laboratory, IPC Science and Technology Press, Ltd., Surrey, England, 1971.

[9] D. B. Marshall, B. N. Cox and A. G. Evans, Acta Met. 33[11] 2013–21 (1985).

[10] B. Budiansky, J. W. Hutchinson and A. G. Evans, J. Mech. Phys. Solids, 34 (1986) 167–189.

[11] L. N. McCartney, Proc. Roy. Soc., A409 (1987) 329–350.

[12] A. G. Evans, Mater. Sci. Eng., in press.

[13] M. He and J. W. Hutchinson, J. Appl. Mech., in press.

[14] M. D. Thouless and A. G. Evans, Acta Metall. 36 [3] (1988) 517–522.

[15] D. B. Marshall and A. G. Evans, J. Am. Ceram. Soc. 68 (1985) 225.

[16] A. C. Kimber and J. G. Keer, Jnl. Mat. Sci. Let. 1 353–354 (1982).

[17] D. B. Marshall and W. Oliver, J. Am. Ceram. Soc. 70 (1987) 542–548.

[18] T. P. Weihs, C. M. Dick and W. D. Nix, MRS Symposium Proceedings, Vol. 120 (Ed. F. D. Lemkey et al.) 1988, p. 247.
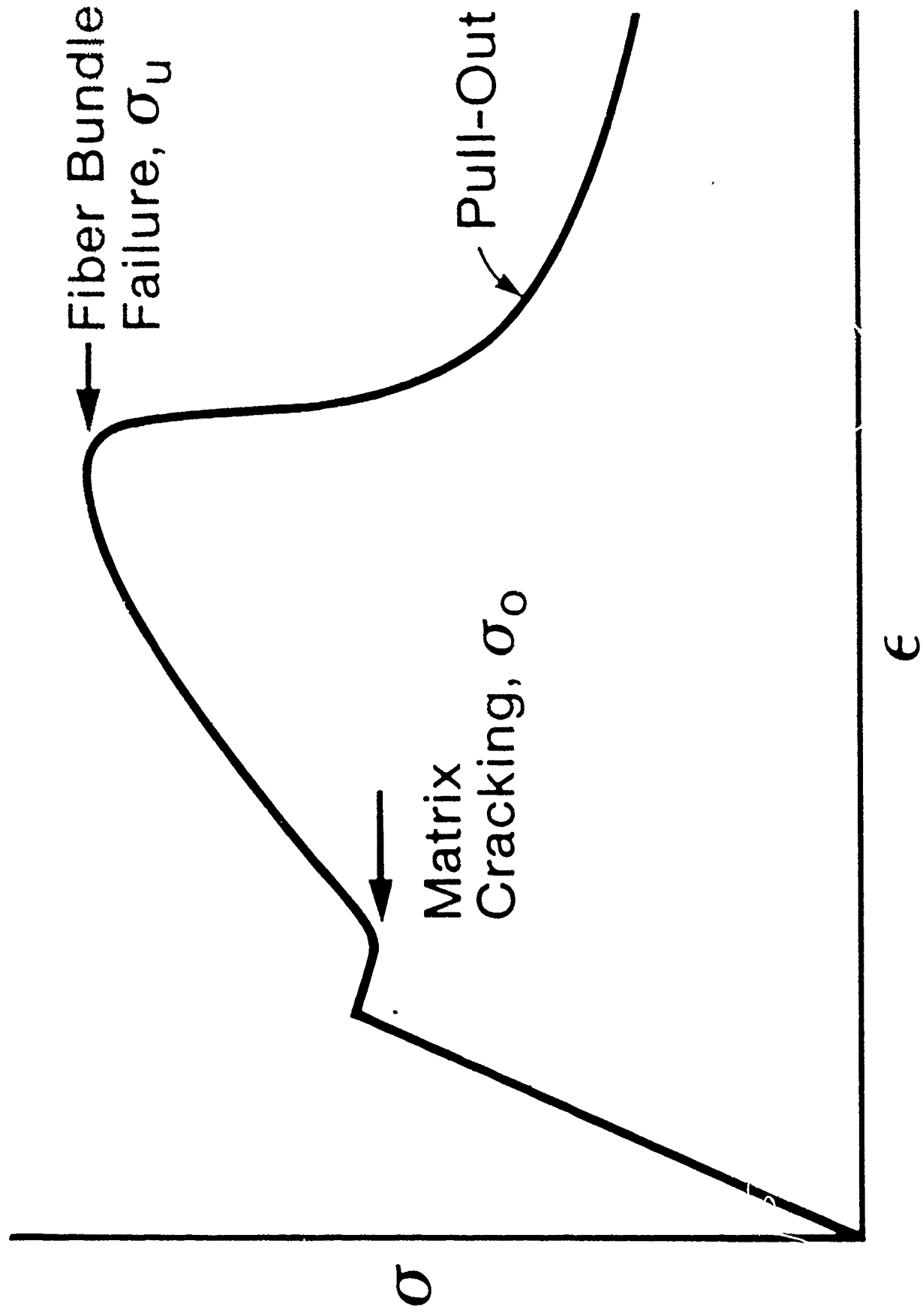
[19]   M. D. Thouless, O. Sbaizero, L. S. Sigl and A. G. Evans, J. Am. Ceram. Soc., in press.

[20]   H. C. Cao and A. G. Evans, Mechanics of Mtls., in press.

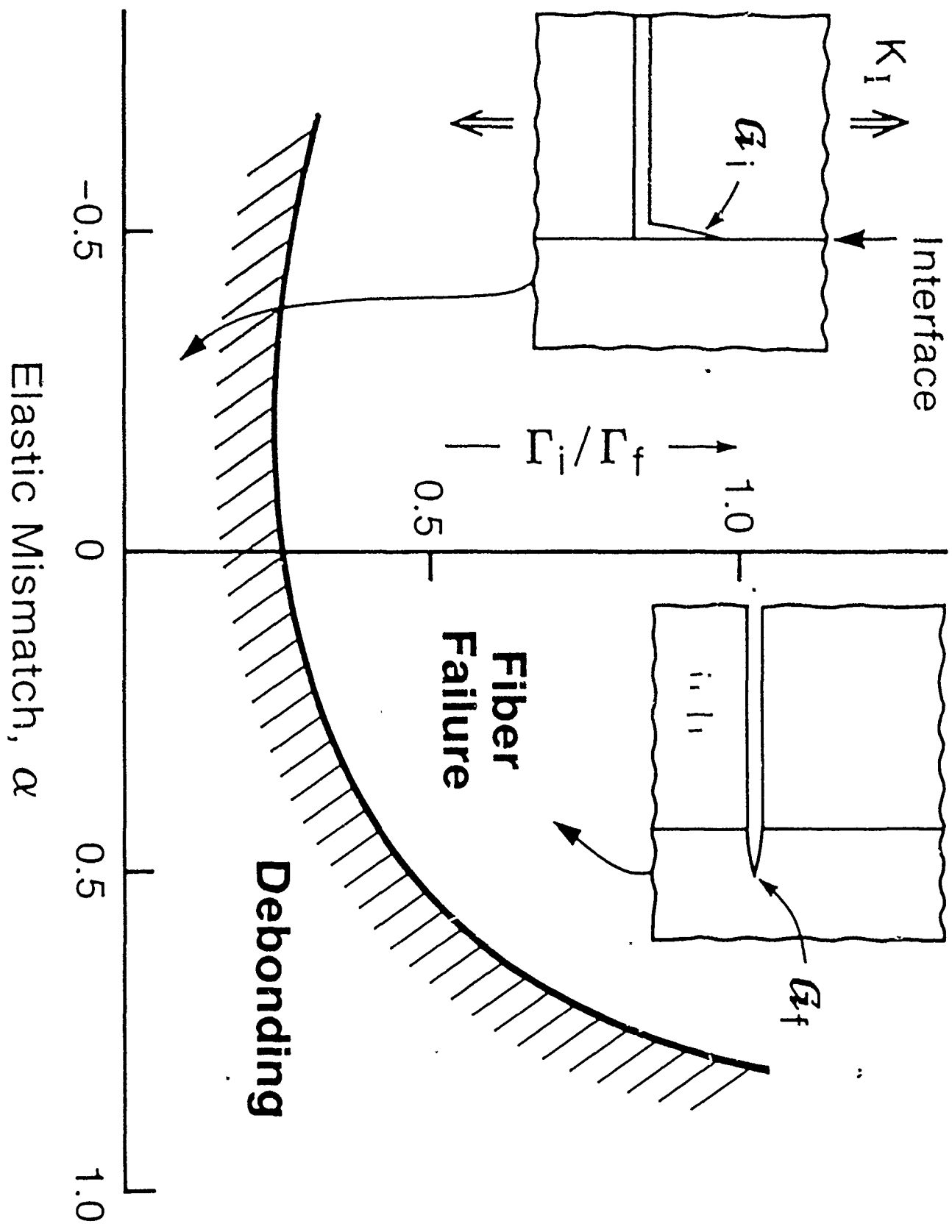[20]   W. Oliver, H. C. Cao and D. B. Marshall, to be published.

FIGURE CAPTIONS
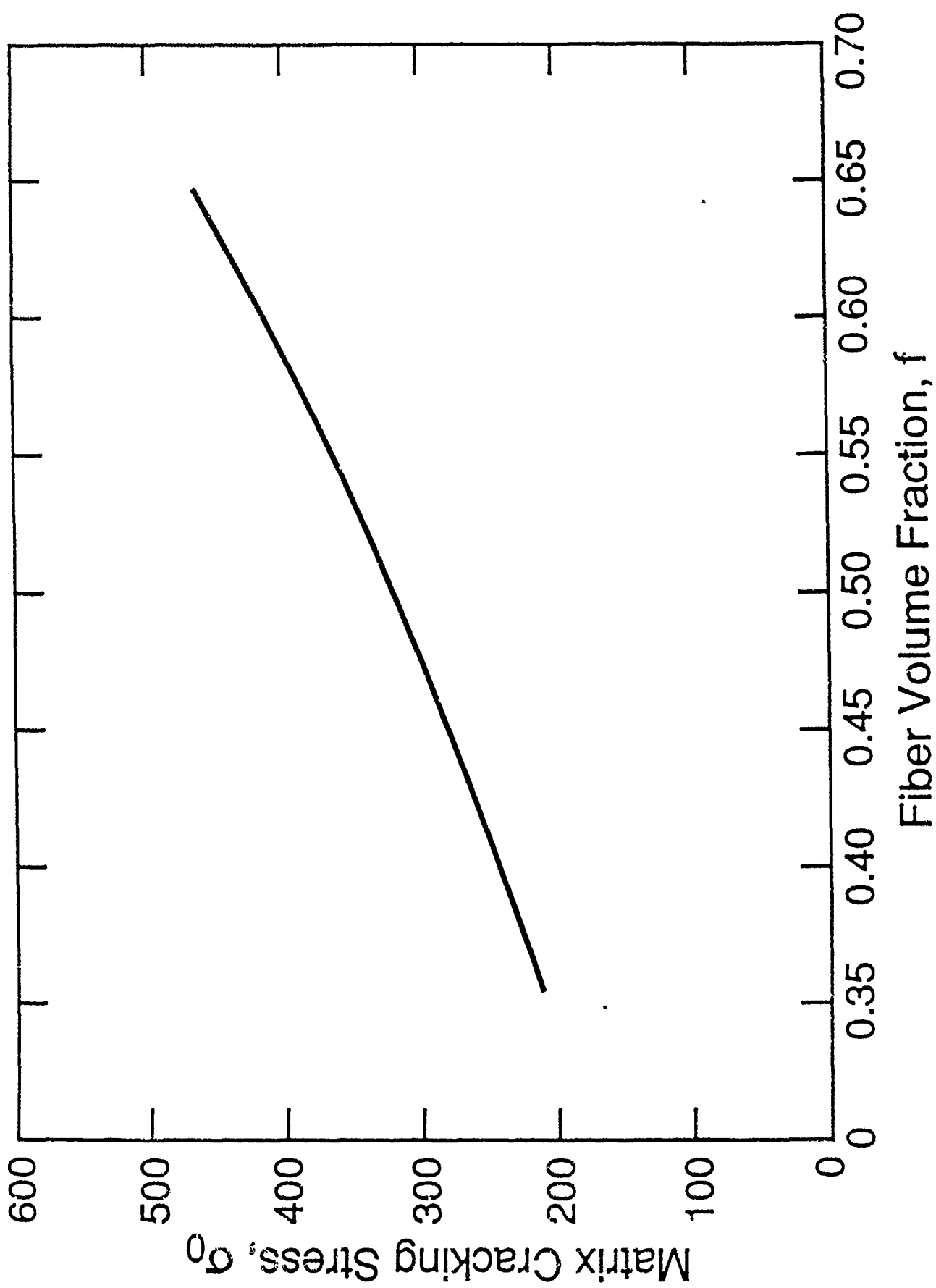
Fig. 1. A tensile stress/strain curve for a "tough" composite

Fig. 2. a) A schematic indicating the roles of interface debonding and sliding in "tough" brittle matrix composites. Debonding along the interface must occur in preference to fiber failure at the crack front. In the crack wake, the matrix tends to close around the fiber and de¹ nding accompanied by frictional sliding occurs.

b) A crack front debond diagram revealing the region of relative interface fracture energy that allows debonding as a function of the elastic mismatch, α.

Fig. 3. The matrix cracking stress as a function of fiber volume fraction computed using Eqn. (4), with properties representative of material C

Fig. 4. a) Tensile stress/strain curves measured for each of the composite materials

b) Magnification of the region near the matrix cracking stress

Fig. 5. Matrix cracks observed in material B

Fig. 6. a) Interactions between matrix and delamination cracks in material C showing the delineation of the matrix cracks

b) A tilted SEM view highlighting the steps between matrix blocks

Fig. 7 Thermal matrix cracks in material D

Fig. 8. Rough surface of fibers revealed on the fracture surface of a tensile specimen of material D. Radial cracking in the matrix is also evident (arrowed), as well as fracture mirrors on the fibers.

Fig. 9. Correlated fiber failure in material D

Fig. 10. A fracture surface observed for material E

Fig. 11. TEM microstructure characterization:
- a) Circumferential debonds in carbon layer in the LAS glass-ceramic matrix material
- b) A carbon layer at the interface, with no debonds in the LAS glass matrix composite

Fig. 12. a) Thin interface layer in aluminosilicate matrix system
- b) Interface debonding associated with matrix cracking

Fig. 13. Very good bond in the silica matrix material, as manifest in the matrix crack which does not debond the interface

Fig. 14. a) Image contrast within interphase layer in the soda-lime glass matrix system, revealing porosity
- b) Debonding within the porous interphase layer

Fig. 15. Distribution function for Nicalon fiber fracture stress measured from mirror sizes on fibers for material C ($S^* = 2.47$GPa, $\omega = 2.1$) and material D ($S^* = 1.38$GPa, $\omega = 3.1$)

Fiber Bundle Failure, σ_u

Pull-Out

Matrix Cracking, σ_o

σ

ϵ

100 μ

A

100μm

B

20μm
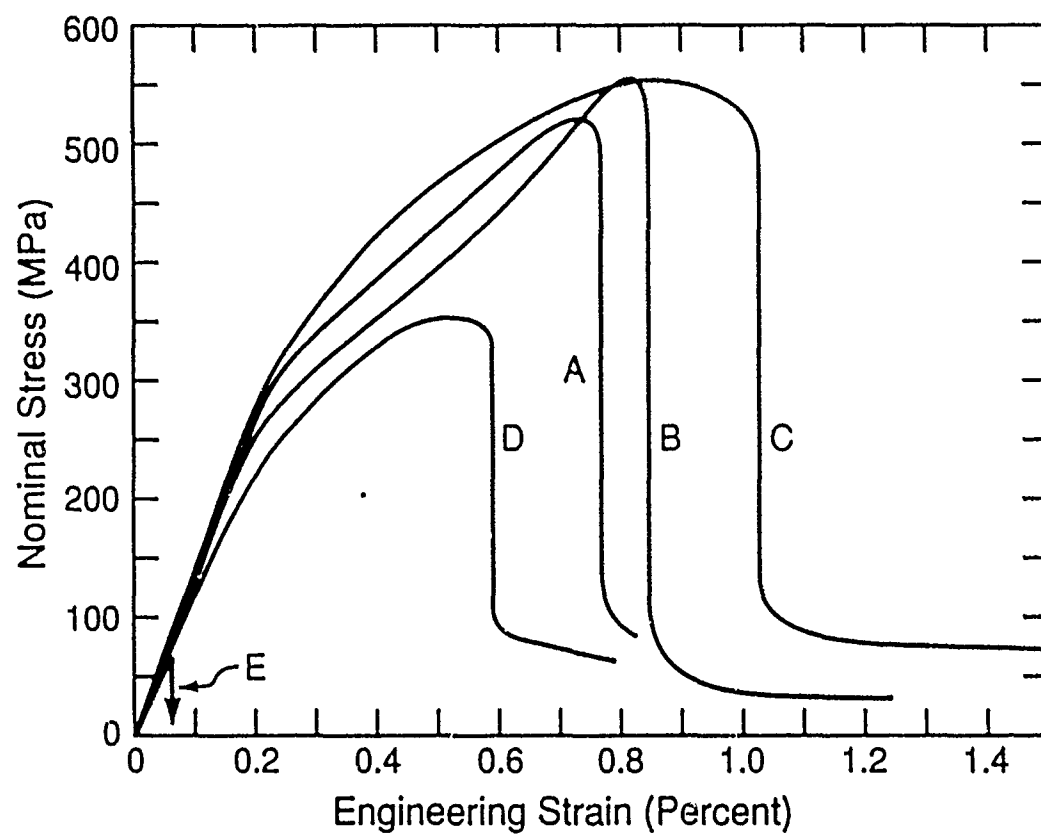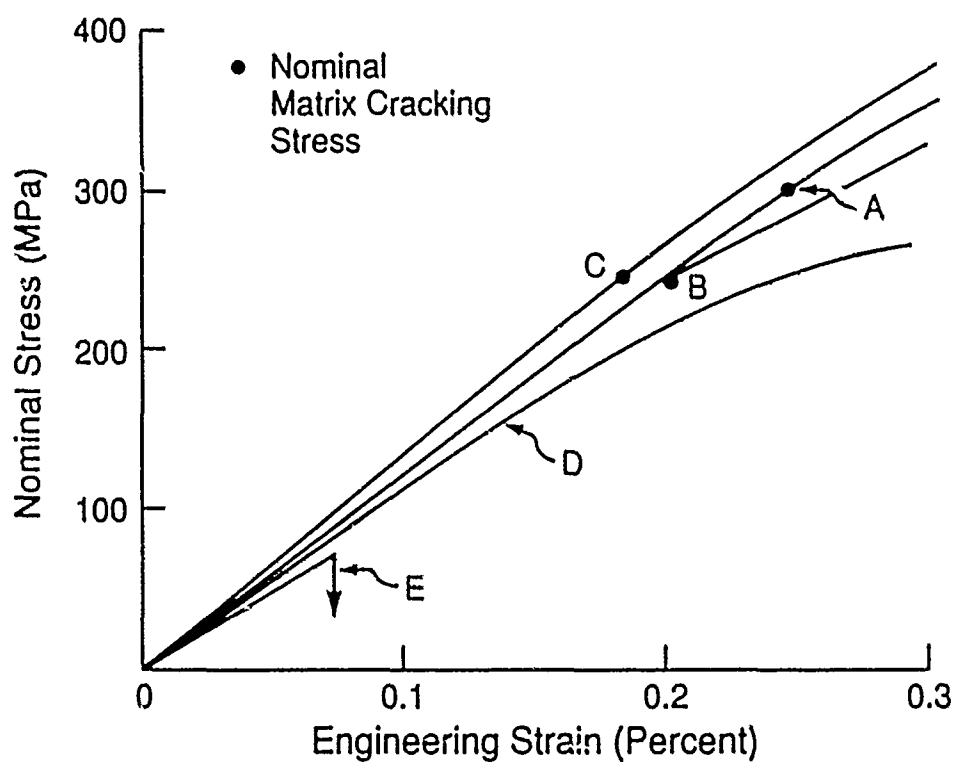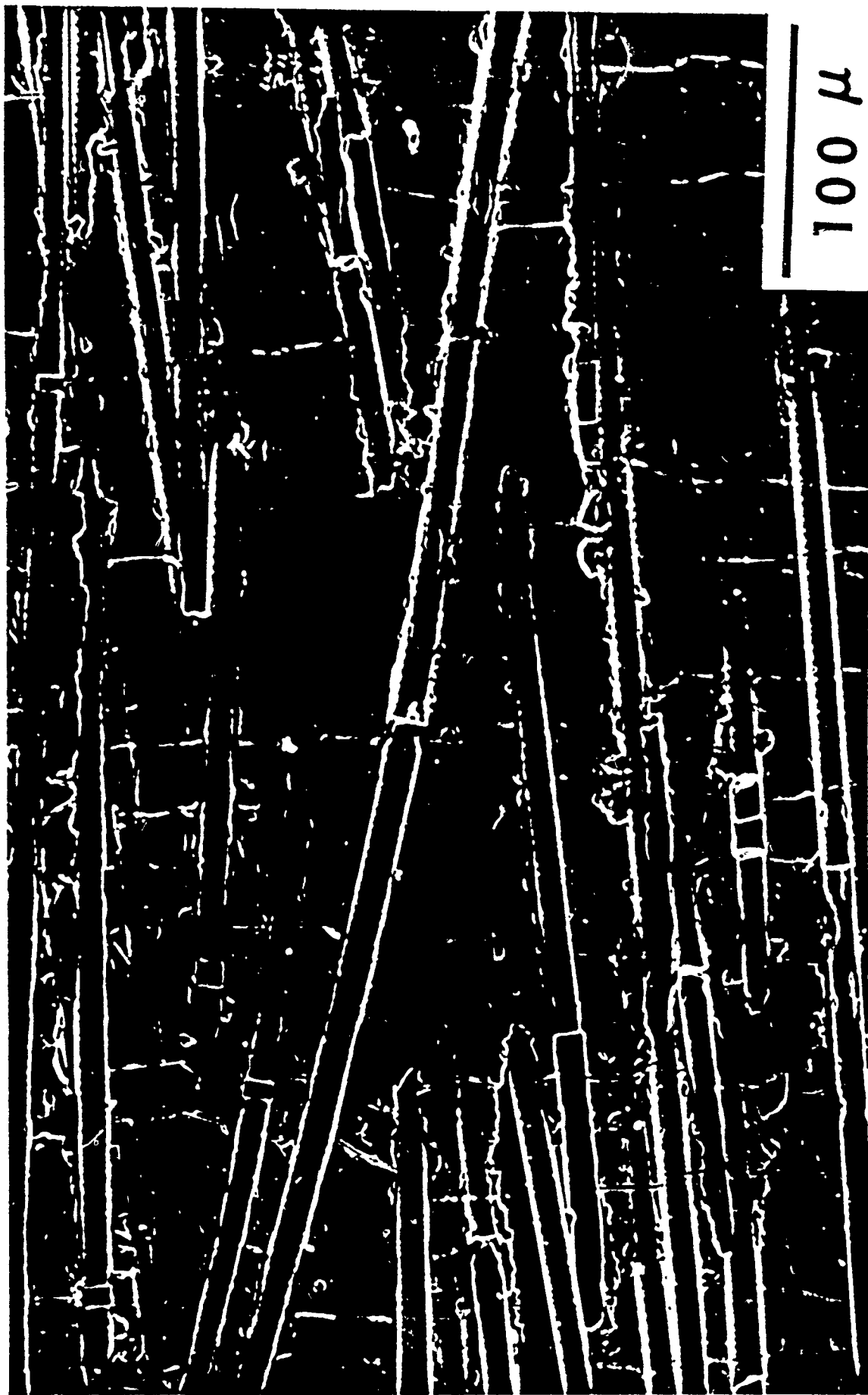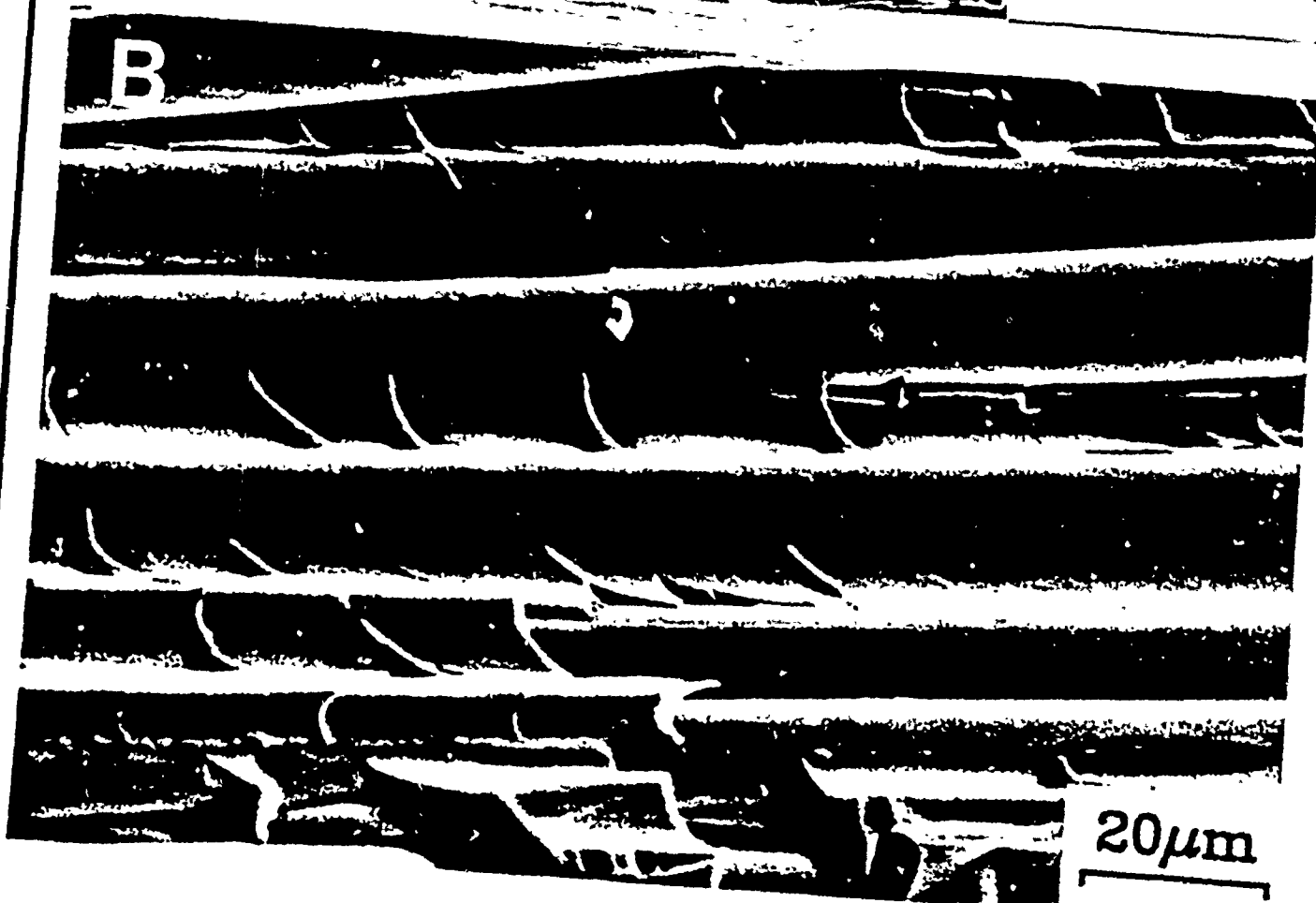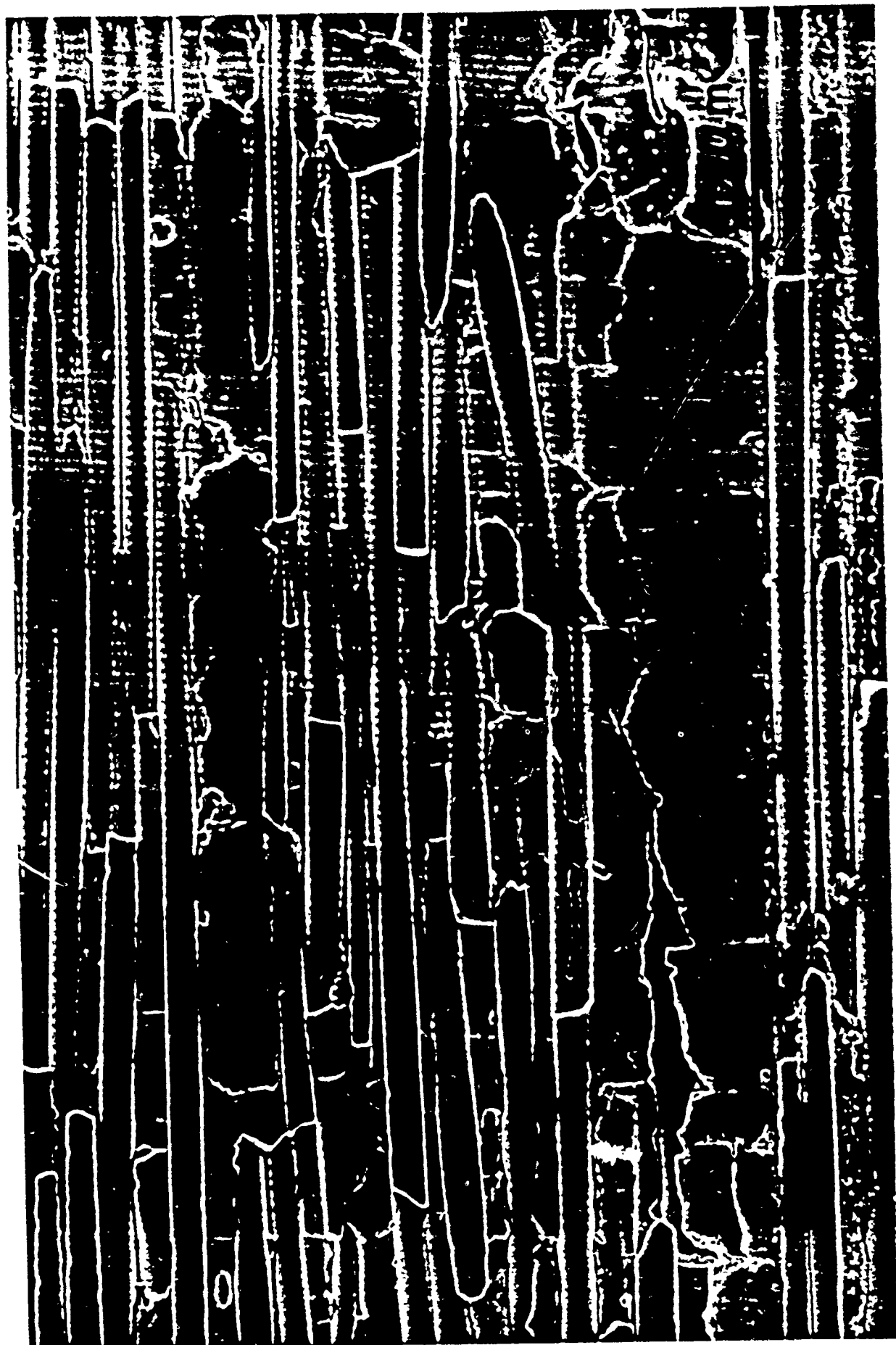
Fracture Mirror

Axial Crack

10μm
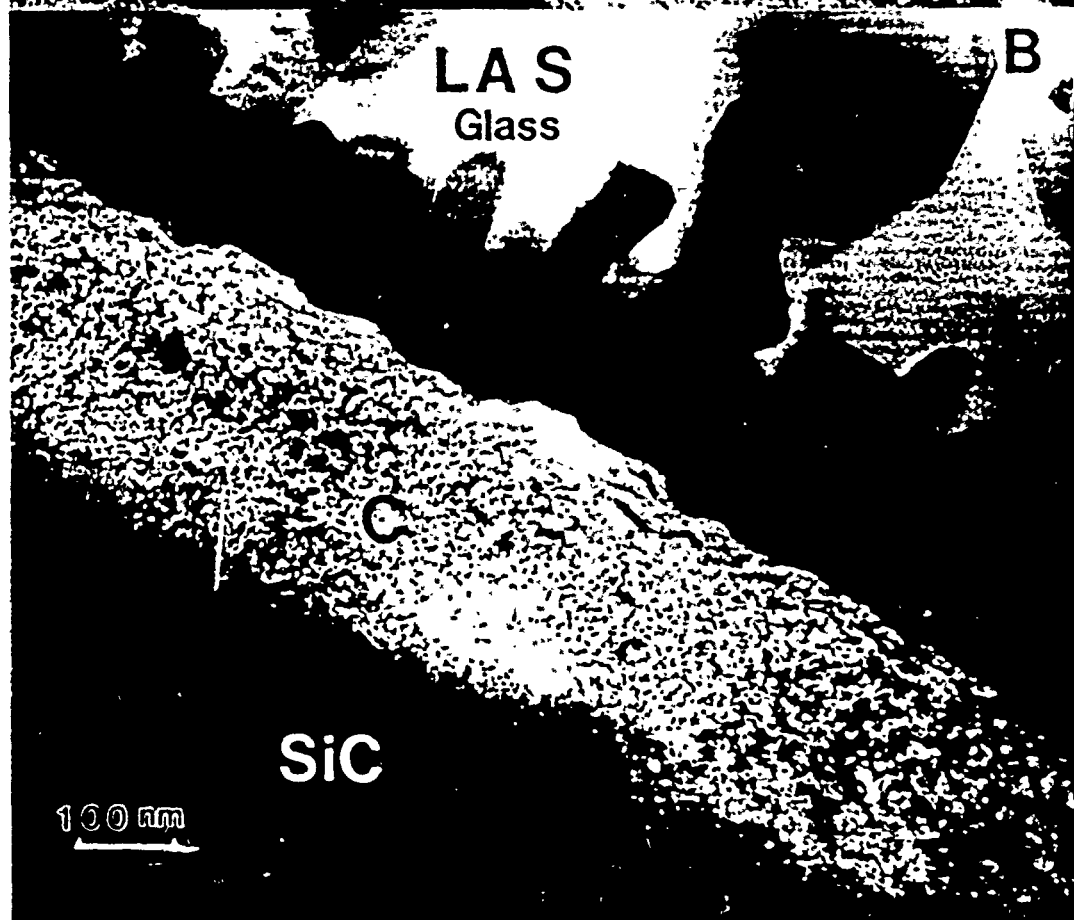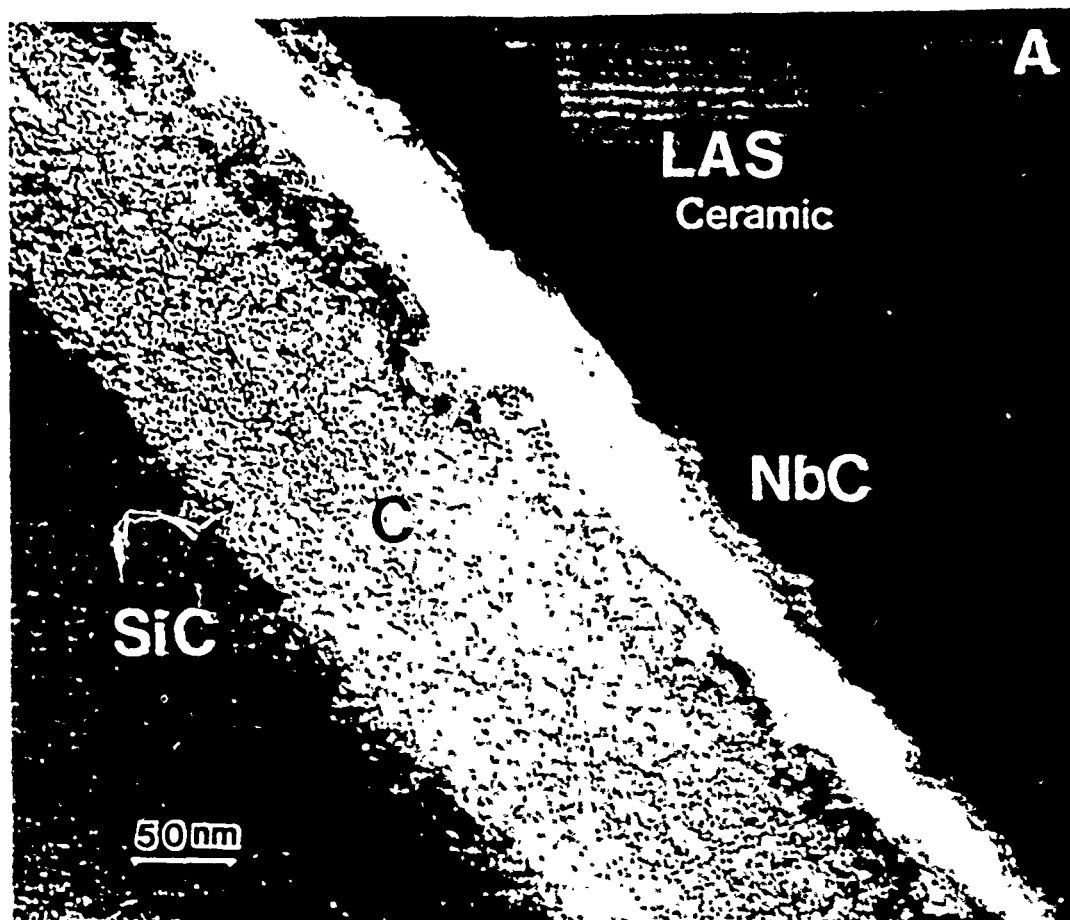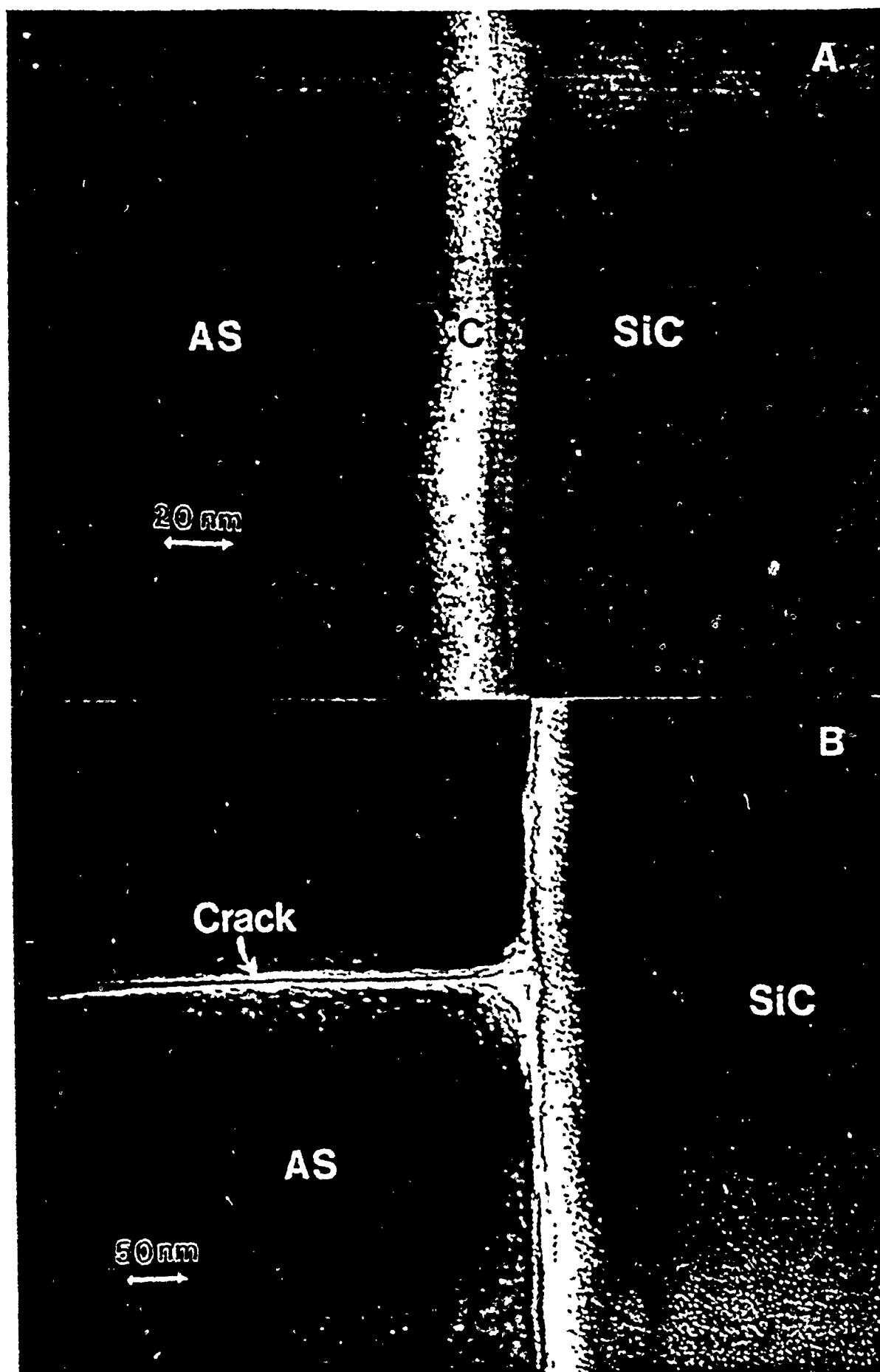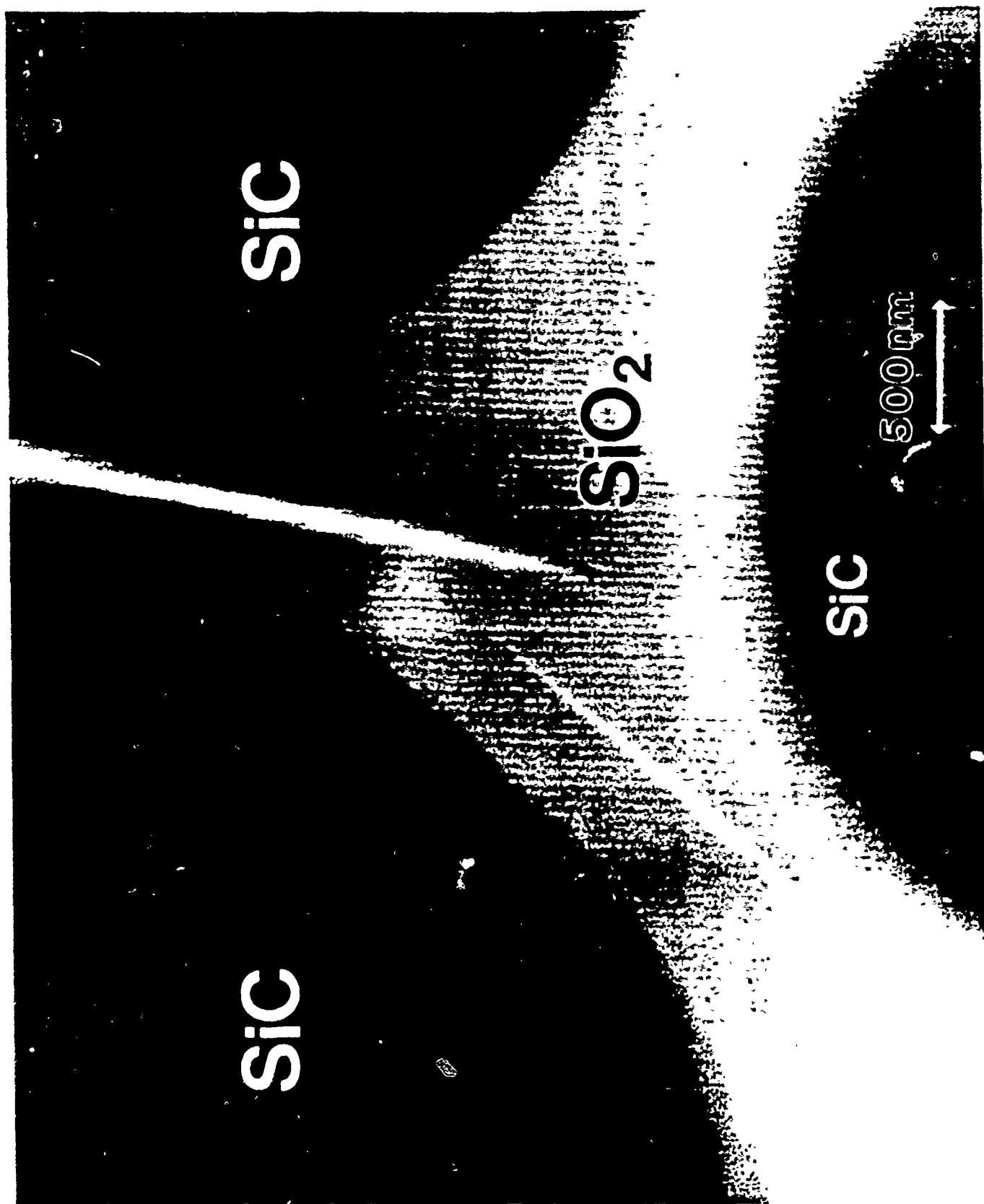
10μm

A

LAS
Ceramic

NbC

C

SiC

50 nm

B

LA S
Glass

C

SiC

100 nm

A

AS   C   SiC

20 nm

B

Crack

SiC

AS

50nm

THE FRICTIONAL RESISTANCE

TO SLIDING OF A SiC FIBER

IN A BRITTLE MATRIX

T. P. Weihs, C. M. Dick and W. D. Nix

Department of Materials Science and Engineering
Stanford University
Stanford, California 94305

THE FRICTIONAL RESISTANCE TO SLIDING OF A SiC FIBER IN A BRITTLE MATIX

T. P. WEIHS, C. M. DICK and W. D. NIX
Dept. of Materials Science and Engineering, Stanford University, Stanford, Ca 94305
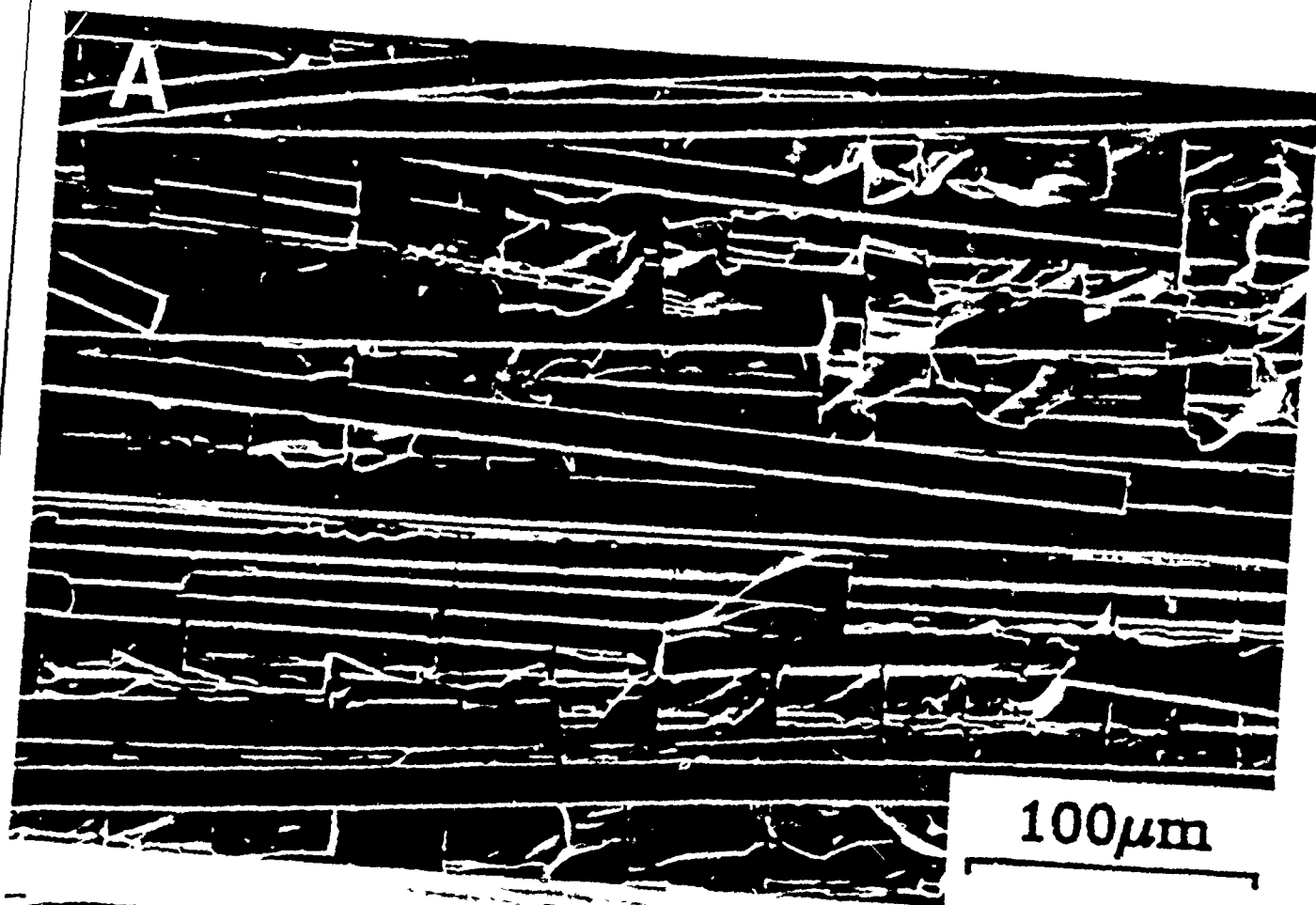
ABSTRACT

The frictional resistance to sliding of a SiC fiber in a brittle, ceramic matrix has been measured with two different experimental techniques. Both techniques utilize a load-controlled indentation instrument. In the first technique, the ends of individual fibers are displaced down into the matrix. The frictional resistance to sliding, τ, was calculated using the elastic model of Marshall and Oliver and the load-displacement data. Alternatively, fibers have been displaced along their complete lengths through thin sections of the matrix. The critical force for complete slip and the sample geometry determined τ for a given fiber. For this technique slip over the complete length of a fiber was verified by the protrusion of that fiber from the bottom of the sample. By inverting the sample and loading the protruding fiber, the frictional resistance to reverse sliding was also measured. The results obtained from the two complementary techniques are in general agreement.

INTRODUCTION

A major goal in the design of ceramic based fiber composites has been to optimize the toughening achieved by fiber pull-out during crack propagation. This toughening is directly related to the frictional work associated with fiber pull-out[1-3]. Therefore, it depends strongly on how easily a fiber can slide in a brittle matrix. If the frictional resistance to sliding is too high, the fibers will fracture in unison with the matrix as a crack passes. In this case no pull-out will occur. If the friction is too low, little work is required to pull the fibers out of their matrix and minimal toughening is achieved. Consequently, characterization of the frictional stresses at the interfaces between fibers and matrix is necessary to understand and to optimize the toughening of these systems. In an attempt to characterize the frictional stresses for a model system, experiments have 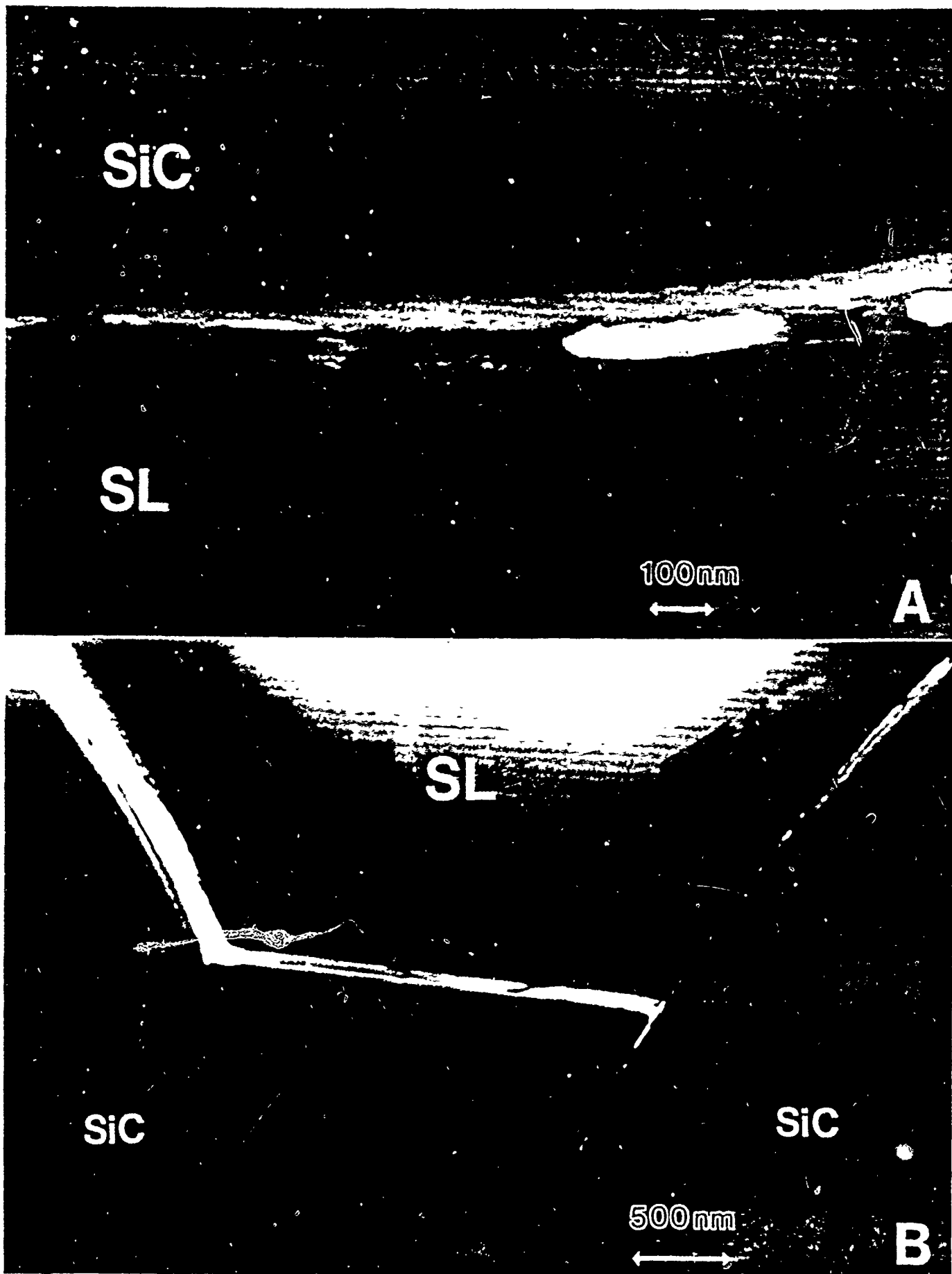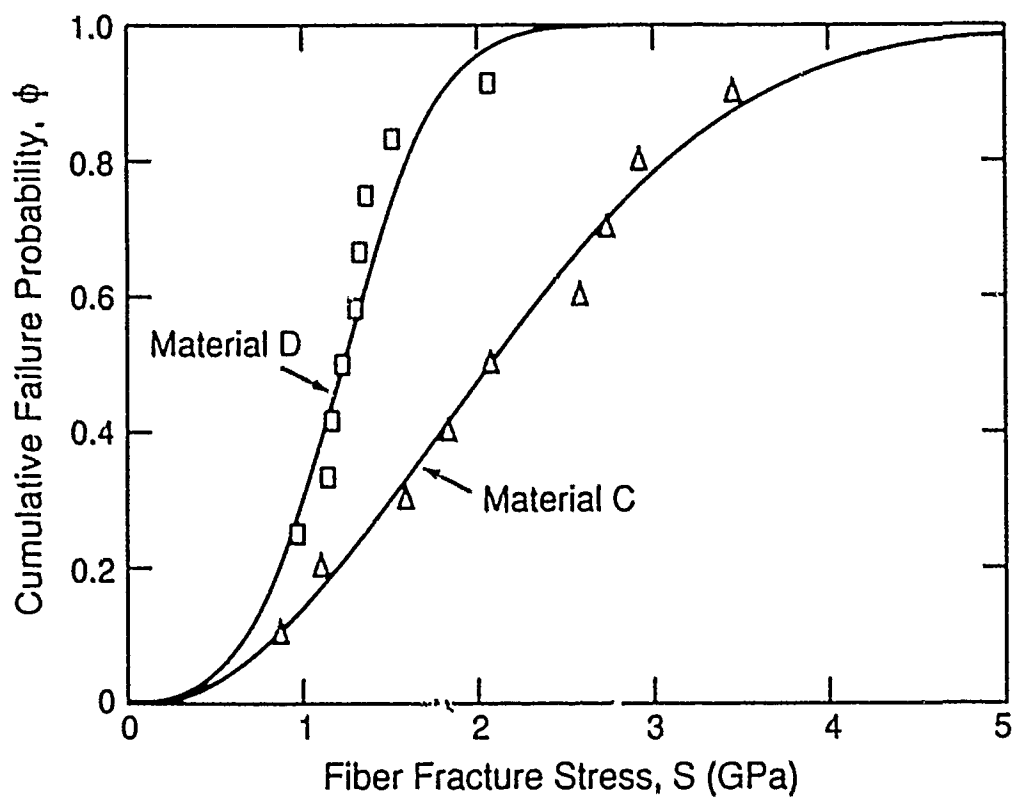been performed using two different experimental techniques[4-5] The frictional resistances to sliding of a SiC fiber in a brittle matrix obtained by these two techniques are presented, and both the testing techniques and the results are compared.

THEORY

The frictional resistance to sliding of a stiff fiber in a brittle matrix can be measured using two different but complementary methods. Consider a fiber loaded as shown in Figure 1. Given sufficient force and a sufficiently weak interface, part of the fiber will debond from the matrix and slide relative to the matrix as it is compressed. Marshall and Oliver (M&O)[4] have demonstrated that the sliding length, L, is determined by the frictional resistance to slip, τ, the applied force, F, and the fiber radius, R (Figure 1). If the interface is homogeneous and the frictional resistance is constant along the interface, the debond (or slip) length should increase linearly with the applied force according to

$$L = F/2\pi R\tau \qquad (1)$$

As the load on the fiber is increased, the fiber will continue to debond and to compress elastically. M&O have also shown that by modeling the compression of the fiber, and by measuring the load on the fiber and the displacement of the top of the fiber, one can determine the frictional resistance, τ.

An alternative experimental technique has been reported recently by Weihs and Nix[5]. They have shown that if the sample in Figure 1 is thin enough, a fiber can be forced to slide along its entire length. Such a technique yields a more direct measurement of τ. For a sample of

thickness t, the critical force, F_c, for complete slip is given by

$$F_c = 2\pi R t \tau \qquad (2)$$

If a load-controlled instrument (such as a Nanoindenter [6,7]), applies the critical force, F_c, to a fiber, it will continue to slide until the indenter contacts the matrix surrounding the fiber. The length of slip is determined by the shape of the indenter and the radius of the fiber. For a blunt indenter, like the one used here, a typical fiber will slide 1 to 2 microns. Such a protrusion of the fiber from the bottom of the sample can be seen easily to verify slip along the complete length of the fiber. An additional benefit to the critical force technique is achieved by inverting a sample and loading a protruding fiber: the frictional resistance to reverse sliding can be measured.

PROCEDURE

The model composite tested consisted of SiC fibers (Nicalon) in a lithium-alumino-silicate ceramic matrix, SiC/LAS III.* The composite was hot-pressed at 1250°C and then heated (cerammed) in Argon at 1135°C to crystallize the matrix. The SiC fibers tested varied in diameter from 9 to 24 µm while the average diameter was 15.4 µm.

To prepare samples for testing, thin rectangular sections (5.0 x 3.0 mm with thickness ranging from 0.3 to 0.7 mm) were cut from a larger rectangular bar. The samples were cut so that one half of the fibers were perpendicular to the face of the sample and one half were parallel to it. Next, both faces of the samples were polished to a 0.25 µm finish with diamond paste. However, for the thinnest sample (0.3 mm prior to polishing), fibers were found to protrude up to 0.05 mm from one face of the sample after it was cut from the rectangular bar. The formation of these protrusions could not be avoided during the cutting procedure. Subsequent polishing of the rough face of the thinnest sample forced protruding fibers to slide down into the matrix and out the back side of the sample. The significance of such sliding prior to testing will be discussed later. One point to note here is that the protrusion of the fibers from the bottom of the thinnest sample prevented the study of reverse sliding in this specimen. When the sample was inverted after an initial test, the fibers that had slipped could not be distinguished from the other fibers since all fibers were protruding from the bottom of the sample.

The thicknesses of the two samples tested (to be labeled 1 and 2) were measured after polishing to be 0.696 mm and 0.128 mm, respectively. Once measured, the thick sample was mounted on two closely spaced glass plates to form a simple beam. For the thinner, more fragile sample, washers were bonded to the top and bottom of the faces of the sample to reduce the chance of cracking during handling and testing.

Using a Nanoindenter[6,7], a load-controlled indentation instrument, the ends of fibers were displaced into the matrix as shown schematically in Figure 1. The loading rate was controlled to displace the indenter tip at a constant velocity between 3 and 6 nm/sec. Once a force of 120 mN was applied to the fiber (the maximum loading capability of the instrument), the load was removed at a constant rate. During each test the force applied by the Nanoindenter and the displacement of the indenter tip were continuously recorded. In the case of the thicker sample, the specimen was inverted in order to load protruding fibers in the reverse direction. All tests were performed at room temperature.

To determine the displacement of the fiber, the penetration of the indenter tip into the fiber, u_f, had to be subtracted from the total displacement of the indenter tip. (Figure 1). Following the procedure used by M&O[4], a separate sample was annealed in air at 1000°C for 2 hrs. This heat treatment permitted strong bonds to form at the fiber/matrix interface that prevented the displacement of fibers upon testing. The lack of displacement was verified by SEM analysis and by cyclic loading of the fibers. The load-depth curve for an indentation into a SiC fiber is presented in Figure 2. An equation fitted to the curve in Figure 2 was used to determine the average indentation depth into a SiC fiber for any applied load. The indentation depth was then subtracted from the total displacement to obtain the fiber displacement in the

---

* United Technologies Research Center, East Hartford, Ct.

above experiments.

RESULTS

Figure 3 presents a plot of the square of the force versus fiber displacement (F^2 vs u) for a fiber in Sample 1. Based on the elastic analysis presented by M&O [4], if the frictional stress is
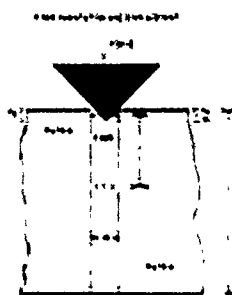
Fig. 1. Schematic of Test Configuration
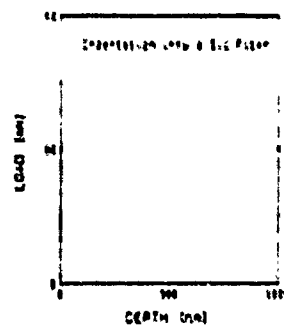
Fig. 2. Load/Depth Curve for an Indentation into a SiC Fiber
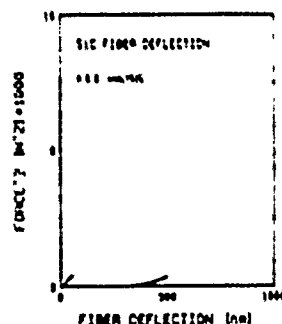
Fig. 3. Load Squared/Displacement Curve for a Fiber in Sample 1.
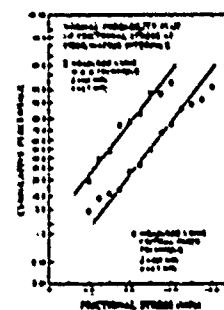
Fig. 4. Normal Probability Plot of Frictional Resistance to Sliding

constant along the fiber/matrix interface and if the interface is homogeneous, then the loading part of the curve should be linear and its slope should determine τ for that fiber. Results similar to the one in Figure 3 were obtained for 30 other fibers in Sample 1. These tests were used to determine the distribution of the values of τ based on the M&O technique. In determining this distribution, the results from tests on fibers in Sample 2 were not considered because they showed unusually low (< 1.0 MPa) values of τ compared to the other sample and to previous results [4]. The unreasonably low values are partially attributed to the large compliance of the

thin sample. Based on simple elastic beam and circular plate[8,9] theory, Sample 2 could be expected to deflect by amounts which are smaller than, but similar in magnitude, to the deflections of the individual fibers being tested. Since deflections of the whole sample are not considered in the analysis of the load-deflection data, this large compliance could significantly lower the slope of the loading curves (Figure 3) and thereby lower the calculated values of τ as seen. Consequently, the M&O analysis has been applied only to tests on the thicker sample which is expected to have only negligible bending deflections.

The results from a M&O analysis of the tests from Sample 1 are plotted on normal probability paper in Figure 4. This particular type of plot was used to present the data for three different reasons. First, it allows one to qualitatively judge whether or not the quantity of interest, namely τ, is normally distributed[10,11]. A normal distribution is characterized by a linear spread of data between 16 and 84 cumulative percent. The plotted points below and above these percentages typically show more deviation as the number of data points in these regions is small. Secondly, given a normal distribution, which is expected for the frictional resistance[10], the mean and standard deviation of the quantity can be graphically determined[10,11]. The mean is given by the intersection of the 50% horizontal line and the line fitted to the data between 16 and 84 cumulative percent. Similarly, the standard deviation is given by the difference between the mean and the quantity given by the intersection of the 16% horizontal line and the fitted line. Lastly, a normal probability plot provides an informative means for graphically comparing the results obtained by the two techniques.

With regard to the data from the M&O analysis (Figure 4), the values of τ fall close to the fitted line within the percentages of 16 and 84. This linear behavior suggests that the frictional stress follows a normal distribution. As mentioned earlier, such behavior is expected since the frictional stresses are thought to be determined by the additive effects of random events[10]. The small deviations from linearity at high percentages are often seen in normal distributions and do not contradict the linearity of the bulk of the data. The fitted curve in Figure 4 gives a value of 6.0 MPa for the mean and a standard deviation of 2.7 MPa.

Figure 5(a) presents the displacement of a fiber that was reported earlier[5]. (This fiber, called Fiber A, was from Sample 1.) During the initial loading, Fiber A was steadily compressed into the matrix. However, once the critical load was reached, the fiber moved rapidly through the matrix at a velocity greater than 2-4 µm/sec and protruded from the bottom of the sample. During the reverse loading, Fiber A showed similar behavior and slipped at about the same critical force
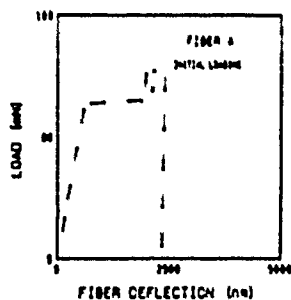

Fig. 5(a). Load/Displacement Curve for the Initial Loading of Fiber A
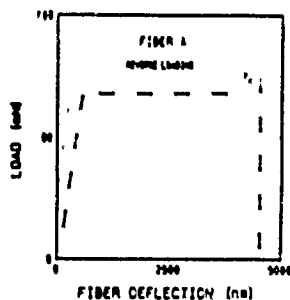
Fig. 5(b). Load/Displacement Curve for the Reverse Loading of Fiber A

Fig. 6. SEM Micrograph of SiC Fiber A (rad = 11 μm) Protruding from the Sample
after Reverse Loading

as for the initial loading (Figure 5(a) & (b)). An SEM micrograph of Fiber A protruding from
the matix after a reverse loading is presented in Figure 6. One can notice that an indentation from
the initial loading marks the top face of the fiber. Results similar to those for Fiber A were
obtained for 2 of the other 30 fibers tested in Sample 1 and 44 of the 45 fibers tested in Sample 2.

To analyze the distribution of the frictional stresses based on the critical force technique,
only the results from tests on Sample 2 were utilized. For this specimen almost all of the fibers
(44 of 45) were able to slide at loads less than the maximum load of 120 mN. Thus, the
sampling of fibers is not biased towards those fibers with small frictional stresses. (Such a bias
is present for the critical force results from the thicker sample in which approximately 10% of the
fibers slid over their complete length.) The results from Sample 2 are presented in Figure 4
along with those from the M&O analysis. Considering the cumulative percentage range between
16 and 84, the deviations from the fitted line are small. Thus, the critical force data also appears
to follow a normal distribution of τ. However, the calculated mean value is higher than for the
M&O analysis. Following the procedure outlined earlier, the mean and standard deviation of the
frictional stress were determined to be 10.0 MPa and 2.7 MPa, respectively.

DISCUSSION

The two techniques presented here yield similar distributions of the frictional resistance to
sliding of a SiC fiber in a brittle matrix. Both distributions are normal distributions and the
standard deviations are small and equal. However, the mean values are different. To determine
which technique may offer the more accurate mean value of τ, the three fibers which slid over
their complete lengths in Sample 1 should be considered. The frictional stresses for these three
fibers were reported to be 2.27, 3.09, and 2.79 MPa using the critical force technique[5]. (The
M&O analysis for the same tests yielded similar results.) This indicates that at least 10% of the
31 fibers tested in Sample 1 had frictional stresses less than 3.1 MPa. Such a cumulative
percentage agrees with the normal distribution plot in Figure 6 for the M&O analysis, but it does
not agree with the data obtained by the critical force technique. Measurements using the latter
technique suggest that less than 1.0% of the fibers should have frictional stresses under 3.1 MPa.
This disparity implies that the data obtained from Sample 2 using the critical force technique may
be in error.

To examine reasons why τ may be over estimated by the critical force technique, several questions should be addressed. First, does the sliding of the fibers during the preparation of Sample 2 distort the values of τ that are measured? From an earlier work [5] the answer appears to be no for two reasons. First, since the resistance for reverse sliding was equal to that for forward sliding [5], the sliding of the fibers during polishing of the sample should not reduce the friction at the interface. Secondly, although the sliding of the fibers during polishing may induce residual stresses at the fiber/matrix interface, these stresses will be removed by the sliding of the fiber which occurs before F_c is reached.

The second question to be addressed concerns the bending of the sample during the loading of individual fibers. As also reported earlier [5], such bending is negligible for Sample 1. However, for Sample 2, which is approximately 5 times thinner than Sample 1, bending can be significant. Two detrimental effects are produced by this bending. First, a M&O analysis of the data produces unusually low values of τ because the analysis does not account for the additional deflections. (This effect has already been described.) Secondly, stresses in the sample that result from the bending may impede the sliding of fibers and thereby raise the value of τ measured by the critical force technique. Using elastic theory for a circular plate [9], the maximum radial stresses could be as high as 3.0 MPa for a 120 mN load. In future work, this effect will be reduced by minimizing the support length for the sample.

CONCLUSION

The frictional resistance to sliding of a SiC fiber in a brittle, ceramic matrix has been measured using two different experimental techniques. Both techniques yield normal distributions of the frictional stress with similar standard deviations. However, the technique developed by Marshall and Oliver yields a mean value of τ which is 39% smaller than the value of τ measured directly using the critical force technique developed by Weihs and Nix. Although the reason for the difference in mean values is still unclear, the present data suggests that the elastic bending stresses in the thin sample may account for the higher frictional stresses measured using the latter technique.

ACKNOWLEGEMENTS

REFERENCES

1) D. C. Phillips, J. Mat. Sci., 9, 1847, (1974).
2) K. M. Prewo and J. J. Brennan, J. Mat. Sci., 15, 463, (1980).
3) D. B. Marshall and A. G. Evans, J. Am. Cer. Soc., 68, 225, (1985).
4) D. B. Marshall and W. C. Oliver, J. Am. Cer. Soc., 70, 542, (1987).
5) T.P. Weihs and W.D. Nix, Scripta Met., 22, 271, (1988).
6) M. F. Doerner and W. D. Nix, J. Mat. Res., 1, 601, (1986).
7) W. C. Oliver, R. Hutchings, and J. B. Pethica, "Measurements of Hardness at Indentation Depths as Low as 20 Nanometers," in Microindentation Techniques in Materials Science and Engineering, Ed. P. J. Blau and B. R. Lawn (ASTM, STP 889, 1985).
8) S.P. Timoshenko and J.H. Goodier, Theory of Elasticity, (McGraw-Hill, San Francisco, 1970), pp. 385-8.
9) A.C. Ugural, Stresses in Plates and Shells, (McGraw-Hill, San Francisco, 1981), pp. 37-8.
10) L. Blank, Statistical Procedures for Engineering, Management, and Science, (McGraw-Hill, San Francisco, 1980), pp. 428-35.
11) L. Sachs, Applied Statistics - A Handbook of Techniques, (Springer-Verlag, N.Y., 1984), pp. 107-8.

MATERIALS
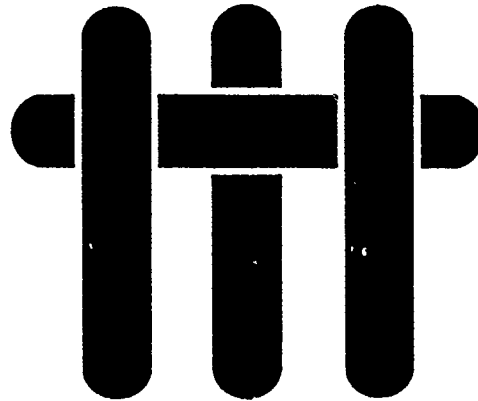
TENSILE TESTS OF CERAMIC-MATRIX

COMPOSITES: THEORY AND EXPERIMENT

H. C. Cao

Materials Department
College of Engineering
University of California, Santa Barbara
Santa Barbara, California 93106

and

M. D. Thouless

IBM Research Division
T. J. Watson Research Center
Yorktown Heights, NY 10598

ABSTRACT

A model describing the salient features of tensile stress/strain curves of ceramic fiber composites has been developed. The model incorporates statistics of fiber failure. Furthermore, the compliance of the testing machine is included so that the onset of instability can be predicted. An experiment conducted on a composite consisting of a glass ceramic matrix reinforced with SiC fiber exhibits excellent agreement with the predicted behavior.

1. INTRODUCTION

The mechanical properties of a brittle material can be dramatically improved by the incorporation of aligned fibers. Under optimum conditions, these composite materials exhibit a substantial degree of non-linear deformation[1-6]. This is a very important feature, since it gives some tolerance against catastrophic failure by the propagation of a dominant flaw.

A schematic illustration of the stress/strain curve for this type of material illustrates three regions of interest[1]: (i) initial linear-elastic behavior, (ii) non-linear deformation and (iii) final failure involving a decreasing load-bearing capacity. The initial elastic deformation occurs with an effective modulus of [1]

$$E_c = f \ E_f \ (\eta + 1)/\eta \tag{1}$$

where f is the volume fraction of fibers in the matrix, and η is defined as

$$\eta = f \ E_f \ /[(1 - f)E_m] \tag{1a}$$

where E_f and E_m are the moduli of the fibers and matrix respectively. The nonlinear deformation begins when the applied load reaches a critical value required to propagate the largest pre-existing flaw across the specimen[1,4,8]. A further increase in the load causes progressively smaller flaws to propagate until, ultimately, the density of matrix cracks is bounded by a saturation value (Fig. 2). The average spacing of the matrix cracks at this point has been calculated to be [9],

$$\ell = 1.337 \left[\frac{(1 - \eta)R\sigma_0}{2\tau f} \right] \tag{3}$$

where σ_0 is the nominal stress in the composite when matrix cracking first appears, R is the fiber radius and τ is the shear resistance of the fiber/matrix interface. An increasing load also leads to consecutive fiber failure at preexisting defects, which are statistically distributed. The load bearing capacity of the composite therefore

reaches a maximum value, and then decreases as progressively fewer fibers are left intact to support the load.

The matrix-cracking stress is an important parameter for engineering design[6-8]. However, the most attractive feature of these composites, in comparison to traditional monolithic ceramics, is their tolerance to damage. It is of interest, therefore, to understand the mechanics at strains in excess of that required to initiate matrix cracking. It is the intent of this communication to model this behavior and in particular, to include the details required to make comparisons with experimental observations. Therefore, the compliance of the testing machine is included in the analysis because it plays an important role in determining the observed load-displacement characteristics. To the author's knowledge this compliance has not previously been included in any analysis or interpretation of the experimental data, obtained for these composites. One result that will be emphasized is the maximum compliance for the testing machine to avoid an instability in the load-displacement trace.

2. Calculation of Stress-Strain and Load-Displacement Curves

2.1 Statistical analysis of fiber bundle failure

A number of simplifying assumptions are made in the analysis that follows. It is assumed that the saturation density of matrix cracks is developed when the applied stress reaches σ_0, and that the distance between the cracks is sufficiently small to enable the stress distribution to be described as that shown schematically in Fig. 3a. Furthermore, it is assumed that once a fiber has broken anywhere within the gauge length of the specimen it is no longer capable of carrying a load. The first assumption is most restrictive when one attempts to describe the behavior at low extensions, near the point at which matrix cracking first occurs. Under these conditions, the stress in the unbroken fibers may have a distribution as shown in

Fig. 3b, and a break in a fiber may be undetectable if it occurs well away from the plane of the matrix crack. The second assumption leads to significant errors as the load-bearing capacity of the composite drops to zero. It is recognized that interaction with the matrix blocks and neighboring fibers[10-12] will result in the broken fibers being able to carry some residual load well away from the fracture site. The importance of this residual load bearing capacity increases as the overall stress level decreases.

If the fibers exhibit a statistical variation of strength that obeys a two parameter Weibull distribution, then the probability that an element of length dz, situated at a distance z from a reference plane, will fail at or below a reference stress of T, is given by [12-13]

$$\phi(T,z)\delta z = \frac{2\pi R}{A_0}\left[\frac{\sigma(T,z)}{S_0}\right]^m \delta z \tag{3}$$

where S_0 and m are the scale and shape parameters respectively, A_0 is a normalizing term with units of area, and $\sigma(T,z)$ is the local stress on the element. With the assumptions described in the previous paragraph and adopting a shear-lag model, the local stress on an element is

$$\sigma_f(T,z) = T - 2\tau z / R \qquad 0 \le z \le \ell/2 \tag{4}$$

provided that $T \ge \tau (1+\eta) \ell/R$, and where the reference stress, T, is taken to be the fiber stress in the plane of the matrix crack. The average stress, σ, applied to the composite, is related to T by

$$\bar{\sigma} = fT[1 - \Phi(T,L)] \tag{5}$$

where $\Phi(T,L)$ is the probability that a fiber will fail anywhere within the gauge length, L, when the reference stress is less than or equal to T:

$$\Phi(T,L)=1-exp\left\{-\frac{4\pi RL}{\ell A_0}\int_0^{\ell/2}\left[\sigma_f(T,z)/S_0\right]^n dz\right\}$$

(6)

Equations (4), (5) and (6) can then be combined to show that the applied stress is

$$\bar{\sigma}=fT exp\left\{-\frac{L}{\ell}\left(\frac{T}{\Sigma}\right)^{n+1}\left[1-\left(1-\frac{\tau\ell}{RT}\right)\right]^{n+1}\right\}$$

(7)

where,

$$\Sigma=\left[\frac{A_0 S_0^n \tau(m+1)}{2\pi R^2}\right]^{1/(m+1)}.$$

The average strain in the composite is governed by that in the fibers, and hence is given by,

$$\bar{\varepsilon}=\frac{2}{E_f\ell}\int_0^{\ell/2}\sigma_f(T,z)dz$$

$$=\frac{T}{E_f}-\alpha$$

(8)

where,

$$\alpha=\frac{\tau\ell}{2E_f R}$$

Consequently, for $\bar{\varepsilon}\geq\sigma_0/[fE_f+(1-f)E_m]$, the nominal stress and strain in the composite are related by

$$\bar{\sigma}=fE_f(\bar{\varepsilon}+\alpha)exp\left\{-\frac{L}{\ell}\left(\frac{E_f}{\Sigma}\right)^{m+1}\left[(\bar{\varepsilon}+\alpha)^{n+1}-(\bar{\varepsilon}-\alpha)^{n+1}\right]\right\}$$

(9)

Often α is very small compared with ε, so that Eqn. 10 can be simplified to

$$\bar{\sigma}=fE_f\bar{\varepsilon}exp\left\{-(m+1)\frac{\tau L}{\Sigma R}\left(\frac{\bar{\varepsilon}E_f}{\Sigma}\right)^m\right\}$$

(10)

Eqn. 10 is plotted in Fig. 4, using the data from Table I. It will be observed that there is a maximum in the stress/strain relation which is identical with the

ultimate tensile strength of the composite, $\bar{\sigma}_m$. The approximate form of the stress/strain relation allows an estimation of $\bar{\sigma}_m$ and the associated strain, $\bar{\varepsilon}_m$ to be obtained as

$$\bar{\sigma}_m = f\Sigma\left(\frac{\Sigma R}{m(m+1)\tau L}\right)^{1/n} \exp\{-1/m\}$$

(11a)

and

$$\bar{\varepsilon}_m = \left(\frac{\Sigma R}{m(m+1)\tau L}\right)^{1/n} \frac{\Sigma}{E_f}.$$

(11b)

2.2 Machine Compliance

Experimentally, the form of the curve that is obtained after this maximum will depend upon the testing conditions. If testing is conducted under load-controlled conditions, the load will drop catastrophically to zero. Conversely, if an infinitely-rigid testing machine is used for displacement control, the full exponentially decaying tail will be developed. In practice, testing is frequently carried out under displacement control but with a machine that has some finite compliance associated with the fixture and loading train. If the testing machine is assumed to act as a spring of compliance C in series with the specimen (Fig. 5), then the nominal stress in the composite can be related to the cross-head displacement, d, by

$$\bar{\sigma} = \frac{L}{CA_c}\left\{\frac{d}{L} - \bar{\varepsilon}\right\}$$

(12)

where A_c is the cross-sectional area of the composite, and L the gauge length of the specimen. Using the experimental values from Table I, some plots of equation (12) for given values of d are superimposed on Fig. 4.

The specimen and loading train can be regarded as two springs in series: one is linear and the other, representing the composite, is nonlinear. For a given cross-head displacement, d, the stress developed in the specimen is determined by the equality of Eqns. 9 and 12. This can be seen graphically in Fig. 4. It can also be noted from this figure that at a critical value of d=d*, when Eqn. 12 is tangential to Eqn. 9, an instability occurs. The elastic energy stored in the loading train is released and absorbed by the composite. The strain in the specimen increases abruptly, while the measured displacement remains constant.

This instability can be avoided, and the full exponentially-decaying tail of the load/displacement plot can be obtained, if the stiffness of the loading train exceeds a critical value, S_0. This critical value is that required to ensure that the slope of Eqn. 12 is always more negative than the slope of Eqn. 9. The critical stiffness can be obtained from these two equations as

$$S_0 \equiv \frac{1}{C_0} = \frac{A_c f m E_f}{L \exp(1+1/m)}$$ 13

3.   Comparison With Experimental Measurement

A previous study has presented the results of tensile tests obtained, using a servo-hydraulic machine# , on a series of glass ceramic matrix composites. One of these composites, which consisted of SiC fibers in a lithium-aluminum-silicate glass-ceramic matrix, has been well characterized[3,5-7]. It was therefore suitable to be used as a comparison with the present model.

The mechanical properties of the composite and testing parameters are summarized in Table I. Upon substituting these parameters into Eqns. 9 and 12, the predicted load/displacement trace could be drawn in Fig. 5. The experimentally

MTS 810, Material Test System, Inc. Minesota.

obtained trace is superimposed, and it will be clear that the essential features are well described by the present model. The effect of machine compliance is vividly illustrated by the discontinuous jump in the load.

4. Concluding Remarks

The most restrictive limit of the present model is that it does not include an accurate description of fiber pull-out. A simplifying assumption was made in the analysis that broken fibers do not carry any load. In practice, frictional effects will probably ensure that broken fibers support some load well away from their points of fracture. Therefore, it is expected that the analysis presented in this communication provides a lower bound on the load-bearing capability of the composite. It will be observed from Fig. 6 that at extreme values of the strain, when most of the fibers are expected to have failed somewhere along their length, the predicted loads are considerably less than the observed ones. If the broken fibers do carry some load then another important effect would be that the present analysis overestimates the sensitivity of the strength of the composite to its length. Such a size effect has not been investigated. Furthermore, after all the fibers have failed within the gauge section, frictional force can provide additional load bearing capacity, which is not accounted for by the present model. This deviation is apparent from the behavior beyound the instability point on the load/displacement curve(Fig. 6).

Finally, to summarize, this communication has presented a simple analysis incorporating the statistics of fiber failure to model the observed tensile behavior of brittle fiber composites. The compliance of the machine used to test the materials has been included in the analysis, as it has a profound influence on the shape of the observed load/displacement curves. The essential features predicted by this analysis appear to be in good agreement with an experimental test.

REFERENCES

1. J. Aveston, G. A. Cooper and A. Kelly, "Single and Multiple Fracture," pp. 15-26 of <u>The properties of Fiber Composites,</u> Conf. Proc. National Physical Lab., IPC Science and Technology Press, (1971).

2. J. Aveston and A. Kelly, "Tensile First Cracking Strain and Strength of Hybrid Composites and Laminates," *Phil. Trans.* Royal Society of London, A294, 519-534, (1980).

3. J. J. Brennan and K. M. Prewo, "Silicon Carbide Fiber Reinforced Glass-Ceramic Matrix Composite Exhibiting High Strength and Toughness." *J. Mater. Sci.*, 17, p. 2371-83, (1982).

4. D. B. Marshall, B. N. Cox and A. G. Evans, " The Mechanics of Matrix Cracking in Brittle-Matrix Fiber Composites," *Acta Metall.*, 33, 2013-2021, (1985).

5. T. Mah, M. G. Mendiratta, A. P. Katz, R. Ruh and K. S. Mazdiyasni, " Room Temperature Mechanical Behavior of Fiber-Reinforced Ceramic-Matrix Composites," *J. Am. Ceram. Soc.*, 68, C27-30, (1985).

6. D. B. Mashall and A. G. Evans, " Failure Mechanisms in Ceramic-Fiber/Ceramic-Matrix Composites," *J. Am. Ceram. Soc.*, 68, 225-231, (1985).

7. H. C. Cao, E. Bishoff, O. Sbzero, M. Ruhle, A. G. Evans, D. B. Marshall and J. Brennen, "The Effect of Interfaces on the Mechanical Performance of Fiber Reinforced Brittle Materials." submitted to *J. Am. Ceram. Soc.*, (1989).

8. L. N. McCartney, Mechanics of Matrix Cracking in Brittle-Matrix Fiber-Reinforeced Composites," *Proc. R. Soc. Lond.*, A409, 329-350, (1987).

9. A. C. Kimber and J. G. Keer, " On the Theoretical Average Crack Spacing in Brittle Matrix Composites Containing Aligned Fibers," *J. Mat. Sci. Let.*, 1, 353-354, (1982).

10. R. L. Smith and S. L. Phoenix, " Asymptotic Distributions for the Failure of Fibrous Materials under Series-Parallel Structure and Equal Load-Sharing," *J. Appl. Mechs.*, 48, 75-82, (1981).

11. S. L. Phoenix and R. L. Smith, "A Comparison of Probabilistic Techniques for the Strength of Fibrous Materials under Local Load-Sharing Among Fibers," *Intl. J. Solids Structures*, 19, 479-496, (1983).

12. H. L. Oh and I. Finnie, "On the Location of Fracture in Brittle Solids -- I: Due to Static Loading," *Int. J. Fracture.*, 6, 287-300, (1970).

13. M. D. Thouless and A. G. Evans, " Effects of Pull-out on the Mechanical Properties of Ceramic Matrix Composites," *Acta. Metall.*, 36, 517-522(1988).

Table I. Material Properties

Material Properties	Value	Reference
Fiber modulus, E_f	200 GPa	5
Fiber radius, R	8 μm	
Fiber volume fraction, f	0.5	
Matrix modulus, E_m	85 GPa	3
Statistical properties of fibers,		
S_0 (A_0=1 m²)	2.988 MPa [#]	7, 14
m	2.1	7, 14
Interface sliding stress, τ	2 MPa	6
Matrix crack spacing, l	400 mm	6
Matrix cracking stress, σ_0	290 MPa	7

[#]   Due to a notation difference, the parameter S_0 can be converted from S_* in

reference 14, in accordance with,

$$S_0 = S \cdot \left(\frac{2\pi RL}{A_0}\right)^{1/m}$$

FIGURE CAPTIONS:

Fig.1 A schematic tensile stres /strain curve for a "tough" fiber composite.

Fig. 2 SEM micrograph showing the saturated matrix cracks

Fig. 3 a) Stress distribution assumed in the present model, for a unbroken fiber .

b) Possible stress distribution in a broken fiber when the spacing between the matrix cracks is large.

Fig. 4 Stress/strain curve predicted by Eqn. 10 and the machine compliance curves which determine the cross-head displacement.

Fig. 5 Schematic illustration of the test specimen loaded by a finite compliance machine which is represented by a spring in series with the sample.

Fig. 6 A comparison of the predicted load/displacement curve with that obtained experimentally.

Fig. 1

Fig. 3

Fig. 4

A_c

$\overline{\sigma}, \overline{\varepsilon}$

L

Specimen

Machine
Compliance, C

P, u

Fig. 5

LAS/SiC Composite

Experimental

Predicted
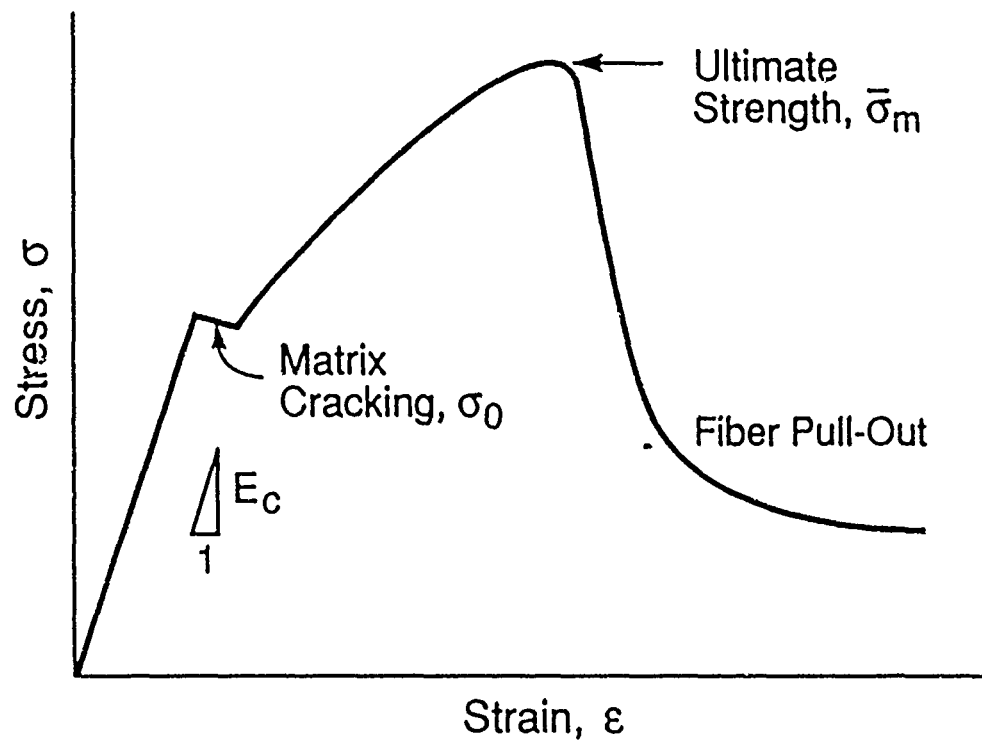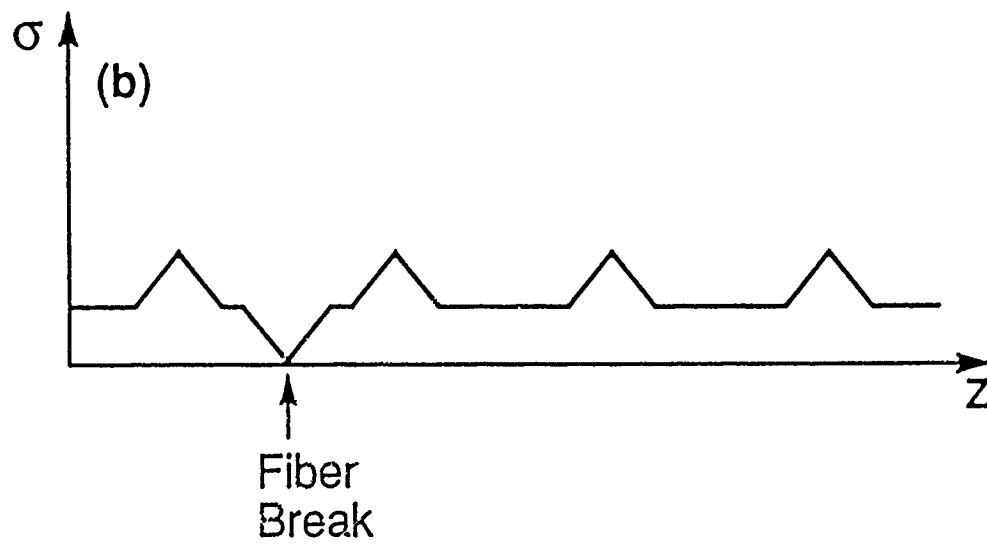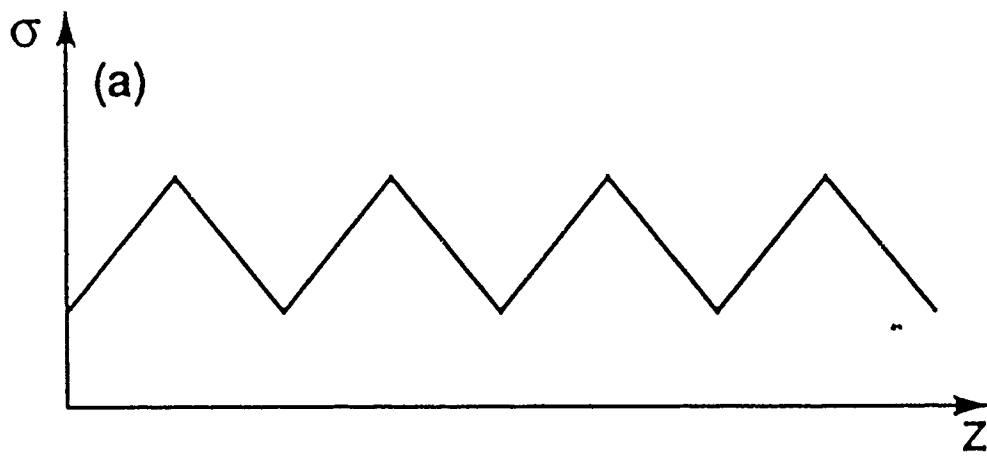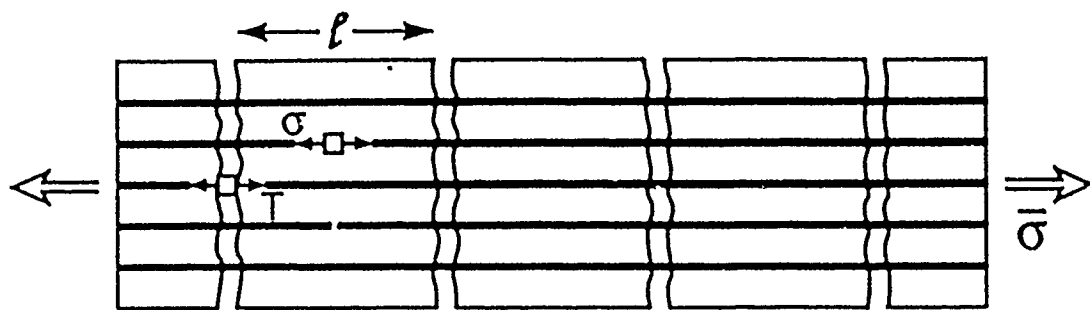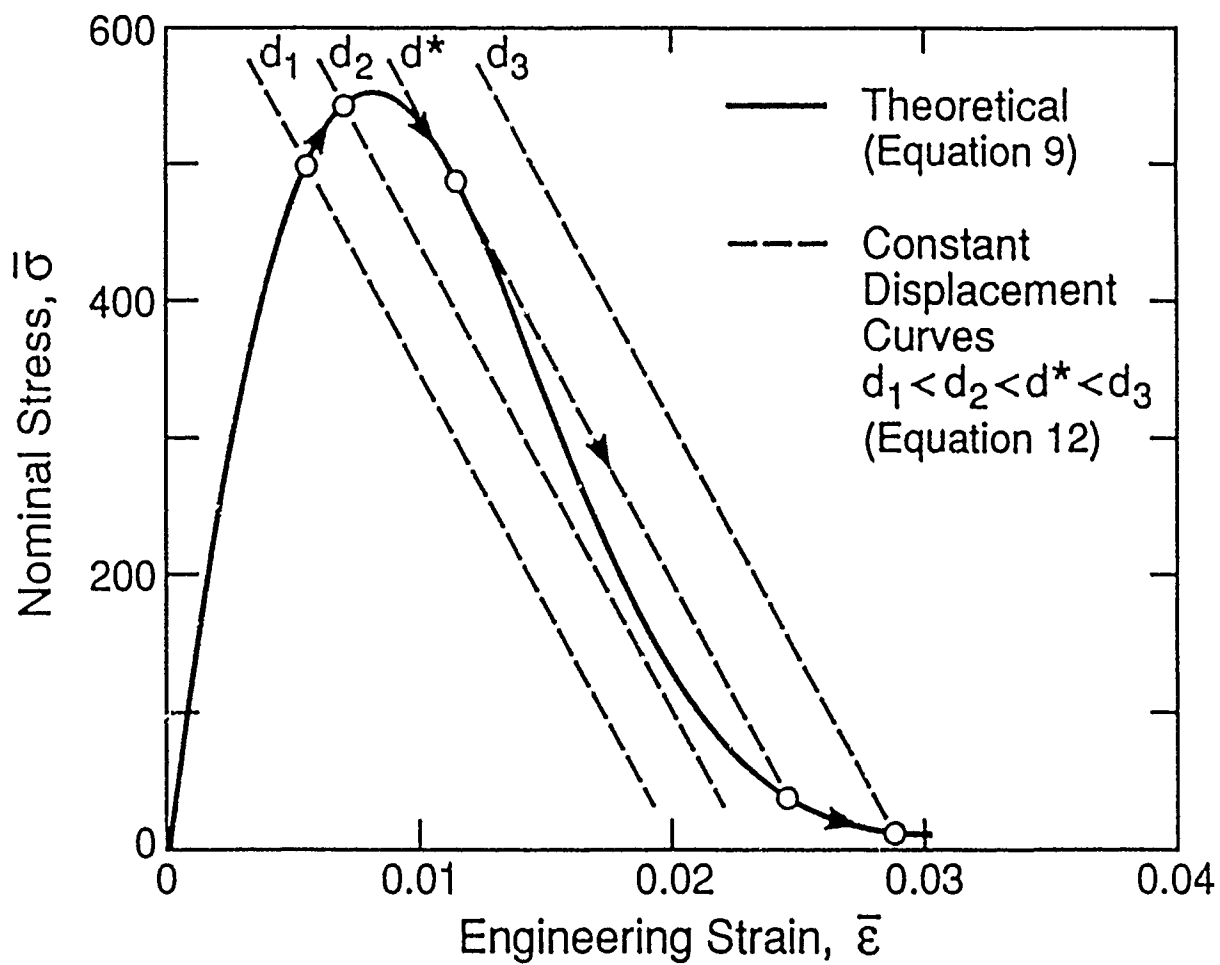
Fig. 6

MATERIALS

EFFECTS OF RESIDUAL STRESS AND FRICTIONAL SLIDING ON CRACKING AND PULL-OUT IN BRITTLE MATRIX COMPOSITES

L. S. Sigl and A. G. Evans

Materials Department
College of Engineering
University of California, Santa Barbara
Santa Barbara, California 93106

EFFECTS OF RESIDUAL STRESS AND FRICTIONAL SLIDING ON CRACKING AND PULL-OUT IN BRITTLE MATRIX COMPOSITES

L.S. SIGL and A.G. EVANS

Materials Department, College of Engineering, University of California, Santa Barbara, CA 93106, U.S.A.

The crack growth resistance and matrix cracking stress for high toughness brittle matrix composites depends on interface debonding, as well as the residual stress, the elastic properties, the friction coefficient along the debond and the fiber strength. A comprehensive analysis is presented of the interrelationships between these variables for uniaxially reinforced systems when the interface is subject to residual compression.

Notation

α	linear thermal expansion coefficient
λ	ratio of Young's modulus $= E_f/E_m$
Σ_{ij}	non-dimensional stress $= \sigma_{ij}/\Delta\alpha\,\Delta T E_f$
σ	stress on fiber between crack surfaces
σ_{rr}	radial stress
$\sigma_{\theta\theta}$	tangential stress
σ_{zz}	axial stress
ϵ	strain
ξ	$(1-f)/[\lambda(1+f)+(1-f)(1-2\nu)]$
ϕ	$\nu(1-f+f\lambda)/[\lambda(1+f)+(1-f)(1-2\nu)]$
τ	interface sliding resistance
τ_{ff}	effective sliding resistance
μ	friction coefficient
ν	Poisson's ratio
a	fiber radius
A_0	reference area for fiber statistics
D	d/a
d	debond length
E	Young's modulus of composite
e_T	stress-free strain $\Delta\alpha\,\Delta T$
F	$P-R$
F_p	non-dimensional pull-out stress
f	fiber volume fraction
G_{IIc}^i	critical mode II strain energy release rate for interface
G_{mc}	critical mode I strain energy release rate for matrix

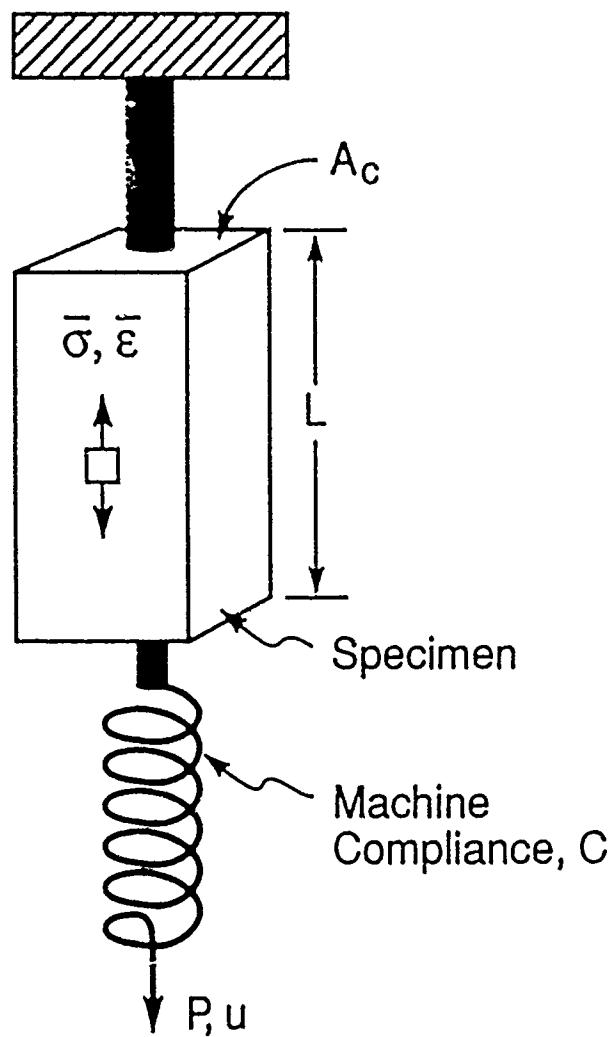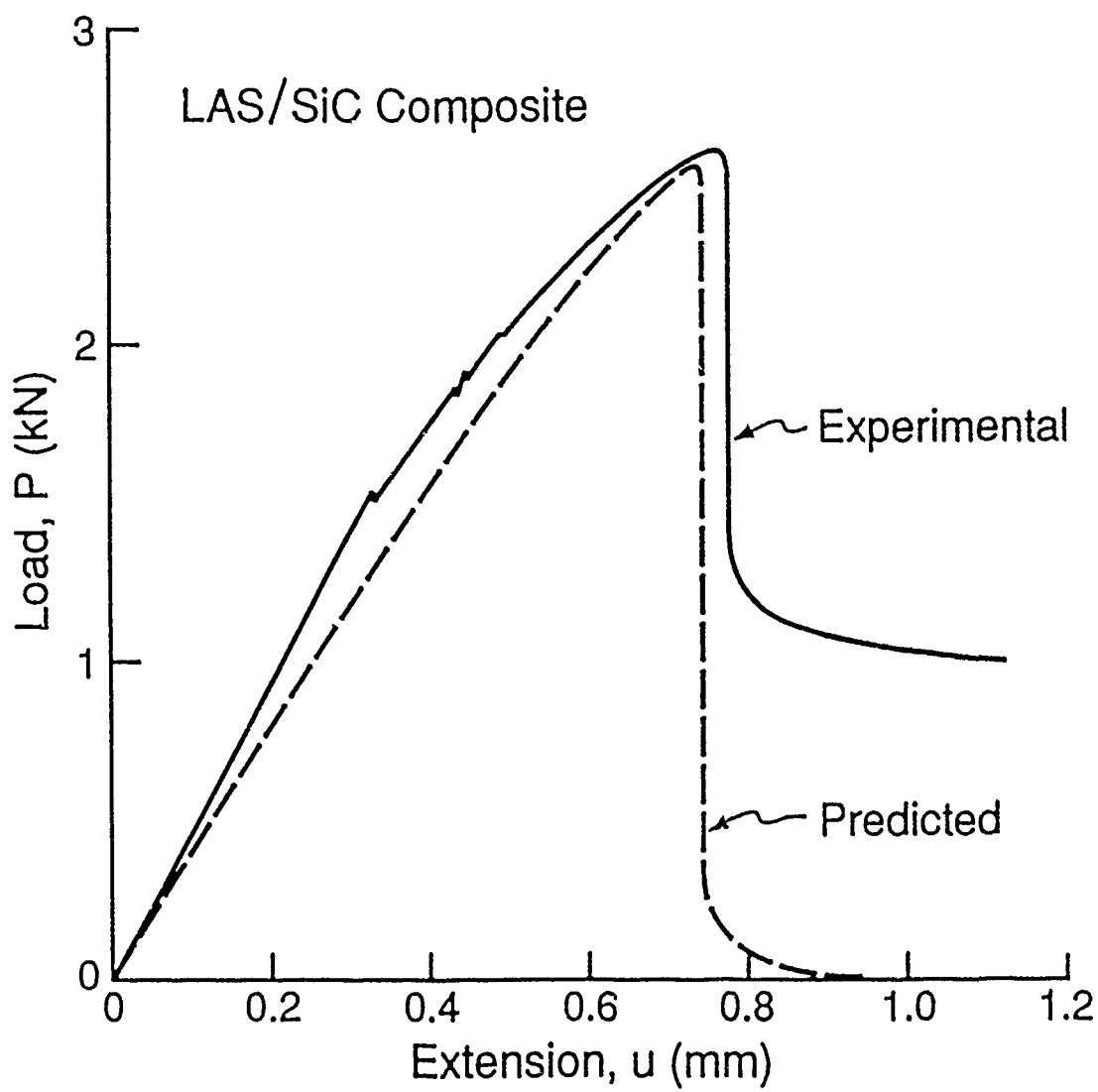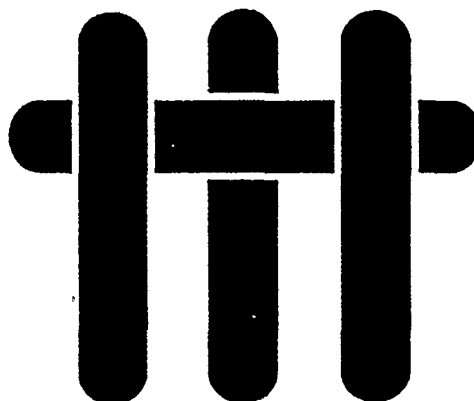|	
h	pull-out length
H	pull-out parameter
l	slip length
m	shape parameter for fiber strength distribution
P	non-dimensional stress on fiber $= \sigma/\Delta\alpha\,\Delta T E_f$
q	normal compressive stress at the interface
Q	non-dimensional interface stress $= q/\Delta\alpha\,\Delta T E_f$
r	distance from center of fiber
R	non-dimensional residual stress in the fiber
S	fiber strength
S_0	scale parameter for fiber strength
ΔT	temperature change that governs the stress-free strain
u	average crack opening
U	non-dimensional crack opening
X	slip length or debond length
z	axial distance from crack plane
Z	z/a
Z_0	location where axial stress in fiber is zero

1. Introduction

The behavior of partially debonded fibers in composites with interfaces subject to residual tension has been analyzed previously (Charalambides and Evans, 1989). That investigation revealed that
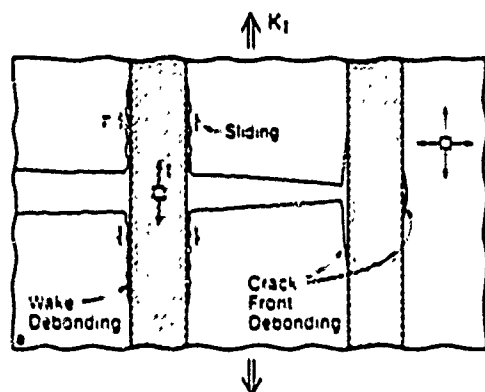
Fig. 1a. A schematic indicating crack front and wake debonding.

the toughening in the absence of fiber surface asperities (that cause frictional sliding resistance) is restricted to crack bridging by intact fibers. The magnitude of the toughening is thus relatively small. However, when a frictional resistance to the pull-out of failed fibers exists, the fracture toughness of the composite can be considerably larger (Thouless and Evans, 1988). Such resistance ob-

Fig. 1b. A schematic illustrating fiber failure and pull-out with effects on composite toughness.

tains either upon asperity contact or when the interface is subject to residual compression (Marshall and Oliver, 1987; Budiansky et al., 1986). The present article presents an analysis of effects that occur in brittle matrix composites that experience frictional sliding and pull-out at debonded interfaces. Such composites are exemplified by Al_2O_3 reinforced with SiC (Nicalon) fibers (Anderson).

The basic premise for the study is that the composite has "weak" interfaces that debond at the matrix crack front (Fig. 1a). *Residual radial compression* then causes the debonded surfaces to come into contact in the crack wake. As the crack extends, further debonding may occur and the crack opening is resisted by frictional sliding along the debond. Subsequently, the fibers may fail in the crack wake, away from the crack plane, and pull-out against the frictional resistance (Fig. 1b). The analysis performed in the present article addresses issues concerned with stresses in intact and failed fibers, subject to prior debonding, and frictional sliding. The results are used to deduce trends in matrix cracking and in toughness with the salient material variables.

2. Stresses in intact fibers

When the thermal expansion coefficient of the matrix, a_m exceeds that of the fiber, a_f, the composite is subject to *residual compression* at the fiber/matrix interface. Frictional sliding then becomes possible along debonded interfaces in the crack wake, resulting in bridging tractions, as well as a pull-out resistance to crack opening (Thouless and Evans, 1988). The initial calculations are conducted by preselecting the debond length and evaluating the stress distributions and the tractions on the fibers, as a function of crack opening. To ascertain the salient trends, an approximate analytical model is developed by using simplifying assumptions. The simplifications are selected by using insights gained from numerical, finite element, calculations and justified by selected comparisons.

The calculations have been conducted for the case wherein Coulomb friction conditions obtain
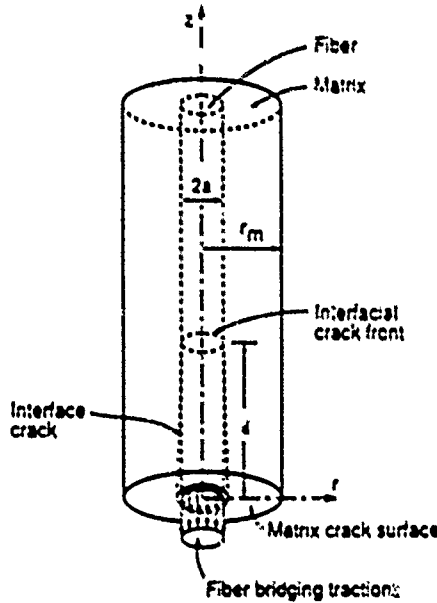
Fig. 2 The composite cylinder used to conduct the analysis.

along the previously debonded region, while elasticity is obeyed beyond the debond. The shear stress τ that exists along the interface within the debond zone is thus,

$$\tau = -\mu q, \tag{1}$$

with q being the normal pressure at the interface and μ the friction coefficient.

The analytical approach selected for present purpose is a *modified shear lag* scheme that neglects gradients in shear stress compared with normal stress gradients. Comparison with numerical results indicates that this approximation has good applicability when the friction coefficient $\mu < 0.1$. A more complete analysis would be needed to solve problems wherein $\mu > 0.1$. Subject to zero radial stress on the outside of the composite cylinder [1] (Fig. 2), the stresses satisfy the following relationships (Timoshenko and Goodier, 1950)

$$\sigma_{rr}^f = \sigma_{\theta\theta}^f = q, \tag{2.1}$$

[1] More rigorously, a zero *average* external radial stress obtains as the operative boundary condition on the outside of the cylinder.

$$\sigma_{rr}^m = \frac{q}{(1-f)}\left[\left(\frac{a}{r}\right)^2 - f\right], \tag{2.2}$$

$$\sigma_{\theta\theta}^m = \frac{-q}{(1-f)}\left[\left(\frac{a}{r}\right)^2 + f\right], \tag{2.3}$$

where the superscripts f and m refer to the fiber and matrix, respectively, a is the fiber radius, f is the fiber volume fraction and r is the distance from the fiber center. The corresponding strains are (Timoshenko and Goodier, 1950):

$$\epsilon_{rr}^f = \epsilon_{\theta\theta}^f = -\alpha_f \Delta T + \left[q(1-\nu) - \nu\sigma_{zz}^f\right]/E_f, \tag{3.1}$$

$$\epsilon_{zz}^f = -\alpha_f \Delta T + \left[\sigma_{zz}^f - 2\nu q\right]/E_f, \tag{3.2}$$

$$\epsilon_{rr}^m = -\alpha_m \Delta T + \left(\frac{1}{E_m}\right)$$
$$\times\left\{\frac{fq}{(1-f)}\left[\frac{\left(\frac{a}{r}\right)^2(1+\nu)}{f} - (1-\nu)\right]\right.$$
$$\left. -\nu\sigma_{zz}^m\right\}. \tag{3.3}$$

$$\epsilon_{\theta\theta}^m = -\alpha_m \Delta T - \left(\frac{1}{E_m}\right)$$
$$\times\left\{\frac{fq}{(1-f)}\left[\frac{\left(\frac{a}{r}\right)^2(1+\nu)}{f} + (1-\nu)\right]\right.$$
$$\left. -\nu\sigma_{zz}^m\right\}. \tag{3.4}$$

$$\epsilon_{zz}^m = -\alpha_m \Delta T + \left(\frac{1}{E_m}\right)\left[\sigma_{zz}^m + \frac{2f q \nu}{(1-f)}\right], \tag{3.5}$$

where ΔT is the temperature change (defined here as positive), E is Young's modulus and ν is Poisson's ratio taken for simplicity to be the same for fiber and matrix. Continuity of radial displacements at the interface requires that, at $r = a$,

$$\epsilon_{\theta\theta}^m = \epsilon_{\theta\theta}^f. \tag{4}$$

With this boundary condition, eqns. (2) and (3) can be used to relate the interface pressure q to the axial stresses σ_{zz}, giving.

$$Q = -\xi\left[1 + \nu\Sigma_{zz}^m\lambda - \nu\Sigma_{zz}^f\right],\tag{5}$$

where $Q = q/\epsilon_T E_f$, $\Sigma_{zz} = \sigma_{zz}/\epsilon_T E_f$, $\lambda = E_f/E_m$, and

$$\xi = \frac{(1-f)}{(1-f)(1-2\nu) + \lambda(1+f)}.$$

Further progress requires that the boundary conditions at the interface be specified, in order to provide another relationship between q and σ_{zz}. Different boundary conditions exist within the debond zone, where sliding occurs, and beyond the debond zone, where elasticity prevails. Within the *debond zone*, the shear stress at the interface, τ, is related to q by eqn. (1), such that mechanical equilibrium demands

$$\frac{2\tau}{a} = \frac{\partial\sigma_{zz}^f}{\partial z} = -\frac{(1-f)}{f}\frac{\partial\sigma_{zz}^m}{\partial z}.\tag{6}$$

Substituting for $\partial\sigma_{zz}$ from eqn. (6) into the differential of eqn. (5) gives:

$$\frac{\partial Q}{\partial Z} - 2\mu\phi Q = 0,\tag{7}$$

where

$$\phi = \nu(1 - f + f\lambda)/[\lambda(1+f) + (1-f)(1-2\nu)].$$

A final solution to eqn. (7) requires that the *initial stress* in the composite be established. For this purpose, it is appreciated that the stress/displacement function has an initial offset (Marshall and Evans, 1988) (see Fig. 7) such that, at zero crack opening, a compressive axial stress exists in the fiber (Appendix 1). Then, as the crack opens, the axial stress relaxes to zero, and an initial crack opening develops. The details associated with the initial opening are complex, because it does not occur uniformly. However, by assuming uniform opening and evaluating the resulting axial stresses and displacements, good correspondence with numerical solutions can be demonstrated for the interesting range of material variables.

The boundary condition for the stress is

$$\sigma_{zz}^f = -R\epsilon_T E_f, \quad \text{at } z = 0,$$

with R derived in Appendix 1. Consequently, in the presence of a stress, σ, applied to the fiber between the crack surfaces, the net non-dimensional stress on the fiber, F, at $z = 0$ is

$$F = P - R.\tag{8}$$

where,

$$P = \frac{\sigma}{\epsilon_T E_f}.$$

Then, since σ_{zz}^m is zero at $z = 0$, the stress on the interface is, $-\xi(1 - \nu_f F)$ and eqn. (7) gives

$$Q = -\xi(1 - \nu F)\exp(2\mu\phi Z),\tag{9a}$$

where $Z = z/a$. A related solution has been quoted by Wells and Beaumont (1985). The present solution applies when $F < |1/\nu|$. For larger F, the fiber and matrix separate, and the solutions given elsewhere (Charalambides and Evans, 1989) then apply. Note that, when μZ is small, Q is essentially constant along the fiber (see Fig. 3) and given by

$$Q = -\xi(1 - \nu F).\tag{9b}$$

This limit at small μ is the simple shear lag result.
The corresponding axial stresses are

$$\Sigma_{zz}^f = F + W,\tag{10a}$$

and

$$\Sigma_{zz}^m = -fW/(1-f),\tag{10b}$$

where

$$W = 2\mu\int_0^Z Q\,dZ$$
$$= -\xi(1 - \nu F)[\exp(2\mu\phi Z) - 1]/\phi.$$

For small μZ, the axial stresses reduce to

$$\Sigma_{zz}^f = F - 2\mu\xi Z(1 - \nu F).\tag{10c}$$
$$\Sigma_{zz}^m = 2\mu\xi Z(1 - \nu F)/(1 - f).\tag{10d}$$

Note that the stress in the fiber changes sign from tension to compression at a location

$$Z_0 = F/2\mu\xi(1 - \nu F).\tag{10e}$$
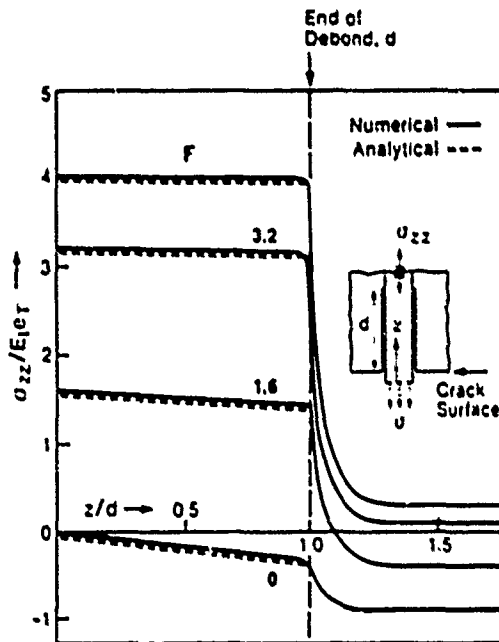
Fig. 3. Trends in axial stress with applied stress, analytical and numerical results; $E_f = E_m$, $\nu_f = \nu_m = 0.25$, $f = 0.3$, and $\mu = 0.05$

Fig. 5. Trends in axial stress with friction coefficient: $E_f = E_m$ and $\nu_f = \nu_m = 0.25$.

Fig. 4. Trends in interface stress with applied stress: analytical and numerical results; $E_f = E_m$, $\nu_f = \nu_m = 0.25$, $f = 0.3$, and $\mu = 0.05$.

These axial stresses apply when z is less than both the slip length, l (Appendix 1) and the debond length, d. Furthermore, when $l < d$, the stresses at $z > l$ are given directly by the applied loads and the initial stresses (Appendix 1). When l is limited by d, singular stresses develop at the end of the debond that can cause further debonding. These stresses are discussed elsewhere (Section 4).

Selected *finite element* solutions (Appendix 2) provide a basic check on the validity of the above analytical solutions for $\mu < 0.1$. Some comparisons are presented in Figs. 3, 4. The only region of significant divergence within the debond zone involves a small region near the matrix crack plane, wherein rapid variations in the interface pressure, q, are missed by the analytical simplifications. This region is of minor importance for present purposes. Some of the salient trends in stresses can now be deduced from the analytical solutions plotted on Figs. 3-6 [2]. When slip is limited by the debond, d, the interface pressure and axial stress vary linearly within the debond zone, except near

[2] Values of μ up to 0.5 are used in the figures to more vividly illustrate the trends. But, it should be recalled that the analytical results become inaccurate when $\mu \gtrsim 0.1$.
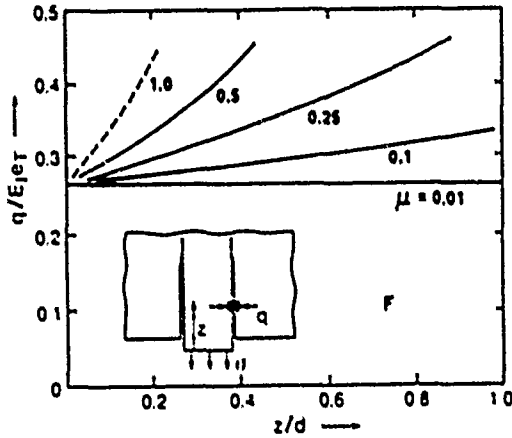
Fig. 6. Trends in radial stress with friction coefficient: $\epsilon_f = E_m$, $\nu_f = \nu_m = 0.25$ and $f = 0.3$.

the matrix crack plane and near the end of the debond. The stress changes are governed largely by the friction coefficient. As the applied stress increases, the axial stress in the fiber increases, but the interface pressure decreases and, as noted above, becomes zero when $F = |1/\nu|$. When $l < d$, the presence of the debond has no effect. Simple "composite" solutions (Budiansky et al., 1986) then obtain at $z > l$.

3. Crack opening displacements

With the simplification, used above, that the crack surfaces be planar, the crack opening u can be estimated from the difference in the axial elastic strains between the fiber and matrix as

$$u = \int_0^y \left(\epsilon_{zz}^f - \epsilon_{zz}^m \right) dz, \tag{11}$$

where y is either the slip length, when $l < d$, or the debond length. The axial strains may be obtained as

$$\epsilon_{zz}^f = \epsilon_T[F + W - 2\nu_f Q] - \alpha_f \, \Delta T,$$
$$\epsilon_{zz}^m = f\epsilon_T[-W + 2\nu_m Q]\lambda/(1-f) - \alpha_m \, \Delta T. \tag{12}$$

Substituting for ϵ_{zz} from eqn. (12) into eqn. (11)

and integrating, the non-dimensional crack opening becomes

$$U = u/\epsilon_T a = \chi\{[(1 + \nu)/\nu] - (1 - \nu F)(1 - 2\nu^2\phi)$$
$$\times [\exp(2\mu\chi\phi) - 1]/2\mu\phi\nu. \tag{13a}$$

with $\chi = l/a$ (Appendix 1) when $l < d$ and $\chi = d/a$ otherwise. For small $\mu\chi$, eqn. (13a) reduces to

$$u/a\chi = \epsilon_T[1 + F + 2\nu\phi(1 - \nu F)]. \tag{13b}$$

Some crack opening trends predicted by eqn. (13) with χ given by eqn. (A3), Appendix 1, are compared with numerical results in Fig. 7. Again, the correspondence is good, except for small openings, wherein the behavior is strongly influenced by the concentrated radial stress near the crack plane. General trends in crack opening obtained from the analytical solution (Fig. 8) reveal that three basic regions exist. For small stress levels (region I), where $l < d$, the behavior is strongly non-linear because l varies with P (eqn. A5), and is greatly influenced by the friction coefficient. At intermediate stress (region II), l is limited by d and linear behavior occurs with the slope now governed
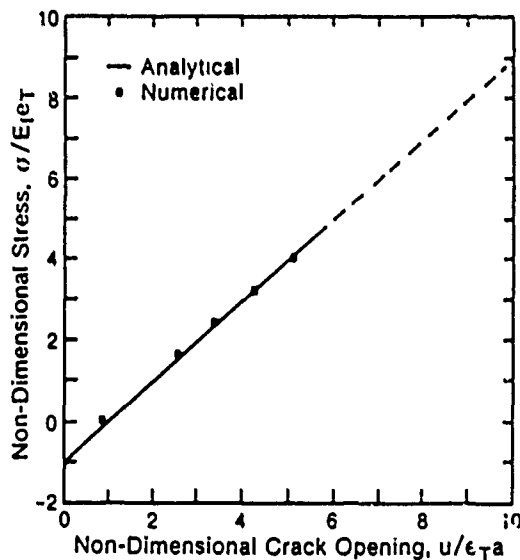
Fig. 7. Trends in non-dimensional crack opening with non-dimension applied stress: $E_f = E_m$, $\nu_f = \nu_m$, $f = 0.3$, $\mu = 0.05$ and $d/a = 10$.
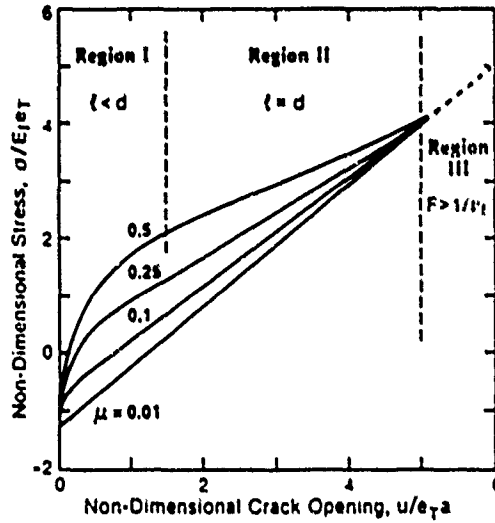
Fig. 8. Generalized crack opening behavior indicating three regions: $d/a = 10$, $f = 0.3$ and $E_f = E_m$.

by both the friction coefficient and the debond length. Finally, at large stresses, $F > |1/\nu|$ (region III), the interface separates and the debond extends unstably (Section 4), resulting in a non-unique relation between u and F.

4. The debond length

The debonding process can be explored by noting that the extension of a debond by δd is accompanied by free energy changes (Marshall et al., 1985; Marshall and Oliver, 1987), including ΔU_s, the strain energy, δW_t, the work done by the forces on the fibers between the crack and ΔW_f the energy dissipated by frictional sliding. Each of these terms is evaluated upon extending a debond, subject to the condition that the slip length $l > d$, whereupon a stress concentration exits at the debond tip.

The relevant strain energies can be estimated by noting that the σ_{zz} stresses are appreciably larger than the σ_{rr} and $\sigma_{\theta\theta}$ stresses (Figs. 3–5) and then calculating the strain energies in the fiber

and matrix associated with σ_{zz}. This procedure gives

$$\delta U_s = \frac{\pi a^2 e_T^2 E_f}{2} \int_d^{d+\delta d} \Sigma_{zz}^2 \, dz, \tag{14a}$$

such that,

$$\frac{\delta U_s}{a^2 E_f e_T^2 \delta d}$$

$$= \frac{\pi}{2} \Big\{ F^2 - 4\mu\xi DF(1 - \nu F)$$

$$+ 4[\mu\xi D(1 - \nu F)]^2 (1 + \lambda f^2/(1 - f)^2) \Big\}, \tag{14b}$$

or for small $\mu d/a$,

$$\frac{\delta U_s}{a^2 E_f e_T^2 \delta d} = \frac{\pi F^2}{2}. \tag{14c}$$

This estimate ignores the contribution from the singular field at the debond tip, which is assumed to be small.

The *work done* during crack opening upon debond growth at constant F is

$$\delta W_t = \pi a^2 \sigma \delta u, \tag{15a}$$

where δu is the relative displacement of the debonded surfaces, as governed by eqn. (11). Inserting δu derived from eqn. (13a), the work done when $\mu d/a$ is small becomes

$$\frac{\delta W_t}{a^2 E_f e_T^2 \delta d} = -\pi F[1 + F + 2\nu\phi(1 - \nu F)]. \tag{15b}$$

The energy dissipated by *frictional sliding* is

$$\delta W_f = -2\pi\delta u a^2 \mu e_T E_f \int_0^{d/a} |Q| \, dz. \tag{16a}$$

Inserting δu from eqn. (13a) gives for small $\mu d/a$

$$\frac{\delta W_f}{a^2 E_f e_T^2 \delta d}$$

$$= -2\pi(1 - \nu F)[1 + F + 2\nu\phi(1 - \nu F)] \, d\mu\xi. \tag{16b}$$
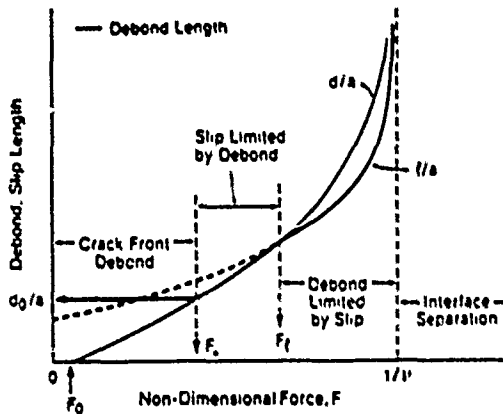
Fig. 9. Trends in wake debond length *d* with the stress on the fibers. Also plotted is the slip length, *l* and the crack front debond length *d*.

The strain energy release for debond growth can be expressed in terms of the energy changes as (Marshall et al., 1985),

$$G = [\delta U_s + \delta W_t + \delta W_t]/2\pi a \delta d, \qquad (17a)$$

which for small $\mu d/a$ becomes

$$G/e_T^2 E_t a = F^2/4 + F/2 - \mu \xi D(1 - \nu F), \qquad (17b)$$

where $D = d/a$. Equating G to the mode II fracture resistance of the interface G_{IIc}^i, the debond length becomes

$$\frac{\mu d}{a} = \frac{F^2 + F - 4F_0^2}{4\xi(1 - \nu F)} \qquad (18)$$

where

$$F_0 = G_{IIc}^i/E_t e_T^2 a$$

represents a *threshold* condition below which debonding does not occur in the crack wake. Trends in d/a with F are schematically illustrated on Fig. 9: notably, an absence of debonding below the threshold, followed by a linear region with slope inversely dependent on the friction coefficient. Finally, as $F \to 1/\nu$, the behavior is strongly non-linear and $d/a \to \infty$ (but the details are poorly described by eqn. (18) which is restricted to small $\mu d/a$).

Since debonding is subject to $l > d$, it is also necessary to plot l/a on Fig. 9, using eqn. (A5). Furthermore, crack front debonding should be superposed. The essential debonding behavior then exhibits four regions. Crack front debonding governs the actual threshold stress F_a ($> F_0$) at which debond extension initiates in the wake. Debonding at $F > F_a$ then occurs subject to eqn. (18). Thereafter, at F_t, the slip length diminishes to the debond length and continued debonding is limited by the slip length (eqn. A5). Finally, at $F = 1/\nu$, debonding becomes unstable.

5. Pull-out

When a fiber fails, the traction on the fiber end drops, because the axial stress on the fiber is eliminated at the fracture site. With the boundary conditions

$$\Sigma_{zz}^f = F_p$$

at $z = 0$, and

$$\Sigma_{zz}^f = 0$$

at $z = h$, where h is the pull-out length, the tractions can be derived from eqn. (10), as plotted on Fig. 10. The result for small $\mu h/a$ can be explicitly derived by noting that, for uniform shear stress along the fiber,

$$F_p = -2\mu Q(h - u)/a. \qquad (19)$$

Inserting Q with $R = 0$ then gives,

$$\frac{u}{a} = \frac{h}{a} - \frac{F_p}{2\mu \xi(1 - \nu F_p)}. \qquad (20)$$

The pull-out force is thus *non-linear* (Fig. 10).

The pull-out length, h, is itself a function of μ and e_T. Rigorous analysis of pull-out is beyond the scope of the present study. However, when $h\mu/a$ is small, insightful analytical solutions are possible. As already noted, for this condition, the pressure along the fiber is essentially uniform (eqn. 9b) and the axial stress in the fiber is approximately linear. The available statistical analysis of pull-out, by Thouless and Evans (1988) which is
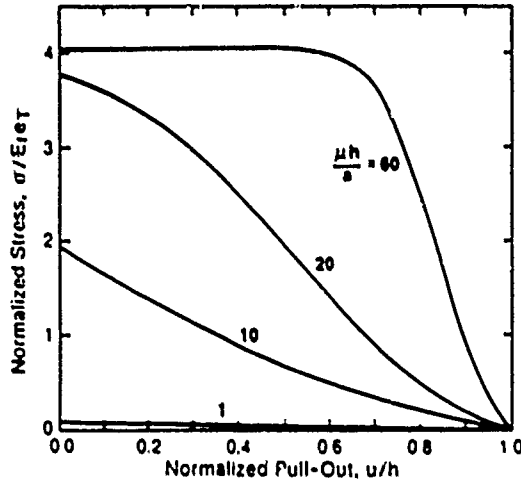
Fig. 10. Variation in pull-out stress with crack opening; $e_f = E_m$, $\nu_f = \nu_m = 0.25$, and $f = 0.3$.

also based on a linearly varying fiber stress may thus be utilized. This analysis uses the fiber stress distribution,

$$\sigma_{zz}^f = \sigma(1 - 2\tau Z/a),\qquad(21)$$

where τ is the *constant* shear stress at the interface. Consequently, by equating eqn. (21) to eqn. (10c), it is possible to derive an effective shear stress for the present problem as

$$\tau_{tt} = E_t e_T \mu\xi(1 - \nu_t F).\qquad(22)$$

This effective shear stress can be incorporated into the Thouless and Evans (1988) analysis by noting that it is only necessary to consider that length of fiber subject to axial tension, $Z < Z_0$ (with Z_0 given by eqn. 10e). The basic statistical relation is

$$h(S) = \frac{4\pi m a}{A_0 S_0^m}\int_0^S \exp\left[-(\sigma/\eta)^{m+1}\right]$$
$$\times \int_0^{z_0} z(\sigma - 2\tau_{tt}z/a)^{m-1}\,dz\,d\sigma\qquad(23)$$

for $\sigma < E_t e_T/\nu$, where m is the shape parameter and S_0 and A_0 are the scale parameters that govern the weakest link fiber strength statistics (Thouless and Evans, 1983) and

$$\eta^{m+1} = A_0 S_0^m \tau_{tt}(m+1)/2\pi a^2.$$

Integration of eqn. (23) with respect to z gives

$$\frac{h(S)}{a} = \frac{\pi a^2}{(m+1)A_0 S_0^m (E_t e_T \mu\xi)^2}$$
$$\times \int_0^s \frac{\sigma^{m+1}\exp\left[-(\sigma/\eta)^{m+1}\right]\,d\sigma}{(1 - \nu\sigma/E_t e_T)^2}.\qquad(24)$$

This integral can be reexpressed in the non-dimensional form

$$\frac{h(v)}{a} = \frac{B}{2\nu_t \mu\xi}\int_0^r \frac{v^{m+1}}{(1-v)^2}$$
$$\times \exp\left[-Bv^{m+1}/(1-v)\right]dv,\qquad(25)$$

where

$$B = \frac{2\pi a^2 (E_t e_T/S_0)^{m+1}}{(m+1)A_0\mu\xi\nu^{m+1}},$$

and $v = S\nu/E_t e_T$. If all of the fibers fail before interface separation occurs (i.e., $F < 1/\nu$), the average pull-out length is

$$\frac{\langle h\rangle}{a} = \frac{2m}{(m+1)\mu\xi\nu}\int_0^1 \frac{v^{m+1}}{(1-v)^2}$$
$$\times \exp\left[-Bv^{m+1}/(1-v)\right]dv$$
$$= \left[\int_0^1 \frac{v^m}{1-v}\exp\left[-Bv^{m+1}/(1-v)\right]dv\right]^{-1},$$
$$\hspace{6cm}(26a)$$
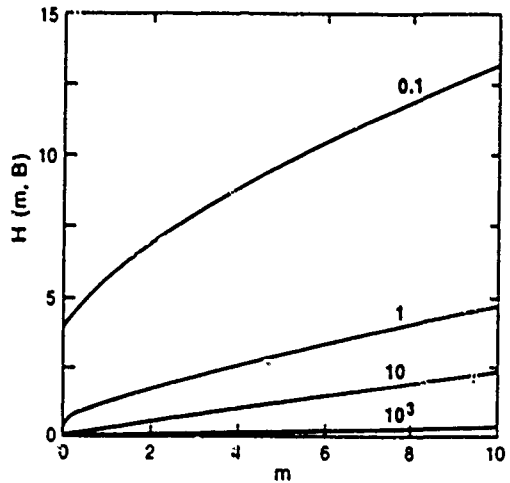
Fig. 11. The non-dimensional pull-out function.

or

$$\langle h \rangle = \frac{2maH(B, m)}{(m+1)\mu\xi\nu}. \qquad (26b)$$

where H is the function plotted in Fig. 11. For an interesting range of composite properties, H satisfies the approximate form

$$H = 1/2B + m/(1 + B). \qquad (27)$$

The function H can thus be used in conjunction with eqn. (26b) to obtain the mean pull-out length $\langle h \rangle$. The pull-out length can, in turn, be used to estimate the pull-out contribution to the composite toughness, as elaborated in the following section.

6. Pull-out toughening

Toughening of brittle matrix composites has contributions from bridging, debonding, residual strain and pull-out. The latter is the most important in high toughness composites (Thouless and Evans, 1988). For long cracks, the steady-state pull-out toughening is given by (Thouless and Evans, 1988)

$$\Delta G_p^u = 2f\int_0^\infty \sigma \, du. \qquad (28)$$

An insightful estimate of ΔG_p^u may be derived from the present analysis by adopting various hypotheses. It is assumed that G_{Ic}^i for the interface is sufficiently small that crack front debonding occurs, followed by additional wake debonding. It is also assumed that fiber failure occurs within the zone of axial tension (Fig. 5). Based on these conditions, a result for ΔG_p^u may be derived by allowing all fibers to have a pull-out length equal to the mean, $\langle h \rangle$, and then evaluating ΔG_p^u using $\langle h \rangle$ as the upper integration limit in eqn. (28).

From eqns. (20) and (28) it follows that

$$\Delta G_p^u = -\frac{fE_f e_T a}{\mu\xi} \int_0^{F_p^*} \frac{F_p \, dF_p}{(1 - \nu F_p)^2}, \qquad (29)$$

where the limit F_p^* may be obtained from eqn. (20) by setting $u = 0$ and $h = \langle h \rangle$, giving

$$F_p^* = \frac{2\langle h \rangle\mu\xi}{[1 + 2\mu\xi\langle h \rangle\nu]}. \qquad (30)$$

Integration of eqn. (30) then gives for small νF_p^*,

$$\Delta G_p^u = 2fE_f e_T \langle h^2 \rangle\mu\xi/a. \qquad (31)$$

Introducing $\langle h \rangle$ from eqn. (26b), the toughening becomes

$$\Delta G_p^u = \frac{8fm^2 E_f e_T H^2(B, m)a}{(m+1)^2\mu\xi\nu^2}. \qquad (32)$$

A general sensitivity study of ΔG_p^u is difficult, because of the number of variables involved. However, when eqn. (27) adequately describes trends in H, the pull-out toughening has a relatively simple form (when $m \ll 1/B$) given by

$$\Delta G_p^u = \frac{fA_0^3\mu\xi\nu^{2m}S_0^{2-m}m^2}{2\pi^2 a^3(E_f e_T)^{2m-1}}. \qquad (33)$$

The only unexpected feature of this prediction concerns the appearance of μ in the numerator. However, it is recalled that the result only applies for small $\mu\langle h \rangle/a$. Indeed, given the complexity of the full solution, a systematic experimental study of trends in toughening with μ and e_T that augments the present analysis would be most insightful.

7. Matrix cracking

Various solutions for steady-state matrix cracking can be derived, depending upon the debond resistance of the interface. A comprehensive study of the spectrum of matrix cracking behaviors would be useful, but is not attempted here. Instead the bound for small G_{Ic}^i is presented. In this case, l and d essentially coincide (Fig. 9) and only slip needs to be included in the analysis of the loads supported by the fibers. The analysis must then take the same form as that derived for a constant shear stress interface (Budiansky et al., 1986), but with τ replaced by eqn. (1), giving the following expression for the cracking stress, σ_0,

$$\frac{\sigma_0}{E} + \frac{\sigma_m^R}{E_m} = \left(\frac{6\mu f^2 E_f G_{mc}}{(1-f)E_m Ea}\right)^{1/3}\left(\frac{q}{E_n}\right)^{1/3}$$

$$= (q/E_m)^{1/3}J. \qquad (34)$$

where G_{mc} is the matrix toughness and σ_m^R the axial residual stress in the matrix as governed by e_T, f and λ (Budiansky et al., 1986). An explicit solution to eqn. (34) can be derived subject to matrix cracking occurring when $F \ll 1/\nu$, viz.

$$\frac{\sigma_0}{E} + \frac{\sigma_m^R}{E_m} = (e_T \lambda \xi)^{1/3} J. \tag{35}$$

This result confirms that an *optimum* residual strain exists that gives the maximum possible matrix cracking stress, as elaborated elsewhere (Budiansky et al., 1986).

8. Implications and conclusions

The mechanical properties of composites subject to residual compression at the fiber/matrix interface involve interactions between interface debonding, frictional sliding along debonds, statistical fiber failure and pull-out. These processes have been modelled in the presence of a matrix crack. The solution provides insights concerning the matrix cracking stress, the evolution of debonding and the fracture resistance of the composite. In particular, trends in these important properties with such variables as the residual stress, the friction coefficient, the fiber strength and the matrix toughness are predicted.

The full solutions for each of these processes have unwieldy forms that obscure the essential trends. Several insightful bounds have thus been identified and emphasized, all applicable when the friction coefficients is small, $\mu \gtrsim 0.1$, typical of high toughness composites (Marshall and Oliver, 1987; Budiansky et al., 1986; Anderson). One bound obtains when the residual strain is also small, such that the mean fiber strength $\bar{S} \gg E_f e_T/\nu$. Then, the interface separates provided that G_{IIc}^i is quite small, whereupon solutions derived for a constant shear strength interface (Budiansky et al., 1986) afford a reasonable description of composite behavior. Another bound obtains when the residual strain is quite large, such that the matrix cracking stress $\sigma_0 \ll E_f e_T \nu$. Then, matrix cracking occurs subject to an essentially constant interface sliding stress, μq, and

previous solutions for matrix cracking obtain. Most interestingly, an optimal residual strain exists at which the matrix cracking stress is a maximum (Budiansky et al., 1986).

Further progress on the above problem, given the complexity of the full solutions, involves pull-out experiments, as well as crack growth experiments on composites, as needed to provide insight capable of elucidating the bounds wherein simplified solutions have validity.

References

Anderson, C.A., unpublished research.

Budiansky, B., J.W Hutchinson and A.G. Evans (1986) *J. Mech. Phys. Solids 34*, 167.

Charalambides, P.G. and A G. Evans (1989), *J. Amer. Ceram. Soc. 72*, 746.

Marshall, D.B. and A.G. Evans (1988), *Mater. Forum*, 11, 304.

Marshall, D.B. and W. Oliver (1987), *J. Amer. Ceram. Soc 70*, 542.

Marshall, D.B., B.N. Cox and A.G. Evans (1985), *Acta Metall. 33*, 2013.

Timoshenko, S. and J.N. Goodier (1950), *Theory of Elasticity*, McGraw Hill.

Thouless, M.D. and A.G. Evans (1988), *Acta Metall. 26*, 517.

Wells, J.F.K. and P.W.R. Beaumont (1985), *J. Mater. Sci. 20*, 1735.

Appendix 1

1. Initial stress in the composite

When matrix cracking occurs, the relaxation of the axial matrix stress at the crack plane causes the crack to open (Fig. 6) and modifies the stress

In the fiber. A convenient reference stress, R, is the non-dimensional axial stress in the fiber along the crack surface plane, when the crack surfaces (assumed flat) just begin to open. Clearly, an applied compression, $R f$, exists on the *composite* element at this stage. Along this plane, $\sigma_{zz}^m = 0$ and thus, from eqn. (9a) with $P = 0$,

$$Q = -\xi[1 + \nu R] \qquad (A1)$$

At the onset of matrix crack opening, the boundary conditions, subject to the assumption that the crack opens uniformly are: $\epsilon_{zz}^f = \epsilon_{zz}^m$. Then, from eqn. (3)

$$Q = (1 - R)\xi/2\phi \qquad (A2)$$

By eliminating Q from eqns. (A1) and (A2), R becomes:

$$\frac{1 + 2\phi}{1 - 2\nu\phi} \qquad (A3)$$

2. The slip length

For slip lengths $l < d$, the load transfer from the fiber to the matrix dictates that

$$P = -2\mu\int_0^{l/a} Q \, dZ \qquad (A4)$$

Integration and rearranging yields

$$l/a = \ln[1 + \phi P/\xi(1 - \nu F)]/2\mu\phi \qquad (A5a)$$

which for small $\mu l/a$ becomes

$$l/a = P/2\mu\xi(1 - \nu F) \qquad (A5b)$$

As the stress increases, l approaches d and, at $l = d$, part of the load transfer begins to take place along the ideally bonded interface beyond the debond. Thereafter, l is limited by d, until further debonding occurs.

Appendix 2

The finite element scheme

The finite element calculations were performed using a mesh described elsewhere (Charalambides and Evans, 1989). The calculations were performed for debond ratios ranging from $5 < d/a < 20$. The load was applied in accordance with the following steps. Firstly, with full bonding between matrix and fiber along the future debond length, cooling over a temperature range ΔT was simulated with the outer surface of the cylinder constrained to remain vertical and zero net force normal to this surface. In the next step, a matrix crack was introduced by setting the normal and shear stress on the crack plane to zero and interface debonding was allowed by deactivating the interface elements and changing the boundary conditions, in order to satisfy eqn. (1) along the debond and elasticity beyond the debond. External load was then applied by uniformly displacing the upper boundary of the model.

MATERIALS
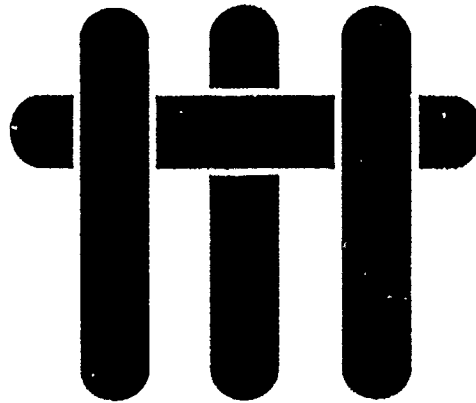
EFFECT OF INTERFACE MECHANICAL PROPERTIES ON PULLOUT IN A SiC-FIBER-REINFORCED LITHIUM ALUMINUM SILICATE GLASS-CERAMIC

Michael D. Thouless, Orfeo Sbaizero, Lorenz S. Sigl and A. G. Evans

Materials Department
College of Engineering
University of California, Santa Barbara
Santa Barbara, California 93106

Effect of Interface Mechanical Properties on Pullout in a SiC-Fiber-Reinforced Lithium Aluminum Silicate Glass-Ceramic

Michael D. Thouless,* Orfeo Sbaizero,
Lorenz S. Sigl, and Anthony G. Evans*

Materials Department, College of Engineering,
University of California, Santa Barbara, California 93106

The pullout of fibers in the crack wake makes an important contribution to the toughness of ceramic-matrix composites. The pullout is, in turn, influenced by the properties of the fibers and by the sliding resistance of the interface. Basic relationships governing the pullout are developed analytically and investigated experimentally using a lithium aluminum silicate/silicon carbide (LAS/SiC) composite subjected to various heat treatments. The experiments involve determining the strengths of single fibers and then measuring the pullout distributions. The results are used to provide a consistent view of the pullout process and related changes in mechanical properties. [Key words: composites, mechanical properties, interfaces, silicon carbide, fibers.]

I. Introduction

Fibers typically fail at appreciable distances from the crack plane in a ceramic composite that exhibits a high toughness (Fig. 1)[1-3] The broken fibers slide against the matrix and enhance the toughness by resisting crack opening.[1,4] The location of the fiber-fracture site with respect to the

crack plane, h, and the interfacial sliding resistance, τ, are therefore critical toughening parameters.[4] An existing analysis of this phenomenon of pullout in ceramic-matrix composites[4] assumes that the fibers fracture in the crack wake and that there is negligible fiber failure ahead of the crack. One intention of the present study was an evaluation of this premise achieved by comparing predicted trends in the distribution of the lengths of broken fibers with experimental observations made on a heat-treated 0°/90° laminated lithium aluminum silicate/silicon carbide (LAS/SiC) composite.[5]

Companion studies of the interfacial microstructure in the LAS/SiC composites have revealed that the interface is often partially debonded.[6] This debonding occurs upon cooling because of a thermal expansion mismatch between the fiber and the matrix. Further debonding caused by the passage of a matrix crack can be anticipated,[7] resulting in appreciable debond lengths over which fiber sliding can occur. Fiber bridging and pullout occurring at a constant value of τ therefore appear to provide a reasonable preliminary hypothesis for a toughening model.[4] The mechanical properties of composites of this type can be related to the net tractions exerted on the matrix-crack surface by both the intact fibers bridging the crack and fractured fibers pulling out of the matrix (Fig. 1).[4] The tractions are a function of crack opening and depend upon a broad range of material properties. The overwhelmingly important variables are τ and the sta-

Michael Thouless is a Research Staff Member in the IBM Research Division at Yorktown Heights, NY. He read Engineering at the University of Cambridge and received a B.A. in 1981. Thouless obtained a Ph.D. in Materials Science from the University of California at Berkeley in 1984. He worked as an Assistant Research Engineer in the University of California at Berkeley and then at Santa Barbara until 1988 when he took up his present appointment.

Anthony G. Evans is Alcoa Professor and Chair of the Materials Department at the University of California at Santa Barbara. A native of Wales, he earned his B.S. in metallurgy in 1964 and Ph.D. in physical metallurgy in 1967, both from Imperial College, London, England. During 1967 to 1971 he was with the Atomic Energy Re-

search Establishment. Harwell. In 1971 Evans came to the United States as visiting scholar at the University of California at Los Angeles. He then worked at the National Bureau of Standards from 1972 to 1974, Rockwell International Science Center from 1974 to 1978, and the University of California at Berkeley from 1978 to 1985. He has more than 200 technical papers to his credit.

A Fellow of the American Ceramic Society, Evans is a past chair of the Basic Science Division and a past vice president of the Society. He received the Society's Ross Coffin Purdy Award in 1975 presented the Sosman Lecture in 1980, and was recipient of the Fulrath Award in 1981. Evans will deliver the Edward Orton, Jr. Memorial Lecture and receive the John Jeppson Medal and Award during the 1989 Annual Meeting of the Society. He is a member of the National Institute of Ceramic Engineers.

Lorenz S. Sigl is a research engineer with ESK GmbH, Kempten, Federal Republic of Germany, a leading European manufacturer of non-oxide ceramics. He received his undergraduate and Ph.D degrees, both with first-class honors, in Materials Science from the University of Leoben, Austria, in 1982 and 1985. Dr Sigl was associated with the Max-Planck-Institute for Metals Research, Stuttgart FRG, while working on his graduate studies. He was an assistant research engineer with the University of California at Santa Barbara. Dr. Sigl's interests include the toughening of brittle solids, fracture statistics, and the design of ceramic components.

Orfeo Sbaizero is Associate Professor at the Applied and Industrial Chemistry Institute at the University of Trieste, Italy, where he is responsible for courses relating to the chemistry of materials and for the staff that is studying ceramic composites. He received his diploma in engineering from Trieste in 1977 and his doctorate in 1981. Dr Sbaizero was a visiting professor at the University of California at Santa Barbara.

tistical parameters that govern the fiber strength.[4]

The present study emphasizes experimental approaches for evaluating the interface and fiber parameters by examining mechanical property changes associated with heat treatment in air. As shown in the companion study,[5] such heat treatment causes the original carbon layer at the fiber/matrix interface to be replaced by silica. The SiO_2 layer formed after a relatively brief heat treatment of ~2 h and thickened with exposure time to eventually fill the gap left by removal of the carbon. The associated changes in the important composite quantities were evaluated and the results correlated with the interface observations[5] and the fracture properties. Finally, the implications of the observations and analyses for the role of interfaces in the mechanical properties of ceramic-matrix composites are briefly summarized.

II. Theory

The fiber failure analysis uses a strength distribution that satisfies weakest-link statistics. The explicit form is given by the two-parameter Weibull distribution, in which the probability $S(\sigma)$ that the flaws in a surface area of fibers, A_0, have a strength $<\sigma$ is given by

$$S(\sigma) = \int_0^\sigma g(S)\,dS = (\sigma/S_0)^m / A_0 \quad (1)$$

where S_0 and A_0 are the scale parameters and m is the shape parameter. A_0 is a quantity of area which is introduced for dimensional purposes. For simplicity, A_0 will be later equated to 1 m² but it must be appreciated that S_0 depends on the choice of A_0.

The probability density function, $\phi(z,T)$, for weakest-link failure of a fiber occurring behind the crack tip at a distance z from the crack plane can then be derived with the assumption that T is constant:[4]

$$\phi(z,T) = \frac{2\pi R m}{A_0 S_0^m}(T-z/\lambda)^{m-1}$$

$$\times \exp[-(T/\Sigma)^{m+1}] \quad (2a)$$

where

$$\lambda = \frac{R}{2\tau}$$

$$\Sigma = \left[\frac{A_0 S_0^m \tau(m+1)}{2\pi R^2}\right]^{1/(m+1)}$$

T is the maximum stress in the fiber between the crack surfaces and R is the fiber radius. The probability that a fiber will fail in the crack wake, at a location between z and $z+\delta z$ from the crack plane when the tractions are

between T and δT is equal to $\phi(z,T)$ $dz\,dT$. Consequently, for fixed T the cumulative probability that the pullout length will be $\leq h$ is

$$\Phi(h,T)\,dT = 2\int_0^h \phi(z,T)\,dz\,dT \quad (h < \lambda T)$$

$$= 2\int_0^{\lambda T} \phi(z,T)\,dz\,dT \quad (h \geq \lambda T)$$

$$(2b)$$

$$\Phi(h,T)\,dT = \frac{4\pi R\lambda T^m}{A_0 S_0^m}\exp[-(T/\Sigma)^{m+1}]$$

$$\times \begin{cases} 1-\left(1-\dfrac{h}{\lambda T}\right)^m & (h < \lambda T) \\ 1 & (h \geq \lambda T) \end{cases}$$

$$(2c)$$

The factor 2 in Eq. (2b) arises because the fiber is stressed on both sides of the crack plane. Integration of $\Phi(h,T)$ over all possible values of T ($0 \leq T \leq \infty$) yields the cumulative probability for the pullout lengths which will be observed on a fracture surface:

$$\Phi(h) = \int_0^\infty \Phi(h,T)\,dT \quad (3a)$$

which may be conveniently expressed in a nondimensional form as

$$\Phi(\zeta) = 1 - \int_0^\infty (1-\zeta\beta^{-m})^m$$

$$\times \exp[-\beta]\,d\beta \quad (3b)$$

where $\beta = (T/\Sigma)^{m+1}$ and $\zeta = h/(\lambda\Sigma)$. Numerical integration of Eq. (3b) yields the nondimensional cumulative distributions plotted in Fig. 2. Note that as m increases, the pullout lengths decrease and become zero when $m \to \infty$.

It is also possible to calculate the mean pullout length from Eq. (1)[5]

$$\langle h \rangle = \frac{\lambda\Sigma}{m+1}\Gamma\left(\frac{m+2}{m+1}\right) \quad (4)$$

Debonding and Sliding Processes
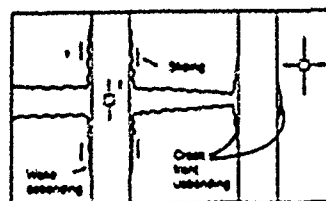
- Debonding is a prerequisite for toughening.
- Sliding governs toughening.

Crack propagation and fracture in ceramic-matrix composites involve debonding and sliding processes.

where Γ is the gamma function. The distribution of the pullout lengths therefore contains information about the parameters τ, S_0, and m.

The above analysis, as well as that conducted by Thouless and Evans,[4] assumes that the failure of one fiber does not affect the stresses in neighboring fibers, except through changes in the stress T between the crack surfaces induced by such failures. Consequently, the results are only applicable when the sliding resistance of the interface and the volume fracture of fibers are sufficiently small that fiber breaks do not cause stress concentrations in surrounding fibers. Interactive effects would cause fiber failure and pullout lengths that exhibit significant spatial correlation. Consequently, one measure of the applicability of the above statistical results is the spatial randomness of pullout length, as elaborated below.

A second distribution of interest includes measurements made of mirror radii on the fracture surfaces of the fibers. These measurements enable the local stress at which the fiber fails, S, to be determined. It is noted that T and S are related by

$$T = S + 2\tau h/R \qquad (5)$$

Consequently, if simultaneous measurements are made of h and S, the mean value of T can be found from

$$\langle T \rangle = \langle S \rangle + 2\tau \langle h/R \rangle \qquad (6)$$

From Eq. (1), this is equal to

$$\langle T \rangle = 2 \int_S^{T_{max}} \int_0^{\tau T} T\phi(T,z)\, dz\, dT$$

$$\langle T \rangle = \Sigma \int_0^{\beta_{max}} \beta^{'\,m+1} \exp(-\beta)$$

$$\times\ d\beta = \Sigma\gamma\left\{\frac{m+2}{m+1},\beta_{max}\right\} \qquad (7)$$

where $\beta_{max} = (T_{max}/\Sigma)^{m+1}$. T_{max} is the largest value of T represented by the test population, and γ is the incomplete gamma function. A comparison of Eqs. (6) and (7) can be made in order to independently check the magnitudes of τ, S_0, and m.

The transition between steady-state cracking and fracture from a dominant flaw is one of the most fundamental changes in mechanical properties. Steady-state cracking occurs at an applied stress[8-10]

$$\sigma_s = [6\tau K_m^2 f^2(1-f)(1+\xi)/R]^{1/3} \qquad (8)$$

where K_m is the matrix toughness. Good experimental confirmation of this stress has been obtained on several composite systems.[10,11] As τ increases, σ_0 increases so that the steady-state cracking stress eventually exceeds the maximum stress that can be sup-

ported by the fibers. At this stage the macroscopic fracture process should change to one with a low failure strain. An approximate statistical analysis of fiber failure in the presence of steady-state cracking with multiple cracks has shown that the peak stress supported by the fibers is given by[12]

$$\dot{\sigma}_m = fS$$

$$\times \exp\left\{-\frac{\left[1-\left(1-\frac{\tau d}{RS}\right)^{m+1}\right]}{(m+1)\left[1-\left(1-\frac{\tau d}{RS}\right)^m\right]}\right\} \qquad (9)$$

where

$$\left(\frac{RS}{\tau d}\right)^{m+1} = \left(\frac{A_2}{2\pi RH}\right)\left(\frac{RS_0}{\tau d}\right)$$

$$\times\left[1-\left(1-\frac{\tau d}{RS}\right)^m\right]^{-1} \qquad (10)$$

H is the specimen length and the crack spacing d is[3]

$$d \approx \frac{\sigma_s R}{2f\tau} \qquad (11)$$

When $\dot{\sigma}_m$ becomes less than σ_s, abrupt fracture is predicted to occur at the matrix-cracking stress, resulting in a low failure strain.

III. Experimental Procedure

(1) Mechanical Properties

Test specimens of a 0°/90° cross-ply laminated LAS/SiC with a fiber volume fraction of 0.44 were prepared for tensile and flexural testing, as described elsewhere[13] Four-point flexure tests were performed with the loading axis normal to the laminate plane. The test dimension (4 mm×3 mm with inner and outer spans of 6 and 25 mm, respectively) provided a ratio of tensile to shear stress >10. The specimens were heat-treated in air at 800°C for 2, 4, 8, 16, and 100 h, because prior research[14] had indicated that heat treatment at this temperature caused systematic changes in the mechanical properties. The principal results of the mechanical tests (Fig. 3) concerned the change in fracture strain that occurred, after even brief heat treatments. This change coincided with a transition from steady-state matrix cracking to a more brittle failure from a single dominant flaw. This transition has a profound effect on the structural utility of the composite.

(2) Single-Fiber Tests

Single fibers with a gauge length of 10 mm were tested in uniaxial tension. Tests were conducted on Nicalon fibers that had been heat-treated in air at 800°C for 4, 8, and 16 h. The result-
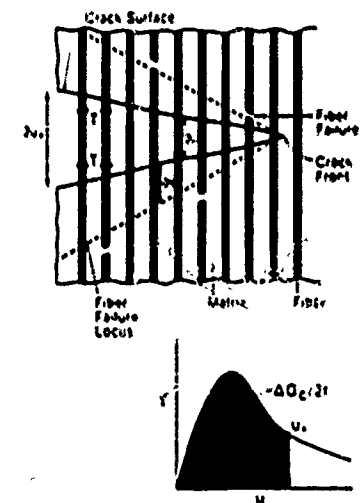

Fig. 1. Schematic illustration of fiber failure occurring away from the matrix crack plane
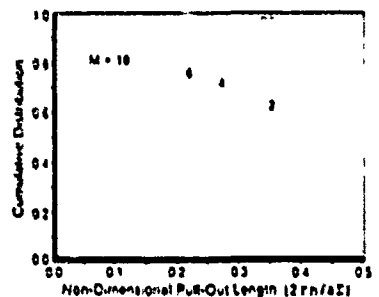
Fig. 2. Trends in the predicted cumulative pullout distributions with the statistical parameter, m

ant cumulative strength distributions are plotted in Fig 4, and the statistical parameters m and S_0 (with A_0 equated to 1 m²) are summarized in Table I It is apparent that both m and S_0 diminished systematically upon heat treatment

The fracture surfaces of each fiber were examined by scanning electron microscopy (SEM) so that the fracture origin and the mirror dimensions could be determined (see Fig 6(A)). Almost without exception, the fibers failed

The Most Probable Failure Site

↱ Because of flaw-size *distribution*, failure of the fiber does not occur at the location of maximum stress.
● The stress field seeks out the largest flaws within the decaying stress field.
● Weakest-link statistics allows the most probable site to be determined.

Fiber failure is statistical, leading to the concept of the most probable fiber failure site (Eq. (2b)).

Fig. 3. Mechanical property results on heat-treated composites (A) tensile tests, (B) flexural tests.
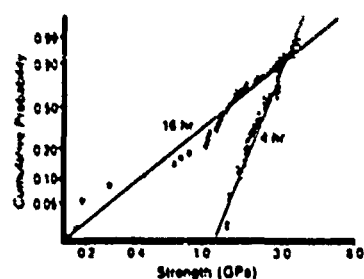
Fig. 4. Cumulative strength distributions obtained from single-fiber tests. Results are shown for tests on fibers heat-treated for 4 and 16 h at 800°C.
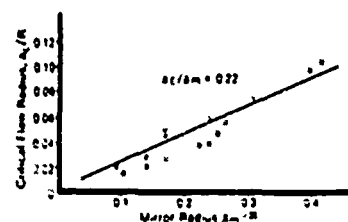
Fig. 5. Relationship between mirror and flaw radii

from surface flaws. The formulation for Eq. (1) in which surface flaws were assumed to be critical therefore appears to be justified The mirror radius, a_m, is expected to be proportional to the critical flaw radius, a_c, when the ratio a_m/R is small The two quantities are governed by the relationships[15]

$$K_f \sim S\sqrt{a_m}/3.5 \tag{12}$$

and

$$a_c/a_m \sim 0.22 \tag{13}$$

where K_f is the fracture toughness of the fiber and S is the stress on the fiber at the flaw plane.

A plot of a_m/R against a_c/R with the predicted slope of 0.22 superimposed (Fig. 5) reveals that, although

appreciable scatter exists, the relationship between the two quantities is consistent with expectations. The fracture toughnesses of the fibers were estimated using Eq. (12) (Table I) The resultant values ($K_f \sim 1$ MPa m¹ᐟ²) seem reasonable for such a fine-grained, nonstoichiometric material[*]

(3) Pullout Measurements

The fracture surfaces of the four-point flexure specimens were examined by SEM (Fig. 6) The pullout lengths were measured by using one fiber as a reference, measuring all projected lengths with respect to that fiber, and then tilting the specimen to measure the actual length of the reference fiber. A certain degree of ambiguity exists concerning the measurements of small pullout lengths. In some cases, the crack appears to have simply deflected at the fiber or not interacted at all with it, whereas other examples exhibit pullout characteristics (Fig. 6(A)). A quantitative estimate of the relative occurrences of

Table I.   Composite Properties Obtained for Single-Fiber and Pullout Tests[*]

Heat-treatment time[†] (h)	m	S_0 (MPa)[‡]	K_f (MPa·m¹ᐟ²)	τ (MPa)	l_e
4	4.2	80	1.03 [°]	30	0.91
8	3.0	17	0.79	30	0.65
16	1.7	0.33	0.76	200	0.54

[*]Mean radius of fibers $R = 7$ μm. [†]At 800°C [‡]$A_0 = 1$ m²

*Note that K_c for polycrystalline SiC is ~2 MPa m¹ᐟ² while that for most amorphous ceramics is ~0.5 to 1 MPa m¹ᐟ²

pullout and crack-front failure can be established by analysis, as elaborated in the next section. The resultant histograms of the pullout lengths are presented in Fig. 6(A). It is evident that while an abrupt change in the pullout distribution occurred upon initial heat treatment (4 h at 800°C), more modest changes occurred during subsequent annealing (up to 16 h). However, it is worth noting that the sample that was heat-treated for 100 h showed no pullout and the fracture surface was essentially featureless.

Effect of Sliding Stress on Fiber Failure
A Weakest-Link Failure Problem

Large τ Case

Small pullout length, *h*

The most probable fiber failure site is close to the matrix crack because the axial stress in the fiber drops rapidly with z.

Small τ Case

- Stress transfer from intact fiber to matrix occurs gradually.
- σ_t decreases slowly with z.
- The fiber failure site is remote from the matrix crack.

The failure site is strongly influenced by the sliding stress τ.

In order to address correlations among fiber fracture sites and thus pullout lengths, the dependence of the pullout distribution on lateral location has been examined. At the simplest level, the existence of extensive interactive effects can be discounted on the basis that pullouts do not exhibit local "clumping", i.e., patches that have many large or small pullouts are not evident (Fig 6(B)). A more rigorous analysis of possible interaction effects and their importance awaits further study.

*Chemical solutions which allow dissolution of the matrix (e.g. HF) also remove the SiO₂ film on the fibers in the heat-treated materials and thus such a procedure for ascertaining in situ fiber strength degradation would be of questionable merit.

The fracture surfaces of the fibers from the four-point bend specimens were also examined by SEM. Where possible, the effective radii of the fracture mirrors were measured (Fig. 6(C)) and related to the corresponding pullout length *h*. The mirror size directly corresponded to the local stress, S, at which the fiber failed Eq. (12). The fracture mirrors always initiated at the fiber surface, as for single fibers. Furthermore, only relatively large mirror radii could be accurately measured. The population of strengths, S, represented by these measurements is thus censored to include about half the population and is limited to relatively low values $S_{-},, = 1.1$ GPa. The relationship between *h* and S (Fig. 8) reveals that the distribution of S is independent of *h* and insensitive to heat-treatment time. Such behavior is consistent with a spatially random distribution of flaws in the fibers.

IV. Analysis of Results

The assumed fiber-fracture/toughening model has three unknown material variables the statistical parameters for fiber failure S_0 and *m* and the interfacial shear resistance τ These parameters also govern the fiber strengths and the pullout distributions It should therefore be possible to determine them from the experiments described in the previous section They cannot be independently evaluated from each set of experiments so the results had to be analyzed with the assumption that the values of *m* and S_0 determined from the single-fiber tests were appropriate for the fibers in the matrix Values of τ could then be estimated from the other measurements, and a consistency check made by comparing the different values of τ This approach relies on the assumptions that the characteristics of the fibers do not change upon incorporating them into the composite and that the effects of heat treatment do not change substantially when the fibers are surrounded by a matrix. This premise is difficult to verify, because of the problems involved in extracting undamaged fibers from the composite, especially when the SiO₂ caused by oxidation is present.¹ Careful extraction studies conducted on the as-ceramed composite¹⁶ (no SiO₂ layer) have indicated that some fiber degradation is possible during processing, probably associated with Al and Mg diffusion into the fiber However, the effect is relatively small Furthermore, it is not clear whether the degradation caused by oxidation would be influenced by such processing effects.

The first estimate of τ was obtained from the measured pullout distribution (Fig. 7), using Eq. (3b), as elaborated in the Appendix For this purpose, the
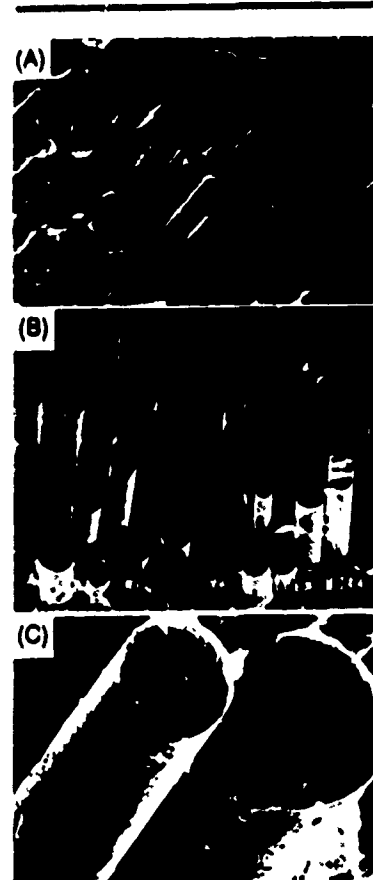

Fig. 6. Scanning electron micrographs of (A) fiber pullout showing some fibers that fail at the crack front (arrowed). (B) the lack of obvious spatial correlation between fiber failure sites. (C) the fracture mirrors observed on two fibers (arrowed)
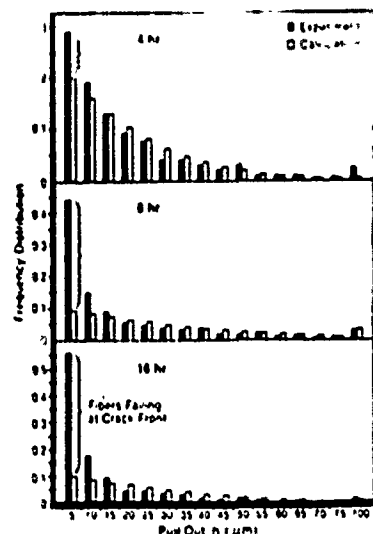

Fig. 7. Frequency distribution of pullout lengths: measured and predicted values indicating the fibers that fail at the crack front

quality in fiber failure was recognized. The values of m and S_n obtained from the single-fiber test (Table I) were used to determine the magnitude of τ that gives a best fit to the pullout distributions for $h>5$ μm. The comparisons are shown in Fig. 6(C) and the associated values of τ are summarized in Table I. It is apparent from these comparisons that the percentage of fibers in the 0- to 5-μm interval found experimentally exceeds that expected by extrapolation of the pullout data obtained from $h>5$ μm. If it is assumed that this excess arises from fibers that fail at the crack tip, then a reduced volume fraction of fibers that pullout, f_e, can be deduced (Table I). It is supposed that the fraction given in Table I represents that proportion of fibers that do not fail at the crack front and therefore contribute to the toughening process. Evidently, this fraction decreases with increase in heat-treatment time.

A useful check on the magnitude of τ can be achieved by using Eqs (6) and (7) in conjunction with the results presented in Fig. 8. First, $\langle T \rangle$ was obtained from Eq. (6) by using the test data and the values of τ deduced from

Fig. 8. Relationship between pullout length and fiber failure stress obtained from measurements of the mirror size

In-Situ Fiber Strength

Mirror Schematic

● Calibration has shown that the stress S on the fiber when it fails is related to mirror radius a_m (Eq. 12).
● Therefore, the fiber failure stress in the composite can be evaluated.

In-situ fiber strengths can be assessed from fracture mirrors.

the pullout measurements (Table I). Second, using the same initial choices for τ, T_{m}, was determined from the datum on Fig. 8 that gives the largest value of T. A corresponding value of $\langle T \rangle$ was calculated from Eq. (7). The

Stress–Strain Curve for Composite
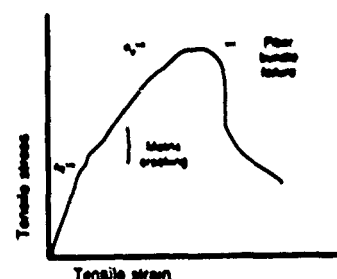
● σ_0 increases as τ increases.
● The material is macroscopically brittle when $\sigma_0 > \sigma_u$.
● This happens in Fig. 5 after a heat treatment longer than 4 h.

The composite stress–strain curve is affected by the interface sliding resistance.

magnitude of τ was then changed and the process iterated until similar values of $\langle T \rangle$ were obtained from both Eqs. (6) and (7). This analysis is sensitive to T_{m}, and therefore the accuracy of this method was limited by the relatively small number of measurements obtained in the present study. Nevertheless, the analysis revealed that τ was of the order 30 to 40 MPa in specimens annealed for either 4 or 8 h and 100 to 200 MPa in those specimens annealed for 16 h. Such values of τ are in agreement with those determined from the pullout distribution (Table I).

V. Discussion

Trends in the steady-state cracking stress σ_s can be predicted using Eq. (8) with l replaced by l_e. In the as-ceramed composites σ_s is predicted to be $\sim$100 MPa, consistent with measurements (Fig. 3). A much higher value, $>$500 MPa, is predicted after heat treatment when the original carbon layer is replaced by SiO_2,[5] based on the τ given in Table I. Estimates of the ultimate strength, σ_m, given by Eq. (9) indicate that, in the as-ceramed state, this strength should be $\sim$300 MPa, decreasing slightly to $\sim$250 MPa after 8-h heat treatment. Such predictions would therefore imply that a transition to a low strain failure mode should occur after heat treatment of $\sim$4 h. Such behavior is consistent with the mechanical property measurements. It should be noted that *this* transition does not correspond to the criterion suggested elsewhere[3,4] in which the fibers bridging a

Initial Debonding

Carbon Coatings on Nicalon
Debond

No Debonding

● This explains fiber failures on
the matrix crack plane as
noted by an arrow in Fig. 6(A)

Debonding is governed by the proper-
ties of the fiber coating.
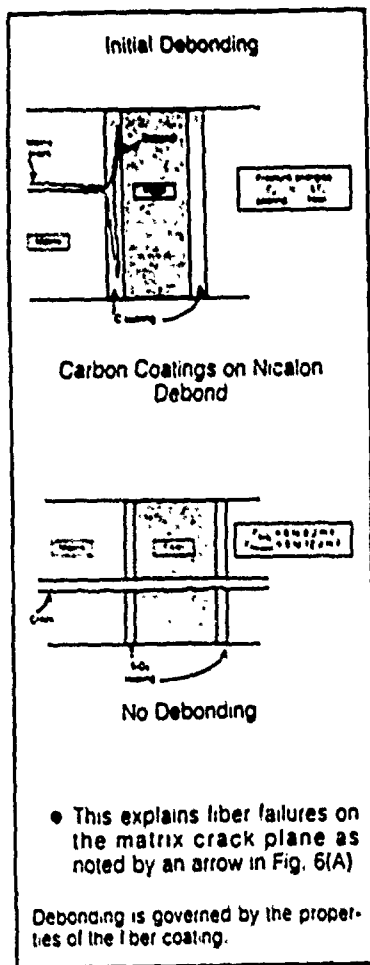
single matrix crack are incapable of
supporting the applied load. Ration-
alization of this point is the subject of
further study

The systematic reduction in pullout
length with heat treatment clearly indi-
cates that τ and h are interrelated.
Prediction of trends in pullout toughen-
ing, being governed by the product
τh^2,[1,4] thus requires that the interrela-
tionship $h(\tau)$ be rigorously established.
The original hypothesis concerning
$h(\tau)$, that fiber failures occur in the
crack wake, is qualitatively supported
by the good correspondence between
measured and predicted pullout distri-
butions (Fig. 7).

Based on limited data, it appears as
if the sliding resistance is character-
ized by three regimes. Originally,
when carbon is present, τ is small and
of order 2 MPa.[3,10] Upon heat treat-
ment, when the carbon is removed
and replaced by silica, τ increases
substantially. Since the debond gap is
similar in the two instances,[4] this
change in τ is presumed to be associ-
ated with an increase in friction coeffi-
cient, μ. Noting that μ for the carbon
layer has been estimated as ~0.01,[15]
an increase in τ by over an order of

magnitude suggests that μ should be
of the order of unity in the presence of
silica consistent with measured val-
ues ($\mu \approx 0.3$ to 0.8).[17]

VI. Concluding Remarks

Measurements of mechanical prop-
erties and of fiber pullout lengths used
in conjunction with statistical analysis
of fiber failure provide a consistent de-
scription of the behavior of a model
ceramic-matrix composite. Most im-
portant, the transition from steady-
state cracking to brittle fracture from a
single dominant flaw that occurs upon
heat treatment in air has been inter-
preted in terms of changes that occur
at the fiber-matrix interface. Specifi-
cally the replacement of a carbon layer
by a silica layer causes the frictional
sliding of unbonded fibers over the
matrix to become substantially more
difficult, resulting in fiber failure closer
to the crack plane. The increase in
sliding resistance has been attributed
to an increase in the friction coeffi-
cient. The importance of interfaces
having a low friction coefficient thus
emerges as a major conclusion of this
research.

Pullout Toughening

● The material is more brittle as τ
increases.
● This happens when SiO_2
replaces C at the interface
(Fig. 2).
● Frictional *sliding* along the
debonded interface is a major
contribution to toughness,
which varies as $\tau h^2/R$.
● Energy is dissipated (as heat)
by frictional sliding; this is a
large effect.
● As τ decreases, h increases
rapidly and toughness
increases.

The sliding resistance τ influences the
pullout length h and this controls the
toughness.

APPENDIX

Method for Obtaining τ from Pullout Distribution

To facilitate the evaluation of τ from the pullout distribution, the following statistical results are useful. For the single-fiber tensile tests, the failure probability can be represented by

$$\Phi = 1 - \exp\left[-\frac{2\pi RL}{A_0}\left(\frac{S}{S_0}\right)^m \right] \qquad (A-1)$$

where L is the gauge length. The median strength S_1 is thus related to the statistical parameters by

$$A_0 S_0^m = 2\pi RL S_1^m/(\ln 2) \qquad (A-2)$$

Substituting for $A_0 S_0^m$ in Eq. (4) then gives

$$\langle h \rangle = \frac{R}{2(m+1)\tau^{1/m+1}}$$
$$\times \left[\left(\frac{L}{R}\right)\frac{S_1^m(m+1)}{\ln 2} \right]\Gamma\left[\frac{m+2}{m+1}\right] \qquad (A-3)$$

Rearranging Eq. (A-3) to give τ results in

$$\frac{\tau}{S_1} = \left\{ \frac{\Gamma\left[\dfrac{m+2}{m+1}\right]}{2(m+1)}\left(\frac{R}{\langle h \rangle}\right) \right\}^{(m+1)/m}$$
$$\times \left[\frac{(m+1)L}{R\ln 2}\right]^{1/m} \qquad (A-4)$$

where $\langle h \rangle$ represents the mean pullout length, excluding the fibers that failed at the crack front. Equation (A-4) provides a preliminary estimate of τ, which may be refined by small iterations that provide the best fit to the full distribution at $h > 5$ μm.

References

[1] D C Phillips, "Interfacial Bonding and the Toughness of Carbon-Reinforced Glass and Glass-Ceramics." *J Mater Sci*, 9, 1847–54 (1974)

[2] E Y Luh and A G Evans "High-Temperature Mechanical Properties of a Ceramic-Matrix Composite." *J Am Ceram Soc*, 70 [7] 466–69 (1987)

[3] D B Marshall and A G Evans, "Failure Mechanisms in Ceramic-Fiber/Ceramic-Matrix Composites." *J Am Ceram Soc*, 68 [5] 225–31 (1985)

[4] M D Thouless and A G Evans, "Effect of Pull-Out on the Mechanical Properties of Brittle-Matrix Composites." *Acta Metall*, 36 [3] 517–22 (1988)

[5] K Prewo and J J Brennan, "Silicon Carbide Fiber Reinforced Glass-Ceramic Matrix Composites Exhibiting High Strength and Toughness." *J Mater Sci*, 17, 1201 (1982)

[6] E Bischoff, M Ruhle, O Sbaizero, and A G Evans, "Microstructural Studies of the Interfacial Zone of a SiC-Fiber-Reinforced Lithium Aluminum Silicate Glass-Ceramic" to be published in *J Am Ceram Soc*

[7] P G Charalambides and A G Evans, "Effects of the Interface Fracture Resistance on the Mechanical Properties of Some Brittle Matrix Composites", to be published in *J Am Ceram Soc*

[8] D B Marshall, B N Cox, and A G Evans "The Mechanics of Matrix Cracking in Brittle-Matrix Fiber Composites." *Acta Metall*, 33 2013–21 (1985)

[9] L Budiansky, J W Hutchinson, and A G Evans, "Matrix Fracture in Fiber-Reinforced Ceramics." *J Mech Phys Solids*, 34, 167–89 (1986)

[10] D B Marshall, "Interfaces in Ceramic Fiber Composites", pp 858–68 in Ceramic Microstructures. The Role of Interfaces Edited by J A Pask and A G Evans Plenum Press, New York, 1985

[11] K Prewo, "Fiber Reinforced Ceramics New Opportunities for Composite Materials", presented at the 4th U S –Japan Conference on Composite Materials, Washington, DC, June 1988.

[12] D B Johnson-Walls, M S Thesis, University of California, Berkeley, CA, 1986

[13] O Sbaizero and A G Evans, "Tensile and Shear Properties of Laminated Ceramic Matrix Composites" *J Am Ceram Soc* 69 [6] 481–86 (1986)

[14] J J Brennan, "Interfacial Chemistry and Bonding in Fiber Reinforced Glass-Ceramic Matrix Composites" pp 387–400 in Ceramic Microstructures The Role of Interfaces. Edited by J A Pask and A.G. Evans Plenum Press, New York, 1988

[15] R W Rice, Treatise on Materials Science and Technology, Vol 11, p 199 Academic Press, New York, 1976

[16] K Prewo, "Tension and Flexural Strength of Silicon Carbide Fibre-Reinforced Glass Ceramics." *J Mater Sci*, 21, 3590–600 (1986)

[17] S M Wiederhorn, unpublished research   □

MATERIALS
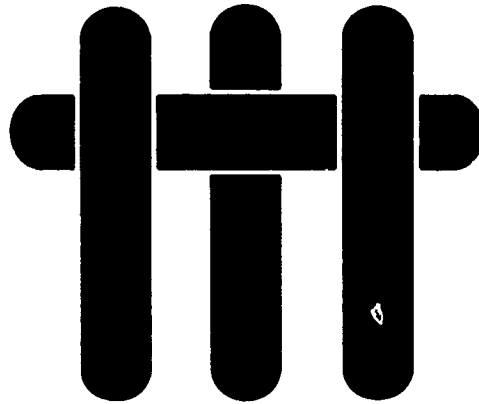
DEBONDING PROPERTIES OF RESIDUALLY

STRESSED BRITTLE-MATRIX COMPOSITES

P. G. Charalambides and A. G. Evans

Materials Department
College of Engineering
University of California, Santa Barbara
Santa Barbara, California 93106

Debonding Properties of Residually Stressed Brittle-Matrix Composites

P.G. Charalambides and Anthony G. Evans*

Materials Department, College of Engineering, University of California,
Santa Barbara, California 93106

Trends in interface debonding have been calculated during fiber pullout for composites with interfaces subject to residual tension. The debond behavior is shown to depend sensitively on the thermal expansion mismatch. The results are used as the basis for designing a pullout test specimen suitable for measuring the mixed-mode fracture energy of bimaterial interfaces. The solutions also provide the background needed to assess the role of debonding in the toughening of ceramics by fibers. [Key words: composites, fracture, interfaces, mechanical properties, fibers.]

I. Introduction

EXPERIMENTAL observations reported in companion studies[1,2] suggest that, in an important class of tough ceramic composites, a low fracture resistance interface exists with interfaces subject to residual *tension*, such that partial debonding occurs on cooling. When the matrix crack front approaches the fiber, the initial debonds extend along the interface (Appendix A) and inhibit fiber failure (Fig. 1).[3] Many of the fibers thus remain intact and allow toughening by bridging and pullout.[4]

Understanding of the subsequent events involved in fiber failure can be achieved by analyzing the behavior of debond cracks, as the intact fibers are axially loaded in the crack wake between the crack surfaces (Fig. 1). One of the important issues concerns the ability of the interface to further debond in the crack wake. The incidence and extent of such debonding has a strong influence on the stress in the fiber and thus on pullout toughening, through the influence of this stress on the location of fiber

failure.[4] In order to address this issue, the stress and displacement fields near the debond tip, as well as relationships with the critical values for debond growth, are required. Some basic mechanics of interface cracks[5-7] (Appendix B) indicate that this problem can be studied by using the crack tip stresses and displacements to calculate the strain energy release rate $\mathcal{G}$ and the phase angle of loading, ψ, at the debond (Appendix B). The latter is a measure of the mixity of opening and shear along the surface of the debond crack. A numerical method is used in the present study to calculate both $\mathcal{G}$ and ψ.

Further background is provided by recent investigations of the fracture energy of interfaces,[5,8] $\mathcal{G}_{ic}$, which indicate that such fracture can be characterized by a locus involving $\mathcal{G}_{ic}$ and ψ. Moreover, for *all-brittle* constituents, $\mathcal{G}_{ic}$ typically becomes large as $\psi \to \pi/2$ (Fig. 2),[8] because of asperity contacts on the debond surfaces within a bridging zone near the debond tip. Evaluation of the phase angle thus emerges as a vitally important aspect of the study. Such analysis is performed in the conventional manner by ignoring the shear tractions that exist along asperity contacts in the bridging zone. Then the frictional contacts govern the fracture $\mathcal{G}_{ic}(\psi)$, but do not enter the mechanics.

Several other phenomena having importance for composites are also examined using the present analysis. First, the calculation of $\mathcal{G}$ and ψ can be used to interpret *pullout experiments* which are designed to *measure* the debond fracture energy, $\mathcal{G}_{ic}$, at large values of the phase angle. Furthermore, the magnitudes of $\mathcal{G}$ and ψ also provide the basis for determining whether fibers are able to fail from the end of the debond rather than within the debond length, by weakest-link statistics. Understanding of these fiber failure possibilities is critical to the analysis of pullout toughening.[4] Finally, analysis of the compliance of debonded fibers provides new insight about the bridging contribution to toughness.

II. Debonding Mechanics

(1) Stress-Free Composites

The stress on a debonded fiber caused by matrix opening results in a stress intensification at the end of the debond such that, in the absence of contacting asperities, steady-state conditions ($\mathcal{G}$ independent of debond length) must obtain when the debond length is somewhat larger than the fiber radius. Furthermore, *in the absence of residual stress*, the approximate steady-state strain energy release rate $\mathcal{G}$ can be analytically derived. This is achieved for the composite cylinder shown in Fig. 2(A) by noting that the axial stresses are substantially larger than the radial and tangential stresses, whereupon $\mathcal{G}$ is closely related to the strain energies, U, in regions (i) and (ii) of Fig. 2(B) by

$$\mathcal{G} = (U_i - U_{ii})/2\pi a \Delta \ell \tag{1}$$

where a is the fiber radius and $\Delta \ell$ is an increment in debond length (Fig. 2(B)). It is straightforward to derive the strain energies as

$$U_i = \frac{\pi a^2 \Delta \ell}{2 E_f} t^2 \tag{2a}$$

$$U_{ii} = \frac{\pi a^2 \Delta \ell}{2 E_f} \left[\left(\frac{\sigma_f}{t} \right)^2 + \frac{1-f}{f} \frac{E_f}{E_m} \left(\frac{\sigma_m}{t} \right)^2 \right] t^2 \tag{2b}$$
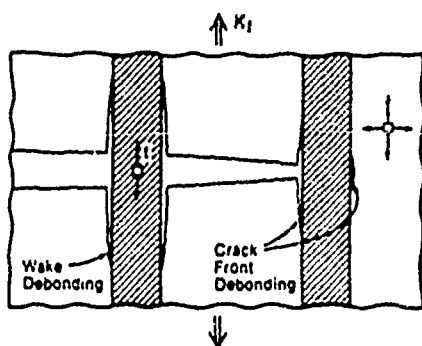
Fig. 1. Schematic diagram indicating crack front and wake debonding in fiber-reinforced ceramics.
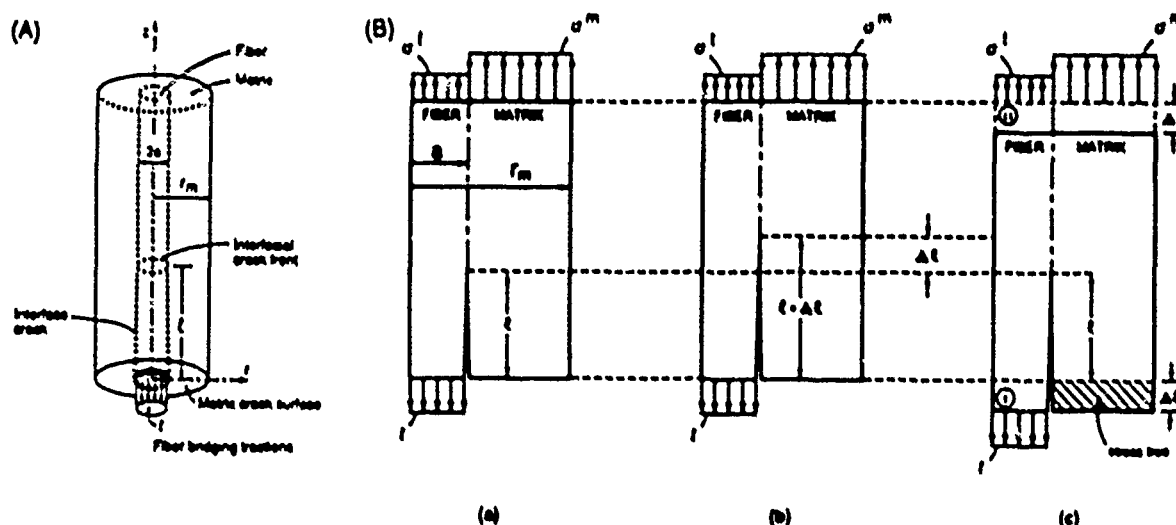
Fig. 2. (A) The composite cylinder used for analysis and (B) the regions of stress release in steady state.

where E is Young's modulus,[*] and the stresses σ_f and σ_m are given by

$$\sigma_f = \frac{f}{f + \Sigma(1-f)} t$$

$$\sigma_m = \frac{f\Sigma}{f + \Sigma(1-f)} t$$

with $\Sigma = E_m/E_f$. Inserting U from Eqs. (2) into Eq. (1) gives

$$\frac{\mathcal{G}E_f}{t^2 a} = \frac{1}{4} \frac{\Sigma}{\Sigma + \frac{f}{1-f}} \qquad (3)$$

It is noted that in bimaterial systems with equal Poisson's ratios (i.e., $v_f = v_m$) loaded with an axial stress t, the interface pressure and therefore the radial and tangential stresses are zero. In this instance, the expression for $\mathcal{G}$ given by Eq. (3) is exact. The trends in nondimensional $\mathcal{G}$ are plotted in Fig. 3.

Further progress is achieved by numerically evaluating the strain energy release rate and the phase angle at the debond front, using a finite-element procedure developed for interface cracks[*] (Appendix C). The finite-element equations were solved for the fiber/matrix unit-cell boundary value problem shown in Fig. 2(A). Because of the axisymmetry of the problem, it is sufficient to solve the finite-element equations in only a radial plane of the unit cell. A typical finite-element mesh with the boundary conditions is depicted in Fig. 4. The results of the finite-element calculations are summarized in Figs. 3, 5, and 6.[*] Steady-state conditions are confirmed when the debond length $\ell \geq a$ (Fig. 2(A)) such that the steady-state nondimensional strain energy release rates, $E_f\mathcal{G}/t^2 a$, agree closely with the analytical solutions (Fig. 3). The steady-state phase angles are strong functions of the relative modulus, E_f/E_m, and of the relative Poisson ratio v_f/v_m. It is convenient to express these trends by means of a nondimensional phase angle, ψ^* (Appendix B), as depicted in Fig. 6 and Table I. The phase angle is typically large ($\psi^* > 1$), indicative of large relative shear displacements along the debond surfaces. It is also noted that $\mathcal{G}$ has a finite value at $\ell = 0$, governed by the matrix crack singularity. The associated nondimensional $\mathcal{G}$ for the homogeneous material is 0.06,[10] consistent with the present calculations (Fig. 5).

Fig. 3. Trends in steady-state strain energy release rate with volume fraction: both approximate analytical and numerical results are plotted. The numerical results were obtained for Poisson's ratios $v_f = v_m = 0.25$; $\Sigma = E_m/E_f$.
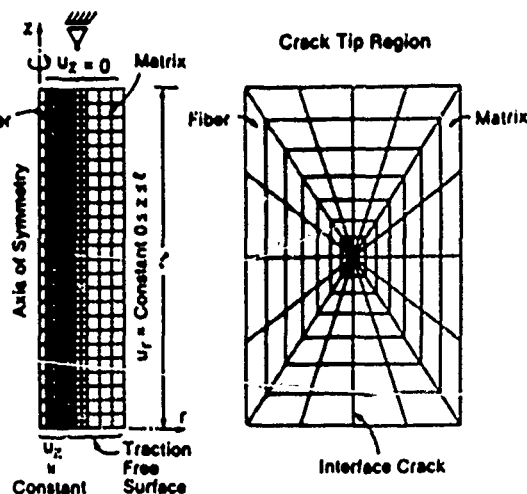
Fig. 4. Typical finite-element mesh and the boundary conditions used in solving the problem shown in Fig. 2(A).

---

[*]Henceforth, the subscripts f and m will be used to represent quantities relevant to the fiber and matrix, respectively.

[*]These results correspond to a crack tip system (see Fig. B1) where the matrix is taken as material 1 and the fiber as material 2.
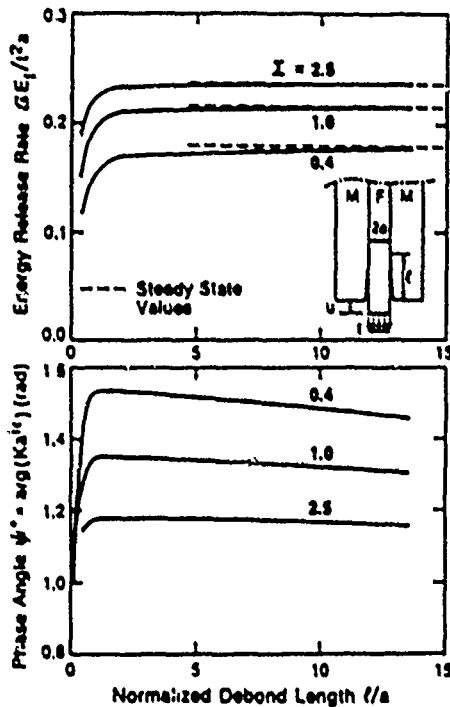
Fig. 5. Nondimensional strain energy release rate $'\mathcal{GE}_f/t^2a$ and nondimensional phase angle,$\psi°$: trends with debond length ℓ/a for a fiber volume fraction $f = 0.15$ and Poisson's ratios $\nu_f = \nu_m = 0.25$.
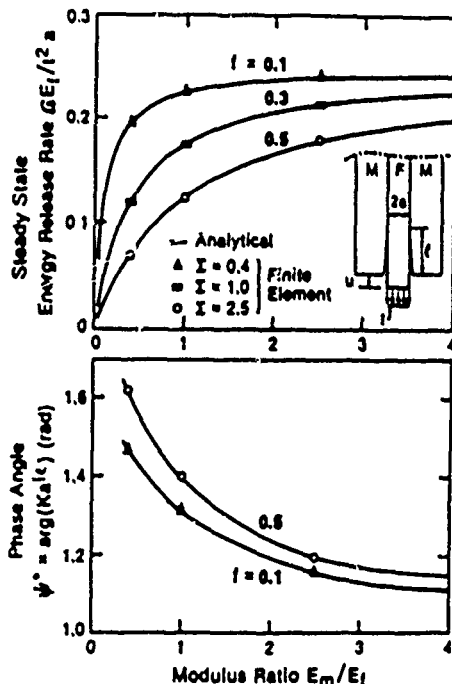
Fig. 6. Nondimensional strain energy releases rate and phase angle: trends with modulus ratio and volume fraction for $\nu_f = \nu_m = 0.25$.

Table I. Poisson's Ratio Effects on the Stress Intensities at the Crack Tip of a Debonded Fiber, $E_m/E_f = 1$

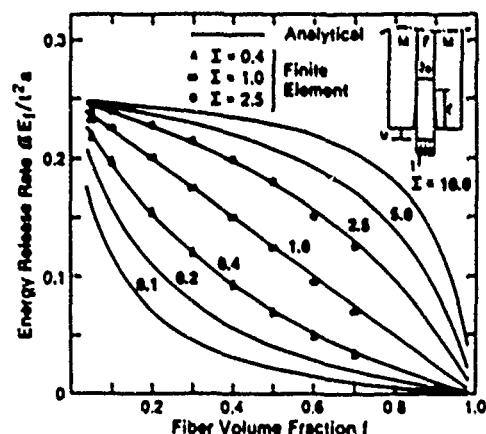| f	ν_f	ν_m	$\dfrac{\text{Re }(K a^u)}{t\sqrt{a}}$	$\dfrac{\text{Im }(K a^u)}{t\sqrt{a}}$	$\dfrac{\mathcal{G}^s}{a t^2}$	$\dfrac{\mathcal{G}^u}{a t}$
0.15	0.3	0.2	0.132	0.461	0.215	10.5
0.15	0.25	0.25	0.117	0.463	0.214	10.5
0.15	0.2	0.3	0.106	0.467	0.214	10.5
0.30	0.3	0.2	0.112	0.419	0.176	10.2
0.30	0.25	0.25	0.094	0.421	0.175	10.2
0.30	0.2	0.3	0.079	0.426	0.175	10.3
0.50	0.3	0.2	0.079	0.357	0.125	9.9
0.50	0.25	0.25	0.060	0.358	0.124	10.0
0.50	0.2	0.3	0.044	0.362	0.124	10.0

(2) Residually Stressed Composites

When the thermal expansion coefficient of the fiber, α_f, exceeds that of the matrix, α_m, the interface is subject to residual tension upon cooling and the debond energy release rates are enhanced. These energy release-rates can be calculated by noting that the stress intensities from the applied loads, and from the residual field, can be linearly superposed. The stress intensities in steady state provided by the residual and applied fields have thus been calculated using finite elements[*] (Appendix C) with the boundary adjusted to ensure that the shrinkage of the unit cell shown in Fig. 2(A) is compatible with its neighboring cells. For an elastically homogeneous composite ($\Sigma = 1$), the net stress intensities K^r on the stressed fibers in the matrix crack wake are

$$\frac{K_i^r}{E\Delta\alpha\Delta T\sqrt{a}} = 0.28 + 0.11\tau \qquad (4a)$$

$$-\frac{K_u^r}{E\Delta\alpha\Delta T\sqrt{a}} = -0.51 + 0.45\tau \qquad (4b)$$

where $\Delta\alpha = \alpha_f - \alpha_m$, and ΔT is negative and $\tau = t/E\Delta\alpha\Delta T$. Corresponding results for composites having inhomogeneous elastic properties can be expressed in general by

$$\frac{\text{Re }(K^r a^u)}{E_f\Delta\alpha\Delta T\sqrt{a}} = c_1 + c_2\tau_f \qquad (5a)$$

$$\frac{\text{Im }(K^r a^u)}{E_f\Delta\alpha\Delta T\sqrt{a}} = c_3 + c_4\tau_f \qquad (5b)$$

where $\tau_f = t/E_f\Delta\alpha\Delta T$, Re and Im refer to the real and imaginary components of K, respectively (Appendix B), and the coefficients c_i depend on the elastic properties, as summarized in Table II. The results can now be expressed in terms of a strain energy release rate $\mathcal{G}^r/E_f a(\Delta\alpha\Delta T)^2$ and the nondimensional phase angle, $\psi°$ (Appendix B), as

$$\frac{\mathcal{G}^r}{E_f a(\Delta\alpha\Delta T)^2} = k_1 + k_2\tau_f + k_3\tau_f^2 \qquad (6a)$$

$$\psi° = \arctan\left[\frac{\text{Re }(K^r a^u)}{\text{Im }(K^r a^u)}\right] = h(\tau_f) \qquad (6b)$$

with k_i being the coefficients presented in Table II, leading to the trend in $\mathcal{G}^r$ plotted in Fig. 7(A); $\psi°$ is the function plotted in Fig. 7(B). Several aspects of the results are noteworthy. Before a stress t is applied, $\mathcal{G}$ has a residual value and a large negative phase angle. Application of stress initially causes $\mathcal{G}$ to decrease, because the phase angle governed by the applied loading and the residual field have opposite sign. Consequently, $\psi°$ changes sign from negative to positive at a stress $t \approx E_f\Delta\alpha\Delta T$. As t becomes larger than $E_f\Delta\alpha\Delta T$, $\mathcal{G}$ increases monotonically with t, and when $t \geq 5E_f\Delta\alpha\Delta T$, $\mathcal{G}$ has essentially the value expected from the applied load alone (Eqs. (6)).

III. Crack Surface Compliances

The relationship between the fiber tractions, t, and the crack opening, u, which governs the bridging contribution to toughness can also be deduced from the numerical results, as summarized in Fig. 8. Linear behavior obtains, as expected for steady state, such that in the absence of residual stress

$$\frac{uE_f}{t\omega} = \lambda_1(f, \Sigma) + \lambda_2(\Sigma)\frac{\ell}{c} \qquad (7)$$

where λ_i ($i = 1, 2$) are coefficients that vary minimally with Σ and f (Fig. 8 and Table III). Upon asperity contact, smaller values of λ obtain and are subject to further study.

A generalized expression for the total matrix crack opening u^T produced by the applied loads t and thermal stress $E_f \Delta \alpha \Delta T$ can also be obtained using the finite-element results as

$$u^T = a\Delta\alpha\Delta T(g_2 + g_1 \tau_f) \qquad (8a)$$

where

$$g_1 = \lambda_1(f, \Sigma) + \lambda_2(\Sigma)\frac{\ell}{a} \qquad (8b)$$

$$g_2 = \lambda_3(f, \Sigma) + \lambda_4(\Sigma)\frac{\ell}{a} \qquad (8c)$$

with λ_i ($i = 1, 4$) given in Table III (see also Fig. 8). These results will be used below to discuss toughening.

IV. Fiber Cracking

Some understanding of *fiber cracking* can be achieved by estimating the strain energy release rates, $\mathcal{G}^i$, associated with a small kink crack in the fiber, at the end of the debond. For a kinked crack in a homogeneous elastic body ($\Sigma_m = 1$) the stress intensity factors at the kink, K_1 and K_2, are

$$K_1 = C_{11}K_1 + C_{12}K_{II} \qquad (9a)$$

$$K_2 = C_{21}K_1 + C_{22}K_{II} \qquad (9b)$$

where K_1 and K_{II} refer to the primary crack and[10]

$$C_{11} = \frac{1}{4}\left(3\cos\frac{\beta}{2} + \cos\frac{3\beta}{2}\right) \qquad (10a)$$

$$C_{12} = -\frac{3}{4}\left(\sin\frac{\beta}{2} + \sin\frac{3\beta}{2}\right) \qquad (10b)$$

E_m/E_f	C_1	C_2	C_3	C_4	a_1	a_2	a_3
0.4	0.174	0.021	−0.296	0.307	0.189	−0.280	0.152
1.0	0.278	0.110	−0.508	0.449	0.314	−0.370	0.200
2.5	0.388	0.235	−0.778	0.548	1.486	−0.430	0.228

$$C_{21} = \frac{1}{4}\left(\sin\frac{\beta}{2} + \sin\frac{3\beta}{2}\right) \qquad (10c)$$

$$C_{22} = \frac{1}{4}\left(\cos\frac{\beta}{2} + 3\cos\frac{3\beta}{2}\right) \qquad (10d)$$

with β being the kink angle (Fig. 9). The energy release rate $\mathcal{G}^i$ of the kink crack is thus

$$\mathcal{G}^i = \frac{1 - \nu^2}{E}(K_1^2 + K_2^2)$$

$$= \frac{1 - \nu^2}{E}[(C_{11}K_1 + C_{12}K_{II})^2 + (C_{21}K_1 + C_{22}K_{II})^2]$$

$$= \frac{1 - \nu^2}{E}(a_1K_1^2 + a_2K_1K_{II} + a_3K_{II}^2) \qquad (11)$$

or

$$\frac{\mathcal{G}^i}{\mathcal{G}^T} = \frac{a_1 + a_2\arctan(\psi) + a_3[\arctan(\psi)]^2}{1 + [\arctan(\psi)]^2} \qquad (12)$$

where

$$a_1 = \frac{1}{8} + \frac{1}{2}\cos^2\frac{\beta}{2} + \frac{1}{4}\cos\beta + \frac{1}{8}\cos 2\beta$$

$$a_2 = -\sin\beta - \frac{1}{2}\sin 2\beta$$

$$a_3 = \frac{5}{8} + \frac{1}{2}\sin^2\frac{\beta}{2} + \frac{3}{4}\cos\beta - \frac{3}{8}\cos 2\beta$$

Differentiation to obtain the maximum in the *fiber* gives

$$\frac{d\mathcal{G}^i}{d\beta} = 0 \longrightarrow \frac{da_1}{d\beta}K_1^2 + \frac{da_2}{d\beta}K_1K_{II} + \frac{da_3}{d\beta}K_{II}^2 = 0 \qquad (13)$$
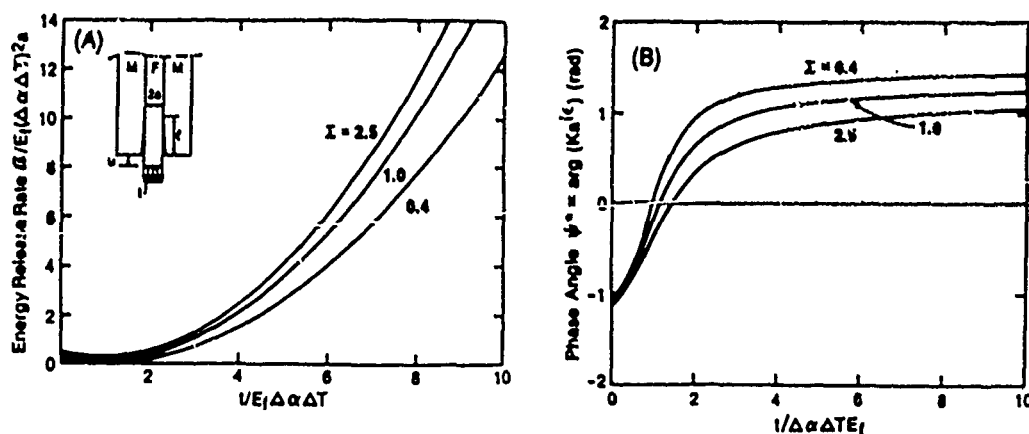

Fig. 7. (A) Variations in total nondimensional debond strain energy release rate with nondimensional applied stress for several elastic modulus ratios and fixed Poisson's ratios, $\nu_f = \nu_m = 0.25$. (B) Trends in phase angle with nondimensional stress for several elastic modulus ratios.
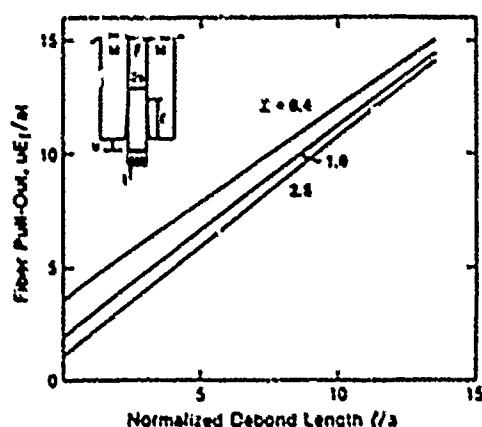
Fig. 8. Trends in nondimensional compliance with debond length for $f = 0.15$ and $v_f = r_n = 0.25$

where

$$\frac{da_1}{d\beta} = -\frac{1}{2}\sin\beta(1 + \cos\beta)$$

$$\frac{da_2}{d\beta} = 1 - \cos\beta(1 + 2\cos\beta)$$

$$\frac{da_3}{d\beta} = -\frac{1}{2}\sin\beta(1 - 3\cos\beta)$$

The resultant maximum is plotted in Fig. 9. It is apparent that $\mathcal{G}$ for the kink crack is only slightly larger than that for the interface crack at all t, indicating that *debonds are not expected to cause fiber cracking*. This conclusion has been confirmed[11] by further studies for the general case, $\Sigma \neq 1$. The problem of fiber failure in the wake, as it relates to toughening, thus appears to be dominated by statistical considerations, as elaborated below.

V. Wake Debonding

The trends in $\mathcal{G}$ with the traction t exerted by the extending matrix crack provide insight concerning debonding in the crack wake. First, it is noted that for the case of tensile residual stress at the interface, the steady-state nature of $\mathcal{G}$ would cause the debond, once critical, to extend a considerable distance along the interface. However, in many cases such extensive debonding would be inhibited either by friction at asperities on the debond interfaces (which causes $\mathcal{G}$ to become smaller than indicated

by the present calculations) or by fiber failure, as elaborated below. It is also evident from the nondimensional parameter $\mathcal{G}/E_f a(\Delta\alpha\Delta T)^2$ that debonding is more likely ($\mathcal{G}$ increases) as the fiber radius, the fiber stiffness, and the misfit strain increase. Furthermore, since $\mathcal{G}$ initially decreases upon fiber loading ($t > 0$), a threshold stress must be involved in debond extension in the crack wake. Specifically, $\mathcal{G}$ must at least exceed the value at $t = 0$ before the debond extends.

A quantitative assessment of debonding would require knowledge of the interface fracture locus $\mathcal{G}_{ic}(\psi)$ as well as the fiber bundle strength S_b, given by[12]

$$S_b = S_0(\ell/\ell_0)^{-1/m}(me)^{-1/m}$$ (14)

where S_0 and ℓ_0 are the scale parameters and m is the shape parameter, as governed by the fiber strength distribution. Specifically, the competition between debonding and fiber failure in the wake may be addressed if t in Eq. 6(u) is replaced by S_b (Eq. (14)) and $\mathcal{G}^t$ equated to $\mathcal{G}_{ic}$ at the relevant ψ. In particular, the magnitude of the debond length ℓ^* at which fiber failure occurs in preference to further debonding can be readily derived as

$$\ell^*/\ell_0 = \frac{(S_0/E_f\Delta\alpha\Delta T)^m}{me\left\{-\frac{k_2}{2k_3} + \frac{1}{2k_3}\left[k_1^2 + 4k_3\left(k_1 - \frac{\mathcal{G}_c}{aE_f(\Delta\alpha\Delta T)^2}\right)\right]^{\frac{1}{2}}\right\}^m}$$ (15)

Debonding would proceed until ℓ reaches ℓ^*, whereupon fiber failure would occur. The actual locations of the fiber failures are given by statistical arguments.[4]

VI. Toughening

When the composite is subject to tensile residual stress at the interface, the present analysis has revealed that a *positive* mode I exists along the debond. Consequently, sliding and classical *pull-out* contributions to toughness only exist if the fibers are rough and friction is provided by asperity contact. In practice, fibers are not straight and debonded interfaces are not smooth.[1] A sliding resistance thus usually exists,[13] having magnitude governed by the frictional characteristic of the debonded interface.

When conditions of debonding without friction exist, the fibers primarily contribute to toughness through crack *bridging*. The bridging contribution to toughness can be derived from the compliance relations derived in Section III by noting that the asymptotic toughening is[14]

$$\Delta\mathcal{G}_c = 2\int_0^{t=S} t(u)\,du$$ (16)

where S is the axial stress of which the fibers fail. This topic is elaborated elsewhere.[15]

Table III. Coefficients λ^i ($i = 1, 4$) Used in the Interpolation of the Matrix Crack Opening

Σ	$\lambda_i(\Sigma, f)$							
	$f = 0.05$	$f = 0.1$	$f = 0.2$	$f = 0.3$	$f = 0.4$	$f = 0.5$	$f = 0.6$	$f = 0.7$
0.4	3.22	3.42	2.04	1.76	1.55	1.40	1.28	1.19
1.0	1.85	1.96	1.30	1.14	1.00	0.87	0.75	0.63
2.5	0.96	1.01	0.72	0.64	0.57	0.49	0.41	0.30

Σ	$-\lambda_i(\Sigma, f)$							
	$f = 0.05$	$f = 0.1$	$f = 0.2$	$f = 0.3$	$f = 0.4$	$f = 0.5$	$f = 0.6$	$f = 0.7$
0.4	2.59	2.75	1.64	1.42	1.25	1.12	1.03	0.95
1.0	1.73	1.84	1.23	1.07	0.94	0.81	0.70	0.59
2.5	1.05	1.11	0.79	0.71	0.62	0.54	0.44	0.33

Σ	$\lambda_4(\Sigma)$	$-\lambda_4(\Sigma)$
0.4	0.838	1.062
1.0	0.910	1.058
2.5	0.964	1.043

Subsequent to fiber failure, some closure of the debond surface generally occurs and the pullout motion of the fibers is typically resisted by frictional contact at asperities, as expressed by a shear resistance, τ_s. Pullout then has a profound effect on the mechanical properties. This phenomenon intimately involves statistical considerations through the location of fiber failure.[4] However, fiber failure and pullout based on a *constant* shear resistance τ_s[4] is clearly an oversimplification, especially prior to fiber failure when asperity contact can be affected by opening of the debond surfaces. A more complete analysis of the pullout that incorporates these effects is in progress.

VII. Closure

The present article has provided rigorous solutions for the mechanics of debonded interfaces in composites with interfaces subject to residual tension. Steady-state behavior at the debonds has been demonstrated with a phase angle that depends sensitively on the residual/applied stress ratio and on the elastic properties of the fiber and the matrix. The results of this analysis have been used to derive conditions for fiber debonding in the crack wake, to ascertain fiber failure criteria pertinent to fiber pullout and toughening and to examine the role of debonding and residual stress in fiber bridging toughness.

The actual fiber response in the crack wake is undoubtedly more complex than the symmetrical debond configuration considered in the present analysis. However, debonding should proceed in a manner that restores symmetry, since asymmetric debonds are subject to antiplane shear as well as in-plane shear and opening. Consequently, while more complex calculations would be envisioned, it does not appear that additional insight would emerge.

APPENDIX A

Crack Front Debonding

In a composite containing fibers with partial thermal debonds (Fig. A1), growth of the debonds can occur upon passage of the matrix crack. Specifically, the debond experiences a biaxial stress, in-plane strain, from the approaching matrix crack given by

$$\sigma_M = \frac{K_m}{\sqrt{2\pi r}} \qquad (A-1a)$$

$$\sigma_n = \frac{2\nu K_m}{\sqrt{2\pi r}} \qquad (A-1b)$$

where K_m is the matrix toughness, and r is the distance from the crack front. The stress-intensity factors at a debond subject to biaxial stress σ are[16] ($\Sigma = 1$)

$$\frac{K_I}{\sigma\sqrt{\pi a}} \approx \frac{\left[\frac{1}{2}\sin \alpha(1 + \cos \alpha)\right]^{1/2}}{1 + \frac{1}{2}\sin^2\alpha} \qquad (A-2a)$$

$$\frac{K_{II}}{\sigma\sqrt{\pi a}} \approx \frac{\left[\frac{1}{2}\sin \alpha(1 - \cos \alpha)\right]^{1/2}}{1 + \frac{1}{2}\sin^2\alpha} \qquad (A-2b)$$

where 2α is the angle included by the debond (Fig. A1). The modulus of K is thus

$$\frac{|K|}{\sigma\sqrt{\pi a}} \approx \frac{\sin\frac{1}{2}\alpha}{1 + \frac{1}{2}\sin^2\alpha} \equiv g(\alpha) \qquad (A-3)$$

where $g(\alpha)$ is plotted in Fig. A1. Noting that σ derives from both the crack tip field and the residual stress q gives
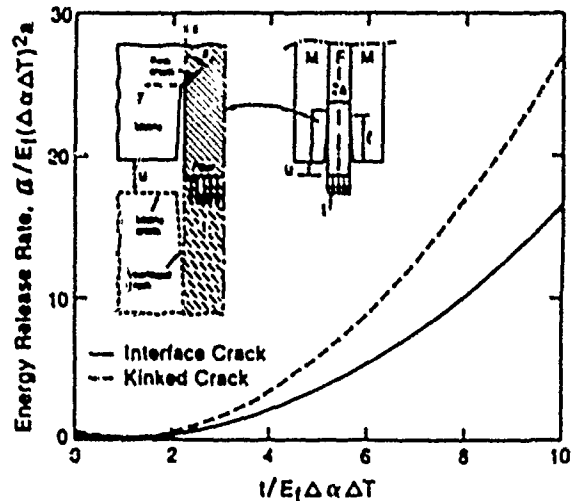
Fig. 9. Variations in nondimensional maximum energy release rate for a kink crack, with nondimensional applied stress; homogeneous system ($\Sigma = 1$); comparison with 'S'.

$$\sigma = q + \frac{1}{2}(\sigma_M + \sigma_n) \qquad (A-4)$$

whereupon Eq. (A-3) becomes

$$\frac{|K|}{g(\alpha)} = q\sqrt{\pi a} + \frac{1 + 2\nu}{2\sqrt{2}}K_m\sqrt{\frac{a}{r}} \qquad (A-5)$$

The quantity $|K|$ attains a maximum as $r \to a$. While not strictly valid in this limit, it is insightful to obtain the maximum from Eq. (A-5) as

$$\frac{|K|_{max}}{K_m g(\alpha)} = \frac{q\sqrt{\pi a}}{K_m} + \frac{1 + 2\nu}{2\sqrt{2}} \qquad (A-6)$$

It is apparent from the functional form of $g(\alpha)$ depicted in Fig. A1 that a *lower bound* condition exists below which debonding cannot occur. This condition involves the peak value of $g(\alpha)$ that occurs when $\alpha \approx 0.3\pi$

$$g(\alpha) \approx 0.76 \qquad (A-7)$$
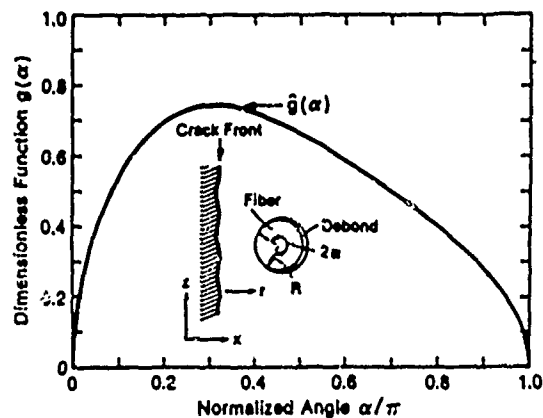
Fig. A1. Normalized modulus $|K|$ of the stress intensity factor at fiber thermal debonds due to the presence of the matrix crack.

① E_1, ν_1

Interfacial Crack

Crack Tip

Interface

② E_2, ν_2 $\phi = \tan^{-1}(v/u)$
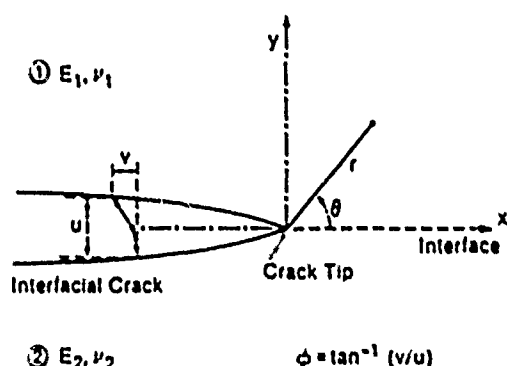
Fig. B1. Displacement field associated with a crack at a bimaterial interface.

Consequently, by equating $|K|_{\max}$ to the fracture resistance of the interface $|K_{ic}|(\psi)$, the lower bound debonding condition becomes

$$\frac{|K_{ic}|(\psi)}{K_m} < 0.76\left(\frac{1+2\nu}{2\sqrt{2}} + \frac{q\sqrt{\pi a}}{K_m}\right) \qquad (A-8)$$

This result is used in Section V to conclude that wake debonding is preferable to fiber failure at the end of the debond (recognizing that the critical values of K for the fiber and matrix are typically of similar magnitude).

Another important feature of the debonding problem evident from Fig. A1 is the realization that complete circumferential debonding is unlikely to occur, because $g(\alpha) \to 0$ as $\alpha \to \pi$. Consequently, the matrix crack is unlikely to encounter a fully debonded fiber. This realization emphasizes the importance of the conclusions reached in Section V that wake debonding occurs more readily than fiber failure when condition (A-8) is satisfied.

An analysis similar to that presented in this appendix has been independently conducted by Nix.[17]

APPENDIX B

Mechanics of Interface Cracks

The small strain linear elasticity singularity solution in the crack tip region can be developed using the bimaterial constant ε, which for plane strain is defined following Rice and Sih[5] and Rice[6] as

$$\varepsilon = \frac{1}{2\pi} \ln \frac{1+\beta}{1-\beta} \qquad (B-1)$$

where

$$\beta = -\frac{1}{2}\left[\frac{G_1}{G_2}(1-2\nu_2) - (1-2\nu_1)\right] \Big/ \left[\frac{G_1}{G_2}(1-\nu_2) + (1-\nu_1)\right]$$

is one of the plane strain Dundurs parameters[18] and G_i and ν_i ($i = 1, 2$) are the shear modulus and Poisson's ratio for materials 1 and 2, respectively. The traction at a distance r ahead of the crack tip is then given by

$$\sigma_{22} + i\sigma_{12} = \frac{K}{\sqrt{2\pi r}}r^{i\varepsilon} \qquad (B-2)$$

where $i = \sqrt{-1}$ and $K = \mathrm{Re}\,(K) + i\,\mathrm{Im}\,(K)$ is the complex stress intensity factor introduced by Rice[6] and Hutchinson *et al.*[19] Furthermore, the relative plane strain displacements of two points at distance r behind the crack tip on the top and bottom crack

surfaces, Δu_x and Δu_y (Fig. B1), are also given in terms of the complex K and the bimaterial constant ε as follows:

$$\Delta u_y + i\Delta u_x = \frac{2\left(\frac{1-\nu_1}{G_1} + \frac{1-\nu_2}{G_2}\right)K}{(1+2i\varepsilon)\cosh(\pi\varepsilon)}\sqrt{\frac{r}{2\pi}}r^{i\varepsilon} \qquad (B-3)$$

The energy release rate per unit of new crack area $\mathcal{G}$ in terms of the complex stress intensity factor K is

$$\mathcal{G} = \frac{\frac{1-\nu_1}{G_1} + \frac{1-\nu_2}{G_2}}{4\cosh^2(\pi\varepsilon)}|K|^2 \qquad (B-4)$$

where $|K|^2 = K\bar{K}$ is the modulus of the complex stress intensity factor, K.

The complex stress intensity factor K can be expressed in terms of its modulus $|K|$ and phase angle ψ:

$$K = |K|e^{i\psi} \qquad (B-5)$$

When all complex quantities are expressed in polar form, Eq. (B-3) yields an expression for the phase angle ψ, such that

$$\psi = \phi + B - \varepsilon \ln r \qquad (B-6)$$

where $\phi = \arctan(\Delta u_x/\Delta u_y)$ and $B = \arctan(2\varepsilon)$ are both nondimensional, whereas the $\varepsilon \ln r$ term is unit sensitive. This peculiarity of the phase angle has been recently examined by Rice[6] with the conclusion that ψ provides a proper characterizing parameter, provided that lengths are measured using consistent units (typically micrometers). While it is important to use ψ to describe fracture data, it is convenient to present calculated phase angles using a scale-invariant form:

$$Ka^{i\varepsilon} = |K|e^{i\psi^*} \qquad (B-7)$$

where $\psi^* = \psi + \varepsilon \ln a$ with a being a characteristic dimension, in this case the fiber radius.

APPENDIX C

A known finite-element solution to a linear elastic boundary value problem which involves a crack with traction-free surfaces can be used in conjunction with Parks' stiffness derivative method[20] to evaluate with sufficient accuracy the associated energy release rate $\mathcal{G}$.[21] In summary, $\mathcal{G}$ is given by

$$\mathcal{G} = -\frac{1}{2}\sum_{n=1}^{\mathrm{No.\ of\ elements}} \{u_N\}^T \frac{\partial[S]}{\partial\ell}\{u_N\} \qquad (C-1)$$

where $\{u_N\}$ denotes the nodal displacement vector, $[S]$ the stiffness matrix, and $\partial/\partial\ell$ differentiation with respect to crack length. The symbol Σ implied summation over all the distorted elements during the virtual crack extension. The method is still valid in the case of bimaterial crack problems as long as the crack surfaces remain traction free.

Consider a bimaterial problem for which it is desired to compute $\mathrm{Re}\,(K)$ and $\mathrm{Im}\,(K)$. First, solve the boundary value problem by the finite-element method and find $\{u_N\}$. From this, compute $\mathcal{G}$ by the virtual crack extension technique summarized by Eq. (C-1). Then add to $\{u_N\}$ the displacements $\{\Delta u_N^1\}$ for a problem in the same geometry but for which $\mathrm{Im}\,(K) = 0$ and $\mathrm{Re}\,(K) = \Delta\,\mathrm{Re}\,(K)$.

A new value $\mathcal{G} + \Delta_1\mathcal{G}$ can now be obtained through Eq. (C-1) for the nodal displacements $\{u_N + \Delta u_N^1\}$. The result for this calculation can be shown to be such that the change in the value of $\mathcal{G}$ is

$$\Delta_1\mathcal{G} = \frac{1}{H}[\Delta\,\mathrm{Re}\,(K)^2 + 2\,\mathrm{Re}\,(K)\Delta\,\mathrm{Re}\,(K)] \qquad (C-2)$$

Solving for $\mathrm{Re}\,(K)$ gives

$$\text{Re}(K) = \frac{H}{2}\frac{\Delta_l\delta}{\Delta\,\text{Re}(K)} - \frac{1}{2}\Delta\,\text{Re}(K) \qquad (C\text{-}3)$$

The second term can be neglected compared with the first if $\Delta\,\text{Re}(K)^2$ is selected to be small. The procedure can be repeated for an added vector $\{\Delta u_n^g\}$ such that $\text{Re}(K) = 0$ and $\text{Im}(K) = \Delta\,\text{Im}(K)$, in which case an expression for $\text{Re}(K)$ can also be derived.

The vectors $\{\Delta u_n^I\}$ and $\{\Delta u_n^g\}$ comprise sets of virtual displacements and can represent any problem. Furthermore, it should be noted that the virtual field is needed only for the nodes associated with the distorted ring of elements. In view of this, the asymptotic crack tip displacements can be used everywhere as a suitable field.

When $\text{Im}(K) = 0$ and $\text{Re}(K) = \Delta\,\text{Re}(K)$

$$\Delta u_j^I = \frac{\Delta\,\text{Re}(K)}{2G_j}\sqrt{\frac{r}{2\pi}\frac{e^{\pi\epsilon}}{1+e^{2\pi\epsilon}}}f^I(r,\theta,\epsilon,\mu_j) \qquad (C\text{-}4)$$

whereas when $\text{Re}(K) = 0$ and $\text{Im}(K) = \Delta\,\text{Im}(K)$

$$\Delta u_j^g = \frac{\Delta\,\text{Im}(K)}{2G_j}\sqrt{\frac{r}{\pi}\frac{e^{\pi\epsilon}}{1+e^{2\pi\epsilon}}}f^g(r,\theta,\epsilon,\mu_j) \qquad (C\text{-}5)$$

where

$$f_1^I(r,\theta,\epsilon,\mu_j) = D_j + 2\delta_j\sin\theta\sin\phi$$

$$f_2^I(r,\theta,\epsilon,\mu_j) = -C_j - 2\delta_j\sin\theta\cos\phi$$

$$f_1^g(r,\theta,\epsilon,\mu_j) = -C_j + 2\delta_j\sin\theta\cos\phi$$

$$f_2^g(r,\theta,\epsilon,\mu_j) = -D_j + 2\delta_j\sin\theta\sin\phi$$

The constants C_j, D_j, δ_j, and ϕ are functions of the material constants and location in the continuum. They are given as follows:

$$\delta_1 = e^{-(\pi-\theta)\epsilon}$$

$$\delta_2 = e^{-(\pi+\theta)\epsilon}$$

$$\phi = \epsilon\ln r + \frac{\theta}{2}$$

$$C_j = \bar\beta\gamma_j\cos\frac{\theta}{2} - \beta\bar\gamma\sin\frac{\theta}{2}$$

$$D_j = \beta\gamma_j\cos\frac{\theta}{2} + \bar\beta\bar\gamma\sin\frac{\theta}{2}$$

$$\beta = \frac{0.5\cos(\epsilon\ln r) + \epsilon\sin(\epsilon\ln r)}{0.25 + \epsilon^2}$$

$$\bar\beta = \frac{0.5\sin(\epsilon\ln r) - \epsilon\cos(\epsilon\ln r)}{0.25 + \epsilon^2}$$

$$\gamma_j = \mu_j\delta_j - \frac{1}{\delta_j}$$

$$\bar\gamma_j = \mu_j\delta_j + \frac{1}{\delta_j}$$

Also

$$\gamma_j = \begin{cases} 3 - 4\nu_j, & \text{plane strain} \\ (3 - \nu_j)/(1 + \nu_j), & \text{plane stress} \end{cases}$$

In the above equations, j is a material index which takes the values 1 and 2 for materials 1 and 2, respectively (Fig. B1).

References

[1] E. Bischoff, M. Rühle, O. Sbaizero, and A. G. Evans, "Microstructural Studies of the Interfacial Zone of a SiC-Fiber-Reinforced Lithium Aluminum Silicate Glass-Ceramic," *J. Am. Ceram. Soc.*, 72 [5] 741–45 (1989).

[2] M. D. Thouless, O. Sbaizero, L. S. Sigl, and A. G. Evans, "Effect of Interface Mechanical Properties on Pullout in a SiC-Fiber-Reinforced Lithium Aluminum Silicate Glass-Ceramic," *J. Am. Ceram. Soc.*, 72 [4] 525–32 (1989).

[3] A. G. Evans, "The New Generation of High Toughness Ceramics"; to be published in ASTM Special Technical Publication, Fracture Mechanics.

[4] M. D. Thouless and A. G. Evans, "Effects of Pull-out on the Toughness of Reinforced Ceramics," *Acta Metall.*, 36, 517 (1988).

[5] J. R. Rice and G. C. Sih, "Plane Problems of Cracks in Dissimilar Media," *J. Appl. Mech.*, 32, 418–23 (1965).

[6] J. R. Rice, "Elastic Fracture Mechanics for Interfacial Cracks," *J. Appl. Mech.*, 55, 98 (1988).

[7] P. G. Charalambides, J. Lund, R. M. McMeeking, and A. G. Evans, "A Test Specimen for Determining the Fracture Resistance of Bimaterial Interfaces"; to be published in *J. Appl. Mech.*

[8] J. W. Hutchinson and A. G. Evans, "On the Mixed Mode Fracture Resistance of Interfaces," *Acta Metall.*, 37 [3] 909–16 (1989).

[9] P. P. L. Matos, R. M. McMeeking, P. G. Charalambides, and M. D. Drory, "A Method for Calculating Stress Intensities in Bimaterial Fracture"; to be published in *Int. J. Fract.*

[10] B. Cotterell and J. R. Rice, "Slightly Curved or Kinked Cracks," *Int. J. Fract.*, 16, 155 (1980).

[11] M. He and J. W. Hutchinson, Harvard Report, MECH-119, Cambridge, MA, April 1988.

[12] H. T. Corten; p. 27 in Modern Composite Materials. Edited by L. J. Broutman and R. H. Krock. Addison-Wesley, New York, 1967.

[13] D. B. Marshall and A. G. Evans, "Failure Mechanisms in Ceramic-Fiber/Ceramic-Matrix Composites," *J. Am. Ceram. Soc.*, 68 [5] 225–31 (1985).

[14] A. G. Evans and R. M. McMeeking, "On the Fracture Toughness of Strong Reinforcements," *Acta Metall.*, 34, 2435 (1986).

[15] P. G. Charalambides, "Toughening Caused by Elastic Bridging of Debonded Fiber"; unpublished work.

[16] G. C. Sih, Handbook of Stress Intensity Factors. Lehigh University Press, Bethlehem, PA, 1972.

[17] W. D. Nix, unpublished research presented at the Winter Study Group, Santa Barbara, CA, Jan. 1988.

[18] J. Dundurs, "Discussion," *J. Appl. Mech.*, 36, 650–52 (1969).

[19] J. W. Hutchinson, M. E. Mear, and J. R. Rice, "Crack Paralleling an Interface Between Dissimilar Materials," *J. Appl. Mech.*, 53, 828–32 (1987).

[20] D. M. Parks, "A Stiffness Derivative Finite Element Technique for Determination of Elastic Crack Tip Stress Intensity Factors," *Int. J. Fract.*, 10, 487–502 (1974).

[21] J. R. Rice, "Mathematical Analysis in the Mechanics of Fracture"; pp. 191–311 in Fracture, An Advanced Treatise. Edited by H. Liebowitz. Academic Press, New York, 1968. □

M A T E R I A L S
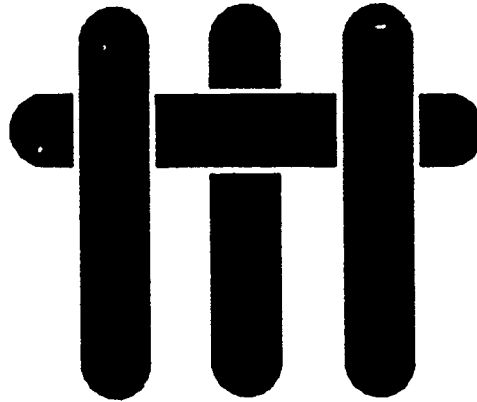
FIBER DEBONDING IN RESIDUALLY STRESSED
BRITTLE MATRIX COMPOSITES

by

P. G. Charalambides [*] [†]

Materials Department
College of Engineering
University of California
Santa Barbara, California 93106

July 1989

---

[*] Member American Ceramic Society

[†] Current Address: Department of Mechanical Engineering & Engineering Mechanics,
Michigan Technological University, Houghton, Michigan, 49931

Abstract

The competition between initial fiber debonding versus fiber failure marks a crucial event of the microstructural failure process in fiber reinforced brittle matrix composites. In this study, the role of a thermal residual stress field on the debonding conditions is examined theoretically and analytically. The analysis is based on two critical observations, the first being that the mechanics at the tip of a kink crack are driven *only* by the *singularity* at the main crack tip. Following from the first is the second observation that any thermal stress effects on the debonding criteria should enter only through the phase angle ψ^T of the total stress intensity factor at the main crack tip. In general, this stress intensity factor has a thermal as well as a mechanical load contribution. It is shown that when the thermal and mechanical stress intensities, K^R and K^t respectively, are *in-phase*, i.e. $\psi^R = \psi^t$, the existing debonding conditions are universal and can be used even in the presence of thermal loads. On the contrary, when K^R and K^t are *out of phase*, i.e. $\psi^R \neq \psi^t$, events such as the delamination of *thick* films or debonding of *inclined aligned fibers* in brittle matrix composites become sensitive to the presence of the thermal stresses.

1. Introduction

The "ductility" and toughness of brittle matrix fiber reinforced composite systems crucially depend on the competing effect of initial fiber debonding versus fiber failure [1,2]. The choice of the favored event is made at the microstructural level by the matrix crack early on in the failure process of the composite. Initiation of *matrix cracking* marks the first step of failure of the composite. The mechanics for this phenomenon have been extensively analyzed in recent years [3-5]. Subsequent to matrix cracking initiation, the matrix crack driven by the mode I [6] stress intensity factor, K_I, propagates through the matrix and intercepts the fiber reinforcements (Fig. 1a), an event that signifies the beginning of the second step of microstructural failure. At this configuration (Fig. 1a), the matrix crack, still dominated by the opening mode (mode I), eventually favors one of two virtual crack paths: the mode I straight-forward path (Fig. 1b) or the mixed mode [7-11] interface path (Fig. 1c). In the first case, if the available energy release rate at the $0°$

1

fiber kink crack (Fig. 1b) exceeds the fracture toughness of the fiber $\mathcal{G}_{fc}$, the matrix crack encounters no further resistance and thus propagates catastrophically through the fiber reinforcements triggering a *brittle type failure* of the composite resulting in minimum or no macroscopic "ductility" and composite toughness. On the other hand, if the crack kinks at a 90° angle relative to the initial matrix crack plane, i.e., *fiber debonding* along the fiber matrix interface (Fig. 1c), substantial toughening can occur due to fiber bridging and/or subsequent frictional fiber pull-out as discussed elsewhere [7,12-15]. Thus, in optimally designed high toughness fiber reinforced systems, initial fiber debonding is a salient feature of the composite microstructural failure and marks the activation of various toughening processes in the composite. Despite its importance, rigorous solutions pertinent to initial fiber debonding conditions were unavailable until recently.

In characterizing the debonding process, He and Hutchinson [9], Evans *et al.* [10] and Thouless *et al.* [11], derived conditions for fiber failure versus initial fiber debonding pertinent to the competing fracture processes depicted in Figs. 1b and 1c respectively. Such debonding conditions were obtained [9,10] for a wide range of bimaterial systems, interface characteristics and fiber orientation. In their studies, He and Hutchinson [9] were concerned with two competing incipient kink cracks (cracks of infinitesimal length), i.e., the fiber and the debond kink cracks shown schematically in Figs. 1b and 1c respectively. To assure generality of their solutions, the energy release rates and the phase angles at the tip of each of these incipient cracks were obtained from an *existing* singular stress field at the tip of the main matrix crack and the corresponding kink angle relative to the matrix crack plane. Subsequently, fiber debonding conditions were derived from the ratio $\mathcal{G}^k/\mathcal{G}^T$, where $\mathcal{G}^k$ and $\mathcal{G}^T$ are the computed energy release rates at the tip of the interface (Fig. 1c) and fiber (Fig. 1b) kink cracks respectively. In summary, for a homogeneous composite system and for a network of reinforcements aligned in the direction of the applied loads at 90° from the matrix crack plane (Fig. 1a), fiber debonding was found to be favored over fiber failure when $\mathcal{G}_{ic}/\mathcal{G}_{fc} \leq 1/4$ is satisfied, where $\mathcal{G}_{ic}$ and $\mathcal{G}_{fc}$ are the fracture toughnesses of the interface and the fiber respectively. In this particular example, the matrix crack is dominated by a mode I stress intensity factor even in the presence of thermal loads. To the extent of the above assumptions, the existing criteria [8-11] for cracks kinking out of

2

interfaces or cracks deflecting along weak interfacial paths are general and can be used to study fiber debonding in brittle matrix composite systems. However, recent discussions yielded an additional need to assess and clarify the role, if any, of a thermal residual stress field on fiber debonding.

Composite systems develop thermal residual stresses during processing due to thermal expansion mismatches between the fiber and the matrix. These stresses are known to substantially influence the mechanical properties and toughness in these composites. For example, Charalambides and Evans [7], from a finite element analysis in composites with interfacial residual tension, found that the mechanics at the tip of a debond crack (kink crack of finite length) sensitively depend on the thermal stresses. In light of this, a fundamental question is put forward. The findings of He and Hutchinson are for a kink crack of infinitesimal length: Can these results be used to predict fiber debonding conditions in the presence of appreciable thermal residual stresses?

In this work, a theoretical argument and analytical considerations in the case of a homogeneous system are employed to clarify the stated question. The analysis employed in this study is general and applies to systems with main cracks under *out of phase* complex stress intensities caused separately by the thermal and mechanical loads. Special cases of practical interest are presented as examples such as fiber debonding in unidirectionally fiber reinforced composite systems and delamination of thick films subjected to both mechanical and thermal stresses. Furthermore, some of the issues presented in this analysis are similar to those encountered in the analysis for continuing fiber debonding versus fiber failure at the tip of a finite debond crack, an equally important step in completing our understanding of the microstructural failure process in brittle matrix composites. This phenomenon is taken on in the discussion section of the present study.

2. Debonding Mechanics

For the sake of the analysis let us consider the cylindrical unit cell shown in Fig. 2. This configuration corresponds to a fully cracked matrix while the crack is bridged by the intact fiber reinforcements. The stresses and strains in the crack tip region (homogeneous system) are dominated by the singularity of the main matrix crack. Due to the symmetry

3

of the unit cell and for both the applied and thermal load cases, the matrix crack is constrained to a symmetrical relative crack surface opening such that only K_I, the mode I stress intensity factor is non-zero. These observations essentially determine the mechanics of fiber debonding. In particular, the competing effects of initial fiber debonding versus fiber failure can be examined by comparing the energy release rate $\mathcal{G}^k$ at the tip of the kink crack (kink angle 90°), to that of the main crack $\mathcal{G}^T$ due to the combined effects of applied and thermal loadings. However, as discussed by Cotterell and Rice [16], the stress intensity factors at the tip of an infinitesimal kink crack depend only on the original singular stresses at the main crack tip. Any non-singular stress terms, including thermal stresses and contacting asperity tractions, cancel out or if introduced on the kink crack surfaces, will give zero contribution to the kink crack stress intensities and energy release rate. Moreover, as indicated above, both the applied and thermal loads give rise only to a mode I stress intensity factor. Thus the stress intensities at both kinds of kink cracks are proportional to the main crack K_I, and the ratio $\mathcal{G}^K/\mathcal{G}^T$ is that which would be produced by mechanical loading alone. It follows that under these assumptions, the conditions derived by He and Hutchinson [8,9], Evans et al. [10] and Thouless et al. [11] can be used to predict which of the critical events would occur first even in the presence of thermal loads. However, there is an additional interest in cases wherein the assumption is violated that the mechanical and thermal loads produce only mode I matrix crack stress intensities. Such conditions for instance prevail during delamination of thermally bonded *thick* films and possibly during debonding of *inclined aligned* fiber reinforcements. For these systems, a more rigorous analysis is needed in order to clarify the thermal effects on initial debonding/delamination conditions. Such analysis, based on near-tip mechanics is presented below.

2.1 *Cracks kinking out of a mixed mode crack tip*

In this section the analysis is extended to include the thermal effects on debonding or crack kinking at the tip of a mixed mode crack. To be more specific, consider a situation in which an applied load t and a thermal load σ^R, with $\sigma^R = \bar{E}\Delta\alpha\Delta T$ being a residual stress measure, are imposed on the composite. There are then two contributions to the

4

complex stress intensity factor K^T at the main matrix crack tip (Fig. 2): i) K^t due to the applied loads t and ii) K^R being the contribution of the thermal loads σ^R. From existing solutions [6,7] and dimensional analysis, the above stress intensities can be written in a complex form as,

$$K^t = K_I^t + iK_{II}^t = ta^{\frac{1}{2}}F^t\left(\cos\psi^t + i\sin\psi^t\right) \tag{1a}$$

$$K^R = K_I^R + iK_{II}^R = \sigma^R a^{\frac{1}{2}}F^R\left(\cos\psi^R + i\sin\psi^R\right) \tag{1b}$$

Then, the combined total complex stress intensity factor K^T, at the tip of the main crack is obtained via linear superposition as follows,

$$K^T = K_I^T + iK_{II}^T = \left(1 + \frac{K_I^R}{K_I^t}\right)K_I^t + i\left(1 + \frac{K_{II}^R}{K_{II}^t}\right)K_{II}^t \tag{2}$$

The total energy release rate at the matrix crack tip is obtained in terms of $|K^T|$, the modulus of K^T, via Irwin's relationship for cracks in homogeneous bodies, i.e.,

$$\mathcal{G}^T = \frac{1-\nu^2}{E}\left((K_I^T)^2 + (K_I^T)^2\right) = \frac{1-\nu^2}{E}(K_I^T)^2\left(1 + \tan^2\psi^T\right) \tag{3}$$

with E being the Young's modulus and ν the Poisson's ratio of the material. Following Cotterell and Rice [16], the combined stress intensity factor at the tip of the kink crack has two components, K_1^k and K_2^k and can be obtained from K^T the total stress intensity factor at the tip of the main crack, as follows,

$$K_1^k = c_{11}K_I^T + c_{12}K_{II}^T \tag{4a}$$

$$K_2^k = c_{21}K_I^T + c_{22}K_{II}^T \tag{4b}$$

where c_{ij}, ($i, j = 1, 2$) are geometric factors which for a homogeneous system are given in terms of the kink angle θ (Fig. 3) and coincide with Cotterell and Rice values [16] for low values of θ. From Irwin's relationship and in light of the above equations, the total energy release rate at the kink crack $\mathcal{G}^k$ becomes,

$$\mathcal{G}^k = \frac{1-\nu^2}{E}\left((K_1^k)^2 + (K_2^k)^2\right)$$

$$= \frac{1-\nu^2}{E}(K_I^T)^2 C(c_{ij}(\theta), \psi^T) \qquad (5)$$

where

$$C(c_{ij}(\theta), \psi^T) = c_{11}^2 + c_{21}^2 + 2\left(c_{11}c_{12} + c_{21}c_{22}\right)\tan\psi^T + \left(c_{11}^2 + c_{21}^2\right)\tan^2\psi^T \qquad (6)$$

and $\tan\psi^T = K_{II}^T/K_I^T$ is the phase angle for the total stress intensity factor at the tip of the matrix crack and is obtained from equation (2) as follows,

$$\tan\psi^T = \frac{K_{II}^T}{K_I^T} = \frac{1 + \frac{F^R}{F^T}\frac{\sin\psi^R}{\sin\psi^T}\frac{\sigma^R}{t}}{1 + \frac{F^R}{F^T}\frac{\cos\psi^R}{\cos\psi^T}\frac{\sigma^R}{t}}\tan\psi^t \qquad (7)$$

2.2 Debonding conditions

The competing effects of crack kinking (fiber debonding, Fig. 1c) versus fiber failure (Fig. 1b) can be established using equations (3) and (5) to obtain a condition for the toughness ratio $\mathcal{G}_{ic}/\mathcal{G}_{fc}$ which is the fracture toughness of the interface to the fracture toughness of the fiber. Such an analysis is based on the implicit assumption that the system is ideally brittle and that fracture at the tip of the competing kink cracks is driven by the energy release rate alone. Also implicit in the analysis is the assumption that any possible increases in $\mathcal{G}_{ic}$ due to the increased mode mixity ψ^k at the kink crack tip ($\psi^k \approx 42°$, [9]) are neglected. However, as discussed by Evans and Hutchinson [17], non unique values for $\mathcal{G}_{ic}$ are obtained at non-zero phase angles $\psi \neq 0$. The increase in $\mathcal{G}_{ic}$ with ψ is primarily due to contacting asperities on the crack surfaces behind the crack tip as discussed elsewhere [17]. In the case of an incipient kink crack, i.e., a kink crack of infinitesimal length, such effects are minimal and therefore an energy release rate criterion can be used to predict kink crack initiation as implemented by He and Hutchinson [8,9], Evans et al. [10] and Thouless et al. [11]. Thus, in the absence of any shielding effects

6

at the kink crack tip due to contacting asperities and in an ideally brittle environment, fracture occurs when $\mathcal{G}^k \geq \mathcal{G}_{ic}(\psi^k = 0°)$, with $\mathcal{G}_{ic}(\psi^k = 0°)$ being the mode I fracture toughness of the interface. In particular when the competition is between a kink crack at 90° from the plane of the main crack (Fig. 1c) and fiber failure (Fig. 1b), fiber debonding is favored when

$$\frac{\mathcal{G}_{ic}}{\mathcal{G}_{fc}} \leq \frac{\left[c_{11}^2 + c_{21}^2 + 2\left(c_{11}c_{12} + c_{21}c_{22}\right)\tan\psi^T + \left(c_{11}^2 + c_{21}^2\right)\tan^2\psi^T\right]_{\theta=\pi/2}}{1 + \tan^2\psi^T} \tag{8}$$

On the other hand, if kinking occurs at an angle other than 90° with respect to the plane of the main crack such as the case of debonding along the interface of inclined fibers (Fig. 4), the favored event is obtained by comparing the solutions for the energy release rate at the tip of two competing inclined kink cracks as shown in Figs. 4b and 4c. In this instance, fiber debonding is favored over fiber failure if

$$\frac{\mathcal{G}_{ic}}{\mathcal{G}_{fc}} \leq \frac{\left[c_{11}^2 + c_{21}^2 + 2\left(c_{11}c_{12} + c_{21}c_{22}\right)\tan\psi^T + \left(c_{11}^2 + c_{21}^2\right)\tan^2\psi^T\right]_{\theta=\theta_i}}{\left[c_{11}^2 + c_{21}^2 + 2\left(c_{11}c_{12} + c_{21}c_{22}\right)\tan\psi^T + \left(c_{11}^2 + c_{21}^2\right)\tan^2\psi^T\right]_{\theta=\theta_f}} \tag{9}$$

where θ_i and θ_f are the kink angles for the debond and fiber kink cracks, and are shown schematically in Figs. 4b and 4c respectively. It becomes clear from equations (8) and (9) that the thermal loads influence the debonding condition via the phase angle ψ^T *only* which is given by equation (7). To be more specific, when $\psi^R = \psi^t$, i.e. *in-phase* thermal-mechanical stress intensities, equation (7) yields that $\psi^T = \psi^t$ and the thermal effects do not enter the conditions given by equations (8) and (9). On the contrary, when $\psi^R \neq \psi^t$ the above conditions become sensitive to the thermal loads via equation (7) in which case additional analysis is needed in order to clarify the thermal effects.

To further explore and quantify each of the above possibilities, studies pertinent to debonding in homogeneous systems with interfaces is presented below for two special cases. Initially, we consider the case in which the thermal and mechanical loads when applied

7

independently give rise to *in-phase* stress intensities at the tip of the main crack so that $\psi^T = \psi^t = \psi^R$ and the thermal effects drop out of the debonding conditions. Subsequently, we consider the case in which the thermal and mechanical stress intensities are *out of phase*, i.e. $\psi^R \neq \psi^t$, and debonding does depend on the thermal loads.

3. Debonding independent of thermal loads

3.1 *In-phase mechanical and thermal loadings*

In the case where the mechanical and thermal loads independently give rise to *in-phase* stress intensities at the main crack tip, i.e. $\psi^t = \psi^R$, equation (7) yields $\psi^T = \psi^t = \psi^R$. As a result, the debonding conditions expressed via equations (8) and (9) become *independent* of the thermal loads and can be determined from the mechanical loads alone. Some of the conditions derived by He and Hutchinson and Evans *et al.* implicitly assumed in-phase mode I thermal and mechanical stress intensities and are universal to the extent of the above assumption. To demonstrate the validity of those results, we shall now consider the fiber debonding processes for the composite unit cell shown in Fig. 2. As discussed earlier in this work, the matrix crack (Fig. 2) is dominated by a mode I stress intensity factor due to either mechanical or thermal loading and thus, $\psi^T = \psi^R = \psi^t = 0$. These conditions prevail at the tip of matrix cracks in systems such as fiber reinforced composites with the network of fiber reinforcements aligned in the direction of the applied stress at 90° relative to the matrix crack plane (Fig. 1) or composite systems reinforced by a randomly oriented network of chopped fibers, (Fig. 4) where on the average the thermal shear stress goes to zero. Also similar mode I conditions due to thermal and applied loads exist at the tip of the notch in the plane strain mode I pre-notched bimaterial beam shown in Fig. 5. Therefore, in these systems and in light of equation (8) fiber debonding or onset of delamination of the top layer (Fig. 5) will be favored if

$$\frac{\mathcal{G}_{ic}}{\mathcal{G}_{fc}} \leq \left[c_{11}^2 + c_{21}^2 \right]_{\theta = \pi/2} \tag{10}$$

which is a universal constant independent of thermal stresses. Furthermore, by using the approximate values for c_{11} and c_{21} obtained by Cotterell and Rice [16] in the case of a

8

homogeneous system and for a kink angle $\theta = 90°$, the condition for fiber debonding given by equation (10) takes the form, $\mathcal{G}_{ic}/\mathcal{G}_{fc} \leq 1/4$ first reported by Thouless et al. [11].

4. Debonding dependent on thermal loads

4.1 Out of phase mechanical and thermal loadings

In the general case when the stress intensity factor at the main crack tip due to the thermal loads is out of phase with that due to the mechanical loads, i.e $\psi^R \neq \psi^t$, the debonding conditions (equations (8) and (9)) are indeed sensitive to the presence of the thermal stresses via equation (7). To demonstrate the thermal effects on the above conditions we shall consider the example of the plane strain pre-notched delamination four-point flexure specimen shown in Fig. 5. Without loss of generality, let us assume that the system is elastically homogeneous, i.e. $E_1 = E_2$ and $\nu_1 = \nu_2$, with E and ν being the Young's modulus and Poisson's ratio respectively and the subscripts 1 and 2 denoting quantities for the top and bottom layers respectively, (Fig. 5). For the sake of the analysis let us also assume that the two thermally bonded layers have different thermal expansion coefficients, i.e. α_1 and α_2. Under these conditions and for the special case of a specimen with layers of equal thickness, $h_1 = h_2$, analytical solutions exist for the steady-state delamination mechanics [18-20] due to the applied and thermal loads. In particular, Charalambides et al. [18] and Suo and Hutchinson [19], found that the mechanical complex stress intensity factor due to the applied loads P is given by,

$$K^t = \frac{1}{4}(\frac{2}{\sqrt{3}} + i)th_2^{\frac{1}{2}} = th_2^{\frac{1}{2}}\sqrt{\frac{7}{48}}e^{i\,0.49\pi}\pi \tag{11}$$

where $t = 3P\ell/bh_2^2$ is the maximum normal stress due to bending of the bottom layer alone. Thus, in this example the mechanical loads are characterized by a phase angle ψ^t such that $\tan\psi^t = \sqrt{3/2}$ or $\psi^t = 0.4089\pi/1.8(rad)$ which is to a good approximation equal to 40.89°. In addition, the corresponding stress intensity factor due to the thermal loading $\sigma^R = E(\alpha_2 - \alpha_1)\Delta T$, was found by Charalambides et al. [20] to be a pure mode II, and is given below,

9

$$K^R = i\frac{1}{4}\sigma^R h_2^{\frac{1}{2}} = \frac{1}{4}\sigma^R h_2^{\frac{1}{2}} e^{i\frac{\pi}{2}} \tag{12}$$

The thermal phase angle is $\psi^t = \pi/2$ and thus the thermal and mechanical loads give rise to *out of phase*, i.e. $\psi^R \neq \psi^t$, stress intensities at the delamination crack tip. In light of equations (11) and (12), the expression for the phase angle of the total stress intensity factor ψ^T obtained from equation (7) reduces to

$$\tan\psi^T = \frac{\sqrt{3}}{2}(1 + \tau) \tag{13}$$

with $\tau = \sigma^R/t$. Further progress is made in the analysis by adopting for $c_{i,j}$, $(i,j = 1,2)$ the approximate expressions derived by Cotterell and Rice [16]. Following Charalambides and Evans [7] and with the aid of equation (8), fracture at the tip of an incipient kink crack inclined at an angle β from the delamination crack plane (Fig. 3) is favored over further delamination when[†]

$$\frac{\mathcal{G}_{fc}}{\mathcal{G}_{ic}} \leq \frac{a_1(\beta) + a_2(\beta)\tan\psi^T + a_3(\beta)\tan^2\psi^T}{1 + \tan^2\psi^T} \tag{14}$$

with

$$a_1(\theta) = c_{11}^2 + c_{21}^2 = \tfrac{1}{8} + \tfrac{1}{2}\cos^2\tfrac{\theta}{2} + \tfrac{1}{4}\cos\theta + \tfrac{1}{8}\cos 2\theta$$

$$a_1(\theta) = 2\left(c_{11}c_{12} + c_{21}c_{22}\right) = -\sin\theta - \tfrac{1}{2}\sin 2\theta \tag{15}$$

$$a_3(\theta) = c_{12}^2 + c_{22}^2 = \tfrac{5}{8} + \tfrac{1}{2}\sin^2\tfrac{\theta}{2} + \tfrac{3}{4}\cos\theta - \tfrac{3}{8}\cos 2\theta$$

and β is the value for the kink angle θ for which $\mathcal{G}^k(\theta)$ given by equations (5) and (15) becomes maximum. That is to say, from all virtual kink cracks the one with the maximum energy release rate is activated. This is usually assumed in the case of cracks kinking out of an interface [8] (Fig. 5). Thus the situation considered here is somewhat different

---

[†] Equation (14) in this article is identical to equation (12) in reference [7] where *tan* was erroneously replaced by *arctan*.

from those considered in the previous sections in this study. In those cases, e.g. fiber debonding, the angle β was fixed and taken to be equal to the interface orientation angle relative to the matrix crack plane (Fig. 1). On the contrary, the crack deflection angle in this analysis is unknown and is obtained as a part of the solution through an energy maximizing process. The maximum in $\mathcal{G}^k$ is obtained by first combining equations (5) and (15) and then differentiating with respect to θ such that,

$$\frac{d\mathcal{G}^k}{d\beta} = 0 \quad \Rightarrow \quad \frac{da_1}{d\beta} + \frac{da_2}{d\beta}\tan\psi^T + \frac{da_3}{d\beta}\tan^2\psi^T = 0 \tag{16}$$

where

$$\frac{da_1}{d\beta} = -\frac{1}{2}\sin\beta(1+\cos\beta)$$

$$\frac{da_2}{d\beta} = 1 - \cos\beta(1+2\cos\beta) \tag{17}$$

$$\frac{da_3}{d\beta} = -\frac{1}{2}\sin\beta(1-3\cos\beta)$$

The trends for the total phase angle ψ^T and the kink angle β with the thermal to mechanical stress ratio σ^R/t for which a maximum in $\mathcal{G}^k$ is observed are shown in Fig. 6 in dash and solid lines respectively. The corresponding trend in the ratio $\mathcal{G}^T/\mathcal{G}^k$ is plotted on Fig. 7. It is of interest to observe some limiting cases. For example, as shown in Fig. 6 the phase angle of the total stress intensity factor ψ^T becomes negative for $r < -1.0$ which is consistent with equation (13). When the stress ratio $r = -1.0$, the total phase angle takes the value $\psi^T = 0$ in which case the delamination crack is dominated by only the mode I component of the applied stress intensity factor given by equation 10. In this instance, the maximum kink energy release rate occurs straight ahead of the delamination crack , i.e., $\beta = 0$ (Fig. 6), and the energy release rate ratio takes the value $\mathcal{G}^T/\mathcal{G}^k = 1.0$. Thus under ideally brittle conditions and when $r = -1.0$, the only favored fracture event is the failure of the interface under the influence only of the mode I component of the applied stress intensity factor. On the other hand, as the ratio $r = \sigma^R/t$ increases, failure of the bottom layer is favored over further delamination, as indicated by the failure map in Fig. 7. As shown in this figure, the competition between further delamination and failure

11

in one of the two layers is most sensitive to the thermal stresses for small values of r, i.e. $-2.0 \leq \tau \leq 2.0$. Outside this interval the thermal effects become minimal.

5. Discussion

In this work, the effects of thermal stresses on the conditions for fiber debonding in brittle matrix composites and on the delamination criteria for thermally bonded plane strain layers have been examined. The analysis assumed elastically homogeneous systems but can be extended to include bimaterial cases. Departing from the observation that the mechanics of incipient kink cracks are driven only by the singular stresses at the main crack tip, two distinct situations were examined in regard to the thermal effects on the debonding criteria. The first is the case when the thermal and mechanical loads give rise to *in-phase* stress intensities, i.e., $\psi^R = \psi^t$, in wh' case the criteria for crack kinking are independent of the thermal loads. On the contrary, when the stress intensities are *out of phase*, i.e. $\psi^R \neq \psi^t$, the criteria for delam...ation of thermally bonded layers and in some special cases the conditions for fiber debonding in brittle matrix composites, become sensitive to the presence of the thermal stresses.

In general, in fiber reinforced brittle matrix composites, matrix cracking is a mode I process and remains as such even in the presence of thermal stresses. Thus the existing [8-10] debonding criteria derived from a mode I matrix crack singularity can be used even in the presence of thermal loads. For example, earlier in this work, it was demonstrated that systems reinforced with an aligned fiber network oriented at 90° from the crack plane (Fig. 1) experience an in-phase mode I stress intensity at the matrix crack tip due to independent application of the applied and thermal loads. Thus the condition for debonding reduces to equation (10) which is indeed independent of the thermal loads.

By analogy, the same conclusion must apply to systems reinforced with randomly oriented chopped fibers. Again in those systems, due to the randomness of the fiber orientation a mode I stress intensity is induced at the matrix crack tip by both the thermal and applied loads. Thus the debonding condition remains unaffected by the presence of thermal loads even if the fiber is intercepted at an angle by the matrix crack. Results for such systems are reported in the article by Evans, He and Hutchinson [10].

12

Unlike the previous two cases a somewhat more complex situation is encountered in systems where the fiber reinforcements are both inclined and aligned relative to the matrix crack. For example, consider the near tip schematic shown in Fig. 8. If the composite system is brittle, such that fiber failure (Fig. 8a) at the matrix crack surface is favored over fiber debonding (Fig. 8b), the stress intensity at the mechanically mode I matrix crack tip must remain mode I even in the presence of thermal loads. This is especially true for long matrix cracks (cracks extending over a substantial number of fibers), where the average thermal shear traction acting on the crack surfaces over the total crack length must be zero. As a result, a fiber failure criterion independent of thermal stresses must be obtained. On the other hand, when fiber debonding occurs prior to fiber failure (Fig. 8b), the inclined fibers would bridge the crack over a certain distance from the matrix crack tip, as shown schematically in Fig. 8b. Furthermore, debonding of inclined fibers is most likely geometrically asymmetric and thus a mode II thermal component at the otherwise mode I matrix crack tip may exist. Under these conditions, fiber debonding would be influenced by the presence of thermal stresses. However, further studies are needed to clarify this case.

Fina.   ple of thermally dependent kinking/delamination conditions was presented, via   thickness, elastically homogeneous four-point flexure beam specimen shown in Fig   the delamination process is primarily mixed mode [18-21] and in cases other than the thin film decohesion process [21], the thermal and mechanical stress intensities are not in-phase. Thus, the delamination process in such systems must indeed depend on the thermal stresses as demonstrated earlier in this work and fracture maps similar to that shown in Fig. 7 are needed to study these phenomena.

In light of the above observations, we now proceed to examine the processes of initial fiber debonding and further debond extension (delamination) in fiber reinforced brittle matrix composites. In doing so, we employ the aid of Fig. 9 where the phase angles at the debond tip due to the applied load t and thermal load σ^R are plotted as a function of the debond crack length. The curve for ψ^t, the phase angle due to the applied loads, was obtained numerically by Charalambides and Evans [7] using finite elements. The curve for ψ^R (the thermal phase angle) is representative of composite systems stressed

residually with their interfaces in tension and is qualitatively correct in the sense that only the steady-state result is reported in the literature [7]. Thus knowing the steady-state result [7] together with the kink crack solution [9], i.e. $(\psi^R)_{a=0} \approx 42.2°$, the transient branch for ψ^R is plotted qualitatively as shown in Fig. 9. However, the shape of this part of the curve is of no significance to the present analysis.

As shown in Fig. 9, at the limit $a \to 0$, the phase angles at the 90° debond kink crack due to the thermal and applied loads are equal, i.e. $\psi^R = \psi^t$. This is obtained due to the dominance of the mode I singularity at the main matrix crack tip. Thus, using this result and by the virtue of earlier observations, initial debonding is insensitive to the presence of thermal stresses and the criteria for this process to occur are given by He and Hutchinson [9] and Evans et al. [10]. On the contrary, as the debond crack grows and enters the steady-state regime, i.e. $a \geq 5.0R$ [7], the thermal and applied debond-tip stress intensities are out of phase (Fig. 9) and the delamination process (debond extension) becomes indeed sensitive to the thermal stresses as discussed elsewhere [7].

6. Concluding Remarks

The effects of a thermal residual stress field on the condition for kink crack initiation relevant to fiber debonding in brittle matrix composite systems and on the delamination of layers in plane strain, have been addressed. The analysis in this work is based on two critical observations. The singular stresses alone at the main crack tip drive the mechanics at the tip of all virtual kink cracks associated with that main crack tip. Given the above, any thermal effects on the kinking (fiber debonding/ delamination) conditions enter via the phase angle ψ^T of the total stress intensity at the main crack tip. In particular, when ψ^T is independent of the thermal loads, i.e. $\psi^R = \psi^t$, the conditions for debonding are also independent and the existing criteria for fiber debonding can be used even in the presence of thermal stresses. However, when $\psi^R \neq \psi^t$, the coupled phase angle ψ^T does depend on the thermal stresses and the criteria for crack kinking versus further delamination or debond extension are thermally sensitive. Thus, such competing effects can only be studied using fracture maps involving the thermal stresses as well as the relative fracture toughnesses in the directions of the competing fracture events.

14

Acknowledgements

## References

[1] A. G. Evans. "New High Toughness Ceramics", *The Processing and Mechanical Properties of High Temperature/High Performance Composites*. (Department of Materials, University of California, Santa Barbara, 1988).

[2] A. G. Evans, "The Mechanical Performance of Fiber Reinforced Ceramic Matrix Composites". *Material Science and Engineering*, A107, 227-239 (1989).

[3] D. Marshall and A. G. Evans, "Failure Mechanisms in Ceramic-Fiber/Ceramic-Matrix Composites", *J. Am. Ceram. Soc.*, 68[5], 225-231 (1985).

[4] D. B. Marshall, B. N. Cox and A. G. Evans, "The Mechanics of Matrix Cracking in Brittle Matrix Fiber Composites", *Acta Metall.* 33[11], 2013-2021 (1985).

[5] B. Budiansky, J. W. Hutchinson and A. G. Evans, "Matrix Fracture in Fiber-Reinforced Ceramics", *Jnl. Mech. Phys. Solids*, 34, 167-189 (1986).

[6] G. C. Sih, "Handbook of Stress Intensity Factors", Lehigh Univ. Press (1972).

[7] P. G. Charalambides and A. G. Evans, "Debonding Properties of Residually Stressed Brittle Matrix Composites", *J. Am. Ceram. Soc.*, 72[5], 746-753 (1989).

[8] M. Y. He and J. W. Hutchinson "A Crack Kinking Out of an Interface", Harvard University Report, MECH.-113 (1988).

[9] M. Y. He and J. W. Hutchinson "On Interface Debonding and Fiber Cracking in Brittle Matrix Composites". (To be published).

[10] A. G. Evans, M. Y. He and J. W. Hutchinson "A Crack Kinking Along the Interface". (To be published).

[11] M. D. Thouless, H. C. Cao and P. A. Mataga, "Delamination from Surface Cracks in Composite Materials". *J. Mat. Science*, in press.

[12] P. G. Charalambides. (Unpublished research).

[13] G. Campbell, M. Ruhle, B. J. Dalgleish and A. G. Evans, "Whisker Toughening: A Comparison Between Al_2O_3 and Si_3N_4 Toughened With SiC". (To be published).

[14] M. D. Thouless and A. G. Evans, "Effects of Pull-Out on the Mechanical Properties of Ceramic-Matrix Composites", *Acta Metall.*, 36[3], 517-522 (1988).

[15] M. D. Thouless, Orfeo Sbaizero, Lorenz S. Sigle and Anthony G. Evans, "Effects of Interface Mechanical Properties on Pullout in SiC-Fiber Reinforced Lithium Aluminum Silicate Glass-Ceramic", *J. Am. Ceram. Soc.*, 68[4], 225-231 (1989).

[16] B. Cotterell and J. R. Rice, "Slightly Curved or Kinked Cracks", *Int. J. Fract.* 16, 155 (1980).

[17] A. G. Evans and J. W. Hutchinson, "Effects of Non-Planarity on the Mixed Mode Fracture Resistance of Bimaterial Interfaces", *Acta Metall*, in press.

[18] P. G. Charalambic__, . Lund, A. G. Evans and R. M. McMeeking, "A Test Specimen for Determining the Fracture Resistance of Bimaterial Interfaces", *J. Appl. Mech.*, 56, 77-82 (1989).

[19] Z. Suo and J. W. Hutchinson, *Material Science and Engineering* A(107), 135-143 (1989).

[20] P. G. Charalambides, H. C. Cao, J. Lund and A. G. Evans, "Development of a Test Method for Measuring the Mixed Mode Fracture Resistance of Bimaterial Interfaces", (submitted to *Acta Metall.*, September 1988).

[21] M. D. Drory, M. D. Thouless and A. G. Evans, "On the Decohesion of Thin Films", *Acta Metall.*, 36, 2019-2028 (1988).
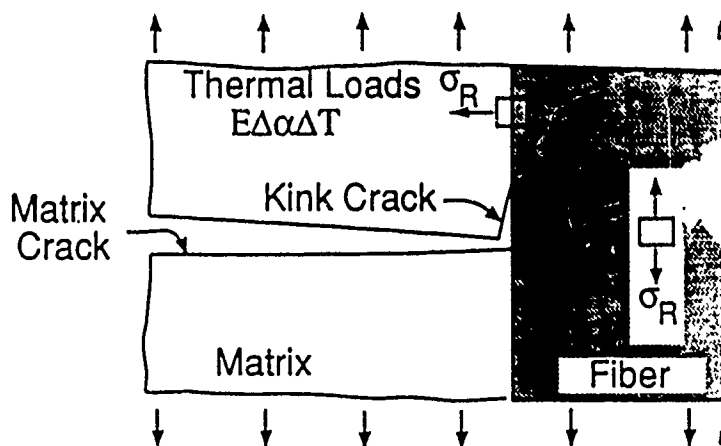
Figure Captions

Fig. 1 A schematic of composite microstructural failure:

   a) The Fiber is intercepted by the matrix crack

   b) Fiber failure. For a homogeneous system, *fiber failure* will be favored over initial fiber debonding (Fig 1c) if $\mathcal{G}_{ic}/gs_{if} > 1/4$, as discussed in Refs [8-10].

   c) Onset of initial fiber debonding. For a homogeneous system, if $\mathcal{G}_{ic}/gs_{if} \leq 1/4$ (Refs [8-10]) *initial fiber debonding* is favored over fiber failure (Fig 1b).

Fig. 2 The axisymmetric cylindrical unit cell wherein the matrix crack is bridged by an aligned network of fiber reinforcements.

Fig. 3 A schematic of a main crack kinking under mixed mode conditions.

Fig. 4 A schematic of competing events of debonding versus fiber failure for systems with interfaces inclined relative to the matrix crack plane.

Fig. 5 The four-point delamination flexure specimen. The delamination process is competing against incipient kink cracks at the delamination crack tip.

Fig. 6 The trends in the steady-state phase angle ψ^T (dash line) and kinking angle β for which $\mathcal{G}^K$ is maximized (solid line) with the stress ratio σ^R/t, for the special case of a beam with $h_1 = h_2$.

Fig. 7 The trends in the ratio $\mathcal{G}^k/\mathcal{G}^T$ with the stress ratio σ^R/t in an otherwise elastically homogeneous system with thermal expansion mismatches between the top and bottom layers ($h_1 = h_2$).

Fig. 8 Schematics of the microstructural failure brittle matrix composites reinforced with an aligned and inclined fiber network.

   a) Fibers failing with out debonding. Low toughness system.

   a) Fibers failing after debonding. High toughness system.

Fig. 9 The trends in the debond tip phase angles in a homogeneous system with normalized crack length. The curve for ψ^t marked by the solid line was derived numerically (see reference [7]) via the method of finite elements for the case of an applied stress t alone. The dash curve due to the thermal loads σ^R was interpolated between the steady-state numerical value reported in reference [7] and the kink crack solution derived in reference [9].
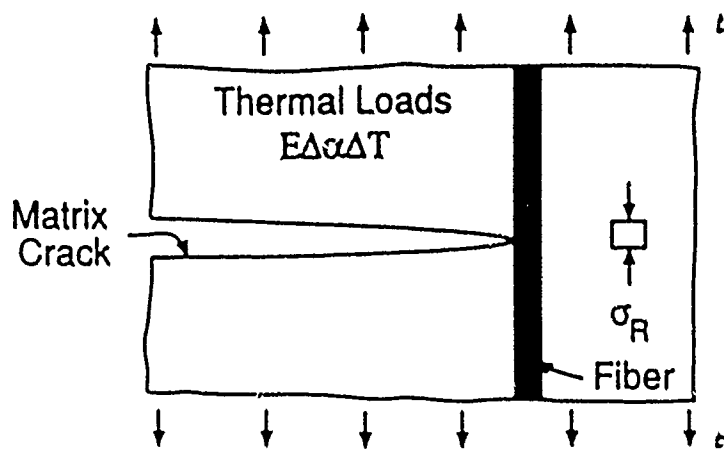
a) Fiber intercepted by the matrix crack
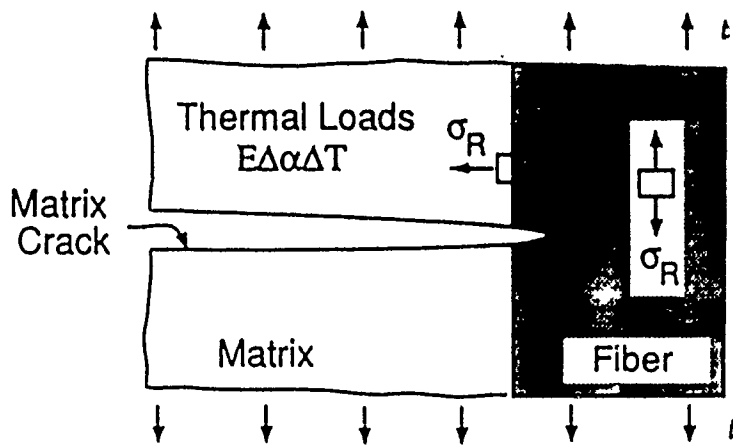
b) Fiber Failure $\quad \mathcal{G}_{ic}/\mathcal{G}_{fc} > 1/4$

c) Initial Fiber Debonding $\quad \mathcal{G}_{ic}/\mathcal{G}_{fc} < 1/4$

Fig. 1

Fig. 2

Fig. 3

a) An Inclined Fiber intercepted
   by the matrix crack

b) Fiber Failure $\mathcal{G}_{ic}/\mathcal{G}_{fc} > \mathcal{G}^{k}/\mathcal{G}^{T}$

c) Initial Fiber Debonding $\mathcal{G}_{ic}/\mathcal{G}_{fc} < \mathcal{G}^{k}/\mathcal{G}^{T}$

Fig. 4

Fig. 5

Kink Crack Angle β

Phase Angle ψ'ʳ

Normalized Stress Ratio, $\frac{E\Delta\alpha\Delta T}{t}$

(Degrees)
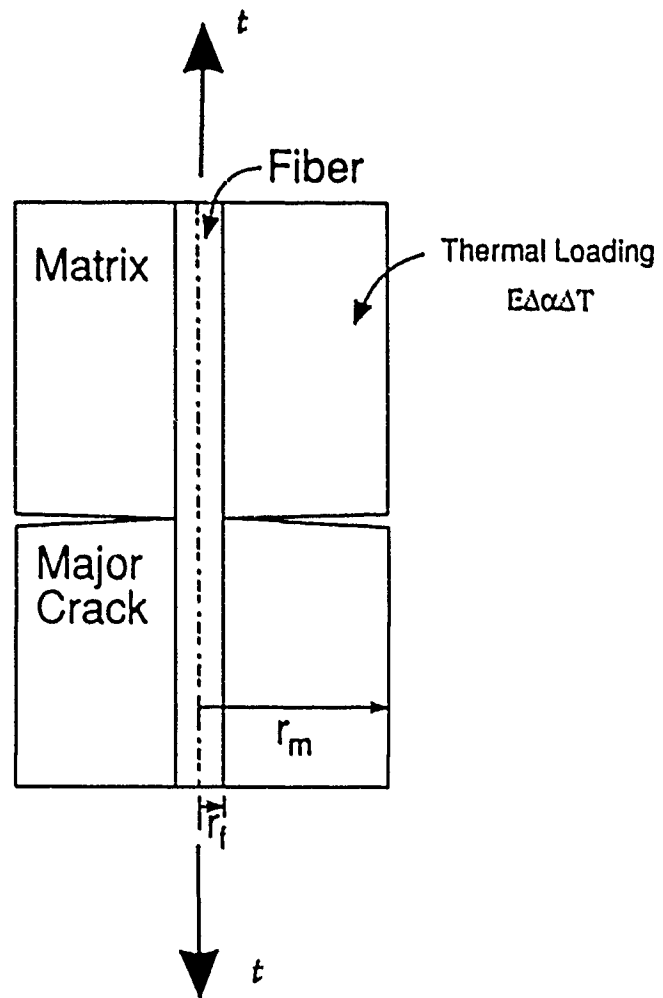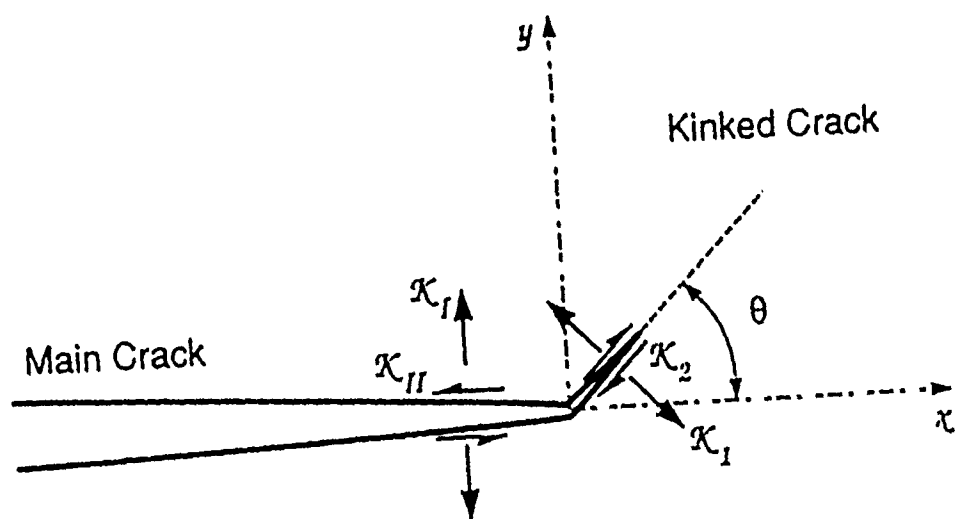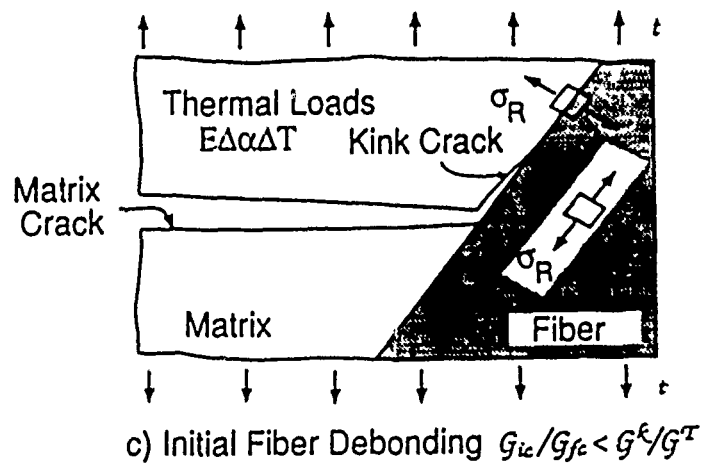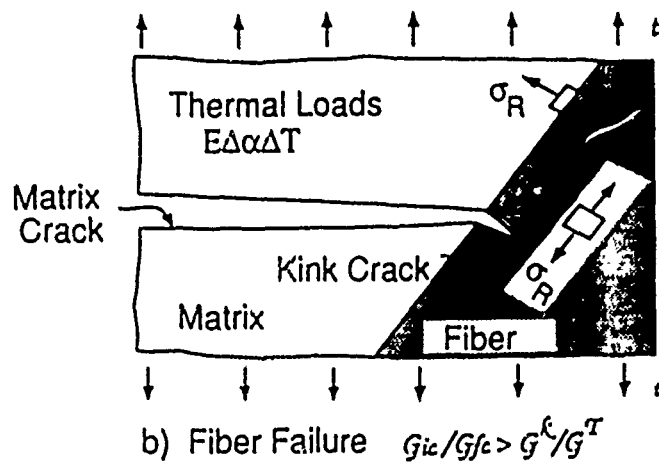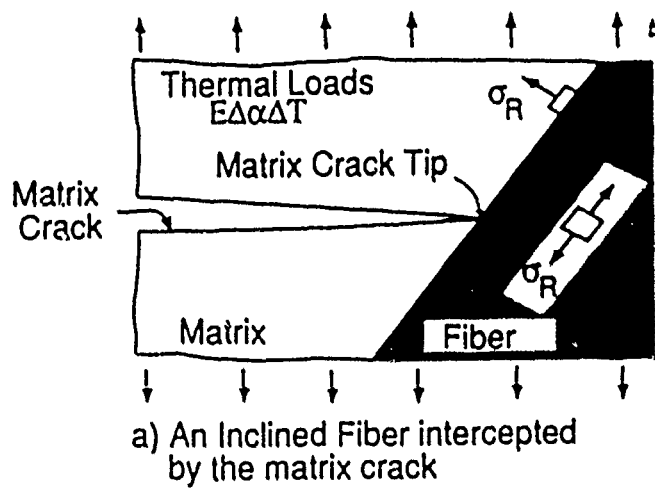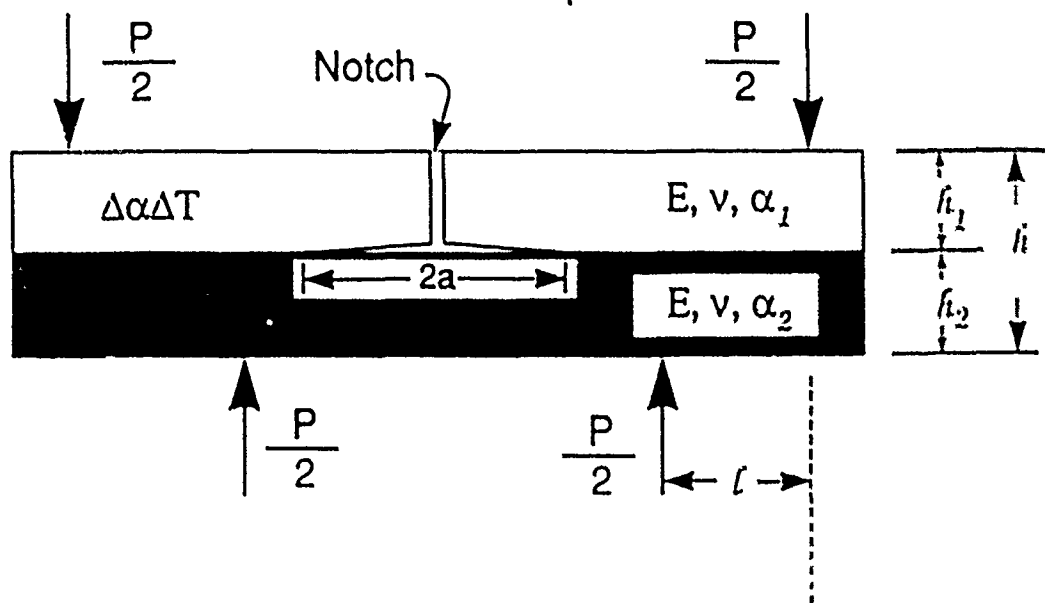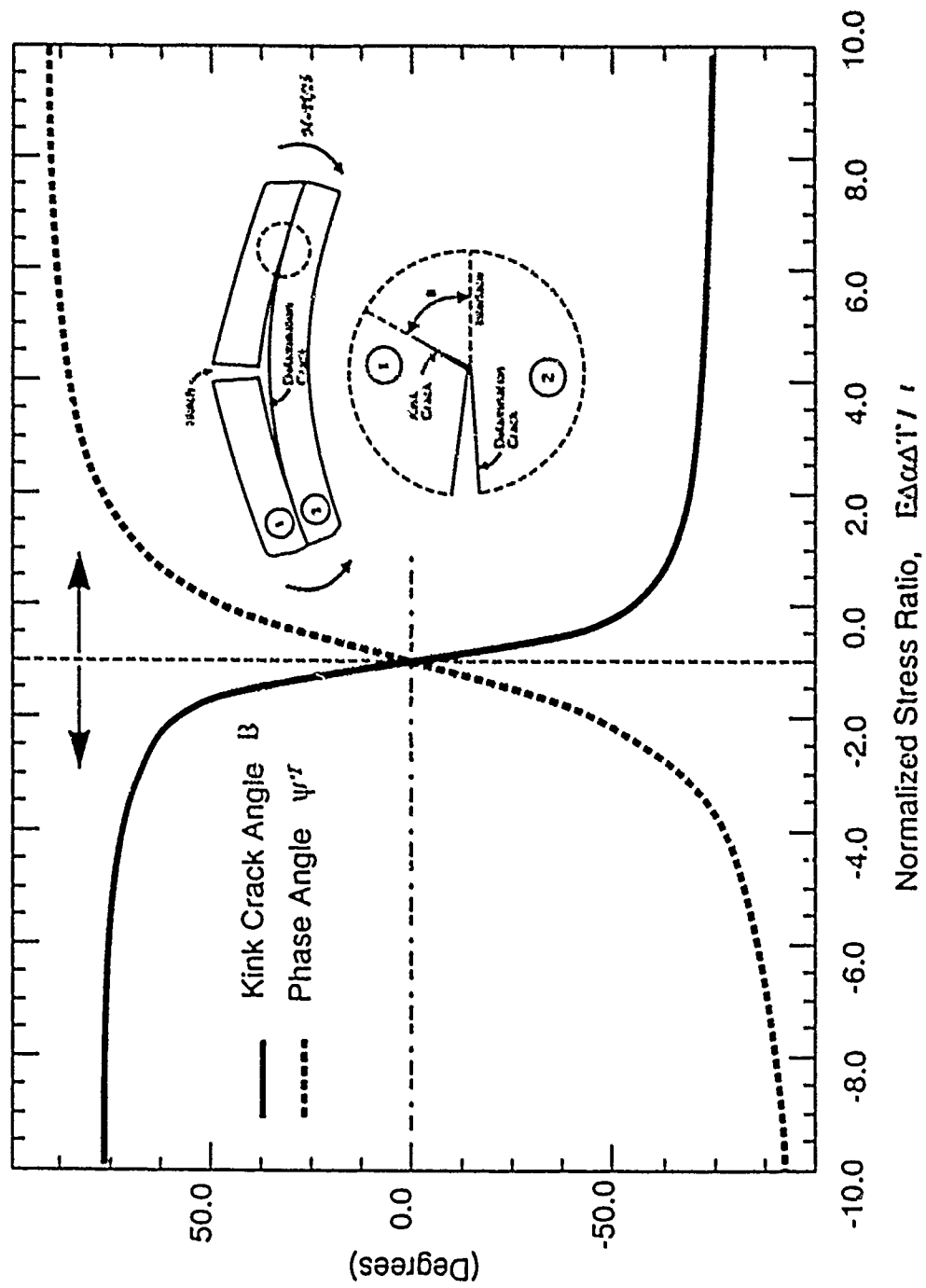
Fig. 6
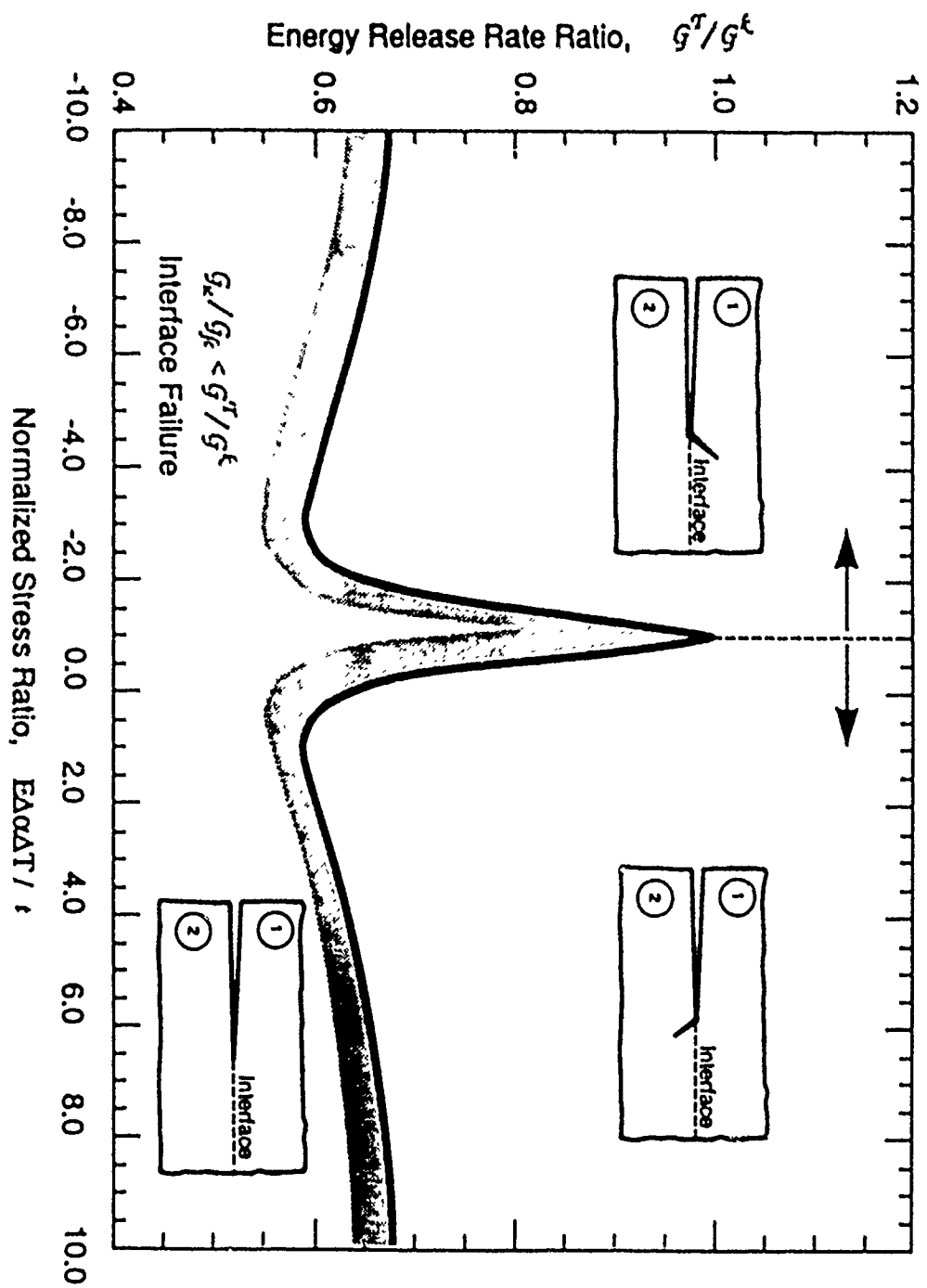
Fig. 7
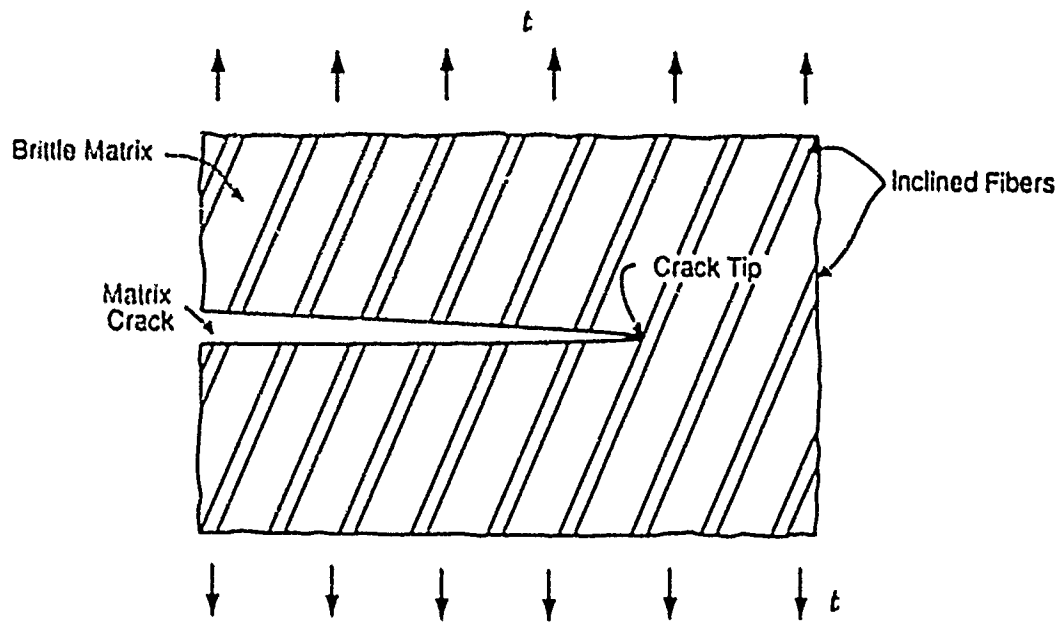
a) Brittle Composite Failure
(Thermally Insensitive Process)
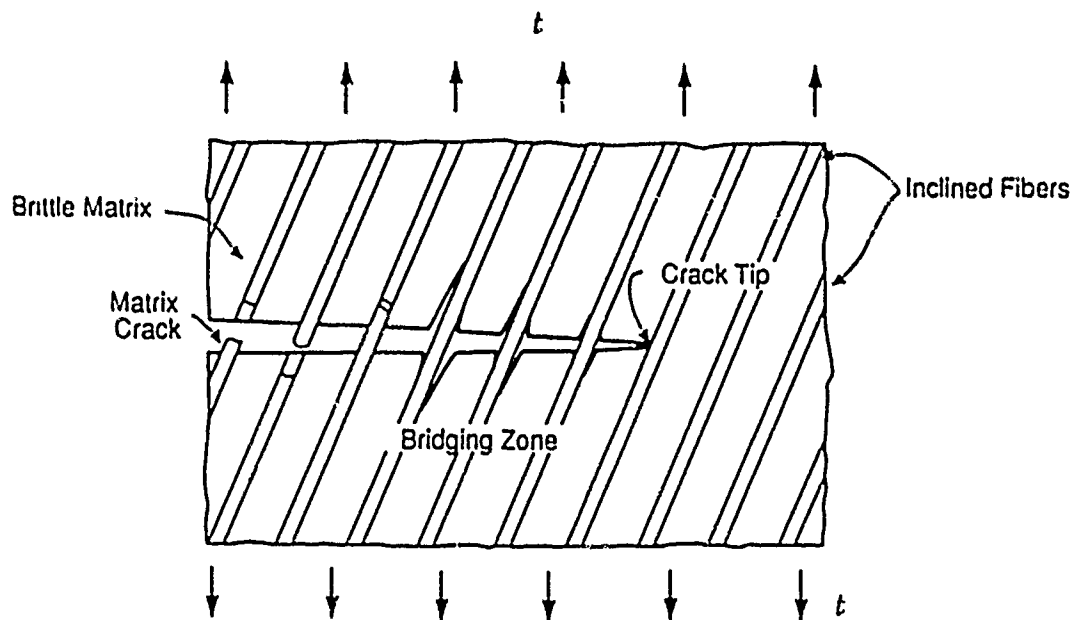
b) Debonding of Inclined Fibers
(Thermally Sensitive Process)

Fig. 8
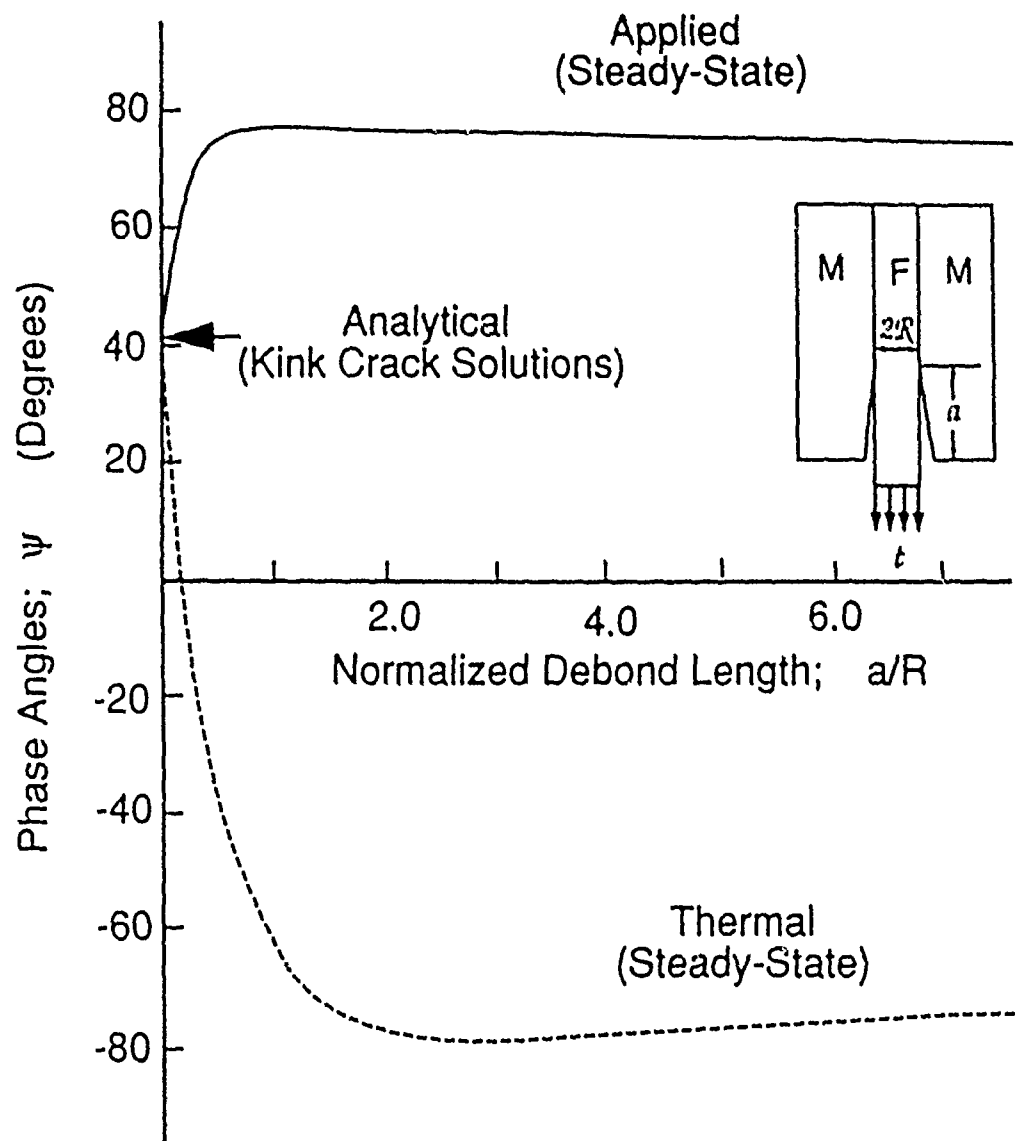
Fig. 9

MATERIALS
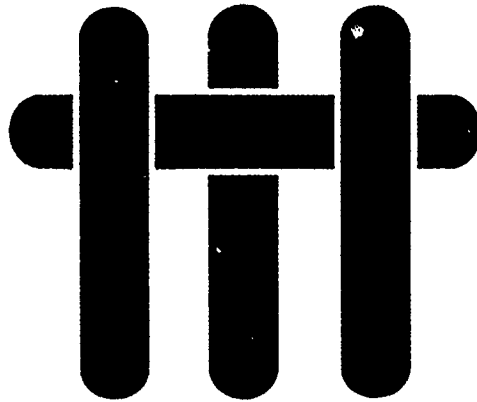
CRACK DEFLECTION AT AN INTERFACE

BETWEEN

DISSIMILAR ELASTIC MATERIALS

Ming-Yuan He*

Institute of Mechanics
Chinese Academy of Sciences
Beijing, People's Republic of China

and

John. W. Hutchinson

Division of Applies Sciences
Harvard University
Cambridge, Massachusetts 02138

---

* Visiting Scholar, University of California, Santa Barbara

CRACK DEFLECTION AT AN INTERFACE
BETWEEN DISSIMILAR ELASTIC MATERIALS

Ming-Yuan He†
Institute of Mechanics, Chinese Academy of Sciences, Beijing,
People's Republic of China

and

John W. Hutchinson
Division of Applied Sciences, Harvard University, Cambridge, MA 02138, U.S.A.

Abstract—A crack impinging an interface joining two dissimilar materials may arrest or may advance by either penetrating the interface or deflecting into the interface. The competition between deflection and penetration is examined in this paper when the materials on either side of the interface are elastic and isotropic. The energy release rate for the deflected crack is compared with the maximum energy release rate for a penetrating crack. The results can be used to determine the range of interface toughness relative to bulk material toughness which ensures that cracks will be deflected into the interface.

1. INTRODUCTION

In this paper several problems are analyzed which provide insight and quantitative information on the role an interface between dissimilar elastic materials plays when approached by a crack. At issue is whether a crack impinging on an interface will pass through the interface or be deflected into the interface. Such questions are of importance, for example, in the design of the interface between fiber and matrix in fiber reinforced ceramic composites where it is desired that any matrix crack approaching a fiber deflect along the interface, thereby allowing the fiber to survive. The results from this study provide estimates of the relative toughness of the interface to that of the material on the uncracked side of the interface necessary to ensure that a crack will deflect into the interface rather than penetrate it.

The four sets of problems analyzed are shown in Fig. 1. In set A, a symmetrically loaded, semi-infinite main crack impinges the interface at a right angle. The three problems analyzed (problems A1, A2 and A3) permit an assessment of the competition between penetration of the interface and deflection. Set B in Fig. 2 addressed the same competition when the main crack impinges on the interface at an oblique angle. An unusual feature of the oblique problem for the main crack (with $a = 0$) is the fact that there is a *single* dominant mode of deformation at the crack tip when the materials across the interface are dissimilar. Thus the asymptotic behavior at the crack tip is influenced by the remote loads only through a single stress intensity factor. The competition between penetration and deflection as posed in problems B1 and B2 does not depend on the nature of the remote loads in a strict asymptotic sense when the branch length a is arbitrarily small compared to the length of the main crack.

A consequence of the existence of a single dominant mode of the main crack impinging the interface at an oblique angle is a tendency for a crack approaching the interface to turn either into or away from the interface, depending on the relative stiffnesses of the materials on either side of the interface. In problem C in Fig. 1 the behavior of a straight wedge-loaded, semi-infinite crack is determined as the crack approaches the interface. This problem gives further insight into the tendency of a crack to curve into or away from the interface when it approaches at an oblique angle. Finally, in problems D1 and D2 the competition between penetration through the interface or deflection into it is analyzed for an oblique

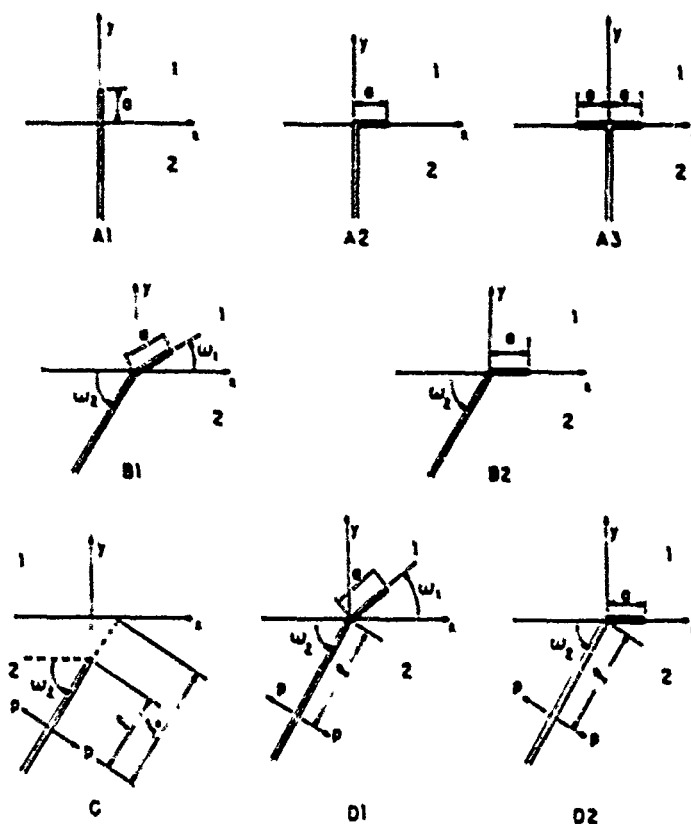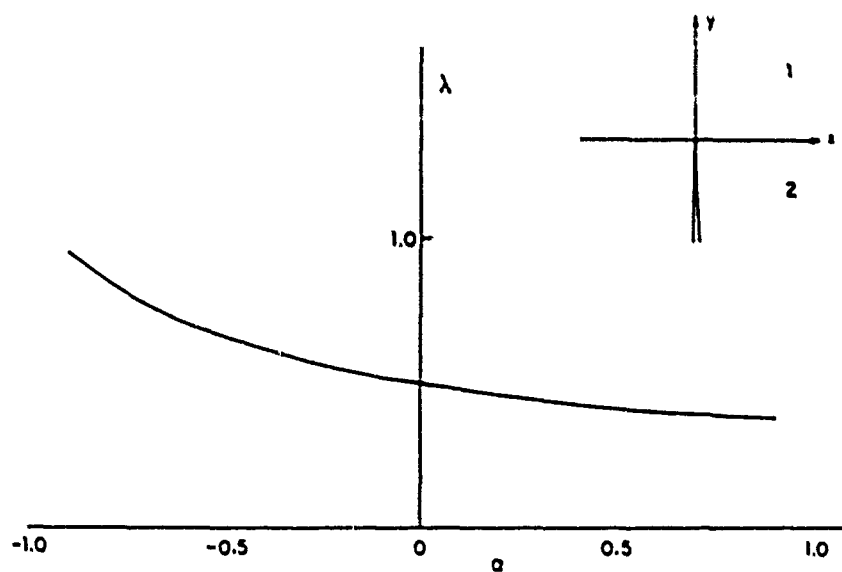† Visiting Scholar, Harvard University, August 1987–August 1988.

Fig. 1 Crack geometries.

Fig. 2. Stress singularity exponent for $\beta = 0$.

wedge-loaded crack These problems are solved for finite values of a/l where l is the distance of the wedge loads from the interface. The behavior as $a/l \to 0$ is discussed in relation to the problems in set B.

There are a number of earlier studies which analyze details of crack penetration and/or deflection at an interface without specifically focussing on the competition between the two modes of cracking. The solution procedures used in the present study are similar to, or extensions of, the integral equation methods used in these earlier papers. Cook and Erdogan (1972) and Erdogan and Biricikoglu (1973) investigate the behavior of a crack penetrating the interface at right angles. Goree and Venezia (1977) analyze several problems involving penetration and deflection for a main crack impinging the interface at right angles. Additional work along these same lines is reported by Lu and Erdogan (1983). The tendency for a crack approaching an interface or a free surface at an oblique angle to be deflected one way or the other has been elucidated by studies of Erdogan and Arin (1975) and more recently by Lardner et al. (1989).

In all cases the materials on either side of the interface are taken to be elastic and isotropic with shear modulus μ_i and Poisson's ratio ν_i where $i = 1$ and 2 correspond to the arrangement shown in Fig. 1. For the plane strain, traction boundary value problems considered, the solution variables of interest depend on only two non-dimensional combinations of the material parameters. These are the Dundurs' (1969) parameters

$$\alpha = [\mu_1(1-\nu_2) - \mu_2(1-\nu_1)]/[\mu_1(1-\nu_2) + \mu_2(1-\nu_1)] \tag{1}$$

$$2\beta = [\mu_1(1-2\nu_2) - \mu_2(1-2\nu_1)]/[\mu_1(1-\nu_2) + \mu_2(1-\nu_1)]. \tag{2}$$

The first parameter is most readily interpreted when expressed as $\alpha = (\bar{E}_1 - \bar{E}_2)/(\bar{E}_1 + \bar{E}_2)$ where $\bar{E} = E_i/(1-\nu^2)$ is the plane strain tensile modulus. The solutions to the four sets of problems are presented and discussed in the following sections. The problems are formulated and analyzed in the Appendices.

2. DEFLECTION VERSUS PENETRATION FOR A CRACK PERPENDICULAR TO THE INTERFACE (PROBLEMS A)

In the set A of problems the semi-infinite reference crack with $a = 0$ is perpendicular to the interface with its tip at the interface. A symmetric loading with respect to the crack plane is applied and the traction ahead of the crack in material 1 is characterized by

$$\sigma_{yy}(0,y) = k_1(2\pi y)^{-\lambda} \tag{3}$$

where λ is real and depends on α and β according to (Zak and Williams, 1963)

$$\cos \lambda\pi = \frac{2(\beta-\alpha)}{1+\beta}(1-\lambda)^2 + \frac{\alpha+\beta^2}{1-\beta^2}.$$

A plot of λ as a function of α for $\beta = 0$ is shown in Fig. 2. The amplitude factor k_1 is proportional to the applied load. Explicit knowledge of k_1 is not needed here. The reference crack is imagined to advance in the three ways indicated in Fig. 1: one by penetration straight through the interface (A1) and two by deflection into the interface (A2 and A3).

In the case of penetration, the stress state at the advancing tip is pure mode I. By dimensional considerations its stress intensity factor must depend on k_1 and a according to

$$K_1 = c(\alpha,\beta)k_1 a^{1/2-\lambda} \tag{4}$$

where c is dimensionless. The energy release rate is

$$\mathcal{G}_p = \frac{1-\nu_1}{2\mu_1} K_1^2 = \frac{1-\nu_1}{2\mu_1} c^2 k_1^2 a^{2\lambda}. \tag{5}$$

The traction on the interface directly ahead of the right-hand tip of either of the deflected cracks (A2 or A3) is characterized by (Rice, 1988)

$$\sigma_{yy}(x,0) + i\sigma_{xy}(x,0) = (K_1 + iK_2)(2\pi r)^{-1/2} r^{i\varepsilon} \tag{6}$$

where $r = x - a$, $i = \sqrt{-1}$, and

$$\varepsilon = \frac{1}{2\pi} \ln\left(\frac{1-\beta}{1+\beta}\right). \tag{7}$$

In these cases, dimensional considerations require

$$K_1 + iK_2 = k_1 a^{\lambda - 1/2} [d(\alpha,\beta)a^{i\varepsilon} + e(\alpha,\beta)a^{-i\varepsilon}] \tag{8}$$

where d and e are dimensionless complex valued functions of α and β. The energy release rate of the deflected crack is

$$\mathcal{G}_d = [(1-\nu_1)/\mu_1 + (1-\nu_2)/\mu_2](K_1^2 + K_2^2)/(4\cosh^2 \pi\varepsilon) \tag{9}$$

where

$$K_1^2 + K_2^2 = k_1^2 a^{2\lambda - 1}[|d|^2 + |e|^2 + 2R_e(de)]. \tag{10}$$

In each of the three cases the energy release rate goes to zero or becomes unbounded as $a \to 0$ depending on whether λ is less than or greater than 1/2. But the dependence of $\mathcal{G}$ on a is very weak since λ differs only slightly from 1/2 except for $\alpha < -0.7$ (cf. Fig. 2). More importantly, the ratio $\mathcal{G}_d/\mathcal{G}_p$ is independent of a (and k_1) and is given by

$$\mathcal{G}_d/\mathcal{G}_p = [(1-\beta^2)/(1-\alpha)][|d|^2 + |e|^2 + 2R_e(de)]/c^2. \tag{11}$$

Thus the *relative* tendency of a crack to be deflected by the interface or to pass through it can be assessed using this ratio.

Integral equation methods have been used to solve for the function $c(\alpha,\beta)$ for the case of the penetrating crack and for $d(\alpha,\beta)$ and $e(\alpha,\beta)$ for the two cases involving deflected cracks. The details of the solution procedures are given in Appendices I and II. The ratio $\mathcal{G}_d/\mathcal{G}_p$ is plotted as a function of α in Fig. 3 for $\beta = 0$ for each case. The effect of β has not been systematically explored since it is felt that α is the more important of the two parameters. In any case, the effect of β on the ratio is not expected to be large, as was seen in a similar problem (He and Hutchinson, 1989). Note, for example, that β appears explicitly in (11) only to order β^2. The relative amounts of K_1 and K_2 at the right-hand tip of the deflected cracks are presented in Fig. 4 using the measure $\psi = \tan^{-1}(K_2/K_1)$.

Let $\mathcal{G}_{ic}$ be the toughness of the interface (which may depend on ψ) and let $\mathcal{G}_c$ be the mode I toughness of material 1. The impinging crack is likely to be deflected into the interface if

$$\mathcal{G}_{ic}/\mathcal{G}_c < \mathcal{G}_d/\mathcal{G}_p \tag{12}$$

since then the condition for propagation in the interface will be met at a lower load than that for penetration across the interface. Conversely, the crack will tend to penetrate the interface when the inequality is reversed. The deflected crack branching to one side (as opposed to the crack with the double branch) generally controls the condition for deflection into the interface since it corresponds to the highest ratio $\mathcal{G}_d/\mathcal{G}_p$, although the double branching crack could control if $\mathcal{G}_{ic}$ depends strongly on ψ. For α not too different from
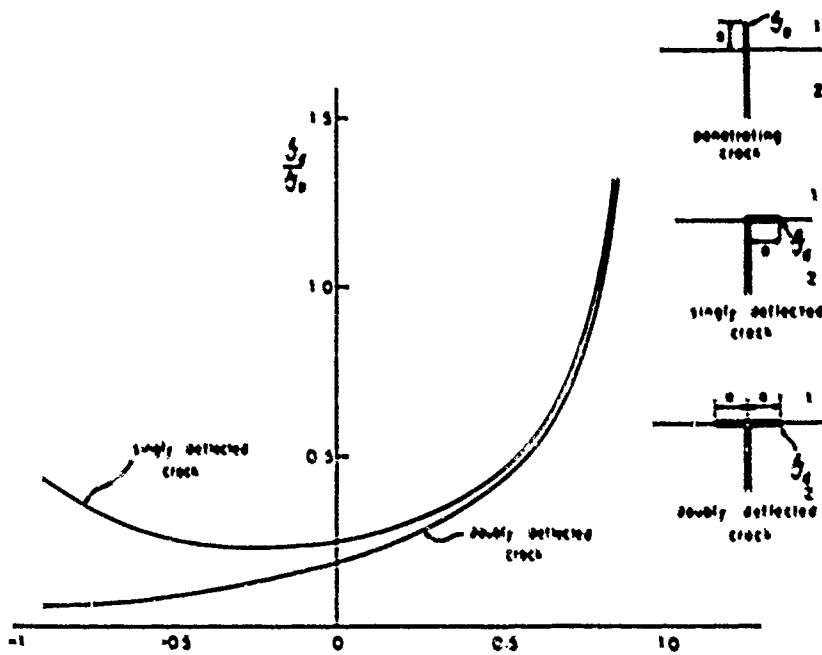
Fig. 3. Ratio of energy release rate of deflected crack to penetrating crack at same amount of crack advance *a*

zero, the critical ratio is approximately 1/4. It increases to approximately 1.2 when $x = 1/2$, corresponding to a plane strain tensile modulus of material 1 being three times that of material 2.

The analysis has not addressed the question of the load level required for the crack to deflect into the interface or to penetrate it. Rather, it has exploited the fact that the energy release rates of the competing crack trajectories depend on crack advance *a*, in exactly the same way. Thus the relative energy release rates can be unambiguously determined and used to assess which of the competing trajectories will be selected. When $\lambda < 1.2$ it is
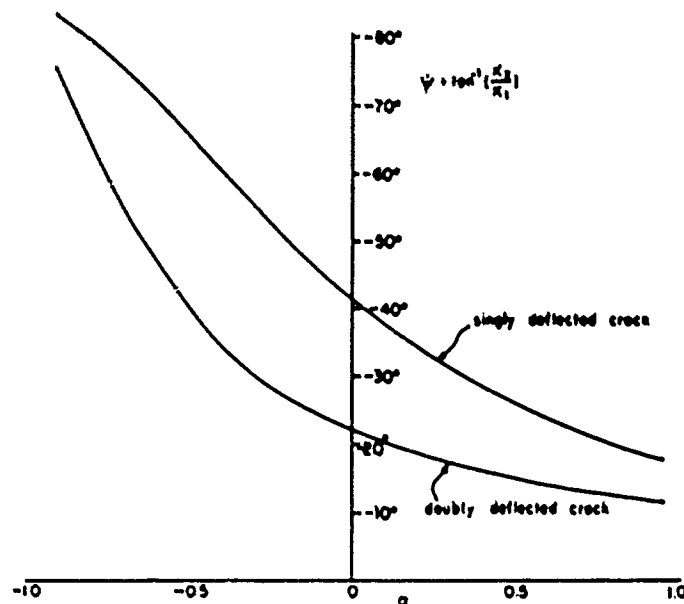
Fig. 4. Combination of interface stress intensity factors at right-hand tip of deflected crack.
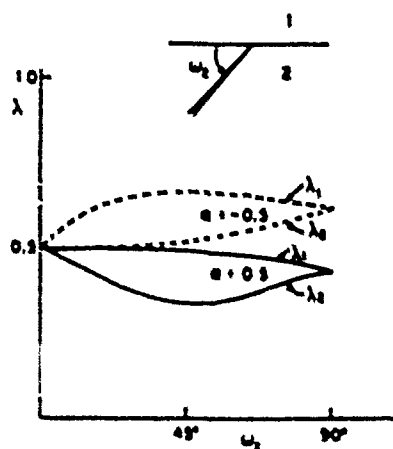
Fig. 5 Stress singularity exponents for crack impinging interface at an oblique angle ($\beta = 0$)

necessary to invoke intrinsic flaws in either the interface or in material 1 for the crack to grow from the tip when $\alpha = 0$. The condition (12) implicitly assumes these intrinsic flaws of comparable size. The above conclusions are also drawn under the assumption that the crack approaches the interface quasistatically. Dynamic effects may alter the conclusions somewhat when the impinging crack is traveling at a significant fraction of the elastic wave speed.

3 CRACK TERMINATING AT AN INTERFACE AT AN OBLIQUE ANGLE

There is a peculiarity to the problem of a crack impinging on an interface at an oblique angle which makes a discussion of the relative tendency for deflection or penetration somewhat more complicated than the case of the perpendicularly impinging crack. The peculiarity concerns the nature of the singular stress fields for an oblique crack terminating at the interface with the geometry shown in the insert in Fig. 5.

For a homogeneous material ($\alpha = \beta = 0$) or for the crack making a right angle with the interface between two different materials ($\omega_1 = \pi/2$), the most singular stress fields of physical interest at the tip can be written as

$$\sigma_{ij} = k_1 r^{-\lambda} \sigma_{ij}^I(\theta) + k_{II} r^{-\lambda} \sigma_{ij}^{II}(\theta) \tag{13}$$

where $\lambda = 1/2$ for the homogeneous material and λ is given in Fig. 2 for ($\omega_1 = \pi/2$). In these cases, the eigenvalue problem for the exponent λ has a double root yielding two linearly independent fields σ_{ij}^I and σ_{ij}^{II} which can be taken to be symmetric and anti-symmetric relative to the crack plane. When the crack lies on the interface ($\omega_1 = 0$) the eigenvalue is also double with $\lambda = 1/2$ when $\beta = 0$.

For values of ω_1 between 0 and $\pi/2$ the eigenvalue problem no longer has double roots when the materials are dissimilar. Instead of (13), the two most singular fields of interest are

$$\sigma_{ij} = k_1 r^{-\lambda_1} \sigma_{ij}^{(1)}(\theta) + k_2 r^{-\lambda_2} \sigma_{ij}^{(2)}(\theta) \tag{14}$$

where λ_1 and λ_2 are real for $\beta = 0$. Corresponding to each eigenvalue is only one eigenfunction instead of two. The two exponents λ_1 and λ_2 are plotted as a function of ω_2 in Fig. 5 for $\alpha = \pm 0.5$ with $\beta = 0$. If λ_1 is identified as the larger of two exponents, the dominant singular field is
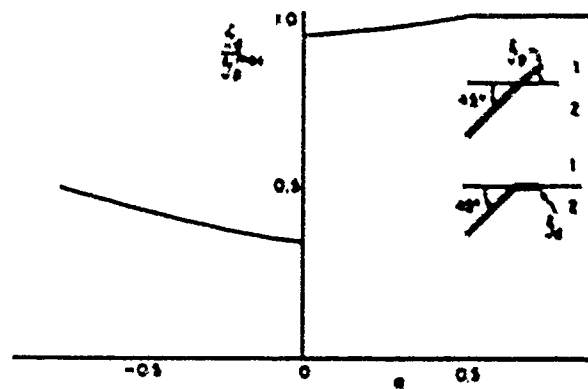
Fig. 6. Ratio of ratio of energy release rate of deflected crack to maximum energy release rate of penetrating crack at same α for asymptotic problem characterized by (15) when $\alpha = 0$ ($\beta = 0$)

$$\sigma_\mathrm{ij} = k_1 r^{\lambda-1} \sigma_\mathrm{ij}^{(1)}(\theta) \tag{15}$$

where $\sigma_\mathrm{ij}^{(1)}(\theta)$ is a mixed mode θ-variation which depends on ω_2 and α.

Thus, unlike the problems mentioned above—indeed, unlike most linear crack problems—the oblique crack terminating at an interface has a *fixed* mixed mode (i.e. a fixed θ-variation) independent of the remote loading combinations acting on the body. The zone of dominance of (15) may be very small and must vanish as α and β vanish since then the two-term representation (13) holds. Similarly, dominance must vanish as $\omega_2 \to 0$ or $\pi/2$. In spite of the limited range of dominance expected for (15), we have considered the competition between penetration and deflection at an interface for an oblique crack where (15) specifies the dominant field at the tip of the main crack. These results are discussed in the next section. In the last two sections, we circumvent the issue of limited dominance of the asymptotic problem by analyzing an oblique crack under a specific wedge-loading.

4 ASYMPTOTIC LIMITS FOR DEFLECTION VERSUS PENETRATION FOR AN OBLIQUE CRACK (PROBLEMS B)

In problems B1 and B2 (cf Fig. 1) the dominant singularity field (15) is imposed as the remote field on the main semi-infinite crack. The competition between penetration of the interface and deflection into the interface parallels that discussed in Section 2 for the perpendicular crack under symmetric load. Now, however, the direction taken by the crack penetrating into material 1, ω_1, must be determined. The direction chosen will be that which maximizes the energy release rate.

The stress intensity factors at the tip of the penetrating crack are related to k_1 and a by

$$K_1 + iK_{11} = c(\alpha, \omega_1, \omega_2) k_1 a^{1/2 - \lambda_1} \tag{16}$$

where c is a dimensionless complex-valued function and attention will be focussed on material combinations with $\beta = 0$. The energy release rate of the penetrating crack is

$$\mathscr{G}_p = \frac{1-\nu_1}{2\mu_1} |c|^2 k_1^2 a^{1-2\lambda_1}. \tag{17}$$

The maximum energy release rate with respect to ω_1 for fixed a is denoted by $\mathscr{G}_p^{max}$. The interface stress intensity factors of the deflected crack can be expressed as (8) with $\epsilon = 0$ and k_1 and λ replaced by k_1 and λ_1, respectively. The ratio of the two energy release rates is again independent of a and is given by

$$\mathscr{G}_d / \mathscr{G}_p^{max} = (1-\alpha)^{-1} [|d|^2 + |e|^2 + 2R_e(de)]/|c|^2. \tag{18}$$

Numerical results for this ratio as a function of α are shown in Fig. 6 for the case where

$\omega_2 = 45$. When material 1 is stiff compared to material 2 ($x > 0$) the maximum energy release rate of the penetrating crack is only slightly larger than that of the deflected crack. In fact, when x is greater than about 0.5 the maximum energy release rate of the penetrating crack is attained for $\omega_2 = 0$ so that the critical penetrating crack coincides with the deflecting crack. When material 1 is the more compliant material the energy release rate of the penetrating crack significantly exceeds that of the deflecting crack.

The discontinuity in $\mathscr{G}$, $\mathscr{G}_p^{max}$ in Fig. 6 at $x = 0$ is associated with exchange in roles of (λ_1, λ_2) and $(\sigma^{\theta\theta}(\theta), \sigma^{r\theta}(\theta))$ in (14) as x changes sign. The θ-variation of the dominant singularity field (15) changes discontinuously as x changes sign. As has already been mentioned, the dominance of the single field (15) vanishes as $x \to 0$.

We proceed from here by considering the specific wedge-opening loading indicated in problems C and D in Fig. 1. One consequence of a *single* dominated mixed mode for the crack terminating at the interface is that a straight crack approaching the interface will necessarily experience a mixed mode at its tip. This is illustrated by example in the next section where its implications are discussed. In Section 6 we reconsider the competition between penetration and deflection for the oblique crack under the wedge loading for finite values of a/l.

5. STRAIGHT CRACK UNDER WEDGE LOADING APPROACHING AN INTERFACE AT AN OBLIQUE ANGLE (PROBLEM C)

With the tip of the crack in material 2, the near tip fields are a combination of modes I and II. Here we examine the history of K_I and K_{II} for the semi-infinite, straight crack loaded by the opening wedge forces per unit thickness P shown as C in Fig. 1. The solution for the stress intensity factors can be written as

$$K_I + iK_{II} = cPl^{-1/2} \tag{19}$$

where l is the distance of the tip from the loads and where c is a dimensionless, complex function of x, β, ω_2 and l/l_a. When l is small compared to l_a the crack tip is in mode I with the well-known result

$$K_I \to \left(\frac{2}{\pi}\right)^{1/2} Pl^{-1/2} \quad \text{for} \quad l/l_a \ll 1 \tag{20}$$

As l increases the crack tip interacts with the interface and some amount of mode II is induced. Plots of K_{II}/K_I as a function of l/l_a are given in Fig. 7 for three angles of approach ($\omega_2 = 30$, 45 and 60) for two material combinations ($x = 0.5$ and $x = -0.5$, each with $\beta = 0$). These results have been computed using an integral equation approach given in Appendix B.

When the crack approaches a more compliant material across the interface ($x < 0$) K_{II} become negative, although it is very slightly positive for an initial range of l/l_a. If it were free to curve following a path with K_{II} always zero, the crack would curve toward the interface since the straight crack has $K_{II} < 0$. Conversely, when the straight crack approaches a stiffer material across the interface ($x > 0$), K_{II} becomes positive suggesting that an actual crack trajectory satisfying $K_{II} = 0$ would curve away from the interface. Conjectured trends are sketched in Fig. 8. Similar conclusions have been drawn in the studies of Erdogan and Arin (1975) and Lardner et al. (1989).

The variation of the energy release rate

$$\mathscr{G} = \frac{(1 - \nu_2)}{2\mu_2} |c|^2 \frac{P^2}{l} \tag{21}$$

with l/l_a is shown in Fig. 9 for $\omega_2 = 60$ and for $x = 0$ and ± 0.5 with $\beta = 0$. These variations reflect the behavior that is well-known for a crack approaching an interface at right angles.
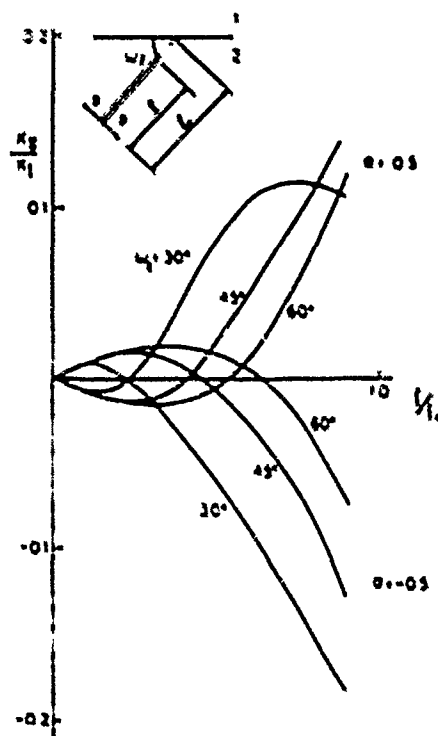
Fig. 7 Ratio of K_{II} to K_I for wedge loaded straight crack approaching the interface at several angles.
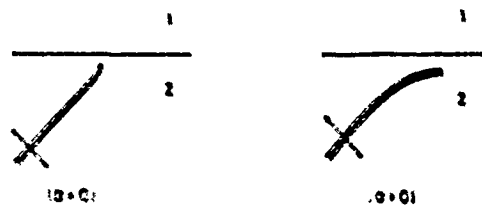
Fig 8 Conjectured trends for crack approaching an interface

When the material across the interface is stiffer than that where the crack resides $(x > 0)$, $\mathcal{G}$ must drop to zero as the interface is approached. But note from Fig. 5 that λ_1 is only very slightly smaller than 1/2 for $\omega_2 = 60°$ and $\alpha = 0.5$, and thus $\mathcal{G}$ has not yet started to drop steeply even when $l/l_0 = 0.95$. When $x = -0.5$, corresponding to a more compliant material across the interface, $\lambda_1 = 0.67$ and the increase in $\mathcal{G}$ as the interface is approached is more dramatic.

6. DEFLECTION VERSUS PENETRATION OF A WEDGE-LOADED CRACK IMPINGING AN INTERFACE AT AN OBLIQUE ANGLE (PROBLEMS D)

The main semi-infinite crack in Set D in Fig. 1 is subject to opening wedge loads, P, a distance, l, from the interface along the crack line. Competition between penetration (D1) and deflection (D2) is analyzed. As noted in the previous section an oblique crack under the wedge-opening loading is not expected to approach the interface as a straight crack. Nevertheless, the problems analyzed in this section should give further insight into the crack deflection process. Moreover, the results of this section place the behavior of the perpendicular crack in perspective.

The solution for the stress intensity factors in problem D1 can be written as
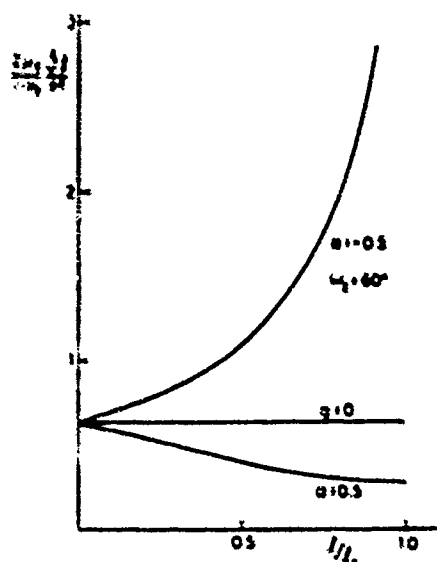
Fig. 9. Normalized energy release rate for straight crack approaching an interface at $\omega_2 = 60°$ $(\beta = 0)$.

$$K_1 + iK_{II} = c(\alpha, \omega_1, \omega_2, a/l) P l^{-1/2} \tag{22}$$

where c is a dimensionless complex-valued function of the arguments indicated (β is again taken to be zero). The energy release rate is

$$\mathcal{G}_p = \frac{(1-\nu_1)}{2\mu_1} c^2 \frac{P^2}{l} \tag{23}$$

The maximum value of $\mathcal{G}_p$ with respect to ω_1 for fixed a/l is denoted by $\mathcal{G}_p^{max}$.
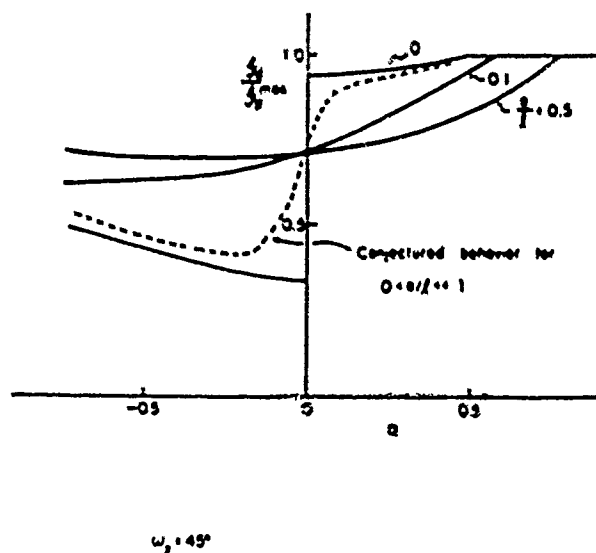
$\omega_2 = 45°$

Fig. 10. Ratio of energy release rate of deflected crack to maximum energy release rate of penetrating crack at same a for $\omega_2 = 45°$ and $\beta = 0$.
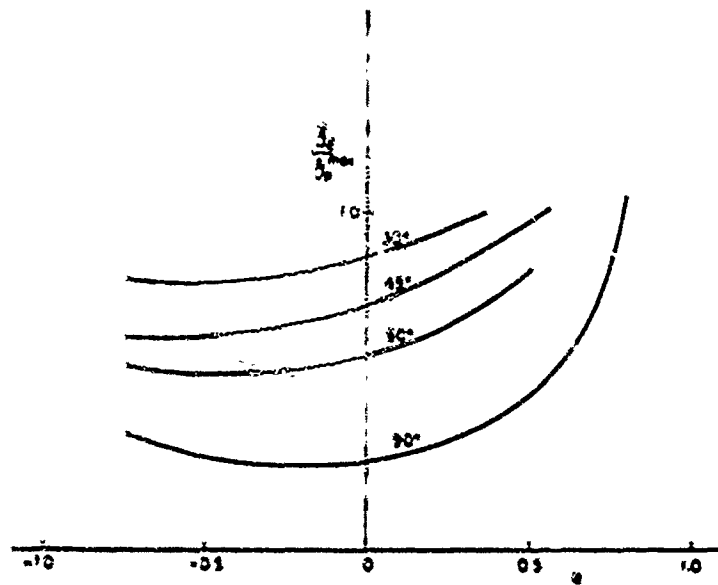
Fig. 11. Ratio of energy release rate of deflected crack to maximum energy release rate of penetrating crack at same α for wedge loaded crack with ω₂ = 30, 45, 60, α/l = 0.1 and β = 0. The curve for ω₂ = 90 is from Fig. 3.

With $\beta = 0$, the interface intensity factors for the deflected crack can be expressed in a manner similar to (22), i.e.

$$K_1 + iK_2 = d(\alpha, \omega_2, a/l) P l^{-1/2} \tag{24}$$

The energy release rate of the deflected crack, $\mathcal{G}_d$, is again given by (9) (with $\epsilon = 0$) where $K_1^2 + K_2^2 = d^2 P^2 / l$.

The ratio of the competing energy release rates is
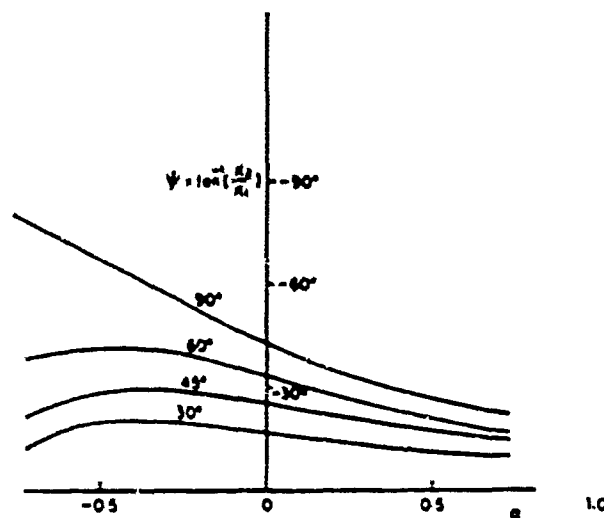
Fig. 12. Combination of interface stress intensity factors at tip of deflected crack for ω₂ = 30, 45, 60 and 90

$$\mathscr{G}_d \, \mathscr{G}_p^{\,rin} = (1-x)^{-1} |d|^2 \, |c|^2. \tag{25}$$

This ratio is plotted as a function x for $\omega_2 = 45$ in Fig. 10 for $a/l = 0.5$ and 0.1; the asymptotic limit of Section 4 for $a/l \to 0$ is also included, taken from Fig. 6. Equation (25) has a finite limit as $a \to 0$, and we believe that this limit must be the asymptotic result of Section 4. We have not attempted to compute the ratio (25) for values of a/l smaller than 0.1. However, we conjecture that results for significantly smaller a/l will approach the asymptotic limit in the manner indicated in Fig. 10.

Curves of $\mathscr{G}_d \, \mathscr{G}_p^{\,rin}$ as a function of x are shown in Fig. 11 for $a/l = 0.1$ and $\omega_2 = 30^\circ$, 45, and 60. Included also is the curve from Fig. 3 for the singly deflected crack with $\omega_2 = 90$. The associated measure ψ of the relative combination of the stress intensity factors of the deflected crack is given in Fig. 12. As one would expect intuitively, the competition between deflection and penetration becomes more favorable to deflection the more oblique is the crack impinging the interface. If one desires to design the toughness of an interface such that a crack of any orientation will be deflected, then the results for the perpendicularly impinging crack ($\omega_2 = 90$) control the choice of interface toughness. For x-values in the range of -0.5 to about 0.25 the toughness of the interface (measured in energy units) must be less than about one quarter of the toughness of the material across the interface if all cracks are to be deflected.

REFERENCES

Cook, T. S. and Erdogan, F. (1972) Stresses in bonded materials with a crack perpendicular to the interface. Int. J. Engng Sci. 10, 677-697

Dundurs, J. (1969) Edge-bonded dissimilar orthogonal elastic wedges. J. Appl. Mech. 36, 650-652.

Erdogan, F. and Arin, K. (1975) Half plane and a strip with an arbitrary located crack. Int. J. Fract. 11, 191-204.

Erdogan, F. and Bincikoglu, V. (1973) Two bonded half planes with a crack going through the interface. Int. J. Engng Sci. 11, 745-766.

Gutce, J. G. and Venezia, W. A. (1977) Bonded elastic half-planes with an interface crack and a perpendicular intersecting crack that extends into the adjacent material. Int. J. Engng Sci. 15, Part I, 1-17, Part II, 19-27

He, M. Y. and Hutchinson, J. W. (1989) Kinking of a crack out of an interface. To be published in J. Appl. Mech. (in press)

Hein, V. L. and Erdogan, F. (1971) Stress singularities in a two material wedge. Int. J. Fract. Mech. 7, 317-330.

Lu, M-C. and Erdogan, F. (1983) Stress intensity factors in two bonded elastic layers containing cracks perpendicular to and on the interface. Engng Fract. Mech. 18, Part I, 491-506, Part II, 507-528.

Lardner, T. J., Ritter, J. E., Shiao, M. L. and Lin, M. R. (1989) Behavior of cracks near free surfaces and interfaces. To be published.

Rice, J. R. (1988) Elastic fracture concepts for interfacial cracks. J. Appl. Mech. 55, 98-103.

Zak, A. R. and Williams, M. L. (1963). Crack point singularities at a bi-material interface. J. Appl. Mech. 30, 142-143

APPENDIX A: INTEGRAL EQUATIONS

In this Appendix we set up the integral equations for the plane strain problem specified in Fig. A1, which is representative of several of the various problems.

Let $u_r(\eta_1)$ and $u_\theta(\eta_1)$ be the r and θ components of an edge dislocation located on the radial line $\theta = \omega_1$ at $Z_1 = \eta_1 e^{i\omega_1}$, and let $h_r(\eta_2)$ and $h_\theta(\eta_2)$ be the r and θ components of an edge dislocation located on the radial line $\theta = -\omega_2$ at $Z_2 = \eta_2 e^{-i\omega_2}$. The stresses induced by a dislocation can be obtained using the Muskhelishvili method and are given as follows.
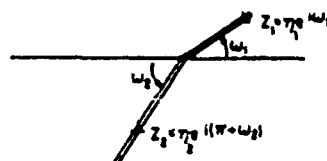

Fig. A1. Geometry conventions.

The stress components σ_{rr} and $\sigma_{r\theta}$ at a point $Z = t_1 e^{i\omega}$ on the radial line $\theta = \omega$ induced by the dislocation at $Z_1 = \eta_1 e^{i\omega}$ are given by

$$\sigma_{rr} + i\sigma_{r\theta} = 2B(\eta_1) e^{i\omega} (\eta_1 - t_1) + B(\eta_2)G_1(\eta_2, t_1) + B(\eta_2)G_2(\eta_2, t_1) \tag{A1}$$

Similarly, the stresses at a point $Z = t_1 e^{i\omega}$ on the radial line $\theta = \omega$, induced by the dislocation at $Z_2 = \eta_2 e^{i\omega}$ are given by

$$\sigma_{rr} + i\sigma_{r\theta} = B(\eta_2)F_1(\eta_2, t_1) + B(\eta_2)F_2(\eta_2, t_1). \tag{A2}$$

The stresses at a point $Z = t_2 e^{i\omega}$ on the radial line $\theta = \omega$, induced by the dislocation at $Z_1 = \eta_1 e^{i\omega}$ are given by

$$\sigma_{rr} + i\sigma_{r\theta} = 2A(\eta_1) e^{i\omega} (t_2 - \eta_1) + A(\eta_1)F_1(\eta_1, t_2) + A(\eta_1)F_2(\eta_1, t_2) \tag{A3}$$

The stresses at a point $Z = t_2 e^{i\omega}$ on the radial line $\theta = \omega_2$ induced by the dislocation at $Z_2 = \eta_2 e^{i\omega}$ are given by

$$\sigma_{rr} + i\sigma_{r\theta} = A(\eta_2)G_3(\eta_2, t_2) + A(\eta_2)G_4(\eta_2, t_2) \tag{A4}$$

where $i = \sqrt{-1}$, $(\bar{\ })$ denotes the complex conjugate, and

$$A(\eta_1) = \mu_1 [4\pi i(1 - \nu_1)](\omega_1 - \omega_2) e^{i\omega}$$
$$B(\eta_2) = \mu_2 [4\pi i(1 - \nu_2)](b - ib) e^{i\omega} \tag{A5}$$

and where

$$C_1 = -\delta\left(\frac{1}{(z - \bar{z}_2)} - \frac{z_2 - z_1}{(z - z_2)^2} + e^{2i\omega} \frac{z_2 - t}{(z - \bar{z}_2)^2}\right)$$

$$G_2 = -\delta\left(\frac{1}{z - z_2} - \frac{z_2 - z_2}{(z - z_2)^2} + e^{2i\omega} \frac{(z_2 - \bar{z}_2)(z - \bar{z}_2 - 2\bar{z})}{(z - \bar{z}_2)^3}\right) - \frac{\Delta}{z - \bar{z}_2} e^{2i\omega}$$

$$G_3 = \frac{1 - \Delta_1}{z - \bar{z}_1} + e^{2i\omega} \frac{\bar{z}_2(1 - \Delta_1) - z(1 - \Delta_1) - z_2(\delta_1 - \Delta_1)}{(z - \bar{z}_1)^2}$$

$$G_4 = \frac{(1 - \Delta_1)}{z - z_1} + e^{2i\omega} \frac{(1 - \delta_1)}{z - \bar{z}_1}$$

$$F_1 = -\delta_1\left(\frac{1}{z - \bar{z}_1} - \frac{z_1 - z_1}{(z - z_1)^2} + e^{2i\omega} \frac{(z_1 - t)}{(z - \bar{z}_1)^2}\right)$$

$$F_2 = -\delta_1\left(\frac{1}{z - z_1} - \frac{z_1 - z_1}{(z - z_1)^2} + e^{2i\omega} \frac{(z_1 - \bar{z}_1)(z - \bar{z}_1 - 2\bar{z})}{(z - \bar{z}_1)^3}\right) - \frac{\Delta_1}{z - z_1} e^{2i\omega}$$

$$F_3 = \frac{(1 - \Delta)}{z - \bar{z}_1} + e^{2i\omega} \frac{(1 - \delta)z_1 - z(1 - \Delta) - z_2(\Delta - \delta)}{(z - \bar{z}_1)^2}$$

$$F_4 = \frac{(1 - \Delta)}{z - z_1} + e^{2i\omega} \frac{(1 - \delta)}{z - \bar{z}_1}. \tag{A6}$$

In the above

$$\delta = \frac{\beta - \alpha}{1 + \beta} \quad \Delta = \frac{\alpha + \beta}{\beta - 1} \tag{A7}$$

$$\delta_1 = \frac{\alpha - \beta}{1 - \beta} \quad \Delta_1 = \frac{\alpha + \beta}{1 + \beta}. \tag{A8}$$

The semi-infinite reference crack corresponding to $0 \leqslant \eta_2 \leqslant \infty$ is represented by a distribution of dislocations $B(\eta_2)$, and the segment of crack corresponding to $0 \leqslant \eta_1 \leqslant a$ is represented by a distribution $A(\eta_1)$. The $B(\eta_2)$ and $A(\eta_1)$ are chosen such that the net tractions resulting from eqns (A1), (A2), (A3) and (A4) are zero everywhere on the crack surface. Since the a-dependence of the solution is known from dimensional considerations, a can be taken to be unity. The dual integral equations are then

$$2\int_0^a \frac{B(\eta_2)\,e^{-\cdots}}{(\eta_2-t_2)}\,d\eta_2 - \int_0^a [B(\eta_2)G_1(\eta_2,t_2) - B(\eta_2)H_2(\eta_2,t_2)]\,d\eta_2 + \int_a^\cdots [A(\eta_1)G_1(\eta_1,t_2) - A(\eta_1)G_4(\eta_1,t_2)]\,d\eta_1 = 0$$

$$2\int_0^a \frac{A(\eta_1)\,e^{-\cdots}}{(t_1-\eta_1)}\,d\eta_1 + \int_0^a [B(\eta_2)F_1(\eta_2,t_1) + B(\eta_2)F_2(\eta_2,t_1)]\,d\eta_2$$

$$+ \int_0^a [A(\eta_1)F_1(\eta_1,t_1) + A(\eta_1)F_2(\eta_1,t_1)]\,d\eta_1 = 0. \quad \text{(A9)}$$

With the changes of variables

$$\eta_2 = (1+\xi_2)/(1-\xi_2), \quad t_2 = (1+u_2)/(1-u_2) \qquad \text{(A10)}$$

The integral equations (A9) can be rewritten as

$$\int_{-1}^1 \frac{B(\xi_2)(1-u_2)}{(\xi_2-u_2)(1-\xi_2)}\,d\xi_2 - \int_{-1}^1 [D(\xi_2)G_1(\eta_2,t_2) - D(\xi_2)G_2(\eta_2,t_2)](1-\xi_2)^{-1}e^{-\cdots}\,d\xi_2$$

$$- \frac{1}{2}\int_a^\cdots [A(\eta_1)G_1(\eta_1,t_2) - A(\eta_1)G_4(\eta_1,t_2)]\,e^{-\cdots}\,d\eta_1 = 0$$

$$\int_0^a \frac{A(\eta_1)\,d\eta_1}{(t_1-\eta_1)} + \int_{-1}^1 [D(\xi_2)F_1(\eta_2,t_1) - D(\xi_2)F_4(\eta_2,t_1)](1-\xi_2)^{-1}e^{-\cdots}\,d\xi_2$$

$$- \frac{1}{2}\int_0^a [A(\eta_1)F_1(\eta_1,t_1) + A(\eta_1)F_2(\eta_1,t_1)]\,e^{-\cdots}\,d\eta_1 = 0 \quad \text{(A11)}$$

where $D(\xi_2) \approx B(\eta_2)$. The representations of $A(\eta_1)$ and $D(\xi_2)$ for the different problems are constructed in Appendix B. The stress intensity factors at the tip of a deflected crack are given by

$$K_1 + iK_{II} = (2\pi)^{1/2}\,e^{-\cdots}\lim_{\eta_1\to 1}\{(1-\eta_1)^{1/2}A(\eta_1)\} \qquad \text{(A12)}$$

APPENDIX B· DISLOCATION REPRESENTATIONS

The representation of the dislocation distributions for the different problems are summarized here.

Problems A1 and B1

The remote field imposed on the semi-infinite crack is (3) in A1 and (15) in B1. Let $\delta = u(r, -\pi-\omega_2) - u(r, \pi+\omega_2)$ be the relative displacements of the crack faces associated with these fields. From the singularity analysis for the crack terminating at the interface, the remote dislocation distribution can be obtained from $b = d\delta/d\eta_2$ and eqn (A5) as

$$B(\eta_2) = c_\omega \eta_2^{-k} \qquad \text{(B1)}$$

where $k = k_1$ in A1, and $k = k_1$ and $\lambda = \lambda_1$ in B1. The complex constant c_ω is determined by the singularity analysis.

The most singular stresses in the vicinity of the kink of the crack (at $x = y = 0$) have the form $\delta \sim r^{-p}d(\theta)$ where, in general, p is a complex number depending on α, β, ω_1 and ω_2. Hein and Erdogan (1971) have obtained the equation for p. When $\beta = 0$, p is real. In the neighborhood of the kink $B \sim \eta_2^p$ and $A \sim \eta_1^p$.

The representation of $D(\xi_2)$ which builds-in the correct singularity at the kink and which approaches eqn (B1) remote from the interface is

$$D(\xi_2) = \left(\frac{1-\xi_2}{2}\right)^k \left(\frac{1+\xi_2}{2}\right)^{-p}\left[c_0 k + (1-\xi_2)\sum_{i=1}^{\overline{n}} d_i T_{i-1}(\xi_2)\right] \qquad \text{(B2)}$$

where the ds are complex coefficients which must be obtained in the solution and process and $T_i(\xi_2)$ is the Chebyshev polynomial of first kind of degree i. The representation for $A(\eta_1)$ is taken as

$$A(\eta_1) = \eta_1^{-p}(1-\eta_1)^{-1/2}\sum_{i=1}^{n} a_i\eta_1^{i-1} \qquad \text{(B3)}$$

and, by (A12), the stress intensity factors at the tip of the crack are

$$K_1 + iK_{II} = (2\pi)^{1/2}\,e^{-\cdots}\sum_{i=1}^{n} a_i. \qquad \text{(B4)}$$

By substituting (B2) and (B3) into the two integral equation (A11) one obtains the two equations.

$$\sum_{i=1}^{m}[d_i E_{1i}(w_j)-\bar{d}_i F_{1i}(w_j)]-\sum_{i=1}^{n}[a_i \cdots w_{i-1}-\bar{a}_i H_{1i}(w_j)] = L_1(w_j) \tag{B5}$$

$$\sum_{i=1}^{m}[d_i E_{2i}(t_j)+\bar{d}_i F_{2i}(t_j)]-\sum_{i=1}^{n}[a_i G_1(t_j)+\bar{a}_i H_2(t_j)] = L_2(t_j) \tag{B6}$$

where integral expressions for E_i, F_i, G_i, H_i, and L_i are readily identified. To determine the $m+n$ complex coefficients d_i and a_i, (B5) is satisfied at m Gauss-Legendre points on the interval $-1 < w_2 < 1$, and (B6) is satisfied at n Gauss-Legendre points on the interval $0 < t_1 < 1$. On the basis of numerical experimentation with various choices of m and n, the calculations were carried out with $m = n = 8$. We believe the results for the energy release rates reported in the figures are accurate to within about one percent. In the case of problem A1, symmetry implies that the real parts of d_i and a_i are zero.

Problem D1

The formulation of problem D1 is similar in most respects to B1 except that the concentrated wedge loads must be applied. This is accomplished by considering the solution for a concentrated force P acting on an otherwise traction-free boundary of a semi-infinite plane. The singular behavior of $N(\eta_2)$ near $\eta_2 = 1$ must be consistent with this solution, i.e.

$$N(\eta_2) \to -P e^{\cdots}[2\pi^2(\eta_2-1)] \tag{B7}$$

as $\eta_2 \to 1$. The dislocation density remote from the wedge loading will have the form

$$B(\eta_2) \propto \eta_2^{-1} \quad \text{for} \quad \eta_2 \to \infty \tag{B8}$$

where λ^* is the eigenvalue of the problem in Section 3 which is the next larger than λ_1 and λ_2 in (14). This exponent characterizes the asymptotic outer solution to the semi-infinite crack problem for a loading which is confined to the vicinity of the tip.

A representation for $D(\xi_2)$ consistent with the above features and the singularity at the kink is

$$D(\xi_2) = (1-\xi_2)^{\alpha}(1-\xi_2)^{\beta}\left[C(\xi_2-\xi_0)^{-1} - \sum_{i=1}^{m} d_i F_i(\xi_2)\right] \tag{B9}$$

where

$$C = -P e^{\cdots}(1-\xi_0)^{2-\alpha}(1+\xi_0)^{\beta}(4\pi^2) \tag{B10}$$

and $\xi_0 = (l-1)(1+l)$. The representation for $A(\eta_1)$ is still given by eqn (B3). The integral equations reduce to the form given in (B5) and (B6), and the solution procedures are the same as described above. The results reported were computed with $m = n = 8$.

Problems A2, A3, B2 and D2

The formulation of these problems differs from their counterparts above only in that the portion of the crack beyond the kink lies along the interface. When $\beta = 0$, eqn (A3) gives the traction on the interface when $w_i = 0$ with $F_1 = 0$ and $F_2 = -(\delta_i - \Delta_i)(t_i-\eta_i)$. The second integral equation in (A11) reduces to

$$(1-\alpha)\int_{-1}^{1}\frac{A(\eta_1)\,d\eta_1}{(t_i-\eta_1)} - \int_{0}^{1}[D(\xi_2)F_1(\eta_2,t_i)-\bar{D}(\xi_2)F_1(\eta_2,t_i)](1-\xi_2)^{-1}\,d\xi_2 = 0. \tag{B11}$$

The representations for $A(\eta_1)$ and $D(\xi_2)$ are still given by (B2) and (B3), and the interface stress intensity factors are given by

$$K_1+iK_2 = (1-\alpha)(2\pi)^{1/2}\sum_{j=1}^{m} d_j \tag{B12}$$

Problem C

The integral equation governing the dislocation distribution $B(\eta_2)$ for the wedge loaded crack approaching the interface is

$$2\int_{0}^{l} B(\eta)(\eta-t)^{-1}e^{\cdots}\,d\eta + \int_{0}^{l}[B(\eta)G_1(\eta,t)+\bar{B}(\eta)G_2(\eta,t)]\,d\eta = 0 \tag{B13}$$

where η and t are zero at the crack tip. The distribution $B(\eta)$ must be consistent with the wedge loading (B7) and a square root singularity at the crack tip. The representation used is the same as that in (B9) and (B10) with $p = 1$ 2. The integral equation is reduced to algebraic equations for the m complex coefficients d_i as in the previous problems. The results reported in Figs 7 and 9 were computed with $m = 20$ for $l/l_0 < 0.7$ and $m = 30$ for $l/l_0 \geq 0.7$.

MATERIALS
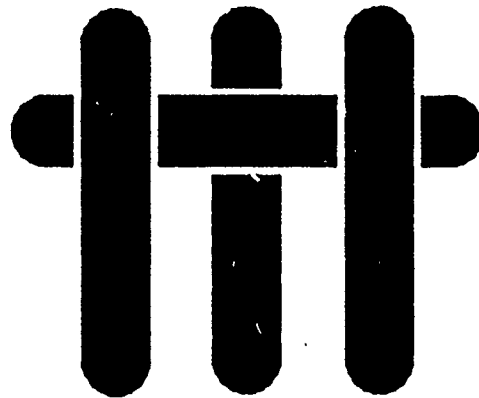
ON INTERFACE DEBONDING AND FIBER CRACKING IN BRITTLE MATRIX COMPOSITES

by

A. G. Evans and M. Y. He

Materials Department
College of Engineering
University of California
Santa Barbara, California 93106

and

J. W. Hutchinson

Applied Sciences Division
Harvard University
Cambridge, MA 02138

ABSTRACT

Analyses of debonding along interfaces and of the kinking of interface cracks into a fiber have been used to define the role of debonding in fiber reinforced, brittle matrix composites. The results reveal that, for <u>aligned</u> fibers, debonding requires an interface fracture Γ_i energy less than about one-fourth that for the fiber, Γ_f. Furthermore, once this condition is satisfied, fiber failure does not occur by deflection of the debond through the fiber. Instead, fiber failure is governed by weakest link statistics. However, the debonding of <u>inclined</u> fibers/whiskers is possible when Γ_i/Γ_f is larger than one-fourth and additionally, debonds can deflect onto the fiber and cause fiber failure at inclinations $\gtrsim 60°$.

1. INTRODUCTION

Brittle matrices reinforced with brittle fibers exhibit high "toughness" when fiber failure is suppressed at the matrix crack front.[1-5] This process involves interface debonding at the crack front and probably further debonding in the crack wake, accompanied by frictional sliding along the debonded interfaces (Fig. 1). Fiber failure in the crack wake then results in a pull-out contribution to toughness, which becomes large when the distance between the fiber failure site and the matrix crack plane (i.e., the pull-out length) is also large. Consequently, it is important to understand the mode of fiber failure and the relationships which govern the fiber failure site. Existing analyses of pull-out toughening have assumed that fiber failure involves weakest link statistics, whereupon the failure site depends on fiber strength parameters. Such solutions have dictated present approaches for fiber development which emphasize strength. However, implicit in these analyses is the premise that fiber failure does not occur by kinking from the debond crack tip into the fiber. Clearly, should fiber failure instead proceed by kinking, the relevant fiber property would be its toughness rather than its strength, resulting in very different emphasis for fiber development. The existence of a kinking mechanism of fiber failure has been illustrated in SiC whisker reinforced Al_2O_3 (Fig. 2), albeit at a whisker acutely inclined to the matrix crack plane.

Analyses that contain much of the information relevant to initial debonding and fiber failure by kinking have been completed recently.[6, 7] The intent of the present article is to utilize this information and to present solutions that specifically address these issues.

3

2. THE BASIC MECHANICS

2.1 INITIAL DEBONDING

The incidence of initial debonding at the matrix crack front, rather than failure of the fiber, can be obtained from a comparison of the strain energy release rate, G_i, for a small kink along the interface emanating from the matrix crack, with that for a small coplanar kink into the fiber, G_f[6] (Fig. 3). Specifically, debonding is expected to occur when G_i/G_f is larger than the ratio of critical values, Γ_i/Γ_f, at the relevant phase angle of loading at the interface crack, ψ_i. For brittle matrix composites with <u>aligned</u> fibers, the relevant debonding diagram considers a matrix crack normal to the interface (Fig. 3).* The solution indicates that <u>high modulus</u> fibers tend to <u>encourage</u> debonding. Furthermore, it is noted that this condition for initial debonding is <u>not</u> affected by the residual strain.

In a composite with randomly oriented fibers and/or whiskers, G_i/G_f increases as the interface angle θ decreases,[5] such that debonding occurs subject to less stringent requirements as evident from Fig. 4.

2.2 WAKE DEBONDING

When the condition for initial debonding represented by Fig. 3 is satisfied, the crack can only deviate from the interface if the phase angle of loading at the debond changes. Phase angle changes become possible when the debond length exceeds the fiber radius. Then, crack geometry changes, coupled with residual strain effects, as well as changes in loading on the fiber, exert an influence on ψ_i.[10] Good insight into these effects can be gained by examining the behavior of a fiber in the

---

*Delamination by matrix crack propagation parallel to the fibers can also occur;[4] this problem is not addressed by the present study.

immediate crack wake (Fig. 5). For this case, the phase angle initially increases as the debond extends (up to debond lengths of ~5R).[10] More significantly, when residual strain exists, the phase angle changes rapidly, at fixed debond length, as axial loads are exerted on the fiber between the crack surfaces. The change in phase angle between the crack front and the crack wake could, in principle, cause fiber failure from the debond, in the crack wake, as elaborated below.

2.3   FIBER FAILURE

The problem of fiber failure from the debond is characterized by a plane strain crack along the interface with a kink extending into the fiber[7] (Fig. 6). Specifically, the <u>maximum</u> energy release rate for the kink, compared with the energy release rate for continued extension along the interface, dictates the tendency for fiber failure. Calculations of these energy release rates compared with critical values for the fiber and interface, as a function of the phase angle for the debond crack, provide the fiber failure diagram indicated on Fig. 6. In this diagram the locus of initial debonding refers to debond requirements in Γ_i/Γ_f plotted against ψ such that *each point* refers to a specific α. Three such α values are indicated on the figure. It is now vividly apparent that fiber failure typically requires larger values of Γ_i/Γ_f than initial debonding. Consequently, if the ratio Γ_i/Γ_f is fixed and thus independent of the phase angle ψ_i, a debond, once initiated, would *always remain at the interface*, except when the fiber axis is within ~30° of the matrix crack plane. Possible changes in this conclusion, based on phase angle effects, are discussed below.

2.4 THE CRITICAL ENERGY RELEASE RATE

The interface fracture energy Γ_i, is often influenced by the phase angle, ψ_i,[11] as illustrated in Fig. 7. The role of the phase angle is not fully understood; one hypothesis is that crack surface contact at asperities on the interface crack surface becomes increasingly important as ψ_i increases, causing a corresponding increase in Γ_i. Alternative mechanisms that could cause Γ_i to increase with ψ_i have yet to be explored.

The fracture resistance of the fiber Γ_f does not involve similar considerations of the phase angle in the fiber, ψ_f, because the maximum energy release rate essentially coincides with the orientation at which $\psi_f \approx 0$,[7] consistent with the condition that crack propagation in homogeneous brittle solids seek the trajectory having $\psi = 0$.[12]

.

3. DEBONDING AND FIBER FAILURE

The critical property requirement for good composite performance, based on the need for debonding, is governed solely by the fracture resistance ratio, Γ_i/Γ_f, as summarized by the debond diagrams (Fig. 3, 4) at the appropriate phase angle, ψ_i. The tendency for further debonding in the wake, compared with fiber fracture, depends on additional variables. The basic characteristics are summarized in composite diagram (Fig. 8). Such diagrams reveal that, when Γ_i is independent of the phase angle, ψ_i, fiber failure can <u>never</u> occur from the end of the debond, unless the fiber axis has an inclination with the matrix crack plane, $\theta < 30°$. Instead, fiber failure must be statistical in nature.[13] However, when Γ_i increases with increase in ψ_i as encouraged by a rough debond interface, the possibility of fiber failure from the debond extends to a larger orientation range. To understand this possibility, the

6

switch in phase angle ψ_i that occurs between the debond at the crack front and when the debond exists at an intact fiber in the crack wake is invoked. The relevant behavior is illustrated for the case $\alpha = 0$ (Fig. 8). At the crack front $\psi_i \approx 45°$, whereas in the crack wake, ψ_i varies as the fiber becomes stressed in the crack wake and a maximum steady-state level, $\psi_i \approx 75°$, is rapidly reached. The change in Γ_i between this range of phase angles is thus of relevance. Few data exist regarding the possibility of a sufficient increase in Γ_i (over this range) to cause the fracture energy path, $\Gamma_i(\psi_i)$ to intersect the fiber failure boundary. However, it is noted that such an intersection becomes more likely as the amplitude of the interface fracture surface roughness increases.[11] It is also reemphasized that, when Γ_i is not strongly influenced by phase angle, the composite diagram (Fig. 8) dictates that small kinks near the debond tip will not propagate in preference to further debonding in aligned fiber reinforced materials having fibers coincident with the stress axis. In such cases, fiber failure occurs in accordance with weakest link statistics.[13]

As the fiber axis deviates from the normal to the crack plane, crack front debonding can occur at larger Γ_i/Γ_f (Fig. 4). Consequently, inclined fibers that debond could experience fiber fracture from the debond tip as the phase angle shifts upon passage of the matrix crack. Specifically, fiber fracture can occur from the debond when the fiber axis orientation $\theta \lesssim 60°$, even when Γ_i is phase angle independent (given a sufficient phase angle switch). This important influence of orientation explains the observation (Fig. 2) that inclined whiskers can crack from the debond tip.

4. CONCLUDING REMARKS

The preceding discussion suggests that, in composites with aligned fibers, interface debonding should occur, provided that the fracture resistance of the "weakest" interface (matrix/coating or coating/fiber) satisfies the inequality, $\Gamma_i/\Gamma_f \lesssim 1/4$. When this condition is satisfied, further debonding can occur in preference to fiber failure from the debond, unless an interface mechanism exists that causes Γ_i to increase rapidly with increase in phase angle, ψ_i. Consequently, the influence of the mechanical properties of the _fiber_ on composite behavior is contained exclusively in the statistical parameters that govern their tensile _strength_. A rough debond interface seems to be one important way in which Γ_i can increase with ψ_i, by means of a crack surface contact mechanism and thereby inhibit further wake debonding and violate the above conclusion

In composites with randomly oriented whiskers or chopped fibers, debonding occurs more readily at the more acutely inclined reinforcements. Then, in cases wherein debonding only occurs at the inclined reinforcements, fiber failure by kink fracture from the debond is seemingly feasible. For such materials, _toughness_ rather than strength is the fiber property that governs the composite toughness.[14]

REFERENCES

[1]   K. M. Prewo, Jnl. Mater. Sci. 21, (1986) 3590.

[2]   J. Aveston, G. A. Cooper and A. Kelly, The Properties of Fiber Composites, IPC Science and Technology (1971) p. 15.

[3]   D. B. Marshall and A. G. Evans, J. Am. Ceram. Soc. 68 (1985) 2013.

[4]   A. G. Evans, Mat. Sci. Eng., in press.

[5]   B. Budiansky, J. W. Hutchinson and A. G. Evans, Jnl. Mech. Phys. Solids, 34 (1986) 167.

[6]   M. Y. He and J. W. Hutchinson, Harvard University Report, MECH.-133 (1988) (To be published).

[7]   M. Y. He and J. W. Hutchinson, Harvard University Report, MECH.-113 (1988), J. Appl. Mech., in press.

[8]   J. Dundurs, Mathematical Theory of Dislocations (ASME, NY) (1969) p. 70.

[9]   K. K. Lo, Jnl. Mech Phys. Solids 31 (1983) 287.

[10]   P. G. Charalambides and A. G. Evans, Jnl. Am. Ceram. Soc., in press.

[11]   A. G. Evans and J. W. Hutchinson, Acta Met., in press.

[12]   M. D. Thouless, A. G. Evans, M. F. Ashby and J. W. Hutchinson, Acta Met. 35 (1987) 1333.

[13]   M. D. Thouless and A. G. Evans, Acta Met. 36 (1988) 517.

[14]   A. G. Evans, M. Rühle and M. D. Thouless, Materials Research Society Proceedings, 78 (1987) 259.

FIGURE CAPTIONS

Fig. 1. A schematic indicating the debonding and sliding behaviors that accompany matrix crack propagation in a brittle matrix composite.

Fig. 2 Debonding of an inclined SiC whiskers in an Al_2O_3 matrix. A thin (~ 5nm) amorphous silicate layer at the interface allows debonding. Also note that a whisker crack has formed from the end of one of the debonds.

Fig. 3. A crack front debond diagram indicating the range of relative interface fracture energy, Γ_i/Γ_f in which debonding occurs in preference to fiber failure: α is a measure of the elastic mismatch ($\alpha = (\bar{E}_f - \bar{E}_m)/(\bar{E}_f + \bar{E}_m)$, where $\bar{E} = E/(1 - \upsilon^2)$ is the plane strain tensile modulus — positive α refers to a fiber having higher shear modulus than the matrix).

Fig. 4. The effect of interface orientation on the debonding requirements

Fig. 5. Trends in phase angle at the debond for a fiber loaded in the crack wake
a) effect of debond length when mismatch strain is zero
b) effect of positive mismatch strain in the steady-state region

Fig. 6. A fiber cracking diagram for a fiber loaded in the crack wake, for three values of α. Also shown is the locus for crack front debonding, over the same range of α. This locus is the debond boundary in Γ_i/Γ_f, ψ space with each point on the boundary referring to a specific α: for reference purposes, three typical values of α are shown. This figure indicates the extent to which Γ_i/Γ_f must increase between the crack front and the wake in order to have debond deflection into the fiber.

Fig. 7. Some trends in critical energy release rate for interface cracking, Γ_i with the phase angle of loading ψ_i obtained for a model system (glass/polymer). Also shown are predicted values for a rough interface with H being the amplitude and L the wavelength of the roughness.

Fig. 8. Composite diagram concerning fiber failure. Trajectories of Γ_i with ψ_i that lead to debond deflection into the fiber and debonding without fiber failure ($\alpha = 0$). To obtain this result, the kink angle that gave the maximum value of the energy release rate in the fiber was used and this energy release rate was equated to Γ_f.

FIG. 1

1μm
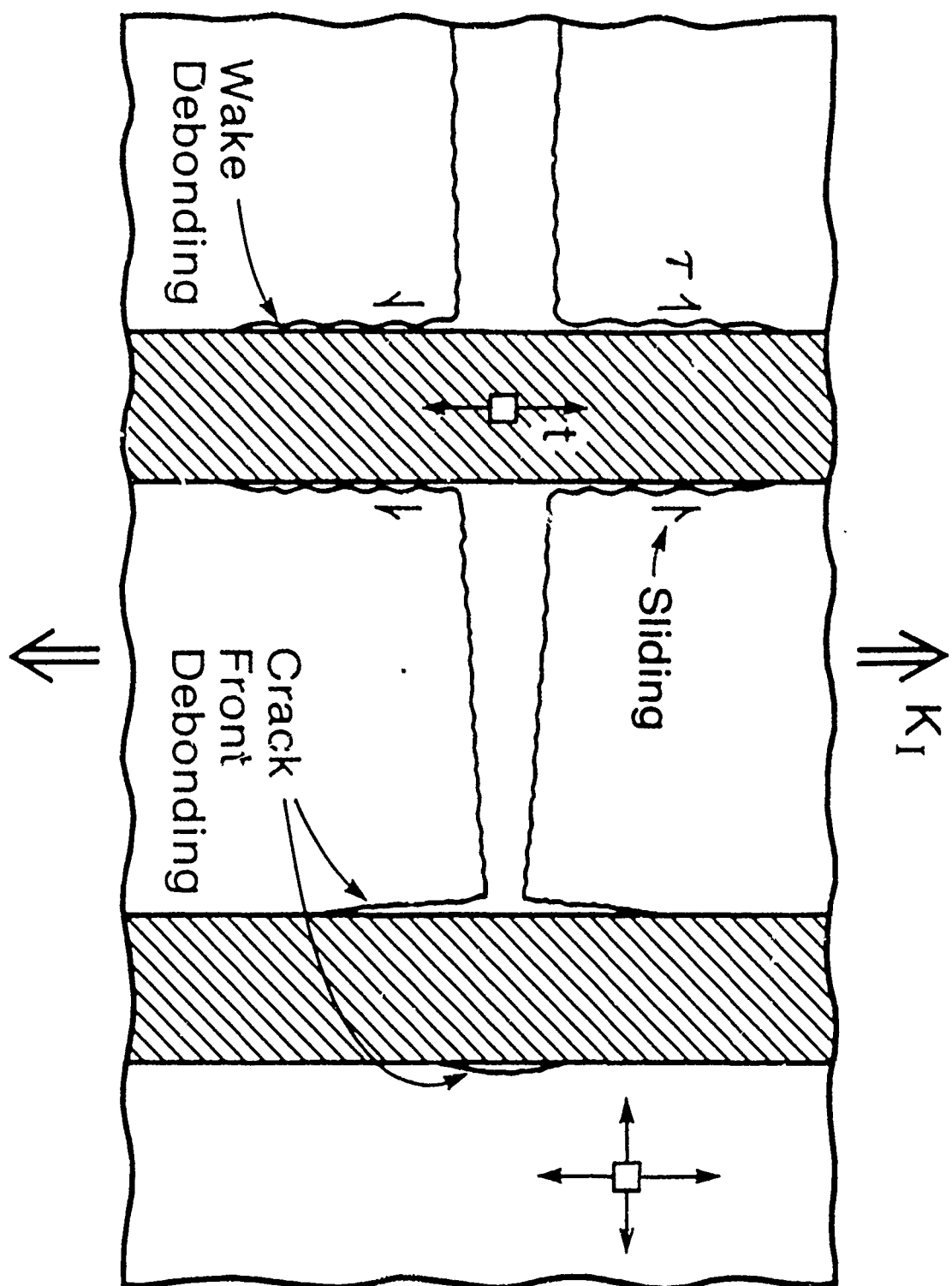
FIG. 2
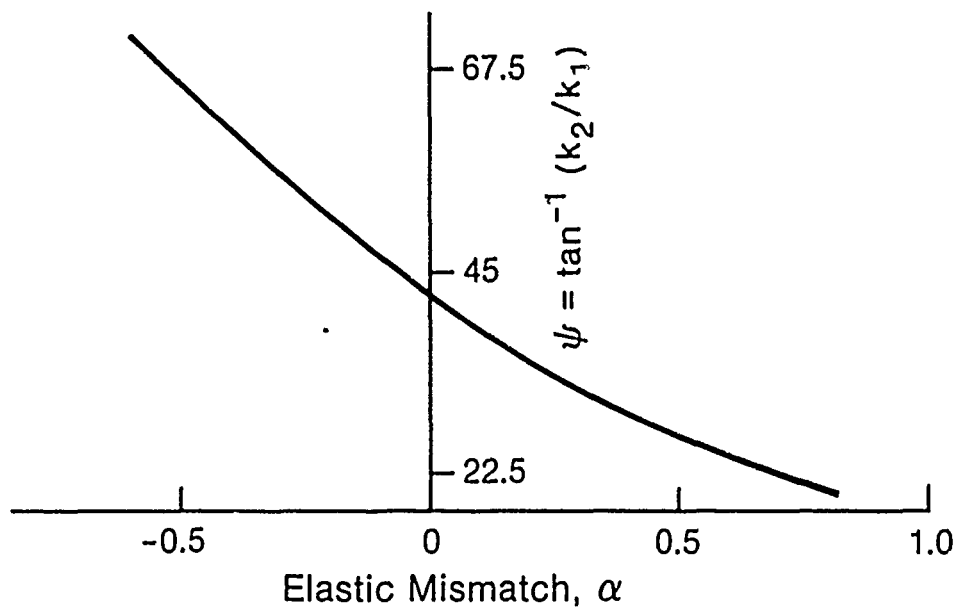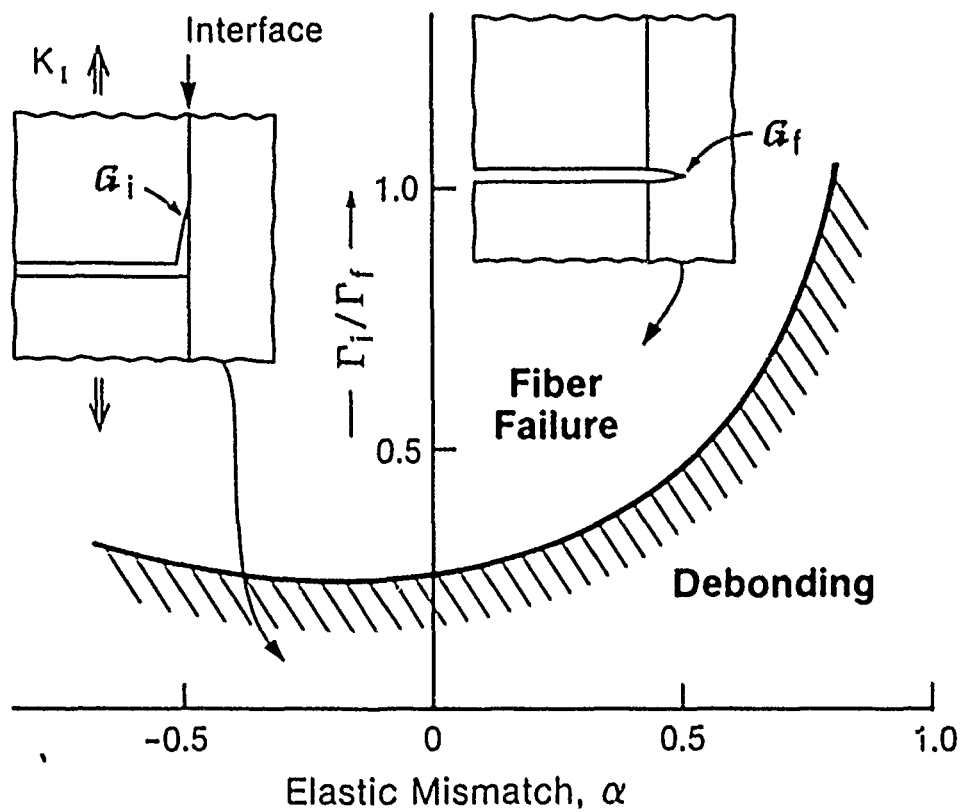
FIG. 3
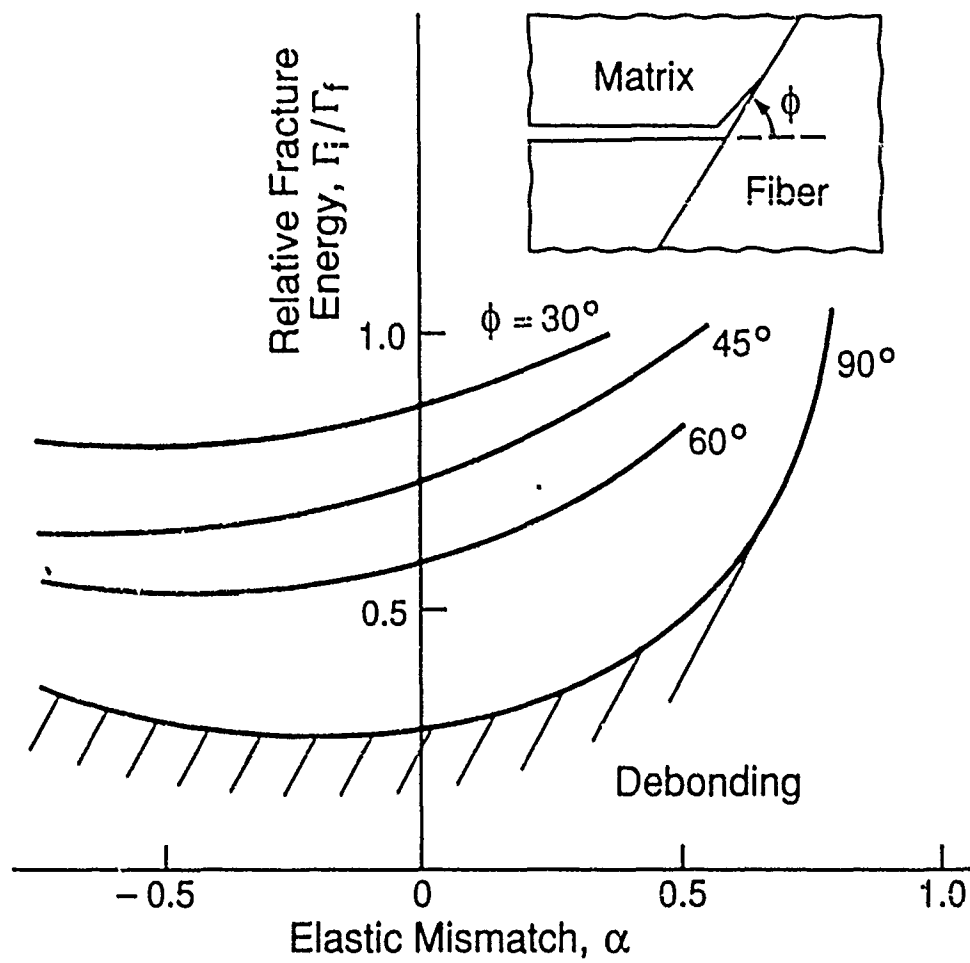
FIG. 4
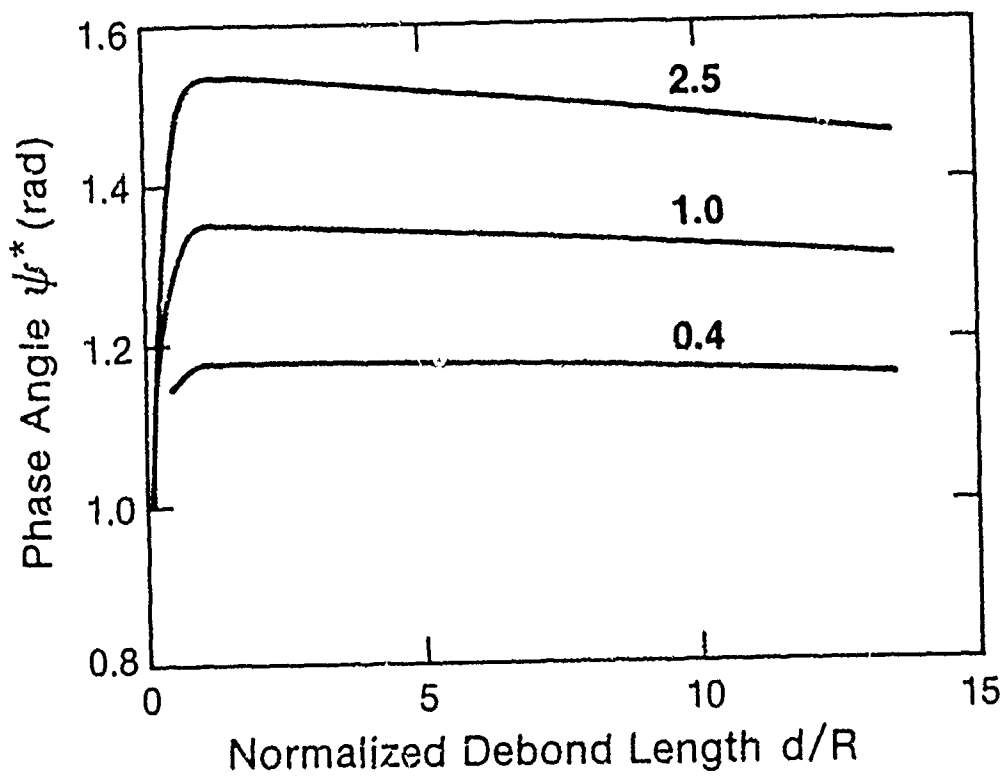
FIG. 5A
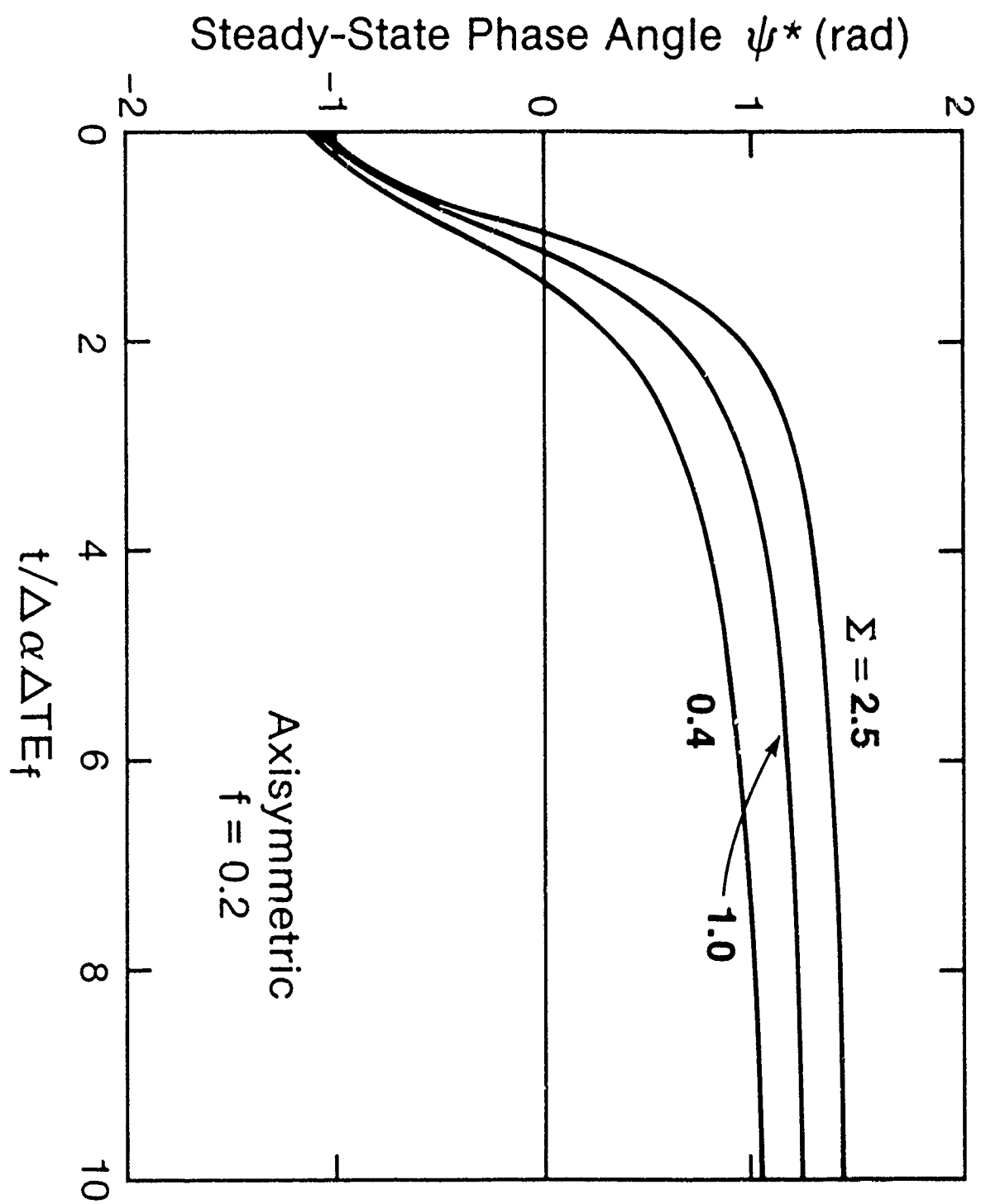
FIG. 5B
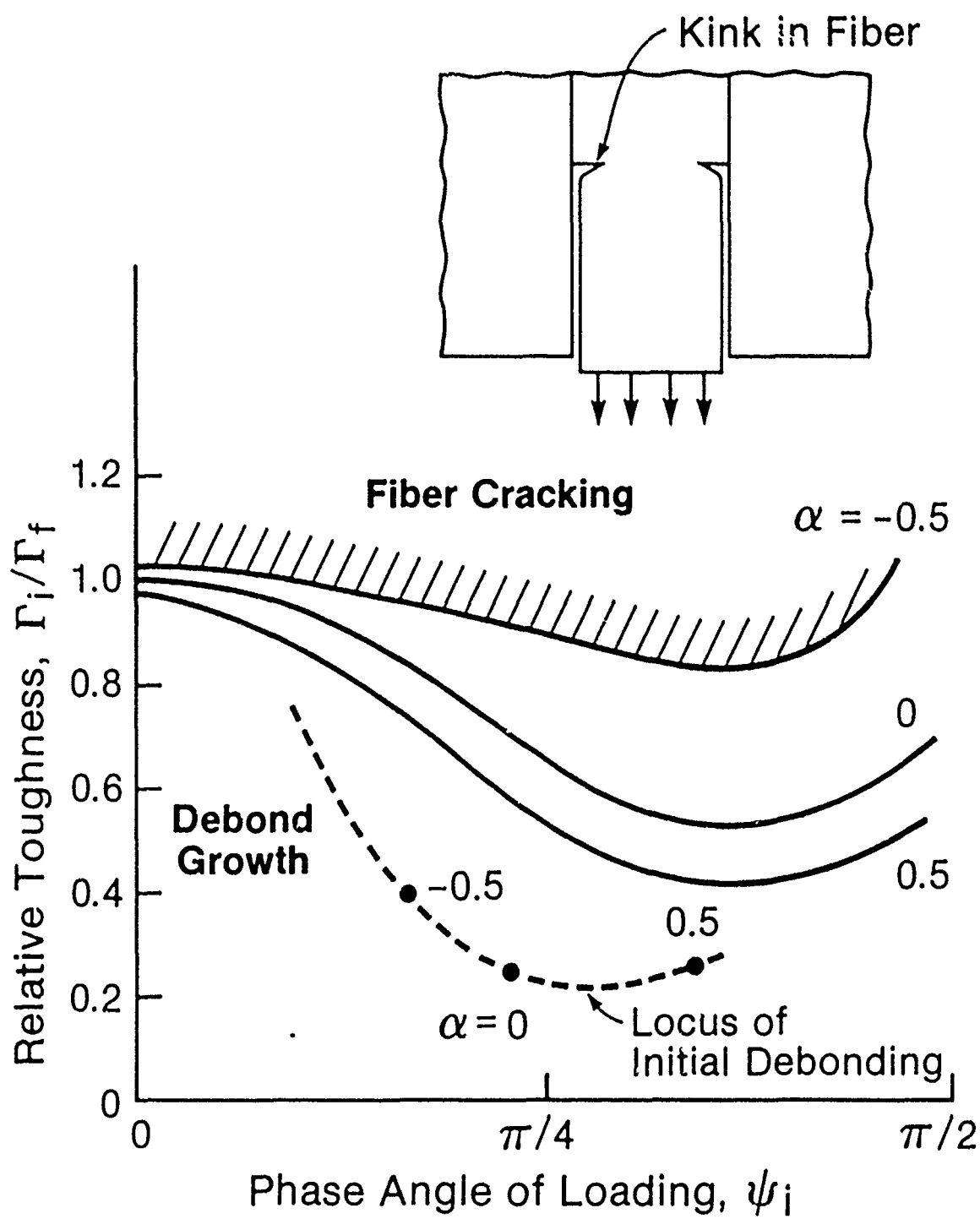
FIG. 6
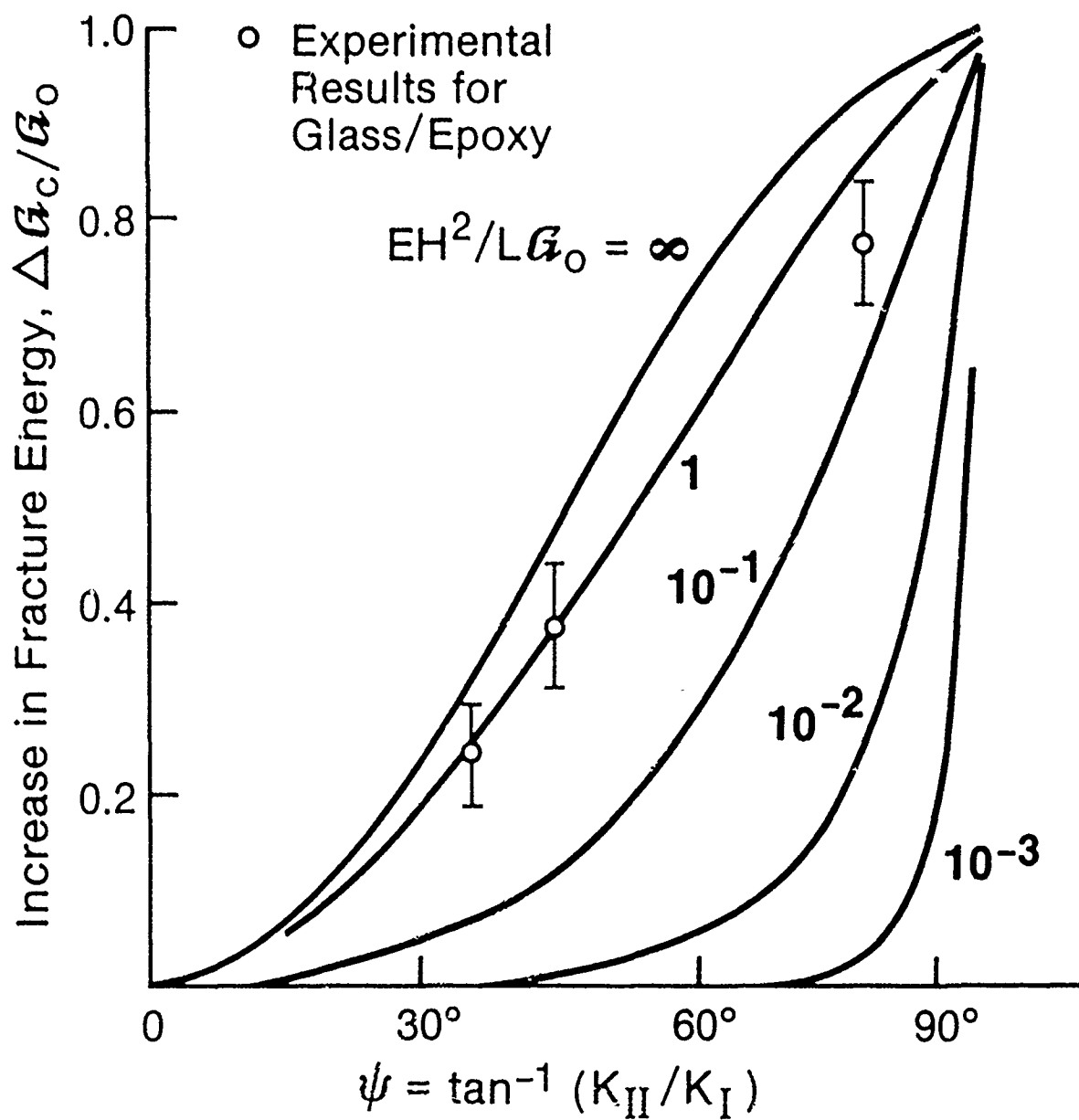
FIG. 7
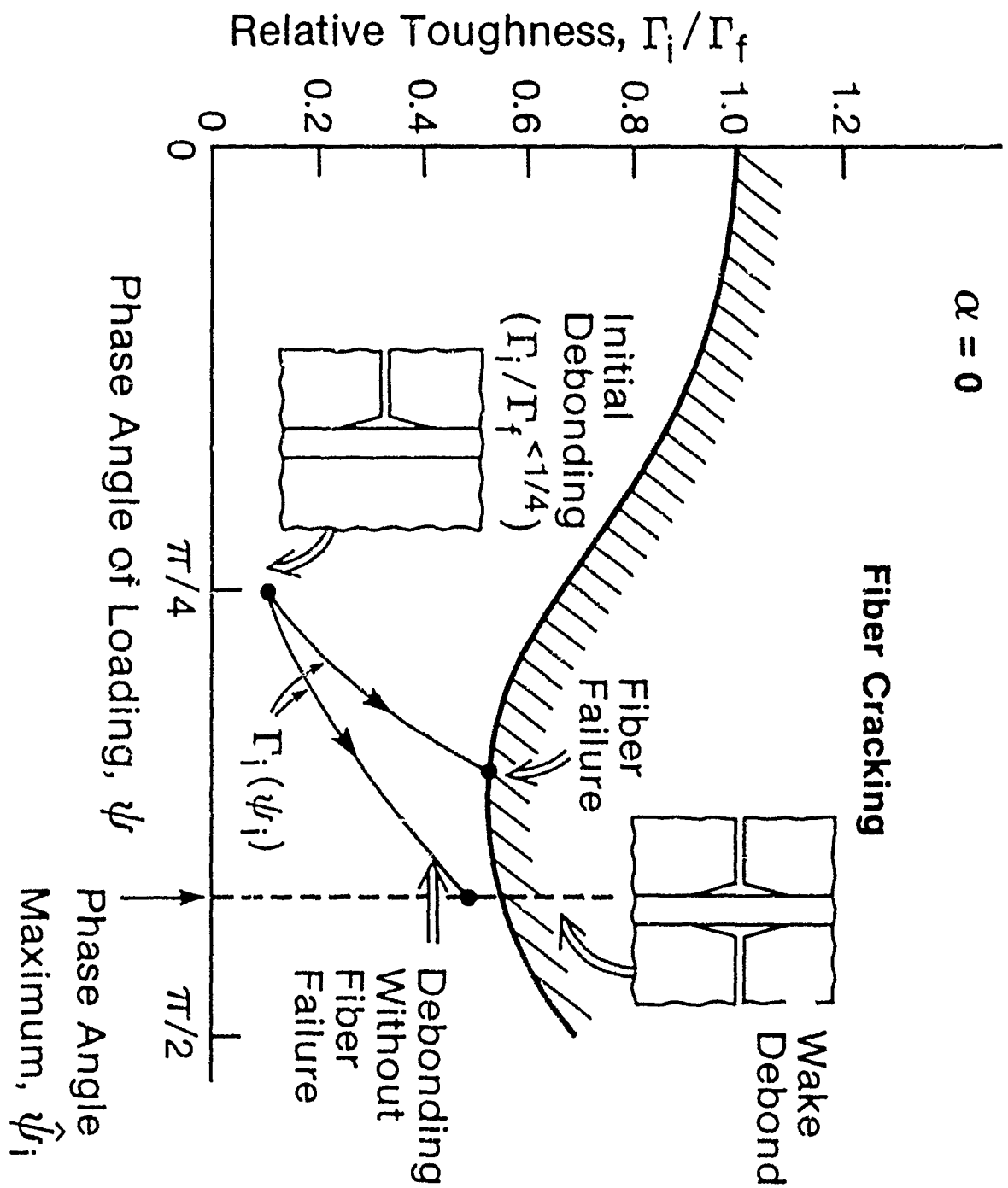
FIG. 8

MATERIALS
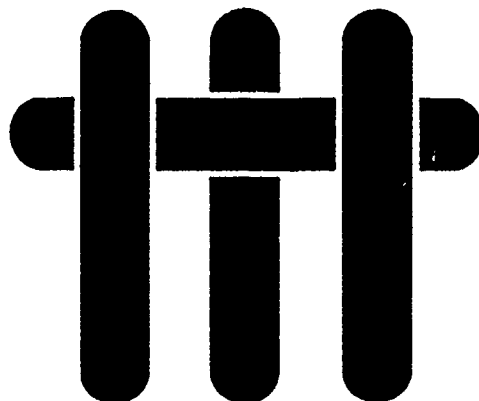
MICROSTRUCTURAL STUDIES OF THE INTERFACIAL ZONE OF A SiC-FIBER-REINFORCED LITHIUM ALUMINUM SILICATE GLASS-CERAMIC

Ewald Bischoff, *Manfred Rühle, Orfeo Sbaizero and A. G. Evans

Materials Department
College of Engineering
University of California, Santa Barbara
Santa Barbara, California 93106

* Now at Max-Planck-Institut für Metallforschung, Institut für Werkstoffwissenschaft, Seestraße 92, D–7000 Stuttgart, FRG

Microstructural Studies of the Interfacial Zone of a SIC-Fiber-Reinforced Lithium Aluminum Silicate Glass-Ceramic

Ewald Bischoff, Manfred Rühle,* Orleo Sbaizero, and Anthony G. Evans*

Materials Department, College of Engineering, University of California,
Santa Barbara, California 93106

Transmission electron microscopy studies have been conducted on interfaces in a lithium aluminum silicate/SiC-fiber-reinforced composite. In the as-processed state, interphases of amorphous C and carbides of Nb have been confirmed, with circumferential thermal debonds evident in the C layer. After heat treatment in air at 800°C, the C is found to be replaced by amorphous SiO_2, and the carbides of Nb replaced by oxides. The SiO_2 thickens with exposure time and typically contains circumferential separations. Some Mg and Al diffusion also accompanies the heat-treatment process and eventually leads to the formation of MgO and Mg silicates in the interfacial zone. [Key words: composites, mechanical properties, interfaces, microstructure, silicon carbide.]

I. Introduction

IT IS now well substantiated that ceramic matrix composites have mechanical properties strongly influenced by the sliding and debonding resistance of the interfacial region.[1-3] In the absence of interfacial bonding, and with small sliding resistance, matrix cracking precedes fiber failure and the resultant composites have nonlinear behavior and a large work of fracture.[1-3] However, an increased interfacial resistance causes a transition to notch sensitive behavior, wherein fiber fracture, pullout, and matrix cracking occur simultaneously.[6] Then, the toughness becomes an appropriate characterizing parameter.[7,9] The contribution to the

toughness caused by fibers that remain intact in the crack wake, and bridge the crack,[7,9] as well as the additional toughening that derives from pullout,[10] after fiber failure, have been calculated in previous studies. The principal intent of the present series of papers[11-13] is to conduct an experimental examination of the coupled influence of fiber bridging and pullout on the fracture of fiber-reinforced ceramics. For this purpose, studies are conducted on a material that exhibits systematic changes in interfacial sliding resistance, upon heat treatment.[8,13,14] The material is a laminated 0/90 composite consisting of SiC (Nicalon) fibers in a lithium aluminum silicate (LAS) glass-ceramic matrix.[8,13,14] The present paper describes the changes in the nature of the fiber/matrix interfacial zone. As such, it provides an informed basis for the companion studies of mechanical properties and of fiber pullout.[11,13] In these studies,[11] test specimens were heat-treated in air to 800°C for 2, 4, 8, 16, and 100 h, because prior research[13,14] had indicated that heat treatment at this temperature caused systematic changes in the mechanical properties. The principal results of the mechanical tests (Fig. 1) concern the changes in fracture strain that occur, even after brief heat-treatment periods, in both tension and flexure. This change coincides with a transition from steady-state matrix cracking in the as-ceramed* composite to more brittle failure from a single dominant flaw after heat treatment. This transition has a profound effect on the structural utility of the composite and requires explanation in terms of microstructural changes at the interface and associated effects on fiber failure and pullout.

II. Interface Structure

Samples of the as-ceramed and heat-treated composite were mechanically dimpled in orientations having the fibers either nor-
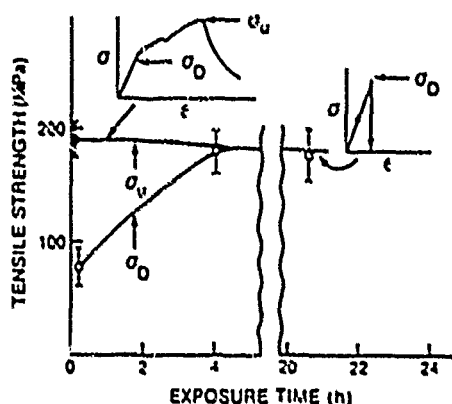
Fig. 1. Trend in tensile strength and stress-strain behavior with heat treatment.

mal or parallel to the section plane. Ion beam thinning was then conducted in the conventional manner to obtain foils suitable for TEM analysis. The forces applied during mechanical polishing and dimpling were sufficiently small that no damage could be identified in the specimens. Such procedures are based on experience gained in the preparation of foils that allows the investigation of microcracks.[13] The foils were investigated with a transmission electron microscope[*] operating at 200 kV. Chemical analysis with spatial resolution of ~15 nm was performed with energy dispersive X-ray spectroscopy (EDS) and electron energy loss spectroscopy (EELS). Low-magnification images in the as-ceramed state[13,14] of the composite reveal that in many instances circumferential cracks exist around the fibers. These cracks extend around $1/2$ to $1/3$ the circumference (Fig. 2(A)). When such cracks are not present, small cracklike flaws are usually evident at the interface (Fig. 2(A)). Studies conducted on other systems have also revealed the presence of debonds.[16,17]

Careful studies were performed to ensure that the flaws identified in Fig. 2(A) are predominantly debonds rather than thinning-

Fig. 2. (A) Bright-field shadow image showing circumferential cracking, as well as flaws arrowed) around fibers. (B) Bright-field image of a region close to the carbon interface. Close to the interface, the thicknesses of the LAS, the carbon layer, and the SiC fiber are approximately the same.
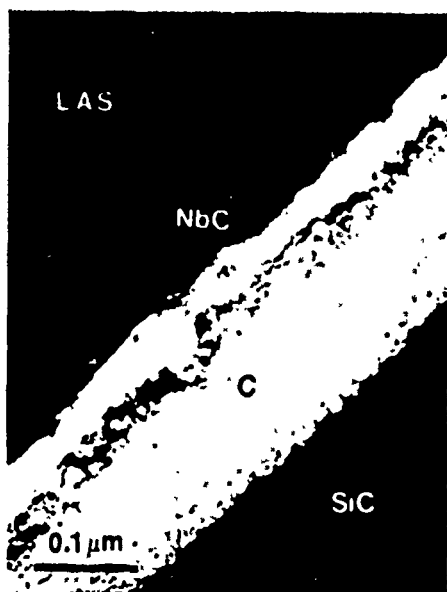
Fig. 3. Bright-field micrograph of the interface between fiber and matrix in the as-processed composite.

induced artifacts (i) It was established that the thinning rates of the LAS glass, the SiC fiber, and the interface are similar, resulting in specimens of homogeneous thickness It was also independently determined that interfacial layers are not thinned preferentially. For example, a quantitative thickness evaluation of a bright-field image of the interface region indicated no deviation from uniformity (Fig. 2(B)). (ii) As elaborated below, it has been verified that the basic debonding criteria are satisfied in this material system. (iii) The surface separations, δ (see Fig. 3), are consistent with values expected from the thermal expansion differences. Specifically, by noting that the thermal strain $\Delta\alpha\Delta T$ is ~3 × 10^{-3} and that debonding occurs only on one side, the separation should be of order $\delta \approx 2R\Delta\alpha\Delta T \approx 40$ nm. This value compares favorably with the openings measured from Fig. 3. (iv) The low values of the transverse elastic modulus and thermal expansion coefficient[1] are only explicable if the fibers are thermally debonded.

At higher resolutions, two distinct interfacial zones are apparent between the fiber and the matrix (Fig. 3). The zone adjacent to the fiber, which always exhibits a *bright* (positive) contrast, is amorphous. The *dark*, second layer consists of small grains about 20 to 100 nm in diameter having a thickness ranging between 20 and 200 nm. The circumferential cracks are found to always occur *within* the bright, inner layer, close to the interface with the dark layer (Fig. 3). Analysis by EELS established that the *bright* layer is amorphous C (Fig. 4). Analysis of the *dark* layer by EELS

(Fig. 5) and by EDS indicated that the grains are primarily NbC, consistent with previous studies.[13,17,18] Heat treatment in helium for 4 h at 800°C did not change the size and chemistry of these interfacial zones.

Heat treatment in air between 2 and 100 h at 800°C resulted in a drastic change of the interfacial layers. A similar bright-field appearance was obtained (Fig. 6), but there were essential differences in the composition, compared with the as-processed state. Chemical analysis by EELS revealed that the amorphous layer was SiO_2; a typical EELS spectrum is shown in Fig. 4. At a few locations, amorphous carbon was still present in small pockets. The SiO_2 layer also contained Al, with the Al content decreasing upon annealing from 5.9 wt% at 4 h to 2.5 wt% at 100 h, consistent with previous investigations of Al diffusion.[14,17] Simultaneously, the thickness of the SiO_2 layer increased from 50 to 100 nm at 2 h to 200 to 300 nm after 100 h (Fig. 7). Circumferential separations again appeared. At times up to 16 h these occurred on the outside of the SiO_2 layer (Fig. 6) and the number density of fibers that exhibit separations remained essentially constant with annealing time. After 100 h, the bond layer became sufficiently "strong" that circumferential cracks, when present, often extended partially into the matrix (Fig. 8). Composites containing SiO_2 layers were detected in previous studies,[16,17] but usually formed during processing rather than upon postprocessing heat treatment.

Chemical analysis of the darker outer layer (Fig. 5) showed that it contained fine, crystalline sub-oxides of Nb, but the analytical techniques used (EELS, EDS) did not allow unique determination of the composition.[*] Considerable Mg (10 to 15 wt%) and some MgO particles were also present. After 100 h, a third Mg-rich layer containing a crystalline magnesium-silicate phase was detected between the bright and dark layers (Fig. 9).

III. Discussion

The oxidation of the SiC fiber results in a SiO_2 layer (and fugitive CO_2). The volume of the SiO_2 layer is larger than that of the original SiC by ~1.8. This volume increase results in a closure of the gap between the fiber and the LAS matrix caused by C removal and oxidation of the SiC. The SiO_2 layer thickness is also spatially quite uniform and consistent with parabolic kinetics up to thicknesses of the order of the original C layer thickness (~150 nm (Fig. 7)). At this stage, it is reasonable to suppose that the gap caused by C oxidation closes. Oxygen access to the interface must then be restricted such that the further thickening of the oxide occurs at a reduced rate, as noted in Fig. 7. The interface separations observed for heat treatments up to ~8 h can clearly be attributed to the existence of a gap caused by removal of the C layer. Conversely, the separations observed in the as-ceramed state and after extensive heat treatment are presumed to be thermal debonds. Such debonds can occur when the fiber has a larger thermal expansion coefficient than the matrix, such that interfacial residual tension exists, and the interphase has a relatively low fracture resistance. Indeed, SiC has a larger thermal expansion coefficient than LAS (~4 × 10^{-6} and ~1 × 10^{-6} K^{-1}, respectively) and interlayers observed either initially (C) or after heat treatment in air (SiO_2) both exhibit a relatively low fracture resistance.

In thermal debonding,[12,19] the strain energy release rate approaches zero as the circumferential crack extends fully around the circumference. The crack thus tends to arrest, resulting in partial debonds, consistent with present observations (Fig. 2(A)). A lower bound condition for thermal debonding of a cylinder has previously been established as[12,19]

$$K_{ic}/q\sqrt{a} < \phi \qquad (1)$$

where K_{ic} is the fracture toughness of the debond layer, a is the fiber radius, ϕ is a coefficient ~1.4, and q is the residual tensile stress at the interface, given by[5]

[*]However, thermodynamic reasons suggest that the layer consists of the most stable oxide, Nb_2O_5.
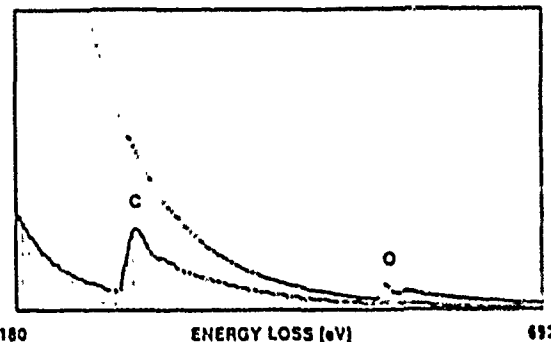
Fig. 4.   Partial EELS spectra of the bright interfacial layer. The base plot (hatched) from the as-processed composite shows an edge consistent only with amorphous carbon. The overlay plot from the sample annealed for 4 h at 800°C shows an oxygen edge.

$$q = \frac{E_m(1 - f)\Delta\alpha\Delta T}{2\lambda(1 - \nu_m)} \qquad (2)$$

with

$$\lambda = \{1 - (1 - E/E_f)(1 - \nu_f)/2$$
$$+ (1 - f)(\nu_m - \nu_f)/2$$
$$- (E/E_f)[\nu_f + (\nu_m - \nu_f)fE_f/E]^2\}/$$
$$(1 - \nu_m)\{1 + \nu_f + (\nu_m - \nu_f)fE_f/E\}$$

E is Young's modulus of the composite, $E = fE_f + (1 - f)E_m$, ν is Poisson's ratio, $\Delta\alpha$ is the difference in thermal expansion between fiber and matrix, and ΔT is the cooling range.

The fracture toughness of the amorphous C layer is unknown. Results for "glassy" C (dense, amorphous C) at a reasonable crack velocity (~10^{-3} m·s^{-1}) would suggest that $K_{ic} \approx 0.9$ MPa·m$^{1/2}$.[20,21] However, the C layer is expected to be less dense than "glassy" C and thus have a lower K_{ic}. Indeed, the results of nanoindenter tests[22] suggest an *upper bound* on K_{ic} of only 0.1 MPa·m$^{1/2}$. Based on the latter K_{ic} value, the nondimensional debond parameter $K_{ic}/q\sqrt{a} \approx 0.1$ is more than 1 order of magnitude less than the lower bound debond criterion given by Eq. (1). The viability of thermal debonding is thus verified. The fraction of fibers that actually exhibit debonding is then governed by probabilistic issues based on interface flaw populations. Such flaw populations are likely to vary with heat treatment, as elaborated in a companion paper.[11]
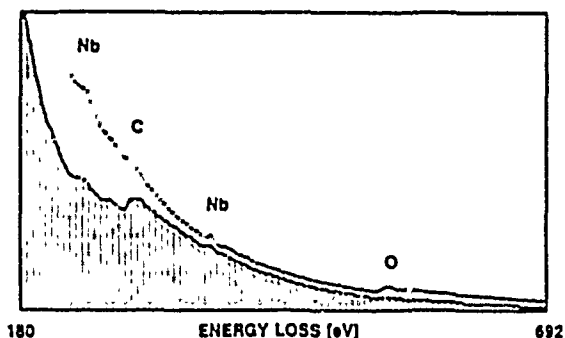
Fig. 5.   Partial EELS spectra of the dark interfacial layer showing niobium and carbon in the as-processed composite (base plot, hatched) and niobium and oxygen in the 4-h annealed material (overlay plot).
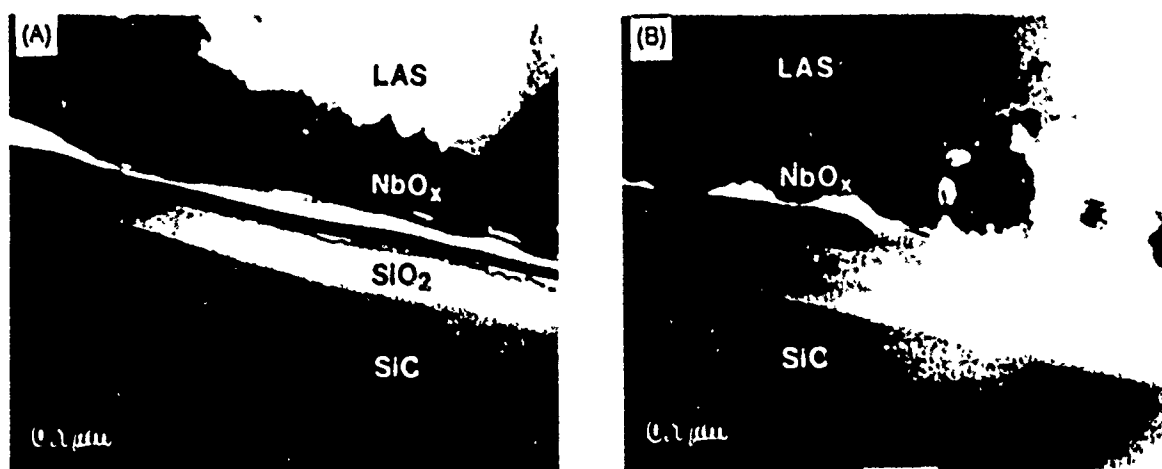
Fig. 6. TEM bright-field images of the interfacial layers after annealing in air (A) 4 h and (B) 16 h at 800°C.
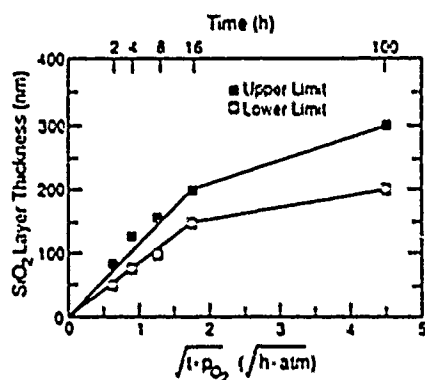
Fig. 7. SiO_2 interfacial layer thickness after exposure to air at 800°C. p_{O_2} refers to the oxygen partial pressure and t is the time. Note the transition in rates that occurs at a thickness of ~150 nm after ~16 h. This thickness coincides with the original C layer thickness.

IV. Implications and Conclusion

The marked change in the mechanical properties of LAS/SiC composites caused by heat treatment in air can clearly be attributed to the replacement of the C layer by SiO_2. The principal effect of the change in the interphase seemingly coincides with the corresponding, abrupt increase in *sliding resistance* (friction coefficient), between fiber and matrix, as elaborated in the companion papers.[11,12] This conclusion immediately implies that the optimum interphase for high-temperature toughness is a material that behaves essentially as a *solid lubricant:* either a layered structure or a soft metal thermodynamically compatible with fiber and matrix. A coupled issue concerns the thermal expansion mismatch and the incidence of thermal debonding. The expansion mismatch and the fracture resistance of the amorphous C and SiO_2 layers seemingly satisfy lower bound conditions for circumferential thermal debonding and such debonds are observed at an appreciable fraction of fiber/matrix interfaces.

The observation that some interfaces do not debond asserts that thermal debonding involves a statistical population of interface flaws having, as yet, uncertain origin. Consequently, the lower bound criterion is not a sufficient condition for thermal debonding. Furthermore, a duality in fiber response to matrix cracks might be anticipated from these observations, whereby some fibers fracture at the matrix crack front rather than pullout in the wake. Evidence for such duality is presented in a companion paper,[11] with attendant implications for mechanical behavior.
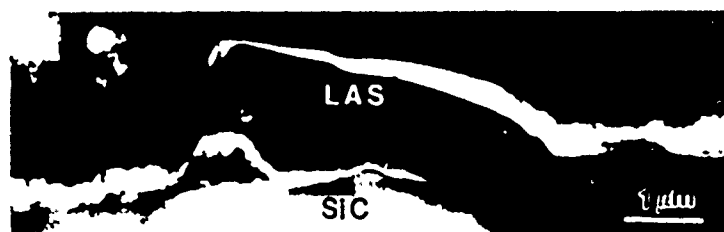
Fig. 8. TEM micrograph of sample annealed for 100 h in air showing cracks running into the matrix.

Fig. 9. TEM micrograph of the fiber/matrix interface from a sample annealed for 100 h showing that a crystalline intermediate layer has formed.

References

[1] K. M. Prewo and J. J. Brennan, "Silicon Carbide Fiber Reinforced Glass-Ceramic Matrix Composites Exhibiting High Strength and Toughness," *J. Mater. Sci.*, 17, 1201–12 (1982)

[2] D. C. Phillips, "The Fracture Energy of Carbon Fiber Reinforced Glass," *J. Mater. Sci.*, 7, 1175–82 (1972)

[3] D. B. Marshall and A. G. Evans, "Failure Mechanisms in Ceramic-Fiber/Ceramic-Matrix Composites," *J. Am. Ceram. Soc.*, 68 [5] 225–31 (1985).

[4] D. B. Marshall, B. N. Cox, and A. G. Evans, "The Mechanics of Matrix Cracking in Brittle-Matrix Fiber Composites," *Acta Metall.* 33, 2013 (1985)

[5] B. Budiansky, J. W. Hutchinson, and A. G. Evans, "Matrix Fracture in Fiber-Reinforced Ceramics," *J. Mech. Phys. Solids*, 34 [2] 167 (1986)

[6] J. Aveston, G. Cooper, and A. Kelly, "Single and Multiple Fracture," pp. 15–26 in Conference Proceedings of the National Physical Laboratory. Properties of Fiber Composites. IPC Science and Technology Press, Surrey, England, 1971

[7] B. Budiansky, Micromechanics II, Tenth U.S. Congress on Applied Mechanics. June 1986, Austin, TX

[8] E. Y. Luh and A. G. Evans, "High-Temperature Mechanical Properties of a Ceramic Matrix Composite," *J. Am. Ceram. Soc.*, 70, 466–69 (1987)

[9] D. B. Marshall and A. G. Evans, "Tensile Failure of Brittle-Matrix Fiber Composites," in Proceedings of the 5th International Conference on Composite Materials (ICCM-V). Edited by W. C. Harrigan, J. Strife, and A. K. Dhingra. Metallurgical Society, Warrendale, PA. 1985

[10] M. D. Thouless and A. G. Evans, "Effects of Pullout on the Mechanical Properties of Ceramic Matrix Composites," *Acta Metall.* 36 [3] 517 (1988)

[11] M. D. Thouless, O. Sbaiterro, L. S. Sigl and A. G. Evans, "Effect of Interface Mechanical Properties on Pullout in a SiC-Fiber-Reinforced LAS Glass-Ceramic," *J. Am. Ceram. Soc.* 72 [4] 525–32 (1989)

[12] P. G. Charalambides and A. G. Evans, "Effects of the Interface Fracture Resistance on the Mechanical Properties of Some Brittle-Matrix Composites," *J. Am. Ceram. Soc.*, 72 [5] 746 (1989)

[13] J. J. Brennan, "Interfacial Chemistry and Bonding in Fiber-Reinforced Glass-Ceramic Matrix Composites," pp. 387–400 in Ceramic Microstructures 86. The Role of Interfaces. Edited by J. A. Pask and A. G. Evans. Plenum Press, 1987

[14] J. J. Brennan, "Interfacial Characterization of Glass and Glass-Ceramic Matrix Nicalon Fiber Composites," p. 549 in Tailoring Multiphases and Composite Ceramics. Edited by R. Tressler et al. Plenum Press, New York, 1986

[15] M. Ruhle, A. G. Evans, R. M. McMeeking, P. G. Charalambides, and J. W. Hutchinson, "Microcrack Toughening in Alumina/Zirconia," *Acta Metall.*, 35, 2701–10 (1987)

[16] B. A. Bender, D. Lewis, W. S. Coblenz, and R. W. Rice, "Electron Microscopy of Ceramic Fiber–Ceramic Matrix Composites—Comparison with Processing and Behavior," *Ceram. Eng. Sci. Proc.*, 3 [7–8] 513–29 (1984).

[17] B. Bender, D. Shadwell, C. Bulik, L. Incorvati, and D. Lewis, "Effect of Fiber Coatings and Composite Processing on Properties of Zirconia-Based Matrix SiC Fiber Composites," *Am. Ceram. Soc. Bull.*, 65 [2] 363–69 (1986).

[18] R. Chaim and A. H. Heuer, "The Interface Between (Nicalon) SiC Fibers and a Glass-Ceramic Matrix," *Adv. Ceram. Mater.*, 2 [2] 154–58 (1987).

[19] Y. M. Iu, M. Rosenblatt, L. Y. Cheng, F. F. Lange, and A. G. Evans, "Cracking in Particulate Composites Due to Thermal Mechanical Stress," *Int. J. Fract.*, 17, 483–89 (1981)

[20] J. S. Nadeau, "Subcritical Crack Growth in Vitreous Carbon at Room Temperature," *J. Am. Ceram. Soc.*, 57 [7] 303–306 (1974).

[21] M. Sakai, R. C. Bradt, and D. B. Fishbach, "Fracture Toughness Anisotropy of a Pyrolytic Carbon," *J. Mater. Sci.*, 21, 1491–92 (1986)

[22] D. B. Marshall and W. C. Oliver, "Measurement of Interfacial Mechanical Properties in Fiber-Reinforced Ceramic Composites," *J. Am. Ceram. Soc.*, 70 [8] 542–48 (1987)   □

MATERIALS
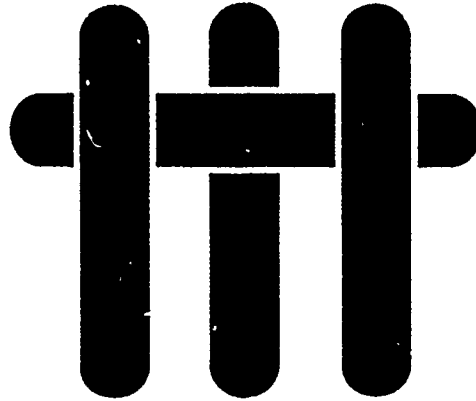
THE MECHANICAL BEHAVIOR

OF CERAMIC MATRIX COMPOSITES

A. G. Evans

Materials Department
College of Engineering
University of California, Santa Barbara
Santa Barbara, California 93106

and

D. B. Marshall

Rockwell International Science Center
1049 Camino Dos Rios
Thousand Oaks, California 93160

OVERVIEW NO. 85

THE MECHANICAL BEHAVIOR OF CERAMIC MATRIX COMPOSITES

A. G. EVANS[1] and D. B. MARSHALL[1]

[1]Materials Department, College of Engineering, University of California, Santa Barbara, CA 93106 and
[2]Rockwell International Science Center, 1049 Camino Dos Rios, Thousand Oaks, CA 93160, U.S.A.

Abstract—This article summarizes the current understanding of relationships between microstructure and mechanical properties in ceramics reinforced with aligned fibers. Emphasis is placed on definition of the micromechanical properties of the interface that govern the composite toughness. Issues such as the debond and sliding resistance of the interface are discussed based on micromechanics calculations and experiments conducted on both model composites and actual composites.

Résumé—Cet article résume la compréhension courante des relations qui existent entre microstructure et propriétés mécaniques dans les céramiques renforcées par des fibres alignées. L'accent est mis sur la définition des propriétés mécaniques de l'interface qui régissent la résistance du composite. On discute les conséquences telles que la résistance a l'arrachement et au glissement à l'interface, en se basant sur des calculs de micromécanique et sur des expériences réalisées a la fois sur des composites modèles et sur des composites réels.

Zusammenfassung—Dieser Artikel stellt den gegenwärtigen Stand im Verständnis des Zusammenhanges zwischen Mikrostruktur und mechanischen Eigenschaften von Keramiken, die mit ausgerichteten Fasern verstärkt sind, zusammen. Besonderer Wert wird auf die Definition der mikromechanischen Eigenschaften der Grenzfläche gelegt, welche die Zähigkeit des Werkstoffes bestimmen. Bestimmte Fragenkreise, wie die Ablösung oder der Gleitwiderstand an der Grenzfläche, werden auf der Grundlage von mikromechanischen Rechnungen und von Experimenten, die an Modell- und echten Werkstoffen durchgeführt wurden, diskutiert.

1. INTRODUCTION

Practical ceramic matrix composites reinforced with continuous fibers exhibit important failure damage behaviors in mode I, mode II and mixed mode I-II, as well as in compression. The failure sequence depends on the applied stress state as well as on whether the reinforcement is uniaxial, laminated or woven. However, the underlying failure processes are conveniently illustrated by the behavior of uniaxially reinforced systems. The basic features are sketched in Fig. 1. The intent of the present article is to provide an assessment of relationships between the properties of the constituents (fiber, matrix, interface) and the overall mechanical performance of the composite. At the outset, it is recognized that the composite properties are dominated by the interface and that upper bounds must be placed on the interface debond and sliding resistance in order to have a composite with attractive mechanical properties. A major emphasis of the article thus concerns the definition of optimum properties for coatings and interphases between the fibers and the matrix, subject to high temperature stability and integrity. Residual stresses in the composite caused by thermal expansion differences are also very important and are confronted throughout.

The strong dependence of ceramic matrix composite properties on the mechanical properties of the interface generally demands consideration of fiber coatings and or reaction product layers, at least for high temperature use. Thus, while low temperature matrix infiltration procedures, such as chemical vapor infiltration (CVI), can create composites that exhibit limited interface bonding and, therefore, have acceptable ambient temperature properties, experience indicates that moderate temperature exposure causes diffusion, coupled with the ingress of O_2, N_2, etc., from the environment, resulting in chemical bonding across the interface. The resultant interphases consisting of oxides, nitrides, carbides (either separately or in combination) invariably have sufficiently high fracture resistance that desirable composite properties are not retained. Consequently, a major objective of this article and of continuing research on ceramic matrix composites is the identification of interphases that are both stable at high temperature and bond poorly to either the fiber or the matrix. Certain refractory metals and intermetallics seem to have these attributes, as elaborated in the following chapters.

The basic philosophy of this article is that the overall mechanical behavior is sufficiently complex
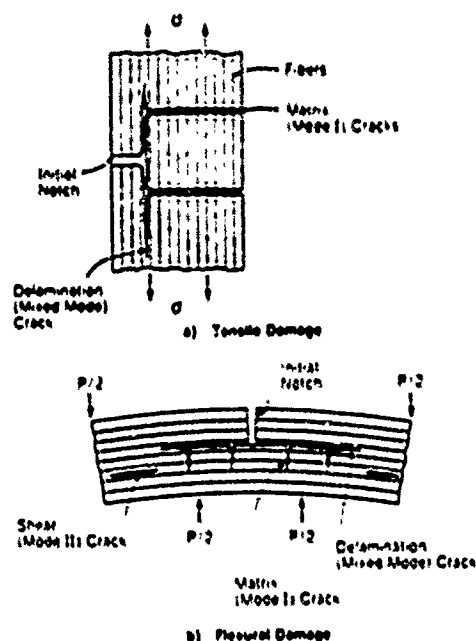
Fig. 1 A schematic illustrating the failure modes observed in high toughness uniaxially reinforced ceramic matrix composites. (a) Tension. (b) Flexure.

and involves a sufficiently large number of independent variables that empiricism is an inefficient approach to microstructural optimization. Instead, optimization only becomes practical when each of the important damage and failure modes has been described by a rigorous model, validated by experiment. The coupling between experiment and theory is thus a prevalent theme. It is also noted that this objective can only be realized if the models are based on homogenized properties that describe representative composite elements, while also taking into account the constituent properties of the fibers, matrix and interface. Models that attempt to discretize microstructural details have little merit in the context of the above objective. In this regard, the present philosophy is analogous to that used successfully to describe process zone phenomena such as transformation and microcrack toughening [1–5], as well as ductile fracture [6, 7], wherein the behavior of individual particles, dislocations, etc. provides input to the derivation of constitutive properties that describe the continuum behavior.

The behavior of the composite is intimately coupled to the basic features of crack propagation and sliding along interfaces. This is demonstrated first by examining the damage and fracture processes that occur in each of the important modes depicted in Fig. 1. The results of these studies will indicate the need for studying interface responses in judiciously selected test specimens. The basic mechanics and the implications of tests used to study interface debonding and sliding are then presented. Finally, implica-

tions for the choice of matrices, fibers and coatings that provide good mechanical properties are discussed. The tensile properties are discussed initially in qualitative terms, involving consideration of both debonding and sliding at fiber/matrix interfaces, as well as pullout, in accordance with the sequence depicted in Fig. 2. Then, the special but important case of unbonded fibers will be given quantitative attention.

2. TENSILE BEHAVIOR OF UNIAXIAL COMPOSITES

2.1. Debonding and sliding

Present understanding of the "toughening" of ceramics by brittle fibers is consistent with the debonding and sliding events illustrated in Fig. 2. To allow crack bridging by the fibers, debonding at the fiber/matrix interface must occur in preference to fiber failure at the matrix crack front. When this condition is satisfied, the sliding resistance, τ, of the debonded interface has the important role of governing the rate of load transfer from the fiber to the matrix. Specifically, large τ enhances load transfer, causing the axial stress in the fiber to decay rapidly with distance from the matrix crack plane. Consequently, weakest link statistical arguments dictate that the fibers fail at locations close to the crack plane, thus diminishing the vitally important pull-out contribution to the mechanical properties. A *small* sliding resistance along the debond thus promotes high "toughness".

The extent of debonding at the crack tip is typically small when residual compression exists at the interface, but can be extensive when the interface is in residual tension. However, more importantly, further debonding is typically induced in the crack wake [8]. The extent of debonding is again governed largely by the residual field. Residual radial tension encourages extensive debonding, whereas in the presence of residual compression, debonding is stable. The extent
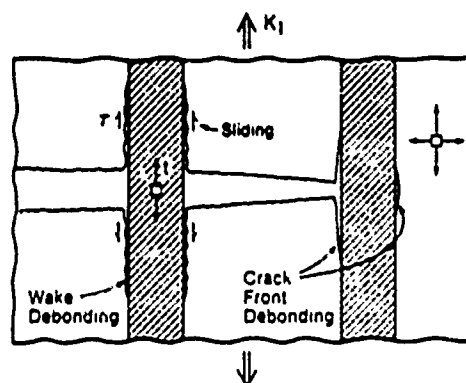
Fig. 2. A schematic illustrating the initial debonding of fibers at the crack front and fiber debonding in the crack wake.
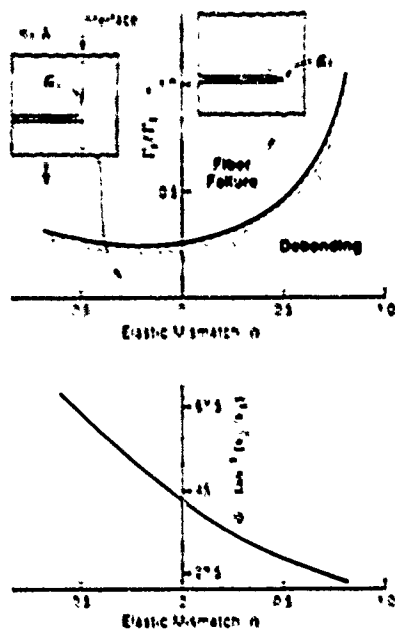
Fig. 3. The critical energy release rate required for crack front debonding.

of debonding is determined by the friction coefficient and morphology of the debonded interface.

Analysis of fiber debonding at the tip of a matrix crack (Section 5.2) indicates that debonding rather than fiber failure occurs, provided the fracture energy of the interface, $\mathcal{G}_d$, is sufficiently small compared with that of the fiber, $\mathcal{G}_{f_c}$ (Fig. 3) [9]

$$\mathcal{G}_d \cdot \mathcal{G}_{f_c} \leqslant 1.4$$

There is no direct experimental validation of this requirement. However, various observations of crack interactions with fibers and whiskers support the general features [10, 11]. In particular, experiments on LAS·SiC composites reveal that as-processed materials with a carbon interlayer debond readily and demonstrate extensive pullout [Fig. 4], whereas

Fig. 5. LAS matrix·SiC fiber composite heat treated in air for 16 h at 800 C indicating a complete SiO$_2$ layer and no pullout.

composites heat treated in air to create a continuous SiO$_2$ layer between the matrix and fiber exhibit matrix crack extension through the fiber without debonding (Fig. 5). Furthermore, composites with a thin interface layer of SiO$_2$ having a partial circumferential gap exhibit intermediate pull-out characteristics (Fig. 6). The associated constituent properties are summarized
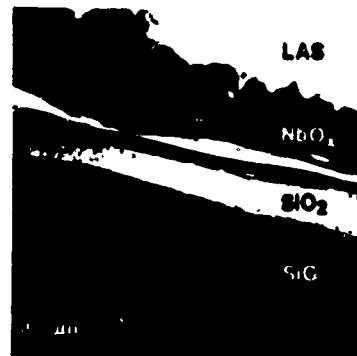
Fig. 6. LAS matrix·SiC fiber composite heat treated in air for 4 h at 800 C indicating a partial SiO$_2$ layer—with gap—and variable pullout.

Fig. 4. Interfaces and pullout in a composite consisting of LAS matrix and SiC (Nicalon) fibers: as-processed indicating C interlayer, thermal debonding and extensive pullout.

Table 1. Constituent properties of LAS/Nicalon composite

	E(GPa)	(J/m²)	(K)
Fiber (Nicalon)	200	4.4*	4 × 10
Matrix (LAS)	85	40	1 × 10⁻⁸
Interface Amorphous C	—	<1*	—
Amorphous SiO₂	90	8	1 × 10⁻¹

*Determined from fracture mirror radii
*Determined by indentation takes into account initial thermal debonding (Fig. 3)

In Table 1. Based on these properties, the preceding arguments would indicate that crack front debonding should not occur when a complete SiO₂ layer exists at the interface; whereas, appreciable crack front debonding should obtain when the C layer is present. In accord with the observations [10, 11] The composites with only a partial SiO₂ interface layer are also interesting. For these materials, $\mathcal{G}$ is related to the fraction of the circumference that bonds the fiber to the matrix: typically 1-3. Reference to Table 1 and to the initial debonding requirement (Fig. 3) would thus indicate that debonding, while marginal, is possible

2.2. Stress-strain curves

As alluded to above, the axial tensile properties are dictated by the mechanical properties of the fiber/matrix interface, the strength of the fibers and residual stresses due to different contractions of the fibers and matrix upon cooling after fabrication. For suitable combinations of these properties, a non-catastrophic mode of failure can be obtained, as characterized by the tensile stress-strain curve of Fig. 7 [12, 13]. Qualitatively, this failure mechanism is favored in composites with "weak" interfaces, high-strength fibers and tensile residual stresses normal to the fiber/matrix interface. Changes in any of these parameters can lead to a transition in failure mechanism to one which is catastrophic, with linear stress-strain curve to failure.

The initial departure from non-linearity in both

type of stress-strain curve results from cracking of the matrix For the non-catastrophic mode of failure, the first crack in the matrix extends indefinitely, breaking only a small fraction of fibers [13, 14]. Further loading causes formation of periodic matrix cracks, with spacing dictated by a characteristic stress transfer length associated with the bridging fibers. These cracks divide the composite into "blocks" of matrix held together by intact fibers. The increasing non-linear portion of the stress-strain curve is dictated by the properties of the fibers, as qualified by frictional interactions with the matrix "block" The ultimate strength is determined by fiber bundle failure, with the tail of the curve corresponding to pullout of broken fibers. This type of failure mechanism has been observed in a wide range of composite materials, including reinforced cements, glasses and glass-ceramics [15-18]. If, on the other hand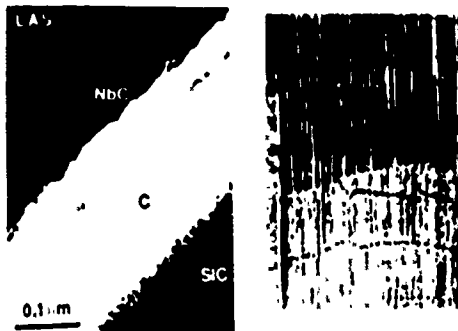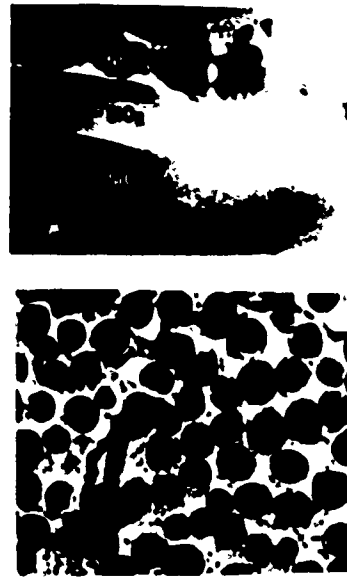, a substantial proportion of the fibers break in the wake of the first matrix crack as it extends, then failure of the composite is catastrophic. In this case, the ultimate strength is limited by the growth of a single dominant crack and is determined by a fracture resistance curve [19]. The nature of the resistance curve and the magnitude of the steady-state toughness is governed by the zone of bridging fibers behind the crack tip. The composite properties associated with the above failure mechanisms are discussed below, along with the criteria that dictate the transition between mechanisms.

2.3. Some basic mechanics

The opening of a crack bridged by fibers involves stretching of fibers between the crack surfaces. This stretching may be characterized by a relation between the stress, σ, in the fibers and an average local crack opening displacement, u, as depicted in Fig. 8. The form of this relation depends on the details of the bridging mechanism and reflects properties such as fiber-matrix debonding and frictional sliding, as well as elastic stretching of the fiber. The peak value, $t = S$, represents the "strength" of the fiber, whereas the decreasing portion depends on the nature and location of fiber failure.
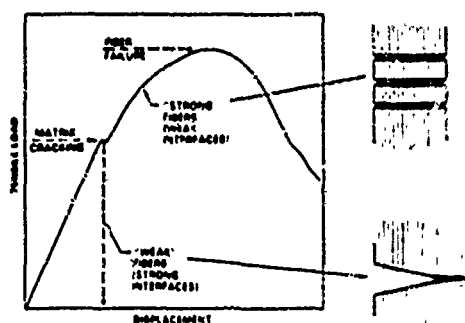
Fig. 7. A tensile stress-strain curve for a "tough" ceramic composite.

Fig. 8. A schematic illustrating various trends in crack opening with stress.

The $t(u)$ relations in Fig. 8 represent the range of behavior exhibited by brittle reinforcing fibers. At one extreme, for a fiber that is sufficiently well bonded that no debonding occurs when the crack circumscribes it, the $t(u)$ relation is linear to failure. At the other extreme, for a fiber that is not bonded at all to the matrix, frictional forces resist pullout. Initially, the $t(u)$ relation is an increasing function of u until the fibers break, then $t(u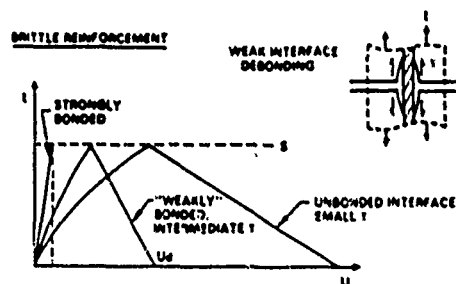)$ decreases as the broken fibers pull out of the matrix. Intermediate $t(u)$ relations result from partial debonding and frictional sliding over the debonded crack surfaces.

The influence of bridging fibers on fracture of the composite can be evaluated by two equivalent approaches, both of which model the composite around the crack as a continuum and employ the $t(u)$ relation as the link between the constitutive properties of the composite and its macroscopic continuum behavior. In one approach, the stresses in the bridging fibers are viewed as crack surface closure tractions which reduce the stresses at the crack tip [14]. The corresponding reduction in crack tip stress intensity factor is calculated from these surface tractions using a standard Green's function. The criterion for crack growth is obtained by setting the resultant crack tip stress intensity factor in the matrix equal to the toughness of the unreinforced matrix. The alternative approach is to use the J-integral to evaluate the effect of the bridging tractions on the energy flux [20, 21]. In general, both of these approaches require numerical solution of an integral equation to calculate the crack opening displacements, in order to specify the distribution of closure tractions over the crack surface. However, for steady-state configurations, the J-integral approach provides simple analytical results and is thus more useful.

2.4. Matrix cracking

Matrix cracking originates from preexisting flaws, typified by a crack in the matrix with intact bridging fibers over its entire surface. If the composite is subject to uniform applied tensile stress, σ_a, normal to the crack, the crack opening displacement, u, and the crack surface pressure, $p = ft$, increase monotonically with distance behind the crack tip. For sufficiently long cracks, u and p approach asymptotic limits equal to u_a and σ_a (p cannot exceed σ_a) at the mouth of the crack (Fig. 9). This is a steady-state configuration; the stresses at the crack tip increase as the applied stress increases, but are independent of the total crack length. Consequently, the critical stress, σ_c, to extend the crack in the matrix is also independent of crack length. Therefore, provided $\sigma_c < Sf$, where S is the strength of the fibers, the crack extends indefinitely in the matrix (i.e. completely across the specimen) at constant applied stress, without breaking fibers in its wake. If, on the other hand, the preexisting matrix crack is not sufficiently long for the asymptotic opening to be achieved at $\sigma_a = \sigma_c$, then the critical

stress is a decreasing function of crack length, as illustrated in Fig. 10 [14].

Analysis of steady-state matrix cracking provides the following relation from which the stress σ_c can be evaluated once the stress–displacement relation $p(u)$ is specified [20, 22]

$$\mathcal{G}_m(1-f)/2 = \sigma_c u_c - \int_0^{u_c} p(u)\,du \qquad (1)$$

where u_c is the asymptotic crack opening corresponding to $\sigma_a = \sigma_c$, and $\mathcal{G}_m$ is the fracture energy of the unreinforced matrix. The right-hand side of equation (1) is the complementary energy, represented by the shaded area in Fig. 11(a). The critical condition for matrix cracking is determined by the applied stress at which this area is equal to $\mathcal{G}_m(1-f)/2$. Thus, for a given matrix and volume fraction of reinforcement, this area is constant and, consequently, the effect of changing the nature of the bridging ligaments on the matrix cracking stress can be readily deduced. Generally, changes that stiffen the loading portion of the $p(u)$ curve must increase σ_c, whereas changes to the maximum value of $p(u)$ or to the region of the curve beyond the peak have no influence on σ_c.

2.5. Resistance curves and toughening

If the steady-state matrix cracking stress given by equation (1) exceeds the stress, fS, that can be supported by the fibers, then the fibers within a fully-bridged crack break before the crack extends in the matrix. The consequent reduction in bridging forces causes the crack tip stresses to increase (at constant applied stress), resulting in unstable crack extension in the matrix, accompanied by further fiber failure [23]. The corresponding stress–displacement curve is linear to the peak load and failure is catastrophic.

A preexisting crack without bridging fibers (e.g. a notch cut by a saw) grows in the matrix initially without breaking fibers. A bridging zone develops behind the advancing crack front, resulting in increasing closure tractions as the crack grows. Consequently, the applied stress intensity factor needed for continued crack growth increases, so that crack growth is dictated by an increasing crack resistance curve (R-curve), as depicted in Fig. 12. In general,
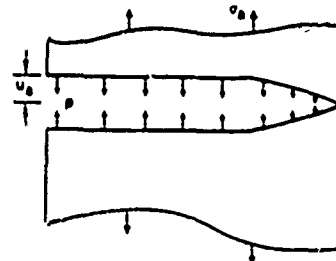
Fig. 9. Steady-state cracking indicating the uniform opening u_s in the crack wake.
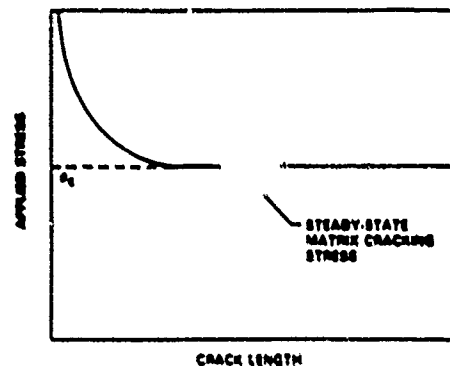
Fig. 10. Variation in matrix cracking stress with crack length

calculation of the rising part of the R-curve and the amount of crack extension needed to achieve steady state, requires numerical solution of an integral equation to obtain the crack opening displacements [23]. In composites with small bridging zones, the steady-state toughness increment is of primary interest. However, in composites with large bridging zones, the entire R-curve must be specified, because the steady-state toughness may never be achieved by a stable crack (e.g. if the crack extension needed is larger than the specimen width).

A simple analytical solution of the steady-state toughness increment has been derived using the J-integral [20, 21]

$$\Delta \mathcal{G}_c = 2 \int_0^{u_0} p(u)\, du \qquad (2)$$

where u_0 is the crack opening at the end of the bridging zone. For the steady-state crack, u_0 is the displacement above which the bridging forces are zero and $\Delta\mathcal{G}_c$ is given by the area beneath the $p(u)$ curve, as depicted in Fig. 11(b). Therefore, if the $p(u)$ relation is specified, then $\Delta\mathcal{G}_c$ can be evaluated without having to determine the crack opening displacements
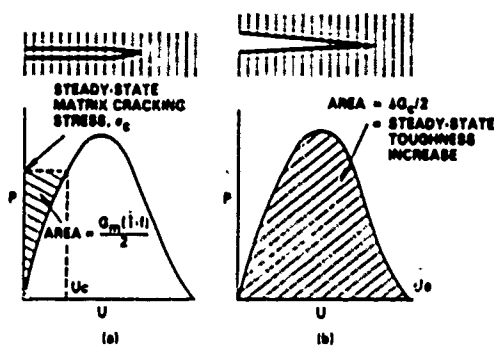
Fig. 11. Stress, crack opening curves for (a) steady-state cracking and (b) steady-state toughening.
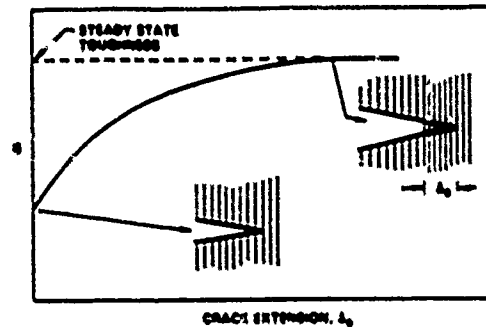
Fig. 12. A schematic resistance curve for crack extension in a uniaxial composite.

2.6. Transition in failure mechanism and optimization of properties

The results of the previous two sections allow some general conclusions to be drawn concerning the dependence of steady-state toughness and steady-state matrix cracking stress on microstructural properties. If we begin with a composite that fails by the non-catastrophic, multiple matrix cracking mechanism, then, as discussed previously, any change in the nature of the bridging ligaments that stiffens the increasing portion of the $p(u)$ relation causes the steady-state matrix cracking stress to increase. However, if σ_c exceeds the peak in the $p(u)$ curve, a transition in failure mechanism must occur and the steady-state toughness is given by the area beneath the $p(u)$ curve. Then, further increase in stiffness of the increasing portion of the $p(u)$ relation would usually lead to a decrease in toughness, provided that the peak value of $p(u)$ remains constant. Therefore, the optimum properties (i.e. maximum σ_c or $\Delta\mathcal{G}_c$) occur in the vicinity of the transition between the two failure mechanisms.

2.7. Residual stress

Residual microstructural stresses arise generally from thermal contraction during cooling from an elevated processing temperature. The residual stresses before cracking are of opposite sign in the reinforcing ligaments and matrix, and the average residual stress normal to a potential crack plane that spans many microstructural units is zero. Therefore, in the absence of a bridging zone, the microstructural residual stresses have no effect on the steady-state fracture toughness. Moreover, the fracture mechanics analysis of bridging, expressed in terms of the $p(u)$ relation, is unaffected by the presence of residual microstructural stresses. However, the residual stresses influence the $p(u)$ relation and thereby the magnitudes of the matrix cracking stress and the fracture toughness [24].

The influence of the residual stress on the $p(u)$ relation is dependent upon the mechanisms of interfacial sliding and fiber failure. An offset in the origin always occurs by an amount

$$\sigma_0 = -qE^f E_m \qquad (3)$$

Table 2. Effect of residual stress on toughness

Stress displacement law		Rupture condition	Residual stress in fiber Compression	Tension
Linear		Stress	Decrease	Increase
		Displacement	Increase	Decrease
Frictional with pullout	Surface toughness	Stress	---	Negligible
	Coulomb friction	Stress	Decrease	---

where q is the axial residual stress in the matrix and E and E_m are the Young's moduli of the composite and the matrix. The remainder of the $p(u)$ curve is simply translated by σ_u for some composites, but in general, the shape of the $p(u)$ curve may be modified as well.

For composites in which residual stress translates the $p(u)$ relation uniformly by σ_u, it is readily deduced from Fig. 11(a) that the *matrix cracking stress* σ_c is either increased (q compressive) or decreased (q tensile) by σ_u. However, the sign and magnitude of the steady-state *toughness* change induced by the residual stress depends on the mechanism of interfacial sliding and fiber failure, as summarized in Table 2.

2.8. Transverse failure

The transverse strengths of high toughness composites are generally very low. There have been no systematic studies of this property. However, experimental studies on composite laminates [25] indicate that the transverse cracks typically propagate along the interface layer and through the matrix between neighboring fibers. Furthermore, because the interfaces have sufficiently small fracture energy to allow debonding, overall failure is preceded by interface failure. This process occurs at a critical stress, σ^*, which can be determined in a manner analogous to that for the steady-state cracking of thin films [26], to give

$$\sigma^* \approx \sqrt{2E\mathcal{G}_i/\pi R} - q. \qquad (4)$$

In some cases, q is sufficiently large that $\sigma^* < 0$ and the interfaces debond upon cooling (Fig. 4).

3. TENSILE BEHAVIOR OF COMPOSITES WITH UNBONDED REINFORCING FIBERS

Composites with little or no bonding at the fiber-matrix interface ($\mathcal{G}_i \approx 0$) are an important, special case that have been extensively studied, both theoretically and experimentally, and thus merit separate consideration. The non-catastrophic failure mechanism depicted in Fig. 7 is most likely in such composites. Moreover, with fiber pullout being dictated by sliding, evaluation of the $p(u)$ relation is relatively straightforward compared with the composites that have significant debond energies. In the latter case, rigorous analysis involves complications of interfacial fracture between materials of differing

elastic constants, a topic that will be addressed in Section 5.

Composites comprising glass or glass-ceramic matrices and C or SiC fibers have been observed to fail in the "weakly" bonded category. One particular composite with SiC fibers and lithium-alumina-silicate (LAS) glass-ceramic matrix has been extensively studied and has served as a reference for most comparisons with theoretical modelling [13, 15, 16]. In this composite, the fiber/matrix interface contains a C layer (Fig. 4) which governs the "weak" interfacial bonding [10].

3.1. Pullout

Rigorous analysis of the $p(u)$ relation governed by fiber sliding requires consideration of fiber fracture statistics and the effect of residual and applied stresses on the frictional resistance, τ, through their influence on the normal interfacial stress. In principle, with a statistical distribution of fiber strengths, some fiber failure occurs ahead of the crack tip as well as in the crack wake. Analysis of fiber failure ahead of the crack has not been attempted, partly because the problem is complex and partly because of a perception that fiber failures close to the crack plane that cause pullout are most likely to occur in the crack wake. Such behavior has indeed been observed in glass reinforced plastics [27]. However, there is no direct evidence that fiber failure ahead of the matrix crack can be neglected in ceramic matrix composites.

Nevertheless, it is insightful to examine solutions for the $p(u)$ relation based on wake failure in composites having debonded interfaces subject to small, constant sliding resistance, τ, and negligible residual stress [28]. The analysis involves calculation of the distribution of fiber failure sites as a function of applied stress, σ, and hence, the reduction in stress due to fiber failure. The fiber strengths are taken to be defined by a Weibull distribution with shape and scaling parameters m and S_0. The results summarized in Fig. 13 indicate that the initial, rising portion of the $p(u)$ curve is dominated by intact fibers, the peak is dominated by multiple fiber failures, analogous to bundle failure, and the tail is governed by pullout. The *initial rising* portion of the curve is closely approximated by the limiting solution ($m = \infty$) for all m [14]

$$p = \left[\frac{4\tau f^2 E_f E^2}{R E_m^2 (1-f)^2} \right]^{1/2} u^{1/2} \qquad (5)$$
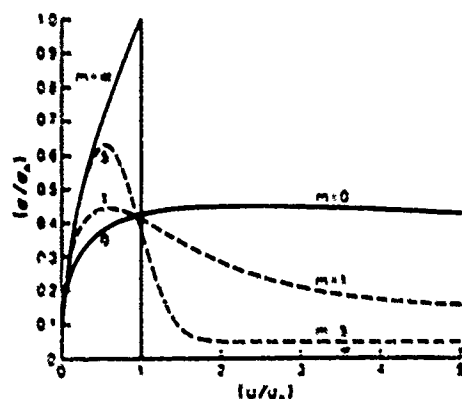
Fig. 13 Non-dimensional stress, crack opening curves for bridging plus pullout for various values of the statistical shape parameter, m

where R is the fiber radius, f the volume fraction of fibers and E_f, E_m and E are the Young's moduli of the fibers, matrix and composite. However, the tail of the curve is more sensitive to m as m decreases, corresponding to a broader distribution of fiber strengths, more fibers fail further from the matrix crack, causing the extent of *pullout* to increase.

Correlation of calculated and experimentally measured pull-out lengths on the fracture surfaces of broken test pieces provides a route for measuring the statistical parameters and interfacial sliding resistance [11, 29]. The calculated cumulative probability that the pull-out length will be $\leqslant h$ is plotted in Fig. 14. The results indicate that the pull-out lengths tend to increase as m decreases, as expected. Preliminary estimates of the effects of residual strain suggest that the pull-out length usually decreases as the residual strain increases, when the residual stress at the interface is compressive. However, specific trends are sensitive to m, as well as to the friction coefficient μ. Measurements in the LAS/SiC system will be discussed below.

3.2. Matrix cracking

For composites in which the interfacial residual stress is tensile or zero and the sliding resistance can
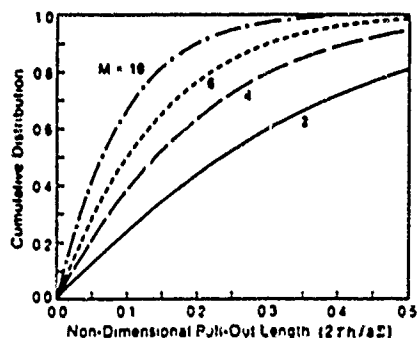
Fig. 14. The cumulative pull-out distribution for several values of the shape parameter, m.

be represented by a unique stress, τ, the $p(u)$ relation is given by equation (5) and the steady-state matrix cracking stress evaluated from equation (1) is [12, 14]

$$\frac{\sigma_c}{E} = \frac{\sigma_m}{E} - \frac{q}{E_m}$$

with

$$\sigma_m = \left[\frac{6\mathscr{G}_{mc}\tau E_f E_m f^2}{RE(1+f)}\right]^{1/3} \tag{6}$$

where $\mathscr{G}_{mc}$ is the fracture energy of the unreinforced matrix and q is the axial residual stress in the matrix. Experiments conducted on a number of ceramic matrix composites are consistent with equation (6). When the interface is subject to residual compression, τ depends on the local applied stress and solution for σ_c is more complex. However, to first order, τ may be simply replaced by μq, where μ is the friction coefficient and q, the residual stress normal to the interface).

When the applied stress exceeds σ_c, multiple matrix cracking is expected [12, 14] and observed [12, 13]. The saturation crack spacing D, is between one and two times the distance over which the applied stress in the matrix builds up from zero at the crack surface to the value for an uncracked composite. For unbonded fibers, this is the distance over which sliding occurs at the interface. In this case, the range of crack spacings is given by

$$\sigma_m R(1-f)/2f\tau < D < \sigma_m R(1-f)/f\tau. \tag{7}$$

Experimental observations [13] have again confirmed this feature of matrix cracking.

The most crucial aspects of the above interpretation of steady-state cracking and of behavior prediction concern determination of τ and q for actual composite systems. Both are difficult to measure. Two basic approaches have been used to measure the *sliding resistance* τ: indentation [30, 31] and measurement of crack opening hysteresis [13]. Both approaches are readily applicable when $\mathscr{G}_{ic}$ and τ are small. The former method is most insightful when used with a nanoindenter system, whereupon τ can be obtained on single fibers either from a push through force on thin sections or from the hysteresis in the loading/unloading cycle on thick sections [Fig. 15(a)]. This method has the obvious disadvantage that the fiber is in axial compression so that the interface is also compressed during the test, with attendant changes in τ. However, this effect has been shown to be negligible for ceramic composites systems having very small sliding stresses ($\tau \leqslant 10$ MPa). Calculation of τ from direct measurement of crack opening hysteresis during load cycling [Fig. 15(b)] avoids this complication because the fibers are subjected to axial tensile loading. However, this approach also has several drawbacks. Measurements are obtained only *after* matrix cracking and so correspond to a range of crack opening displacements beyond those that dictate formation of the matrix cracks. Furthermore,
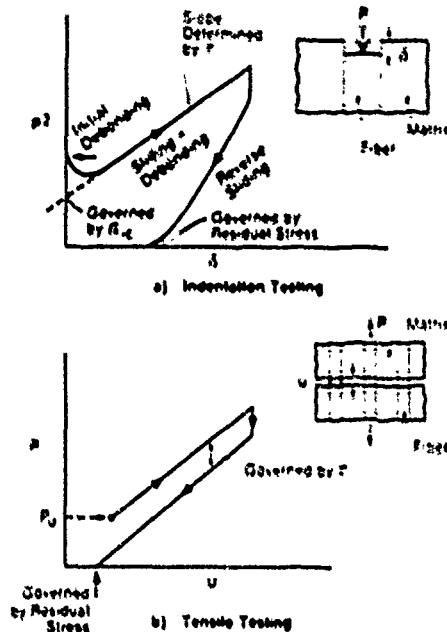
Fig. 15 (a) A load/unload cycle for nanoindentation of a fiber. (b) Crack opening hysteresis for a composite with intact fibers revealing the trends in both sliding resistance and residual stress.

interpretation of the results is complex when appreciable fiber failure accompanies matrix cracking. Consequently, other approaches applicable to composites having larger τ are being investigated. One of these is discussed in the following section.

3.3. Ultimate strength

Following multiple matrix cracking, the axial stress in each of the fibers varies from the maximum, equal to $\sigma_a f$, between the crack surfaces to a minimum, $\geqslant \sigma_a E_f/E$, halfway between adjacent matrix cracks. The probability and location of fiber failure subject to weakest link statistics in such a stress field can be readily derived. However, calculation of the maximum load supported by the composite (i.e. a bundle of such fibers) requires that the stress redistribution caused by the fractured fibers be modelled. Such an analysis has not been attempted. Nevertheless, a lower bound for the maximum load can be derived by simply allowing failed fibers to have no load bearing ability. Then, a modified bundle failure analysis yields the following expression for the ultimate strength

$$\sigma_u = fS \exp\left[-\frac{\{1-(1-\tau D/RS)^{m+1}\}}{(m+1)\{1-(1-\tau D/RS)^m\}}\right] \quad (8)$$

where

$$(RS/\tau D)^{m+1} = (A_0/2\pi RL)(RS_0 \tau D)^m$$

$$\times [1-(1-\tau D \cdot RS)^m]^{-1}$$

with L being the gauge length. In the one composite

system for which analysis of the ultimate strength has been performed (LAS SiC) [11, 29], equation (8) agrees quite well with measured values.

The ultimate strength anticipated from the above argument is expected to be influenced by the residual stress. Specifically, in systems for which the fiber is subject to residual compression, the axial compression should suppress fiber failure and elevate the ultimate strength to a level exceeding that predicted by equation (8) [32]. This effect may be estimated by regarding the matrix as clamping onto the fiber and thus, simply superposing the residual stress onto S.

3.4. Resistance curves

When mode I failure is dominated by propagation of a single matrix crack, accompanied by fiber failure and pullout, the mechanical properties are characterized by a resistance curve. The entire R-curve has been evaluated for fibers with a single-valued strength, S (i.e. $m = \infty$) and small sliding resistance, τ. Although this analysis does not account for pullout of broken fibers (fibers must fail between the crack surfaces for $m = \infty$), some useful trends with microstructural properties are evident. The steady-state toughness increase obtained from equations (2) and (5), is

$$\Delta\mathcal{G}_c = \frac{S^3 Rf(1-f)^2 E_m^2}{6\tau E_f E_c^2} \quad (9)$$

and the amount of crack extension needed to achieve steady state is

$$\Delta c \sim \left[\frac{\mathcal{G}_\infty R^2(1-f)^2 E_m^4}{\tau^2 f^2 E_f^2 E}\right]^{1/3} \quad (10)$$

It is noteworthy that both $\Delta\mathcal{G}_c$ and Δc increase with the ratio R/τ, whereas the steady-state matrix cracking stress decreases [equation (6)]. Furthermore, a simple relationship exists between the steady-state toughening and the matrix cracking stress (Fig. 16) [33]. These results indicate that, for reasonable values of $fS \sigma_a$ (<3), the toughening ratio is, at most, 6 and more typically, 3. It is thus concluded that bridging from unbroken continuous fibers does not permit order-of-magnitude increases in toughness. Instead, the very high toughness obtained in various materials involves an important contribution from pullout.
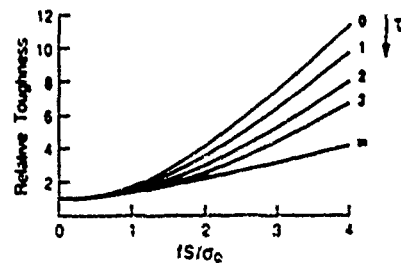
Fig. 16. Trends in toughening ratio with matrix cracking stress. From Ref. [33]

caused by fiber failure away from the matrix crack plane.

The steady-state toughness increase when fibers have a statistical distribution of strengths has been evaluated using the $p(u)$ relations in Fig. 13. The expressions are lengthy in form, but general trends can be specified. The degree of toughening always increases as the scale parameter S_0 increases, thereby establishing *that high fiber strengths are invariably desirable*. However, the dependence on τ and R is ambivalent. The essential details are highlighted by considering separately the contributions from broken and unbroken fibers to the toughness integral [28]. The component due to unbroken fibers is

$$\Delta\mathscr{G}_s = 4fTU' (m + 1) \qquad (11)$$

where $U' = T^2R/4E_f\tau(1+\xi)$ is proportional to $[R^{m-1}\tau^{m-3}]^{1/(m-1)}$. A notable feature is the inversion in the trend with τ that occurs at $m = 2$, and with R at $m = 3$. The corresponding pull-out contribution from broken fibers can be examined by recognizing that the toughening has the form

$$\Delta\mathscr{G}_s \sim \langle h \rangle^2 (\tau/R) \qquad (12)$$

where $\langle h \rangle$ is the average pullout length.

The elimination of $\langle h \rangle$ from this expression using the calculations of pull-out lengths summarized in Fig. 9 then leads to the result that the toughness is proportional to

$$[R^{m-1}S_0^{2m}/\tau^{m-1}]^{1/(m-1)}.$$

The toughness thus increases with increasing R when $m > 5$, and decreases when $m < 3$. Conversely, it increases with increasing τ when m is very small ($\ll 1$), and decreases when $m > 2$. These limits arise because of the competing importance of the contribution to toughness from the intact bridging fibers and the failed fibers that experience pullout. Knowledge of the magnitude of the statistical shape parameter, m, for the fibers *within* the composite is therefore a prerequisite to optimizing the shear properties of the interface for high toughness.

The shape of the rising R-curve is expected to be sensitive to m; in general, the amount of crack growth needed to approach steady state must increase with decreasing m. However, the actual slope of the resistance curve has not yet been evaluated, because numerical methods are needed to determine the upper limit of equation (2), as dictated by the crack opening at the end of the bridging zone. Further research concerning this phenomenon is a major priority.

3.5. Property transition

Non-linear macroscopic mechanical behavior in tension is most desirable for structural purposes. Therefore, analysis of the transition between this and the linear response is important. The transition is dependent upon the nature of preexisting defects in the composite, in particular the length of *unbridged* crack. However, a useful lower bound, which applies
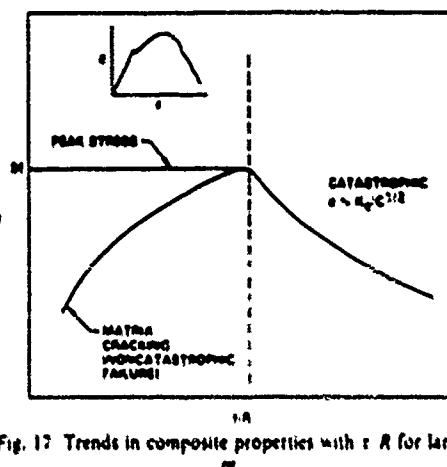
Fig. 17 Trends in composite properties with τ/R for large m.

to preexisting defects that are fully bridged, is given by the requirement that the steady-state matrix cracking stress be smaller than the ultimate strength in order to obtain the non-catastrophic failure mode. For $m = \infty$, this condition is given by setting σ_c in equation (6) equal to the fiber strength S.

Equations (6) and (9) for steady-state matrix cracking and asymptotic toughening (at $m = \infty$) allow the general trends for property optimization, outlined in Section 2.1 to be quantified. The variation in strength of a composite with the ratio τ/R is shown schematically in Fig. 17. In the region of non-catastrophic response, the matrix cracking stress increases with the parameter τ/R, whereas the ultimate strength is not affected (for small m in the ultimate strength is a weakly decreasing function of τ). At a critical value of τ/R, where σ_c exceeds Sf, the transition to linear response occurs. With further increase in τ/R, the fracture toughness decreases (and the strength also decreases if the preexisting flaws remain unchanged).
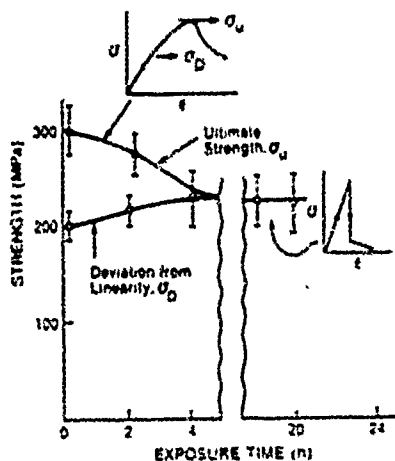
Fig. 18. Effects of heat treatment on the tensile stress-strain behavior of LAS/SiC composites.
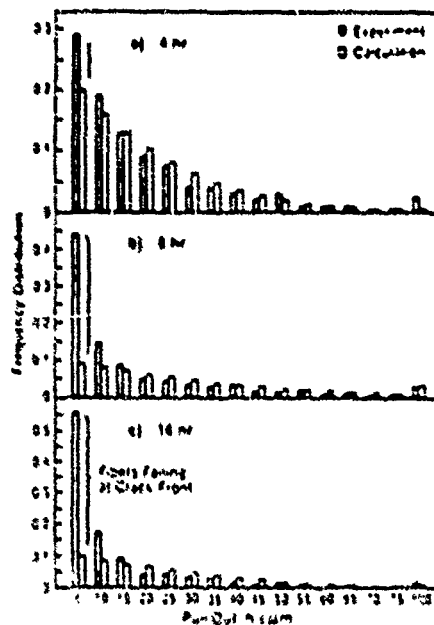
Fig. 19. Histograms indicating trends in pull-out length with heat-treatment.

Therefore, optimum values of τR exist near the transition point.

The behavior illustrated in Fig. 17 has been investigated systematically by heat treating the LAS/SiC composite under conditions where the interfacial graphite layer disappears and is replaced by SiO_2 (Figs 4–6), resulting in an increased frictional sliding resistance. The variation in tensile mechanical properties with heat treatment time are shown in Fig. 18. The influence of heat treatment on interfacial properties can be inferred from measurements of fiber pull-out lengths in broken test pieces and comparison with the calculations of Fig. 14 [29]. The results reveal that the pull-out distribution gradually changes as the gap caused by C removal is filled with SiO_2 (Fig. 19). In particular, the median pullout length decreases and the proportion of fibers that actually pull out exhibit distributions consistent with the predictions of the weakest link fiber failure analysis, such that the interface τ increases by about an order of magnitude when a partial SiO_2 layer replaces C. This change in τ and the accompanying dramatic change in the mechanical properties of the composite are consistent with the response depicted in Fig. 17.

3.6. Residual stress

Large mismatches in thermal expansion coefficient between fiber and matrix are clearly undesirable. In particular, relatively large matrix contraction, $\alpha^m \alpha' \gg 1$, causes premature, or even spontaneous, matrix cracking [equation (6)]. Such behavior is not

necessarily structurally detrimental, but concerns regarding thermal fatigue, the ingress of environmental fluids, etc. have discouraged the development of materials having these characteristics. Conversely, relatively small matrix contractions, $\alpha' \alpha^m \gg 1$, thermally debond the fiber from the matrix. When sufficiently extensive, the resultant radial separations negate the influence of the fibers. Consequently, values of $\alpha' \alpha^m$ close to unity are required. Indeed, mode I axial properties subject to an interface that easily debonds and slides freely along the debond involve an optimum residual stress, with a maximum matrix cracking stress, when the interfacial stress is compressive, given by [34]

$$\sigma_c E = (2/3) [f\mu \mathcal{G}_m \lambda E_m R]^{1/3} \qquad (13)$$

where $\lambda = 1 - (1 - E/E_i)/2$. When $\alpha_f \mathcal{G}_m \gg 1$, such that the interfacial stress is tensile, asperities on the debond surface may provide a discrete sliding stress, τ, that depends on such features as the asperity amplitude. For such cases, the optimum residual strain has not been determined.

The fracture resistance is also influenced by the residual stress. However, the sign and magnitude of the change in toughness induced by residual stress depends on the mechanisms of interface sliding and fiber failure, as summarized in Table 2 [24]. Subject to adequate debonding, the salient results for ceramics reinforced with brittle fibers are that $\Delta\mathcal{G}_c$ is unaffected when the interfacial stress is tensile and the interface is characterized by a unique τ, whereas $\Delta\mathcal{G}_c$ usually decreases with increasing compressive interfacial residual stress because the pull-out lengths decrease, as apparent when τ is equated to μq.

Residual stresses in composites are difficult to measure. Even when the composite is fully elastic, so that no interface debonding or sliding occur on cooling, the residual stresses at the surfaces are complex. Consequently, methods such as X-ray diffr on that probe thin surface layers are difficult to terpret. Neutron diffraction, which typically averages over a much larger volume of material, is usually more satisfactory. Measurement difficulties are exacerbated when debonding and sliding occur on cooling. These processes initiate preferentially at the surface and spread into the body along the interface, thereby alleviating the residual stress over the debond/slip length. For small τ and $\mathcal{G}_c$, these lengths are large (many multiples of the fiber diameter) [13]. Consequently, a valid measure of the residual stress can only be obtained using processes that penetrate well into the material. One independent approach for measuring q that has merit in some cases involves use of the same crack opening measurements described by Fig. 15(b). Specifically, the residual axial stress in the matrix is related directly to the stress at which crack closure occurs [13]. The method is, however, restricted to materials for which matrix cracking is not accompanied by extensive fiber failure.

Fig. 20 Delamination cracking in notched flexure tests.

Fig. 21 Matrix microcracks that precede mode II failure in tough composites.

4. MIXED MODE FAILURE

4.1. Mode II failure mechanisms

Flexural tests performed on uniaxial composites reveal that a shear damage mechanism exists (Figs 1 and 20) [35] and that such damage often initiates at quite low shear stresses, e.g. 20 MPa in LAS SiC. The damage consists of en echelon matrix microcracks inclined at about π 4 to the fiber axis (Fig. 21). With further loading, the microcracks coalesce, causing matrix material to be ejected and resulting in the formation of a discrete mode II crack. The crack is defined by the planar zone of ejected matrix. The crack also has a microcrack damage zone similar to that present upon crack initiation.

The microcracks that govern mode II failure are presumably caused by stress concentrations in the matrix and form normal to the local principal tensile stress, but then deflect parallel to the mode II plane and coalesce. An adequate model that incorporates the above features has not been developed. Consequently, the underlying phenomena are briefly noted without elaboration. The stress concentrations in the matrix have magnitude governed by the elastic properties, the fiber spacing and the interface strength. The growth and coalescence of the microcracks is influenced by the matrix toughness $\mathcal{G}_m$. The shear strength seemingly decreases as the mode I toughness increases.

4.2. Delamination cracking

Delamination is a common damage mode in the presence of notches [13, 25] (Figs 1 and 20). Delamination cracks nucleate near the notch base and extend stably. Analysis of such data is based on the solutions used for mixed mode interface cracking in beams [36], modified to take account of the elastic anisotropy. The fracture resistance is found to increase with crack extension. The existence of a resistance curve is attributed to intact fibers within the crack that resist the displacement of the crack surfaces and thus, shield the crack tip in a manner analogous to fiber bridging in mode I. However, the fracture energies are typically of the same order as the fracture

energy of the matrix, e.g. ~20 Jm⁻² for LAS matrix composite

5. INTERFACIAL DEBONDING AND SLIDING

5.1. Mechanics of interfacial cracks

The results and discussion of the preceding sections point to several problems involving debonding along interfaces that are central to determining mechanical properties of composites. Such debonding occurs both at the tip of a matrix crack and in the crack wake (Fig. 2). It typically involves two materials with different elastic constants and mixed shear and tensile loading. Furthermore, since the interface can have lower fracture resistance than either the matrix or fibers, the debond crack can continue to extend under mixed mode conditions rather than seeking a plane normal to the principal tensile stress. Therefore, it is necessary to direct attention to the dependence of fracture resistance, $\mathcal{G}_i$, on the mix of shear and tensile loading.

The mechanics of cracks at bimaterial interfaces was derived in a series of studies in the 1960s [37-41] and has received renewed interest and elucidation recently [42-45]. An additional complexity in the fracture mechanics arises from the fact that the shear and tensile components of stress and displacement along the crack plane ahead of, and behind, the crack tip are not decoupled as they are in linear elastic fracture mechanics for homogeneous materials, i.e. a tensile (mode I) remote loading generally results in both tensile and shear stresses and displacements near the crack tip. Moreover, the mix depends on the crack length as well as the mismatch in elastic constants and the position relative to the crack tip. Despite this complication, it is possible to specify the crack tip field in terms of a position-independent stress intensity factor, K, which contains all of the information concerning applied loads and the geometrical configuration. However, to accomplish this, the stresses and displacements are expressed in complex notation, with opening and shear components as the real and imaginary parts. In this scheme, the ratio of opening to shear crack tip displacements (u and v
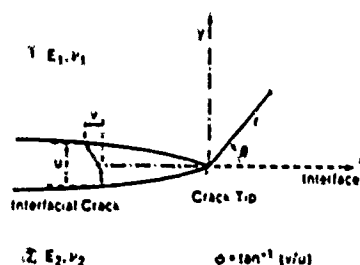

Fig. 22. The displacement of the surface of a crack at bimaterial interface indicating the shear and opening displacement that accompany most external loading conditions.

respectively. Fig. 22) is described by a phase angle $\phi = \tan^{-1}(v/u)$.

Because of the interdependence of the opening and shearing components of the remote loading and the crack tip displacements, ϕ differs from the phase angle of K' ($\psi = \tan^{-1}(K_2'/K_1')$) by an amount that depends on the mismatch of elastic constants and position

$$\phi = \psi + \epsilon \ln r + \tan^{-1} 2\epsilon \qquad (14)$$

where

$$\epsilon = \frac{1}{2\pi} \ln\left(\frac{1-b}{1+b}\right)$$

and

$$b = \frac{G_1(1-2v_2) - G_2(1-2v_1)}{2[G_1(1-v_2) + G_2(1-v_2)]}$$

b is one of Dundurs' parameters [46], with G the shear modulus, v the Poisson's ratio, and r the distance from the crack tip. Because of the ln r term, which describes a slow oscillation in the ratio v/u with r, the value of ψ is dependent upon the choice of length units. However, this does not present a difficulty provided a consistent choice is maintained.

In most practical examples, the parameter ϵ is small, often less than 0.01 [43]. Consequently, several schemes for ignoring the effect of ϵ in equation (14) have been proposed, so that ψ represents the relative proportions of mode II and mode I in the crack tip field [41, 42]. However, even in this case, the proportion of mode I to mode II in the crack tip field differs from that in the applied, remote field.

The strain energy release rate can be calculated in terms of the crack surface displacements [42]

$$\mathscr{G} = \frac{\pi(1 + 4\epsilon^2)(u^2 + v^2)}{8r[(1 - v_1)G_1 + (1 - v_2)G_2]} \qquad (15)$$

Alternatively, $\mathscr{G}$ can be expressed in terms of the modulus of the stress intensity factor, $|K|^2 = K_1^2 + K_2^2$, in a form similar to that for homogeneous materials [41]

$$\mathscr{G} = \frac{C|K|^2}{16\cosh^2(\pi\epsilon)} \qquad (16)$$

where

$$C = 8\left[\frac{1 - v_1^2}{E_1} + \frac{1 - v_2^2}{E_2}\right].$$

The criterion for crack growth is taken as a critical strain energy release rate, $\mathscr{G}_c$. In general, the value is dependent on the ratio of shear to opening stress, i.e. $\mathscr{G}_c$ is a function of ψ. An example of a calculated dependence and some experimental data for a glass/epoxy system are shown in Fig. 23.

5.2. Debonding mechanics

Debonding solutions are required for axisymmetric configurations, representative of the debonding of fibers (Fig. 3), as well as for planar cracks character-
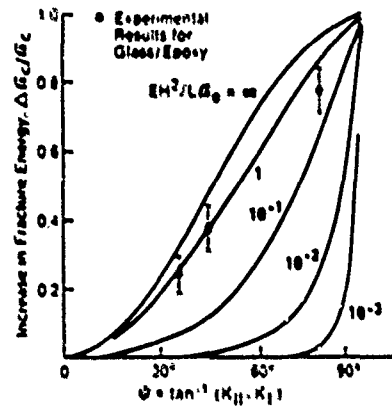
Fig. 23. Experimental data for the fracture energy of a glass/epoxy interface compared with prediction based on a crack surface locking model

istic of macroscopic delamination (Fig. 20). In both cases, $\mathscr{G}$ and ψ are strongly influenced by the residual stress. Furthermore, when the phase angle becomes large, $\psi \rightarrow \pi/2$, frictional sliding and crack surface locking effects become important [47]. A comprehensive set of solutions that fully encompass the spectrum of residual stress and of frictional sliding relevant to composites does not yet exist. Some known solutions are described below.

Axisymmetric solutions exist for composites with interfaces subject to residual radial tension, wherein a net crack opening exists for the full range of applied tensile loads, elastic moduli and fiber volume fractions [8]. All solutions have the general features that $\mathscr{G}$ is small, but non-zero, when the debond length approaches zero and increases to a steady-state value $\mathscr{G}_{ss}$ when the debond length d exceeds $\sim R$ (Fig. 24). Such behavior indicates the insightful bound that a preexisting debond larger than $\sim R$ must extend without limit when $\mathscr{G}_{ss}$ exceeds $\mathscr{G}_c$ at the appropriate ψ. The basic trends in $\mathscr{G}_{ss}$ and ψ relevant to wake debonding, determined using finite elements, are summarized in Fig. 24. The variables in the analysis are: the ratio, Σ, of Young's modulus for the fiber, E_f, to that of the matrix, E_m, the fiber volume fraction, f, the stress-free (residual) strain ($\Delta\alpha\Delta T$), the stress imposed on the fiber, t, and the Poisson's ratios v_m and v_f. Note that the phase angles are typically large, indicative of a large ratio of shear to opening.

Rigorous axisymmetric solutions for interfaces subject to residual radial compression have not been derived. However, some approximate solutions based on a modified shear lag approach are insightful [48]. This approach has merit when the friction coefficient μ is small ($\mu \leqslant 0.2$). For this case, complete crack opening does not occur until t reaches a critical value t_c given by

$$t_c E_f \Delta\alpha\Delta T = 1/v_f. \qquad (17)$$

For $t > t_c$, steady state obtains for long debonds and
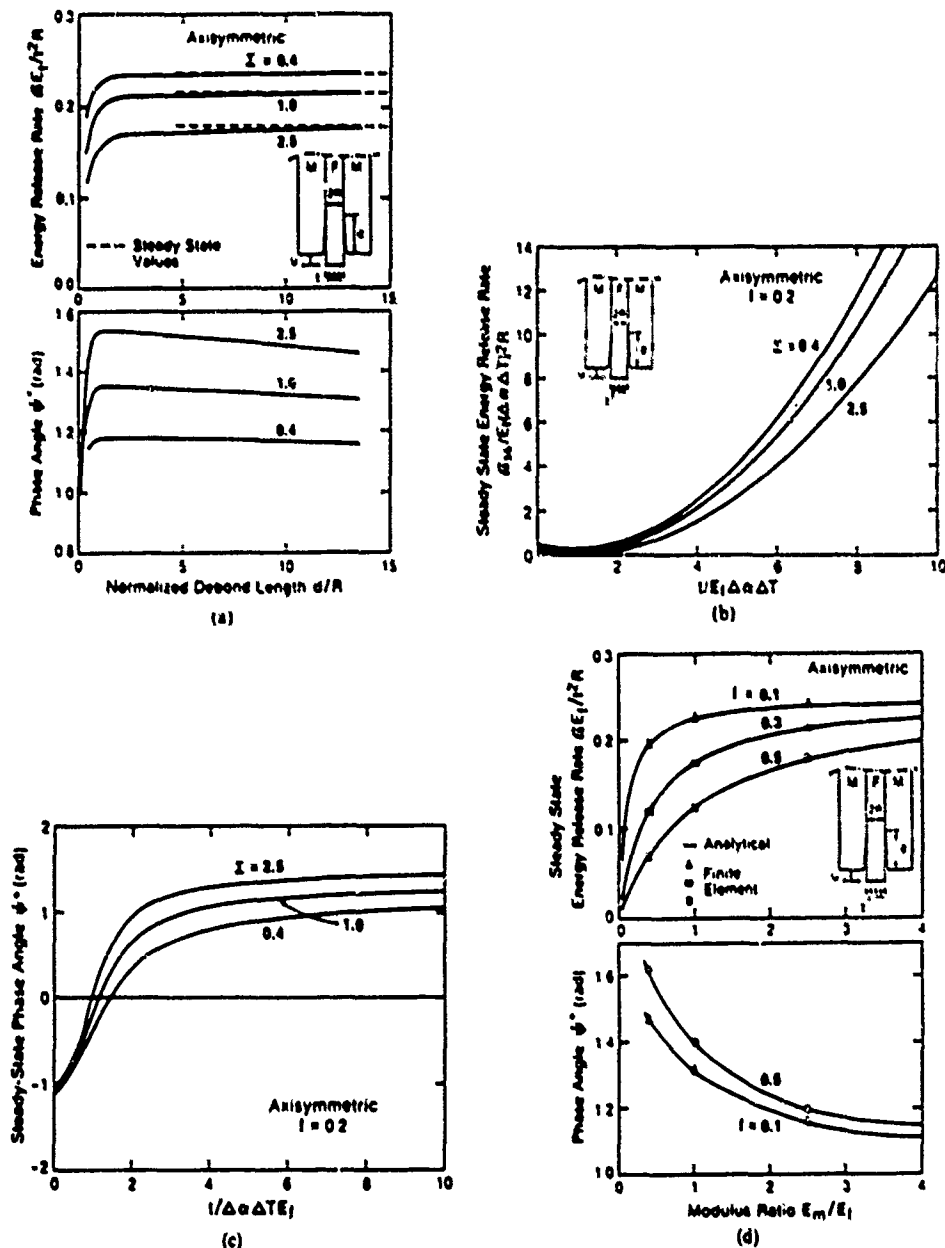
Fig. 24. Trends in energy release rate and phase angle for loads exerted on a fiber in the crack wake (a) Effects of debond length ($\psi^\circ = \psi + \epsilon$ in R). (b) Effects of applied stress $\imath$ on steady-state $\mathcal{G}_\infty$. (c) Effects of applied stress $\imath$ on phase angle ψ in steady-state regime. (d) Effects of elastic modulus ratio of $\mathcal{G}_\infty$ and ψ.

the solutions given in Fig. 24 are directly applicable. For $\imath < \imath_c$, the debond crack is subject to normal compression and resultant friction. In this case, $\mathcal{G}$ diminishes with increase in debond length, d, representative of *stable* crack growth

$$\mathcal{G}/E_f R (\Delta\alpha\Delta T)^2$$

$$\approx F^2/4 + F/2 - \frac{\mu d(1-f)(1-vF)}{R[(1-f)(1-2v)+1+f]} \quad (18)$$

where

$$F = (\imath - q)/E_f \Delta\alpha\Delta T$$

and q is the axial residual stress in the matrix, as governed by $\Delta\alpha\Delta T$, f and Σ. In this instance, $\mathcal{G}$ is strictly mode II and debonding should thus be predicted by equating $\mathcal{G}$ to $\mathcal{G}_\infty$ at $\psi = \pi/2$. Such predictions have not been attempted. However, it is insightful to note that, for "weak" interfaces

($\mathcal{Y}_e \ll \mathcal{Y}_k$), the debond length and the slip length, l, are closely related, with l given by [48]

$$l/R \approx \frac{F[(1-f)(1-2v)+1+f]}{2\mu(1-vF)(1-f)}. \quad (19)$$

For the *plane delamination* problem, a comprehensive analysis exists [44], expressible in terms of imposed axial forces and bending moments. The solution having greatest relevance to problems in ceramic matrix composites involves the four-point bending of a bimaterial beam with debond cracks between the inner loading points [36, 44]. The general form of the solution [(Fig. 25(a)] indicates that $\mathcal{Y}$ rapidly acquires a steady-state level. Trends in the steady-state value $\mathcal{Y}_u$ are summarized in Fig. 25(b). The corresponding non-dimensional phase angle, $\psi^\circ = \psi + \epsilon \ln R$ is ~0.68 for all Σ, when $\Delta z \Delta T = 0$. Clearly, the elastic properties have strong influences on both $\mathcal{Y}_u$ and ψ.

Initial debonding along the *interface* rather than extension of the notch across the interface is ex-
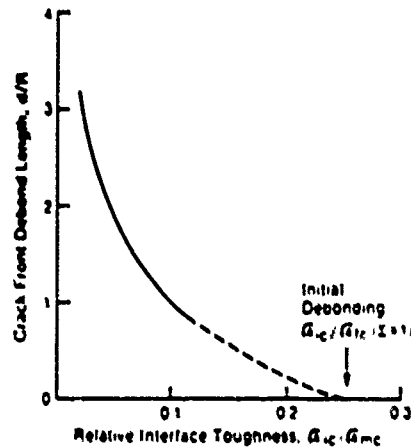
Fig. 26. The energy release rate for crack front debonding

(a)

(b)

Fig. 25. Energy release rates for a bimaterial beam tested in flexure. (a) Trends with crack length for an elastically homogeneous system (b is the beam width). (b) Trends in steady-state energy release rate, $\mathcal{Y}_u$ with modulus and thickness ratios.

pected, provided that $\mathcal{Y}_e$ at $\psi \approx \pi/4$ is less than the critical strain energy release rate for the lower material (the fiber), $\mathcal{Y}_{k}$, by a ratio that depends on the elastic properties of the fiber and matrix (Fig. 3) For the elastically homogeneous case, debonding occurs in preference to fiber failure when [9]

$$\mathcal{Y}_e/\mathcal{Y}_k \lesssim 1/4.$$

The extent of fiber debonding at the tip of a matrix crack has not been rigorously analyzed. However, useful insights can be gained by interpolating between the above initiation condition and an existing solution for long cylindrical debonds (at $\psi = 0$) in a crack tip field. The latter solution indicates that debond lengths substantially larger than the fiber diameter require very small values of $\mathcal{Y}_e$ at the interface compared with that at the matrix crack front, $\mathcal{Y}_m$, given approximately by (Fig. 26)

$$\mathcal{Y}_e/\mathcal{Y}_{mc} \approx 0.1 \, R/d. \quad (20)$$

Consequently, it is surmised that the $\mathcal{Y}_e$ required for continued debonding decreases rapidly as the debond length increases. Extensive crack front debonding thus appears unlikely in the absence of residual stress, even when $\mathcal{Y}_e$ is quite small. This conclusion about crack front debonding is substantially changed when residual stress exists [8].

Initiation of debonding is a necessary but not sufficient condition for good composite properties. It is also required that the debond crack *remain in the interface* and not kink into the fiber to cause premature fiber rupture, either along the crack front or in the crack wake. Analysis of this problem [45] indicates that kinking out of the interface is not expected when the above inequality is satisfied.

5.3. Measurement of the interface fracture resistance

The preceding mechanics analyses provide the essential background needed for the measurement of debond resistances relevant to composite perfor-

mance. Three basic test methods have been identified as being convenient for providing data at $\psi \approx 0$, $\pi/2$ and $\pi/4$ [49, 50]: compact tension tests, flexural tests and pull-out tests. Two critical aspects of interface fracture testing are the initial introduction of a well-defined debond crack and measurement of the residual stress. Another important testing issue concerns friction at the loading points [49]. A procedure that takes frictional effects into account, based on measurements of the hysteresis in loading and unloading compliance has been developed and validated. These rigorous demands on the testing needed to generate valid $\mathcal{G}_{ic}$ data, have limited the extent of available results. Preliminary results indicate that $\mathcal{G}_{ic}$ tends to increase with increase in ψ, especially as $\psi \rightarrow \pi/2$, and furthermore, that the rate of increase depends on the morphology of the fracture interface [42]. Specifically, rough fracture interfaces cause $\mathcal{G}_{ic}$ to increase more rapidly with increase in ψ. Analysis of this phenomenon [42] has modelled the sliding and locking of crack surface asperities that make contact at large phase angles. The material parameter that governs the magnitude of this effect is [47, 50]

$$\chi = EH^2/\mathcal{G}_0 L \qquad (21)$$

where H is the amplitude and L the wavelength of undulations on the fracture interface and $\mathcal{G}_0$ is the intrinsic fracture resistance of the interface. Specifically, large χ results in the greatest effects on $\mathcal{G}_{ic}(\psi)$. The quantity χ is a measure of the length of the contact zone, which increases as either H increases or $\mathcal{G}_0$ decreases.

The magnitude of $\mathcal{G}_0$ is clearly influenced by the presence of interphases, the atomistic structure of the interface, etc. However, as yet, residual stress and morphological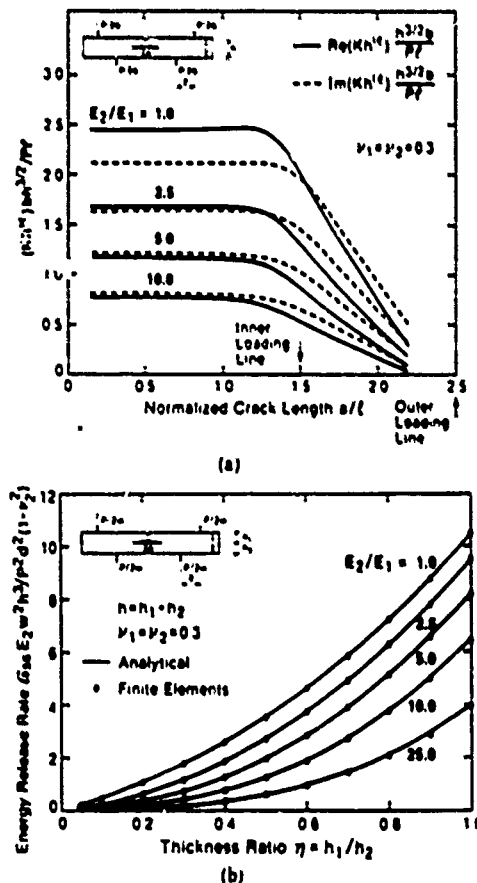 influences have not been sufficiently decoupled to explore these basic relationships. Nevertheless, preliminary measurements reveal that $\mathcal{G}_0$ is typically quite small for oxides bonded to refractory metals (Nb), to intermetallics (TiAl) and to noble metals (Au, Pt) as well as for oxides bonded with inorganic glasses and for carbides and nitrides having graphite boron nitride interlayers.

6. MICROSTRUCTURE DESIGN

Many of the microstructural parameters that control the overall mechanical properties of ceramic matrix composites are now known and validated, as elaborated in the preceding sections. Consequently, various general remarks about microstructure design can be made. However, important aspects of damage and failure are incompletely understood because there have been few organized studies of failure in mode II, mixed mode and transverse mode I. The remarks made in this section thus refer primarily to axial mode I behavior with no special regard to attendant problems in other loading modes.

The basic microstructural parameters that govern mode I failure are the relative fiber/matrix interface

debond toughness, $\mathcal{G}_i$, $\mathcal{G}_{ic}$, the residual strain, $\Delta \alpha \Delta T$, the friction coefficient of the debonded interface, μ, the statistical parameters that characterize the fiber strength, S_0 and m, the matrix toughness, $\mathcal{G}_{mc}$, and the fiber volume fraction f. The prerequisite for high toughness is that $\mathcal{G}_{ic}/\mathcal{G}_{fc} \leqslant 1/4$ ($\Sigma = 1$). Subject to this requirement, the residual strain must be small ($\Delta \alpha \leqslant 3 \times 10^{-4} C^{-1}$) and negative so that the interface is in tension. Furthermore, the friction coefficient along the debonded interface should be small ($\mu \leqslant 0.1$). The ideal fiber properties are those that encourage large pull-out lengths, as manifest in an optimum combination of a high median strength (large S_0) and large variability (small m).

The above conditions can be satisfied, in principle, by creating interphases between the fiber and matrix, either by fiber coating or, *in situ*, by segregation. The most common approach is the use of a dual coating: the inner coating satisfies the above debonding and sliding requirements, while the outer coating provides protection against the matrix during processing. However, the principal challenge is to identify an inner coating that has the requisite mechanical properties while also being thermodynamically stable in air at elevated temperatures. Most existing materials have either C or BN as the debond layer. However, both materials are prone to degradation in air at elevated temperatures. More stable alternatives have been proposed (e.g. Nb, Mo, Pt, NbAl) but have not been evaluated.

REFERENCES

1. A. G. Evans and R. M. Cannon, *Acta metall.* **34**, 761 (1986).
2. J. W. Hutchinson, *Acta metall.* **35**, 1605 (1987).
3. M. Ruhle, A. G. Evans, R. M. McMeeking and J. W. Hutchinson, *Acta metall.* **35**, 2701 (1987).
4. A. G. Evans and K. T. Faber, *J. Am. Ceram. Soc.* **67**, 255 (1984).
5. B. Budiansky, J. W. Hutchinson and J. C. Lambropoulos, *Int. J. Solids Struct.* **19**, 337 (1983).
6. J. W. Hutchinson, *Non-Linear Fracture Mechanics*. Tech. Univ. Denmark (1979).
7. J. R. Rice, *Fracture* (edited by H. Leibowitz), Vol. II. Academic Press, New York (1968).
8. P. G. Charalambides and A. G. Evans, *J. Am. Ceram. Soc.* **72**, 746 (1989).
9. M. He and J. W. Hutchinson, *J. appl. Mech.* In press.
10. E. Bischoff, M. Ruhle, O. Sbaizero and A. G. Evans, *J. Am. Ceram. Soc.* **72**, 741 (1989).
11. M. D. Thouless, O. Sbaizero, L. S. Sigl and A. G. Evans, *J. Am. Ceram. Soc.* **72**, 525 (1989).
12. J. Aveston, G. A. Cooper and A. Kelly, *The Properties of Fiber Composites*, p. 15. IPC Sci. Technol (1971).
13. D. B. Marshall and A. G. Evans, *J. Am. Ceram. Soc.* **68**, 225 (1985).
14. D. B. Marshall, B. N. Cox and A. G. Evans, *Acta metall.* **33**, 2013 (1985).
15. J. J. Brennan and K. M. Prewo, *J. Mater. Sci.* **17**, 2371 (1982).
16. K. M. Prewo and J. J. Brennan, *J. Mater. Sci.* **17**, 1201 (1982).
17. R. A. J. Sambell, A. Briggs, D. C. Phillips and D. H. Bowen, *J. Mater. Sci.* **7**, 676 (1972).

18. A. J. Majumdar, *Proc. R. Soc.* A319, 69 (1970).
19. D. B. Marshall and A. G. Evans, in *Fracture Mechanics of Ceramics* (edited by R. C. Bradt, A. G. Evans, D. P. H. Hasselman and F. F. Lange), pp. 1–15. Plenum Press, New York (1986).
20. L. R. F. Rose, *J. Mech. Phys. Solids* 35, 383 (1987).
21. B. Budiansky, *Micromechanics II, Proc. Tenth U.S. Congr. Appl. Mech.* (1986).
22. D. B. Marshall and B. N. Cox, *Mech. Mater.* In press.
23. D. B. Marshall and B. N. Cox, *Acta metall.* 35, 2607 (1987).
24. D. B. Marshall and A. G. Evans, *Materials Forum* 11, 304 (1988).
25. O. Sbaizero and A. G. Evans, *J. Am. Ceram. Soc.* 69, 481 (1986).
26. M. S. Hu and A. G. Evans, *Acta metall.* 37, 917 (1989).
27. J. K. Wells, Ph.D dissertation, Cambridge Univ. Press (1982).
28. M. D. Thouless and A. G. Evans, *Acta metall.* 36, 517 (1988).
29. D. Johnson Walls, M.S thesis, Univ. of California, Berkeley (1986).
30. D. B. Marshall and W. Oliver, *J. Am. Ceram. Soc.* 70, 542 (1987).
31. T. Wiehs and W. D. Nix, MRS Symposium, Reno, NV, Spring (1988).
32. C. A. Andersson, unpublished research.
33. B. Budiansky and J. C. Amazigo, Harvard Univ. Report MECH 119 (1988).
34. B. Budiansky, J. W. Hutchinson and A. G. Evans, *J. Mech. Phys. Solids* 34, 167 (1986).
35. A. G. Evans, *Mater. Sci. Engng* 71, 3 (1985).
36. P. G. Charalambides, R. M. McMeeking and A. G. Evans, *J. appl. Mech.* 56, 77 (1989).
37. M. L. Williams, *J. appl. Mech.* 49, 199 (1959).
38. A. H. England, *J. appl. Mech.* 32, 400 (1965).
39. F. Erdogan, *J. appl. Mech.* 32, 403 (1965).
40. J. R. Rice and G. C. Sih, *J. appl. Mech.* 32, 418 (1965).
41. G. P. Cherepanov, McGraw-Hill, New York (1979).
42. J. R. Rice, *J. appl. Mech.* 55, 98 (1988).
43. Z. Suo and J. W. Hutchinson, Harvard Univ. Rep. MECH 122 (1988).
44. Z. Suo and J. W. Hutchinson, Harvard Univ. Rep. MECH 118 (1988); *Int. J. Fract.* In press.
45. M. Y. He and J. W. Hutchinson, Harvard Univ. Rep. MECH 113 (1988), *J. Appl. Mech.* In press.
46. J. Dundurs, *Mathematical Theory of Dislocations*, p. 70. Am. Soc. Mech. Engrs, New York (1969).
47. A. G. Evans and J. W. Hutchinson, *Acta metall.* 37, 909 (1989).
48. L. S. Sigl and A. G. Evans, *Mech. Mater.* In press.
49. P. G. Charalambides, H. C. Cao, J. Lund and A. G. Evans, *Acta metall.* In press.
50. H. C. Cao and A. G. Evans, *Mech. Mater.* In press.

NOMENCLATURE

α = linear thermal expansion coefficient
α^m = α for matrix
α^f = α for fibers
μ = friction coefficient
ν = Poisson's ratio of composite
Σ = ratio of Young's modulus of fiber to matrix
σ_c = matrix cracking stress
σ_u = ultimate strength
σ_a = applied stress
σ^* = stress for transverse interface failure
τ = shear resistance of interface after debonding
$\phi(h)$ = cumulative pull-out distribution
ϕ = crack surface shear angle
$\phi(z,t)$ = probability density function for fiber failure
χ = interface fracture parameter = $EH^2/\mathcal{G}_c L$
Ψ = phase angle of loading
β = transition parameter

b = Dundurs' parameter = $\dfrac{G_1(1-2\nu_2)-G_2(1-2\nu_1)}{2[G_1(1-\nu_2)+G_2(1-\nu_1)]}$

D = matrix crack spacing
d = debond length
E = Young's modulus of composite
F = non-dimensional stress
f = fiber volume fraction
G = shear modulus
$\mathcal{G}$ = strain energy release rate
$\mathcal{G}_c$ = critical strain energy release rate for interface
$\mathcal{G}_{ss}$ = steady-state strain energy release rate
$\mathcal{G}_{fc}$ = critical strain energy release rate for the fiber
$\mathcal{G}_{mc}$ = critical strain energy release rate for the matrix
$\mathcal{G}_0$ = intrinsic critical strain energy release rate for the interface
$\mathcal{G}_c(\Delta a)$ = increase in critical strain energy release rate with increase in crack length, Δa
H = amplitude of interface roughness
h = pull-out length
l = slip length
L = gauge length
m = shape parameter for fiber strength distribution
q = residual axial stress in the matrix
q_r = residual stress normal to interface
R = fiber radius
r = distance from crack front
S = fiber strength
S_c = scale parameter for fiber strength distribution
T = pull-out parameter
t = stress acting on fiber between crack surfaces
U = pull-out parameter
u = crack opening displacement
v = crack shear displacement
z = distance from crack plane
σ_a = normalizing stress in statistical analysis of fiber pullout
u_a = normalizing displacement in statistical analysis of fiber pullout

MATERIALS
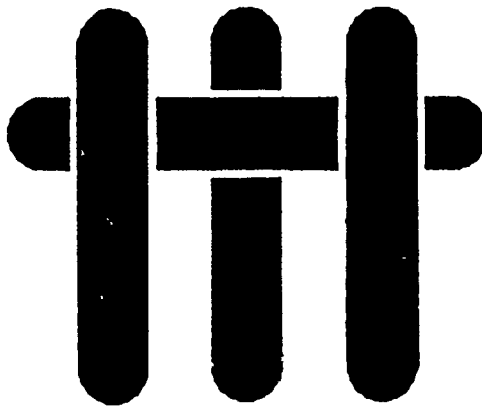
DELAMINATION CRACKING IN A

LAMINATED CERAMIC MATRIX

COMPOSITE

by

O. Sbaizero, P. G. Charalambides and A. G. Evans

Materials Department
College of Engineering
University of California
Santa Barbara, California 93106

ABSTRACT

Delamination crack propagation has been investigated in a laminated fiber reinforced ceramic matrix composite. The crack growth initiation resistance has been shown to be dominated by the critical strain energy release rate for the matrix. However, the resistance increases with crack extension because (`      _`ng effects associated with intact fibers and, in some cases, intact segments of matrix. The delamination cracks also assume a steady-state trajectory within a zero-degree layer close to the 0°/90°C interface.

1. INTRODUCTION

Ceramic matrix composites reinforced with aligned fibers that exhibit high "toughness" in tensile (mode I) loading are often susceptible to delamination (mixed mode) cracking.[1,2] Such cracking, typically encountered in the presence of notches, is also evident in polymer matrix composites,[3] and in wood.[4] The delamination crack nucleates near the base of the notch and propagates axially outward as the load is increased, causing the material to be notch insensitive.[2,3] The intention of this study is to investigate the resistance of a laminated ceramic matrix composite to the mode of crack propagation. The problem is not only of fundamental interest, but also of significant technical importance. The presence and growth of delamination cracks in composite laminates may lead to severe reliability and safety problems, such as the reduction of structural stiffness and exposure of the interior to an adverse environment which may cause the final failure.

The mechanics basis for the study involves analysis of the energy release rates $\mathcal{G}$ and of the phase angles ψ associated with the observed delamination morphologies.[4,5] The product of the study is a characterization of the delamination fracture resistance $\mathcal{G}_R$, which provides the basis for a microstructure based model which relates $\mathcal{G}_R$ to the properties of the matrix, interfaces and fibers. Such characteristics provide the principles needed to predict relative tendencies for composites to exhibit either mode I matrix cracking or mixed mode delamination cracking and thus, establish a framework for design criteria.

2. MECHANICS SUMMARY

The basic mechanics needed to interpret measurements of delamination crack growth have been derived elsewhere.[5,6] The results applicable to the present

experiments are briefly summarized in this section. The experiments utilize test specimens (Fig. 1) in which the notch depth w exceeds the laminate thickness and is about one-third to one-half the specimen thickness, h. For this geometry, tested in four-point flexure, delamination cracks are subject to steady-state conditions, provided that the cracks are between the inner load lines and larger than ~ (1/2)w. Steady-state stress intensity factor solutions for anisotropic beams have been derived[5] and provide the basis for solutions applicable to laminates.[6] The laminate results have the form

$$b_{11} \mathcal{G} B^2 h^3 / P^2 \ell^2 = F(b_{11}/b_{22}, w/h, n) \tag{1a}$$

and

$$\psi = \tan^{-1}\left[\left(\sqrt{3/2}\right) \left(b_{22}/b_{11}\right)^{1/4} \right] \tag{1b}$$

where $\mathcal{G}$ is the energy release rate, ψ is the phase angle of loading, P is the load, ℓ the moment arm (Fig. 1), B the beam width, b_{ij} is the elastic stiffness defined by[5]

$$\varepsilon_i = \Sigma b_{ij} \sigma_j$$

$$i = 1, 2, 6$$

$$j = 1, 2, 6$$

where ε_i is the strain, σ_j the stress and n is the number of laminate layers in the beam. For ten layers, the function F has the trend plotted on Fig. 2.

The experimental data presented below have been obtained in the steady-state regime, allowing direct use of Eqn. (1) to obtain $\mathcal{G}$ and ψ.

3. EXPERIMENTAL PROCEDURES

3.1 MATERIALS

The primary material selected for investigation consists of a 0°/90° cross-ply laminated LAS-II matrix reinforced with SiC Nicalon fibers, prepared by hot pressing and supplied by United Technologies Research Center.[1,2] The fiber volume fraction is ~ 0.44. The material has a thin C layer between fiber and matrix which allows debonding and sliding[7,8] and thus imparts high tensile "toughness," as evident from a tensile stress/strain curve[2] (Fig. 3). This material is also subject to residual strain caused by thermal expansion mismatch, such that the radial stress at the interface is tensile.[8] In some cases, this tensile stress causes thermal interfacial debonding.[8]

3.2 TEST SPECIMENS

Flexural specimens having dimensions 3 x 3 x 35mm were machined from hot pressed plates such that the fiber and specimen axes were coincident. Notches having width, ~ 0.9mm were then introduced using a diamond blade. The location of the base of the notch with respect to the lamination layer was systematically varied. In some cases, the side surfaces were carefully polished, using diamond polishing media, as needed to make observations of cracking and damage in the optical and scanning electron microscopes.

3.3 TEST PROCEDURES

Specimens were loaded in four-point flexure at constant load point displacement rate of ~ 10μm s^{-1}. Loads were monitored and a displacement

transducer, attached to the specimen adjacent to the notch, was used to measure the vertical displacement, u, upon loading. Friction was minimized by emplacing a thin layer of solid lubricant between the specimen and the loading points. Crack lengths were also observed and monitored using a long focal length optical microscope.

Specimens were mostly subject to monotonic displacement rates, resulting in continuous crack extension. In some cases, periodic unloading was performed and the associated hysteresis measured. Crack lengths were also measured in the optical and in scanning electron microscope.

4. RESULTS

4.1 MEASUREMENTS

Some basic load, displacement, crack length characteristics exhibited upon delamination crack extension are depicted in Figs. 4a, b. Crack extension was accompanied by non-linearity and occurred with rising load. Periodic loading and unloading was accompanied by compliance hysteresis (Fig. 4a). The hysteresis was characterized by a residual crack opening displacement (Fig. 5) that increased with crack extension, but gave minimal change in compliance.

Trends in the crack extension load with delamination crack length (Fig. 4b) can be used in conjunction with Eqn. (1) to evaluate the energy release rate as a function of crack extension, as summarized in Fig. 6. In all cases, the fracture resistance, $\mathcal{G}_R$, increased with increase in crack length, a, but is always of order $20 \mathrm{Jm}^{-2}$ at crack growth initiation ($a \to 0$). The slope (tearing modulus), $T = d\mathcal{G}_R/da$, varied appreciably between specimens, but had a systematic dependence on the location of the notch tip. Specifically, T increased as the distance s between the

6

notch tip and the bottom of the next 90° layer increased (Fig. 7). Furthermore, the results that give the largest T refer to cases in which the notch tip is located in a zero-degree layer, resulting in a bridge of intact material at the crack center (see Fig. 9c).

4.2 OBSERVATIONS

Crack path observations (Figs. 8, 9) indicate that the crack always attains a steady-state trajectory when the crack length a ⪎ w/2. This trajectory coincides with a plane just within and near the base of the 90° layer next to the notch tip (Fig. 9). This plane is seemingly selected by the crack whatever the original location of the notch tip (Fig. 8). Such behavior is exemplified in Fig. 8b by a crack which emanates from a notch tip located at the upper interface of a 90° laminate layer. It is evident that the crack initially progressed toward the lower interface as it extended to a length a ⪰ w/2, and thereafter remained in a constant trajectory adjacent to that interface. It is important to emphasize that the steady-state crack did not select the matrix-only interlayer material, but remained just within the fiber reinforced 90° layer (Fig. 9). Furthermore, it is noted that, when the notch tip terminates in the 0° layer, the crack nucleates *beneath* the notch, within the 90° layer (Fig. 9c), such that a bridge of intact material is retained between the notch tip and the delamination crack surface. But again, the crack extends into the same steady-state trajectory.

After appreciable steady-state crack extension, the crack surfaces are found to be bridged by intact fibers that distort and pull out as the crack surfaces open (Fig. 10). These fibers resist crack extension, as elaborated below.

5. DISCUSSION

The observation that the resistance to crack growth initiation is about the same for all test specimens ($\mathcal{G}_c \approx 20Jm^{-2}$) indicates that a common mechanism is involved. Furthermore, the crack extends through a mix of matrix material and interface (Fig. 9) without significant fiber bridging. A first estimate of the fracture resistance is thus;

$$\mathcal{G}_c \approx f\Gamma_i + (1 - f)\Gamma_m \tag{2}$$

where f is the fiber volume fraction, Γ_i is the fracture energy of the interface and Γ_m the fracture energy of the matrix. Prior research on these materials has suggested the values: $\Gamma_m \approx 20{-}40Jm^{-2}$ and $\Gamma_i < 1Jm^{-2}$.[10,11] The resulting fracture resistance $\mathcal{G}_c$, given that $f \approx 0.44$, would thus be in the range 12 to $24Jm^{-2}$, which encompasses the measured value of $20Jm^{-2}$. A reasonably consistent description of crack growth initiation thus obtains.

The dependence of the tearing modulus on <u>notch location</u> (Fig. 7) may be attributed to the ligament of bridging material between the base of the notch and the steady-state crack trajectory (Fig. 8). This ligament acts as a "hinge," which inhibits the deflection of the beam and thus, causes $\mathcal{G}$ to be less than predicted by Eqn. (1a). Consequently, the strictly material-related results are those having the smallest T, obtained when the notch tip essentially coincided with the steady-state trajectory. The magnitude of the tearing modulus in this case is attributed to the tractions caused by the fibers that bridge the crack surface. Elastic spring models could be used to interpret these results.[12]

6.   CONCLUSION

The propagation of delamination crack has been characterized in a 0°/90°C laminated ceramic matrix composite. Crack growth resistance curves have been generated with two principal features. Crack growth initiation has been shown to depend on the fracture resistance of the matrix and the interface in accordance with a simple rule-of-mixture law. However, further crack growth is impeded by intact fibers and, in some cases, intact matrix ligaments that bridge the crack, leading to resistance over characteristics.

The delamination crack trajectory exhibits steady-state characteristics whereby the crack selects a propagation place with a 90-degree layer adjacent to the matrix layer between laminations. This trajectory then includes matrix material and interfaces. The results of this study can be combined with analysis of resistance curves in mode I loading[2] to interpret and predict preferred crack extension paths in laminated ceramic matrix composites.

REFERENCES

[1] K. M. Prewo, Jnl. Mater. Sci. 21, (1986) 3590.

[2] O. Sbaizero and A. G. Evans, J. Am. Ceram. Soc. 69, (1986) 481.

[3] S. S. Wang, Composite Materials: Testing and Design, ASTM STP 674 (Ed. S. W. Tsai) 1979, pp. 642–663.

[4] M. F. Ashby, E. E. Easterling, R. Harrysson and S. K. Maiter, Proc. Roy. Soc., 4398 (1985) 24.

[5] Z. Suo and J. W. Hutchinson, Harvard Report, in press.

[6] P. G. Charalambides, to be published.

[7] J. J. Brennan and K. M. Prewo, Jnl. Mat. Sci. 17, (1982) 2371.

[8] E. Bischoff, O. Sbaizero, M. Rühle and A. G. Evans, J. Am. Ceram. Soc., in press.

[9] D. B. Marshall and A. G. Evans, J. Am. Ceram. Soc. 68, (1985) 225.

[10] D. B. Marshall and W. Oliver, J. Am. Ceram. Soc. 70, (1987) 542.

[11] T. Weihs and W. D. Nix, MRS Proceedings, Reno, NV, March 1988.

[12] B. Budiansky, J. C. Amazigo and A. G. Evans, Jnl. Mech. Phys. Solids 36,(1988) 167.

FIGURE CAPTIONS

Fig. 1. A schematic drawing of the test specimen and an optical micrograph of the laminate layer

Fig. 2. Trends in non-dimensional steady-state energy release rate with relative notch depth for several values of the elastic anisotropy ($n = 10$)

Fig. 3. A tensile stress-strain curve for the composite (after Ref. 2)

Fig. 4. Loading curves obtained during testing
   a) Load, displacement curves showing hysteresis
   b) Trends in the critical crack extension load with crack length

Fig. 5. Variation in residual crack opening with crack length

Fig. 6. Crack resistance curves obtained for a series of six different test specimens

Fig. 7. A plot of trends in the tearing modulus with notch tip location. When $s/S > 1$, the noted tip is in a zero-degree layer and an intact bridge exists at the notch tip.

Fig. 8. An optical micrograph of the steady-state delamination crack trajectory near the base of the 90-degree layer

Fig. 9. A series of optical and scanning electron micrographs which reveal the initial crack trajectory toward the base of the 90-degree layer

Fig. 10. A scanning electron micrograph of fibers bridging the crack surfaces

11
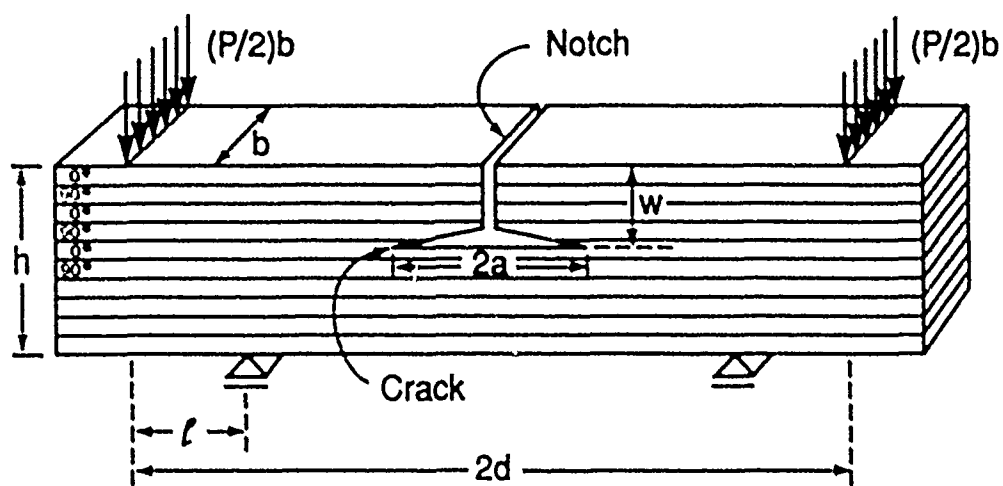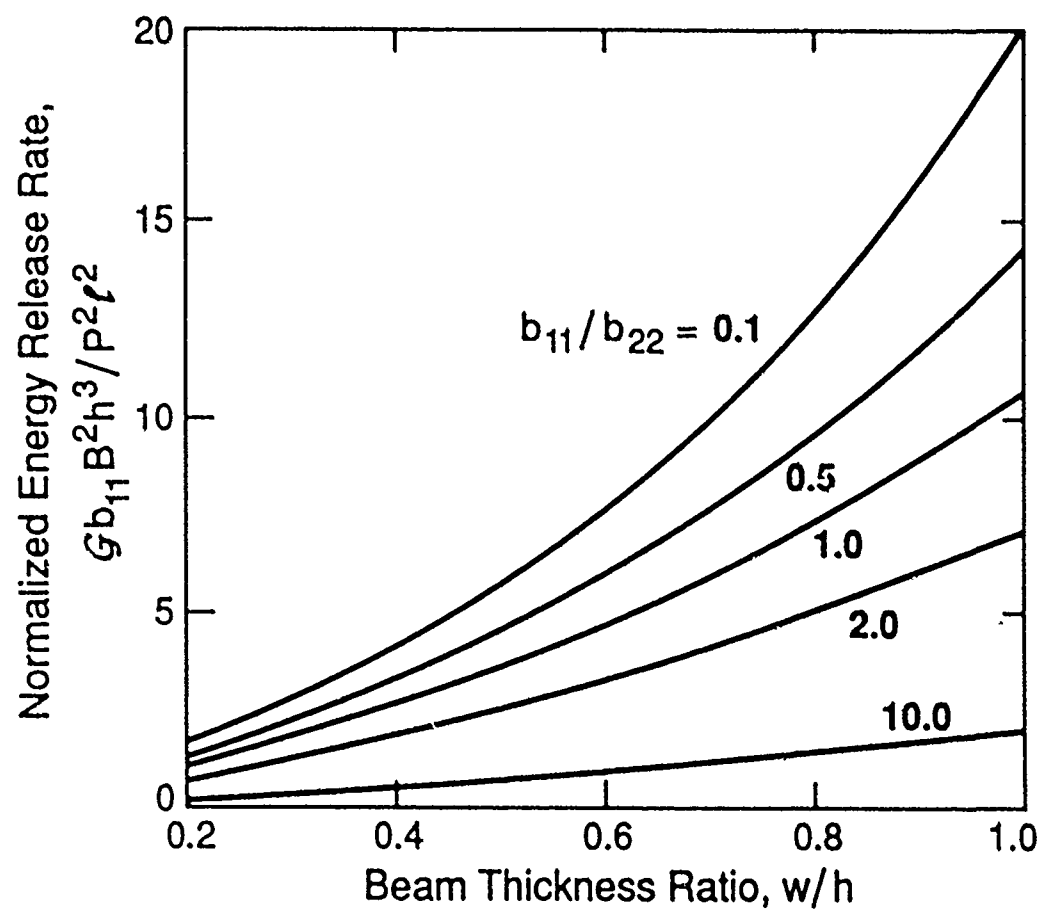
FIG. 2
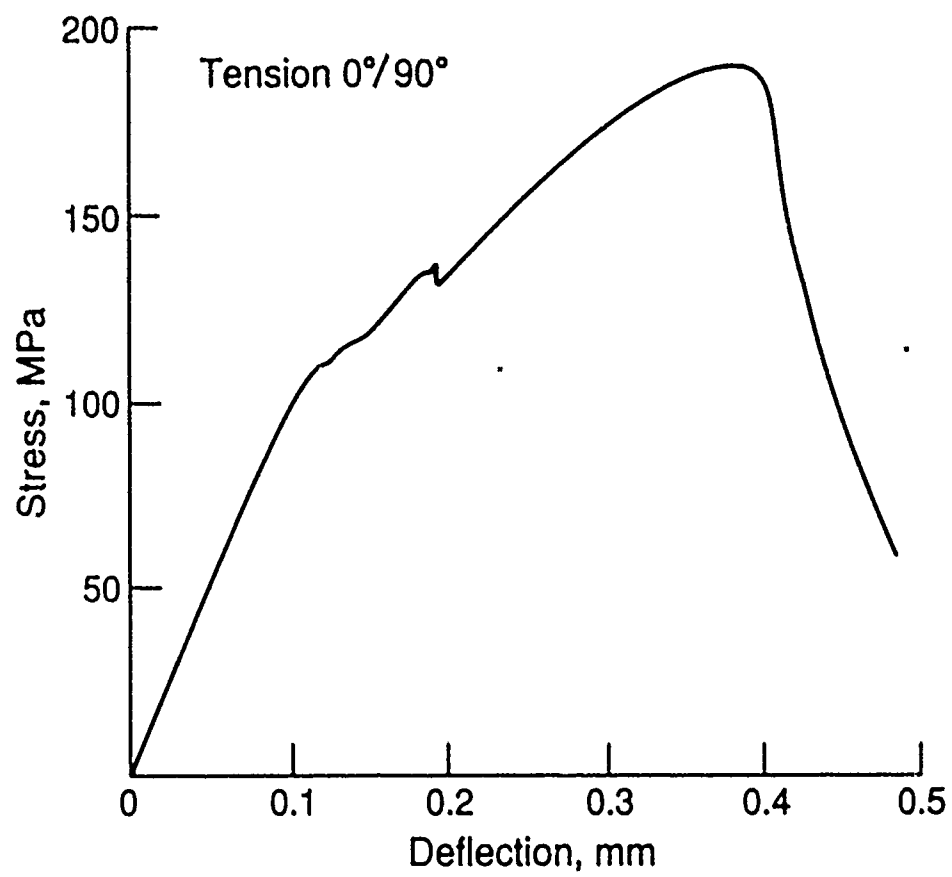
FIG. 3
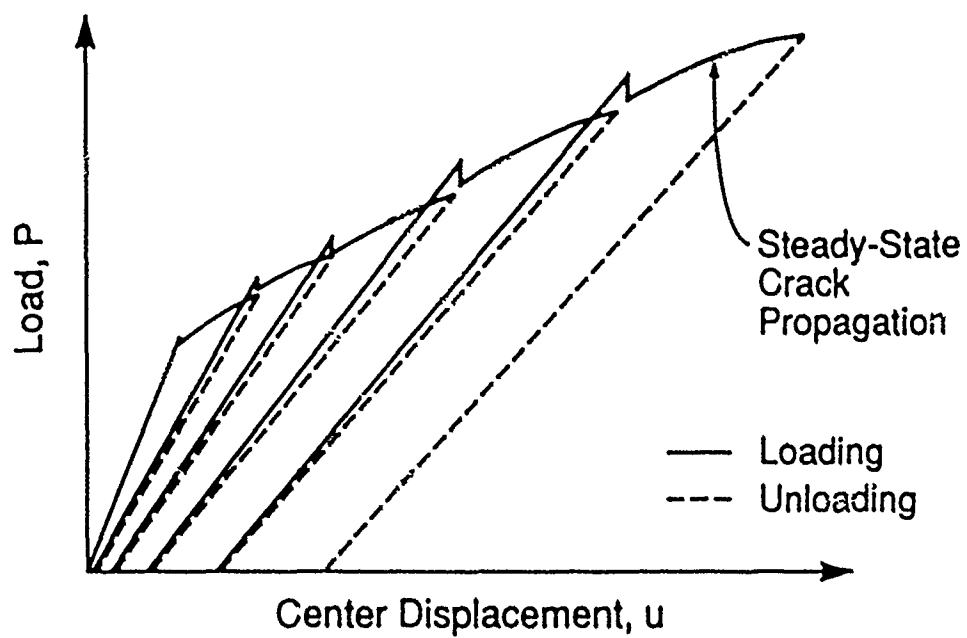
a) Displacements
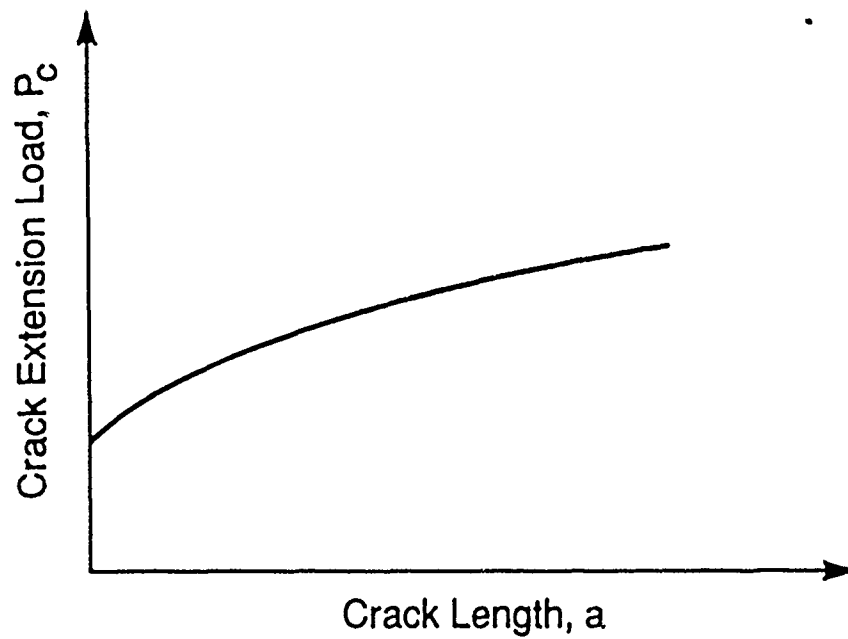
b) Crack Length

FIG. 4

FIG. 5

FIG. 6

FIG. 7

100 μm
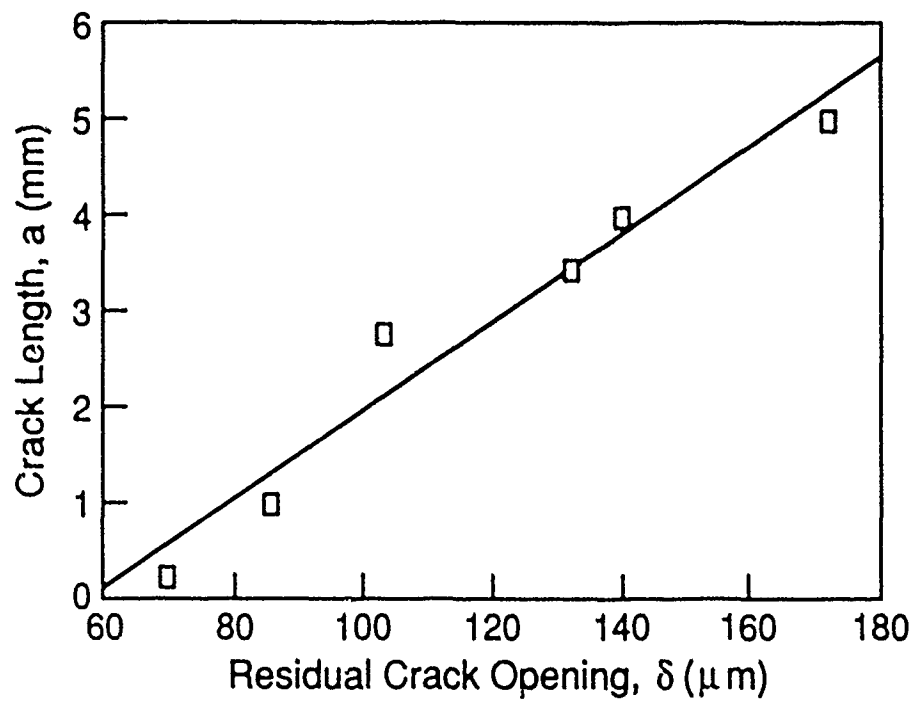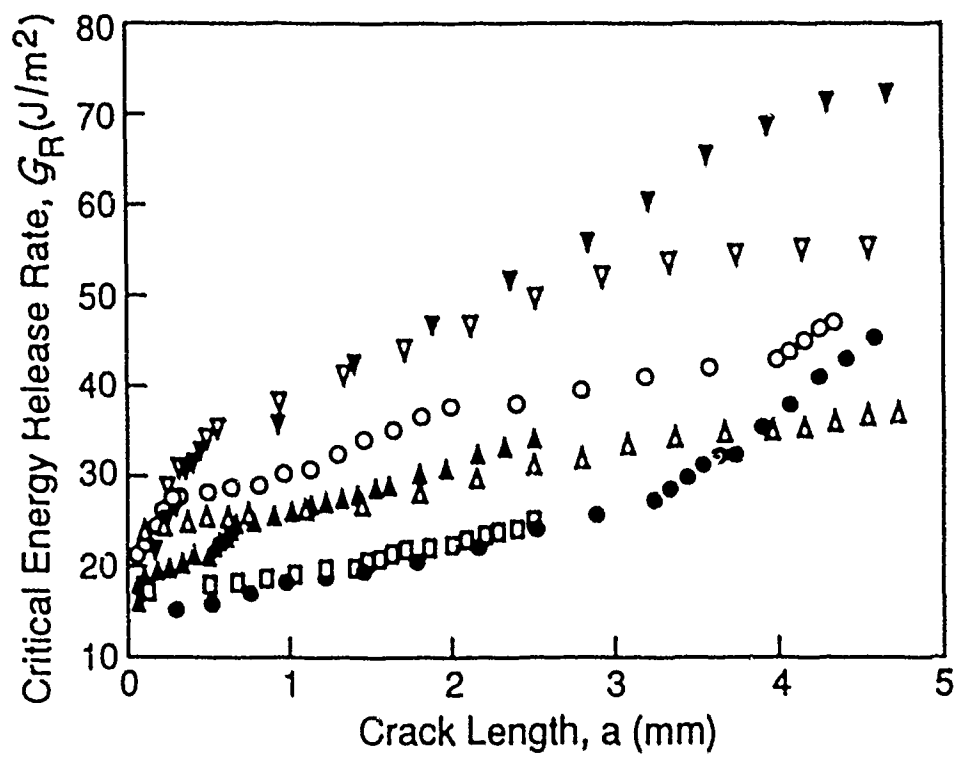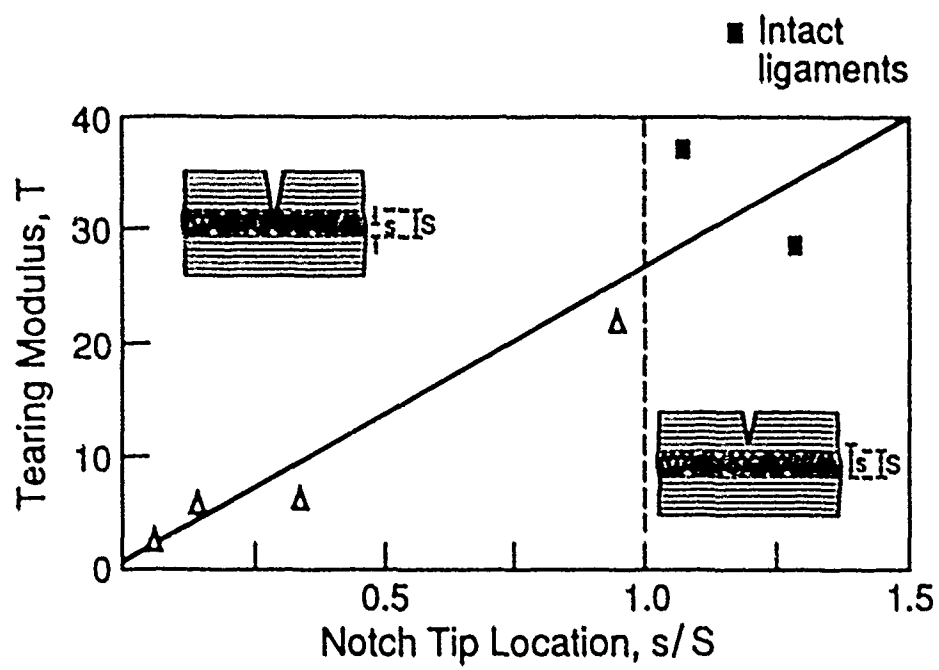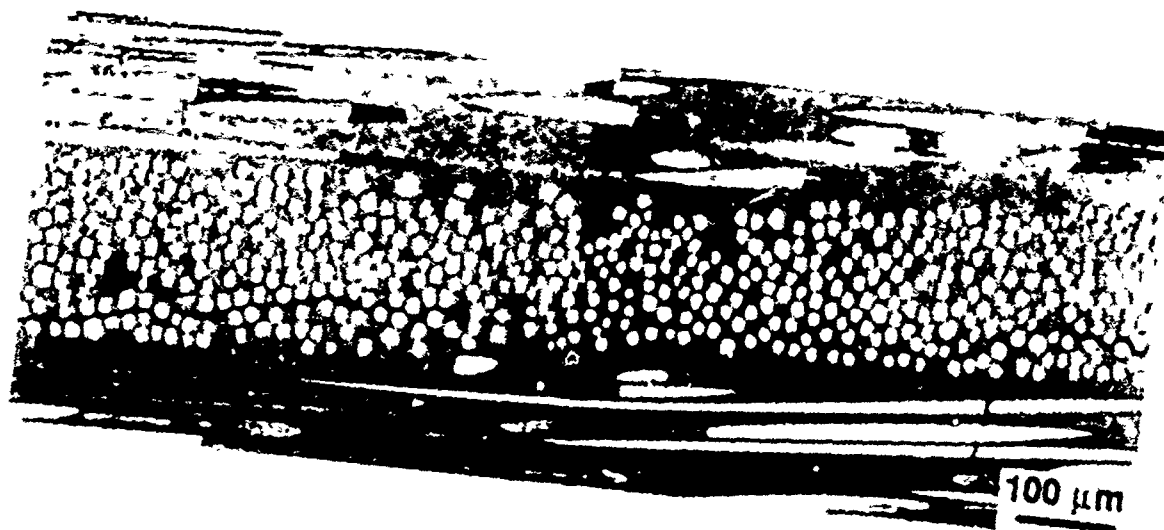
FIG. 8
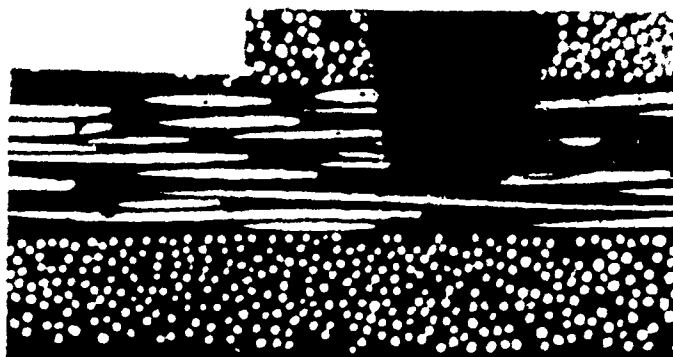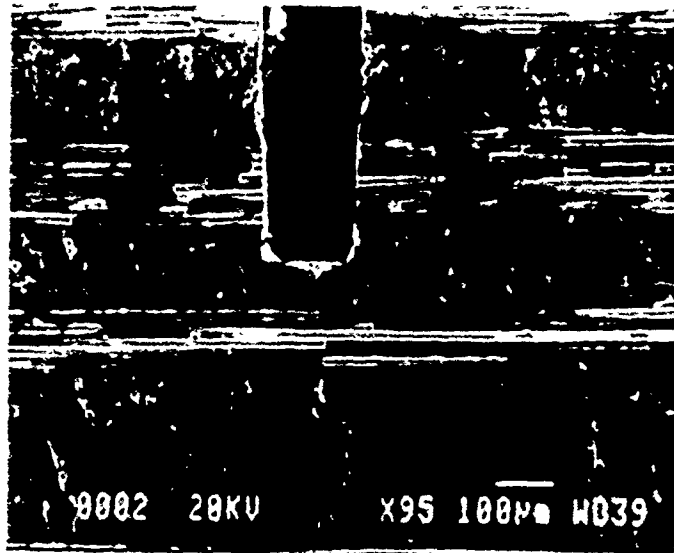
FIG. 9
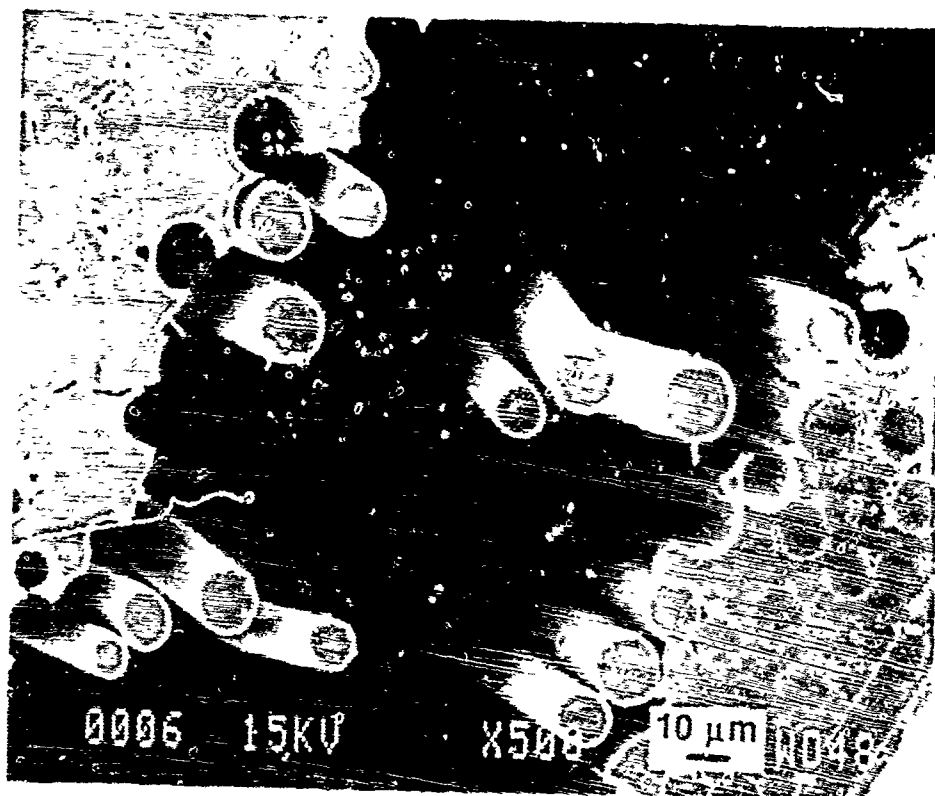
FIG. 10

MATERIALS
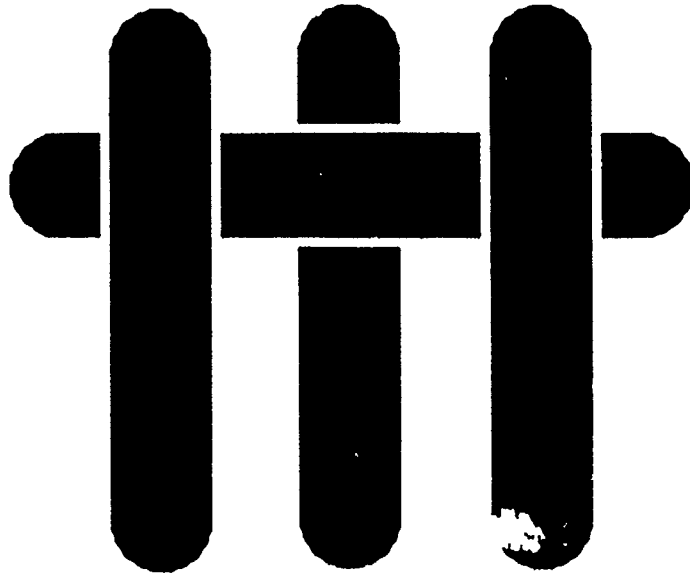
SOME ANISOTROPIC ASPECTS AND THE ANALYSIS OF MIXED MODE
DELAMINATION CRACKING IN FIBER REINFORCED AND LAMINATED
CERAMIC MATRIX COMPOSITES

By

P. G. Charalambides

Department of Materials
College of Engineering
University of California
Santa Barbara, CA 93105

MARCH 1989

SOME ANISOTROPIC ASPECTS AND THE ANALYSIS OF MIXED MODE DELAMINATION CRACKING IN FIBER REINFORCED AND LAMINATED CERAMIC MATRIX COMPOSITES

P. G. CHARALAMBIDES*
*Department of Materials, College of Engineering, University of California, Santa Barbara, CA 93105

1. INTRODUCTION

Tough ceramic matrix composites are susceptible to delamination cracking in the presence of notches [1-4]. Typically, when loaded in either tension or bending, cracks initiate near the base of the notch and extend axially [3] (Fig. 1). Such cracking, also evident in polymer matrix composites [5] t 1 in wood [6], is c' n driven by the anisotropy of the composite. This proce.s essentially alleviates the notch sensitivity of the material and may then be regarded as a desirable characteristic of the composite [2,4]. However, experiments indicate that a susceptibility to delamination cracking usually associates with a low transverse fracture resistance and a low interlaminar shear strength. Therefore, the presence and growth of delamination cracks in fiber reinforced composites and composite laminates may lend to severe reliability and safety problems, such as the reduction of structural stiffness and exposure of the interior to an adverse environment which may cause the final failure.

By analogy to thin film decohesion [7] and to fracture along bimaterial interfaces [8], delamine .ion cracking is a mixed mode process, governed largely by the fracture energies of the matrix and interface. The purpose of the present study is to provide a comprehensive analysis of the crackir menon for typical high toughness ceramic matrix composites and composite lamii ns.

Analysis of the crackir is predicated through relationships between the energy release rate G, the phɛ of loading ψ, the crack length a, and the loading within an elastically anisotropi .y. Calculations are presented for a prenotched four-point flexure geometry with delamination cracks initiating at the end of the notch (Fig. 1) for two composite systems; a unidirectionally fiber reinforced composite and a symmetric laminated beam. Calculations are also presented for the case of a homogeneous orthotropic beam.

For the first composite system, analytical steady-state energy release rates are derived. In this calculation, the effects of the location of the reinforcement are considered. Thus, relationships between the composite longitudinal elastic modulus and the elastic properties of the fiber and the matrix are obtained in terms of the number of fibers along the height of the beam and the fiber volume fraction. The known rule of mixtures result for the homogenized longitudinal effective modulus is recovered for composite systems with number of fibers along the beam height exceeding a critical value.

The laminated systems considered in the second part of this study are, in general, composed of homogeneous orthotropic elastic layers. For example, such elastic behavior is exhibited by fiber reinforced plies that meet the criterion established in the first part of

the analysis. The near-tip delamination mechanics for these laminated systems is investigated analytically via steady-state energy release rate estimates. The determination of the associated phase angle due to interlaminar cracking is not the intent of this study but it is, however, the subject of ongoing research.

In the last part of this work, the analysis is further extended to account for the coupled effects of an applied moment and an axial force on the delamination energy release rate at the tip of a crack parallel to one of the principal orthotropic material directions. A general expression for the energy release rate and phase angle aspects for such a system are discussed.

2. UNIAXIALLY FIBER REINFORCED COMPOSITES

In a typical high toughness fiber reinforced ceramic composite, mixed mode delamination cracks parallel to the principal direction of the fiber initiate at the end of the notch (Fig. 1) when either a moment M and/or an axial load N are applied. By analogy to other cracking problems [7-10], steady-state conditions ($\mathcal{G}$ and ψ independent of crack length) must exist for both tensile and four-point bending loading when the delamination crack length somewhat exceeds the notch depth. For these instances analytical elastic steady-state energy release rates can be obtained. Suo [11] in parallel studies addressed some aspects of steady-state delamination mechanics in orthotropic materials. In his analysis, Suo treated the composite system as homogeneous elastic orthotropic and presented trends for the stress intensities at the delamination crack-tip for a variety of orthotropic materials. As in the cases of cracks in homogeneous isotropic elastic bodies or cracks along bimaterial interfaces, the stress and displacement fields in the region around the crack tip of cracks positioned in one of the principal orthotropic material directions are fully characterized via a stress intensity factor and universal geometry shape functions [11,12]. In addition, opening and sliding of the crack surfaces are related to K_I, the mode I stress intensity factor, and K_{II}, the mode II component. Also, its modulus $|K|$ is related to the energy release rate $\mathcal{G}$ via an Irwin type relationship. Therefore, the task of understanding the mechanics at tips of cracks positioned in a principal direction of an orthotropic material reduces to one wherein only the modulus $|K|$ and the phase angle ψ or $\mathcal{G}$ and ψ are to be determined, where $\psi = \arctan(K_{II}/K_I)$. These quantities, by and large, depend on the load, geometry and the material properties.

Unlike Suo's approach, this analysis is not based on the basic assumption of material orthotropy; rather, the fiber and the matrix are treated individually as linear elastic isotropic materials. Departing from this assumption, analytical elastic steady-state energy release rates for the flexure geometry shown in Fig. 1 are derived in terms of the elastic properties of the two constituents, the fiber volume fraction f, and the relative fiber radius to beam thickness ratio. This result is then used to extract the effective longitudinal elastic moduli of the composite in terms of the above mentioned quantities. This in turn, can be used to provide estimates for the anisotropy parameters ρ and Λ used by Suo [11], thus enabling us to extract the appropriate phase angle from his analysis. With this as a background, we now take on the task of studying the delamination mechanics of a uniaxially fiber reinforced composite system subjected to four-point flexure as shown in Fig. 1.

2.1 Steady – state delamination energy release rates

In a linear elastic system the energy release rate $\mathcal{G}$ can be obtained in terms of the changes in either the total potential energy Ψ or the total strain energy U of the system as the crack grows from length a to $a + \Delta a$, i.e.

$$\mathcal{G} = -\left(\frac{\partial \Psi}{\partial a}\right)_{\substack{\text{Constant} \\ \text{Loads}}} = \left(\frac{\partial U}{\partial a}\right)_{\substack{\text{Constant} \\ \text{Loads}}} \tag{1}$$

For a linear elastic system, $\Psi = -U$. The steady-state delamination energy release rate for the geometry shown in Fig. 1 can now be derived from the changes in U as the crack grows from a to $a + \Delta a$. In doing so, solutions for U in strips of material far behind and far ahead of the crack tip in the fiber reinforced composite beam are required [8]. Such solutions can be obtained for the more general case of an applied moment coupled with an applied axial force. However, such estimates are presented later on in this work for the case of a homogeneous orthotropic material, in which case a more general formula for the energy release rate is obtained. For the purpose of the analyses in this section, we take on the case of an applied moment M alone, which pertains to the flexural specimen shown in Fig. 1.

2.2 Energy release rate

For the case of long cracks compared to the notch depth, the steady-state energy release rate can be obtained via equations (1). Thus,

$$\mathcal{G}_{ss} = \frac{(1 - \nu_m^2)M^2}{2E_m[\lambda f + 1 - f]I}\left[\frac{(1+\xi)^3}{1 + \frac{(1+\xi)^2}{4n^2}\left[\frac{f(\lambda-1)(\frac{3}{2}f-1)}{\lambda f + 1 - f}\right]} - \frac{1}{1 + \frac{1}{4n^2}\left[\frac{f(\lambda-1)(\frac{3}{2}f-1)}{\lambda f + 1 - f}\right]}\right] \tag{2}$$

where $\xi = h_1/h_2$; $\lambda = E_f(1 - \nu_f^2)/E_m(1 - \nu_m^2)$ for plane strain, and $2n$ is the total number of fibers along the beam height as shown in Fig. 2. The derivation of the above formula and a more detailed analysis of the material presented in this work can be found elsewhere [13].

For a fixed fiber volume fraction f, the number n is a measure of the aspect ratio of the fiber radius to beam thickness, i.e. $n = \frac{1}{\sqrt{\pi}}\frac{H}{r_f}\sqrt{f}$ where $2H$ is the beam thickness and $2r_f$ is the fiber diameter. The trends in normalized $\mathcal{G}_{ss}$ with respect to n and therefore the ratio H/r_f are shown in Fig. 2. These results correspond to $\xi = h_1/h_2 = 1.0$ and $f = 0.3$. Notice that in this plot, $\mathcal{G}_{ss}$ is normalized by the rule of mixtures modulus, i.e. $E_1 = (\lambda f + 1 - f)\bar{E}_m$ with $\bar{E}_m = E_m/(1 - \nu_m^2)$. As shown in Fig. 2, for a homogeneous composite system, $\lambda = 1$, the result is that obtained by Charalambides et al [8] and is independent of n. As the system deviates from the homogeneous case, $\lambda \neq 1$, the normalized $\mathcal{G}_{ss}$ is most

sensitive to n for values of $n < 5$ and it asymptotes to the homogeneous system prediction for large $n > 8$. These results suggest that in fiber reinforced composite systems where the number of fibers n exceeds a critical minimum, i.e. $2n > 16$ ($r_f/H \approx 0.03$), the $n \approx \infty$ approximation can be used. The resulting error in $\mathcal{G}_{ss}$ is then less then 1.5%. In such a case the composite can be treated as homogeneous orthotropic with a longitudinal effective modulus E_1, given by the rule of mixtures, i.e. $E_1 = (\lambda f + 1 - f)\bar{E}_m$ for plane strain [14-16].

3. LAMINATED COMPOSITES

When a delamination crack occurs parallel and at close proximity or at an interface between two laminates within a laminated composite, the cracking process must be analyzed using concepts derived for bimaterial interfaces [8,17-19]. For such an interface crack, the mechanics and in particular, the association of an opening and sliding of the crack surfaces to mode I ($\psi = 0$) and mode II ($\psi = \pi/2$) fracture modes have been perplexing, partially due to the coupling of the two modes through a complex stress intensity factor whose phase angle is scale sensitive. In addition, the linear elastic stress and displacement fields in the crack tip region exhibit an oscillatory character leading to near-tip interpenetration of the crack surfaces for non-zero values of the bimaterial constant ε [17]. Although current thinking assumes $\varepsilon = 0$, some of these issues are still the subject of ongoing debate [17,20]. On the other hand, and although the definition of the bimaterial phase angle seems to be ambiguous, the associated energy release rate $\mathcal{G}$ at the tip of an interface crack, is well defined and is characterized by the same units as in the homogeneous case (e.g. J/m^2). Therefore, in an ideally brittle system, $\mathcal{G}$ can be used to characterize fracture. Ultimately, failure loci of $\mathcal{G}_c$ versus phase angle ψ_c [19,21] should be used to account for the increase in $\mathcal{G}_c$ with ψ_c, as the asperities effects at the bimaterial interface become more important. In this section we shall evaluate the steady-state energy release rate at the tip of cracks embedded in laminated structures (a cross-section for a symmetric laminated beam is shown in Fig. 3) subjected to pure bending, in terms of the applied loading and specimen morphology.

3.1 Symmetric laminated systems

A special case of a general laminated system is the symmetric laminated beam whose cross-section is shown schematically in Fig. 3. This geometric morphology represents a typical $0°/90°$ symmetric laminated fiber reinforced composite. In such a case, the longitudinal and transverse moduli and Poisson's ratios for each ply are E_1, ν_{12} and E_2, ν_{23} respectively. The thickness of each layer is t, and the total number of layers is $2n$. Also, as in the first system examined earlier in this work (Fig. 1), the notch depth is h_1 and thus, the delamination crack lies at the interface of the n_1, and $n_1 + 1$ layers from the top. In accordance with equation (1), the associate energy release rate takes the form,

$$\mathcal{G}_{ss} = \frac{(1 - (\nu_{12}^i)^2)M^2}{2E_1^i I_o} \left\{ \frac{1}{\bar{I}_{2c}} - \frac{1}{\bar{I}_c} \right\} \tag{3}$$

The dimensionless moments of inertia appearing in the above equation are: $\hat{I}_c = I_c/I_o$ and $\hat{I}_{2c} = I_{2c}/I_o$, with $I_o = \frac{bh^3}{12}$ and

$$I_c = \frac{bh^3}{12}\frac{1}{2}(1+\lambda)\left[1 + \frac{1-\lambda}{1+\lambda}\frac{1+\xi}{2n}\right] \qquad (3a)$$

$$I_{2c} = \frac{bh^3}{12}\frac{1}{2}(1+\lambda)\frac{1}{(1+\xi)^3}\left\{(1+\xi)^3\left[1 + \frac{1-\lambda}{1+\lambda}\frac{1+\xi}{2n}\right] - 3\xi^2\left[1 + \frac{1-\lambda}{1+\lambda}\frac{1+\xi}{2n}\right]^2 \right.$$
$$\left. - 3\xi(1-\xi^2)\left[1 + 2\frac{1-\lambda}{1+\lambda}\frac{1}{2n}\right] - 4\xi^3\left[1 + \frac{3}{2}\frac{1-\lambda}{1+\lambda}\frac{\xi^2}{(1+\xi)^2}\frac{1+\xi}{2n}\right]\right\} \qquad (3b)$$

For plane strain the width $b = 1$, and from Fig. 1, $M = P\ell/2b$. Also, the parameter λ in the case of a symmetric laminated composite takes the form, $E_2(1 - \nu_{12}^2)/E_1(1 - \nu_{23}^2)$. Transition energy release rates from small to large n values, given by equation (3), are presented in Fig. 3. On this plot, the normalized $\mathcal{G}_{ss}$ is plotted against n for relative notch depth $\xi = h_1/h_2 = 0.6$ and various values of λ. In most symmetric laminate composites, $\lambda < 1$. For these systems and in accordance with Fig. 3 the normalized energy release rate asymptotes to the homogeneous value $(n \to \infty)$ from below. For example, using a typical value of say, $n = 8$ and $\lambda = 0.2$, the normalized $\mathcal{G}_{ss}$ obtained via equation (3) is of the order of 15% lower than the $n = \infty$ value which warns caution when this result instead of the value predicted by equation (3) is used.

4. LIMITING CASE: HOMOGENEOUS ORTHOTROPIC BEHAVIOR

In equations (2) and (3), the effects of the relative fiber radius/layer thickness to beam thickness, on the steady-state delamination energy release rate are obtained via the number n and are shown in Figs. 2 and 3 for fiber reinforced and laminated composites respectively. At the limit $n \to \infty$, a striking similarity for $\mathcal{G}_{ss}$ obtained from each system is observed. In particular, equations (2) and (3) reduce to the following simple expression,

$$\mathcal{G}_{ss} = \frac{M^2}{2E_1 I}\left[(1+\xi)^3 - 1\right] \qquad (4)$$

where $I = bh^3/12$ with h as the total height of the beam and E_1 represents the effective rule of mixtures longitudinal modulus for each system. Thus for fiber reinforced composites, $E_1^f = (\lambda^f f + 1 - f)\bar{E}_m$[†] whereas for $0°/90°$ cross ply fiber reinforced laminated systems, $E_1^s = (E_1^f + E_2^f)/2.0$, and E_2^f is the transverse modulus for each fiber reinforced ply.

[†] Henceforth, the superscripts ( )^s and ( )^f will be used to denote properties of the symmetric laminated and fiber reinforced composites respectively

5. APPLIED MOMENT AND AXIAL FORCE: COUPLED EFFECTS

The coupled effects on the energy release rates of an applied moment M and an axial force N shown in Fig. 4 are presented in this section. As shown earlier via equations (2) and (3) only the effective longitudinal modulus E_1 of the composite enters the expression for the available energy release rate at the delamination crack tip. Furthermore, as $n \to \infty$ (decreasing fiber radius or layer thickness for a fixed fiber/layer volume fraction) the expression for $\mathcal{G}_{ss}$ takes the simple form given by equation (4). In this part of the analysis we treat the composite as one with a small fiber radius or layer thickness, such that the $n \to \infty$ assumption is valid. Under this condition, the effective longitudinal modulus E_1, in fiber reinforced and symmetric laminated composite systems, is given by the rule of mixtures and was obtained earlier in this study. The associated delamination energy release rate can be obtained from the homogeneous beam prediction [8,22,23] where the usual elastic modulus is replaced by the effective modulus E_1. Thus, accounting for the coupled effects of an axial force N and a moment M, $\mathcal{G}_{ss}$ takes the general form:

$$\mathcal{G}_{ss} = \frac{S^2 h^2 \cos^2 \phi}{2 E_1 I_o} \left[\left((1+\xi)^3 - 1\right) - \xi(1+\xi)^2 \tan\phi + \frac{1}{12}\left((1+\xi)(1+3\xi^2) - 1\right)\tan^2\phi \right]$$

(5)

where $\frac{M}{h} = S\cos\phi$ and $N = S\sin\phi$ as shown in Fig. 4. The trends in normalized $\mathcal{G}_{ss}$ with ϕ and thickness ratio ξ are shown in the above figure, where $\mathcal{G}_{ss}$ is plotted against the phase angle of loading ϕ. When $\phi = 0$ the trends are those due to a pure bending and are identical to those obtained by Charalambides et al. [8] whereas for $\phi = 90°$ the trends are those due only to an axial force. These results are general and can be used for a homogeneous, fiber reinforced composite or a laminated system provided the appropriate effective longitudinal modulus is used.

6. ON THE PHASE ANGLE

Phase angle estimates for a crack with its plane parallel to one of the principal orthotropic material directions, were obtained by Suo for the delamination geometry shown in Fig. 4. The effects of a bending moment M and an axial force N on the stress intensity phase angle ψ are coupled only through an angle $\omega(\xi,\rho)$, which is a weak function of $\xi = h_1/h_2$, with ξ as the notch depth and the anisotropy parameter ρ [11]. In addition, exact solutions for the phase angle ψ are given by Suo [11] in the cases of pure bending and pure tension/compression respectively for $\xi = 1.0$, i.e.,

$$\psi = \arctan\left(\frac{\sqrt{3}}{2}\Lambda^{-\frac{1}{4}}\right), \quad \text{pure bending;} \quad \xi = 1.0 \tag{6a}$$

$$\psi = \arctan\left(\frac{2}{\sqrt{3}}\Lambda^{-\frac{1}{4}}\right), \quad \text{axial force only;} \quad \xi = 1.0 \tag{6b}$$

where,

$$\Lambda^f = \frac{E_2^f}{E_1^f} \frac{1 - (\nu_{12}^f)^2 \frac{E_2^f}{E_1^f}}{1 - (\nu_{23}^f)^2}, \qquad \Lambda^s = \frac{E_2^s}{E_1^s} \frac{1 - (\nu_{13}^s)^2}{1 - (\nu_{12}^s)^2 \frac{E_2^s}{E_1^s}} \tag{7}$$

with $\Lambda = \Lambda^f$ and $\Lambda = \Lambda^s$ for a fiber reinforced and a symmetric cross-ply laminated composites respectively. For typical composite systems, the values of ψ predicted via equations (6) are of the order of $40° - 50°$, indicative of the mixed mode nature of delamination cracking under either a pure bending or axial loading. These phase angles in conjunction with the energy release rates derived earlier (see equation 5), fully characterize stress and displacement fields around crack tips of cracks embedded in principal orthotropic direction in homogeneous orthotropic ideally brittle materials. Therefore, delamination cracking in this type of systems can be understood in terms of ψ and $\mathcal{G}_{ss}$. However, these results, in particular those regarding the phase angle, should be used with greater caution when cracking occurs in either a fiber reinforced or a laminated composite. In either of these systems and whenever failure occurs at a scale much smaller than the fiber radius of the layer thickness, concepts from bimaterial fracture may be necessary for the characterization of such cracking process. Despite this difficulty, the phase angles obtained from a homogeneous orthotropic analysis can be used as remote quantities which, as in the case of the sandwich geometry [24], can be linked to the tip values via local mechanics.

7. CLOSURE

The mechanics of delamination cracking for uniaxially fiber reinforced composites and laminated prenotched beams, for the combined loading of an applied moment and an axial force have been presented. As a first step, comprehensive solutions for the delamination steady-state energy release rate $\mathcal{G}_{ss}$ due to a moment M for both systems were developed. These solutions incorporated the effects of arbitrarily small finite number n of fibers/layers in the corresponding composite systems.

It was demonstrated that for large n (i.e. $n > 8$) and when normalized with the appropriate rule of mixtures modulus for each case, $\mathcal{G}_{ss}$ asymptotes to a universal value that depends only on the relative notch depth $\xi = h_1/h_2$. Thus, in composite beams with a large number of fibers/layers, mechanical quantities (energies, stresses, deformations) can be calculated from a statically equivalent homogeneous elastic orthotropic system whose longitudinal modulus is extracted from the original composite via the rule of mixtures. Solutions for the delamination steady-state energy release rate $\mathcal{G}_{ss}$ at the tip of cracks embedded in homogeneous orthotropic materials with their plane along a principal material direction, have been developed for the general case of an applied moment and an axial force. The associated phase angle ψ is of the order of $40° - 50°$, indicative of the mixed mode nature of delamination cracking under either a pure bending or axial loading.

The analysis does not account for possible non-linear failure processes in the region close to the crack-tip which often act as toughening agents. In composites with such operating

mechanisms and under the assumption of a small scale process zone, apparent fracture toughnesses for delamination cracking can be obtained using the results for $\mathcal{G}_{ic}$ derived in this study. Thus, as a major benefit of this work, the results of this analysis can be used in conjunction with experimental data to establish critical delamination energies and crack resistance curves for fiber reinforced/laminated composite systems.

ACKNOWLEDGEMENTS

REFERENCES

[1] O. Sbaizero and A. G. Evans, "Tensile and Shear Properties of Laminated Ceramic Matrix Composites". *J. Am. Ceram. Soc.* **69** (1986), 481-486.

[2] K. M. Prewo, "Tension and Flexural Strenght of Silicon Carbide Fibre-Reinforced Glass Ceramics". *Jnl. Mater. Sci.* 21 (1986), 3590-3600.

[3] O. Sbaizero, P. G. Charalambides and A. G. Evans, "Delamination Cracking in a Laminated Ceramic Matrix Composite" (unpublished).

[4] B. Dalglish and A. G. Evans. "Delamination Cracking in a Fiber Reinforced Ceramic Matrix Composite" (unpublished).

[5] S. S. Wang, "*Composite Materials; Testing and Design.*" ASTM STP 674 (Ed. S. W. Tsai, 1979), 642-663.

[6] M. F. Ashby, E. E. Easterling, R. Harrysson and S. K. Maiter. *Proc. Roy. Soc.* 24 (1985), p. 4398.

[7] M. D. Drory, M. D. Thouless and A. G. Evans, "On The Decohesion of Thin Films". *Acta Metall.* (In press).

[8] P. G. Charalambides, J. Lund, A. G. Evans and R. M. McMeeking, "A Test Specimen for Determining the Fracture Resistance of Bimaterial Interfaces". *J. Appl. Mech.* (In press).

[9] M. D. Thouless, A. G. Evans, M. F. Ashby and J. W. Hutchinson, "The Edge Cracking and Spalling of Brittle Plates". *Acta Metall.* 35 6 (1987), 1333-1341.

[10] P. G. Charalambides, H. C. Cao, J. Lund and A. G. Evans. "Development of a Test Method in Measuring the Mixed Mode Fracture Resistance of Bimaterial Interfaces". *Acta Metall.* (In press).

[11] Z. Suo, "Delamination Specimens for Orthotropic Materials" (unpublished).

[12] G. C. Sih, P. C. Paris and G. R. Irwin, "On Cracks in Rectilinearly Anisotropic Bodies". *Int. J. Fract.* 1 (1965), 189-203.

[13] P. G. Charalambides, "Some Anisotropic Aspects and the Analysis of Mixed Mode Delamination Cracking in Fiber Reinforced and Laminated Ceramic Matrix Composites" (unpublished).

[14] N. J. Pagano and S. W. Tsai, "Micromechanics of Composite Media". *Composite Materials Workshop*, Progress in Material Science Series, Vol. 1, (Technomic Publishing Co. Inc., 1968).

[15] Derek Hull, *An Introduction to Composite Material* Cambridge Solid State Science Series, (Cambridge University Press, 1981).

[16] R. M. Christensen, *Mechanics of Composite Materials* (Wiley, New York, 1979).

[17] J. R. Rice "Elastic Fracture Mechanics Concepts for Interfacial Cracks". *J. Appl. Mech.* 55 1988, 98-103.

[18] J. W. Hutchinson, M. E. Mear and J. R. Rice, "Crack Paralleling an Interface Between Dissimilar Materials". *J. Appl. Mech.* 54 (1987), 828-832.

[19] H. C. Cao and A. C Evans, "An Experimental Study of the Fracture Resistance of Bimaterial Interfac ". *Mechanics of Material*, (In press).

[20] M. Comninou and D. Schmueser, "The Interface Crack in a Combine Tension-Compression and Shear Field". *J. Appl. Mech.* 46 (1979), 345-348.

[21] A. G. Evans and J. W. Hutchinson, "Effects of Non-Planarity on the Mixed Mode Fracture Resistance of Bimaterial Interfaces". *The Processing and Mechanical Properties of High Temperature/High Performance Composites*. (Department of Materials, University of California, Santa Barbara, 1988).

[22] A. G. Evans, M. Rühle,, B. J. Dalgleish and P. G. Charalambides, "The Fracture Energy of Bimaterial Interfaces" (unpublished).

[23] Z. Suo and J. W. Hutchinson, "Interface Crack Between Two Elastic Layers". *Int. J. Fract.* , (In press).

[24] Z. Suo and J. W. Hutchinson, "On Sandwich Geometry Test Specimens for Measuring Interface Crack Toughness" (unpublished).

FIGURE CAPTIONS

Fig. 1 A schematic of a fiber reinforced four-point flexure specimen. At a critical applied load, delamination cracks initiate at the end of the notch.

Fig. 2 The trends in the normalized steady-state energy release rate $\mathcal{G}_{ss}$, with the number of fibers along the height of the beam $2n$. All curves with $\lambda \neq 1$ asymptote to the homogeneous curve result ($\lambda = 1$) as $n \to \infty$.

Fig. 3 The trends in the normalized steady-state energy release rate $\mathcal{G}_{ss}$, with the number of layers in a symmetric laminated beam. In this plot, $\mathcal{G}_{ss}$ is normalized by the the rule of mixtures modulus, i.e. $E_1^s = (\bar{E}_1^f + \bar{E}_2^f)/2.0$. The overbar denotes plane strain conditions and the superscripts ( )^s and ( )^f are used to denote properties of symmetric laminated and fiber reinforced composites respectively.

Fig. 4 The trends in the normalized steady-state energy release rate $\mathcal{G}_{ss}$, with the the loading angle ϕ. The results in this plot are general and can be used for an orthotropic beam with a delamination crack parallel to the principal "1" material axis.
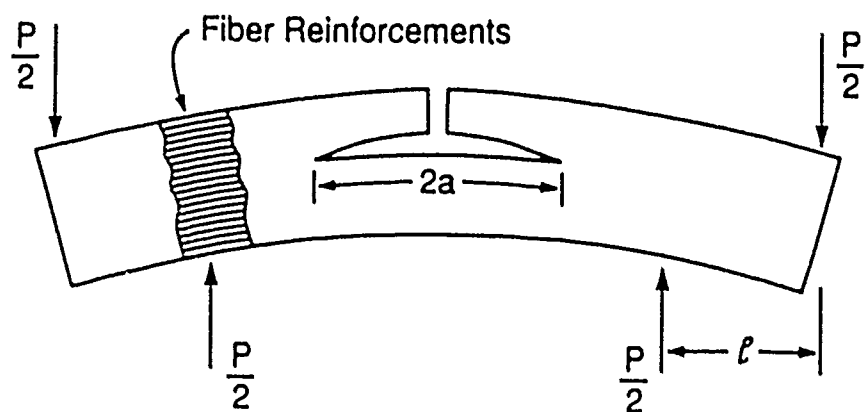
Fig. 1
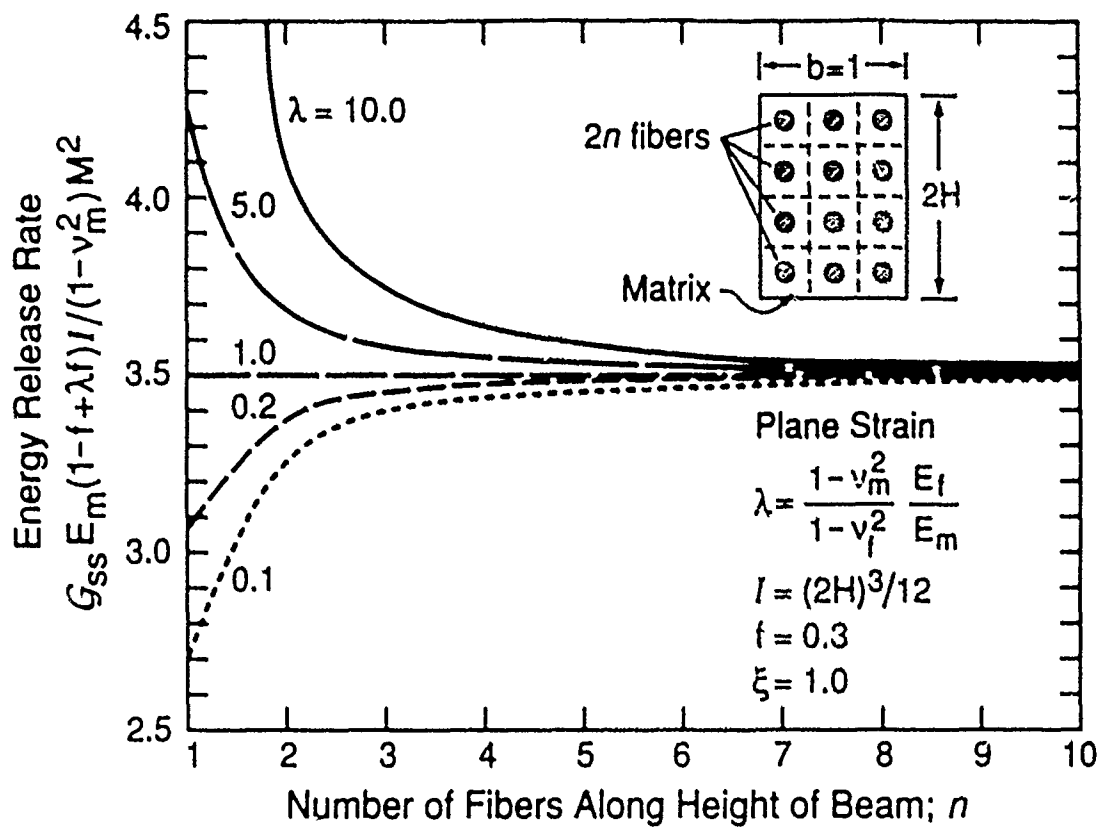
Fig. 2
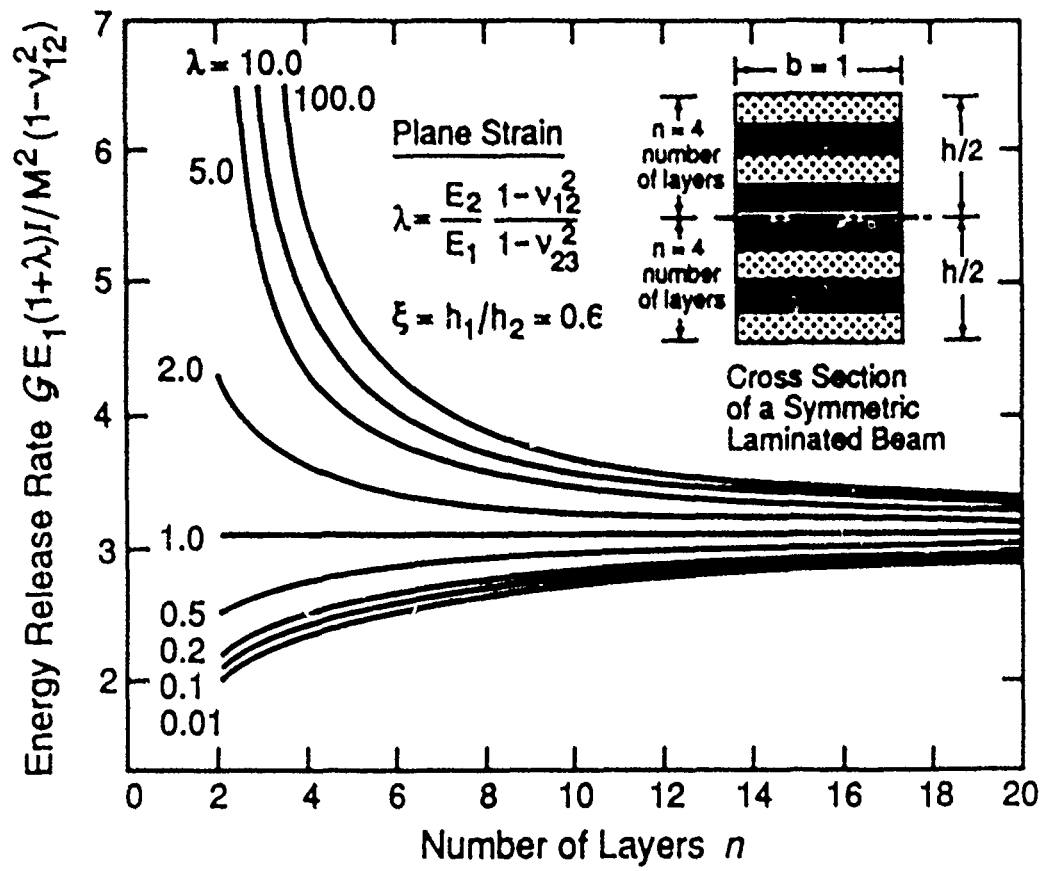
Fig. 3
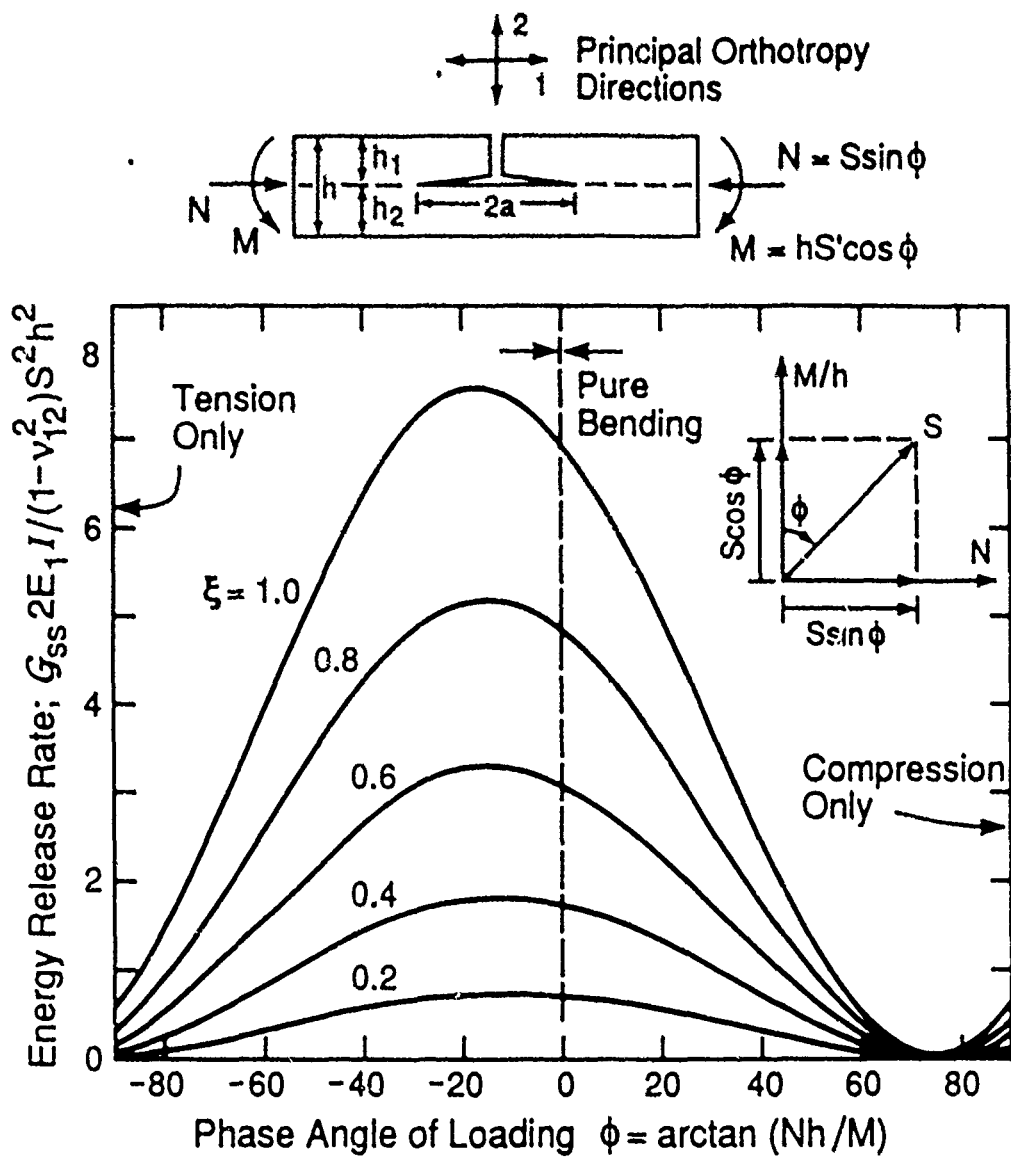
Fig 4

SINGULARITIES, INTERFACES AND CRACKS IN DISSIMILAR

ANISOTROPIC MEDIA

Zhigang Suo

Division of Applied Sciences
HARVARD UNIVERSITY
Cambridge, Massachusetts 02138

March 1989

ABSTRACT

Singularities, such as line forces and dislocations, embedded in elastically anisotropic media are considered in this paper. Interactive solutions for singularity/interface and singularity/interface-crack are obtained. For a non-pathological material pair in which an interface crack displays no oscillatory behavior, it is observed that, apart possibly from the stress intensity factors, the structure of the near-tip field in each of the two blocks is independent of the elastic moduli of the other block. Collinear interface cracks are analyzed under this non-oscillatory condition, and a simple rule is formulated which allows one to construct the complete solutions from the mode III potentials in an isotropic, homogeneous medium. In particular, the stress intensity factors for the above mentioned interface cracks are the same as mode III ones for isotropic, homogen... ... cases. The structure of the oscillatory near-tip fields of an interface crack is identified with only three real normalizing constants. A definition of stress intensity factors is proposed. A peculiar fact is that, due to the anisotropy, the stress intensity factors scaling the oscillatory fields, however defined, do not recover the classical stress intensity factors as the material pair becomes non-pathological. Collinear crack problems are also formulated in this context, and a strikingly simple mathematical structure is identified. The general results are specialized to decoupled antiplane and in-plane deformations. For this important case, it is found that if a material pair is non-pathological for one set of relative orientations of the interface and the two phases, it is non-pathological for any set of orientations. Insight thus gained leads to an extension of an earlier proposal for simplifying the approach to interface fracture mechanics. For bonded orthotropic materials, an intuitive choice of the principal measures of elastic anisotropy and dissimilarity is rationalized. A complex-variable representation is presented for a class of degenerate orthotropic materials. Through out the paper, the equivalence of the Lekhnitskii and Stroh formalisms is emphasized.

1. INTRODUCTION

The interactive solutions for singularity/interface and singularity/crack serve as building blocks for many micromechanics models and computational methods, as indicated by the references cited in Suo (1988a). The impetus to undertake this work came from the recent experimental and theoretical investigations of several research groups, to one of which the writer belongs, on fracture behaviors of woods, composites, bicrystals and oriented polymers (Argon et al. 1988, Ashby et al. 1985, Bassani and Qu 1988, Gupta and Suo 1989, Sbaizero et al. 1988, Suo 1988b, Sweeney et al. 1988, Wang 1988).

Another fact that motivates the present work comes from fundamental concerns of fracture mechanics. About forty years ago, G.R. Irwin, in his pioneering work, identified the three independent singular fields at a crack tip in a homogeneous, isotropic body, which have since been referred to as the *three modes* of singularities. For a given material, each mode is universal for all cracked specimens under arbitrary loadings, except for a normalizing constant, or *stress intensity factor*, which depends on the specific specimen geometry and external loading. Based on this mathematical artifact, Irwin was able to define a material property, *toughness*, a loosely termed jargon among metallurgists then, as the critical value (or combinations) of the stress intensity factor that a material can sustain.

During the last four decades, Irwin's agenda has been pursued for both brittle and ductile solids. Here we will only keep track of the development for brittle solids. Williams (1959) discovered the so-called oscillatory near-tip behavior for an interface crack between two isotropic materials. Significant progress has been made in the interface fracture mechanics, which was assessed by Rice (1988) and Hutchinson (1989). There are still three independent singularity fields for an interface crack between two isotropic materials, however, in the sense that the near-tip fields are universal for a given material pair except for three (real) normalizing factors. The two in-plane modes are coupled and oscillatory,

and can be normalized by a complex stress intensity factor. The mode III field has a square root singularity and can be defined separately with a real stress intensity factor. In another direction, Stroh (1958), Sih, Irwin and Paris (1965), among others, investigated the crack tip fields in an anisotropic homogeneous body. The full singular fields were tabulated by Hoenig (1982) for the most general anisotropy. Again the near-tip fields can be normalized by three stress intensity factors, and moreover, for this situation, the three modes can be separately defined.

The next logical target, a crack along an interface between dissimilar anisotropic media, has been tackled by several authors (Bassani and Qu 1988, Clements 1971, Gotoh 1967, Qu and Bassani 1988a, Tewary et al. 1989a, Ting 1986, Wang 1984, Willis 1971). Several basic crack problems have been solved, and calculation of the oscillatory index has been emphasized. However, it is not clear, from the work published todate, what the structure of the near-tip fields is, and in particular, whether the near-tip fields in general can be normalized by three real factors. This is *not* self-evident. Willis (1971), for example, defined a 'stress concentration vector', which involved three complex, or six real, quantities. A similar situation is found in Wang(1984), Tewary et al. (1989a). Such conceptual ambiguity in defining stress intensity factors, and thus toughness, stands in the way of further development of Irwin's fracture mechanics scheme. One aim of this paper is to show that there are indeed only three independent real normalization factors.

A breakthrough was made recently by considering material pairs with no pathological behavior at interface crack tips (Qu and Bassani 1988 and Bassani and Qu 1988). These authors proved a necessary and sufficient non-oscillatory condition. Under this condition they could define the three modes separately in the conventional fashion, and found the Irwin-type energy release rate expression is simply the average of the corresponding results for the two homogeneous materials. Indeed, in Section 5 of this paper, we observe that for such an interface crack, the near-tip fields (stresses and

displacements) in the two phases do not interact with each other in the sense that, apart from the stress intensity factors, the field in each phase is independent of the moduli of the other phase. Thus the structure of the field in each phase is identical to those for a crack in the corresponding homogeneous material. Collinear interface cracks are also considered, and a simple rule is formulated to construct the complete solutions from the mode III potentials for an isotropic, homogeneous material.

The general oscillatory near-tip fields are derived in Section 6. Of the three singular fields, two are coupled and oscillatory, and the third is non-oscillatory. Each of the three singular fields may contain mixed in-plane and antiplane deformations. A definition of stress intensity factors is proposed. It is found that the stress intensity factors of the oscillatory fields, however defined, do *not* recover the classical stress intensity factors as the material pair degenerates to be non-pathological. This peculiar feature has not been encountered in the previous experience with isotropic material pairs. A revealing example is given in Section 9 for orthotropic bimaterials. A constructive formula is devised to obtain stress intensity factors and complete field solutions for collinear crack problems.

Several known results of dislocation mechanics, such as the solution of a dislocation in a homogeneous material and dislocation/interface interaction are included in this paper for ease of reference. These results, in conjunction with the basic crack solutions, are used to solve singularity/interface-crack interaction problems. The latter problems were also studied recently by Tewary et al. (1989a).

Some basic discussion on interface fracture mechanics for anisotropic media is presented in the final section. For an important situation in which in-plane and antiplane deformations decouple, it is found that a material pair is non-pathological in any relative orientation if it is so in one relative orientation. *Non-pathology* for this special case, as a consequence, is a property that an anisotropic material pair may or may not have, regardless of the relative orientation. Following He and Hutchinson (1988), and Suo and

Hutchinson (1989), we propose that one may interpret and apply toughness data using an imagined non-pathological pair resulting from a slight modification of elastic constants of a given material pair.

Throughout the paper the equivalence is emphasized among several apparently different complex-variable representations of two dimensional elasticity, such as those by Lekhnitskii (1963), Green and Zerna (1954), and Eshelby et al(1953). In other words, for instance, the formulation due to Eshelby et al, which is better known as the Stroh (1958) formalism, is none other than an alternative derivation of the earlier Russian work contained in Lekhnitskii's book. Workers in this field seem to be aware of this fact, but no explicit discussions are found in the established literature. The equivalence allows to take advantage of all these theories, so that one can enjoy many remarkable algebraic results in the Stroh formalism, and also benefit from the explicitness of Lekhnitskii's derivation, as well as many solution techniques developed in his book. In particular, analytic continuation techniques will be exploited throughout the paper, which simplify many earlier works using integral transforms.

One thing that makes the field chaotic is notation. In this paper we have tried to unify the notation by using smallest possible set of matrices, i.e., A, L, B and H. The first three are matrices only involving elastic constants of one material, while the last one, H, is a bimaterial matrix. All of them are complex-valued, and B and H are positive-definite Hermitian matrices.

2. LEKHNITSKII-ESHELBY-STROH (LES) REPRESENTATION

Hooke's law connecting the stresses σ_{ij} and strains ε_{ij} for a generally anisotropic material can be written in one of the following forms

$$\varepsilon_{ij} = \sum_{k,l=1}^{3} S_{ijkl} \sigma_{kl}, \qquad \sigma_{ij} = \sum_{k,l=1}^{3} C_{ijkl} \varepsilon_{kl}$$

$$\varepsilon_i = \sum_{j=1}^{6} s_{ij} \sigma_j, \qquad \sigma_i = \sum_{j=1}^{6} c_{ij} \varepsilon_j \tag{2.1}$$

The standard correspondence is adopted, i.e., $\{\varepsilon_i\} = [\varepsilon_{11}, \varepsilon_{22}, \varepsilon_{33}, 2\varepsilon_{23}, 2\varepsilon_{31}, 2\varepsilon_{12}]^T$ and $\{\sigma_i\} = [\sigma_{11}, \sigma_{22}, \sigma_{33}, \sigma_{23}, \sigma_{31}, \sigma_{12}]^T$. The superscript T denotes the transpose. The fourth-order tensors S and C are referred to as the compliance and stiffness tensors, respectively. The 6×6 matrices s and c ($s = c^{-1}$) are conventional compliance and stiffness matrices. The tensor C_{ijkl} can be replaced by the matrix c_{ij} correspondingly. The relationship between s_{ij} and S_{ijkl} is analogous except that numerical factors are needed, e.g., $s_{11} = S_{1111}$, $s_{14} = 2S_{1123}$, $s_{44} = 4S_{2323}$. To avoid confusion, in this paper *no* summation is assumed implicitly for repeated indices.

It has been shown by Lekhnitskii (1963) and Eshelby et al. (1953), that for a two dimensional problem, i.e., with geometry and external loading invariant in the direction normal to x,y-plane, the elastic field can be represented in terms of *three* functions $\phi_1(z_1)$, $\phi_2(z_2)$, $\phi_3(z_3)$, each of which is *holomorphic* in its argument $z_j = x + \mu_j y$. Here μ_j are three distinct complex numbers with positive imaginary part, which can be solved as roots of a sixth-order polynomial to be listed shortly. With these holomorphic functions, or *complex potentials*, the *representation* for displacements u_i, stresses σ_{ij}, and resultant forces on an arc f_i (the medium is kept on the left-hand side as an observer travels in the positive direction of the arc) is

$$u_i = 2\,\mathrm{Re}\left[\sum_{j=1}^{3} A_{ij} \phi_j(z_j)\right] \qquad f_i = -2\,\mathrm{Re}\left[\sum_{j=1}^{3} L_{ij} \phi_j(z_j)\right]$$

$$\sigma_{2i} = 2\,\mathrm{Re}\left[\sum_{j=1}^{3} L_{ij} \phi_j'(z_j)\right], \qquad \sigma_{1i} = -2\,\mathrm{Re}\left[\sum_{j=1}^{3} L_{ij} \mu_j \phi_j'(z_j)\right] \tag{2.2}$$

Here, ( )' is designated as the derivative with respect to the associated arguments, and A

and L are two matrices depending on elastic constants, which will be defined shortly. Curiously, the derivations by Lekhnitskii and Eshelby et al., and some other authors, notably Green and Zerna (1954), gave entirely different schemes to compute the numbers μ_α and matrices A and L.

On the basis of two Airy-type stress functions, Lekhnitskii found that μ_α satisfy the six-order characteristic equation

$$l_2(\mu)l_4(\mu) - [l_3(\mu)]^2 = 0 \tag{2.3}$$

where

$$l_2(\mu) = s_{55}\mu^2 - 2s_{45}\mu + s_{44}$$

$$l_4(\mu) = s_{11}\mu^4 - 2s_{16}\mu^3 + (2s_{12} + s_{66})\mu^2 - 2s_{26}\mu + s_{22} \tag{2.4}$$

$$l_3(\mu) = s_{15}\mu^3 - (s_{14} + s_{56})\mu^2 + (s_{25} + s_{46})\mu - s_{24}$$

By requiring the compliance matrix to be positive definite, he was able to prove that (2.3) has no real root. If one assumes the roots are distinct, the six roots form three complex conjugate pairs, from which three μ_α with positive imaginary part can be selected. The elements of the matrices A and L are given by

$$L = \begin{bmatrix} -\mu_1 & -\mu_2 & -\mu_3\eta_3 \\ 1 & 1 & \eta_3 \\ -\eta_1 & -\eta_2 & -1 \end{bmatrix} \tag{2.5}$$

and

$$A_{1\alpha} = s_{11}\mu_\alpha^2 + s_{12} - s_{16}\mu_\alpha + \eta_\alpha(s_{15}\mu_\alpha - s_{14})$$

$$A_{2\alpha} = s_{21}\mu_\alpha + s_{22}/\mu_\alpha - s_{26} + \eta_\alpha(s_{25} - s_{24}/\mu_\alpha) \tag{2.6}$$

$$A_{3\alpha} = s_{41}\mu_\alpha + s_{42}/\mu_\alpha - s_{46} + \eta_\alpha(s_{45} - s_{44}/\mu_\alpha)$$

for $\alpha = 1, 2$ and

$$A_{13} = \eta_3(s_{11}\mu_3^2 + s_{12} - s_{16}\mu_3) + s_{15}\mu_3 - s_{14}$$

$$A_{23} = \eta_3(s_{21}\mu_3 + s_{22}/\mu_3 - s_{26}) + s_{25} - s_{24}/\mu_3 \qquad (2.6a)$$

$$A_{33} = \eta_3(s_{41}\mu_3 + s_{42}/\mu_3 - s_{46}) + s_{45} - s_{44}/\mu_3$$

where

$$\eta_\alpha = -l_3(\mu_\alpha)/l_2(\mu_\alpha), \quad \alpha = 1,2, \qquad \eta_3 = -l_3(\mu_3)/l_4(\mu_3) \qquad (2.7)$$

Equations (2.5-2.7) are valid for plane stress deformation. Plane strain deformation can be treated by a change of compliances

$$s'_{ij} = s_{ij} - s_{i3}s_{j3}/s_{33} \qquad (2.8)$$

Evidently unaware of the Russian work, Eshelby et al. (1953) presented their more elegant formalism based on the Navier-Cauchy equations. Their representation has the same structure as (2.2). However, each of the characteristic roots μ_α, as well as each column of A are solved from the eigenvalue problem

$$\sum_{k=1}^{3}[C_{i1k1} + \mu_\alpha(C_{i1k2} + C_{i2k1}) + \mu_\alpha^2 C_{i2k2}]A_{k\alpha} = 0 \qquad (2.9)$$

Each column of A may be normalized arbitrarily. Thus μ_α are the roots with positive imaginary parts of the sixth-order polynomial

$$\left|C_{i1k1} + \mu_\alpha(C_{i1k2} + C_{i2k1}) + \mu_\alpha^2 C_{i2k2}\right| = 0 \qquad (2.9a)$$

The matrix L is given by

$$L_{i\alpha} = \sum_{k=1}^{3}[C_{i2k1} + \mu_\alpha C_{i2k2}]A_{k\alpha} \qquad (2.10)$$

Plane strain deformation is assumed in (2.9) and (2.10). For plane stress problem the following substitution has to be made

$$c'_{ij} = c_{ij} - c_{i3}c_{j3}/c_{33} \qquad (2.11)$$

Now the question of equivalence of the two formulations arises naturally: are μ_α,

A and L defined in the two entirely different ways actually identical? The answer is yes. It is clear in Eshelby et al.(1953) that the representation (2.2) is *uniquely* determined by the elastic constants of a material (up to the three normalization factors for the matrix A), however one derives it. Therefore the Lekhnitskii derivation gives, explicitly, a specially normalized A. In the remaining of the paper, the basic formula (2.2) will be referred to as the *LES representation*. Fundamental results known in different formalisms will be cited freely as needed.

Assuming that the roots of the characteristic equation (2.3) or (2.9a) (they are equivalent) form three *distinct* complex conjugate pairs, Stroh (1958) showed that A and L are non-singular, and moreover, the matrix B is a positive definite Hermitian matrix, where

$$B = i\,AL^{-1} \qquad (2.12)$$

Here $i = \sqrt{-1}$. The matrix B will appear in various solutions. For convenience, a positive definite Hermitian matrix H involving bimaterial elastic constants is defined as

$$H = B_1 + \bar{B}_2 \qquad (2.13)$$

Here and throughout the paper, (¯) denotes the complex conjugation, and the subscripts 1 and 2 attached to matrices and vectors are reserved exclusively to indicate the two materials.

Under an in-plane coordinate rotation

$$[\Omega_{ij}] = \left[\frac{\partial x_i^*}{\partial x_j}\right] = \begin{bmatrix} \cos\phi & \sin\phi & 0 \\ -\sin\phi & \cos\phi & 0 \\ 0 & 0 & 1 \end{bmatrix} \qquad (2.14)$$

where (*) indicates the new coordinate system, Ting (1982) showed that the characteristic numbers transform as

$$\mu_j^* = (\mu_j \cos\phi - \sin\phi)/(\mu_j \sin\phi + \cos\phi) \qquad (2.15)$$

and furthermore, each column of A and L transforms like a vector, namely

$$A^* = \Omega A, \quad L^* = \Omega L \qquad (2.16)$$

It is obvious from (2.16) that under such an in-plane rotation, B and H defined in this paper transform like second order tensors, i.e.,

$$B^* = \Omega B \Omega^T, \quad H^* = \Omega H \Omega^T \tag{2.17}$$

Some consequences of this transformation will be discussed in the final section.

The LES representation breaks down if the roots degenerate. A well known case is an isotropic material, which was treated extensively by Muskhelishvili (1953a) with his famous complex-variable representation. An analogous representation for a class of degenerate orthotropic materials is presented at the end of this paper. Note, however, the matrices B and H are independent of the normalizing factors for A, and have smooth limits even if A and L become singular. This point will be illustrated in Section 9.

Having listed the LES representation and stated the consistency of the two derivations, we now add some words about a particular method, analytic continuation, which will be used in the paper. Stated below is a trivial observation that makes analytic continuation arguments possible:

A function h(z) of z = x + μy is analytic in y > 0 (or y < 0) for any μ if it is
analytic in y > 0 (or y < 0) for one μ, where μ is any complex number with
positive imaginary part.

Consequently, when talking about a function analytic in the upper (or lower) half plane, one needs *not* refer to its argument, as long as the argument has the form z = x + μy (Imμ > 0).

Without loss of any information, we can and *will* present our solutions by the function vector ϕ(z) defined as

$$\phi(z) = \left[\phi_1(z), \ \phi_2(z), \ \phi_3(z) \right]^T \tag{2.18}$$

where the argument has the form z = x + μy (Imμ > 0). A substitution of z_1, z_2 or z_3 is made for each component function when the field quantities are to be calculated from (2.2). Of particular importance is the following set of vectors defined along the x-axis

$$u(x) = \{u_j(x,0)\} = A\phi(x) + \bar{A}\bar{\phi}(x)$$

$$f(x) = \{f_j(x,0)\} = -L\phi(x) - \bar{L}\bar{\phi}(x)$$

$$\sigma(x) = \{\sigma_{2j}(x,0)\} = L\phi'(x) + \bar{L}\bar{\phi}'(x)$$

(2.19)

3. Line Force and Dislocation in a Homogeneous Medium

The solution for a singularity in an *infinite homogeneous* medium is a building block for many subsequent interaction solutions. Consider a dislocation line in the direction perpendicular to x,y-plane, with Burgers vector b, and consider a line force uniformly distributed along that direction, with force per unit length p. Both singularities are at the point (x_0, y_0). The solution is of the form (Eshelby et al. 1953)

$$\phi_j(z) = d_j \ln(z - s_j), \qquad s_j = x_0 + \mu_j y_0$$

(3.1)

where the coefficient vector $d = \{d_j\}$ is to be determined in terms of b and p. The branch points for the ln-functions are at s_j, while, for definiteness, the branch cuts are chosen in the negative x-direction, and the phase angle is measured from the positive x-direction.

With the aid of (2.2), by definition one has

$$b = u^+ - u^- = 2\pi i (Ad - \bar{A}\bar{d}), \qquad p = f^- - f^* = 2\pi i (Ld - \bar{L}\bar{d})$$

(3.2)

Solving for d from the above algebraic equations, one finds

$$d = (2\pi)^{-1} L^{-1} (B + \bar{B})^{-1} b - (2\pi)^{-1} A^{-1} (B^{-1} + \bar{B}^{-1})^{-1} p$$

(3.3)

Hence a complete description of the solution is achieved.

In the above, the subscripts of z are dropped with the understanding mentioned at the end of the last section. When calculating stresses and displacements from (2.2), one needs to reinterpret z by z_j accordingly. The merit of this scheme will be demonstrated in the next section.

Several well-known results are derived below to familiarize ourselves with the

notation. Let the dislocation sit at the origin ($b \neq 0$, $p = 0$). The complex potentials are given by

$$L\phi(z) = (2\pi)^{-1}(B + \bar{B})^{-1}b \ln z \tag{3.4}$$

The traction along the x-axis, calculated from (2.19), is given by

$$\sigma(x) = \frac{1}{2\pi}(B + \bar{B})^{-1}b(\frac{1}{x + 0i} + \frac{1}{x - 0i}) \tag{3.5}$$

In deriving (3.5) one may imagine that the dislocation is infinitesimally *off* the x-axis (upper or below). The notation $x + 0i$ represents a point approaching the x-axis from the upper half-plane, with a similar convention for $x - 0i$. This distinction was suggested by Willis (1971), which is quite crucial when the dislocation solution is used as the kernel to formulate integral equations for cracks, especially for interface cracks. The strain energy of a dislocation is thereby

$$U = \frac{1}{2}b^T \int_r^R \sigma(x) dx = \frac{1}{2\pi}b^T(B + \bar{B})^{-1}b \ln \frac{R}{r} \tag{3.6}$$

The strain energy around a dislocation was first derived by Stroh (1958), and a crack problem was formulated in the same paper using Fourier transforms. However, with the aid of (3.5), the same crack problem can be conveniently simulated by an array of dislocations, as shown in Willis (1971).

4. A SINGULARITY IN A BIMATERIAL

Now the interaction problem in Fig. 1a is taken up. Suppose we know, somehow, the solution for an isolated singularity in an infinite homogeneous medium, designated as $\phi_0(z)$, not necessarily of the form (3.1). The aim is to construct the solution for the same singularity embedded in the bonded inhomogeneous system. Without loss of generality, the singularity is taken to be in material 2, and thus the material constants involved in $\phi_0(z)$ are for material 2. This problem was posed and solved by Tucker (1969), and studied recently by Tewary et al. (1989b). Adapted below is a derivation consistent with the

present notation. The results will be used in Section 7 to examine singularity/interface-crack interactions.

Write the solution for the two blocks formally as

$$\phi(z) = \begin{cases} \phi^1(z), & z \in 1 \\ \phi^2(z) + \phi_0(z), & z \in 2 \end{cases}$$ (4.1)

where z is a complex-variable of the form $z = x + \mu y$ (Im $\mu > 0$). Here and throughout the paper, $z \in 1$ means $y > 0$, and $z \in 2$ means $y < 0$. The task is to solve for $\phi^1(z)$ and $\phi^2(z)$, analytic in upper and lower half planes, respectively, in terms of $\phi_0(z)$. From (2.19), the continuity of forces across the interface requires that

$$L_1 \phi^1(x) + \bar{L}_1 \bar{\phi}^1(x) = L_2 [\phi^2(x) + \phi_0(x)] + \bar{L}_2 [\bar{\phi}^2(x) + \bar{\phi}_0(x)]$$ (4.2)

Rearranging the above one obtains

$$L_1 \phi^1(x) - \bar{L}_2 \bar{\phi}^2(x) - L_2 \phi_0(x) = L_2 \phi^2(x) - \bar{L}_1 \bar{\phi}^1(x) - \bar{L}_2 \bar{\phi}_0(x)$$ (4.3)

Equation (4.3) holds along the whole x-axis. Moreover, the functions at the left-hand side are analytic in the upper half plane, while those on the right-hand side are analytic in the lower half plane. By standard analytic continuation arguments one reaches

$$L_1 \phi^1(z) - \bar{L}_2 \bar{\phi}^2(z) - L_2 \phi_0(z) = 0, \qquad z \in 1$$ (4.4)

Continuity of the displacements across the interface, with the same arguments, gives

$$A_1 \phi^1(z) - \bar{A}_2 \bar{\phi}^2(z) - A_2 \phi_0(z) = 0, \qquad z \in 1$$ (4.5)

Solving from (4.3) and (4.4) for $\phi^1(z)$ and $\phi^2(z)$, one finds

$$\phi^1(z) = L_1^{-1} H^{-1} (\bar{B}_2 + B_2) L_2 \phi_0(z), \qquad z \in 1$$ (4.6)

$$\phi^2(z) = L_2^{-1} \bar{H}^{-1} (\bar{B}_2 - \bar{B}_1) L_2 \bar{\phi}_0(z), \qquad z \in 2$$

Substitution into (4.1) gives the complete solution. When calculating the field quantities via (2.2), one has to substitute z by $z_j = x + \mu_j y$ respectively for each component of $\phi(z)$ of (4.1). Notice that this relation to *construct* a bimaterial solution from a one-material

solution is universal in that no specific information about the singularity is needed.

A singularity in a half-space interacting with a traction-free surface, $y = 0$, can be constructed similarly on the basis of the infinite plane solution, $\phi_0(z)$. The result is

$$\phi(z) = \phi_0(z) - L^{-1}\bar{L}\bar{\phi}_0(z) \tag{4.7}$$

Another interesting case is a singularity in a half plane interacting with a rigidly held surface on $y = 0$. The solution is

$$\phi(z) = \phi_0(z) - A^{-1}\bar{A}\bar{\phi}_0(z) \tag{4.8}$$

The general solution developed above has been used by Gupta and Suo (1989) to study a crack running perpendicular into an interface and crack deflection at an interface. Dislocation solution in a half space was used by Suo (1988b) as kernels in an integral equation formulation of delamination in composites. Here we include several more elementary examples to further familiarize ourselves with notation.

Let a dislocation sit on a bimaterial interface at the origin, with Burgers vector **b**. The corresponding solution for a homogeneous body, $\phi_0(z)$, is given by (3.4), with the elastic constants for medium 2. The solution for bimaterial system is thereby

$$L_1\phi_1(z) = L_2\bar{\phi}_2(z) = (2\pi)^{-1}H^{-1}b\ln z \tag{4.9}$$

A direct calculation using (2.19) gives the traction along the interface

$$\sigma(x) = \frac{1}{2\pi}\left(\frac{H^{-1}}{x+0i} + \frac{\bar{H}^{-1}}{x-0i}\right)b \tag{4.10}$$

The strain energy for a dislocation on the interface is then

$$U = \frac{1}{2}b^T\int_r^R \sigma(x)\,dx = \frac{1}{2\pi}b^T H^{-1}b\ln\frac{R}{r} \tag{4.11}$$

Equation (4.10) was derived by Willis (1971) with the Fourier transform, and used to formulate an interfacial crack problem. Different expressions for the strain energy of a dislocation sitting on the interface analogous can be found in the literature. The present expression seems to agree with a somewhat messy one presented in Bacon et al. (1979,

p.233, also see refs. cited there)

5. INTERFACE CRACK: NON-OSCILLATORY FIELDS

Ting (1986) showed that an interface crack tip is absent of oscillatory behaviors if H is real (his notation is different from that used here). This turns out to be a necessary and sufficient condition (Qu and Bassani 1988). The structure of the crack tip fields and the solution of several crack problems under this condition are strikingly simple. Such a condition at a first glance is quite artificial, i.e., it can only be satisfied by two identical materials and accidentally by some pairs and/or orientations of dissimilar materials, as discussed in Anderson (1988) and Qu and Bassani (1988). However, from the special cases discussed in later sections, one finds that the imaginary part of H is very small for many material pairs. In practice one may choose to ignore the imaginary part of H, which significantly simplifies the approach to interface fracture, as will be clear in the development of this section. This idea, proposed earlier by several authors for isotropic material pairs, will be elaborated on in the final section.

We begin with an asymptotic problem. Consider a semi-infinite, traction-free crack lying along the interface between two homogeneous anisotropic half spaces, with material 1 above, and material 2 below. The two half-spaces are bonded along the positive x-axis and the crack is along the negative x-axis. No specific length and load are present in this problem. Singular fields are sought to satisfy continuity of traction and displacement vectors $\sigma(x)$ and $u(x)$ (defined in (2.19) for each material) across the bonded portion of the interface, as well as traction-free condition along the cracked portion. This is a homogeneous boundary value problem, or an eigenvalue problem.

Let the vector potentials defined in (2.18) for the two blocks be $\phi_1(z)$ and $\phi_2(z)$, respectively. Obviously the traction $\sigma(x)$ defined in (2.19) is continuous across the whole x-axis, *both* the bonded and cracked portions, so that

$$L_1\phi_1'(x) + L_1\bar{\phi}_1'(x) = L_2\phi_2'(x) + L_2\bar{\phi}_2'(x) \tag{5.1}$$

To facilitate the analytic continuation, eqn.(5.1) is rearranged as

$$L_1\phi_1'(x) - L_2\bar{\phi}_2'(x) = L_2\phi_2'(x) - L_1\bar{\phi}_1'(x) \tag{5.2}$$

Equation (5.2) implies that

$$L_1\phi_1'(z) = L_2\bar{\phi}_2'(z), \quad z \in 1 \tag{5.3}$$

Define the displacement jump across the interface as

$$\delta(x) = u(x,0^+) - u(x,0^-) \tag{5.4}$$

With the aid of (5.3), a direct calculation gives

$$\sigma(x) = L_1\phi_1'(x) + L_2\phi_2'(x) \tag{5.5}$$

and

$$i\,\delta'(x) = HL_1\phi_1'(x) - \overline{H}L_2\phi_2'(x) \tag{5.6}$$

A very simple solution can be obtained if the Hermitian matrix H is *real*, that is

$$H = \overline{H} \tag{5.7}$$

Continuity of the displacement across the bonded interface, as inferred from (5.6), implies that $L_1\phi_1'(z)$ and $L_2\phi_2'(z)$ can be analytically extended to the whole plane except on the crack line and satisfy

$$h(z) = L_1\phi_1'(z) = L_2\phi_2'(z), \quad z \in C \tag{5.8}$$

where $h(z)$ is introduced for convenience. Here and later, C is denoted as the crack line (or union of crack lines if several cracks are considered). The traction-free condition on the crack, using (5.5) and (5.8), leads to a homogeneous Hilbert problem

$$h^+(x) + h^-(x) = 0, \quad z \in C \tag{5.9}$$

An obviously admissible singular solution to (5.9) is

$$h(z) = (2\pi z)^{-1/2}k/2 \tag{5.10}$$

where the branch cut for $\sqrt{z}$ is along the crack line. The undetermined constant vector k

appears to consist of three complex constants. However, upon requiring traction to be real, one concludes that k is a *real* vector. The normalization adopted in (5.10) is consistent with the conventional definition of stress intensity factors, with the identification

$$k = [K_I, K_I, K_{III}]^T \tag{5.11}$$

as will be clear in (5.13) below.

The complete asymptotic solution is then given by

$$L_1 \phi_1'(z) = L_2 \phi_2'(z) = h(z) = (2\pi z)^{-1/2} k / 2 \tag{5.12}$$

Assuming L_1 and L_2 are non-singular, one can readily obtain the elastic potentials for the two half spaces. The stresses and displacements can be calculated using the basic representation (2.2), with z properly reinterpreted of course. Examining (5.12) one immediately discovers that the crack tip fields (stresses, displacements) in each block do not depend on the elastic constants of the other block. In other words, the near-tip fields in each block are identical to those of a crack in the corresponding homogeneous anisotropic medium. The latter fields have been completely tabulated in Sih et al. (1965) and Hoenig (1982).

The traction in the interface a distance r *ahead* of the crack tip, and the displacement jump a distance r *behind* of the crack tip, calculated from (5.5) and (5.6), respectively, are given by

$$\sigma(r) = (2\pi r)^{-1/2} k, \qquad \delta(r) = (2r/\pi)^{1/2} Hk \tag{5.13}$$

The energy release per unit newly created crack area, i.e.,

$$G \equiv \frac{1}{2\Delta} \int_0^\Delta \sigma^T (\Delta - r) \delta(r) dr \tag{5.14}$$

where Δ is an *arbitrary* length scale, is thereby

$$G = k^T H k / 4 \tag{5.15}$$

In obtaining (5.15) a special value of the beta function has been used

$$\int_0^1 \left(\frac{t}{1-t}\right)^q dt = \frac{q\pi}{\sin q\pi}, \quad (|\text{Re } q| < 1) \tag{5.16}$$

with $q = 1/2$. This identity will be invoked again in the next section.

Comparison of the strain energy of a dislocation on the interface, eqn. (4.12), and the energy release rate at a crack tip, eqn. (5.15), leads to a simple relation. Both are quadratic forms, and the product of the matrices involved in the two expressions is $1/8\pi$. This relation, for the special case of a crack in a homogeneous medium, was presented by Stroh (1958), Barnett and Asaro (1972). The problem in the present context was formulated earlier by Bassani and Qu (1988) in a different approach.

Having obtained a *complete* description of the asymptotic fields, we turn our attention to a class of crack problems. Consider a set of collinear cracks along the interface between two dissimilar anisotropic half-spaces, with self-equilibrated traction $\sigma_0(x)$ prescribed on the crack faces. Suppose there are n finite cracks in the intervals (a_j, b_j), $j = 1, 2, ..., n$ and two semi-infinite cracks in the intervals $(-\infty, b_0)$ and $(a_0, +\infty)$. The Hilbert problem (5.9) is replaced by a non-homogeneous one

$$h^+(x) + h^-(x) = \sigma_0(x), \qquad x \in C \tag{5.17}$$

where C is the union of all cracks. Equation (5.17) does not have a unique solution. Several auxiliary conditions needed are: $h(z)$ approaches zero faster than $1/z$ as $|z|$ goes to infinity; $h(z)$ has a square root singularity as in (5.10) at the crack tips; and moreover, the net Burger vector for each of the n finite cracks is zero. From (5.6), this latter statement leads to

$$\int_{a_j}^{b_j} [h^+(x) - h^-(x)] dx = 0, \quad j = 1, 2, ..., n \tag{5.18}$$

Notice that the governing equations and the auxiliary conditions for the vector function $h(z)$ are independent of any elastic constants, and *exactly the same* as those for

the mode III potentials in an *isotropic one-material*. A straightforward method thus emerges to *construct* the complete solutions for the above interface crack problems, without much work, from the well-known mode III solutions for isotropic one-materials: each component of the vector function $h(z)$ is the same (except for a factor of $-1/2$) as the mode III potential for collinear cracks in a homogeneous isotropic material, and the latter can be found in Rice (1968); knowing $h(z)$, one can obtain the complete solutions for the two blocks, $\phi_1(z)$ and $\phi_2(z)$, from (5.8). In particular, the stress intensity factors, normalized as (5.10) or (5.13), are *identical* to the classical results for the same crack configuration in an isotropic one-material. Listed below are the general solutions so constructed for the collinear interfacial cracks.

$$h(z) = \frac{\chi_0(z)}{2\pi i} \int_C \frac{\sigma_0(x)dx}{\chi_0^+(x)(x-z)} + P(z)\chi_0(z)$$

(5.19)

where

$$\chi_0(z) = \prod_{j=0}^{n}(z - a_j)^{-1/2}(z - b_j)^{-1/2}$$

(5.20)

Here the branch cuts are chosen along the crack lines so that the product for each finite crack behaves as $1/z$ for large z. And $P(z)$ is a vector involving three polynomials, which should be chosen to satisfy the auxiliary conditions. The interfacial crack solutions for the two important configurations depicted in Fig. 2 are given below (cf. Rice 1968, p. 220).

   i) Semi-infinite crack

$$\chi_0(z) = z^{-1/2}, \quad P(z) = 0$$

(5.21)

The solutions for the two blocks are then given by

$$L_1\phi_1'(z) = L_2\phi_2'(z) = \frac{1}{2\pi\sqrt{z}} \int_{-\infty}^{0} \frac{\sqrt{-x}}{(x-z)}\sigma_0(x)dx$$

(5.22)

Comparing (5.21) with the asymptotic field (5.10), one finds the stress intensity factors

$$k = -\sqrt{\frac{2}{\pi}} \int_{-\infty}^{0} \frac{\sigma_0(x)\,dx}{\sqrt{-x}}$$
(5.23)

ii) Finite crack in the interval (-a, a)

$$\chi_0(z) = (z^2 - a^2)^{-1/2}, \quad P(z) = 0$$
(5.24)

The full solution is given by

$$L_1\phi_1'(z) = L_2\phi_2'(z) = \frac{1}{2\pi\sqrt{z^2 - a^2}} \int_{-a}^{a} \frac{\sqrt{a^2 - x^2}}{(x - z)} \sigma_0(x)\,dx$$
(5.25)

The stress intensity factors are

$$k = -\frac{1}{\sqrt{\pi a}} \int_{-a}^{a} \sqrt{\frac{a + x}{a - x}} \, \sigma_0(x)\,dx$$
(5.26)

The solution to the second problem listed above was obtained earlier by Bassani and Qu (1988) with an integral transform. An exact solution of stress intensity factors for symmetric tilt double-layers has been obtained recently (Suo 1989), which rigorously calibrates some fracture specimens consisting of bicrystals.

6. INTERFACE CRACK: OSCILLATORY FIELDS

In this section, we examine the general case when H is *not* real. The asymptotic fields associated with a traction-free, semi-infinite interface crack will be considered first. It is shown that the mathematical structure of the crack-tip behavior can be decomposed into two types of singular fields. One shows a mixture of singularities $r^{-1/2\pm i\epsilon}$ in stresses, and the other has a $r^{-1/2}$ singularity in stresses. The two fields are scaled by a complex and a real stress intensity factors, K and K_3, respectively. In standard notation ϵ, referred to as the *oscillatory index*, is a nondimensional real number measuring an aspect of elastic dissimilarity of the two materials. The collinear crack problems are also worked out for complex H, which provide a collection of stress intensity factors.

The same collinear crack problems have been solved by several authors (Gotoh

1967, Clements 1971, Willis 1971 and Tewary 1989a), and can be dated back even earlier if one accepts some of the contact problems in the book by Galin (1961) as limiting cases of interface crack problems (rigid/elastic interfaces). Yet these earlier authors seemed to have missed the inherent simplicity of the solutions, and thus they have not been able to interpret their results in the spirit of fracture mechanics. In particular, the 'stress concentration factor' used in these earlier works is a complex column vector with *six* real quantities. We will formulate a derivation that allows one to grasp the simple mathematical structure and read off the stress intensity factors trivially. The method used here, however, is actually not new. Mathematically, it is a variant of those contained in the above references, and was treated thoroughly in general terms by Muskhelishvili (1953b).

The results in the above section up to the introduction of $H = \bar{H}$ in (5.7) are still valid. Continuity of displacement across the bonded interface requires, from eqn. (5.6), the existence of a function h(z) analytic in the whole plane except on the crack lines, such that

$$h(z) = L_1 \phi_1{}'(z) = H^{-1} \bar{H} L_2 \phi_2{}'(z), \qquad z \notin C \tag{6.1}$$

Hence one can focus on $h(z)$, and once $h(z)$ is obtained the full field solution is given by (6.1). In terms of h(z), the traction (5.5) and displacement jump (5.6) can be expressed as

$$\sigma(x) = h^+(x) + \bar{H}^{-1} H h^-(x) \tag{6.2}$$

and

$$i\,\delta'(x) = H\left[h^+(x) - h^-(x)\right] \tag{6.3}$$

Consider the asymptotic problem first. With (6.2), the traction-free condition gives

$$h^+(x) + \bar{H}^{-1} H h^-(x) = 0, \qquad z \in C \tag{6.4}$$

This is a homogeneous Hilbert problem. Let a solution to (6.4) be of the form

$$h(z) = w z^{-1/2 + i\varepsilon} \tag{6.5}$$

where w is a constant vector and ε a constant number, both to be determined. The branch cut for the multi-valued function in (6.5) is chosen to be along the crack line $x < 0$, and the

phase angle of z is measured from the positive x-axis. Substituting (6.5) into (6.4), one obtains an algebraic eigenvalue problem

$$\bar{H}w = e^{2\pi\varepsilon} Hw \tag{6.6}$$

It turns out that the specific structure of eigenpairs of this problem is the key to understanding the results below. We insert following digression to explain this structure.

The following properties hold for a positive definite Hermitian matrix H: the eigenvalue $e^{2\pi\varepsilon}$ is positive, and thus ε is real; if (ε, w) is an eigenpair so is $(-\varepsilon, \bar{w})$, and consequently, since there are only three eigenvalues, $\varepsilon = 0$ is an eigenvalue and the associated eigenvector can be chosen to be real. Therefore, a real number ε ($\neq 0$ iff $H \neq \bar{H}$), a complex vector w, and a real vector w_3 can be found to form three distinct eigenpairs

$$(\varepsilon, w), \quad (-\varepsilon, \bar{w}), \quad (0, w_3) \tag{6.7}$$

satisfying

$$\bar{H}w = e^{2\pi\varepsilon} Hw, \quad \bar{H}w_3 = Hw_3 \tag{6.8}$$

Any two eigenvectors are orthogonal in the sense

$$w^T Hw = w^T Hw_3 = \bar{w}^T Hw_3 = 0 \tag{6.9}$$

Orthogonality conditions involving $\bar{H}$ can be obtained by taking the complex conjugation of the above.

The two vectors w and w_3 are fully determined by the eigenvalue problem except for a complex and a real normalizing constants, respectively. In general they should be normalized to be dimensionless to give conventional dimensions for stress intensity factors (see 6.16 below). We choose to leave the normalization of these vectors otherwise unspecified at this point, since the results presented below are unaffected by the specific normalization.

Every complex-valued vector g can be represented as a linear combination of the

three eigenvectors, that is

$$\mathbf{g} = g_1 \mathbf{w} + g_2 \bar{\mathbf{w}} + g_3 \mathbf{w}_3 \tag{6.10}$$

where the complex numbers g_l can be thought of as the components of vector $\mathbf{g}$, and evaluated by taking inner products, i.e.,

$$g_1 = \frac{\bar{\mathbf{w}}^T H \mathbf{g}}{\bar{\mathbf{w}}^T H \mathbf{w}}, \quad g_2 = \frac{\mathbf{w}^T H \mathbf{g}}{\mathbf{w}^T H \bar{\mathbf{w}}}, \quad g_3 = \frac{\mathbf{w}_3^T H \mathbf{g}}{\mathbf{w}_3^T H \mathbf{w}_3} \tag{6.11}$$

When g is real-valued (for example, g is the traction in the interface or the prescribed traction along the crack faces), one may confirm that $g_2 = \bar{g}_1$, and g_3 is a real number.

Now we return to the main problem. The admissible singular solution to (6.4) is then a linear combination of the three homogeneous solutions of form (6.5):

$$h(z) = z^{-1/2}[a\,\mathbf{w} z^{i\varepsilon} + b\bar{\mathbf{w}} z^{-i\varepsilon} + c\,\mathbf{w}_3] \tag{6.12}$$

where a, b and c are three undetermined complex numbers. Substituting (6.12) into (6.2) and requiring traction to be real along the interface, one concludes

$$a = e^{2\pi\varepsilon}\,\bar{b}, \quad c = real \tag{6.13}$$

thus, only *one* complex constant and *one* real constant are independent, chosen to be K and K_3, respectively, such that

$$h(z) = \frac{e^{\pi\varepsilon} K z^{i\varepsilon} \mathbf{w} + e^{-\pi\varepsilon} \bar{K} z^{-i\varepsilon} \bar{\mathbf{w}}}{2\sqrt{2\pi z}\,\cosh \pi\varepsilon} + \frac{K_3 \mathbf{w}_3}{2\sqrt{2\pi z}} \tag{6.14}$$

Other constants in (6.14) are embedded in a manner similar to the isotropic bimaterial crack tip fields (e.g., Rice 1988). The potentials for the two half spaces are thereby

$$\mathbf{L}_1 \phi_1'(z) = \frac{e^{\pi\varepsilon} K z^{i\varepsilon} \mathbf{w} + e^{-\pi\varepsilon} \bar{K} z^{-i\varepsilon} \bar{\mathbf{w}}}{2\sqrt{2\pi z}\,\cosh \pi\varepsilon} + \frac{K_3 \mathbf{w}_3}{2\sqrt{2\pi z}} \tag{6.15}$$

$$\mathbf{L}_2 \phi_2'(z) = \frac{e^{-\pi\varepsilon} K z^{i\varepsilon} \mathbf{w} + e^{+\pi\varepsilon} \bar{K} z^{-i\varepsilon} \bar{\mathbf{w}}}{2\sqrt{2\pi z}\,\cosh \pi\varepsilon} + \frac{K_3 \mathbf{w}_3}{2\sqrt{2\pi z}}$$

It is interesting to note that the structure of the singular fields is the same for the two half spaces, except for a change of the combination $\pi\varepsilon$ to $-\pi\varepsilon$ everywhere.

Substitution of (6.14) into (6.2) gives the traction in the bonded interface a distance

r ahead of the crack tip

$$\sigma(r) = (2\pi r)^{-1/2}[Kr^{i\varepsilon}w + \bar{K}r^{-i\varepsilon}\bar{w} + K_3 w_3]$$ (6.16)

In words it reads that the interface traction at each fixed point r can be decomposed into two components: one is along w_3 and the other is in the plane spanned by Re[w] and Im[w]. The components, in the sense of (6.11), are

$$\sigma_1(r) = \frac{\bar{w}^T H\sigma(r)}{\bar{w}^T Hw} = \frac{Kr^{i\varepsilon}}{\sqrt{2\pi}}, \quad \sigma_3(r) = \frac{w_3^T H\sigma(r)}{w_3^T Hw_3} = \frac{K_3}{\sqrt{2\pi}}$$ (6.17)

where σ_3 is the w_3 component and σ_1 is the (complex) planar component. These equations may be taken as defining equations for the complex K and real K_3. As r approaches the tip, the w_3 component has a square root singularity and the planar component is oscillatory, with K_3 and K measuring their intensities, respectively. The results are clearly the analog of the corresponding ones for isotropic bimaterial. For an isotropic bimaterial, $\sigma_1(r) = \sigma_{yy} + i\sigma_{xy}$ is the in-plane traction, and $\sigma_3(r)$ is the anti-plane traction.

The displacement jump a distance r behind the tip is

$$\delta(r) = (H + \bar{H})\sqrt{\frac{r}{2\pi}}\left[\frac{Kr^{i\varepsilon}w}{(1 + 2i\varepsilon)\cosh \pi\varepsilon} + \frac{\bar{K}r^{-i\varepsilon}\bar{w}}{(1 - 2i\varepsilon)\cosh \pi\varepsilon} + K_3 w_3\right]$$ (6.18)

Due to the anisotropy, the matrix $(H + \bar{H})$ may rotate the base vectors in (6.18), implying that non-oscillatory direction of the displacement jump may not coincide with that of the interface traction, and similarly for the oscillatory planes.

The energy release rate defined in (5.14) is

$$G = \bar{w}^T(H + \bar{H})w|K|^2/(4\cosh^2 \pi\varepsilon) + w_3^T(H + \bar{H})w_3 K_3^2/8$$ (6.19)

In deriving this the integral identity (5.16) has been used with q = 1/2, 1/2 ± iε.

The structure of the near-tip fields around an interface crack has been identified, with only one real and one complex normalizing factors K_3 and K. In principle, for a given boundary value problem, these factors should be determined by the external geometry and load, and can be used the similar way as the conventional stress intensity factors in Irwin's

fracture mechanics.

Remember that a normalization to the two eigenvectors has not been assigned yet. The different choices of normalization affect the definition of stress intensity factors by a real factor to K_3 and a complex factor to K. As clearly indicated by an example in section 9, it is impossible to find a specific normalization such that the stress intensity factors so defined reduce to the classical stress intensity factors for a crack tip in a homogeneous, anisotropic medium as the two materials become the same. A tentative normalization is proposed as follows, which recovers the stress intensity factor definition for isotropic bimaterials

$$w = [- i/2, *, *]^T, \qquad w_3 = [*, *, 1]^T \tag{6.20}$$

where (*) signifies numbers determined by the eigenvalue problem (6.6). Note this normalization may not always be valid. For example, when w_3 is an in-plane vector containing no anti-plane components, (6.20) is invalid.

Now consider the collinear crack problems specified in Sec. 5 for the complex H. From (6.2), the prescribed traction $\sigma_0(x)$ on the crack lines C results in the Hilbert problem

$$h^+(x) + \bar{H}^{-1} H h^-(x) = \sigma_0(x), \qquad x \in C \tag{6.21}$$

Writing the above equation in its components, or equivalently, taking the inner product of (6.21) with $\bar{w}^T H$, $w^T H$ and $w_3^T H$, one obtains

$$\left. \begin{array}{l} h_1^+(x) + e^{-2\pi\varepsilon} h_1^-(x) = \sigma_{01}(x) \\ h_2^+(x) + e^{+2\pi\varepsilon} h_2^-(x) = \bar{\sigma}_{01}(x) \\ h_3^+(x) + h_3^-(x) = \sigma_{03}(x) \end{array} \right\}, \qquad x \in C \tag{6.22}$$

The components are defined in the sense of (6.10) and (6.11). Note that these equations are decoupled. Furthermore, since they contain no explicit material dependence besides ε, one may conjecture that they should be identical to those for isotropic bimaterials. Indeed they are (cf. England 1965, Erdogan 1965, Rice and Sih 1965). Constructed from the known

solutions for isotropic bimaterials, the complete solution is

$$h(z) = h_1(z)\vec{w} + h_2(z)\bar{\vec{w}} + h_3(z)\vec{w}_3 \tag{6.23}$$

where

$$h_1(z) = \frac{\chi(z)}{2\pi i}\int_C \frac{\sigma_{01}(x)dx}{\chi^+(x)(x-z)}$$

$$h_2(z) = \frac{\bar{\chi}(z)}{2\pi i}\int_C \frac{\bar{\sigma}_{01}(x)dx}{\bar{\chi}^+(x)(x-z)} \tag{6.24}$$

$$h_3(z) = \frac{\chi_0(z)}{2\pi i}\int_C \frac{\sigma_{03}(x)dx}{\chi_0^+(x)(x-z)}$$

In the above $\chi_0(z)$ is the same as that of (5.20) and $\chi(z)$ is the standard function used in isotropic bimaterial interface crack problems, and is defined as

$$\chi(z) = \prod_{j=0}^{n}(z - a_j)^{-1/2-i\epsilon}(z - b_j)^{-1/2+i\epsilon} \tag{6.25}$$

Knowing $h(z)$, one can obtain the full field solution via (6.1).

The stress intensity factors can by easily extracted by comparison with the asymptotic solution. As a matter of fact, by construction the answer should have the same structure as their isotropic bimaterial counterparts. For example, the stress intensity factors for a *semi-infinite crack* are

$$K_3 = -(2/\pi)^{1/2}\int_{-\infty}^{0}(-x)^{-1/2}\sigma_{03}(x)dx \tag{6.26}$$

$$K = -(2/\pi)^{1/2}\cosh \pi\epsilon \int_{-\infty}^{0}(-x)^{-1/2-i\epsilon}\sigma_{01}(x)dx$$

and for an *internal crack* the stress intensity factors are

$$K_3 = -\frac{1}{\sqrt{\pi a}}\int_{-a}^{a}\sqrt{\frac{a+x}{a-x}}\,\sigma_{03}(x)dx \tag{6.27}$$

$$K = -\sqrt{\frac{2}{\pi}}\cosh \pi\epsilon\,(2a)^{-1/2-i\epsilon}\int_{-a}^{a}\left(\frac{a+x}{a-x}\right)^{1/2+i\epsilon}\sigma_{01}(x)dx$$

where the complex σ_{01} and real σ_{03} are the components of the applied traction σ_0 in the sense of (6.11). Without actually re-solving the problems, one can easily write done any other solutions for anisotropic bimaterials, providing one knows the solutions for an isotropic bimaterial.

Notice that in the above the auxiliary conditions discussed in § 5, as well as an arbitrary polynomial in each equation of (6.24), have been omitted. One may confirm that the auxiliary conditions are identical to those for isotropic bimaterials.

7. SINGULARITY/INTERFACE-CRACK INTERACTION

Now the interaction problem illustrated in Fig. 1c can be readily solved by the superposition scheme illustrated in Fig. 1. The only relatively non-trivial part is the integral involved in the process. We will not pursue the interaction problem for the general singularity, as has been done for isotropic materials in Suo (1988a). Instead, we will concentrate on a special problem to illustrate the process. The technique, though, is generally applicable.

Consider, for example, a dislocation or a line force, embedded in material 2, interacting with the traction-free semi-infinite interface crack. The non-oscillatory condition $H = \bar{H}$ is assumed. For the problem in Fig. 1a, from (4.7) the traction in the interface is

$$\sigma(x) = C\phi_0'(x) + \bar{C}\bar{\phi}_0'(x) \tag{7.1}$$

where $\phi_0(z)$ is of the form (3.1), and C is an abbreviation of

$$C = H^{-1}(B_2 + \bar{B}_2)L_2 \quad . \tag{7.2}$$

The negative of this traction is prescribed on the crack faces in Fig. 1b. The solution for this problem has been examined in Section 5. The key is to evaluate the integral (5.19). In the present context, it is

$$h(z) = - \frac{\chi_0(z)}{2\pi i} \int_{-\infty}^{0} \frac{C\phi_0'(x) + \bar{C}\bar{\phi}_0'(x)}{\chi_0^+(x)(x-z)} dx \tag{7.3}$$

where $\chi_0(z) = 1/\sqrt{z}$, with the branch cut along the crack. The integral can be evaluated by a contour integral (for detail see Suo 1988a). The final result is

$$h(z) = -\left[C\phi_0'(z) + \bar{C}\bar{\phi}_0'(z) - z^{-1/2}CD\phi_0'(z) - z^{-1/2}\bar{C}\bar{D}\bar{\phi}_0'(z) \right]/2 \tag{7.4}$$

$$D = diag\left[\sqrt{s_1}, \sqrt{s_2}, \sqrt{s_3} \right]$$

where s_j are defined in (3.1) and *diag*[ ] denotes a diagonal matrix. The complete solution can be obtained using (5.8). Comparison of (7.4) and (5.10) gives the stress intensity factors induced by a dislocation or line force

$$k = -2(2\pi)^{1/2} Re\left\{ H^{-1}(B_2 + \bar{B}_2)L_2\left[d_1 s_1^{-1/2}, d_2 s_2^{-1/2}, d_3 s_3^{-1/2} \right]^T \right\} \tag{7.5}$$

where d_j and s_j are defined in (3.1) with elastic constants for material 2.

The dislocation interacting with a crack was treated in a homogeneous medium by Atkinson (1966). The Green function for an internal interface crack was obtained recently by Tewary et al. (1989a).

8. ANTIPLANE FIELD

Consider materials with x, y-plane as a mirror plane, in which the in-plane and antiplane deformations are decoupled. They will be treated separately in this and the next section.

In equation (2.3), $l_3(\mu)$ is identically zero for a material with such a symmetry. The characteristic equation for antiplane deformation thus becomes

$$l_2(\mu) \equiv s_{55}\mu^2 - 2s_{45}\mu + s_{44} = 0 \tag{8.1}$$

The expression $s_{44}s_{55} - (s_{45})^2$, a principal minor of the compliance matrix, is positive. Hence there are two complex conjugate roots to (8.1). According to the convention the

root with positive imaginary part is chosen, i.e.,

$$\mu_3 = s_{45}/s_{55} + i\left(s_{44}s_{55} - s_{45}^2\right)^{1/2}/s_{55} \tag{8.2}$$

Only one holomorphic function $\phi(z_3)$ is needed to represent antiplane deformations, with $z_3 = x + \mu_3 y$. The LES representation (2.2) reduces to

$$u_3 = 2\text{Re}[A\phi(z_3)], \quad f_3 = -2\text{Re}[L\phi(z_3)] \tag{8.3}$$

$$\sigma_{23} = 2\text{Re}[L\phi'(z_3)], \quad \sigma_{13} = -2\text{Re}[L\mu_3\phi'(z_3)]$$

Now all 3×3 matrices defined in Section 2 reduce to scalars. Keeping the same notation, one has

$$L = -1, \quad A = iB, \quad B = \left(s_{44}s_{55} - s_{45}^2\right)^{1/2} \tag{8.4}$$

Clearly, B can be interpreted as the inverse of an equivalent shear modulus, which reduces to the standard shear modulus as the material degenerates to be transversely cubic, or tetragonal. Subscripts 1 and 2 will be attached to B to signify the two materials. Consistent with Ting's (1982) general results, B is an invariant under an in-plane rotation. The bimaterial matrix, now a scalar, $H = B_1 + B_2$, is identically real! Consequently, for the decoupled deformations, the mode III near-tip field of an interfacial crack is non-oscillatory.

The solution for a screw dislocation with Burgers vector b, and a line shear force with density p at point (x_0, y_0) in an infinite homogeneous medium is

$$\phi(z) = d\ln(z - s_3), \quad s_3 = x_0 + \mu_3 y \tag{8.5}$$

$$d = -(4\pi B)^{-1}b + i(4\pi)^{-1}p$$

The stresses and displacements can be calculated using (8.3) and (8.5) with $z = z_3$.

The potential for a singularity in two bonded blocks, embedded in material 2, say, can be constructed by the potential, $\phi_0(z)$, for the same singularity in an infinite homogeneous medium as

$$\phi(z) = \begin{cases} 2B_2/(B_1 + B_2)\phi_0(z), & z \in 1 \\ \phi_0(z) + (B_2 - B_1)/(B_1 + B_2)\overline{\phi}_0(z), & z \in 2 \end{cases} \tag{8.6}$$

The energy of a screw dislocation with Burgers vector b lying on the interface is

$$U = \left[2\pi(B_1 + B_2)\right]^{-1} b^2 \ln(R/r) \tag{8.7}$$

Near-tip fields for an interfacial crack in the two blocks, respectively, are

$$\phi_1'(z) = \phi_2'(z) = -(2\pi z)^{-1/2} K_{III}/2 \tag{8.8}$$

The traction a distance r ahead of the crack tip is

$$\sigma_{23}(r) = (2\pi r)^{-1/2} K_{III} \tag{8.9}$$

and the displacement jump a distance r behind the crack tip is

$$\delta_3(r) = (2r/\pi)^{1/2}(B_1 + B_2)K_{III} \tag{8.10}$$

The energy release rate is related to the stress intensity factor by

$$G = (B_1 + B_2)K_{III}^2/4 \tag{8.11}$$

Consider a set of collinear cracks lying along the interface, with self-equilibrated traction $\tau_0(x)$ prescribed on the crack faces. The potentials, with proper interpretation of the arguments for the two materials, are *exactly the same* (except for a factor of -1/2) as those for cracks in isotropic homogeneous materials, namely

$$\phi_1'(z) = \phi_2'(z) = -\frac{\chi(z)}{2\pi i} \int_c \frac{\tau_0(x)\,dx}{\chi^+(x)(x - z)} + P(z)\chi(z) \tag{8.12}$$

where $\chi(z)$ is given by (5.19), and the polynomial $P(z)$ should be determined to satisfy some auxiliary conditions (see § 5 for detail).

The solution for a singularity interacting with traction-free cracks can be solved by the superposition scheme illustrated in Section 7. Taking the singularity of form (8.5) as an example, in addition to the contribution due to the singularity in well bonded bimaterial system (eqn. (8.6) and Fig. 1a), one obtains the image contribution due to the presence of a semi-infinite crack (Fig. 1b)

$$\phi_1'(z) = \phi_2'(z) = \frac{2B_2}{B_1 + B_2}\left\{\left(\sqrt{\frac{s_3}{z}} - 1\right)\frac{d}{z - s_3} + \left(\sqrt{\frac{\bar{s}_3}{z}} - 1\right)\frac{\bar{d}}{z - \bar{s}_3}\right\} \tag{8.13}$$

where d and s_3 should be calculated from (8.5) and (8.6), with the elastic constants for material 2. The stress intensity factor is given by

$$K_{III} = 4(2\pi)^{1/2}B_2/(B_1 + B_2)\text{Re}\left[ds_3^{-1/2}\right] \tag{8.14}$$

For a screw dislocation, using (8.5) for d (setting $p = 0$), one obtains a nice result

$$K_{III} = -2b/(B_1 + B_2)\text{Re}\left[(2\pi s_3)^{-1/2}\right] \tag{8.15}$$

The isotropic one-material version of the interactive problem was documented in Thomson (1986).

9. IN-PLANE FIELDS; ORTHOTROPIC MATERIALS

For a homogeneous material with x,y-plane as a mirror plane, the characteristic equation for in-plane deformation, specialized from (2.3), is

$$l_4(\mu) = s_{11}\mu^4 - 2s_{16}\mu^3 + (2s_{12} + s_{66})\mu^2 - 2s_{26}\mu + s_{22} = 0 \tag{9.1}$$

It has been shown by Lekhnitskii (1963) that the roots of eqn. (9.1) can never be real, and thus they occur in two conjugate pairs. Assuming they are distinct, one can choose two different roots, μ_1 and μ_2, with positive imaginary parts, to each of which a complex variable $z_j = x + \mu_j y$ is associated. The field quantities can be expressed by two holomorphic functions $\phi_1(z_1)$ and $\phi_2(z_2)$, as obtained by discarding $\phi_3(z_3)$ in (2.2). The matrices A, L, B and H are 2×2 now. the elements for A and L can be specialized from (2.5) and (2.6) with $\eta_1 = \eta_2 = 0$, while

$$B = iAL^{-1} = \begin{bmatrix} s_{11}\text{Im}(\mu_1 + \mu_2) & -i(\mu_1\mu_2 s_{11} - s_{12}) \\ i(\bar{\mu}_1\bar{\mu}_2 s_{11} - s_{12}) & -s_{22}\text{Im}(\mu_1^{-1} + \mu_2^{-1}) \end{bmatrix} \tag{9.2}$$

In deriving (9.2) the standard relations between roots and coefficients have been used. These algebraic results are basically all one needs to specialize various solutions in the

previous sections.

To gain more insight, we consider below orthotropic materials. The principal axes of each material are taken to be in x and y axes, since other orientations may be treated by in-plane rotations and the associated tensor rules in §2. Given an orthotropic solid, since $s_{16} = s_{26} = 0$, only four elastic constants, s_{11}, s_{22}, s_{12} and s_{66}, enter the plane problem formulation. Following the notation introduced earlier (Suo 1988b), we define two nondimensional parameters as

$$\lambda = s_{11}/s_{22}, \quad \rho = (2s_{12} + s_{66})(s_{11}s_{22})^{-1/2}/2 \tag{9.3}$$

The two parameters measure the anisotropy in the sense that $\lambda = 1$ as the material has transversely cubic symmetry and $\lambda = \rho = 1$ as the material becomes transversely isotropic. The positive definiteness of the strain energy density requires that

$$\lambda > 0 \text{ and } -1 < \rho < \infty.$$

The characteristic equation (9.1) is then

$$\lambda \mu^4 + 2\rho\lambda^{1/2}\mu^2 + 1 = 0 \tag{9.4}$$

The roots with positive imaginary parts are

$$\mu_1 = i\lambda^{-1/4}(n + m), \quad \mu_2 = i\lambda^{-1/4}(n - m), \quad \text{for } 1 < \rho < \infty$$

$$\mu_1 = \lambda^{-1/4}(in + m), \quad \mu_2 = \lambda^{-1/4}(in - m), \quad \text{for } -1 < \rho < 1$$

$$\mu_1 = \mu_2 = i\lambda^{-1/4}, \quad \text{for } \rho = 1 \tag{9.5}$$

$$n = [(1 + \rho)/2]^{1/2}, \quad m = [|1 - \rho|/2]^{1/2}$$

From the above we know the LES representation (2.2) does not hold for the degenerate case $\rho = 1$. The significance of this special case will be discussed in the next section.

The matrix B for an orthotropic material, reduced from (9.2), is

$$B = \begin{bmatrix} 2n\lambda^{1/4}\sqrt{s_{11}s_{22}} & i(\sqrt{s_{11}s_{22}} + s_{12}) \\ -i(\sqrt{s_{11}s_{22}} + s_{12}) & 2n\lambda^{-1/4}\sqrt{s_{11}s_{22}} \end{bmatrix} \tag{9.6}$$

It is interesting to note that B is still well-behaved even if $\rho = 1$ (A and L are singular for

this case). The matrix $\mathbf{H}$ in (2.13) for two orthotropic materials with *aligned* principal axes is

$$\mathbf{H} = \begin{bmatrix} H_{11} & -i\beta\sqrt{H_{11}H_{22}} \\ i\beta\sqrt{H_{11}H_{22}} & H_{22} \end{bmatrix} \tag{9.7}$$

where

$$H_{11} = \left[2n\lambda^{1/4}\sqrt{s_{11}s_{22}}\right]_1 + \left[2n\lambda^{1/4}\sqrt{s_{11}s_{22}}\right]_2$$

$$H_{22} = \left[2n\lambda^{-1/4}\sqrt{s_{11}s_{22}}\right]_1 + \left[2n\lambda^{-1/4}\sqrt{s_{11}s_{22}}\right]_2 \tag{9.8}$$

$$\sqrt{H_{11}H_{22}}\,\beta = \left[\sqrt{s_{11}s_{22}} + s_{12}\right]_2 - \left[\sqrt{s_{11}s_{22}} + s_{12}\right]_1$$

Here β is a generalization of one of the Dundurs (1969) parameters. The non-oscillatory fields can be obtained by the corresponding results in §5 if $\mathbf{H}$ is real, or $\beta = 0$. We will focus on the case $\beta \neq 0$ below.

The oscillatory index ε, solved from the eigenvalue problem in Section 6, is

$$\varepsilon = \frac{1}{2\pi}\ln\frac{1-\beta}{1+\beta} \tag{9.9}$$

The eigenvector normalized as (6.20) is

$$\mathbf{w} = \left[-i/2, \quad (H_{11}/H_{22})^{1/2}/2\right]^T \tag{9.10}$$

and the in-plane traction component defined in (6.11) is

$$\sigma_1 = (H_{22}/H_{11})^{1/2}\sigma_{22} + i\sigma_{12} \tag{9.11}$$

With the complex stress intensity factor $K = K_1 + iK_2$, the traction in the interface is given by

$$(H_{22}/H_{11})^{1/2}\sigma_{22} + i\sigma_{12} = (2\pi r)^{-1/2}Kr^{i\varepsilon} \tag{9.12}$$

The displacement jump across the crack is

$$\sqrt{\frac{H_{11}}{H_{22}}}\,\delta_2 + i\delta_1 = \frac{2H_{11}Kr^{1/2+i\varepsilon}}{(1+2i\varepsilon)\cosh\,\pi\varepsilon\,\sqrt{2\pi}} \tag{9.13}$$

The energy release rate is thereby

$$G = H_{11}|K|^2/(4\cosh^2 \pi\varepsilon) \tag{9.14}$$

The stress intensity factors for this case, however defined, may not reduce to the classical definition as the material pair degenerates to have $\varepsilon = 0$, since $H_{22}/H_{11} \neq 1$ if $\lambda \neq 1$. For the case $\varepsilon = 0$ one may rescale K_1 by $(H_{22}/H_{11})^{1/2}$ to recover the classical stress intensity factor.

The stress intensity factor for an internal crack subjected to traction on the faces is

$$K = -\sqrt{\frac{2}{\pi}}\cosh\,\pi\varepsilon\,(2a)^{-1/2-i\varepsilon}\int_{-a}^{a}\left(\frac{a+x}{a-x}\right)^{1/2+i\varepsilon}\left[(H_{22}/H_{11})^{1/2}\sigma_{22} + i\sigma_{12}\right]dx \tag{9.15}$$

For a traction-free internal crack under remote stresses σ_{22} and σ_{12}, the stress intensity factor at the right hand-side is

$$K = (1+2i\varepsilon)\left[(H_{22}/H_{11})^{1/2}\sigma_{22} + i\sigma_{12}\right](2a)^{-i\varepsilon}(\pi a)^{1/2} \tag{9.16}$$

In addition to β (or ε), another generalized Dundurs parameter α, or Σ, can be defined as

$$\Sigma = \left[\sqrt{s_{11}s_{22}}\right]_2 / \left[\sqrt{s_{11}s_{22}}\right]_1 = (1+\alpha)/(1-\alpha) \tag{9.17}$$

Obviously Σ (and α) measures the relative stiffness of the two materials. It can be shown that, for a composite of two aligned orthotropic materials, α and β (or ε and Σ) are the only *bimaterial* parameters needed for traction prescribed problems, in addition to two anisotropy measures, λ and ρ, for each material.

10. ON SOLUTIONS FOR $\varepsilon = 0$ AND $\rho = 1$

Schemes to ignore ε for an interface crack in isotropic bimaterials were proposed

long time ago (*e.g.* Cherepanov 1979). This simplification has been considered seriously by Hutchinson (1989), He and Hutchinson (1988), and Suo and Hutchinson (1989), motivated by recent efforts to develop an engineering theory of interface fracture. The condition $\varepsilon = 0$ has been referred to as the non-oscillatory condition, and a material pair satisfying this condition has been termed as a non-pathological pair.

Calculations of over hundreds of isotropic bimaterials have indicated that ε seldom exceeds a few percent in magnitude, even for material pairs with very large stiffness ratio Σ (*e.g.* Hutchinson et al. 1987, Suga et al. 1988). The same is true for typical non-metals (taken to be isotropic) bonded with anisotropic metal crystals (tables 1 and 2, plane strain is assumed). Consequently, for many bimaterials the simplification can be achieved in practice by an imagined small perturbation of elastic constants. Such a perturbation, which can be thought of as a mathematical idealization, is not expected to change the assessment of fracture behavior dramatically. After all, man has already imposed many idealizations onto a solid: elastic, isotropic, incompressible, to name a few. It seems pointless to tolerate so many others and then reject this appealing one, especially at this stage of development of interfacial fracture mechanics, when many other important issues are yet to be well understood.

The corresponding non-oscillatory condition for an interface crack between two anisotropic media is that the matrix H is real. A question is whether this condition is a property of a given material pair independent of the relative orientations. Since the matrices B and H are second order tensors under a rotation in (x, y)-plane, two important results can be easily inferred. First, for two materials with a fixed relative orientation, ε is invariant under the rotation of the interface in the (x, y)-plane (Ting 1986). Secondly, for a material pair with the (x, y)-plane as a mirror plane, if H is real ($\varepsilon = 0$) for one relative orientation of the two materials, it is real for any relative orientation. A special case of the latter statement was contained in Qu and Bassani (1988), where bicrystals (mis-oriented

but otherwise identical crystals) are considered. If one focuses on bimaterial composites with the (x, y)-plane as a mirror plane, as a consequence of the two statements, one can talk about the non-pathology without referring to the relative orientations of the constituents with respect to the interface.

For two orthotropic materials so bonded such that the (x,y)-plane is a mirror plane of the composite, the non-oscillatory condition is $\beta = 0$, or equivalently, from (9.8)

$$\left[\sqrt{s_{11}s_{22}} + s_{12}\right]_2 = \left[\sqrt{s_{11}s_{22}} + s_{12}\right]_1 \tag{10.1}$$

where the compliances are referred to the principal material axes, although the two orthotropic materials may *not* be aligned with each other. If the two materials satisfy ρ_1, $\rho_2 > 1$, (most fiber-reinforced composite materials satisfy these conditions), it can be shown β is less than 1/2. Sample calculations indicate that β is usually much smaller than this value.

The reward of the non-oscillatory condition is significant. The near-tip fields are decoupled in two senses: the three modes can be separately defined; and the fields in the two materials do not interact with each other in the sense mentioned earlier. The inherent simplicity of various solutions, as indicated Section 5, makes it straightforward, at least in principle, to implement interfaces into many micromechanics models, such as those of Dugdale (1960) and Rice and Thomson (1974). Three recent examples are a prediction of the plastic zone around a bicrystal crack tip using the Schmid law governing single crystal plastic flow (Bassani and Qu 1988), a cohesive-zone model for an interfacial crack presented in Ortiz and Blume (1988), and a cleavage vs. blunting model for metal/ceramic interfaces (Rice et al. 1989).

By the same token, for an orthotropic material, one may invoke $\rho = 1$ as a simplification. It appears that ρ is typically somewhere in the range from 0 to 5. A more important fact is that the known solutions only weakly depend on ρ (e.g., Suo 1988). Hence we believe that it will turn out that the primary measure of orthotropy for woods and

composites is λ, the ratio of stiffnesses in two principal directions. In terms of compliances, the condition $\rho = 1$ is

$$s_{66} = 2(\sqrt{s_{11} s_{22}} - s_{12})$$ (10.2)

The benefit of this simplification is that for many problems of practical significance, the solutions for the case $\rho = 1$ but $\lambda \neq 1$ can be extracted, without much effort, from the existing solutions for an isotropic material by a rescaling technique, as illustrated in Suo (1988b) and Gupta and Suo (1989).

With those two degenerate values taken, i.e., $\varepsilon = 0$ and $\rho = 1$, only three constants (two one-material parameters λ and one bimaterial parameter Σ) are needed to characterize an aligned orthotropic bimaterial system.

Notice however, the case $\rho = 1$ makes the roots of the characteristic equation (9.4) degenerate. Although it can be treated as a limiting case of the general LES representation when the field quantities have been obtained, it may be more convenient to start from a degenerate formulation. The complex potential formulation is analogous to Muskhelishvili's for isotropic materials. The Airy stress function, U(x,y), can be expressed in terms of two holomorphic functions $\phi(z)$ and $\psi(z)$ as

$$U(x,y) = \text{Re}\left[\bar{z}\phi(z) + \int \psi(z)\,dz \right]$$
$$z = x + i\lambda^{-1/4} y$$ (10.3)

The various field quantities can be derived from

$$\sigma_y + \lambda^{1/2}\sigma_x = 4\text{Re}[\phi'(z)]$$

$$\sigma_y - \lambda^{1/2}\sigma_x + 2i\lambda^{1/4}\tau_{xy} = 2[\bar{z}\phi''(z) + \psi'(z)]$$ (10.4)

$$2\mu(u_x + i\lambda^{1/4}u_y) = \bar{\kappa}\phi(z) - z\bar{\phi}'(\bar{z}) - \bar{\psi}(\bar{z})$$

$$i(\lambda^{1/4}f_x + i f_y) = \phi(z) + z\bar{\phi}'(\bar{z}) + \bar{\psi}(\bar{z})$$

where

$$\tilde{\mu} = \frac{1}{s_{66}} = \frac{1}{2(\sqrt{s_{11}s_{22}} - s_{12})}, \quad \frac{1 + \tilde{\kappa}}{4} = \frac{\sqrt{s_{11}s_{22}}}{\sqrt{s_{11}s_{22}} - s_{12}} = \frac{2\sqrt{s_{11}s_{22}}}{s_{66}} \quad (10.5)$$

ACKNOWLEDGEMENTS

REFERENCES

Anderson, P.M. 1988 *J. Appl. Mech.*, 55, 814-817.

Argon, A.S., Gupta, V., Landis, H.S. and Cornie, J.A. 1988 to appear in *J. Mater. Sci.*

Ashby, M.F., Easterling, K.E., Harrysson, R. and Maiti, S.K. 1985 *Proc. Roy. Soc. Lond. A* 398, 261-280.

Atkinson, C. 1966 *Int. J. Fracture Mech.*, 2, 567-575.

Bacon, D.J., Barnett, D.M.and Scattergood, R.O. 1979 *Progress in Materials Science*, 23, 51-262.

Barnett, D.M. and Asaro, R.J. 1972 *J. Mech. Phys. Solids*, 20, 353-366.

Bassani, J.L. and Qu, J. 1988 to appear in *J. Mech. Phys. Solids*.

Cherepanov, G.P. 1979 *Mechanics of Brittle Fracture*, McGraw-Hill, New York.

Clements, D.L. 1971 *Int. J. Engng. Sci.*, 9, 257-265.

Dugdale, D.S. 1960 *J. Mech. Phys. Solids*, 8, 100-104.

Dundurs, J. 1968 in *Mathematical Theory of Dislocations*, ASME, New York.

England, A.H. 1965 *J. Appl. Mech.*, 32, 400-402.

Erdogan, F. 1965 *J. Appl. Mech.*, 32, 403-410.

Eshelby, J.D., Read, W.T. and Shockley, W. 1953 *Acta Met.*, 1, 251-259.

Galin, L.A. 1961 *Contact Problems in the Theory of Elasticity*, § 1.11, translated by H. Moss, School of Physical Sciences and Applied Mathematics, North Carolina State College Publications.

Gotoh, M. 1967 *Int. J. Fracture Mech.*, 3, 253-260.

Green, A.E. and Zerna, W. 1954 *Theoretical Elasticity*, Oxford at the Clarendon Press.

Gupta, V. and Suo, Z. 1989 work in progress.

He, M.-Y. and Hutchinson, J.W. 1988 to appear in *J. Appl. Mech.*

Hoenig, A. 1982 *Engng. Fracture Mech.*, 16, 393-403.

Hutchinson, J.W. 1989 "Mixed mode fracture mechanics of interfaces", to appear in *Scripta Met.*

Lekhnitskii, S.G. 1963 *Theory of Elasticity of an Anisotropic Body*, Holden-Day, Inc.

Muskhelishvili, N.I. 1953a *Some Basic Problems of the Mathematical Theory of Elasticity*, P. Noordhoff Ltd.,Groningen, Holland.

Muskhelishvili, N.I. 1953b *Singular Integral Equations*, P. Noordhoff Ltd., Groningen, Holland.

Ortiz, M. and Blume, J.A. 1988 to be published.

Qu, J. and Bassani, J.L. 1988 to appear in *J. Mech. Phys. Solids*.

Rice, J.R. 1988 *J. Appl. Mech.*, 55, 98-103.

Rice, J.R. 1968 in *Fracture, An Advanced Treatise, II*, H. Liebowitz, ed., Academic Press.

Rice, J.R., Wang, J.-S. and Suo Z. 1989 "Mechanics and thermodynamics of interfacial failure", to be published in *Scripta Met.*

Rice, J.R. and Sih, G.C. 1965 *J. Appl. Mech.*, 32, 418-423.

Rice, J.R. and Thomson, R. 1974 *Phil. Mag.*, 29, 73-97.

Sbaizero, O., Charalambides, P.G. and Evans, A.G. 1988 to be published

Sih, G.C., Paris, P.C. and Irwin, G.R. 1965 *Int. J. Fracture Mech.*, 1, 189-203.

Stroh, A.N. 1958 *Phil. Mag.*, 7, 625-646.

Suga, T., Elssner, E. and Schmander, S. 1988 *J. Composite Materials*, 22, 917-934.

Suo, Z. 1988a to appear in *Int. J. Solids and Struct*.

Suo, Z. 1988b Harvard University Report Mech-135.

Suo, Z. 1989 *Mechanics of Interface Fracture*, PhD thesis, Harvard University.

Suo, Z. and Hutchinson, J.W. 1989 *Mater. Sci. Engng.*, A107, 135-143.

Sweeney, J., Duckett, R.A. and Ward, I.M. 1988 *Proc. Roy. Soc. Lond.* A 420, 53-80.

Tewary, V.K., Wagoner, R.H. and Hirth, J.P. 1989a,b *J. Mater. Res.*, 4, 113-136.

Thomson, R. 1986 *Solid State Physics*, 39, 1-129.

Ting, T.C.T. 1986 *Int. J. Solids. Struct.*, 22, 965-983.

Ting, T.C.T. 1982 *Int. J. Solids. Struct.*, 18, 139-152.

Tucker, M.O. 1969 *Phil. Mag.*, 19, 1141-1159.

Wang, J.-S. 1988 *J. Mater. Res.* 3, 16-28.

Wang, S.S. 1984 *AIAA J.*, 22, 256-264.

Williams, M.L. 1959 *Bull. Seismol. Soc. Am.*, 49, 199-204.

Willis, J.R. 1971 *J. Mech. Phys. Solids*, 19, 353-368.

Table 1. OSCILLATORY INDEX ε

	Al$_2$O$_3$	Boron	Carbon	E-glass	SiC
Al(fcc)	-.047	-.049	-.062	+.017	-.049
Cr(bcc)	-.025	-.031	-.064	+.061	-.028
Cu(fcc)	-.029	-.032	-.049	+.040	-.030
Pb(fcc)	-.034	-.035	-.039	-.006	-.035
Zr(hcp)	-.042	-.046	-.062	+.030	-.045

Table 2. STIFFNESS RATIO Σ

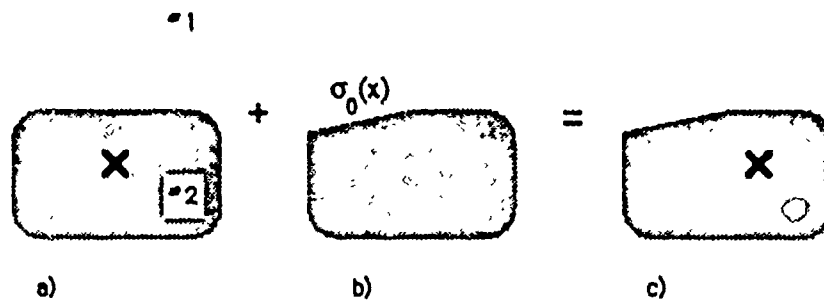|	Al$_2$O$_3$	Boron	Carbon	E-glass	SiC
Al(fcc)	5.5	6.2	9.1	1.0	6.8
Cr(bcc)	1.2	1.3	2.0	0.2	1.5
Cu(fcc)	5.0	5.6	8.3	0.9	6.2
Pb(fcc)	29.5	33.0	49.0	5.6	36.5
Zr(hcp)	3.2	3.5	5.3	0.6	4.0

Fig. 1 Superposition scheme. a) a singularity in a well bonded bimaterial. b) interface crack with traction prescribed on the faces. c) a singularity interacting with a traction-free crack.
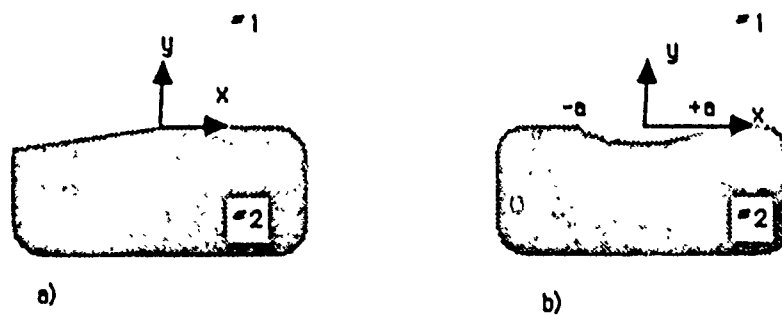

Fig. 2 Two basic crack configurations. a) a semi-infinite crack. b) a finite internal crack.

DELAMINATION SPECIMENS FOR ORTHOTROPIC MATERIALS

Zhigang Suo

Division of Applied Sciences
HARVARD UNIVERSITY
Cambridge, Massachusetts 02138

November 1988

DELAMINATION SPECIMENS FOR ORTHOTROPIC MATERIALS

Zhigang Suo
Division of Applied Sciences
Harvard University
Cambridge, MA 02138

November 1988

ABSTRACT

A semi-infinite crack in an infinite strip of orthotropic material is analyzed. Analytic expressions for mixed mode stress intensity factors are derived with only one parameter undetermined, which is then extracted from numerical solutions to integral equations. The results are relatively simple and complete, and provide the flexibility to simulate a wide range of practical problems, such as fracture specimens and edge delamination phenomena of woods and fiber-reinforced composites. As an illustration, specimens with transverse splitting from notches are analyzed based on the general solution. The validity of using solutions for an isotropic material to calibrate some testing geometries of orthotropic materials is discussed.

1.   Introduction

Cracks in homogeneous, isotropic materials tend to grow under mode I conditions. By contrast, cracks are often trapped, with *mixed mode* local field, to geometrically particular paths such as the fiber direction of woods and uniaxial fiber reinforced composites, the interface of bimaterial systems, and the adhesive layer between bonded joints, owing to anisotropy and/or inhomogeneity in stiffness and toughness. The mixed mode fracture problem is not only of fundamental interest, but also of significant technical importance. High apparent toughness under tension in the fiber direction for woods and composites, for example, is largely attributed to crack splitting, or fiber/matrix debonding (Ashby et al., 1985, Marshall and Evans, 1985, Budiansky et al., 1986). Experimental investigations on fracture in woods and composites appear to be initiated by Wu (1967). Recent efforts in this direction are found in Ashby et al. (1985), Marshall and Evans (1985), Prewo (1986), Michalske and Hellmann (1988), and Sbaizero et al. (1988). Research on analogous situations such as adhesive joints and bimaterial

interfaces, where mixed mode fracture is crucial, are found in Liechti and Hanson (1988), Chai (1988), Argon et al. (1988), and Charalambides et al. (1988a,b). The present work is motivated in part by the intention of using a four-point bend specimen to conduct fracture tests on fiber reinforced composites (Sbaizero et al., 1988).

The basic problem analyzed is introduced in Fig. 1a. A semi-infinite crack in an infinite strip of orthotropic material is considered. More specifically, the strip surfaces are traction-free and in the direction of a principal axis of the material. The crack is parallel to these free surfaces, and driven by the edge loads P_i and M_i, the resultant forces and moments per unit width, respectively. The material is taken to be homogeneous and linearly elastic. Both plane stress and plane strain deformations will be considered. The analysis provides the complete solutions for the mixed mode stress intensity factors. The body of the paper will be devoted to the representation and application of the major results. Mathematical details are grouped into three appendices, which may be of some interest in themselves.

2. Representation of Stress Intensity Factors

For generally anisotropic materials Hooke's law can be written as

$$\varepsilon_i = \sum_{j=1}^{6} s_{ij}\, \sigma_j, \quad i = 1, 2, 3, 4, 5, 6 \tag{1}$$

The standard correspondence is adopted, i.e., $\{\varepsilon_i\} = \{\varepsilon_x, \varepsilon_y, \varepsilon_z, \gamma_{yz}, \gamma_{zx}, \gamma_{xy}\}^T$, $\{\sigma_i\} = \{\sigma_x, \sigma_y, \sigma_z, \tau_{yz}, \tau_{zx}, \tau_{xy}\}^T$, and $[s_{ij}]$ is a six by six symmetric matrix, referred to as the compliance matrix, with twenty-one independent elements. When the material has an elastic symmetry plane normal to z-axis, the stress-strain relation for the deformation in (x, y) plane can be reduced to (see Lekhnitskii, 1963)

$$\varepsilon_i = \sum_{j=1,2,6} b_{ij}\, \sigma_j, \quad i = 1, 2, 6 \tag{2}$$

where

$$b_{ij} = \begin{cases} s_{ij}, & \text{for plane stress} \\ s_{ij} - s_{i3}s_{j3}/s_{33}, & \text{for plane strain} \end{cases} \qquad i,j = 1, 2, 6 \qquad (3)$$

On the other hand if the material is orthotropic with x and y axes coincident with the principal axes of the material, there are only *four* independent elastic constants b_{11}, $b_{12} = b_{21}$, b_{22} and b_{66}, but $b_{16} = b_{26} = 0$.

For any simply connected domain of orthotropic medium with traction prescribed on its boundary, the stresses should only depend on *two* (rather than three) nondimensional elastic parameters (see Appendix I)

$$\lambda = \frac{b_{11}}{b_{22}}, \quad \rho = \frac{2b_{12} + b_{66}}{2\sqrt{b_{11}b_{22}}} \qquad (4)$$

These parameters measure the anisotropy in the sense that $\lambda = 1$ as the material symmetry degenerates to be transversely cubic and $\lambda = \rho = 1$ as the material becomes transversely isotropic. The positive definiteness of the strain energy density requires that $\lambda > 0$ and $-1 < \rho < \infty$. Many nondimensional parameters for orthotropic materials other than those in (4) have been used in the literature, but none of them have offered the unique feature discussed in Appendix I. In Table I, the plane stress values of λ and ρ are listed for some single crystals, woods and composites (no dramatic differences have been found for the corresponding plane strain values). It appears from this list that ρ is typically somewhere in the range from 0 to 5, while λ can be significantly greater or less than 1.

The elastic stress field at the crack tip for generally anisotropic body has a square root singularity. Accordingly, stress intensity factors, K_I and K_{II}, can be defined such that the stresses at a distance r ahead of the crack tip are given asymptotically by

$$\sigma_{yy} = \frac{K_I}{\sqrt{2\pi r}}, \quad \sigma_{xy} = \frac{K_{II}}{\sqrt{2\pi r}} \qquad (5)$$

For a crack in an orthotropic body, lying in a principal plane and with its front in a principal direction, the relative crack face displacements at a distance r behind the crack tip are

$$\delta_y = 8b_{11} \, \lambda^{-3/4} n \, K_I \sqrt{\frac{r}{2\pi}} \quad , \quad \delta_x = 8b_{11} \lambda^{-1/4} n \, K_{II} \sqrt{\frac{r}{2\pi}} \qquad (6)$$

where the frequently encountered constant n is defined by

$$n = \sqrt{\frac{1+\rho}{2}} \qquad (7)$$

The energy release rate, derived from (5) and (6), is related to the stress intensity factors by

$$G = b_{11} \, n \, (\lambda^{-3/4} K_I^2 + \lambda^{-1/4} K_{II}^2) \qquad (8)$$

These results are contained in the work by Sih, Paris and Irwin (1965). The present normalization is related to theirs by $K_I = \sqrt{\pi} \, k_1$, $K_{II} = \sqrt{\pi} \, k_2$. Rearrangements have been made using the two anisotropy measures identified above to suit our purpose.

The analysis of the problem in Fig. 1a is now taken up. The aim is to solve for K_I and K_{II} as functions of the loads P's and M's, geometry specifications h and H, and anisotropy measures λ and ρ. Overall equilibrium provides two constraints among the six loads P_i and M_i. Therefore only four of them are independent, say P_1, P_3, M_1 and M_3. Superposition of the systems in Fig. 1a and 1b gives that in Fig. 1c, with P and M given by

$$P = P_1 - C_1 P_3 - C_2 M_3 / h$$

$$M = M_1 - C_3 M_3 \qquad (9)$$

$$C_1 = \frac{1}{1/\eta + 1} \; , \; C_2 = \frac{6/\eta}{(1/\eta + 1)^3}, \; C_3 = \frac{1}{(1/\eta + 1)^3} \; , \; \eta = \frac{h}{H}$$

Since no stress singularity is present in the beam in Fig. 1b, the stress intensity factors must be identical for both systems in Figs. 1a and 1c. We will concentrate on the reduced problem in Fig. 1c below. Once the latter problem is solved, the solution to the general problem in Fig. 1a can be constructed by the above relations.

The energy release rate for the system in Fig. 1c can be computed exactly by using the energy stored in the structure per unit width per unit length far behind the crack tip (e.g. Rice, 1968). The result is a positive definite quadratic in P and M which can be written as

$$G = \frac{b_{11}}{2} \left[\frac{P^2}{Ah} + \frac{M^2}{h^3} + 2\frac{PM}{\sqrt{AI}\,h^2} \sin\gamma \right] \tag{10}$$

The geometric factors are given by

$$\frac{1}{A} = 1 + 4\eta + 6\eta^2 + 3\eta^3, \quad \frac{1}{I} = 12(1 + \eta^3), \quad \frac{\sin\gamma}{\sqrt{AI}} = 6\eta^2(1 + \eta) \tag{11}$$

where the angle γ is restricted to $|\gamma| < \pi/2$ for definiteness. Without loss of generality, attention will be restricted to $h \leq H$, or equivalently, $0 \leq \eta \leq 1$. The energy release rate given by (10) and (11) is valid even if the material is generally anisotropic.

As shown in Appendix I, for the problem in Figs. 1a and 1c, the combinations $\lambda^{-3/8} K_I$ and $\lambda^{-1/8} K_{II}$ are independent of λ. It will be obvious immediately that this fact simplifies the problem significantly. Equating the two energy release rate expressions (8) and (10), one can verify

$$\sqrt{n} \left| \lambda^{-3/8} K_I + i \lambda^{-1/8} K_{II} \right| = \frac{1}{\sqrt{2}} \left| \frac{P}{\sqrt{hA}} - i e^{i\gamma} \frac{M}{\sqrt{h^3 I}} \right| \tag{12}$$

where $i = \sqrt{-1}$ and $|a|$ stands for the magnitude of a complex number a. Equation (12) states that two complex quantities have the same magnitude. Consequently, they can differ only by a phase angle shift, designated as ω, namely,

$$\sqrt{n} \left(\lambda^{-3/8} K_I + i \lambda^{-1/8} K_{II} \right) = \frac{e^{i\omega}}{\sqrt{2}} \left(\frac{P}{\sqrt{hA}} - i e^{i\gamma} \frac{M}{\sqrt{h^3 I}} \right) \tag{13}$$

On dimensional grounds, ω should be a nondimensional function of nondimensional quantities Ph/M, η, λ and ρ. However, by linearity, ω should not depend on Ph/M; nor should it depend on λ, since both sides of eqn. (13) are independent of λ. Therefore the angle ω depends on η and ρ only, i.e.,

$$\omega = \omega(\eta, \rho) \tag{14}$$

Rewrite eqn.(13) more explicitly as

$$K_I = \frac{\lambda^{3/8}}{\sqrt{2n}}\left[\frac{P}{\sqrt{hA}}\cos\omega + \frac{M}{\sqrt{h^3 I}}\sin(\omega+\gamma)\right]$$

$$K_{II} = \frac{\lambda^{1/8}}{\sqrt{2n}}\left[\frac{P}{\sqrt{hA}}\sin\omega - \frac{M}{\sqrt{h^3 I}}\cos(\omega+\gamma)\right]$$

(15)

so that the stress intensity factors are fully determined apart from the single dimensionless real function $\omega(\eta, \rho)$. From (15) one can restrict ω in the range $0 < \omega < \pi/2$ to recover the positive signs of K_I and K_{II} anticipated for the special case $P > 0$ but $M = 0$.

Specific determination of the function $\omega(\eta, \rho)$ requires that the crack problem in Fig. 1c be solved *rigorously* for a given pair (η, ρ), for an arbitrary set of values of λ, h, P and M. We will show below that ω is around 50°. Some early work on partitioning mixed mode stress intensity factors from the energy release rate was based on unjustified symmetry arguments and contains significant errors (e.g. Tada et al., 1985, pp. 29.2, 29.4, 29.9 and Williams, 1988, Fig. 10a). In the following, an exact solution for ω is found for the case $h = H$, or $\eta = 1$. Numerical solutions are presented for other cases, and a simple estimate is given for practical applications.

i. $\omega(1, \rho)$

Exact solution can be obtained for the this case by considering a special loading $F = 0$, $M = 1$. The geometric factors in eqns. (9) and (11) for $\eta = 1$ are

$$A = \frac{1}{14}, \quad I = \frac{1}{24}, \quad \sin\gamma = \sqrt{\frac{3}{7}}$$

$$C_1 = \frac{1}{2}, \quad C_2 = \frac{3}{4}, \quad C_3 = \frac{1}{8}$$

(16)

Notice that $K_{II} = 0$ due to the symmetry, which, when substituted into eqn.(15), gives $\cos(\omega+\gamma) = 0$. Thus, $\omega = \pi/2 - \gamma = \cos^{-1}\sqrt{(3/7)} \approx 49.1°$. It is striking that $\omega(1, \rho)$ does *not* depend on ρ. This indicates that the function $\omega(\eta, \rho)$ may vary weakly with respect to ρ even if $\eta \neq 1$.

ii. $\omega(\eta, 1)$

This case is equivalent to the isotropic version of the same problem, which has been solved by Suo and Hutchinson (1988a, b). For $0 \leq \eta \leq 1$, an excellent approximation is

$$\omega = 52.1 - 3\eta, \qquad \text{in degrees} \tag{17}$$

iii. $\omega(\eta, \rho)$

An integral equation is formulated and solved numerically in Appendix II for the general case. The extracted values of ω are listed in Table II. One notes immediately that ω is a very weak function of ρ. This implies that eqn. (17) is an adequate estimate for a wide range of ρ for $0 \leq \eta \leq 1$.

3.   Fracture Specimens

3.1   A four-point bend specimen

The specimen illustrated in Fig. 2a is considered first. The beam is cut from an orthotropic material, with its principal axes coincident with the material principal axes. When the crack is long compared with h, but still lying within the central region of the specimen, the specimen can be well approximated by the system in Fig. 2b. It has been shown by finite element calculations (Charalambides et al, 1988a, b) for an analogous specimen that the crack tip field is indifferent to the crack length if it is sufficiently long. Consequently the structure in Fig. 2b can be imagined to be infinitely long in the crack direction. This falls into the class of the problems (Fig. 2a) analyzed in the previous section, with the special loading combination

$$P_1 = M_1 = P_3 = 0, \quad M_3 = -M_0 \tag{18}$$

The equivalent loads controlling the singular field are calculated from eqn.(9), i.e.,

$$P = C_2 M_0/h, \quad M = C_3 M_0 \tag{19}$$

The stress intensity factors are obtained when the above are substituted into (15); that is

$$K_I = \frac{\lambda^{3/8}}{\sqrt{2n}} M_0 h^{-3/2} \left[C_2 A^{-1/2} \cos\omega + C_3 I^{-1/2} \sin(\omega + \gamma) \right]$$

$$K_{II} = \frac{\lambda^{1/8}}{\sqrt{2n}} M_0 h^{-3/2} \left[C_2 A^{-1/2} \sin\omega - C_3 I^{-1/2} \cos(\omega + \gamma) \right]$$

(20)

where ω can be approximated by (17). For the special case $h = H$, or $\eta = 1$, $\omega + \gamma = \pi/2$, $\cos\omega = \sqrt{(3/7)}$, $\sin\omega = \sqrt{(4/7)}$, with various geometric factors given in (16), eqn. (20) can be specialized to

$$K_I = \sqrt{3} \, \lambda^{3/8} \, n^{-1/2} M_0 \, h^{-3/2} , \quad K_{II} = \frac{3}{2} \lambda^{1/8} \, n^{-1/2} M_0 \, h^{-3/2}$$

(21)

This is an exact solution. Notice that from (21)

$$\frac{K_{II}}{K_I} = \frac{\sqrt{3}}{2} \lambda^{-1/4}$$

(21a)

Equation (21a) indicates that mode I and mode II stress intensity factors are comparable for this test arrangement.

3.2   A tensile specimen

Parallel results for the same geometry under tension (Fig. 2c, d) are listed below.

The stress intensity factors are given by

$$K_I = \frac{\lambda^{3/8}}{\sqrt{2n}} Q h^{-1/2} C_1 A^{-1/2} \cos\omega$$

(22)

$$K_{II} = \frac{\lambda^{1/8}}{\sqrt{2n}} Q h^{-1/2} C_1 A^{-1/2} \sin\omega$$

where for an arbitrary value of $\eta = h/H$, C_1 and A are defined in eqns. (9) and (11), and ω can be approximated by (17). The solution for the case $h = H$, or $\eta = 1$, is exact, which is

$$K_I = \frac{\sqrt{3}}{2} \lambda^{3/8} n^{-1/2} h^{-1/2} Q, \quad K_{II} = \lambda^{1/8} n^{-1/2} h^{-1/2} Q$$

(23)

thereby the ratio K_{II}/K_I, for the case $h = H$, is given by

$$\frac{K_{II}}{K_I} = \frac{2}{\sqrt{3}} \lambda^{-1/4} \tag{23a}$$

Again there is a comparable amount of stress intensity of the two modes. This specimen was considered by Williams (1988) who by virtue of unjustified assumptiopns arrived at the conclusion that the near-tip field was pure mode II.

3.3 More specimens

Illustrated in Fig. 3 are geometries utilized predominantly in composite and wood fracture testing. The specimens are cut from bulk materials with principal material axes aligned with specimen axes. A common feature for all these specimens is that no specific length scale is involved in one direction. With such specimens, it has generally been the practice to use the stress intensity factors determined for the corresponding isotropic specimens (e.g. Ashby, et al., 1985, Michalske and Hellmann, 1988). This can be easily justified as follows. The stress intensity factors, in general, depend on the two anisotropy measures, λ and ρ. Exploiting the rescaling technique outlined in Appendix I, one can confirm that, for all configurations in Fig. 3, the stress intensity factors are independent of λ. Given the fact that ρ is typically in the range between 0 and 5, and that the solutions for analogous problems only weakly depend on ρ, one can reasonably expect that the stress intensity factors are *almost* independent of ρ. Consequently, the stress intensity factors for these geometries are nearly independent of any anisotropic factors, and thus the use of solutions for isotropic materials should be appropriate. Evidently unaware of the roles played by λ and ρ, Sweeney (1988) carried out a numerical analysis for an edge crack in an orthotropic half plane (Fig. 3a). The Table I in his paper can be reduced concisely as

$$K_I = Y\sigma\sqrt{\pi a}, \quad Y = 1.12 - 0.011(\rho - 1), \quad \text{for } 1 < \rho < 8 \tag{24}$$

4.   Extension to An Anisotropic Strip

Arguments leading to the stress intensity factor expression (15) have been used successfully in various contexts by Thouless, et al. (1987), Hutchinson, et al. (1988), Drory, et al. (1988) and Suo and Hutchinson (1988a,b,c). The generality may be appreciated by considering the problem with the same configuration as Fig. 1c, but with a generally anisotropic material replacing the orthotropic material considered earlier. The Sih-Paris-Irwin energy release rate expression can be rearranged as

$$G = b_{11}(n_1 \lambda^{-3/4} K_I^2 + n_2 \lambda^{-1/4} K_{II}^2 + 2\sqrt{n_1 n_2}\, \lambda^{-1/2} K_I K_{II} \sin v) \tag{25}$$

Here n_1, n_2 and v can be extracted from the work by Sih et al. (1965) as

$$n_1 = -\frac{1}{2} \mathrm{Im}\,[\,t_1^{-1} + t_2^{-1}], \quad n_2 = \frac{1}{2} \mathrm{Im}\,[\,t_1 + t_2], \quad \sqrt{n_1 n_2} \sin v = \frac{1}{2}\, \mathrm{Im}\,[t_1 t_2] \tag{26}$$

and t_1 and t_2 are roots with positive imaginary parts of

$$t^4 - 2\rho_1 t^3 + 2\rho\, t^2 - 2\rho_2 t + 1 = 0 \tag{27}$$

where ρ_1 and ρ_2 are defined in Appendix I. Comparing (25) with (10) one obtains

$$\left| \sqrt{n_1}\, \lambda^{-3/8} K_I + i\, e^{-iv}\sqrt{n_2}\, \lambda^{-1/8} K_{II} \right| = \frac{1}{\sqrt{2}} \left| \frac{P}{\sqrt{hA}} - i\, e^{i\gamma} \frac{M}{\sqrt{h^3 I}} \right| \tag{28}$$

where A and I are defined by eqn. (11). Again one can introduce a phase angle shift $\omega = \omega(\eta, \rho, \rho_1, \rho_2)$, such that

$$\sqrt{n_1}\, \lambda^{-3/8} K_I + i\, e^{-iv}\sqrt{n_2}\, \lambda^{-1/8} K_{II} = \frac{e^{i\omega}}{\sqrt{2}} \left(\frac{P}{\sqrt{hA}} - i\, e^{i\gamma} \frac{M}{\sqrt{h^3 I}} \right) \tag{29}$$

Consequently, the stress intensity factors K_I and K_{II} are fully determined apart from the function ω. One may anticipate the approximation (17) to be valid for wide ranges of ρ, ρ_1 and ρ_2.

It is not a very difficult exercise to derive a formula analogous to (26) for an interface crack between two layers of dissimilar anisotropic materials, so that such interesting problems as bicrystal specimens (e.g. Wang, 1988) and interlaminar fracture in composites can be addressed. Helpful hints may be found in Suo and Hutchinson (1988a). The corresponding

relation between energy release rate and stress intensity factors of form (22) can be extracted formally from Willis (1971).

Acknowledgements

References

Argon, A.S., Gupta, V., Landis, H.S. and Cornie, J.A., "Intrinsic Toughness of Interfaces between SiC Coatings and Substrates of Si or C Fibers", submitted to *J. Mater. Sci.*

Ashby, M.F., Easterling, K.E., Harrysson, R. and Maiti, S.K., 1985, "The Fracture and Toughness of Woods," *Proc. Roy. Soc. Lond.* A 398, 261-280.

Budiansky, B., Hutchinson, J.W. and Evans, A.G., 1986, "Matrix Fracture in Fiber-reinforced Ceramics", *J. Mech. Phys. Solids*, 34, 167-189.

Chai, H., 1988, "Shear Fracture", *Int. J. Fracture*, 37, 137-159.

Charalambides, P.G., Lund, J., Evans, A.G. and McMeeking, R.M., 1988a, "A Test Specimen for Determining the Fracture Resistance of Bimaterial Interfaces," to be published in *J. Appl. Mech.*

Charalambides, P.G., Cao, H.C., Lund, J. and Evans, A.G., 1988b, "Development of a Test Method for Measuring the Mixed Mode Fracture Resistance of Bimaterial Interfaces", in press.

Drory, M.D., Thouless, M.D. and Evans, A.G., 1988, "The Cracking and Decohesion of Thin Films", *Acta Met.* 36, 2019-2028.

Hutchinson, J.W., Mear, M.E. and Rice, J.R., 1987, "Crack Paralleling an Interface between Dissimilar Materials," *J. Appl. Mech.*, 54, 828-832.

Lekhnitskii, S.G., 1963, *Theory of Elasticity of an Anisotropic Body*, Holden-Day, Inc.

Liechti, K.M. and Hanson, E.C., 1988, "Nonlinear Effects in Mixed-Mode Interfacial Delamination", *Int. J. Fract.*, 36, 199-217.

Marshall, D.B. and Evans A.G., 1985, "Failure Mechanism in Ceramic-Fiber/Ceramic-Matrix Composites", *J. Am. Ceram. Soc.*, 68, 225-231.

Michalske, T.A. and Hellmann, J.R., 1988, "Strength and Toughness of Continuous-Alumina-Fiber-Reinforced Glass-Matrix Composites", *J. Am. Ceram. Soc.*, 71, 725-731.

Prewo, K.M., 1986, "Tension and Flexural Strength of Silicon Carbide Fiber-Reinforced Glass Ceramics", *J. Matter. Sci.* 21, 3590-3600.

Rice, J.R., 1968, "Mathematical Analysis in the Mechanics of Fracture", in *Fracture, An Advanced Treaties*, II, H. Liebowitz, ed., Academic Press, New York, 191-311.

Sbaizero, O., Charalambides, P.G. and Evans, A.G., 1988, "Delamination Cracking in a Laminated Ceramic Matrix Composite", in press.

Sih, G.C., Paris, P.C. and Irwin, G.R., 1965, "On Cracks in Rectilinearly Anisotropic Bodies", *Int. J. Fracture Mech.*, 1, 189-203.

Suo, Z., 1988, "Singularities Interacting with Interfaces and Cracks-II. Anisotropic Materials", manuscript in preparation.

Suo, Z. and Hutchinson, J.W., 1988a, "Interface Crack between Two Elastic Layers", *Int. J. Fract.*, in press.

Suo, Z. and Hutchinson, J.W., 1988b, "Steady-state Cracking in Brittle Substrate beneath Adherent Films", Harvard University Report Mech-132.

Suo, Z. and Hutchinson, J.W., 1988c, " On Sandwich Test Specimens for Measuring Interface Crack Toughness", *Mat. Sci. Eng.*, in press.

Sweeney, J., 1988, "The Stress Intensity for an Edge Crack in a Semi-infinite Orthotropic Body", *Int. J. Fract.*, 37, 233-241.

Tada, H., Paris, P.C. and Irwin, G.R., 1985, *The Stress Analysis of Cracks Handbook*, Del Research, St. Louis, MO.

Thouless, M.D., Evans, A.G., Ashby, M.F. and Hutchinson, J.W., 1987, "The Edge Cracking and Spalling of Brittle Plates", *Acta Met.*, 35, 1333-1341.

Wang, J.-S., 1988, "A New Type of Brittle Fracture in a FCC Metal Bicrystal with Intergranular Segregation", *J. Matter. Res.*, 3, 16-28.

Williams, J.G., 1988, "On the Calculation of Energy Release Rates for Cracked Laminates", *Int. J. Fract.*, 36, 101-119.

Willis, J.R., 1971, "Fracture Mechanics of Interfacial Cracks," *J. Mech. Phys.Solids*, 19, 353-368.

Wu, E.M., 1967, "Application of Fracture Mechanics to Anisotropic Plates," *J. Appl. Mech.*, 34, 967-974.

APPENDIX I   On Material Dependence

Let $U(x,y)$ be the Airy stress function, namely,

$$\sigma_x = \frac{\partial^2 U}{\partial y^2}, \quad \sigma_y = \frac{\partial^2 U}{\partial x^2}, \quad \tau_{xy} = -\frac{\partial^2 U}{\partial x \partial y} \tag{AI.1}$$

Then one can obtain the differential equation of $U(x,y)$ for rectilinearly anisotropic materials from the compatibility equation (cf. Lekhnitskii, 1963)

$$\frac{\partial^4 U}{\partial x^4} - 2\rho_2 \lambda^{1/4} \frac{\partial^4 U}{\partial x^3 \partial y} + 2\rho \lambda^{1/2} \frac{\partial^4 U}{\partial x^2 \partial y^2} - 2\rho_1 \lambda^{3/4} \frac{\partial^4 U}{\partial x \partial y^3} + \lambda \frac{\partial^4 U}{\partial y^4} = 0 \tag{AI.2}$$

where λ and ρ are defined in the body of the paper and $\rho_1 \lambda^{3/4} = b_{16}/b_{22}$, $\rho_2 \lambda^{1/4} = b_{26}/b_{22}$. Now it is obvious that for any simply connected domain of anisotropic medium with traction prescribed on its boundary, the stresses should only depend on four (rather than five) nondimensional elastic parameters. If the material is orthotropic with the principal axes in x and y directions, $\rho_1 = \rho_2 = 0$, the stresses should only depend on two parameters λ and ρ. Moreover, for the problem in Fig. 2a, with no specific length scale in x direction, we are able to show explicitly the way in which stress intensity factors depend on λ. Rescale the x-axis by

$$\xi = \lambda^{1/4} x \tag{AI.3}$$

The boundary value problem in Fig. 2a is then governed by the following differential equation

$$\frac{\partial^4 U}{\partial \xi^4} - 2\rho_2 \frac{\partial^4 U}{\partial \xi^3 \partial y} + 2\rho \frac{\partial^4 U}{\partial \xi^2 \partial y^2} - 2\rho_1 \frac{\partial^4 U}{\partial \xi \partial y^3} + \frac{\partial^4 U}{\partial y^4} = 0 \tag{AI.4}$$

and boundary conditions on (ξ, y) plane

$$\frac{\partial^2 U}{\partial y \partial \xi} = 0, \quad \frac{\partial^2 U}{\partial y^2} = \text{prescribed traction}, \quad \xi \to \pm\infty, \, -H < y < h$$

$$\frac{\partial^2 U}{\partial \xi^2} = \frac{\partial^2 U}{\partial \xi \partial y} = 0, \quad \xi < 0, \, y = 0; \quad -\infty < \xi < \infty, \, y = -H, h \tag{AI.5}$$

Clearly $U(\xi, y)$ will not depend explicitly on λ. This has very strong implication as the stress intensity factors K_I and K_{II} are calculated

$$K_I = \lim_{x \to 0} \sqrt{2\pi x}\; \sigma_y(x, 0) = \lambda^{3/8} \lim_{\xi \to 0} \sqrt{2\pi\xi}\; \frac{\partial^2 U(\xi, 0)}{\partial\xi^2} \qquad (AI.6)$$

$$K_{II} = \lim_{x \to 0} \sqrt{2\pi x}\; \tau_{xy}(x, 0) = -\lambda^{1/8} \lim_{\xi \to 0} \sqrt{2\pi\xi}\; \frac{\partial^2 U(\xi, 0)}{\partial\xi\partial y} \qquad (AI.7)$$

so that the combinations $\lambda^{-3/8} K_I$ and $\lambda^{-1/8} K_{II}$ are independent of λ.

APPENDIX II   Integral Equation Formulation

An integral equation for the plane elasticity problem of Fig.2c is formulated based on the dislocation solutions developed in Appendix III. Since only the function $\omega(\eta, \rho)$ is to be extracted from the numerical solution, one can take

$$\lambda = 1, \quad h = 1, \quad P = 1, \quad b_{11} = 1 \qquad (AII.1)$$

and M will be specified shortly to simplify the numerical analysis.

The semi-infinite crack is simulated by an array of continuously distributed edge dislocations along the negative x-axis, with components $b_\alpha(\xi)$ at $x = \xi$. The traction-free condition along the crack faces results in the integral equations

$$\int_{-\infty}^{0} \frac{2B_\alpha(\xi)}{x - \xi}\, d\xi + \int_{-\infty}^{0} F_{\alpha\beta}(x - \xi)\, B_\beta(\xi)\, d\xi = 0, \quad \text{for} \; -\infty < x < 0 \qquad (AII.2)$$

where the first integral is in the Cauchy principal value sense, and the convention of summing up a repeated Greek suffix is adopted. Here

$$B_\alpha(\xi) = \frac{1}{8\pi n}\, b_\alpha(\xi), \qquad n = \sqrt{\frac{\rho + 1}{2}} \qquad (AII.3)$$

The kernel functions $F_{\alpha\beta}(\zeta)$ are given in Appendix III; they are well-behaved in the whole range $-\infty < \zeta < +\infty$, with asymptotes

$$F_{\alpha\beta}(\zeta) = -\frac{2}{\zeta}\, \delta_{\alpha\beta} + O\left(\frac{1}{\zeta^3}\right) \qquad \text{as} \; \zeta \to \infty \qquad (AII.4)$$

Noticing that by definition the Burgers vector b_α is related to the crack face relative displacement δ_α by

$$b_\alpha(x) = -\frac{\partial}{\partial x} \delta_\alpha(x) \tag{AII.5}$$

one can verify the following asymptotic behaviors for $B_\alpha(\xi)$

$$B_1(\xi) = (2\pi)^{-3/2} \frac{K_{II}}{\sqrt{-\xi}}, \quad B_2(\xi) = (2\pi)^{-3/2} \frac{K_I}{\sqrt{-\xi}} \tag{AII.6}$$

as $\xi \to 0^-$, and

$$B_1(\xi) = \frac{1}{8\pi n} [1 + \eta (4 + 3\eta) - 6M (1 - \eta^2)], \quad B_2(\xi) = \text{constant}$$

$$\tag{AII.7}$$

$$M = - \sqrt{\frac{I}{A}} \sin\gamma$$

as $\xi \to -\infty$, where M has been chosen such that $B_2(-\infty)$ remains finite. And K_I, K_{II} and the "constant" in (AII.7) are not known *a priori*, but must be determined as part of the solution to the integral equations. The integral equations, together with the specified asymptotes, constitute a well-posed mathematical problem for the unknown distributions $B_\alpha(\xi)$. The details of the numerical solution procedure for analogous problems can be found in Thouless, et al. (1987), and Suo and Hutchinson (1988a,b).

Once the $B_\alpha(\xi)$ are obtained for a given pair η and ρ, the stress intensity factors are evaluated from eqn.(AII.6). The function $\omega(\eta,\rho)$ is then extracted by specializing (13) with (AII.1,7) to

$$K_I + i K_{II} = \frac{\cos\gamma}{\sqrt{2nA}} e^{i(\omega + \gamma)} \tag{AII.8}$$

The numerical solution yields both K_I and K_{II} and each results in a value of ω. This provides a consistency check on the accuracy of the solution. For example, knowing K_I and K_{II}, one can calculate $\cos(\omega+\gamma)$ and $\sin(\omega+\gamma)$ independently from (AII.8), and hence the check can be chosen as $[\cos^2(\omega+\gamma)+\sin^2(\omega+\gamma)]^{1/2} - 1$. The results reported in Table II were computed with the consistency check satisfied to better than 0.1%. It is believed that the accuracy of ω is comparable.

APPENDIX III   An Edge Dislocation in Anisotropic Structures

In Appendix II, the solution of an edge dislocation embedded in a strip of cubic material (Fig. 4) is used as the kernel of the integral equation. This solution, together with analytic solutions to a dislocation in an infinite and semi-infinite space of generally anisotropic material, is constructed in this appendix.

It has been shown in Lekhnitskii (1963) that the problems of plane anisotropic elasticity can be conveniently formulated in terms of two analytic functions, $\phi_1(z_1)$ and $\phi_2(z_2)$ with two complex variables, $z_j = x + \mu_j y$. The parameters μ_1 and μ_2 are solved from the algebraic equation

$$b_{11}\mu^4 - 2b_{16}\mu^3 + (2b_{12} + b_{66})\mu^2 - 2b_{26}\mu + b_{22} = 0 \qquad \text{(AIII.1)}$$

The roots of eqn. (AIII.1) can never be real, and thus they occur in conjugate pairs. Here μ_1 and μ_2 are chosen to be the ones with positive imaginary parts. The stresses, resultant forces on an arc and displacements are given by

$$\sigma_x = 2\,\text{Re}\left[\mu_1^2\phi_1'(z_1) + \mu_2^2\phi_2'(z_2)\right]$$

$$\sigma_y = 2\,\text{Re}\left[\phi_1'(z_1) + \phi_2'(z_2)\right]$$

$$\tau_{xy} = -2\,\text{Re}\left[\mu_1\phi_1'(z_1) + \mu_2\phi_2'(z_2)\right]$$

$$f_x = 2\,\text{Re}\left[\mu_1\phi_1(z_1) + \mu_2\phi_2(z_2)\right]$$

$$f_y = -2\,\text{Re}\left[\phi_1(z_1) + \phi_2(z_2)\right] \qquad \text{(AIII.2)}$$

$$u_x = 2\,\text{Re}\left[p_1\phi_1(z_1) + p_2\phi_2(z_2)\right]$$

$$u_y = 2\,\text{Re}\left[q_1\phi_1(z_1) + q_2\phi_2(z_2)\right]$$

where Re[ ] signifies the real part of a complex quantity, and

$$p_j = b_{11}\mu_j^2 + b_{12} - b_{16}\mu_j \, , \quad q_j = b_{22}/\mu_j + b_{12}\mu_j - b_{26} \qquad \text{(AIII.3)}$$

The potentials for an edge dislocation with Burgers vector b_x and b_y at the point (x_0, y_0) in an infinite body are of the form

$$\phi_{j0}(z) = W_j \ln(z - s_j) \, , \quad s_j = x_0 + \mu_j y_0 \qquad \text{(AIII.4)}$$

where the suffix 0 attached to the potentials indicates that the solution is for an infinite body. The complex constants W_1 and W_2 are determined from

$$\begin{cases} \text{Im} [\, W_1 + W_2] = 0 \\[4pt] \text{Im} [\, \mu_1 W_1 + \mu_2 W_2 \,] = 0 \\[4pt] \text{Im} [\, \mu_1^2 W_1 + \mu_2^2 W_2 \,] = - b_x/(4\pi b_{11}) \\[4pt] \text{Im} [\, W_1/\mu_1 + W_2/\mu_2] = - b_y/(4\pi b_{22}) \end{cases} \qquad \text{(AIII.5)}$$

where Im [ ] represents the imaginary part of a quantity. For the special case that the material is cubic with the principal axes along the x and y axes, eqn.(AIII.5) yields

$$W_1 = \frac{1}{\mu_1 - \mu_2}\Big[- B_x + B_y/\mu_1 \Big] \, , \quad W_2 = \frac{1}{\mu_1 - \mu_2}\Big[B_x - B_y/\mu_2 \Big]$$

$$B_\alpha = \frac{b_\alpha}{8\pi m b_{11}} \qquad \text{(AIII.6)}$$

Specializing (AIII.1) to a cubic material ($b_{16} = b_{26} = 0$, $b_{11} = b_{22}$) gives

$$\mu_1 = i\,(n + m), \quad \mu_2 = i\,(n - m), \quad \text{for } 1 < \rho < \infty$$

$$\mu_1 = i\,n + m, \quad \mu_2 = i\,n - m, \quad \text{for } -1 < \rho < 1 \qquad \text{(AIII.7)}$$

$$n = \sqrt{\frac{1+\rho}{2}} \, , \quad m = \sqrt{\left|\frac{1-\rho}{2}\right|}$$

The degenerate value $\rho = 1$ (corresponding to isotropic materials) can be treated as the limiting case. With the dislocation at the origin, i.e., $x_0 = y_0 = 0$, the stresses are

$$\sigma^0_{\alpha\beta}(x,y) = f_{\alpha\beta\gamma} B_\gamma, \qquad f_{\alpha\beta\gamma} = \frac{1}{m}\left[g_{\alpha\beta\gamma}(m) - g_{\alpha\beta\gamma}(-m) \right] \qquad (AIII.8)$$

where

$$g_{111}(m) = -\frac{(n+m)^3 y}{r^2}, \ g_{112}(m) = g_{121}(m) = \frac{(n+m)x}{r^2}$$

$$g_{222}(m) = -\frac{y/(n+m)}{r^2}, \ g_{221}(m) = g_{122}(m) = \frac{(n+m)y}{r^2} \qquad (AIII.9)$$

$$r^2 = x^2 + (n+m)^2 y^2$$

for $\rho > 1$, and

$$g_{111}(m) = \frac{\rho x - my}{r^2}, \ g_{112}(m) = g_{121}(m) = \frac{mx + y}{r^2}$$

$$g_{222}(m) = \frac{mx \cdot \rho y}{r^2}, \ g_{221}(m) = g_{122}(m) = -\frac{x + my}{r^2} \qquad (AIII.10)$$

$$r^2 = (x + my)^2 + (ny)^2$$

for $-1 < \rho < 1$.

For a point-wise singularity, such as dislocation and point force, in generally anisotropic half-space with traction-free boundary $y = 0$, it has been shown by Suo (1988) that the potentials can be constructed with the solution for the same singularity in an infinite body, namely,

$$\phi_1(z) = \phi_{10}(z) + \frac{1}{\mu_1 - \mu_2}\left[(\mu_2 - \overline{\mu}_1)\overline{\phi}_{10}(z) + (\mu_2 - \overline{\mu}_2)\overline{\phi}_{20}(z) \right]$$

$$(AIII.11)$$

$$\phi_2(z) = \phi_{20}(z) + \frac{1}{\mu_1 - \mu_2}\left[(\overline{\mu}_1 - \mu_1)\overline{\phi}_{10}(z) + (\overline{\mu}_2 - \mu_1)\overline{\phi}_{20}(z) \right]$$

A superposition scheme is used here to construct the solution for an edge dislocation embedded in an infinite strip (Fig.3). Attention will be confined to cubic materials with a principal axis along the direction of the strip. A solution without singularity in the strip, which is represented by the Airy stress function $U(x,y)$ in Appendix I, is superposed onto the solution to an edge dislocation in an infinite body to nullify the traction on the the strip boundaries. The

following conventions of the Fourier-cos and -sin transforms for even and odd functions, respectively, will be adopted

$$f(x) = \int_0^{+\infty} \hat{f}(\theta) \cos\theta x \, d\theta, \quad \hat{f}(\theta) = \frac{2}{\pi} \int_0^{+\infty} f(x) \cos\theta x \, dx$$

$$g(x) = \int_0^{+\infty} \hat{g}(\theta) \sin\theta x \, d\theta, \quad \hat{g}(\theta) = \frac{2}{\pi} \int_0^{+\infty} g(x) \sin\theta x \, dx$$

(AIII.12)

Owing to the symmetry of the configuration, the stress function can be expressed by the Fourier integrals

$$U(x, y) = B_x \int_0^{\infty} \{\hat{U}_i(\theta, y)\}^T \{A_i(\theta)\} \frac{\cos\theta x}{\theta^2} d\theta$$

$$+ B_y \int_0^{\infty} \{\hat{U}_i(\theta, y)\}^T \{C_i(\theta)\} \frac{\sin\theta x}{\theta^2} d\theta$$

(AIII.13)

where $\hat{U}$'s are solved from

$$\left[\theta^4 - 2\rho\theta^2 \frac{\partial^2}{\partial y^2} + \frac{\partial^4}{\partial y^4}\right] \hat{U}(\theta, y) = 0$$

(AIII.14)

The solutions are

$$\{\hat{U}_i(\theta, y)\}^T = \begin{cases} \{e^{(n+m)y\theta} \quad e^{(n-m)y\theta} \quad e^{(-n-m)y\theta} \quad e^{(-n+m)y\theta}\}, \rho > 1 \\ \{e^{ny\theta}\sin(my\theta) \quad e^{ny\theta}\cos(my\theta) \quad e^{-ny\theta}\sin(my\theta) \quad e^{-ny\theta}\cos(my\theta)\} \\ \qquad\qquad\qquad -1 < \rho < 1 \\ \{e^{y\theta} \quad y\theta\, e^{y\theta} \quad e^{-y\theta} \quad y\theta\, e^{-y\theta}\}, \quad \rho = 1 \end{cases}$$

(AIII.15)

The stresses are derived form (AI.1).

$$\sigma_{yy}(x,y) = -B_x \int_0^\infty \{\hat{U}_1(\theta,y)\}^T \{A_1(\theta)\} \cos\theta x \, d\theta$$

(AIII.16a)

$$-B_y \int_0^\infty \{\hat{U}_1(\theta, y)\}^T \{C_1(\theta)\} \sin\theta x \, d\theta$$

and

$$\tau_{xy}(x,y) = +B_x \int_0^\infty \{\partial\hat{U}_1(\theta,y)/\partial y\}^T \{A_1(\theta)\} \sin\theta x \, d\theta$$

(AIII.16b)

$$-B_y \int_0^\infty \{\partial\hat{U}_1(\theta, y)/\partial y\}^T \{C_1(\theta)\} \cos\theta x \, d\theta$$

The coefficients A's and C's are used to satisfy the strip boundary conditions. Written in the Fourier transform variables, these conditions become

$$\begin{bmatrix} \{\hat{U}_1(h)\}^T \\ \{\partial\hat{U}_1(h)/\partial y\}^T \\ \{\hat{U}_1(-H)\}^T \\ \{\partial\hat{U}_1(-H)/\partial y\}^T \end{bmatrix} \begin{bmatrix} A_1 & C_1 \\ A_2 & C_2 \\ A_3 & C_3 \\ A_4 & C_4 \end{bmatrix} = \begin{bmatrix} \cdot\hat{f}_{221}(h) & \hat{f}_{222}(h) \\ -\hat{f}_{121}(h) & \hat{f}_{122}(h) \\ \hat{f}_{221}(-H) & \hat{f}_{222}(-H) \\ -\hat{f}_{121}(-H) & \hat{f}_{122}(-H) \end{bmatrix}$$

(AIII.17)

where the Fourier transforms of the functions defined in (AIII.8-10) are

$$\hat{f}_{121}(y) = \frac{1}{m}\left[(n+m) e^{-(n+m)|y|/\theta} - (n-m) e^{-(n-m)|y|/\theta} \right]$$

$$\hat{f}_{222}(y) = \frac{1}{m}\left[-\frac{1}{n+m} e^{-(n+m)|y|/\theta} + \frac{1}{n-m} e^{-(n-m)|y|/\theta} \right]$$

(AIII.18)

$$\hat{f}_{221}(y) = \hat{f}_{122}(y) = \frac{\text{sgn}(y)}{m}\left[e^{-(n+m)|y|/\theta} - e^{-(n-m)|y|/\theta} \right]$$

for $\rho > 1$, and

$$\hat{f}_{121}(y) = 2\left[\cos(my\theta) - n\,\frac{\sin(m\,|y|\theta)}{m} \right] e^{-n|y|\theta}$$

$$\hat{f}_{222}(y) = 2\left[\cos(my\theta) + n\,\frac{\sin(m\,|y|\theta)}{m} \right] e^{-n|y|\theta} \qquad (AIII.19)$$

$$\hat{f}_{221}(y) = \hat{f}_{122}(y) = -2\left[\frac{\sin(my\theta)}{m} \right] e^{-n|y|\theta}$$

for $-1 < \rho < 1$. The dependence on θ has not been noted explicitly.

In the integral equation formulation in Appendix II, the stresses at x induced by the dislocation at $x = 0$ are desired along the line parallel to the strip boundaries with the dislocation on it. They can be written in the form

$$\sigma_{2\alpha}(x) = \frac{2\,B_\alpha}{x} + F_{\alpha\beta}(x)B_\beta \qquad (AIII.20)$$

where F's are to be evaluated numerically using the Fourier integrals (AIII.16) letting $y = 0$. However, for the half-plane problem, i.e., $H \to \infty$, analytic expressions are obtained from (AIII.11). The results are

$$F_{\alpha\beta} = \left(\frac{n}{m}\right)^2 \left[D_{\alpha\beta}(m) + D_{\alpha\beta}(-m) - 2D_{\alpha\beta}(0)/n^2 \right], \quad \alpha = \beta$$

$$\qquad (AIII.21)$$

$$F_{\alpha\beta} = \left(\frac{n}{m}\right)^2 \left[D_{\alpha\beta}(m) + D_{\alpha\beta}(-m) - 2D_{\alpha\beta}(0) \right], \quad \alpha \neq \beta$$

where

$$D_{11}(m) = -\frac{(n+m)\,x}{nr^2}, \quad D_{22}(m) = -\frac{(n-m)\,x}{nr^2},$$

$$\qquad (AIII.22)$$

$$D_{12}(m) = -D_{21}(m) = -\frac{2(n+m)h}{n\,r^2}, \quad r^2 = x^2 + (n+m)^2 h^2$$

for $\rho > 1$, and

$$D_{11}(m) = \frac{x}{r^2} \, , \; D_{22}(m) = \frac{x - 4mh}{r^2}$$

$$\text{(AIII.23)}$$

$$D_{12}(m) = - D_{21}(m) = \frac{2h}{r^2}, \; r^2 = (x + 2mh)^2 + (2nh)^2$$

for $-1 < \rho < 1$.

Table I values of λ and ρ for some materials

Material	$1/\lambda$	ρ
Al (FCC)	1	0.74
Cu (FCC)	1	0.03
Fe (BCC)	1	0.20
Pb (FCC)	1	0.33
Ash	10.5	1.67
Balsa	21.0	2.13
Oak	2.7	1.16
Pine	14.8	1.10
Graphite/Epoxy	9.5	3.34
GY70/Epoxy	42.0	3.36
Boron/Epoxy	14.3	4.91
Graphite/Al	5.0	1.12

Table II $\omega(\eta, \rho)$ (in degrees)

η \ ρ	-5	0	1	2	3	4
0	51.0	51.7	52.1	52.2	52.2	52.3
0.5	50.4	50.4	50.9	51.1	51.1	51.7
1	49.1	49.1	49.1	49.1	49.1	49.1

$$M^* = M + P(H+h)/2$$
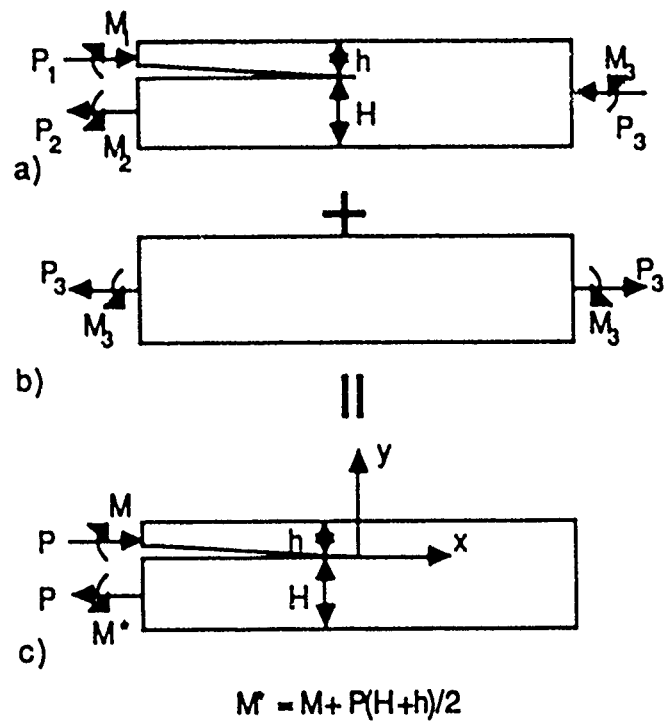
Fig. 1 Superposition scheme for load reduction
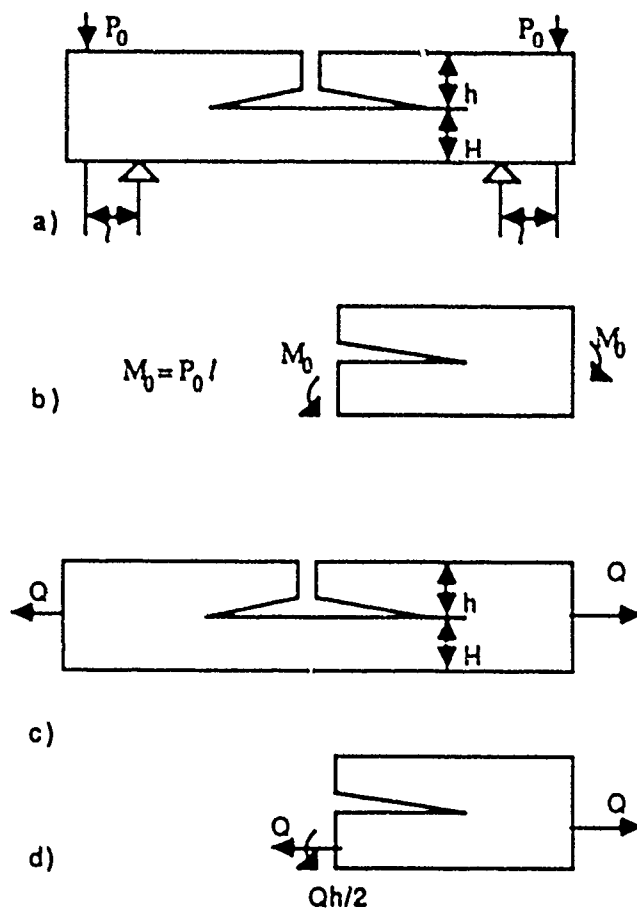
Fig. 2 Transverse splitting from notches.
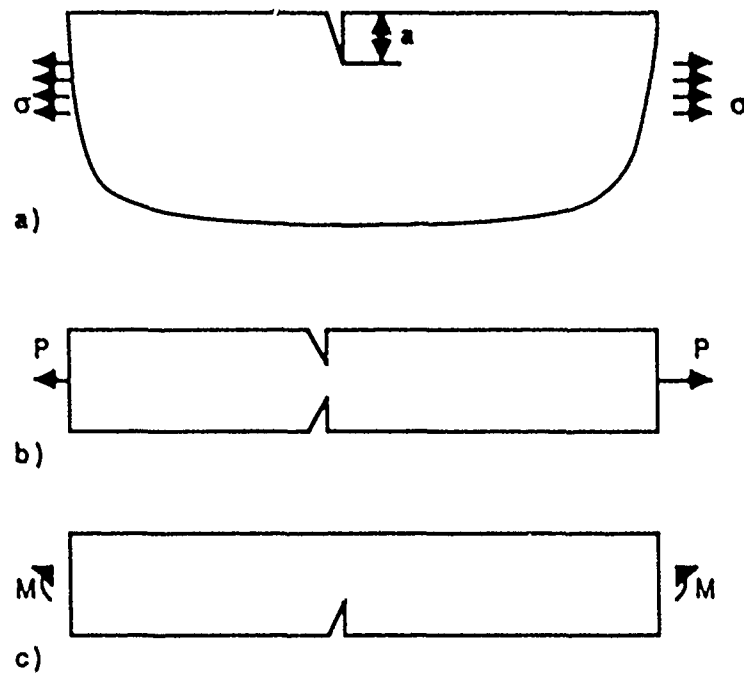
Fig. 3 More specimens.

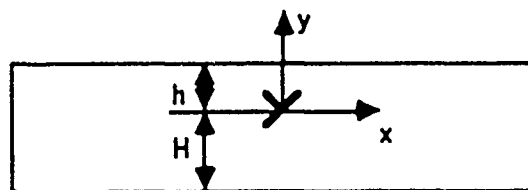Fig. 4 A dislocation in a cubic material strip.

SINGULARITIES INTERACTING WITH

INTERFACES AND CRACKS - I. ISOTROPIC MATERIALS

Zhigang Suo

SINGULARITIES INTERACTING WITH

INTERFACES AND CRACKS - I. ISOTROPIC MATERIALS

Zhigang Suo
Division of Applied Sciences
Harvard University
Cambridge, MA 02138

October 1988

ABSTRACT

Solutions to singularities such as point force, point moment, edge dislocation and transformation strain spot embedded in bonded elastic blocks of dissimilar materials are found to relate to the solutions to the same singularities in an infinite homogeneous plane by a formula independent of the nature of the singularities. This universal result is then used to analyze the interactions between singularities and interface cracks. The complete solutions and stress intensity factors are presented for two important interface crack configurations.

1. Introduction

Recent interest in micromechanics calls for the analyses of the elastic fields for *pointwise singularities*, such as point force, point moment, edge dislocation and circular transformation strain spot, interacting with interfaces and cracks. For example, crack/dislocation interaction plays an important role in understanding the brittle versus ductile response of crystals [1,2]; enhanced toughness in ZrO_2-particle-enriched ceramics has been modeled successfully in recent years [3-7], where an analysis of the transformation strain spot interacting with cracks is usually the first step; embrittlement/ductilization of polycrystals by impurity segregation such as P in Fe and B-doped Ni_3Al alloy have received much attention recently (*e.g.*, see [8]), mechanistic modelling of which has been attempted by considering crack tip (anti-)shielding by impurities (essentially dilatation spots) [9,10]. Along with the intrinsic physical significance of these interaction solutions, they are frequently used as kernel functions of integral equations. A well-known approach to simulate cracks by arrays of dislocations was outlined in the article by Rice [11], and explored extensively by Edogan and his group (e.g. [12]). Recent applications are found to model phenomena such as crack

kinking [13-15], edge spalling [16], composite delamination [17-20], and to analyze some interface fracture specimens [20, 21]. As suggested by the success of a method of analyzing homogeneous cracks [22], use of point force solutions in a cracked bimaterial system as the fundamental solutions, in conjunction with a procedure to extract mixed mode stress intensity factors from path independent integrals [23], may lead to an efficient Boundary Element algorithm for interface crack analyses.

Apparently there are many applications for this class of solutions, which may partially justify a unified presentation for such classical-looking problems. Another fact is that most of the work cited above is confined to cracks in homogeneous materials, and consequently, most singularity/crack interaction solutions scattered in the literature are for homogeneous materials. As a matter of fact, this note results from the investigation of the author, and the research group to which he belongs, on the mechanics of thin film and interface fracture [14-21]. Attention here will be focussed on the construction of the basic solutions. Guidelines for sophisticated applications may be found in the above mentioned papers.

The plane elasticity problem analyzed is depicted in Fig. 1. A singularity interacting with the bimaterial interface is considered first (Fig. 1a). Without loss of generality, singularities are only embedded in material 2. The solution is built on the complex potentials for the same singularity in an infinite homogeneous plane. As illustrated in Fig. 1, the interaction between singularities and interfacial cracks is analyzed by superposition. To make the scheme possible, one needs the solution to the problem specified in Fig. 1b, with interfacial cracks loaded by traction on the crack faces. This latter problem has been solved by several authors in the 1960's [24-26], and will be adapted here by using the two Dundurs' parameters defined below.

The nondimensional elastic moduli dependence of a bimaterial system, with simply connected domain and traction prescribed on its boundary, may be expressed in terms of two *Dundurs' parameters* [27]

$$\alpha = \frac{\Gamma(\kappa_2 + 1) - (\kappa_1 + 1)}{\Gamma(\kappa_2 + 1) + (\kappa_1 + 1)} \, , \qquad \beta = \frac{\Gamma(\kappa_2 - 1) - (\kappa_1 - 1)}{\Gamma(\kappa_2 + 1) + (\kappa_1 + 1)} \tag{1}$$

Subscripts 1 and 2 refer to the two materials, $\kappa = 3 - 4\nu$ for plane strain and $(3-\nu)/(1+\nu)$ for plane stress, $\Gamma = \mu_1/\mu_2$, ν is Poisson's ratio and μ is shear modulus. The physically admissible values of α and β are restricted to a parallelogram enclosed by $\alpha = \pm 1$ and $\alpha - 4\beta = \pm 1$ in the α, β–plane. The two parameters measure the elastic dissimilarity of two materials in the sense that both vanish when the dissimilarity does. Two other bimaterial parameters, Σ, the *stiffness ratio*, and ε, the *oscillatory index*, are related to α and β, respectively, by

$$\Sigma = \frac{c_2}{c_1} = \frac{1 + \alpha}{1 - \alpha} \quad , \quad \varepsilon = \frac{1}{2\pi} \ln \frac{1 - \beta}{1 + \beta} \tag{2}$$

where $c = (\kappa + 1)/\mu$ is a measure of the compliance of a material and will appear again. Thus α can be readily interpreted as a measure of the dissimilarity in stiffness of the two materials. Material 1 is stiffer than 2 as $\alpha > 0$ and material 1 is relatively compliant as $\alpha < 0$. The parameter ε, thus β, as has been discussed extensively in the literature on interfacial fracture mechanics, is responsible for various pathological behaviors at an interfacial crack tip (e.g.[28-30]). However, ε is typically very small. Indeed, since $| \beta | \le .5$, from (2) one finds $| \varepsilon | \le \ln(3)/2\pi \approx 0.175$. Various proposals for handling or ignoring the ε-effects have been considered [21,28]. In this paper no special consideration is given to such effects as crack face contact due to non-zero ε [29,30] in deriving the results for the crack/singularity interaction.

2. Complex Potentials

Stresses and displacements for a homogeneous body under plane deformation can be represented by two standard Muskhelishvili complex potentials $\phi(z)$ and $\psi(z)$ [31]. However, another pair of commonly used potentials, $\Phi(z)$ and $\Omega(z)$, defined as

$$\Phi(z) = \phi'(z) \, , \quad \Omega(z) = [\, z \, \phi'(z) + \psi(z) \,]' \tag{3}$$

prove to be more convenient for our purpose. Stress and displacement components are then derived from

$$\sigma_{xx} + \sigma_{yy} = 2 [\Phi(z) + \overline{\Phi(z)}]$$

$$\sigma_{yy} + i \sigma_{xy} = \overline{\Phi(z)} + \Omega(z) + (\bar{z} - z) \Phi'(z)$$

$$-2i\mu \frac{\partial}{\partial x}(u_y + i u_x) = \kappa \overline{\Phi(z)} - \Omega(z) - (\bar{z} - z)\Phi'(z)$$

(4)

One can confirm a useful coordinate translation rule (see Fig. 2). Suppose that $\Phi\bullet(z\bullet)$ and $\Omega\bullet(z\bullet)$ are the potentials in the coordinate system $z\bullet = x\bullet + i\,y\bullet$, while $\Phi(z)$ and $\Omega(z)$ are the potentials for the same problem in the coordinate system $z = x + i\,y$, where $z\bullet = z - s$, then

$$\Phi(z) = \Phi_\bullet(z - s), \quad \Omega(z) = \Omega_\bullet(z - s) + (s - \bar{s}) \Phi_\bullet'(z - s)$$

(5)

Potentials for singularities in an *infinite homogeneous plane* are the building blocks of this paper. Listed below are some frequently used examples.

An edge dislocation at $z = s$

$$\Phi_0(z) = B[\frac{1}{z - s}], \quad \Omega_0(z) = B[\frac{\bar{s} - s}{(z - s)^2}] + \overline{B} [\frac{1}{z - s}]$$

$$B = \frac{\mu}{\pi i (1 + \kappa)}(b_x + i b_y)$$

(6)

where b_x and b_y are x and y components of the dislocation.

A point force at $z = s$

$$\Phi_0(z) = -Q[\frac{1}{z - s}], \quad \Omega_0(z) = -Q[\frac{\bar{s} - s}{(z - s)^2}] + \kappa \overline{Q}[\frac{1}{z - s}]$$

$$Q = \frac{1}{2\pi(\kappa + 1)}(P_x + i P_y)$$

(7)

where P_x and P_y are force components in x and y directions.

A point moment M at $z = s$

$$\Phi_0(z) = 0, \quad \Omega_0(z) = \frac{M}{2\pi i} \left[\frac{1}{(z-s)^2} \right] \tag{8}$$

A Circular Transformation Strain Spot

Let a circular region of radius R and center $z = s$ in an infinite homogeneous plane undergo a uniform transformation straining $\varepsilon_{\alpha\beta}$. Continuity of tractions and displacements across the circular boundary is maintained. This is a 2D version of the Eshelby problem, which is included in an unpublished report by Hutchinson [32]. The potentials for the elastic field outside the circular spot, $|z - s| > R$, are

$$\Phi_0(z) = -AR^2 \left[\frac{1}{(z-s)^2} \right]$$

$$\Omega_0(z) = (A + 4B)R^2 \left[\frac{1}{(z-s)^2} \right] - 3AR^4 \left[\frac{1}{(z-s)^4} \right] + 2AR^2 \left[\frac{s - \bar{s}}{(z-s)^3} \right] \tag{9}$$

$$A = \frac{\mu}{1+\kappa}(\varepsilon_{xx} - \varepsilon_{yy} + 2i\varepsilon_{xy}), \quad B = \frac{\mu}{1+\kappa}\left(\frac{\varepsilon_{xx} + \varepsilon_{yy}}{2}\right) \quad .$$

3. Singularities Interacting with a Bimaterial Interface

Now the problem in Fig. 1a is considered. Let the potentials for the two blocks be

$$\Phi(z) = \begin{cases} \Phi^1(z) + \Phi_0(z), & z \text{ in #1} \\ \Phi^2(z) + \Phi_0(z), & z \text{ in #2} \end{cases} \quad \Omega(z) = \begin{cases} \Omega^1(z) + \Omega_0(z), & z \text{ in #1} \\ \Omega^2(z) + \Omega_0(z), & z \text{ in #2} \end{cases} \tag{10}$$

where $\Phi_0(z)$ and $\Omega_0(z)$ signify the potentials for a singularity in an *infinite homogeneous plane* of material 2, which could be one of those listed in Section 2. Obviously $\Phi_0(z)$, $\Omega_0(z)$, $\Phi^1(z)$ and $\Omega^1(z)$ are analytic for z above the x axis, while $\Phi^2(z)$ and $\Omega^2(z)$ are analytic for z below the x axis. The task below is to relate $\Phi^1(z)$, $\Omega^1(z)$, $\Phi^2(z)$ and $\Omega^2(z)$ to $\Phi_0(z)$ and $\Omega_0(z)$. The continuity of $\sigma_{yy} + i\sigma_{xy}$ across the interface requires

$$\overline{\Phi}^1(x) + \Omega^1(x) = \overline{\Phi}^2(x) + \Omega^2(x) \tag{11}$$

By the standard analytic continuation arguments it follows that

$$\overline{\Phi^1}(z) = \Omega^2(z), \quad z \text{ in } \#2$$

$$\overline{\Phi^2}(z) = \Omega^1(z), \quad z \text{ in } \#1 \tag{12}$$

The continuity of displacements across the interface, with the aid of (10), leads to

$$(1 - \beta) \, \Omega^2(x) - (\alpha + \beta) \, \overline{\Phi_0}(x) = (1 + \beta) \, \Omega^1(x) - (\alpha - \beta) \, \Omega_0(x) \tag{13}$$

Again by analytic continuity arguments one obtains

$$\Omega^2(z) = \Lambda \, \overline{\Phi_0}(z), \quad \Omega^1(z) = \Pi\Omega_0(z) \tag{14}$$

Here Λ and Π measure the inhomogeneity by

$$\Lambda = \frac{\alpha + \beta}{1 - \beta}, \qquad \Pi = \frac{\alpha - \beta}{1 + \beta} \tag{15}$$

Now with (12) and (14) one can rewrite (10) explicitly as

$$\Phi(z) = \begin{cases} (1 + \Lambda)\Phi_0(z), & z \text{ in } \#1 \\ \Phi_0(z) + \Pi\overline{\Omega}_0(z), & z \text{ in } \#2 \end{cases} \qquad \Omega(z) = \begin{cases} (1 + \Pi)\Omega_0(z), & z \text{ in } \#1 \\ \Omega_0(z) + \Lambda\overline{\Phi}_0(z), & z \text{ in } \#2 \end{cases} \tag{16}$$

so that the singularity solutions in bonded half planes of dissimilar materials can be constructed using the corresponding singularity solutions in an infinite homogeneous plane by eqn. (16). This relation is universal in the sense that it is completely independent of the physical nature of the singularities.

Singularities in a half space interacting with the traction-free surface can be treated as a special case by letting $\alpha = -1$, or $\Lambda = \Pi = -1$. Specializing (16) to this case one obtains

$$\Phi(z) = \Phi_0(z) - \overline{\Omega}_0(z), \quad \Omega(z) = \Omega_0(z) - \overline{\Phi}_0(z) \tag{16a}$$

Continuation arguments have been applied to the 3D version of the same problem in [33,34], where the Kelvin solution was used to construct the point force solutions in a half-space and more generally, in two bonded half-spaces of dissimilar materials.

4. Interfacial Cracks

The singular stress field of an interfacial crack tip shows a $r^{-1/2 + i\varepsilon}$ type singularity [35]. Accordingly, the *complex stress intensity factor*, $K = K_1 + iK_2$, is defined [17] such that the traction in the interface a distance r ahead of the crack tip is

$$\sigma_{yy} + i\sigma_{xy} = \frac{K}{\sqrt{2\pi r}} r^{i\varepsilon} \tag{17}$$

and the relative crack face displacements a distance r behind the crack tip are given by

$$\delta_y + i\delta_x = \frac{c_1 + c_2}{2\sqrt{2\pi} (1 + 2i\varepsilon) \cosh(\pi\varepsilon)} K\sqrt{r} \, r^{i\varepsilon} \tag{18}$$

thereby the energy release rate is [36]

$$G = \frac{c_1 + c_2}{16 \cosh^2 \pi\varepsilon} |K|^2 \tag{19}$$

To make the superposition scheme in Fig. 1 possible, one needs the *complete* solution for the problem in Fig. 1b. Suppose the cracks considered lie on the interface of two dissimilar material blocks. It suffices to consider only the case of traction prescribed on the crack faces, for other methods of loading may be reduced to this case by superposition. This problem was solved in [24-26]. Outlined below is the solution in the present notation. The derivation is simplified to some extent by the use of the Dundurs' parameters.

Let the potentials for the two half-planes in Fig. 1b be written as

$$\Phi(z) = \begin{cases} \Phi^a(z), & z \text{ in } \#1 \\ \Phi^b(z), & z \text{ in } \#2 \end{cases} \qquad \Omega(z) = \begin{cases} \Omega^a(z), & z \text{ in } \#1 \\ \Omega^b(z), & z \text{ in } \#2 \end{cases} \qquad (20)$$

where the supersript "a" indicates that the potential is for the material above, while "b" is for the material below. The continuity of $\sigma_{yy} + i\,\sigma_{xy}$ across the interface requires

$$\overline{\Phi^a}(z) = \Omega^b(z), \quad z \text{ in } \#2$$

$$\overline{\Phi^b}(z) = \Omega^a(z), \quad z \text{ in } \#1 \qquad (21)$$

With (21) one can show that the derivative of displacement jumps across the interface, or the components of the Burgers vector, can be written as

$$-2\,i\,\frac{\partial}{\partial x}(\delta_y + i\,\delta_x) = \frac{c_1 + c_2}{2}\left[(1-\beta)\Omega^b(x) - (1+\beta)\Omega^a(x)\right] \qquad (22)$$

Consequently, due to the continuity of the displacement across the bonded portion of the interface, one can define a function $f(z)$ which is analytic in the whole plane except on the crack lines, such that

$$\Omega^a(z) = (1-\beta)\,f(z), \quad z \text{ in } \#1$$

$$\Omega^b(z) = (1+\beta)f(z), \quad z \text{ in } \#2 \qquad (23)$$

In terms of $f(z)$, the Burgers vector (22) can be written as

$$-2\,i\,\frac{\partial}{\partial x}(\delta_y + i\,\delta_x) = \frac{c_1 + c_2}{2}(1-\beta^2)\left[f(x) - f^+(x)\right] \qquad (24)$$

and the traction on the interface is given by

$$\sigma_{yy} + i\,\sigma_{xy} = (1+\beta)\,f(x) + (1-\beta)\,f^+(x) \qquad (25)$$

The prescribed traction on the cracks thus leads to the following Hilbert problem

$$(1 + \beta)f'(x) + (1 - \beta)f^{*}(x) = \sigma_{yy}(x) + i\,\sigma_{xy}(x), \quad \text{on crack lines} \qquad (26)$$

Suppose there are n finite cracks in the intervals (a_j, b_j) and two semi-infinite cracks in the intervals $(-\infty, b_0)$ and $(a_0, +\infty)$, respectively, on the x axis. Following the methods of Muskhelishvili [31], a homogeneous solution of eqn.(26) (i.e., a solution of f(z) when setting the right hand side of eqn.(26) to be zero) can be written as

$$\chi(z) = \prod_{j=0}^{n} (z - a_j)^{-1/2 - i\epsilon} (z - b_j)^{-1/2 + i\epsilon} \qquad (27)$$

where the branch cuts are chosen along the crack lines so that the product for each finite crack behaves as $1/z$ for large z. The solution to (26) is

$$f(z) = \frac{1}{1 - \beta} \frac{\chi(z)}{2\pi i} \int \frac{\sigma_{yy}(x) + i\,\sigma_{xy}(x)}{\chi^{*}(x)\,(x - z)}\, dx + \chi(z)P(z) \qquad (28)$$

where the integral should be taken over the union of the cracks, and P(z) is a polynomial which should be chosen so that f(z) is bounded at infinity and the net Burgers vector for each of the n finite cracks is zero. From (24) this latter statement leads to n equations

$$\int_{a_j}^{b_j} \left[f(x) - f^{*}(x) \right] dx = 0, \quad j = 1, 2, ..., n \qquad (29)$$

Thus f(z) can be determined and also the potentials $\Phi(z)$ and $\Omega(z)$ by (20), (21) and (23). Once f(z) is obtained, the complex stress intensity factor defined in (17) can be extracted from (25). Noticing that $f^{-}(x) = f^{+}(x) = f(x)$ on the bonded portion of the interface, one obtains

$$K = \sqrt{2\pi}\ \lim_{x \to a}\ 2(x-a)^{1/2 - i\epsilon}\, f(x) \qquad (30)$$

if the crack tip is at $x = a$, running in the direction of positive x-axis.

Two configurations depicted in Fig. 3 are of particular importance in the application. The cracks are loaded by equal but opposite tractions $\sigma_{yy} + i\,\sigma_{xy} = -T(x)$ on the crack faces. One can verify for the semi-infinite crack

$$\chi(z) = z^{-1/2 + i\varepsilon}, \quad P(z) = 0 \tag{31}$$

Thus $f(z)$ can be determined from (28). And the complex stress intensity factor is given by

$$K = \sqrt{\frac{2}{\pi}} \cosh\pi\varepsilon \int_{-\infty}^{0} \frac{T(t)}{(-t)^{1/2 + i\varepsilon}} \, dt \tag{32}$$

In the case of a finite crack of length 2a the corresponding results are

$$\chi(z) = (z-a)^{-1/2 + i\varepsilon}(z+a)^{-1/2 - i\varepsilon}, \quad P(z) = 0 \tag{33}$$

and the stress intensity factor at the right-hand side tip is

$$K = \sqrt{\frac{2}{\pi}} \cosh\pi\varepsilon \, (2a)^{-1/2 - i\varepsilon} \int_{-a}^{+a} \left(\frac{a+t}{a-t}\right)^{1/2 + i\varepsilon} T(t) \, dt \tag{34}$$

A short list of stress intensity factors for some special loading cases can be found in [23].

5. Singularities Interacting with Interfacial Cracks

Now the interaction problem illustrated in Fig. 1c can be readily solved by the superposition of the solutions obtained in the last two sections. This scheme was used in [2] to construct the interaction solution of dislocation and a crack in a homogeneous body.

The potentials for a singularity at $z = s$ in an infinite homogeneous plane can be written in general as

$$\Phi_0(z) = \sum_{m=1}^{M} \frac{A_m}{(z-s)^m}, \quad \Omega_0(z) = \sum_{m=1}^{M} \frac{B_m}{(z-s)^m} \tag{35}$$

where the coefficients A_m and B_m may depend on s and the nature of the singularity. Several examples are given in Section 2. Suppose the potentials (35) are known, the potentials for the same singularity embedded in one of two bonded blocks as in Fig. 1a are readily constructed by (16). In particular, the stresses along the interface in Fig. 1a are

$$\sigma_{yy}(x) + i\,\sigma_{xy}(x) = (1 + \Lambda)\,\overline{\Phi}_0(x) + (1 + \Pi)\,\Omega_0(x) \qquad (36)$$

The negative of these stresses are applied to the faces of the crack in Fig. 1b. It follows from (28) that

$$f(z) = -\frac{1}{1 - \beta}\frac{\chi(z)}{2\pi i}\int \frac{(1 + \Lambda)\overline{\Phi}_0(x) + (1 + \Pi)\Omega_0(x)}{\chi^+(x)\,(x - z)}\,dx \qquad (37)$$

Here we have set $P(z) = 0$. One has to specify the crack configuration in order to evaluate the integral

$$I = \frac{1}{2\pi i}\int \frac{(1 + \Lambda)\overline{\Phi}_0(x) + (1 + \Pi)\Omega_0(x)}{\chi^+(x)\,(x - z)}\,dx \qquad (38)$$

where the integral should be taken on the crack lines. Only the two configurations depicted in Fig. 3 will be analyzed below. Consider the following contour integral

$$J = \frac{1}{2\pi i}\oint \frac{(1 + \Lambda)\overline{\Phi}_0(\xi) + (1 + \Pi)\Omega_0(\xi)}{\chi\,(\xi)\,(\xi - z)}\,d\xi \qquad (39)$$

with the contours specified in Fig. 4. It is easy to confirm

$$J = J_\infty + \frac{2}{1 - \beta}I \qquad (40)$$

where J_∞ is the same integral as (39) integrated over a circle $|z| = R$ as $R \to \infty$. It can be shown that

$$J_\infty = (1 + \Lambda)\overline{A}_1 + (1 + \Pi)B_1 \qquad (41)$$

for the finite crack and $J_\infty = 0$ for the semi-infinite crack. On the other hand J can be evaluated by its residues

$$J = \frac{1}{\chi(z)}\left[(1+\Lambda)\bar{\Phi}_0(z) + (1+\Pi)\Omega_0(z)\right] + \sum_{m=1}^{M}\left[(1+\Lambda)\bar{A}_m F_{m-1}(z,\bar{s}) + (1+\Pi)B_m F_{m-1}(z,s)\right] \quad (42)$$

where

$$F_n(z, s) = \frac{1}{m!}\frac{d^m}{d\xi^m}\left[\frac{1}{\chi(\xi)(\xi - z)}\right]_{\xi = s} \quad (43)$$

Consequently, one obtains

$$f(z) = -\frac{1}{2}\left[(1+\Lambda)\bar{\Phi}_0(z) + (1+\Pi)\Omega_0(z)\right] \quad (44)$$

$$-\frac{\chi(z)}{2}\sum_{m=1}^{M}\left[(1+\Lambda)\bar{A}_m F_{m-1}(z,\bar{s}) + (1+\Pi)B_m F_{m-1}(z,s)\right]$$

for the semi-infinite crack ar ‘

$$f(z) = \frac{\chi()}{2}\left[\; ： ´ \;_1 + (1+\Pi)B_1\right] \quad (45)$$

$$-\frac{1}{2}\left[(1+\ldots;\Phi_0(z) + (1+\Pi)\Omega_0(z)\right]$$

$$-\frac{\chi(z)}{2}\sum_{m=1}^{M}\left[(1+\Lambda)\bar{A}_m F_{m-1}(z,\bar{s}) + (1+\Pi)B_m F_{m-1}(z,s)\right]$$

for the finite crack. Therefore the potentials for the problem in Fig. 1b can be obtained from (20), (21) and (23) with $f(z)$ given in (44) and (45). The potentials for the interaction problem in Fig. 1c are thus the superposition of (16) and those for Fig. 1b.

Since no stress intensity is present in the structure in Fig. 1a, one can deduce the stress intensity factors from (44) and (45). The results are

$$K = -\sqrt{2\pi} \sum_{m=1}^{M} \left[(1+\Lambda)\overline{A}_m F_{m-1}(0, \bar{s}) + (1+\Pi)B_m F_{m-1}(0, s) \right]$$

$$F_m(0, s) = \frac{1}{m!} \prod_{k=0}^{m-1} \left(-\frac{1}{2} - i\varepsilon - k \right) s^{-1/2-i\varepsilon-m}$$

(46)

for the semi-infinite crack and

$$K = +\sqrt{2\pi}(2a)^{-1/2-i\varepsilon} \left[(1+\Lambda)\overline{A}_1 + (1+\Pi)B_1 \right]$$

$$- \sqrt{2\pi}(2a)^{-1/2-i\varepsilon} \sum_{m=1}^{M} \left[(1+\Lambda)\overline{A}_m F_{m-1}(a,\bar{s}) + (1+\Pi)B_m F_{m-1}(a,s) \right]$$

(47)

$$F_m(a,s) = \frac{1}{m!} \frac{d^m}{d\xi^m} \left[\left(\frac{\xi+a}{\xi-a} \right)^{1/2+i\varepsilon} \right]_{\xi=s}$$

for the finite crack.

The stress intensity factors induced by point forces, dislocations and transformation strains for some 3D crack configurations in a homogeneous body are found in [37,38].

6. Summary

Complete solutions to three problems for bimaterial systems specified in Fig. 1 can be found in this paper. Singularities of an arbitrary physical nature are treated within the same framework. In particular, a universal relation is found between the potentials for singularities in an infinite homogeneous plane and in bonded blocks of dissimilar materials (eqn. (16) above). Stress intensity factors are identified for the two crack configurations for both face-loaded problem (see Fig. 1b and eqns.(32,34)) and the interaction problem (see Fig. 1c and eqns.(46,47)). It is believed that the present work will be helpful for those who are interested in micromechanics modelling as illustrated in the Introduction. Parallel results for cracks on the interface between dissimilar anisotropic bodies will be reported in the sequel of this paper.

References

1. J.R. Rice and R. Thomson, Ductile versus brittle behavior of crystals, *Phil. Mag.* 29 (1974) 73-97.

2. R. Thomson, Physics of fracture, in *Solid State Physics*, H. Ehrenreich and D. Turnbull, eds., Academic Press, Inc., 39, 1-129, 1986.

3. R.M. McMeeking and A.G. Evans, Mechanics of transformation toughening in brittle materials, *J. Am. Ceram. Soc.* 69 (1982) 242-246.

4. B. Budiansky, J.W. Hutchinson and J.C. Lambropoulos, Continuum theory of dilatant transformation toughening in ceramics, *Int. J. Solids Structures.* 19 (1983) 337-355.

5. J.W. Hutchinson, Initial crack growth tearing resistance in transformation toughening ceramics, in *Advanced Materials for Severe Service Applications*, K. Iida, ed., 1987, 77-90.

6. J.C. Amazigo and B. Budiansky, Steady-state crack growth in supercritically transforming materials, *Int. J. Solids Structures*, 24 (1988) 751-755.

7. D.M. Stump and B. Budiansky, Crack growth resistance in transformation-toughened ceramics, Harvard University Report Mech-124, 1988.

8. J. R. Rice and J.S. Wang, Embrittlement of interfaces by solute segregation, to appear in *Mater. Sci. Eng.*

9. J. Weertman and J.E. Hack, Stress intensity factor for crack tip shielding or anti-shielding by impurity atoms, *Int. J. Fract.* 30 (1986) 295-299.

10. J. Weertman and J.E. Hack, Crack tip shielding/anti-shielding by impurity atoms, *Int. J. Fract.* 36 (1988) 27-34.

11. J.R. Rice, Mathematical analysis in the mechanics of fracture, in *Fracture, An Advanced Treatise*, II, H. Liebowitz, ed., Academic Press, New York, 1968, 191-311.

12. F. Erdogan, Fracture problems in composite materials, *Eng. Fract. Mech.*, 4 (1972) 811-840

13. K. Hayashi and S. Nemat-Nasser, On branched interface cracks, *J. Appl. Mech.*, 48 (1981) 529-533.

14. M-Y. He and J.W. Hutchinson, Kinking of crack out of an interface, to appear in *J. Appl. Mech.*

15. M-Y. He and J.W. Hutchinson, Crack deflection at interface between dissimilar materials, Harvard University Report MECH-133, 1988.

16. M.D. Thouless, A.G. Evans, M.F. Ashby and J.W. Hutchinson, The edge cracking and spalling of brittle plates, *Acta Met.* 35 (1987) 1333-1341.

17. J.W. Hutchinson, M.E. Mear and J.R. Rice, Crack paralleling an interface between dissimilar materials, *J. Appl. Mech.*, 54 (1987) 828-832.

18. Z. Suo and J.W. Hutchinson, Steady-state cracking in brittle substrate beneath adherent films, Harvard University Report Mech-132, 1988.

19. Z. Suo, A crack in an orthotropic material strip, manuscript in preparation.

20. Z. Suo and J.W. Hutchinson, Interface crack between two elastic layers, Harvard University Report MECH-118, 1988.

21. Z. Suo and J.W. Hutchinson, On sandwich test specimens for measuring interface crack toughness, to appear in *Mater. Sci. Eng.*

22. H. Mews and G. Kuhn, An effective numerical stress intensity factor calculation with no crack discretization, *Int. J. Fract.*, 38 (1988) 61-76.

23. C. F. Shih, R.L. Asaro, Elastic-plastic analysis of cracks on bimaterial interfaces: part I-small scale yielding, *J. Appl. Mech.*, 55(1988) 299-316.

24. A.H. England, A crack between dissimilar media, *J. Appl. Mech.* 32 (1965) 400-402.

25. F. Erdogan, Stress distribution in bonded dissimilar materials with cracks, *J. Appl. Mech.* 32 (1965) 403-410.

26. J.R. Rice and G.C. Sih, Plane problems of cracks in dissimilar media, *J. Appl. Mech.*, 32 (1965) 418-423.

27. J. Dundurs, Elastic interaction of dislocations with inhomogeneities, in *Mathematical Theory of Dislocations*, American Society of Mechanical Engineering, New York, pp.70-115, 1968.

28. M. Comninou, The interface crack, *J. Appl. Mech.*, 44 (1977) 631-636.

29. M. Comninou and D. Schmueser, The interface crack in a combined tension-compression and shear field, *J. Appl. Mech.*, 46 (1979) 345-348.

30. J.R. Rice, Elastic fracture concepts for interfacial cracks, *J. Appl. Mech.*, 55 (1988) 98-103.

31. N.I. Muskhelishvili, *Some Basic Problems of the Mathematical Theory of Elasticity*, P. Noordhoff Ltd., Groningen, Holland, 1953.

32. J.W. Hutchinson, On steady quasi-static crack growth, Harvard Report DEAP S-8, 1974.

33. J.L. Sanders, Jr., Note on the Mindlin problem, in *Mechanics of Material Behavior (D.C. Drucker Anniversary Volume)*, G.J. Dvorak and R.T. Shield, eds, Elsevier, 345-349, 1984.

34. J.R. Rice, Point force solution for bonded dissimilar elastic halfspaces, unpublished results.

35. M.L. Williams, The stresses around a fault or crack in dissimilar media, *Bull. Seismol. Soc. Am.*, 49 (1959) 199-204.

36. B.M. Malyshev and R.L. Salganik, The strength of adhesive joints using the theory of crack, *Int. J. Fract.*, 1 (1965) 114-128.

37. H.F. Beuckner, Weight functions and fundamental fields for the penny-shaped and half-plane crack in three space, *Int. J. Solids Structures*, 23 (1987) 57-93.

38. H. Gao, Application of 3-D weight function-I. formulations of crack interactions with transformation strains and dislocations, to appear in *J. Mech. Phys. Solids.*
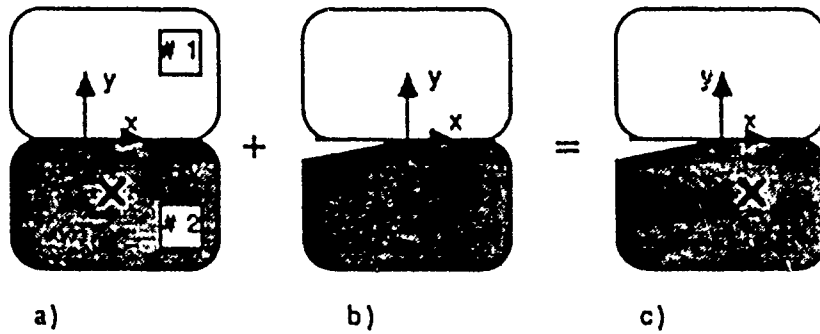
a)   b)   c)

Fig. 1 Superposition scheme. a) a singularity embedded in one of two well bonded blocks. b) interface crack with traction prescribed on the faces. c) interaction between a singularity with a traction-free crack.
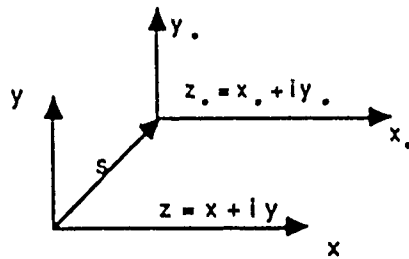
Fig. 2 A coordinate translation.
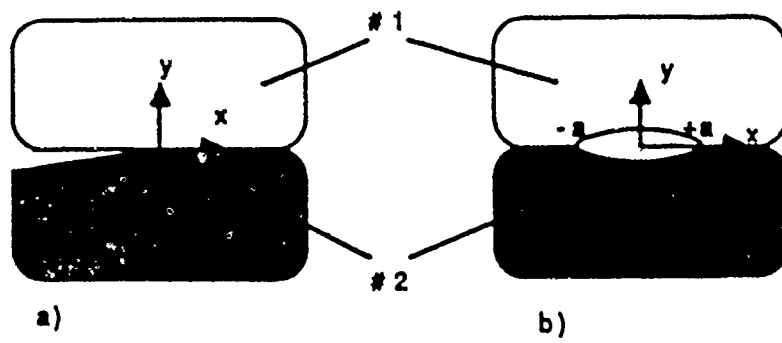
Fig. 3 Two crack configurations.
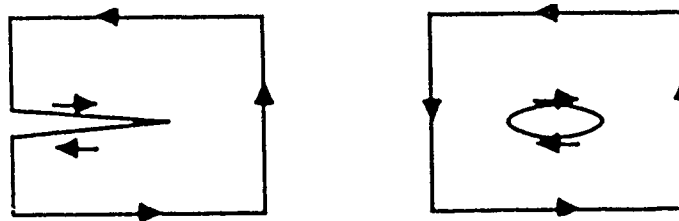
Fig. 4 Integration contours.

MATERIALS
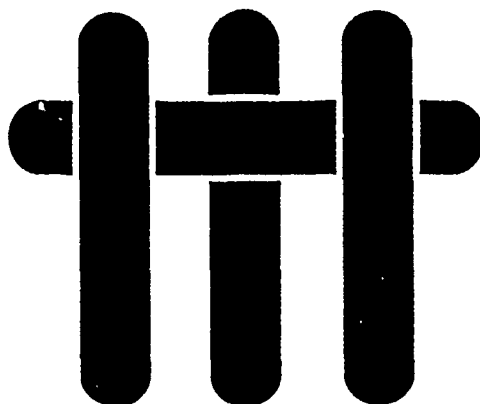
DUCTILE REINFORCEMENT

TOUGHENING OF γ-TiAl:

EFFECTS OF

DEBONDING AND DUCTILITY

by

H. E. Dève, A. G. Evans, G. R. Odette, R. Mehrabian,
Materials Department
College of Engineering
University of California
Santa Barbara, California 93106

M. L. Emiliani and R. J. Hecht
Pratt & Whitney
United Technologies Corp.
West Palm Beach, FL

ABSTRACT

The effects of reinforcement debonding and work hardening on ductile reinforcement toughening of γ-TiAl have been examined. Debonding has been varied by either the development of a brittle reaction product layer or by depositing a thin oxide coating between the reinforcement and matrix. The role of work hardening has been explored by comparing an Nb reinforcement that exhibits high work hardening with a solution hardened Ti-Nb alloy that exhibits negligible work hardening. It is demonstrated that a high work of rupture is encouraged by extensive debonding when the reinforcement exhibits high work hardening. Conversely, debonding is not beneficial when the reinforcement exhibits minimal work hardening.

1. INTRODUCTION

Substantial toughening of intermetallics and ceramics by ductile reinforcements has been established.[1-5] It has also been demonstrated that the toughening due to bridging, $\Delta \mathcal{G}_c$, has a steady-state magnitude given by[6,7]:

$$\Delta \mathcal{G}_c = \sigma_o f R \chi \tag{1}$$

where σ_0 is the uniaxial yield strength, f is the area fraction of reinforcements, 2R is the reinforcement thickness and χ is a work of rupture parameter that can vary between ~ 1/2 and ~ 6, depending upon the extent of interface debonding and the reinforcement constitutive behavior.[1-3,8] Furthermore, the magnitude of χ is reflected in the non-dimensional stress-stretch relationship

$$\chi = \int_0^{\alpha^*} (\sigma/\sigma_0) \, d\alpha \tag{2}$$

where, $\alpha = u/R$, with u being the crack opening displacement and α^* is the value of α at the rupture displacement, u^*. The principal intent of the present study is to examine the specific, yet coupled, effects of debonding and work hardening on χ, including the role of the interface/coating properties.

The systems selected for investigation consist of γ-TiAl reinforced with Nb and Ti-Nb alloys. These systems have been demonstrated to exhibit appreciable toughening in composite form [4,9,10] and also are susceptible to interface debonding when a brittle reaction product (e.g., σ phase) forms between the reinforcement and the matrix.[3] Furthermore, extremes of work hardening behavior, as well as a substantial range of flow strength, are accessible in this system.[3]

Tests that reflect toughening characteristics may be conducted using either composite cylinders[2,3] (Fig. 1a) or laminates[10] (Fig. 1b). Test specimens are more readily produced for the latter geometry, by direct diffusion bonding. Furthermore, this geometry is typical of that used for ductile phase reinforced intermetallics.[4] Consequently, a test procedure based on a plane strain laminate geometry (Fig. 1b) is devised and used to evaluate the toughening potential, based on Eqn. (2).

The degree of debonding can be independently varied by introducing a non-reactive coating between the matrix and the reinforcement. For this purpose, the potential for thin oxide coatings is given explicit consideration, with the extent of debonding assessed in terms of the fracture properties of the oxide material.

2. MATERIALS

Matrix plates (1.5 mm thickness) of TiAl (Ti-50.5 at%Al) have been prepared from HIPed and forged billets by electro-discharge machining (EDM), followed by a homogenization heat treatment at 1000 °C for 20 hrs. The resultant microstructure consists of predominantly equiaxed grains of γ-TiAl (grain size 100 μm) with small amounts of α_2 in a $(\alpha_2 + \gamma)$-lath structure. Thin reinforcement plates (from 0.12 to 0.17 mm thickness) of either pure Nb or Ti-33 at%Nb produced by hot rolling have been annealed in vacuum at 1066°C for 4 h. This material consists of single phase β with equiaxed grains.

Some of the reinforcement plates are coated on both sides with ~ 2 μm of either Al_2O_3 or Y_2O_3. Coatings are deposited by radio-frequency reactive sputtering of 99.9% pure aluminum or yttrium metal targets using a 50%-50% mixture of research grade argon and oxygen. Substrates are rotated at ~1 rpm during sputtering to ensure uniform coverage, and are not externally cooled, heated or biased. As-

4

deposited coatings were examined by SEM and found to correspond to a zone 1 or zone T microstructure, as determined by Thornton.[12]

Laminates suitable for testing (Fig. 1b) are produced by diffusion bonding. To achieve representative microstructures, the TiAl plates are carefully polished to provide good planarity and inserted into a bonding fixture depicted in Fig. 2. The diffusion bonding is carried in vacuum under a 10 MPa pressure at 1066°C for times varying between 1 hr. for the Ti-Nb alloys to 4 hrs. for the pure Nb. In some cases, split plates of TiAl are used to facilitate matrix precracking, as indicated on Fig. 2.

3. MICROSTRUCTURES

The bonded laminates have been investigated by both scanning (SEM) and transmission (TEM) electron microscopy on sections normal to the interface. Analytical electron microscopy has indicated the following general features. In the absence of oxide coatings, both SEM and TEM investigation, (Fig 3a,b), showed that the Nb reacts with the TiAl to form T_2 and σ intermediate phases[3]; whereas Ti-33%Nb produces α_2, and a duplex α/β layer[3] (Fig. 3c,d). Coatings of Y_2O_3 are found to be essentially inert and also prevent the formation of reaction products between the reinforcements and the matrix (Fig. 4a).

The Al_2O_3 coating was subject to extensive reaction with the Ti-Nb reinforcement and fully reacted during diffusion bonding to form a complex multiphase reaction product zone (Fig. 4b). These specimens were not subjected to mechanical testing. Conversely, little reaction occurred upon bonding with the Nb reinforcement (Fig. 4b). The incidence of reactions in the presence of Al_2O_3 is consistent with previous studies, which have revealed that high purity Nb bonds to

5

Al_2O_3 without reaction product formation,[13] whereas Ti reacts with Al_2O_3 to form a multiphase Ti aluminide layer.[14]

4. MECHANICAL CHARACTERISTICS

4.1 TENSILE PROPERTIES

The mechanical properties of the laminates were evaluated by conducting uniaxial tensile tests, using the geometry indicated on Fig. 1b. Symmetric precracking of the TiAl outer layers prior to tensile testing was an essential feature of the experiment. This was most systematically achieved when the split plate bonds were used, followed by tensile loading. Some tests were conducted in a servohydraulic machine with displacements monitored from an axial extensometer. Other tests were conducted *in situ* in the scanning electron microscope. Tests were also conducted on the reinforcements, without bonding to the TiAl. Tensile stress/strain characteristic obtained on the unbonded Nb and Ti-Nb reinforcements (Fig. 5a) confirm previous studies[3] which revealed that appreciable work hardening occurs in the Nb, but that Ti-Nb exhibits early unstable plastic flow due to a low work hardening rate. It must be pointed out that since Ti-Nb undergoes localized plastic deformation, the nominal strain plotted n Fig. 5a is dependent on the initial gauge length. Tests on laminates indicate marked differences in behavior between the Nb and Ti-33 at%Nb reinforcements and between specimens with and without oxide coatings, as summarized in Table I and in Fig. 5.

The presence of oxide coatings encouraged extensive debonding, which initiated with minimal plastic deformation of the reinforcement (Fig. 6) at stresses of the order of the uniaxial yield strength σ_0 . The debonding occurred primarily

between the oxide and the reinforcement. Detailed investigation revealed that the debond lengths, d, for the Nb reinforcements coated with either Y_2O_3 or Al_2O_3 (Figs. 6b,c) were substantially larger than those for uncoated reinforcements. The largest debonds occurred for Y_2O_3, d ~ 24R, while the Al_2O_3 coating gave, d ~ 7-10R, and the uncoated reinforcements gave, d ~ 5R, (Fig. 6d). Furthermore, for oxide coated Nb reinforcements, the rupture stretch, u*, is found to be proportional to the debond length, d (Fig. 7). Accordingly, the work of rupture χ is largest with Y_2O_3 coatings (χ ~ 8) and of intermediate magnitude for Al_2O_3 coatings (χ ~ 4), such that χ exhibits a linear dependence on either d/R (Fig. 8) or u*/R.

The behavior of the composite can be most effectively understood by comparing the above stress/stretch characteristics of the laminates with the corresponding curves for the unbonded reinforcements, configured such that the gauge length coincides with the final debond length observed in the laminates. Then, the plastic stretch, u, and the nominal strain, ε, are related by: $u = \varepsilon d$. The results are plotted on Fig. 9. A comparison of the normalized stress/nominal strain curves for the Nb laminates with those for unbonded reinforcements, (Fig. 9) indicates that the peak stresses σ^{max}/σ_0 are similar, but that this peak occurs at a lower value of the nominal strain for the laminates, whereas the nominal strain <u>at failure</u> is similar for both laminated and unbonded reinforcements. It is apparent from the value of σ_y/σ_0 ~ 1.5, (Table I), that despite the large amount of early debonding there is still a significant constraint effect. Frictional sliding and ligament bridging along the debond surface, (Figs. 6b, c, d), could contribute to the constraint and modify the subsequent work hardening, (Fig. 9). For the Ti-Nb reinforcements (Fig. 5c), somewhat different behavior is obtained. Notably, this material does not exhibit a stage of uniform plastic deformation. Consequently, the displacement to failure in a tensile test is dependent on the initial gauge length. Accordingly, an equivalent measure of the plastic stretch, u, for unbonded Ti-Nb,

(Fig. 5c), is simply the difference between the current and the initial gauge length. Based on this choice, it is evident (Fig. 5c) that the stress/stretch behavior is essentially the same for both the coated Ti-Nb laminate and the unbonded reinforcement.

In the <u>absence of oxide coatings</u>, the behavior has similar features to that noted in previous studies on composite cylinders[3] and on actual composites.[4,9,10] Notably, the σ phase that forms with the Nb behaves as a debond layer (Fig. 6d), and debonding extends primarily in the σ phase. Necking then initiates and rupture occurs at a stretch u ~ 2R, such that the work of rupture is of intermediate magnitude, χ ~ 2.5. Consequently, it is apparent that the σ phase is not as effective a debond medium as either the Y_2O_3 or Al_2O_3 coatings. The Ti-33 at%Nb reinforcement does not form a brittle reaction product[3]. However, the present observations (Fig. 6e) indicate that the TiAl matrix can crack parallel to the interface. Such cracks inhibit the development of full constraint and apparently encourage the formation of shear bands that lead to reinforcement rupture. The work of rupture χ ~ 1.5 is comparable than that apparent when the Y_2O_3 coating is used, although some constraint (σ ~ $2\sigma_0$) develops before the matrix cracks nucleate. Nevertheless, the complete avoidance of matrix debonding might be desirable, since it would lead to high crack growth resistance while maintaining similar values of toughness.[10]

4.2 DEBOND FRACTURE ENERGIES

The fracture energies of some of the interfacial layers have been measured using the UCSB flexural test[15] (Fig. 10). For this test, sandwich specimens are notched in the TiAl layer on the tensile side and loaded in three-point flexure to introduce a precrack along the interface. Subsequently, the specimen is loaded in four-point flexure to cause further crack extension along the interface. The crack

extension load and the specimen dimensions may then be used to give the fracture energy Γ_i.[15] Tests conducted on specimens with Y_2O_3 coatings gave $\Gamma_i \approx 25\,Jm^{-2}$, with crack propagation occurring primarily between the Y_2O_3 and the reinforcement. This value is typical of the fracture energy found for polycrystalline oxides. Tests conducted on the TiAl/Nb specimens with a σ reaction product phase gave $\Gamma_i \approx 45\,Jm^{-2}$, with crack growth occurring primarily within the σ phase.

5. IMPLICATIONS

5.1 DEBONDING

Debonding in ductile reinforcement toughened intermetallics is strongly influenced by the fracture properties of the phases that exist between the reinforcement and the matrix. Oxide coatings that have a small fracture energy ($\Gamma_i \approx 25\,Jm^{-2}$ for Y_2O_3) debond extensively prior to significant plastic deformation of the reinforcement. Simple elastic calculations would suggest steady-state energy release rates[15] and predict unlimited symmetric debonding at a critical stress. In practice, the debond is found to arrest. The actual extent of debonding is thus influenced by other factors, such as frictional sliding and bridging ligaments along the debond surface (Fig. 6 b, c, d). Additionally, the somewhat larger debond resistance of the σ-phase ($\Gamma \approx 45\,Jm^{-2}$) is apparently sufficient to substantially stabilize the debonding. Finally, it is noted that matrix debond cracking is possible with high strength Ti-Nb reinforcements. This occurs, albeit erratically, subject to a fracture energy[4], $\Gamma \approx 200\,Jm^{-2}$.

5.2 TOUGHENING

The present experiments provide a definite rationale for the attainment of an optimum steady-state toughness, as manifest in the work of rupture, χ. The largest values of χ (~ 8) occur for reinforcements that work harden substantially and for interfaces that debond readily. *The work hardening coefficient applicable to Nb (n = 0.3) coupled with an interface fracture energy typical of that for oxides,* (Γ_i ≈ 25 Jm^{-2}) *satisfies these requirements.* Conversely, a fracture energy applicable to the σ-phase reaction product (Γ_i ≈ 45 Jm^{-2}) is apparently too large to allow the requisite debonding. To further relate χ to debonding, the behavior of the reinforcement over the debond length is addressed. For fixed d, the engineering strain in this region, ε, is related to u and d, such that

$$\varepsilon = u/d \tag{3a}$$

or, at rupture,

$$\varepsilon^* = u^*/d \tag{3b}$$

The engineering plastic strain at rupture is governed by the work hardening coefficient n, viz.,

$$\varepsilon^* \approx e^n - 1 \tag{4}$$

Consequently, for fixed d, u* and d are expected to be related by:

$$u^* \approx d\,(e^n - 1) \tag{5}$$

This result is indeed consistent with the measured trend, summarized in Fig. 7. Based on the same simplification that d remains constant, χ can also be estimated by re-expressing equation (1) as

$$\chi = \frac{d}{\sigma_o R} \int_0^{\varepsilon^\bullet} \sigma d\varepsilon \tag{6}$$

Then, based on a power law hardening representation where,

$$\sigma_t = \sigma_o \left(\varepsilon_t / \varepsilon_o \right)^n \tag{7}$$

σ_t and ε_t are the true stress and true strain. Assuming that the true strain at failure is $\varepsilon_t^\bullet \approx n$, then integration of equation (6) gives;

$$\chi \approx \left[n^{n+1} / \varepsilon_o^n (n+1) \right] (d/R) \tag{8}$$

The trend in χ predicted by equation (8), plotted on Fig. 8, conforms quite well with the present experimental results, and rationalizes the influence of debonding.

The behavior typified by the Ti-Nb reinforcement provides an important contrast. This reinforcement gives a desirably large work of rupture without debonding. Seemingly, in this case, when cracking of the matrix is suppressed, moderate constraint accompanied by appreciable plastic dissipation within shear bands is possible.

To further comprehend the significance of the above results, an important duality in behavior is noted, based on related research.[17] The work of rupture provided by the Nb reinforcements can only be <u>partially utilized</u> to give *composite toughness*. This limitation arises because of resistance curve and large scale bridging issues, which become accentuated as the debond length increases.[16,17] Consequently, strictly on the basis of toughness, the Ti-Nb reinforcements, which do not debond and have a high yield stress, are superior to the coated Nb

reinforcements. However, the full plastic di..., tion allowed by debonding of the reinforcement can be utilized in loading situations that sample the complete range of material resistance, such as *Charpy tests*.[17] Therefore, when the criterion used for material selection is based on the Charpy energy, oxide debond coatings, and reinforcements with high work hardening are preferred. The duality in behavior associated with debonding suggests that, in some cases, when both high Charpy energy and high toughness are needed, a dual reinforcement scheme may be required: one reinforcement debonds and contributes to the Charpy energy, whereas the other bonds well and has the strength needed to provide a large toughness.

6. CONCLUDING REMARKS

The present set of experiments clarify the influence of debonding on the work of rupture, χ, of intermetallics toughness with highly ductile reinforcements, such as Nb. In particular, for such reinforcements, it has been established that χ exhibits a linear dependence on the debond length, d. It is also apparent that inert oxide coatings emplaced between the reinforcement and the matrix have a sufficiently low fracture energy that extensive debonding is induced, leading to enhanced values of χ. However, it remains to explicitly relate the debond length to the specific fracture energy of the coatings. Furthermore, it has been demonstrated that debonding is undesirable when the reinforcements have limited intrinsic ductility, caused by an absence of work hardening, as exemplified by Ti-Nb reinforcements.

ACKNOWLEDGEMENTS

TABLE I

Summary of Parameters Obtained from Composite Laminate Tests

REINFORCEMENT	(1) σ_y/σ_o	u°/R	d/R	χ
Nb	~ 1.4	~ 2	~ 5	~ 2.5
Nb Y$_2$O$_3$ coating	~ 1.7	~ 6	~ 24	~ 8
Nb Al$_2$O$_3$ coating	~ 1.7	~ 3	~ 7 to 10	~ 4
Ti/Nb	~ 2	~ 1.4	cracking length ~ 1.5R	~ 1.5
Ti/Nb Y$_2$O$_3$ coating	1	~ 2	~ 25	~ 1.4

(1) σ_y is the reinforcement yield stress.

13

FIGURE CAPTIONS

Fig. 1. a) Schematic of a composite cylinder test specimen

  b) Schematic of a composite laminate test specimen

Fig. 2. The split plate geometry used for a convenient precrack specimen by diffusion bonding

Fig. 3. A summary of reactions that occurred upon diffusion bonding

  a) The Nb/TiAl interfaces showing an SEM micrograph of the σ phase and T_2 reaction layer and the associated phase diagram[18] with the reaction paths indicated

  b) TEM micrograph of T_2 and σ phase reaction product layers shown in (a)

  c) The TiNb/TiAl interface showing an SEM micrograph of the α_2 and α_2 & β matrix product layers, and the associated phase diagram[18]

  d) TEM micrograph of the α_2 and α_2 & β layer for (c)

Fig. 4. a) Optical micrograph of Y_2O_3 coating between TiAl and both Nb and TiNb after diffusion bonding showing the absence of reaction products

  b) Micrograph of Al_2O_3 coatings between TiAl and both Nb and TiNb after diffusion bonding

Fig. 5. a) Tensile stress/strain curve for the unbonded reinforcement. The specimen gauge length was 10mm.   Tensile stress/stretch curves for produced laminates b) Nb c) TiNb.   The letters refer to the points on the curve that correspond with the   *in situ* SEM pictures shown in Fig. 6

Fig. 6. *In situ* SEM views of the laminate specimens used to generate the stress/stretch curves shown in Fig. 5: a) TiNb with Y_2O_3 coating; b) Nb coated with Y_2O_3; c) Nb coated with Al_2O_3; d) uncoated Nb: note bridging ligament along the debond with σ phase; e) uncoated TiNb

Fig. 7 Trend in the critical plastic stretch u*/R with debonded length d/R for Nb reinforcements. The line is the prediction from equation (5)

Fig. 8 Trend in the work of rupture χ with the debond length, d/R, for Nb reinforcements. The line is the prediction from equation (8)

Fig. 9. A comparison of the normalized stress/nominal strain curves for bonded Nb laminates and unbonded Nb reinforcements

Fig. 10 A schematic of the test specimen used to measure the interface fracture energy

REFERENCES

[1] L. S. Sigl, A. G. Evans, P. Mataga, R. M. McMeeking and B. J. Dagleish, *Acta Metall.* 36, 946, (1988).

[2] M. F. Ashby, F. J. Blunt and M. Bannister, *Acta Metall.* 37, 1847, (1989).

[3] H. C. Cao, B. J. Dalgleish, H. E. Dève, C. Elliott, A. G. Evans, R. Mehrabian and G. R. Odette, (In press), *Acta Metall.*

[4] C. K. Elliott, G. R. Odette, G. E. Lucas and J. W. Sheckard, *MRS Proceedings*, vol 120, p. 95, (1988).

[5] V. D. Krstic, *Phil Mag.* A 48, 695 (1983).

[6] B. Budiansky, J. C. Amazigo and A. G. Evans, *J. Mech. Phys. Solids* 36, 167, (1988).

[7] A. G. Evans and R. M. McMeeking, *Acta Metall.* 34, 2435, (1986).

[8] P. A. Mataga, *Acta Metall.*, (in press).

[9] E. Aigeltinger, C. Elliot, N. Glumack, G. Lucas and W. Shekhard, Proceedings of Symposium on High Temperature Intermetallics. (In press)

[10] G.R. Odette, H.E. Deve, C.K. Elliott, A. Harigowa and G.E. Lucas, Proceeding of TMS Symposium on Interfaces on Composites, to be published, (1990).

[11] B. J. Dalgleish, K. Trumble and A. G. Evans, Acta Metall., 37, 1923, (1989).

[12] J.A. Thornton, *Ann. Rev. Mat. Sci.*, 7, 239, (1977).

13] W. Mader and M. Rühle, *Acta Metall.* 37, 853, (1989).

[14] R. E. Tressler, T. L. Moore and R. L. Crane, *J. of Mat. Sci.*, 151, (1973).

[15] P. G. Charalambides, J. Lund, A. G. Evans and R. M. McMeeking, *J. of Appl. Mech.* 56, 77, (1989).

[16] F. Zok and C. Hom, to be published.

[17] F. Zok, S. Jansson, A. G. Evans and V. Nardonne, to be published.

[18] T. J. Jewett, J. C. Lin, N. R. Ronda, L. E. Seitzmon, K. C. Hsieh, Y. A. Chang and J. H. Perepezko, Proc. MRS Fall Meeting (1988).

Figure 1a

Figure 1b

Pressure

TiAl split plates

Nb/Ti alloy
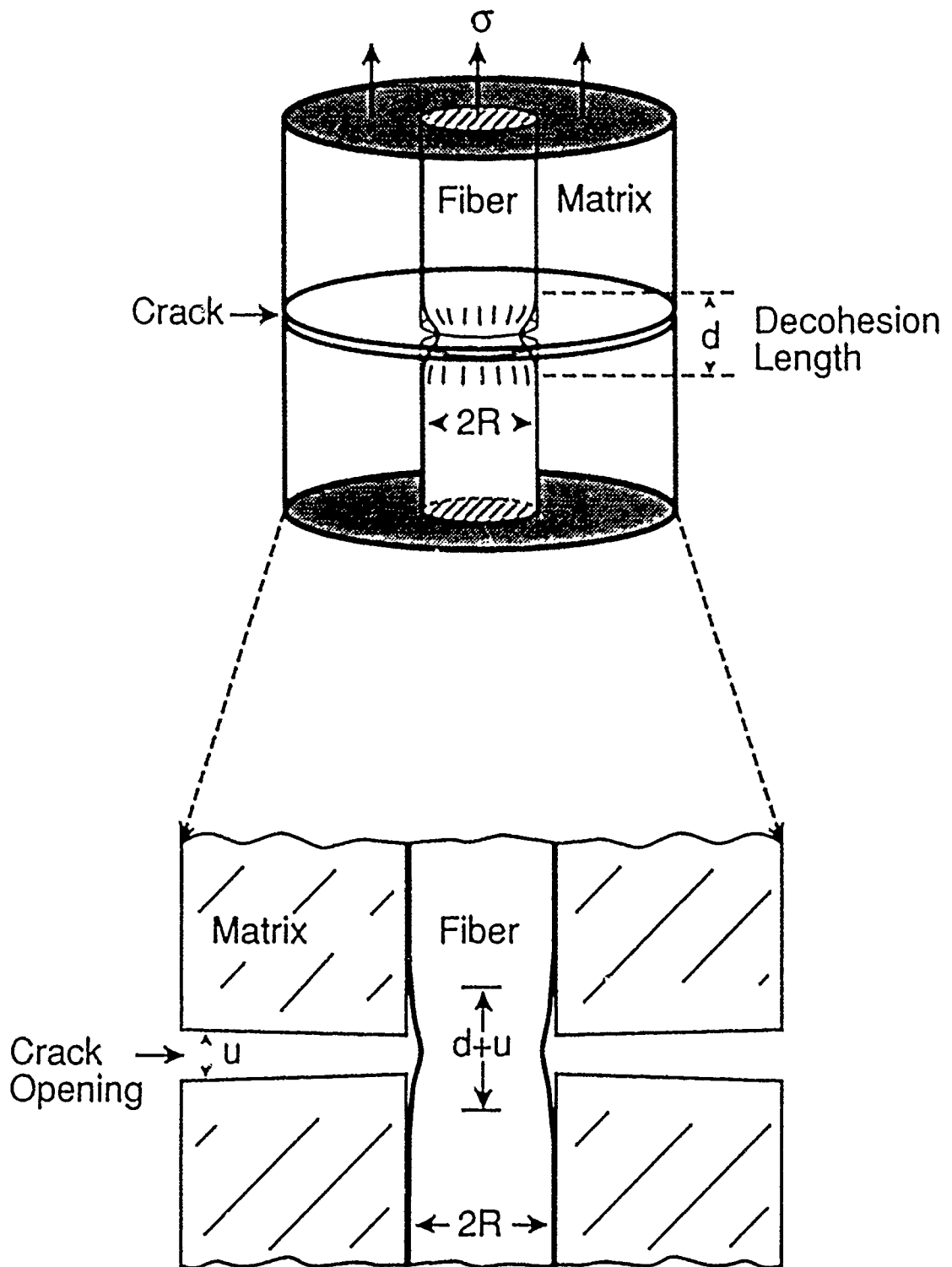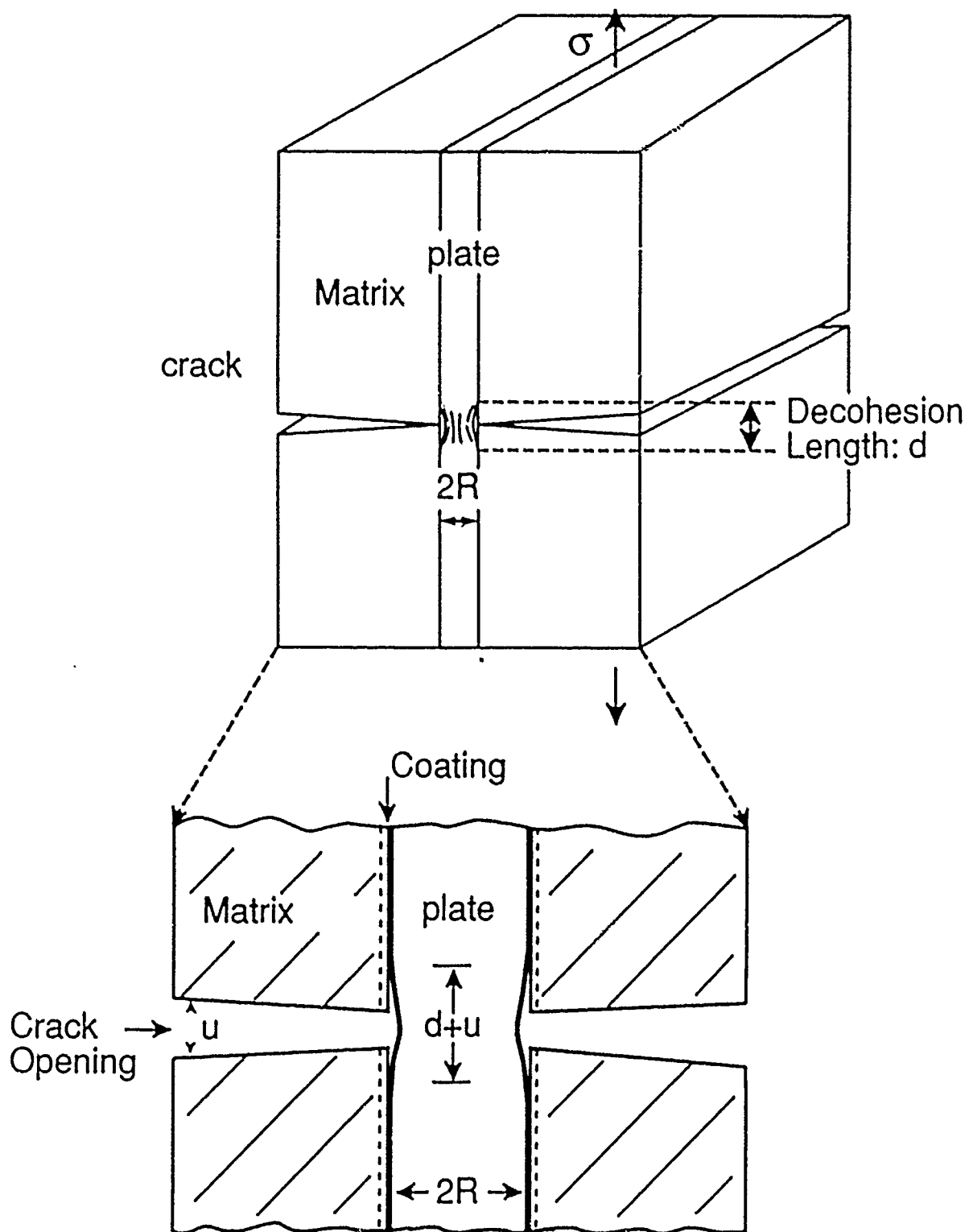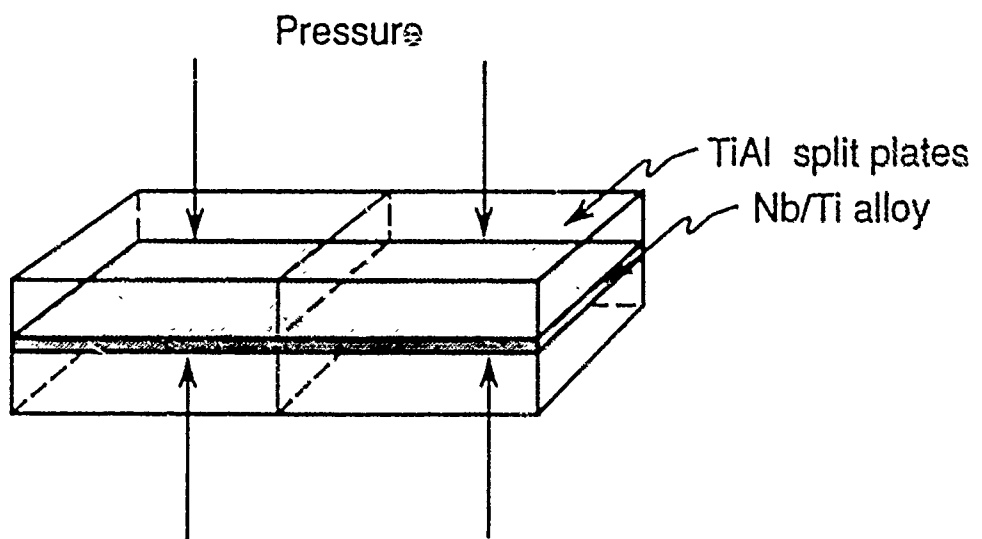
Figure 2

Nb-Ti-Al 1200°C

Figure 3a

TiAl/Nb Reaction Zone

200nm

γ-TiAl   T₂   σ
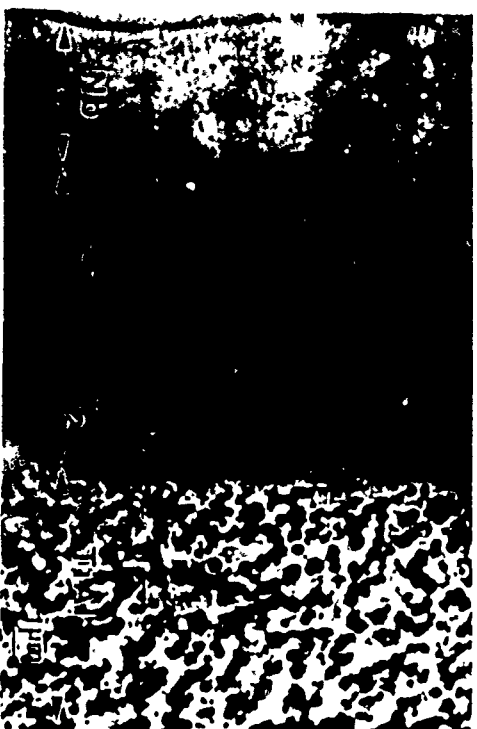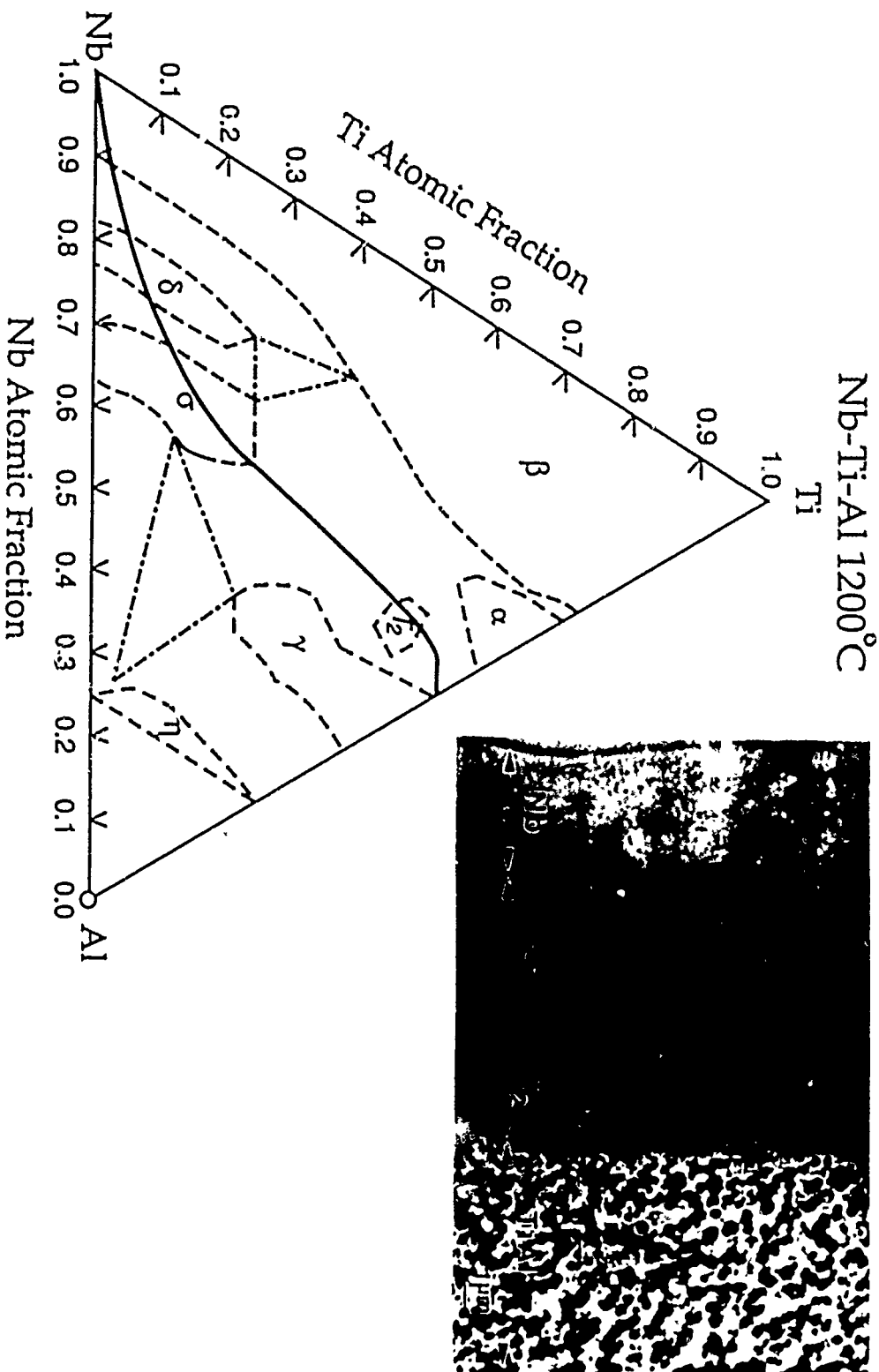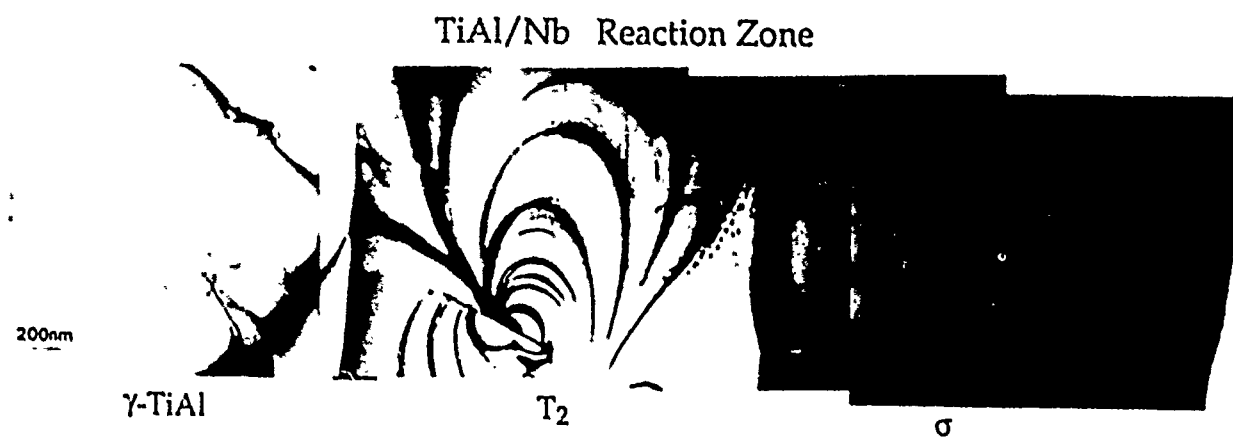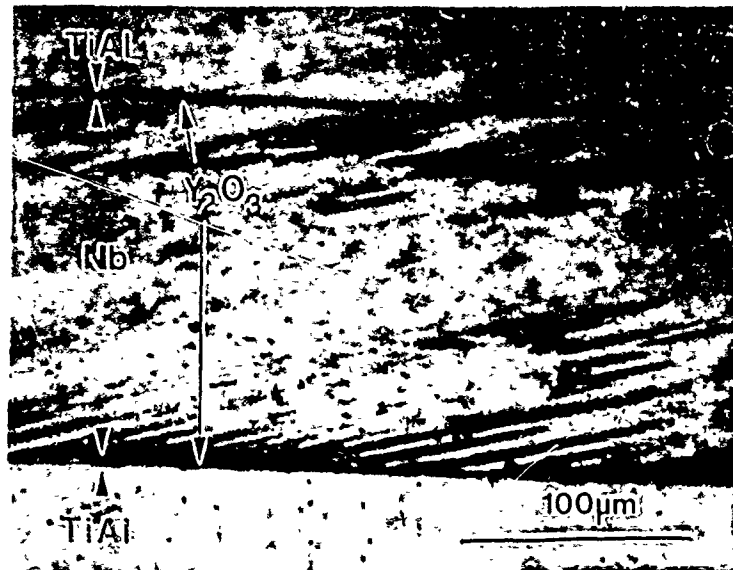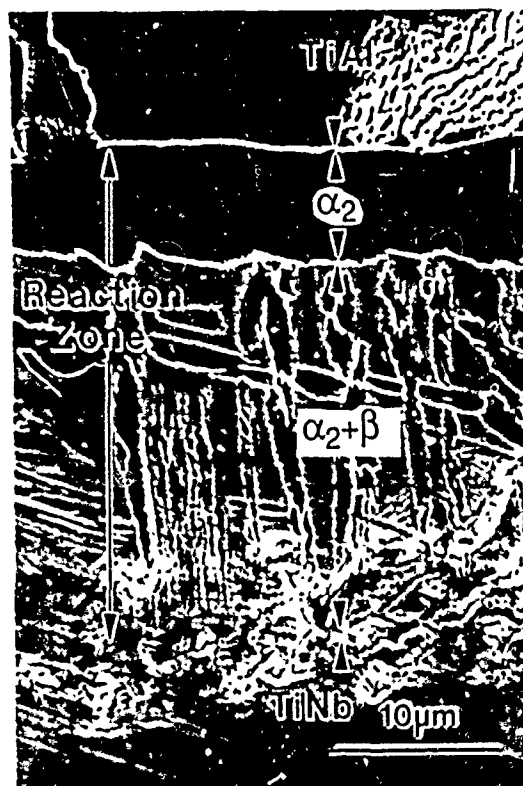
Figure 3b

Nb-Ti-Al 1200°C
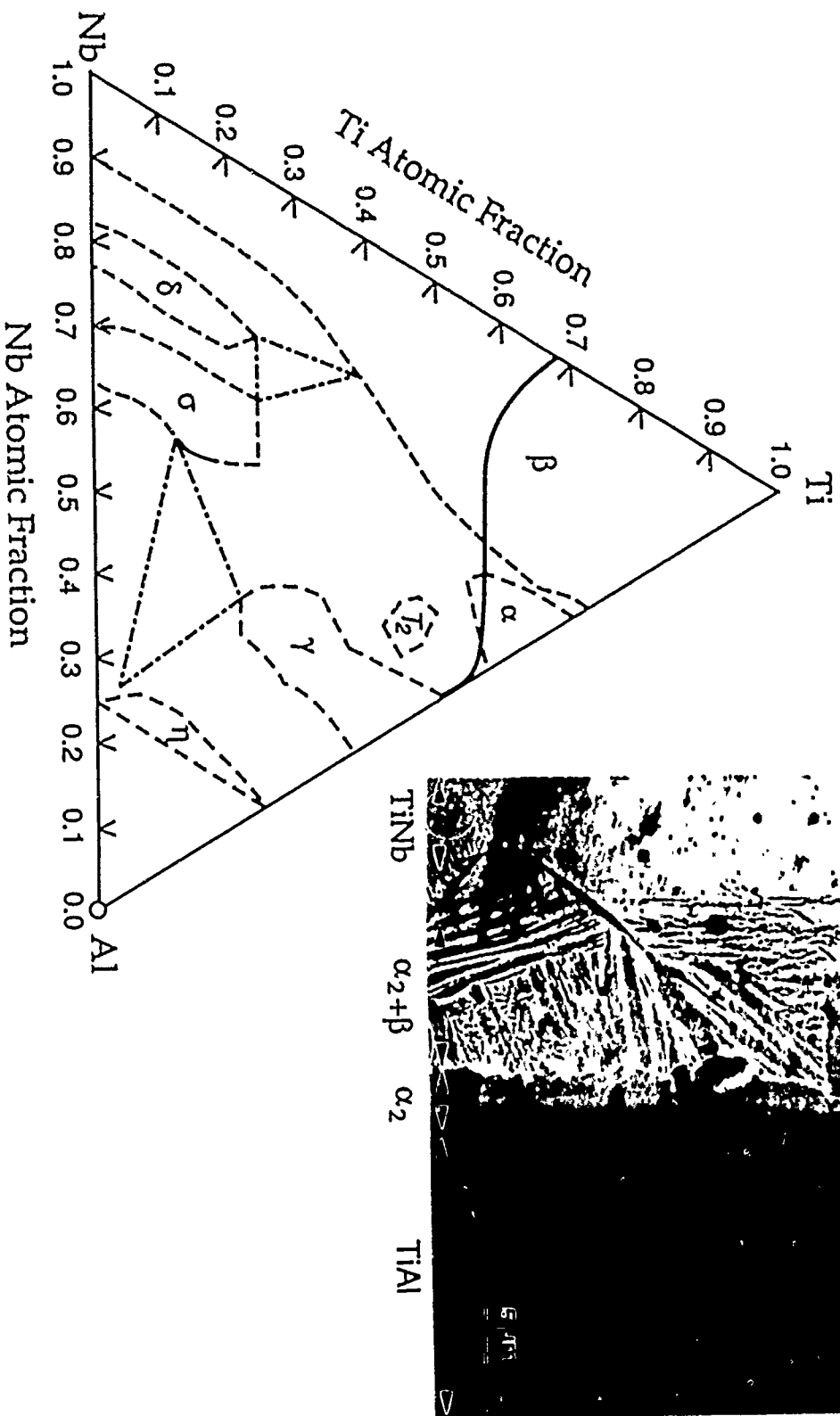
Figure 3c
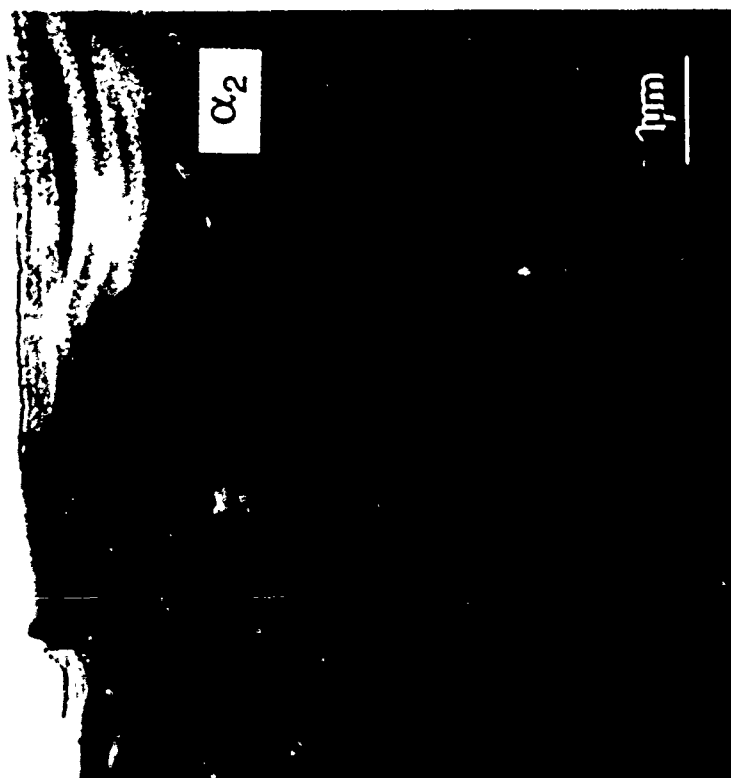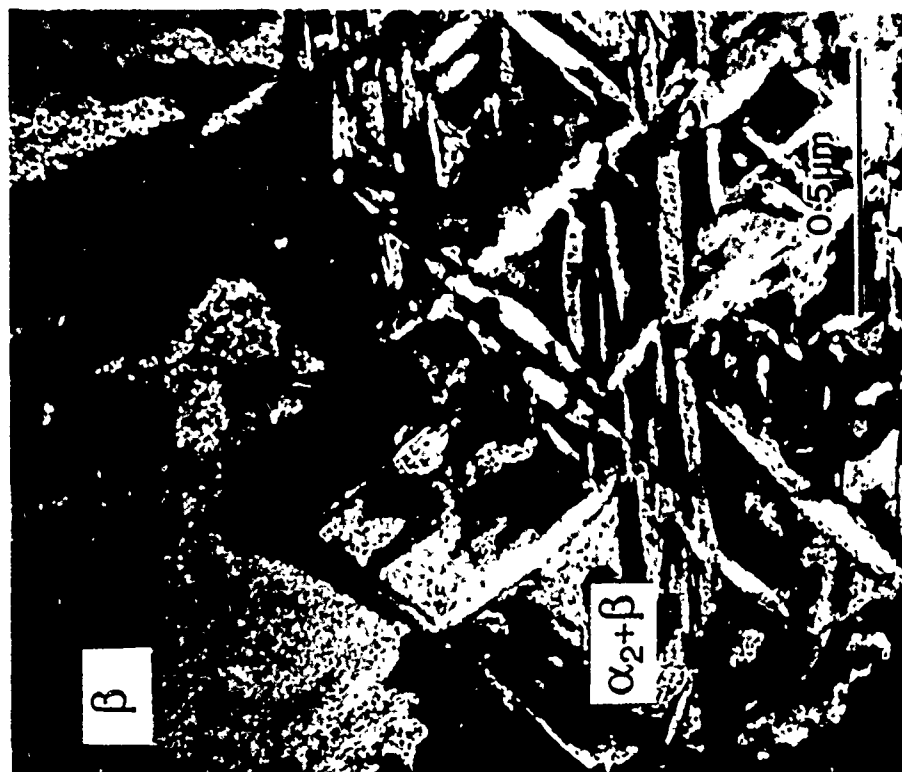
Figure 3d
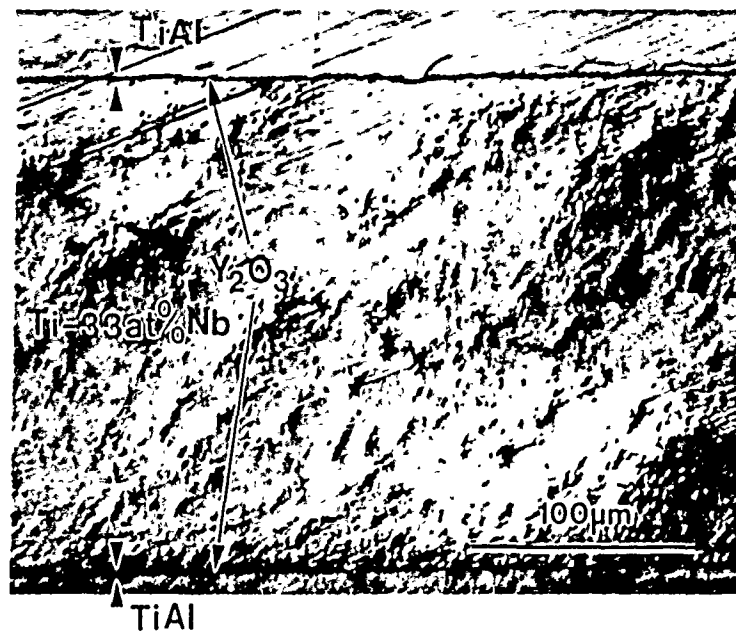
Figure 4a
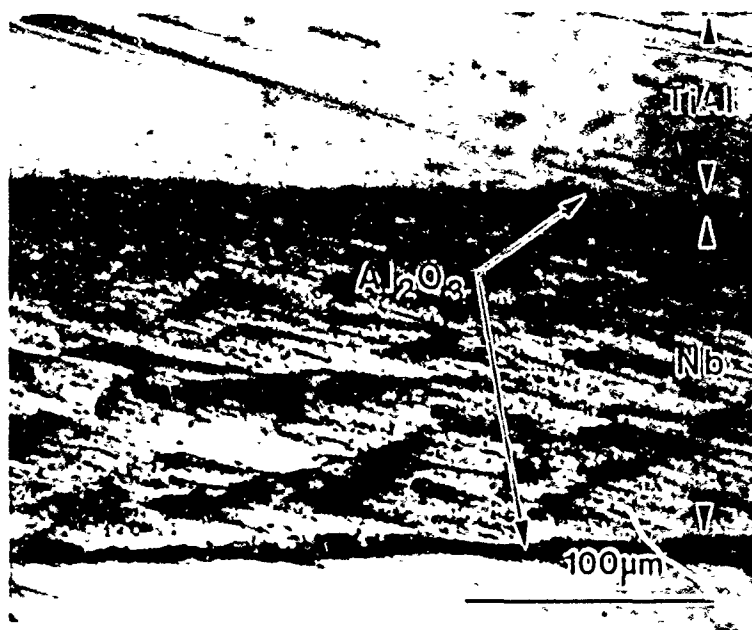
Figure 4b

Figure 5a

TiAl/Nb Laminates
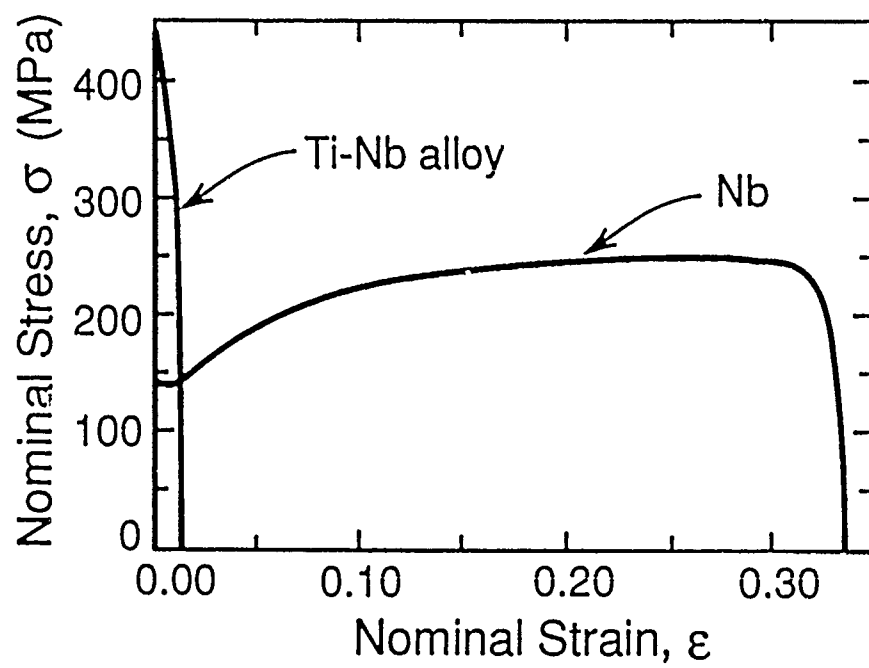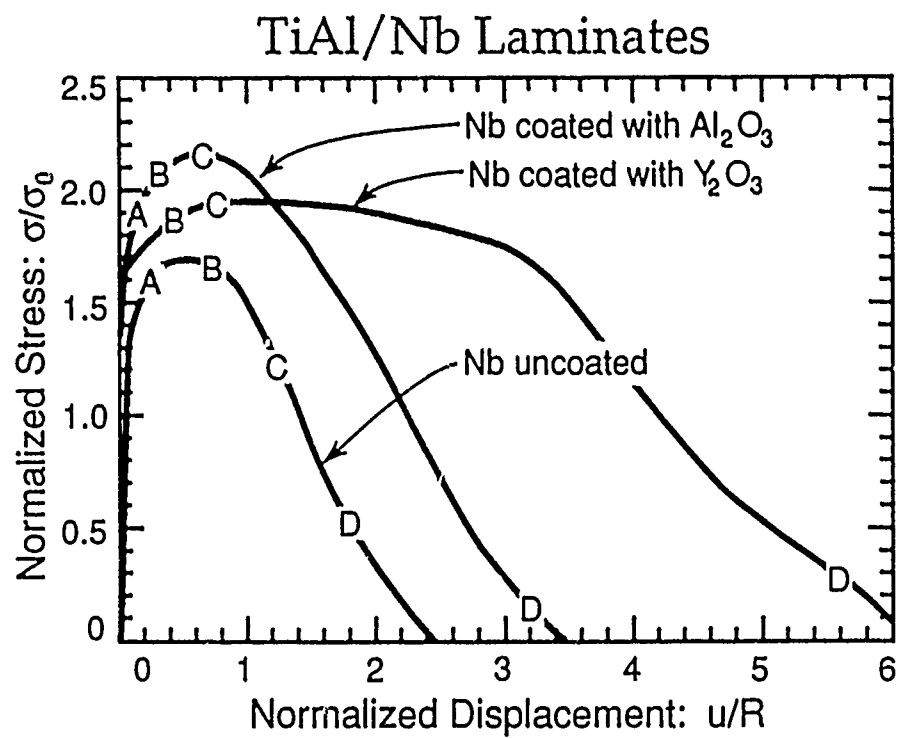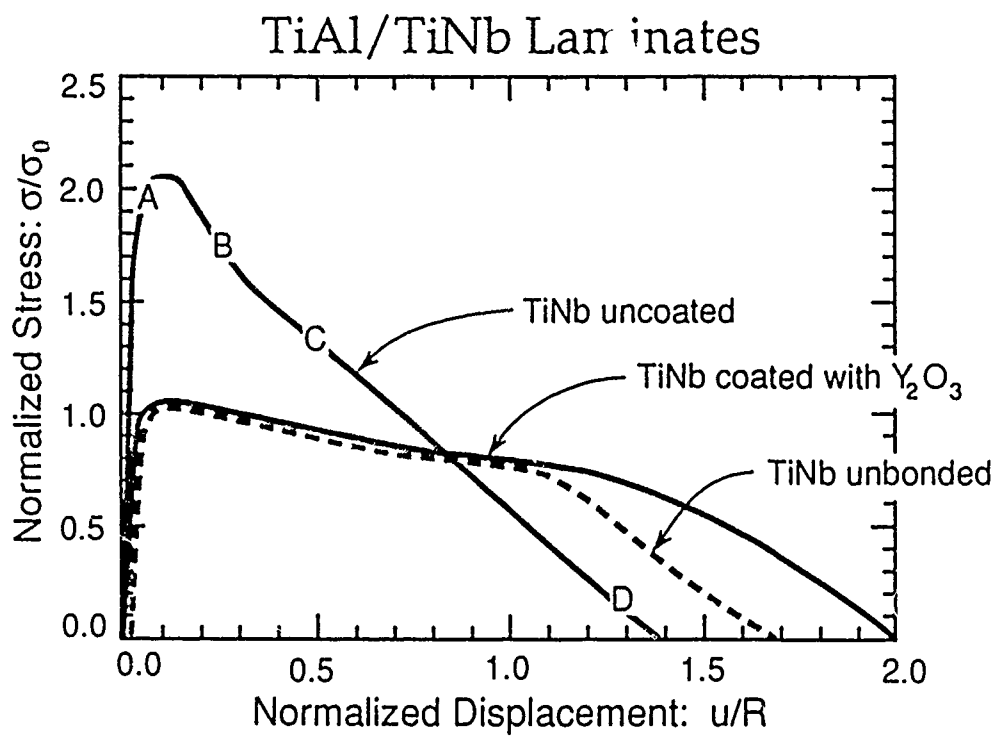

Figure 5b

Figure 5c

TiAl/TiNb - Y_2O_3 Coating
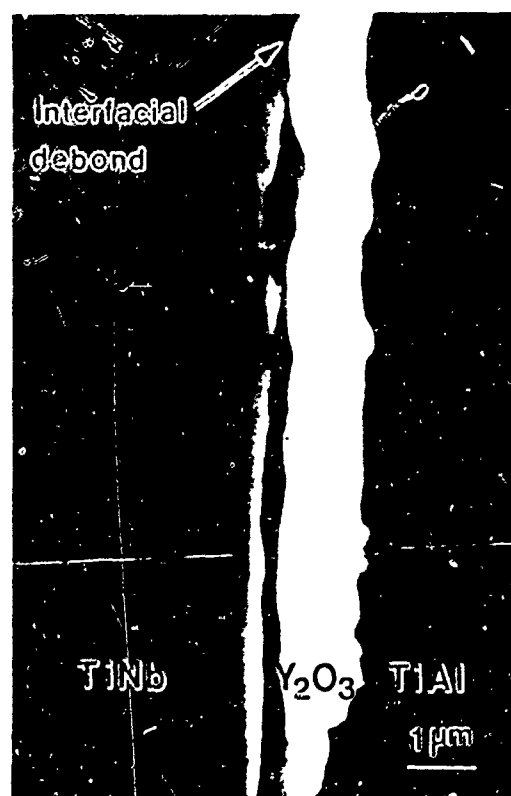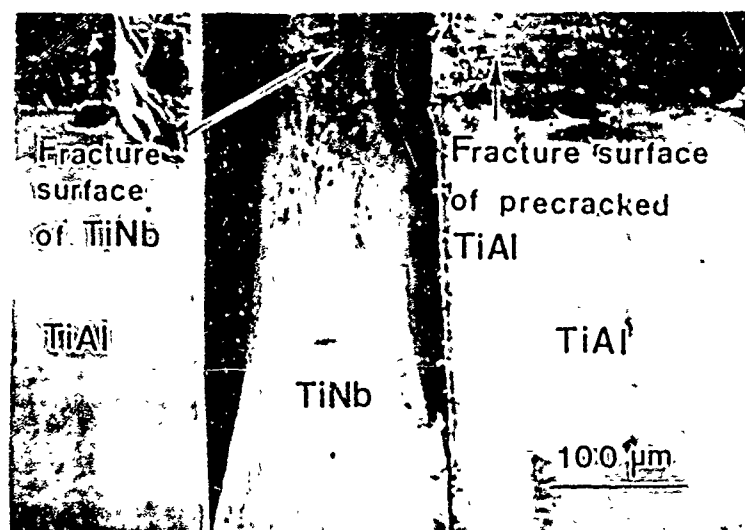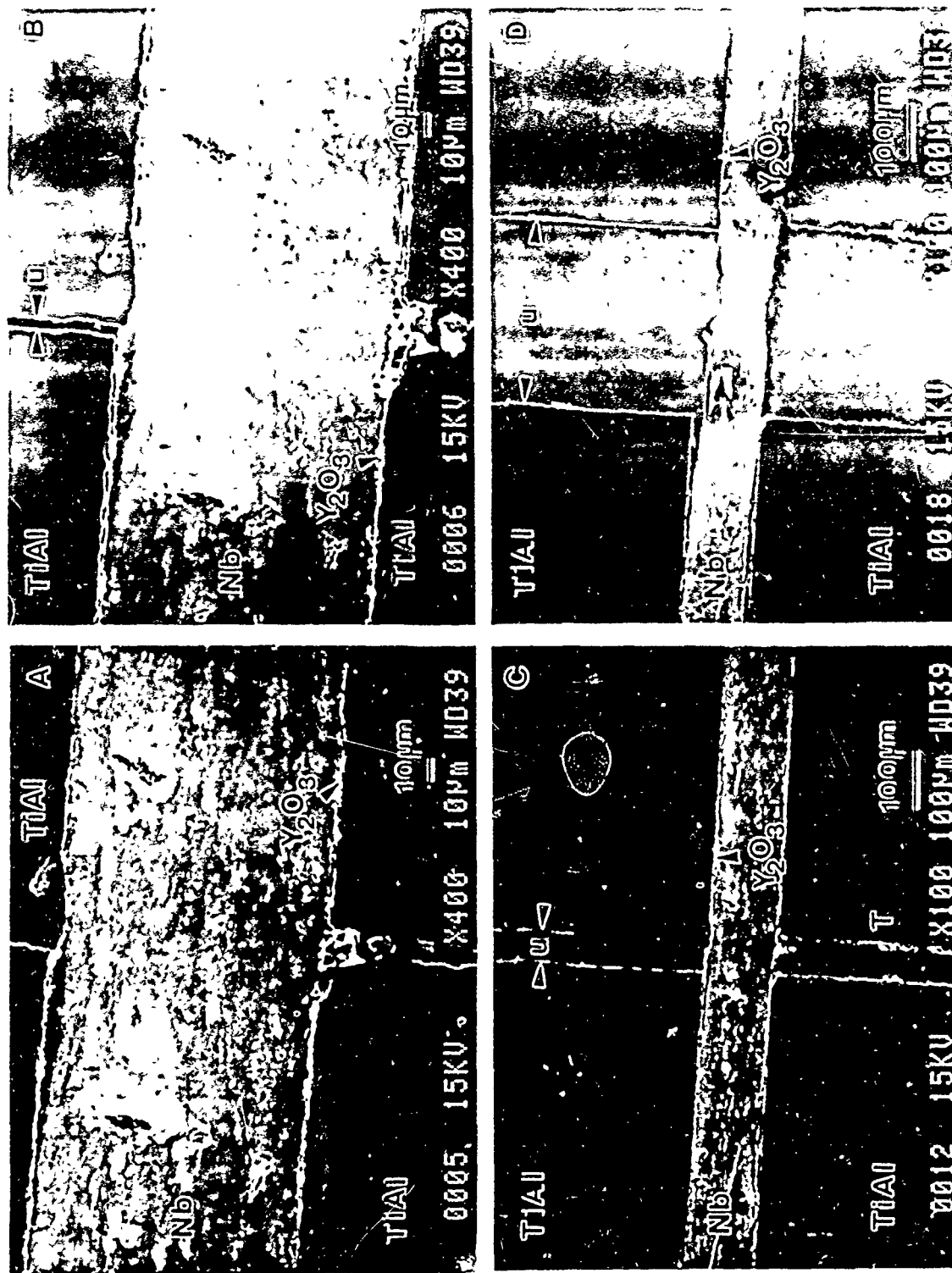
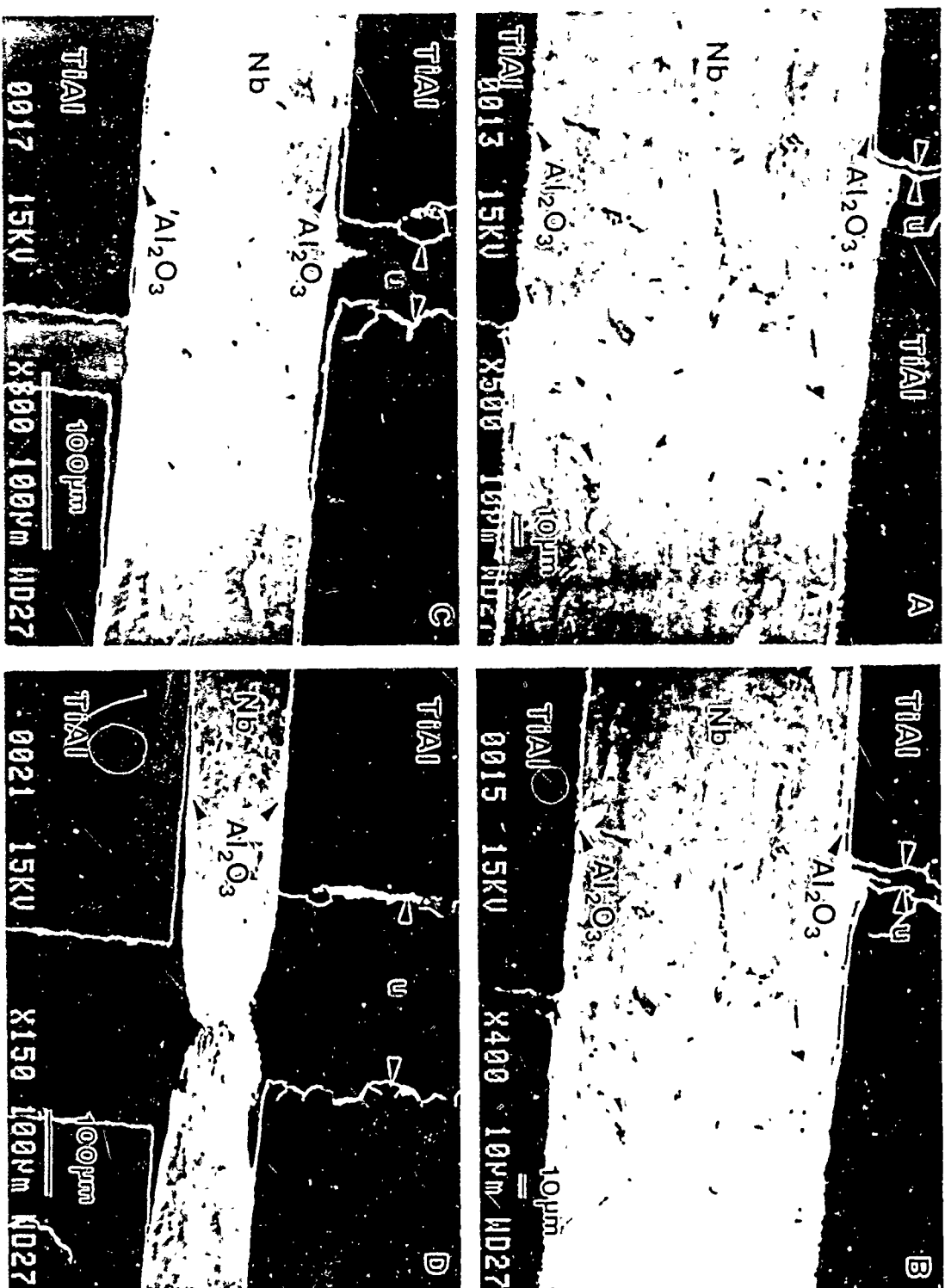

Figure 6a

TiAl/Nb Coated with Y_2O_3
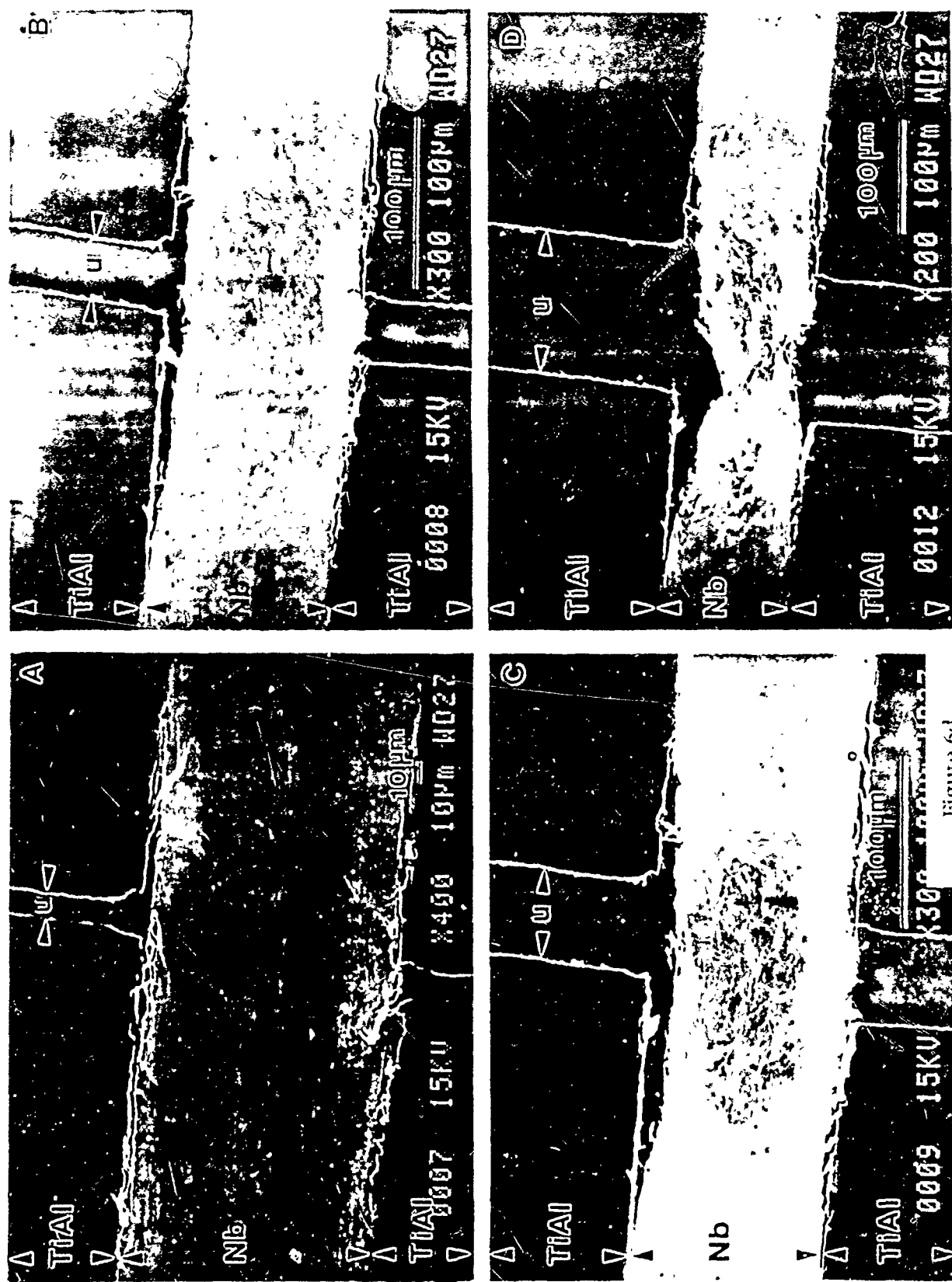

Figure 6b

TiAl/Nb Coated with Al_2O_3
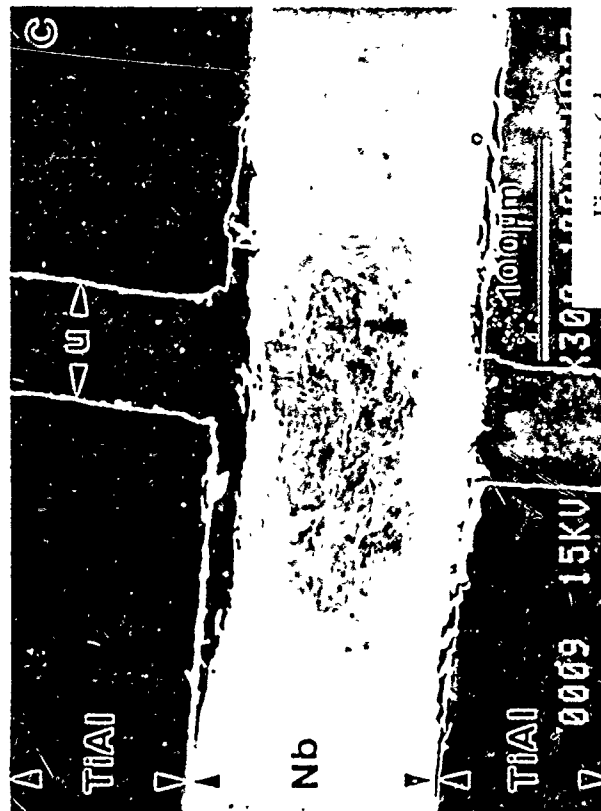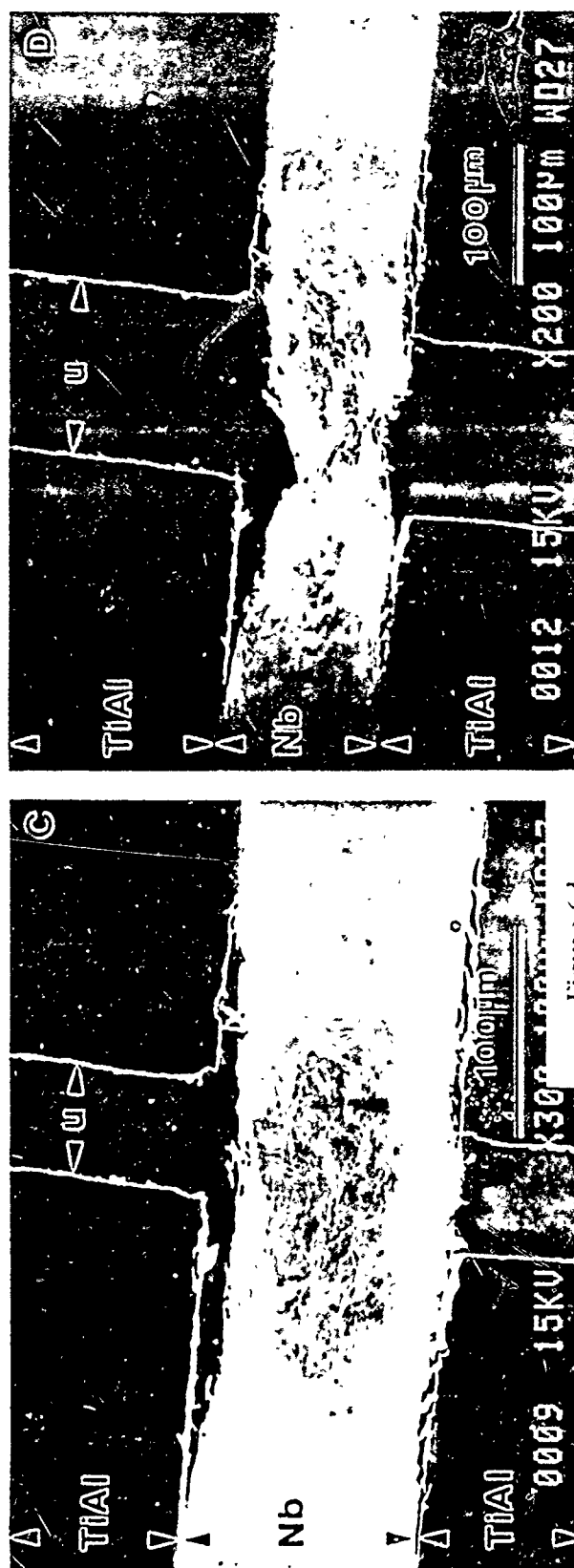

Figure 6c

TiAl/Nb

Figure 6d

TiAl/Nb
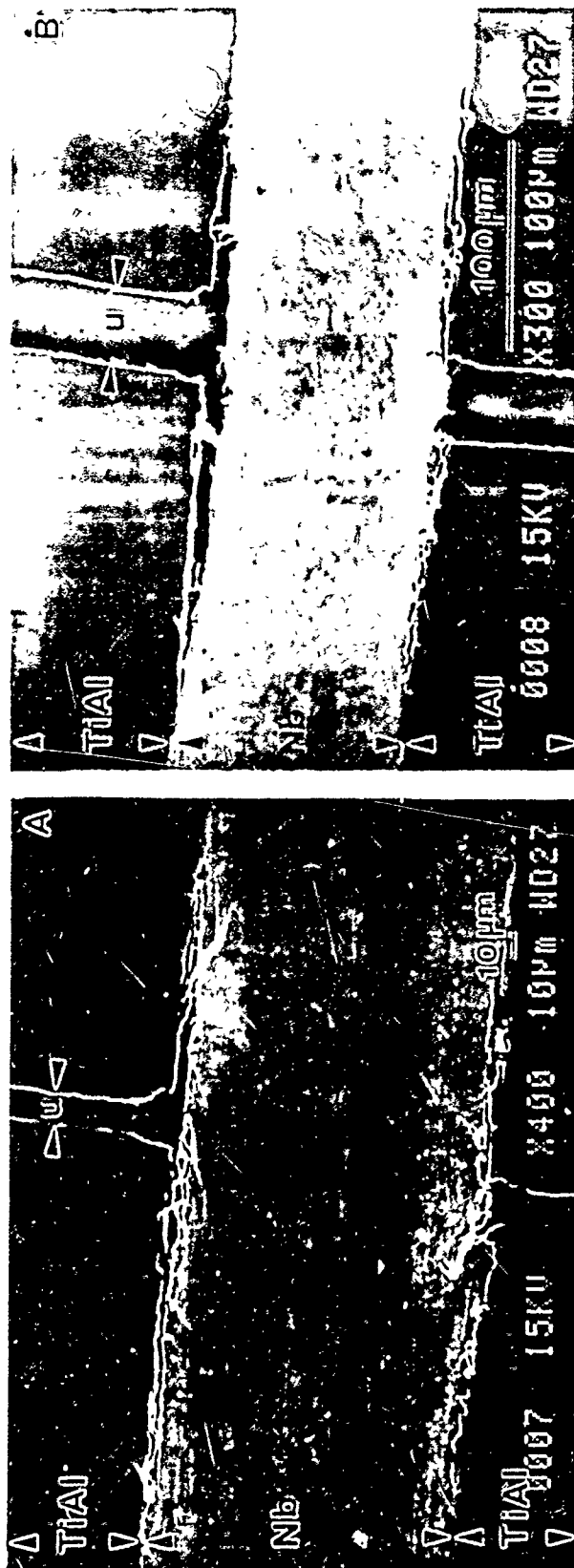
Figure 6d

TiAl/TiNb
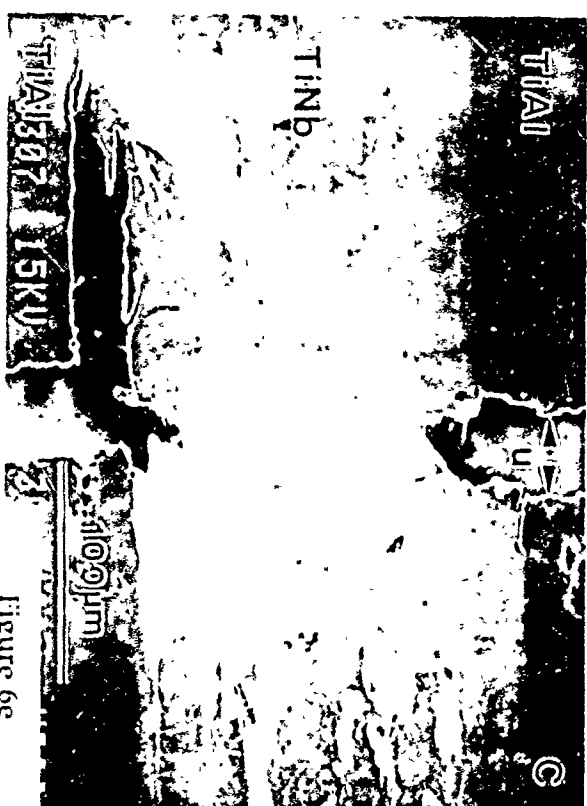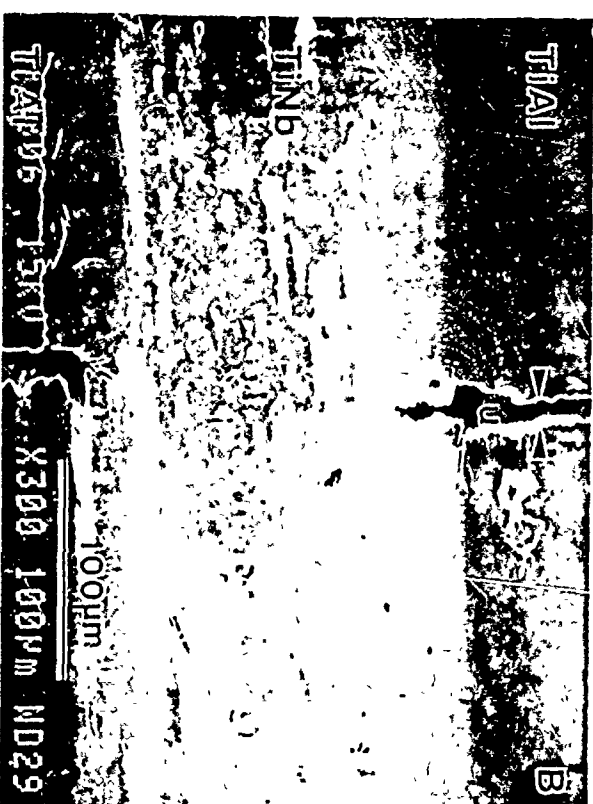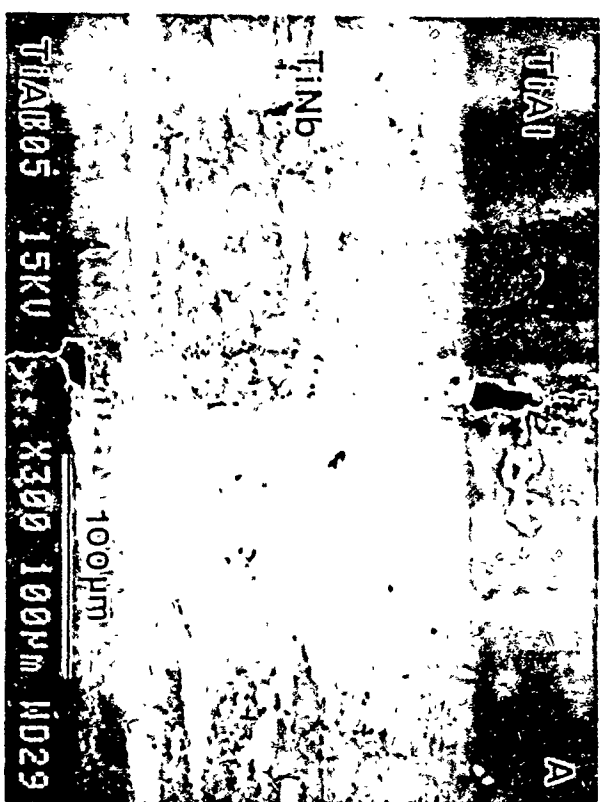
Figure 6e
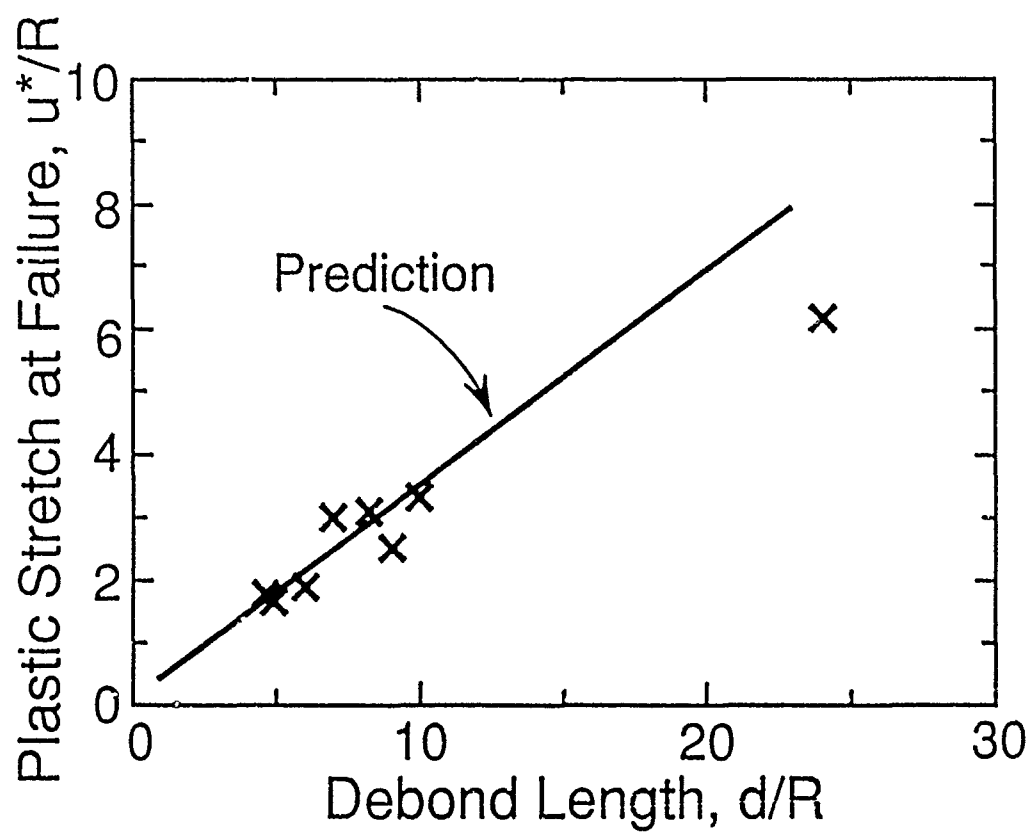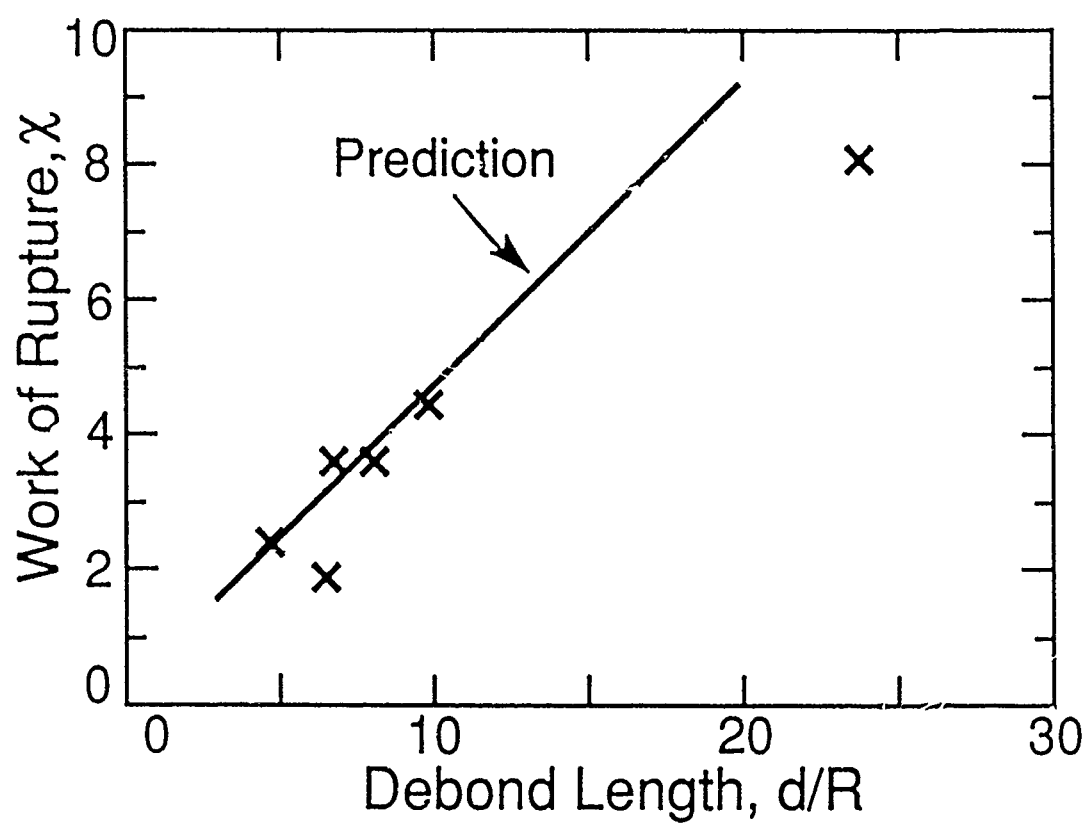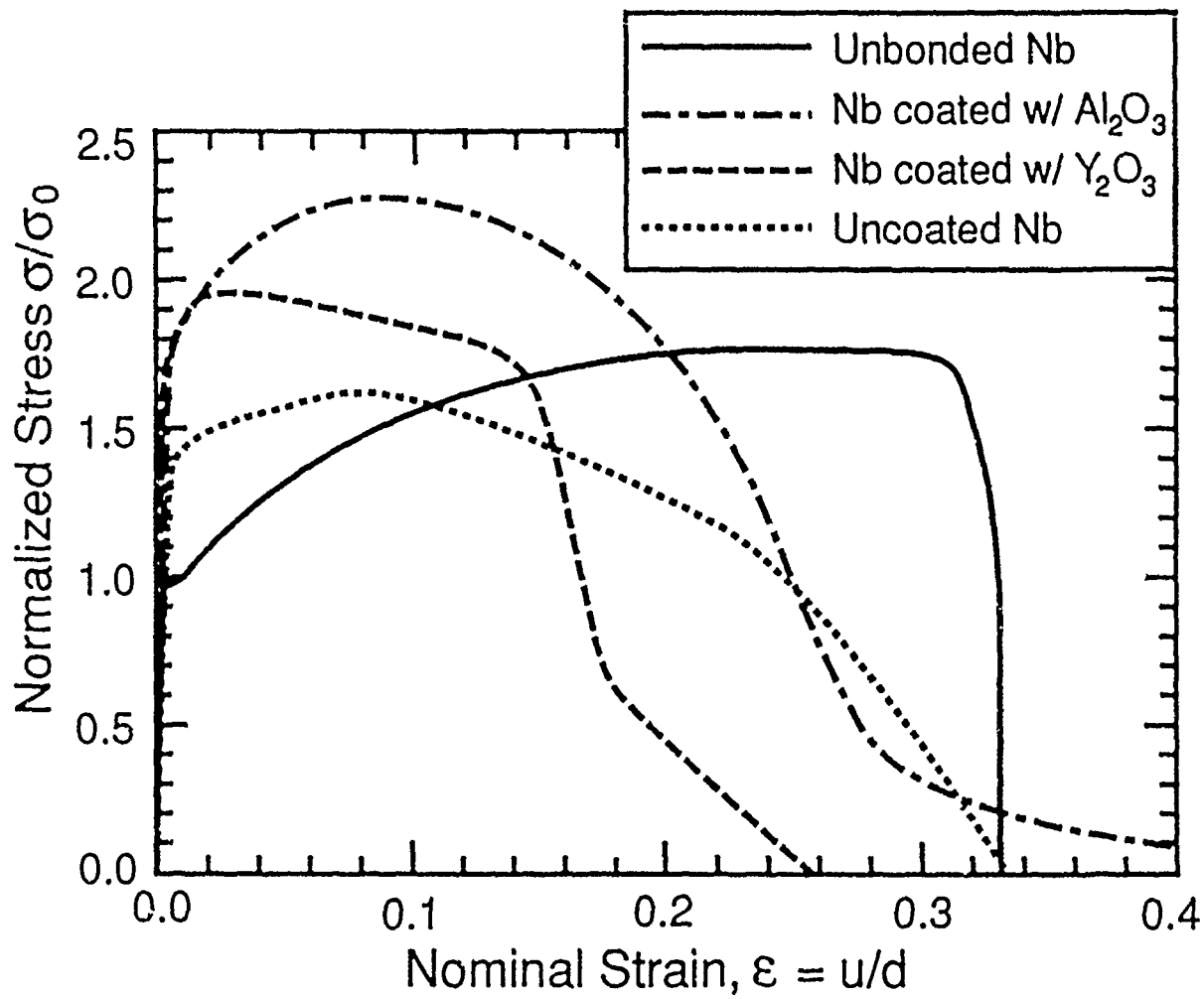
Figure 7
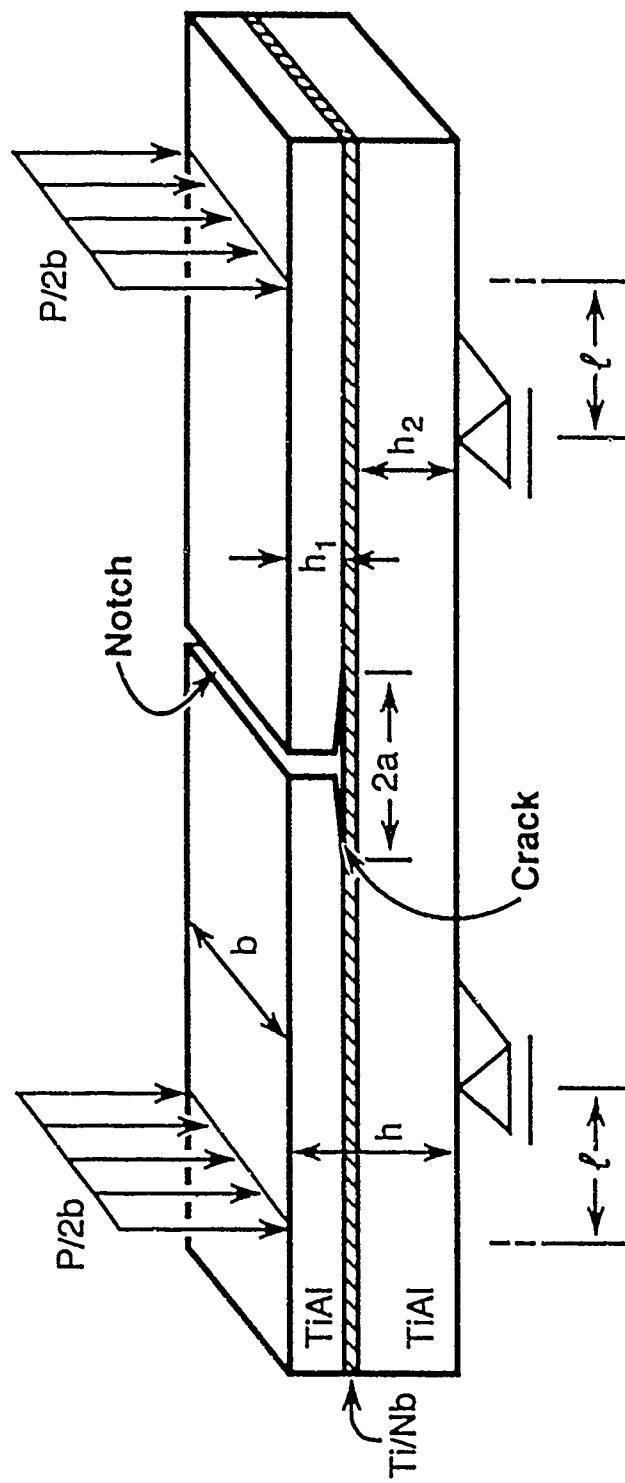
Figure 8

Figure 9

Figure 10

FLOW CHARACTERISTICS OF HIGHLY
CONSTRAINED METAL WIRES

M. F. ASHBY, F. J. BLUNT and M. BANNISTER

University Engineering Department, Trumpington Street, Cambridge CB2 1PZ, England

Abstract—Brittle solids can be toughened by incorporating ductile inclusions into them. The inclusions bridge the crack and are stretched as the crack opens, absorbing energy which contributes to the toughness. To calculate the contribution to the toughness it is necessary to know the *force displacement* curve for an inclusion, constrained (as it is) by the stiff, brittle matrix. Measured force displacement curves for highly constrained metal wires are described and related to the unconstrained properties of the wire. The constraint was achieved by bonding the wire into a thick walled glass capillary, which was then cracked in a plane normal to the axis of the wire and tested in tension. Constraint factors as high as 6 were found but a lesser constraint gives a larger contribution to the toughness. The diameter of the wires (or of the inclusions) plays an important role. Simple, approximate, models for the failure of the wires are developed. The results allow the contribution of ductile particles to the toughness of a brittle matrix composite to be calculated.

Résumé—Il est possible de curcir des matériaux fragiles en leur incorporant des inclusions ductiles. Les inclusions traversent la fissure et s'allongent lorsque la fissure s'ouvre, absorbant de l'energie qui contribue à la résilience. Pour calculer la contribution à la résilience, il est nécessaire de connaître le travail force–déplacement d'une inclusion, quand elle est contrainte par la matrice fragile et rigide. Nous décrivons les courbes expérimentales force–déplacement de fils métalliques fortement contraints, et nous les relions aux propriétés du fil non contraint. La contrainte est créée en fixant le fil à l'intérieur d'un capillaire en verre à parois épaisses, que l'on écrase ensuite dans un plan perpendiculaire à l'axe du fil, et que l'on déforme en traction. Les facteurs de contrainte peuvent atteindre 6, mais une contrainte moins élevée participe davantage à la résilience. Le diamètre des fils (ou celui des inclusions) joue un rôle important. Nous développons des modèles approchés simples de la rupture des fils. Les résultats permettent de calculer la contribution des particules ductiles à la résilience d'un composite à matrice fragile.

Zusammenfassung—Spröde Festkörper können mit eingebrachten duktilen Einschlüssen gehartet werden. Wenn sich der Riß öffnet, überbrücken die Einschlüsse den Riß, sie werden gedehnt und absorbieren Energie und tragen so zur Festigkeitserhöhung bei. Um dessen Höhe zu berechnen, muß man die Kraft-Weg-Kurve für einen Einschluß, eingeengt durch die steife und spröde Matrix, kennen. Die an entsprechenden Metalldrähten gemessenen Kraft-Weg-Kurven werden beschrieben und mit Messungen des Verhaltens freier Drähte verglichen. Die Einschrämkung wurde dadurch erzeugt, daß der Draht in dickwandige Glaskapillaren eingebettet wurde; diese wurden dann in einer Ebene senkrecht zur Drahtachse gebrochen und im Zugversuch verformt. Es ergeben sich Einschränkungsfaktoren bis zu 6, allerdings tragen geringere Faktoren starker zur Zähigkeit bei. Der Durchmesser der Drähte unter der Einschlüsse ist sehr wichtig. Es werden einfache angenaherte Modelle für den Bruch der Drahte entwickelt. Die Ergebnisse ermöglichen, den Beitrag der duktilen Einschlusse zur Zähigkeit einer spröden Matrix zu berechnen.

1. INTRODUCTION

Brittle solids can be toughened by incorporating ductile inclusions into them. Alumina and magnesia have been toughened in this way by dispersing aluminium and nickel particles in them [1, 2]; brittle glass-enamels are made more resistant to cracking by the inclusion of metal particles [3, 4]; brittle metals are toughened by the incorporation of more ductile fibres into them [5–7]; and the toughness of cermets derives from the ductility of the cobalt binder included in the WC framework [8–11]. The physical mechanism of toughening is straightforward enough (see Fig. 1): if ductile ligaments span the advancing crack, they must stretch as the crack opens until they fracture or decohere; the work-of-stretching contributes to the overall toughness of the solid.

If the particle is so weakly bonded to the matrix that it easily pulls free as the crack approaches, then it is not stretched and there is almost no contribution to the toughness. But if it is strongly bonded, it is *constrained*; and then its force–displacement curve is very different from that of the unconstrained material as measured (for instance) in an ordinary tensile test. This is an important difference because the energy absorbed in stretching the particle, crucial in calculating the contribution to the toughness, depends strongly on the degree of constraint.

This paper describes experimental measurements of the force–displacement curve of highly constrained

Table 1 Symbols, definitions and units

a_p	particle or wire radius (m)
E	Youngs modulus (GPa)
ε	strain
ε_y	yield strain
G	shear modulus (GPa)
G_c	toughness (J m²)
ΔG_c	increment in toughness caused by ductile inclusions (J m²)
l	pile-up length (m)
l_c	decohesion length (m)
n	strain hardening exponent $\sigma_c = \sigma_0 \left[\dfrac{\varepsilon}{\varepsilon_y} \right]^n$
R	radius of neck (m)
r	radial coordinate (m)
σ	stress (MPa)
σ_c	flow stress at strain ε (MPa)
σ_0	initial flow stress at yield strain ε_y (MPa)
u	axial extension equal to crack-opening displacement (m)
u_0	initial crack-opening displacement (m)
u^*	crack-opening displacement at failure of ductile wire or particle (m)
V_f	volume fraction of ductile reinforcement
W	work of fracture per unit area of a single particle or wire (J m²)

metal wires which are strongly bonded within a hard, brittle, matrix The results show that several *failure mechanisms* are involved (they are described in Section 4.2); the shape of the force–displacement curve and the total energy absorbed depends on which mechanism is dominant. The results provide the necessary experimental data to validate models for constrained plasticity, and for the development of an understanding of the toughening of ceramics by ductile inclusions.

The symbols used in the text are defined in Table 1

2. BACKGROUND TO THE EXPERIMENT

A number of attempts have been made to analyse the plastic stretching of a plastically-deformable enclave within an elastic medium The earliest [1, 5–7] assumed that the flow strength and fracture strain of the plastic material was the same as that measured in a simple tensile test on the unconstrained material, but this assumption is false.

Approximate calculations which recognise the constraint have appeared in the last 2 years. All have the objective of calculating the *nominal stress*

$$\sigma(u) = \frac{F(u)}{\Pi\, a_0^2} \tag{1}$$

carried by the stretching particle for a given *crack opening*, u, and relating this to the uniaxial stress-strain curve of the particle material (Here F is the force and a_0 the radius of a particle, as shown in Fig. 2.) The function $\sigma(u)$, once derived, relates directly to the increase in toughness of the composite

$$\Delta G_c = V_f \int_0^{u^*} \sigma(u)\, du \tag{2}$$

where V_f is the area-fraction of ductile material intercepted by the crack and u^* is the crack opening
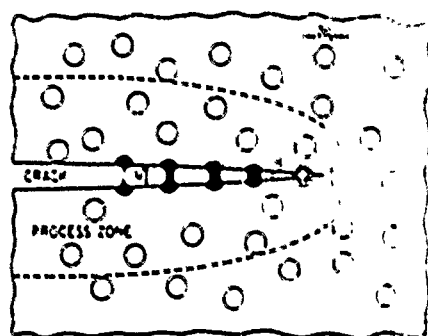
Fig 1 A crack in a brittle matrix, intersected by ductile particles The particles stretch and fail as the crack opens The work of stretching contributes to the toughness of the composite

at the point when the ductile material fails, as shown in Fig. 1. For later convenience, we define

$$W = \int_0^{u^*} \sigma(u)\, du. \tag{3}$$

It has the units of J m², and is a measure of the toughening capacity of a given ductile reinforcement Then

$$\Delta G_c = V_f W \tag{4}$$

Three methods of analysing the problem have been tried: finite element methods [12], a slip-line field analysis [13] and an approximate plasticity approach based on the Bridgeman analysis for necking [14, 15] They compliment each other. The slip-line field analysis and the plasticity approach are most easily applied to the later stages of deformation, when a stretch-zone has formed in the middle of the particle. The finite element calculations are possible only for the early stage when the geometry change of the particle is small Combined, they give a broad indication of the way $\sigma(u)$ varies from initial yield ($u = u_0$) to final failure ($u = u^*$).

These predictions are shown in Fig 2 Here the normal stress in the particle $\sigma(u)$ is normalised by
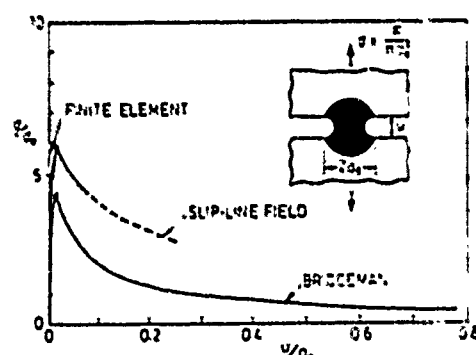
Fig. 2 The normalised particle stress σ/σ_0 plotted against the normalised crack-opening, u/a_0 Here σ_0 is the initial yield strength of the material of the particle in uniaxial tension, and a_0 is the initial particle radius

σ_0, the initial unconstrained yield strength of the inclusion; and the displacement u is normalised by the particle radius a_0. Work hardening affects the curve. The results plotted here are for a work hardening coefficient, n, of 0.1 where n is defined in unconstrained uniaxial tension by

$$\sigma_t = \sigma_0 \left(\frac{\epsilon_t}{\epsilon_0}\right)^n \tag{5}$$

and ϵ is the yield strain and σ_t is the true stress at a true strain ϵ_t.

The important features of the figure, to be compared with experiments and a new set of models in a later section, are

(a) The steep rise in stress to a peak value of $\sigma \cdot \sigma_0$ of between 5 and 6, reflecting the very large constraint imposed by the matrix on the particle; and

(b) the sharp decline in stress from the peak, falling to near zero at a displacement of about $a_0.2$.

Through useful, considerable uncertainty underlies the calculations which led to Fig. 2. First, it is not certain that the physical model is appropriate: the *mechanism* may not be that of pure plastic rupture but (as we shall see) may involve cavitation, debonding, or even brittle fracture of the matrix. Second, the calculations involve *assumptions* which, while they do not alter the general shape of the curve, certainly make the peak stress and the failure displacement uncertain. Before proceeding with further modelling, it is helpful to seek guidance from experimental measurements of the force–displacement curve and from direct observations of the mechanisms.

3. EXPERIMENTAL

Lead was introduced into thick-walled pyrex capillary tubing using the following procedure. Lengths of tube were degreased with acetone and dried in an oven. Analar grade lead (m.p. 327°C) was melted in an alumina crucible and drawn by suction into the tubes. These were then immediately transferred to a furnace at 300°C and cooled gradually to room temperature over a period of 12 h. This treatment gave a consistent structure to the lead and minimised thermal stresses (the expansion coefficients of pyrex and of lead are 5×10^{-6}/K and 29×10^{-6}/K respectively so the thermal mis-match is large). Lead introduced in this way adheres strongly to the glass.

The capillary tubes were 90 mm long with inside diameters of 1.3 and 2.1 mm, and a wall thickness of 3.5 mm. Samples were selected in which the lead was free from bubbles and other defects over a length of at least 40 mm. These were scored round the circumference with a glass cutter, glued with epoxy resin into brass holders, and mounted in a table-model Instron test machine. A hot flame applied briefly to the scored line nucleated a crack which propagated through the glass, but arrested at the central lead
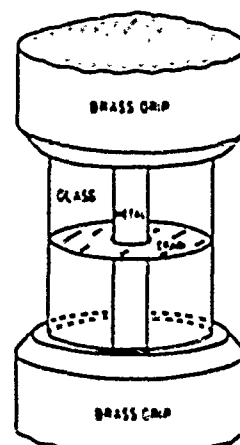

Fig. 3 A diagram of the sample immediately before testing The crack is introduced by scoring the glass with a diamond and applying a small, intense, heat source

core. The cracked specimen was allowed to cool to room temperature before the load–displacement curve, in tension, was recorded. A sketch of a sample, roughly to scale, is shown in Fig. 3.

Lead wires were extracted from uncracked specimens by etching away the glass with 20–30% hydrofluoric acid. The bare wires were mounted in brass chucks and tested to give unconstrained stress–strain curves for the lead. The fracture surfaces of both the constrained and the unconstrained samples were mounted and photographed in the scanning electron microscope.

4. EXPERIMENTAL RESULTS

4.1. Force–displacement curves and associated observations

Nominal stress–strain curves for the unconstrained lead wires (etched out of glass) are shown in Fig. 4. they failed by drawing down to a point or a wedge as shown in Fig. 5. A value of 5.3 MPa was taken for the initial yield strength, σ_0, of the lead; it was the mean of 10 samples. Plots of $\log(\sigma_t)$ vs $\log(\epsilon_t)$ (the true stresses and strain) are shown in Fig. 6. They give an average work hardening index of 0.25. The true stress–strain curve of the lead, up to the onset of localisation is thus described approximately by

$$\sigma_t = 5.3 \left[\frac{\epsilon_t}{\epsilon_0}\right]^{0.25} \text{MPa}. \tag{6}$$

When constrained in glass, the response of the lead was quite different. Fractographs showed that, almost always, the lead core had developed a single large internal void like that shown in Fig. 7(a) and (b). The first figure shows no sign of decohesion; the second shows a little: decohesion occurred when the glass was not properly cleaned before introducing the lead. Occasionally, several voids grow simultaneously, as in Fig. 7(c), which also shows limited
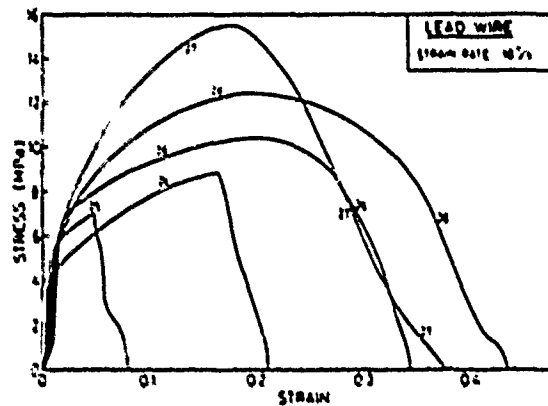
Fig. 4. Stress-strain curves for lead wires. Curves 26, 27 and 28 typify polycrystalline curves, curves 24 and 25 typify occasional single-crystal wires
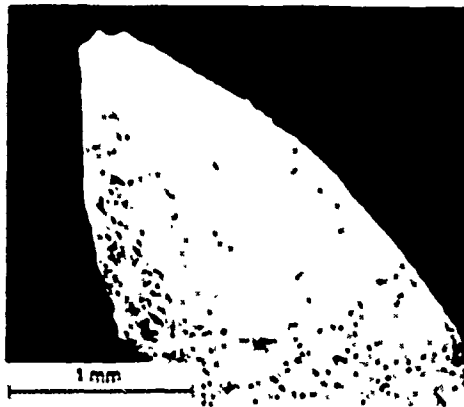
Fig. 5 A fracture surface of a lead wire

fracture was extensive, there was no central void in the lead, which drew down to a point [Fig. 7(d)]

The stress displacement records were sorted into three groups, based on the microscopic examination, as follows

(a) samples with perfect adhesion between lead and glass, and minimal damage to the glass itself, always with a central void,

(b) samples with partial loss of adhesion between lead and glass,

(c) samples with good adhesion between lead and glass, but with extensive damage to the glass

Plots of σ σ_a vs u_a were grouped accordingly and are shown in Fig. 8(a), (b) and (c). The area under each curve

$$\frac{W'}{\sigma_a u_a} = \int_0^{u} \frac{\sigma}{\sigma_a} \frac{du}{u_a} \qquad (7)$$

was measured; this dimensionless number gives a measure of the energy absorbed in stretching the lead to fracture. The results are given in Table 2 In all the plots the stress σ/σ_a rose rapidly to a peak at

decohesion. When the lead remained bonded to the glass, the glass itself often fractured by the formation of cracks concentric with the core, as shown in Fig. 7(d). Occasionally, when decohesion or glass
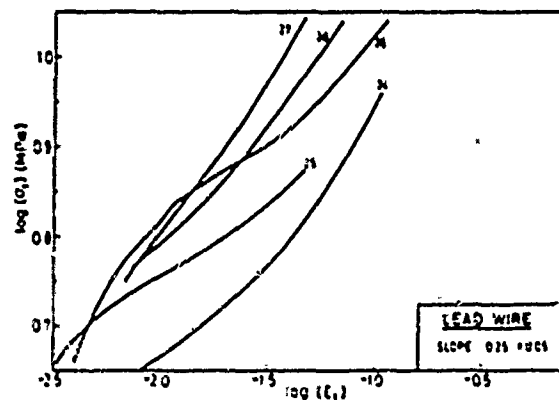
Fig. 6 A plot of $\log \sigma$ vs $\log \epsilon$, (where σ is the true stress and ϵ, the true strain) for the lead wires of Fig. 4. The work hardening index is close to 0.25
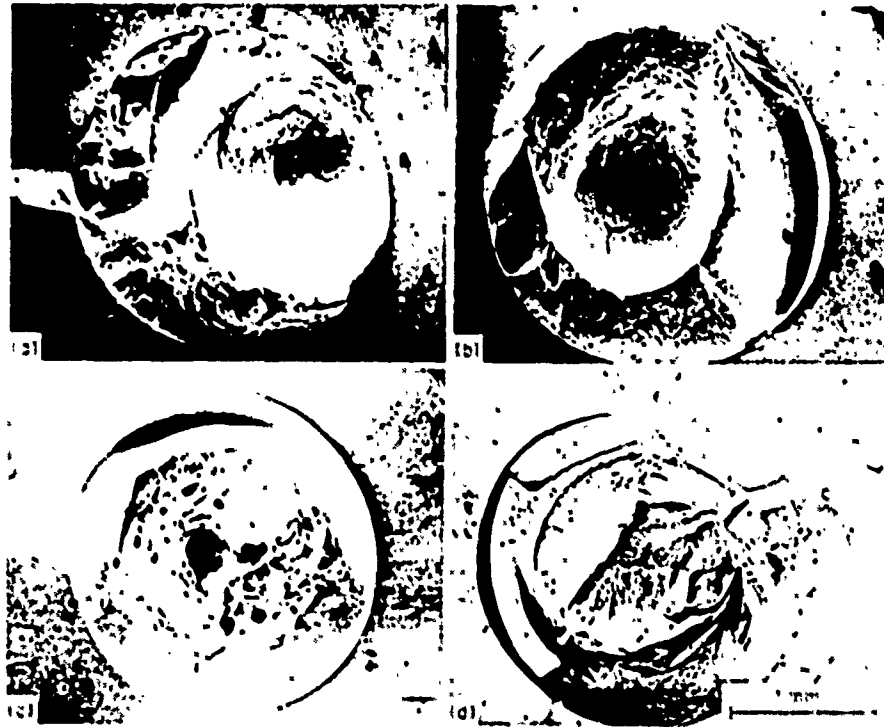
Fig 7 (a) Failure by the growth of a single internal void The lead glass junction remained intact and glass was not fragmented (b) Failure involving decohesion plus the growth of an internal void. The lead has been turn away from the glass over part of its circumference (c) Failure involving decohesion with multiple voiding. (d) Failure involving matrix cracking. The lead glass junction remained intact, but concentric cracks formed in the surrounding glass and the fracture surface is cavity-free

displacement u/a, of about 0.05 It then fell away, although in quite a number of samples in categories (b) and (c) there was a second shallow maximum which suggested work hardening in the lead.

Plots of samples in category (a) [Fig. 8(a)] had maxima of σ/σ_h of about 6. The normalised areas under these curves were small: between 1.5 and 2.0 The displacement at failure, u/a_a, was 0.6 in those
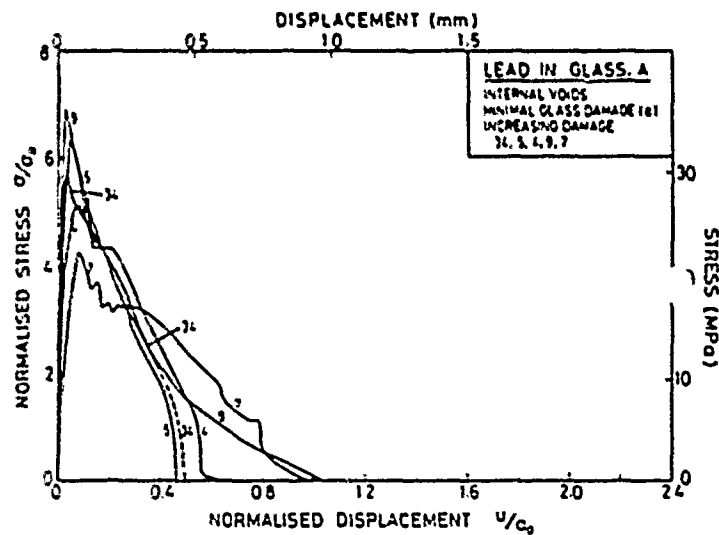
Fig. 8. (a) Caption overleaf

(b)

(c)
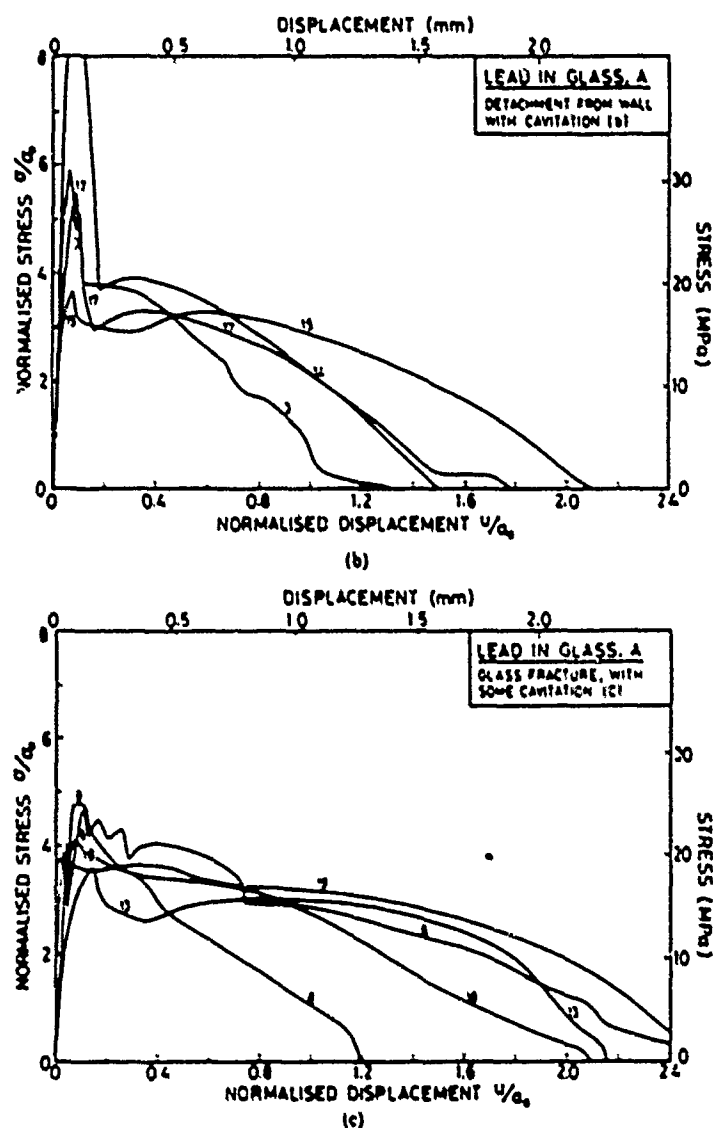
Fig. 8. (a) Lead in glass, type (a) failure: internal cavities with minimal glass damage. The order of increasing damage to the glass was: 34, 5, 4, 9, 7. (b) Lead in glass, type (b) failure: internal cavities plus detachment from the wall. The exceptional initial peaks are caused by incomplete fracture of the glass. (c) Lead in glass, type (c) failure: glass fracture with some cavitation.

with least glass damage, rising to approximately 1.0 with slightly more glass damage.

Force–displacement curves for samples in categories (b) and (c) [Fig. 8(b) and (c)] showed more variation and cannot easily be distinguished from one another. The initial maximum in σ/σ_0 was smaller: between 3.6 and 5.1, but the areas under these curves were larger: from 2.0 to 6.5. In category (b) it was not possible to perceive any positive correlations between the area under the curve and the extent to which adhesion between lead and glass was lost. However in category (c) there was a positive correlation between the length of lead with glass fragments

attached drawn out from the core and the area under the curve.

In a few instances, there was an exceptionally large peak in the force–displacement curve, followed by a precipitate fall. It was caused by incomplete cracking of the glass: the pattern of internal stress caused by thermal contraction of the lead caused the initial crack to arrest just short of the lead core. When the pre-cracked sample was loaded, the pop-in of the crack to the glass–metal interface could usually be heard. In these instances it was not possible to obtain a reliable value of the peak σ/σ_0, but the area was not much affected.

Table 2 The normalised peak stress and energy absorption 2

Sample No	Area C	Peak σ/σ_s	u^*/u_s	Wire diameter (mm)

Type (a) Failures: central void, minimal decohesion or glass fracture

14	1.5	5.7	0.54	2.1
12	2.0	6.1	0.6	2.1
5	1.5	6.1	0.42	2.1
3	1.7	5.1	0.62	2.1
9	2.0	—	1.03	2.1
7	2.0	—	0.97	2.1
111	1.9	6.1	0.66	1.3

Type (b) Failures: some loss of cohesion, no glass fracture

19	1.5	4.2	0.61	2.1
41	1.9	1.7	1.12	2.1
16	2.1	—	1.0	2.1
27	2.6	4.0	1.44	2.1
1	2.9	—	1.1	2.1
14	4.1	—	1.5	2.1
17	3.5	—	1.75	2.1
15	4.8	1.6	2.09	2.1
10	2.8	5.1	1.1	2.1
16	5.0	—	2.15	2.1
18	4.0	1.9	1.94	2.1
G1	3.1	3.1	1.2	1.3
G6	4.3	3.5	1.97	1.3
G7	3.8	3.7	1.69	1.3
111	4.1	1.1	2.01	1.3

Type (c) Failures: perfect adhesion, but glass fracture

8	2.7	4.7	1.2	2.1
17	3.1	4.1	1.33	2.1
22	3.3	—	1.33	2.1
32	3.1	—	1.33	2.1
31	3.4	3.6	1.38	2.1
40	3.5	4.3	1.42	2.1
11	4.3	4.8	1.74	2.1
18	4.6	4.1	2.09	2.1
42	4.9	—	2.34	2.1
11	5.2	3.6	2.14	2.1
N	5.9	—	2.38	2.1
6	5.9	4.7	2.96	2.1
19	6.5	3.7	2.56	2.1
21	3.1	4.6	1.51	2.1
30	3.9	—	1.62	2.1
G3	6.4	4.2	2.22	1.3

4.2 Mechanisms of failure

We distinguish four *mechanisms of failure*. It is convenient for the analysis of Section 5 to treat them as distinct and separate, although in practice they superimpose to some extent.

First, there is the mechanism assumed by the models described in Section 2: that the ductile inclusion deforms plastically to zero section without decohesion, cavitation or matrix fracture; the mechanism implies the inward flow of material as in classical necking creating a conical peak on both fracture surfaces. A very few of our samples approached this state, though all those which did showed some decohesion.

Most of our samples failed by the second mechanism, the nucleation of a single internal cavity which grew until it occupied most of the section. Material flows radially outward, from the growing void and inward from the original crack front, allowing the stretching of the remaining cylindrical ligament, which fails leaving a rim like that of a volcano on both fracture surfaces.

When the lead-glass bond was weak, a third mechanism appeared: the interface separated over a length of between 0.1 and 1.0 u_s, giving a "gauge length" of lead which was less constrained and could draw down, at a lower stress but with a greater elongation, that before. When decohesion was extensive, no internal cavity was found. The peak stress was lower, but the energy absorption greater, than for mechanism 2

A fourth mechanism—that of brittle fracture of the brittle matrix—was frequently observed. The fracture frees a length of lead from the glass (though with fragments of glass still adhering to it), giving a longer "gauge length", as with decohesion The process was characterised by a more gentle fall in stress and a larger energy absorption than mechanism 2

4.3. Dependance of absorbed energy on peak stress and displacement

The important results are plotted in Fig. 9 The first of the two figures shows how the peak stress falls and the maximum displacement increases as constraint is lost Perfect bonding without glass fracture gives a

(a)

(b)

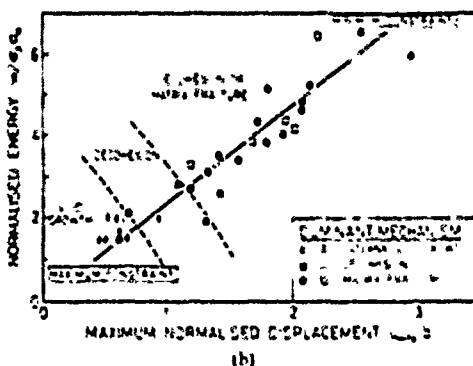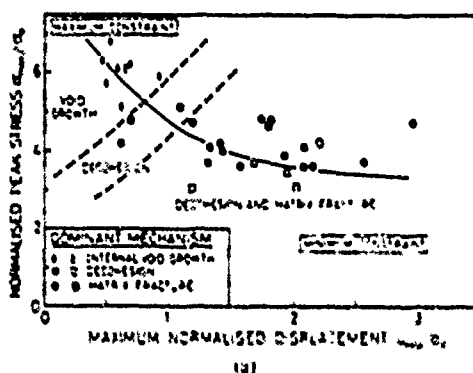Fig. 9 (a) The normalised peak stress σ/σ_s plotted against maximum displacement at failure u/u_s for constrained lead wires Symbols identify the dominant mechanism of failure (b) The normalised energy of fracture plotted against maximum displacement at failure for the same samples Note that data for thin (open symbols 1.3 mm) and thick (solid symbols: 2.12 mm) wires fall, when normalised, on the same curve

constraint factor as high as 7, but with failure displacements u/a_0 around 0.5. Decohesion and glass fracture lower the constraint but increase the failure displacement in such a way that the total energy absorbed increases. The second figure shows this increase, which is substantial: from about 1.5 (in units of $\sigma_0 a_0$) to about 6.5. If energy absorption is the goal, full constraint is not ideal; some (limited) decohesion or matrix fracture is desirable.

The pair of figures illustrate another important point. Data for the two different wire diameters are distinguished by full and open symbols: the normalisation brings the two sets of data into coincidence. The results can be summarised by the equation

$$W' = C\sigma_0 a_0 \qquad (8)$$

where the constant C from Fig. 9(b), depends on the constraint, and thus on the strength of the particle–matrix interface, but *not* on the wire diameter, as expected. It is approximately described [Fig. 9(b)] by

$$C \approx 2.5 \frac{u_{max}}{a_0}. \qquad (9)$$

In the next section, a simple, approximate model for each mechanism is analysed. The models explain much of the observed behaviour, but it should be remembered that, in reality, one mechanism rarely operates in isolation, and that the patterns of flow are more complicated than those assumed by the models.

5. MODELLING OF THE FORCE-DISPLACEMENT CURVE

A set of approximate analytical models for the force–displacement curve is presented in this section. They are simpler than the models described in Section 2, but have the advantages that they include, more explicitly, the geometry changes, and that they treat all the mechanisms in a consistent way.

5.1. The initial, rising, part of the load–deflection curve

When the composite is first loaded, there is a concentration of stress where the crack meets the metal wire. Dislocations nucleated here propagate across the metal and pile up at the metal–ceramic interface as shown in Fig. 10. The number of dislocations which emanate from the crack tip determines the crack opening. A shear stress σ_s compresses a pile-up of n dislocations of Burger's vector b into a length L where (16)

$$nb = \frac{4\sigma_s L}{G} \qquad (10)$$

and where G is the shear modulus. Figure 10 shows that for slip planes at $45°$ to the tensile axis $L \approx 2\sqrt{2}a_0$ and that the initial stage crack opening is $u_0 = \sqrt{2}nb$. Thus

$$u_0 = \frac{16\sigma_s a_0}{G}.$$
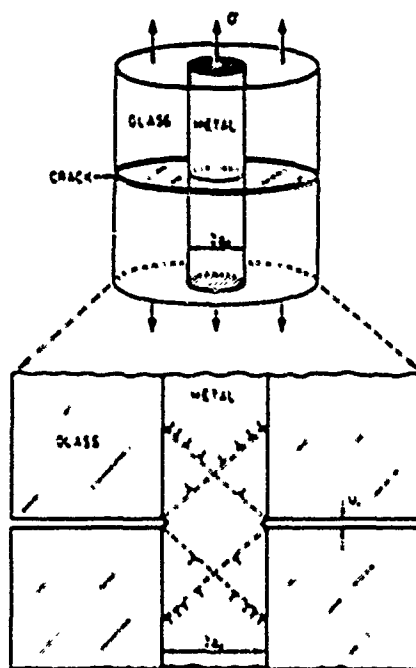
Fig. 10. The initial crack opening, u_0, can be calculated from the dislocation theory of the pile-up.

Replacing σ_s by $\sigma/2$ and G by $3E/8$ gives

$$\frac{u_0}{a_0} \approx 20 \left[\frac{\sigma_0}{E} \right] \frac{\sigma}{\sigma_0}. \qquad (11)$$

The value of σ_0/E for the lead used in the experiments described earlier is 2.8×10^{-4} giving the equation for the rising part of the load deflection curve for this composite as

$$\frac{\sigma}{\sigma_0} \approx 170 \frac{u}{a_0} \qquad (12)$$

The slip distance inside a constrained sphere is smaller, by a factor of about 2, than that in a wire. We therefore expect, for the spherical inclusion

$$\frac{u_0}{a_0} \approx 10 \left[\frac{\sigma_0}{E} \right] \frac{\sigma}{\sigma_0} \qquad (13)$$

5.2. The later, falling, part of the load deflection curve

The post-peak behaviour depends on the *mechanism*. We distinguish three mechanisms and develop simple models for each. The three mechanisms are:

(a) Fully constrained deformation without internal decohesion, matrix fracture or internal voiding (Fig. 11).

(b) Deformation with limited decohesion or matrix fracture but no internal voiding (Fig. 12).

(c) Deformation with internal voiding but no decohesion or matrix cracking (Fig. 13).

(a) Fully constrained deformation. A kinetically admissable flow field is shown in Fig. 11. Deforma-
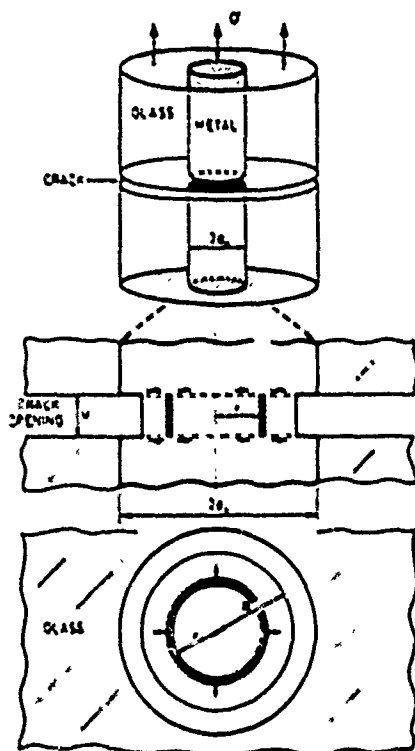
Fig. 11. Fully constrained deformation with no decohesion. Internal voiding or matrix cracking is possible by the flow field shown here. It gives an upper bound for the force–displacement curve.
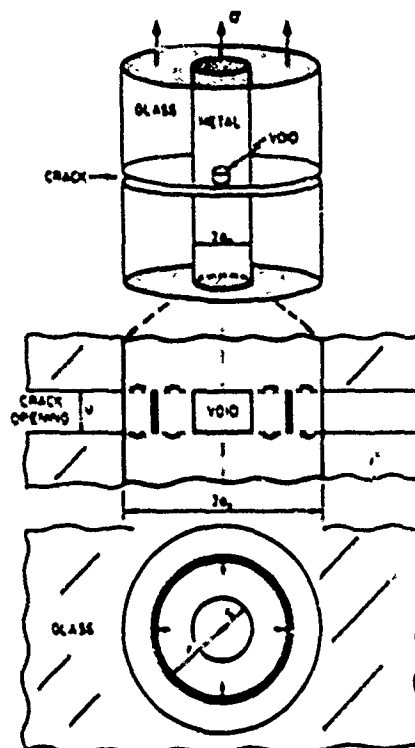
Fig. 13. Internal voiding, frequently observed, is possible by the flow field shown here. It requires a lower force than does the fully constrained deformation of Fig. 11
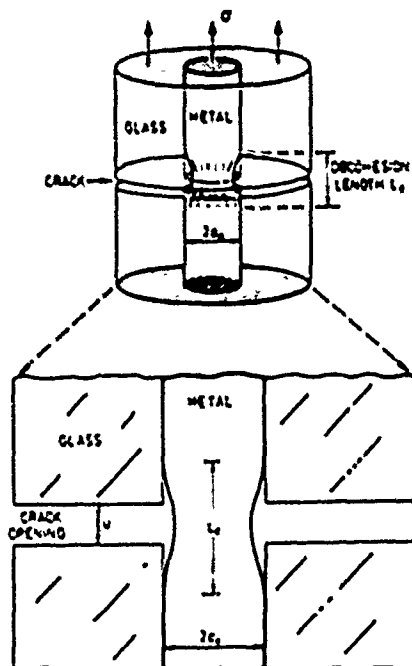
Fig. 12. Decohesion over a length l_d reduces the constraint and modifies the force-displacement curve as analysed in the text and shown in Fig. 8(b)

tion is confined to the solid cylinder of height u and diameter $2R$. As the cylinder extends it shrinks inwards so that its volume remains constant. This condition leads immediately to two equations. The first describes the overall conservation of volume

$$\Pi a_0^2 u_0 = \Pi R^2 u \qquad (14)$$

where u_0 is the initial crack opening and $2a_0$ is the original wire diameter. The second describes the inward radial displacement δr of any point lying at a radius r caused by an axial extension δu. It is obtained by noting that, for any radius, $\Pi r^2 u =$ constant. Differentiation then gives

$$\delta r(r) = -\frac{r}{2u}\delta u. \qquad (15)$$

We now equate the work done by the external stress σ in a small increment of crack opening δu to the plastic work done on the cylinder. There are two contributions to this plastic work: that associated with extending the cylinder and that caused by its shrinking relative to the rest of the wire

$$\sigma \Pi a_0^2 \delta u = \Pi R^2 \sigma_s \delta u + 2 \int_0^R \sigma_s 2\Pi r \, \delta r(r) \, dr \qquad (16)$$

where σ_s is the shear flow-strength of the wire. Substituting for δr from the previous equation,

writing $\sigma_s = 2\sigma$, integrating with respect to r and replacing R u_a using equation (14) gives

$$\frac{\sigma}{\sigma_s} = \frac{u_a}{u}\left[1 - \frac{1}{3}\left[\frac{u_a}{u}\right]^{12}\frac{u_a}{u}\right]. \qquad (17)$$

In general σ_s increases with strain because of work hardening [equation (3)]. The strains in the cylinder are hard to calculate exactly but they are obviously of the order of $(u/u_a - 1)$. The main equation then becomes

$$\frac{\sigma}{\sigma_s} = \left[\frac{1}{c_n}\left[\frac{u}{u_a} - 1\right]\right]^n\frac{u_a}{u}\left\{1 - \frac{1}{3}\left[\frac{u_a}{u}\right]^{12}\frac{u_a}{u}\right\}. \qquad (18)$$

(b) Limited decohesion The theory remains the same as above, but the "gauge length" is no longer the initial crack opening but is equal to the decohesion length $(l_s + u_a)$ shown in Fig 12. Reworking the problem using the method of the last section leads immediately to

$$\frac{\sigma}{\sigma_s} = \left[\frac{1}{c_n}\left[\frac{u - u_a}{l_s + u_a}\right]\right]^n\left[\frac{l_s + u_a}{l_s - u}\right]$$

$$\times\left\{1 - \frac{1}{3}\left[\frac{l_s + u_a}{l_s + u}\right]^2\left[\frac{u_a}{l_s + u}\right]\right\} \qquad (19)$$

(c) Internal voiding. The third mechanism is that of internal void growth A kinematically admissable flow field is shown in Fig. 13; the thick annular ring extends along the tensile axis and shrinks in thickness by the internal radius moving outwards. Constancy of volume now gives

$$\Pi a_s^2 u_a = [\Pi a_s^2 - \Pi r^2] u$$

and

$$\delta r(r) = \left[\frac{a_s^2 - r^2}{2ru}\right]\delta u.$$

Equating the external work to the plastic dissipation gives

$$\frac{\sigma}{\sigma_s} = \left[\frac{1}{c_s}\left[\frac{u}{u_a} - 1\right]\right]^n\frac{u_a}{u}$$

$$\times\left\{1 + \frac{u_a}{3u_a}(2 - 3\left[1 - \frac{u_a}{u}\right]^{13}\right.$$

$$\left.+ \left[1 - \frac{u_a}{u}\right]^{13}\right\} \qquad (20)$$

with the same correction for work hardening as used in case (a).

5.3. Results of the models

The models are evaluated in Figs 14 and 15 Figure 14 is a comparison between the force displacement curve for cases (a) and (c) using

$$u_a/u_a = 0.05 \quad n = 0.25 \quad c_a = 0.004.$$

It shows that the force required to expand the void is a little less than the required to pull material inwards. The shape of the curve is superficially like that of the experiments, but the initial fall is too steep. The long tail results from the drawing out of the ligament without allowing for local necking or further void nucleation, both of which will truncate the curve.

Figure 15 shows the effect of decohesion As the decohesion-length increases, the peak in the curve falls and the curve broadens. A small decohesion length, $l_s = 0.1 u_a$, gives a curve which has a peak height and overall shape which is close to that observed.

6. CONCLUSIONS

Metal wires, constrained by bonding them to a strong brittle matrix so that deformation was
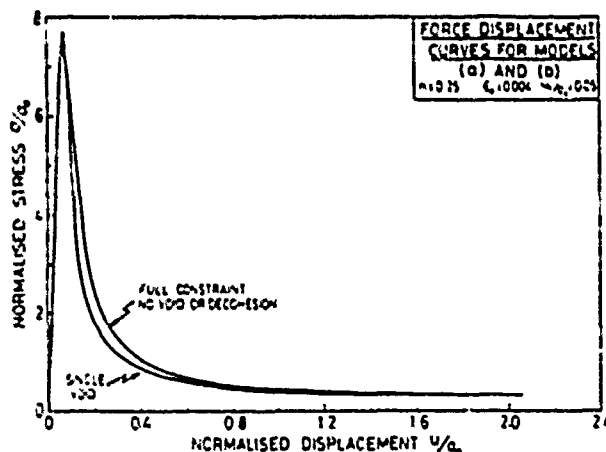

Fig. 14 The force displacement curves for the fully constrained and the internal-void mechanisms
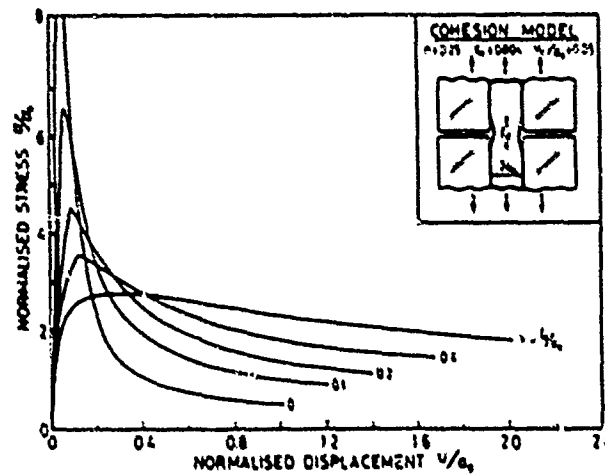
Fig. 15. The effect of decohesion length on the force-displacement curve.

restricted to a small segment of the wire, show a force-displacement curve which is strongly influenced by the constraint. Three failure mechanisms were observed: internal void growth in the metal; decohesion at the metal-matrix interface; and cracking in the brittle matrix.

The overall shape of the force-displacement curve resembles that predicted by Sigl et al. (1988), even though the mechanism assumed by them differs from those observed in our experiments. A set of simple models for the mechanisms give insight into the ways in which the shape of the force-displacement curve is influenced by decohesion, work hardening, wire dimensions and so forth.

The experiments and models establish the necessary basis for understanding and designing ceramic-metal composites with a toughness larger than that of the simple ceramic. Provided the crack is attracted to particles (and does not by-pass them) they should contribute to the toughness in the same way as wires. For both the energy absorbed is

$$\Delta G_c = V_f \int \sigma(u)\, du \qquad (21)$$

$$= C V_f \sigma_0 a_0 \qquad (22)$$

where V_f is the area fraction of ductile material intersected by the crack plane. The constant C is equal to 1.6 for complete bonding with no matrix fracture, but rises to as much as 6 with limited debonding or matrix fracture. The result can be rewritten

$$\Delta K_c = \tilde{n}\left[C V_f \frac{\sigma_0}{E} a_0 \right]^{1.2}. \qquad (23)$$

The greatest toughening is obtained from inclusions with a high modulus, E, a high strength σ_0/E, and a large diameter. As an example, a volume fraction of 5% of well-bonded lead inclusions of diameter 10 μm contribute only 0.25 MPa m$^{1/2}$ to the toughness, whereas the same volume fraction of niobium inclusions gives 3.25 MPa m$^{1/2}$ and of tungsten gives 13.5 MPa m$^{1/2}$. If limited decohesion is allowed, the contributions more than double. Large inclusions are more effective than small ones: the same volume fraction of 100 μm inclusions gives a 3 times greater increase in fracture toughness.

REFERENCES

1. P. Hing and G. W. Groves, J. Mater. Sci. 1, 427 (1972).
2. B. J. Dalgleish and A. G. Evans. To be published.
3. V. V. Kristic and P. S. Nicholson, J. Am. Ceram. Soc. 64, 499 (1981).
4. M. J. Stowell, Private communication (1988).
5. W. W. Gerberich, J. Mech. Phys. Solids 19, 71 (1971).
6. G. A. Cooper and A. Kelly, J. Mech. Phys. Solids 15, 279 (1967).
7. G. A. Cooper, J. Mech. Phys. Solids 18, 179 (1970).
8. J. L. Chermant and F. Osterstock, J. Mater. Sci. 11, 1939 (1976).
9. L. S. Sigl, H. E. Exner and H. F. Fischmeister Inst Phys. Ser 75, Chap. 7, in 3rd Int. Conf. Science Hard Mater. (1986).
10. M. Sleaser, J. Dusza and L. Parilak, Inst. Phys. Conf Ser 75, Chap. 7, in 2nd Int. Conf. Science Hard Mater (1986).
11. L. S. Sigl, Acta metall. To be published.
12. P. Mataga and R. M. McMeeking. To be published.
13. A. G. Evans and R. M. McMeeking, Acta metall 34, 2435 (1988).
14. P. W. Bridgeman, Studies of Large Plastic Flow and Fracture. Harvard University Press.
15. L. S. Sigl and A. G. Evans. To be published
16. J. Friedel Dislocations, p. 257. Pergamon Press, Oxford (1964).

MATERIALS
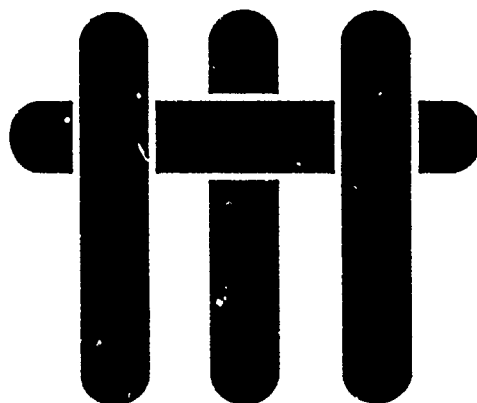
THE INFLUENCE OF THE REACTION LAYER STRUCTURE AND PROPERTIES ON DUCTILE PHASE TOUGHENING IN TITANIUM ALUMINIDE-NIOBIUM COMPOSITES

G. R. Odette, H. E. Dève, C. K. Elliott, A. Hasegawa
and G. E. Lucas

Materials Department
College of Engineering
University of California, Santa Barbara
Santa Barbara, California 93106

Introduction

The concept of toughening brittle matrix composites by the introduction of a modest volume fraction of a ductile phase has now been demonstrated for a number of systems (1-5). For example, incorporation of about 20 volume percent of approximately 35 μm thick pancake-shaped titanium-niobium particles has been shown to increase the toughness of γ-TiAl matrix composites by factors of more than three (5). The toughening is primarily due to shielding of the crack tip stress intensity from remote loads by the bridging zone of unbroken ductile particles left in the wake of the growing crack. In some cases, additional extrinsic toughening is also provided by crack deflection and branching induced by the particles.

For conditions of small scale yielding, bridge toughening produces a resistance curve, or an increasing toughness, ΔK, with crack extension, L, up to a steady-state value. ΔK_{ss}. Steady-state occurs when a balance between the creation and loss of the particles in the bridging zone is achieved. This condition is characterized by a steady-state bridge length, L_{ss}, which is controlled by the crack face opening, u(L), at the point of particle fracture, u^* (Figure 1a). The most fundamental measure of toughening from ductile reinforcements of a given size, a_0, and yield stress, σ_0, is the normalized stress $s(u')$ (= $\sigma(u')/\sigma_0$) versus the normalized crack opening displacement, u^* (= u/a_0) function. The steady-state toughness increment is simply proportional to the area under the $s(u')$ curve or the work of fracture, χ (Figure 1b). Expressed in terms of the J-integral, $\Delta J_{ss} = f_p \sigma_0 a_0 \chi$, where f_p is the fraction of ductile phase particles on the fracture surface (6).

Much of the discussion about ductile phase toughening has been directed at approaches to maximizing χ. Both theoretical considerations (2) and model experiments reported by Ashby et. al.(6) have shown that in some systems χ increases with increasing debonding between the brittle matrix and ductile phase. More generally, deformation of the ductile phase takes place under evolving conditions of constraint due to debonding, strain-hardening, the spread of plasticity and large geometry changes due to necking, crack propagation and shear band formation.
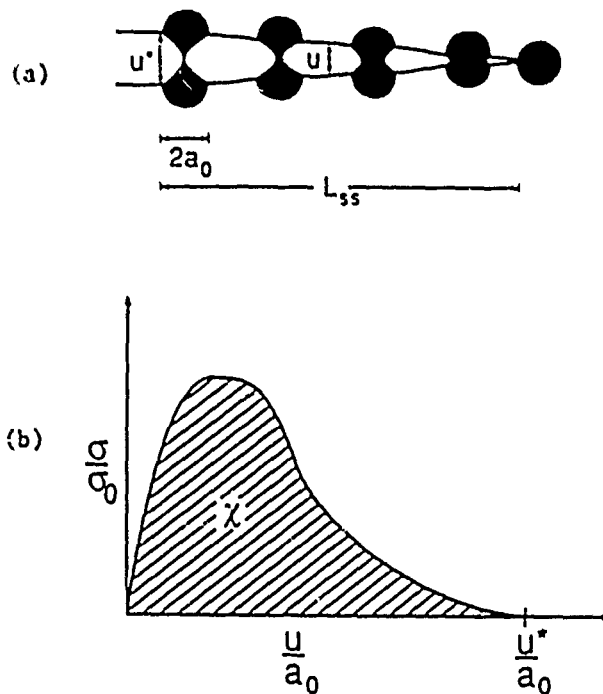

Figure 1 -- Schematic illustration of a) key crack bridging zone parameters; and b) the work of fracture, χ, from the normalized stress displacement curve.

Hence, the behavior of the particle-matrix interface, or reaction layer, which controls debonding can be critical to ductile phase toughening. Conceptually, adherent interfaces lead to constrained deformation with correspondingly high effective stresses and low values of u'*. In this case fracture occurs by localized plasticity and crack propagation generally resulting in low values of χ. In contrast, extensive debonding results in lower constraint and effective stresses but higher values of u'*. In this case, the plastic deformation is distributed in a larger volume, leading to higher values of χ. Thus the debond length, d, is also a key ductile phase toughening parameter and is conveniently defined in a dimensionless form as, d' $(= d/a_0)$

There are, however, several complications to this simple picture. For example, higher strength is beneficial to toughening if it does not lead to a proportionally larger reduction in χ. Further, the constitutive behavior and microscopic deformation mechanisms of the ductile phase can also play an important role in mediating χ and its relation to debonding. While extensive debonding may lead to high values of χ, impractically large crack growth may be required to achieve steady-state conditions. Indeed, the initial slope of the resistance curve, or the tearing modulus, T_R, and its corresponding influence on crack growth stability, may often be a more important engineering property than the steady-state toughness. Debonding would be expected to decrease T_R. In many applications, there may also be significant effects of specimen/structure size and geometry (i.e., large scale yielding) which alter the relation between χ and the maximum useful toughness increment. Finally, crack deflection and branching contribute to toughening and may also exert an indirect influence on bridging mechanics by modifying the particle deformation geometries.

Appropriate measures of s(u') can, in principle, be used both to specify the entire resistance curve due to bridging for any arbitrary size and geometry and help isolate the bridging from crack deflection contributions. Complementary estimates of s(u') can be obtained from both resistance curve along with u(L) and L_{ss} measurements as well as model experiments on special specimens such as laminates.

Hence, the focus of this report is on the interactive roles of the interface, matrix and ductile phase properties on particle deformation and toughening. The behavior of γ-TiAl alloys reinforced with either Nb or TiNb phases is compared and contrasted.

Review of Toughening Observations in Nb and TiNb Reinforced γ-TiAl

The resistance curves for the alloy composites produced by powder consolidation techniques have been evaluated by testing small (0.25 and 0.5 cm thick) three point bend specimens (4,5). The particles were in the form of irregular pancakes, produced by hot forging. The processing times and temperatures were about 4 h and 1066°C respectively. The characteristic dimension, a_0, was taken as the average pancake half-thickness. The ductile phase parameters and estimates of their mechanical properties are tabulated elsewhere (5). The γ-TiAl matrix toughness, K_0, was about 8 MPa$\sqrt{m}$ in both cases.

TiAl-Nb

The 10 volume percent of Nb particles produced an apparent maximum toughness of about 16 MPa$\sqrt{m}$ for the orientation (E) where the crack intercepted the thin edge of the pancake. In this case the crack surface was flat, with undeflected cracks bypassing the particles. The maximum apparent toughness was larger at about 20 MPa$\sqrt{m}$ in the orientation (F) where the cracks intercepted the broad face of the pancakes. In the latter case the crack path is highly tortuous. Normalization of an energy-equivalent toughening increment ($[K \cdot K_0]^2$) by dividing by the ratio of the total crack to projected crack length resulted in a superposition of the resistance curves for the two orientations (4,5). The steady-state toughness contribution from bridging for small scale yielding conditions was estimated to be about 4 MPa$\sqrt{m}$ based on application of a correction for the finite specimen size (7,8).

Intersections of the cracks with the pancake face produced jumps or deflections and a modest amount of crack branching, with an average deflection angle of about 45°. The deflections appeared to be associated with matrix crack renucleation near localized strain concentrations in the deformed particles. An average d' of about 2 was observed, with debonding sometimes, but not

always, on both sides of the particle. Debonding generally occurred between a thin ($\approx 3\ \mu m$) reaction layer and the matrix. The variation in the crack opening with distance from the crack tip was approximately linear, and the particles failed by a highly ductile knife edge rupture process at u'^* values of about 1.6. Tensile deformation of Nb was characterized by fine slip, high strain-hardening exponents, significant uniform strains and fracture following diffuse necking.

Based on a steady state toughness increment of 4 MPa$\sqrt{m}$ and the shape of the resistance curve, $s(u')_{max}$ was estimated to be about 1.7 near the crack tip ($u' \approx 0$) decreasing approximately linearly to zero at u'^*. The corresponding estimate of χ was about 1.3.

TiAl-TiNb

The 20 volume percent of TiNb particles produced much higher maximum apparent toughness levels of about 36 MPa$\sqrt{m}$ in the E-orientation and 40 MPa$\sqrt{m}$ in the F-orientation. Considerable crack deflection and branching (multiple cracking) were observed in both orientations. Again, however, crack length normalization resulted in superposition of the resistance curves. The steady-state toughness contribution from bridging for small scale yielding conditions was estimated to be about 15 MPa$\sqrt{m}$.

Particle deformation was associated with very coarse slip bands which spread over a surprisingly large volume of the particle, typically distances of $2a_0$ or more above and below the crack faces. Significant debonding was not observed, although there was limited cracking at both the matrix reaction zone interface and in the nearby matrix. Final fracture occurred by coalescence of coarse slip bands into a primary crack or shear band at a u'^* of about 0.7. The tensile deformation of TiNb was characterized by coarse slip zones (much like Luder's bands), minimal strain hardening, low uniform strains with fracture following local necking.

Based on a steady state toughness increment of 15 MPa$\sqrt{m}$ and assuming the triangular shape for $s(u')$, similar to that for Nb, $s(u')_{max}$ was estimated to be about 3.1 and χ about 1.1. Note the shape of the resistance curve suggested that $s(u')$ decreases somewhat less rapidly than assumed, hence, these values are approximate. Indeed, the $s(u')$ parameter estimates are also imprecise due to a variety of other sources of uncertainty, including: corrections for specimen size and crack deflection; estimates of the ductile phase yield stress after processing; and scatter in the resistance curve, crack parameter and microstructural measurements.

Crack Particle Interaction and Particle Deformation Observations

A special mechanical testing stage was developed to provide direct observations of crack-particle interactions and ductile phase deformation and fracture in a JEOL 840A Scanning Electron Microscope (SEM). Both loads and displacements were monitored during the tests which were continuously recorded on video tape; the tests were also interrupted periodically to record higher quality still pictures. These in-situ SEM experiments were complementary to both previous SEM observations of statically loaded cracked specimens as well as similar optical observations (albeit with a somewhat lower resolution and depth-of-field capability) during crack growth resistance curve tests in a stiff servohydraulic load frame. The tests permitted the evaluation of the detailed history of a bridging particle from the point of crack intersection to final failure. Details of these experiments will be presented elsewhere, but a summary of the results is provided below.

TiAl-Nb

The debonding and deformation histories of individual particles varied considerably. For example, debonding was observed first on both the front and back of a particle and both prior to and after the crack has bypassed a particle. Often only one side extensively debonded. Debonding usually occurred at relatively low particle strains and increased only slightly with additional deformation. Debonding generally occurred between the reaction layer and matrix. Much larger than average debonding was observed in some cases while some particles appear bonded to the matrix up to the point of fracture. In part this variability in behavior appears to be due to differences in the particle morphology and crack-particle geometry, and in part due to the range of the inherent strength of the reaction layer. The crack jumps and debonding appeared to correlate

with the overall macroscopic character of the particle deformation geometry. Offset cracks tended to produce shear bands while planer cracks tended to produce diffuse necks.

Figure 2a to c illustrates several examples of the behavior noted above for a set of particles in the F-orientation. The first particle (a) does not debond and fractures by crack propagation. The second particle (b) experiences limited debonding on the front side and a large crack jump; failure occurs by shear band formation. The third particle (c) debonds extensively on the back side before crack propagation and also fails in shear. Figure 2d shows an example of particle failure after symmetric debonding by the formation of a diffuse neck.

TiAl-TiNb

In contrast, the TiNb particles do not appear to experience significant debonding as illustrated in the sequence of micrographs shown in Figure 3a to d for a particle in the F-orientation. The micrographs also demonstrate the extensive spread of deformation in the particles. In Figure 3a the crack has by-passed the particle prior to significant deformation but is just approaching it on its front (right side). In Figure 3b the crack is just penetrating the reaction zone (by slip line shear cracks); however, the crack has initiated a region of slip in the particle extending far above the fracture plane. The enormous extent of this region is illustrated at lower magnification in Figure 3c, when the crack had intersected, but not yet penetrated the particle. The higher magnification micrograph shown in Figure 3d shows that in spite of the extensive deformation, the minimal debonding was confined to a small region near the top of the front crack and a slightly more extended region below the back crack (not shown).

Another TiNb-particle sequence is shown in Figure 4a to d. Figure 4a shows a fine matrix crack blunting as it intersects the reaction zone. In Figure 4b the crack has penetrated the reaction zone and significant slip has again been initiated in the particle. A lower magnification shot at this loading point in Figure 4c shows a main shear band forming between the jogged crack as well as the initiation of a secondary crack on the back of the particle running at about 45°. Figure 4d shows that at larger openings the particle has deformed by an extensive region of coarse slip associated with both the primary and secondary crack and that a roughly horizontal tertiary crack has also formed on the back side of the particle. Final fracture took place by crack propagation between the tertiary crack and the primary region of intense slip.

Microstructures, Microchemistries and Deformation Substructures in the Ductile, Reaction Zone and Matrix Phases

A three step thinning procedure involving selected area dimpling, twin-jet electropolishing and ion milling was developed to permit detailed transmission electron microscopy (TEM) imaging, selected area diffraction (SAD) and energy dispersive x-ray spectroscopy (EDS) measurements of adjacent ductile, reaction zone and matrix phases in both undeformed and deformed regions near a crack face. Details of the techniques and extensive micrographic illustrations will be presented elsewhere, and only the most salient results are summarized here.

TiAl-Nb

The compositional variations in the Nb alloy are shown on the 1200°C ternary phase diagram in Figure 5 (9). A simplified overview of the TEM observations is schematically illustrated in Figure 6. The characteristics of the undeformed material can be summarized as follows. The Nb phase had a fine subgrain structure (≈ 3 μm) and a low dislocation density, indicating recovery during hot forging. A reaction layer approximately 3μm thick formed between the β-Nb phase and the $\gamma(L1_0)$-TiAl. A thin (≈ 300 nm) layer composed of only one or two clean equiaxed grains formed immediately adjacent to the Nb. Although identification by diffraction analysis in the reaction zone was not carried out, EDS measurements indicate that this was δ-phase. The next region, out to about 1.5 μm, was composed of approximately 500 nm grains containing spherical inclusions and was compositionally consistent with the σ-phase. The remaining reaction layer was compositionally and microstructurally complex. The spectra were consistent with successive regions of T_2 and α_2-phase. However, the boundaries between these regions were not well defined. The γ-matrix is fine grained (2-5μm) containing a low density of dislocations, typically
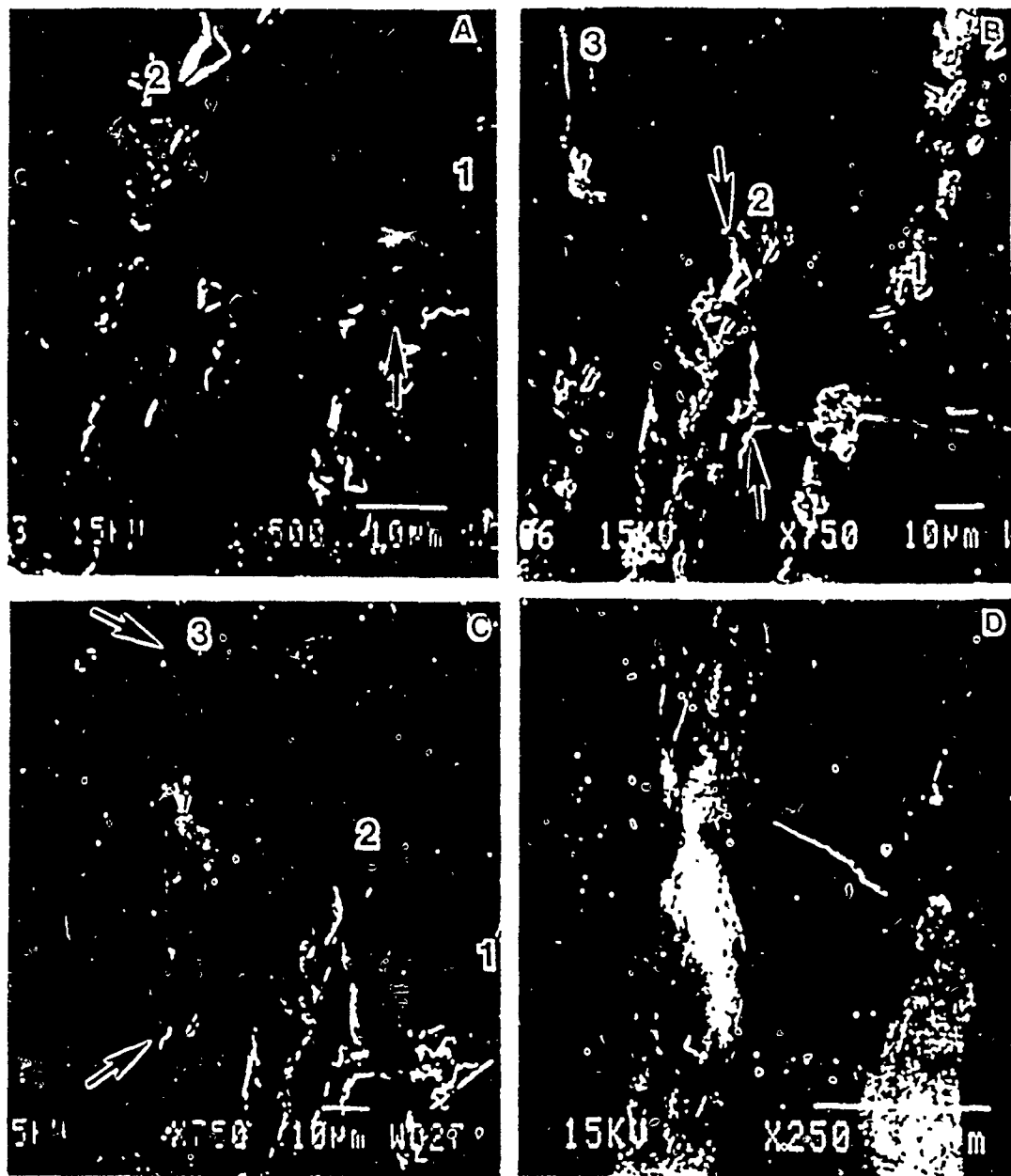
Figure 2 -- Some representative examples of debonding, deformation and fracture characteristics of Nb particles.
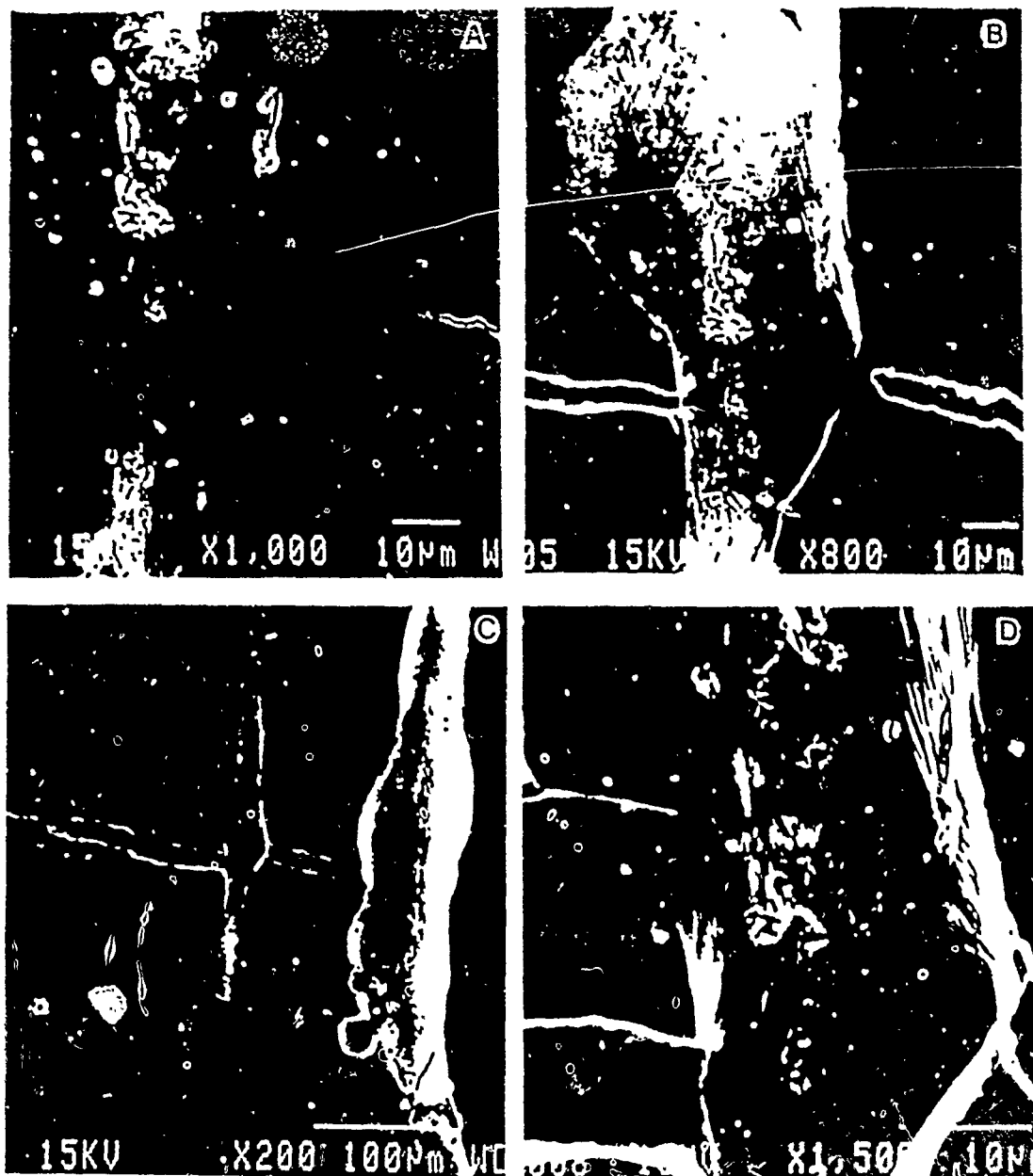
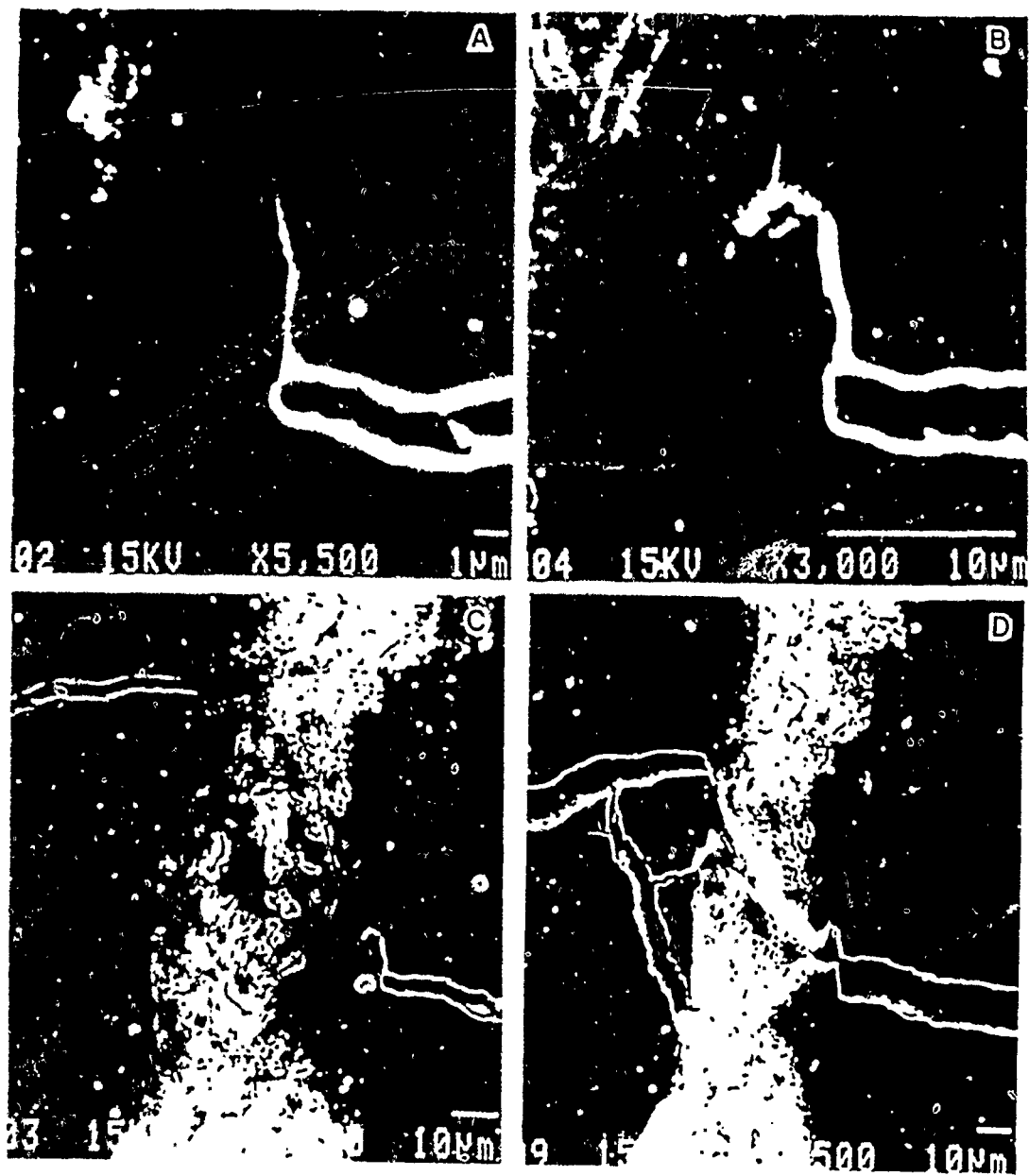Figure 3 -- An example of the deformation history of a TiNb particle.

Figure 4 -- Another example of the deformation history of a TiNb particle.

pinned by relatively large (about 100 nm) spherical features. A low density of twins was also observed in the matrix. The Nb content quickly dropped to small levels (<2 at.%) consistent with the bulk matrix composition.

Deformation substructures could not be observed in the Nb due to the foil thickness in this area. The reaction layer showed no evidence of deformation, as neither dislocations nor twinning were observed. Microscopic cracking was primarily observed near the δ-phase region, in contrast to macroscopic evidence of debonding between the γ-matrix and σ-phase. Significant deformation was observed within about 20 μm of the crack face in the γ-TiAl phase primarily by <111>{112} twinning, but also with heterogeneously distributed regions of a high density of tangled dislocations having a/2<111>-type Burgers vectors, indicating considerable slip. Cracks were observed emanating from ledges formed by twin intersections at the γ-matrix/σ-reaction layer interface.

TiAl-TiNb

The compositional variations in the TiNb alloy are also shown on the ternary phase diagram in Figure 5. An simplified overview of the TEM observations is schematically illustrated in Figure 6. Three regions were observed in the undeformed TiNb-particles which had an average grain size of about 10μm. Normal solid solution β-phase was found at distances greater than about 5 μm from the particle interface with the distinct reaction zone. This β region contained a low density of rafted dislocations having a/2<111>-type Burgers vectors on {110} planes. Aluminum replaced niobium at concentrations of several percent in this region. Extra spots also indicated the presence of a diffuse ω-phase; however, the intensities were too low to obtain dark field images of the precipitate structure. Within about 5 μm of the interface, the diffraction patterns indicated the existence of both ordered B2 and diffuse ω-phases. Superdislocation pairs were observed in

Figure 5 --The composition profiles between the γ-TiAl and the Nb (triangles) and TiNb (circles) particles plotted on the 1200°C Ti-Al-Nb isotherm (9). The numbers or letters on the larger symbols reference positions shown in Figure 6. The smaller symbols are for spectra taken at other nearby positions.

rafted boundary pile-ups, consistent with the ordering. Within about 1.5μm of the interface a region of mixed α_2, B_2 and diffuse ω-phases were observed. The α_2 was in the form of thin (~ 200nm) lath-shaped particles. The dislocation structure in this region was similar to that found in the B_2 region. The Nb concentration dropped to about 20% and the aluminum concentration increased to about 17% approaching the interface. However, there is an indication of a reversal of this trend in the immediate vicinity of the interface where increases in the Nb and decreases in the Al content were observed.

The interface between the particle and the distinct reaction layer was sharp. The 3 to 5 μm thick reaction layer consisted of 2 to 3 grains (about 1 to 3μm diameter) of α_2 (DO_{19}) - phase, but with a c/a-ratio of about 0.929, rather than the nominal 0.801 for Ti_3Al. This distortion may be due to Nb which largely replaces Al, at a level of about 10 atom-percent. The α_2 microstructure was fairly clean with only a few small unidentified features apparent. A low density of long straight dislocations was observed in the undeformed α_2 reaction layer The γ-TiAl matrix region is similar to that found in the TiAl-Nb alloy.

Deformation greatly increased the dislocation density in all regions. The deformation in the TiNb consisted of extensive localized parallel slip on planes separated by about 0.2 to 2μm, and rafted dislocation pile-ups against internal boundaries were frequently seen. The Burgers vectors of the dislocations were identified to be of the a/2<111>-type and slip planes were {110}. Dislocation pairing could not be observed due to the restricted imaging conditions. Cross slip and
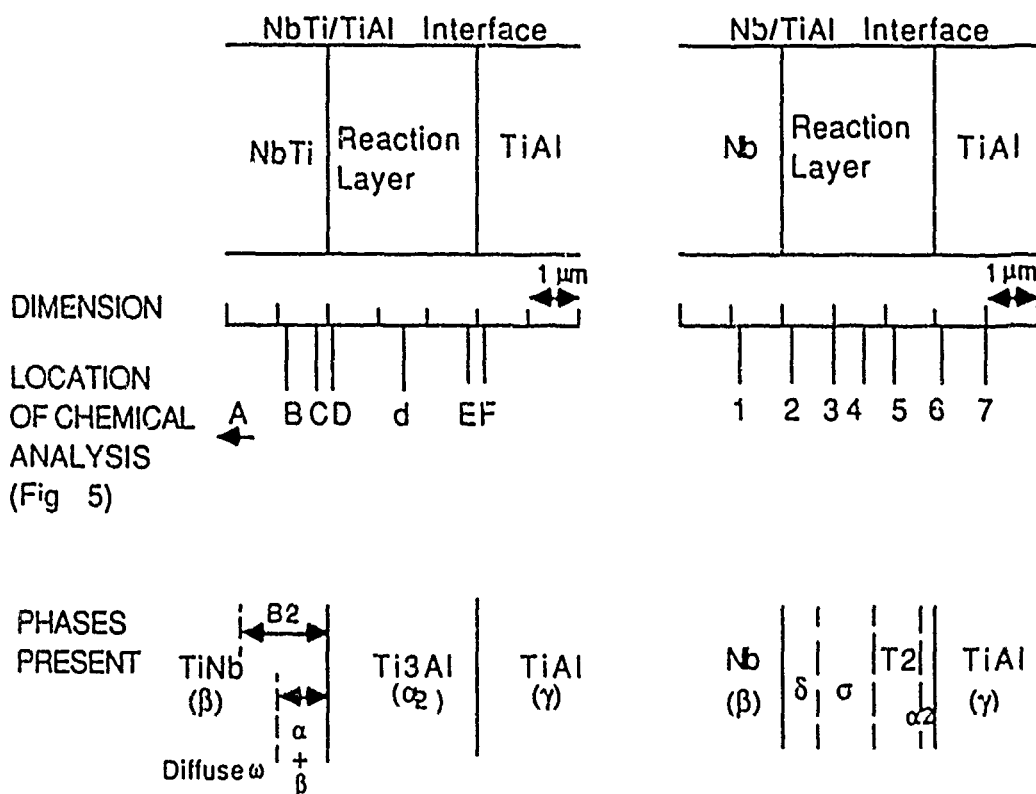

Figure 6 -- A schematic illustration of the size scale and phases observed in particle, reaction layer and matrix regions. The dashed lines demarcating phases indicate variability in the location of these phases.

the formation of dislocation networks were seen in high strain regions. However, no evidence of dislocation cell formation or twinning was found. Suppression of twinning and cell formation may be due to the presence of ω-phase, interstitial gaseous impurities and Al substitutional solutes. The dislocation structures in regions near localized necks in deformed TiNb tensile specimens were also evaluated. Intense bands of paired superdislocations and elongated loops were found, in spite of the fact that neither B_2 nor ω-phase spots were observed in the bulk alloy.

Rafted pileups of paired superdislocations against boundaries were also observed in the deformed α_2-phase. The pile-ups occurred at most frequently at the $B_2 + \alpha_2$ boundary. The dislocation density decreased in the direction of the the TiAl matrix phase. The α_2 phase dislocations had <1120>-type Burgers vectors in the basal planes. Some non-basal plane dislocations were also observed in association with low angle subboundaries. Deformation substructures in the γ-TiAl were similar to those observed in the TiAl-Nb alloys, viz. - twinning and heterogeneous dislocation tangles. Twinning ledges at the γ-α_2 interfaces were observed but did not appear to nucleate microcracks.

In summary, considering influence of differences between processing temperatures and the phase diagram isotherm, the microchemistry of the particles, reaction layer and matrix were in reasonable agreement with published data (9, 10). Further, with a few exceptions, the substructures of the individual phases were consistent with other independent evaluations (11-18). Some notable observations included: a fine subgrain structure in the niobium following processing, which may add to the strength of the particles; significant ductility in the adherent α_2 reaction layer around the TiNb particles in contrast to the brittle debonding σ and δ phases around the Nb particles; evidence of both slip and twinning in the γ-matrix near the crack and α_2 reaction layer; crack nucleation at twinned γ-σ interfaces, but not γ-α_2 interfaces; and highly localized slip processes in the TiNb particles.

Constrained Deformation and Fracture Experiments on Sandwich Specimens

The irregular particles, deformation geometries and other effects noted above make it difficult to accurately extract s(u') curves and χ directly from resistance curves. Further, relating constrained deformation experiments to continuum mechanics models requires controlled and relatively simple (symmetric, low dimensional) deformation geometries. Finally, limitations imposed by surface observations of crack-particle interactions and particle deformation processes are mitigated by conditions which enhance uniformity in the process zone.

Hence, we have developed techniques for fabricating and testing simple sandwich specimens composed of relatively thick outer layers of γ-TiAl diffusion bonded to a thin (about 100μm) Nb or TiNb central foil with a variety of sharp pre-crack geometries. These specimens can be tested in either tension or bending and can be used to evaluate deformation with symmetric or asymmetric cracks. They can also be used to evaluate interface toughness; and by precracking only one side they can be used to study particle bypass mechanisms. The tests were monitored with either a high resolution optical system or on the SEM mechanical testing stage described above. Note that this technique can also be applied to other brittle matrix-ductile reinforcement combinations of interest. Some key results are summarized here for specimens with symmetric, planar precracks tested in tension (Figure 7). Typical diffusion bonding conditions were 10MPa at 1066°C for 4 h. Details of the experimental techniques and additional tests results are described elsewhere.

A typical s(u') curve for the TiNb reinforcement is shown in Figure 8a as the solid line. Micrographs corresponding to various points on this curve are shown in Figure 9. The peak in the normalized stress curve, $s(u')_{max}$, was about 2.1. The peak is bounded by conditions of a completely adherent interface (Point A/Figure 9a) on the rising part of the curve and the formation of a matrix debond crack just beyond the peak stress (Point B/Figure 9b). The load drops progressively as an approximately 50° shear band formed between the primary crack and the bottom of the debond (Point C/Figure 9c). Final fracture at u'* of about 1.75 was approached when a secondary shear band formed and linked with the primary deformation zone (Point D/Figure 9d). The work of fracture parameter, χ, was about 1.5 in this case.
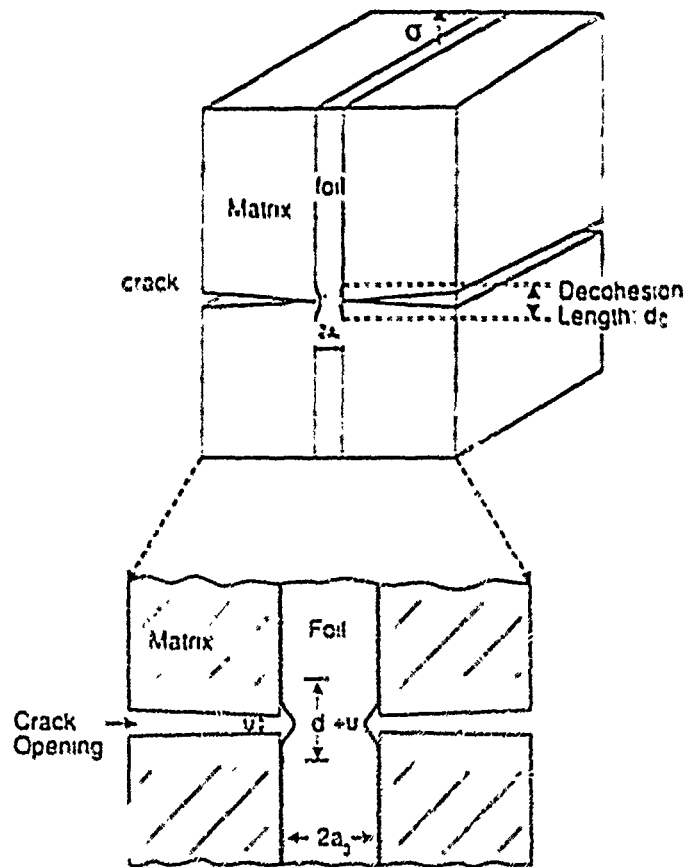
Figure 7 -- The sandwich specimen geometry used in this work to evaluate normalized stress displacement curves.
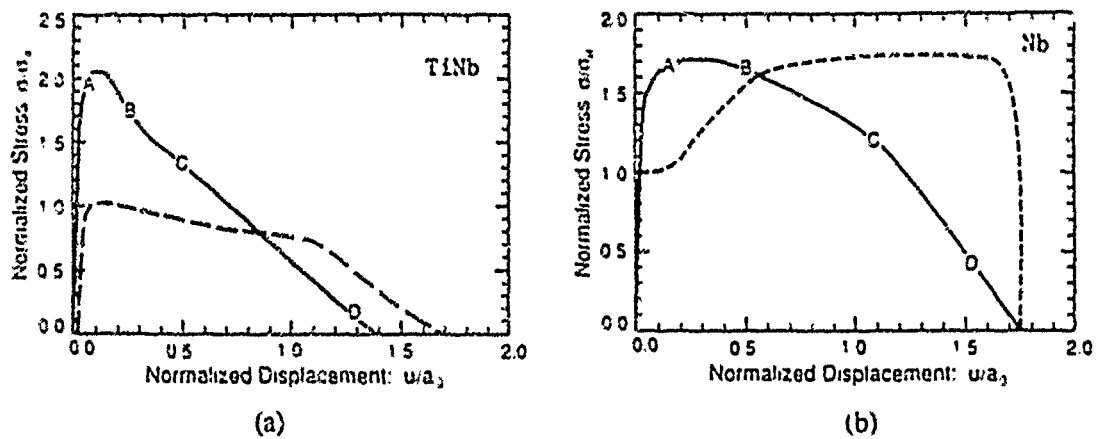

(a)

(b)

Figure 8 -- Normalized stress-displacement curves (solid lines) for a) TiNb and b) Nb foils. The letters reference micrographs shown in Figures 9 and 10. The dashed lines show corresponding curves for uniaxial tensile tests based on the displacement normalizations described in the text.
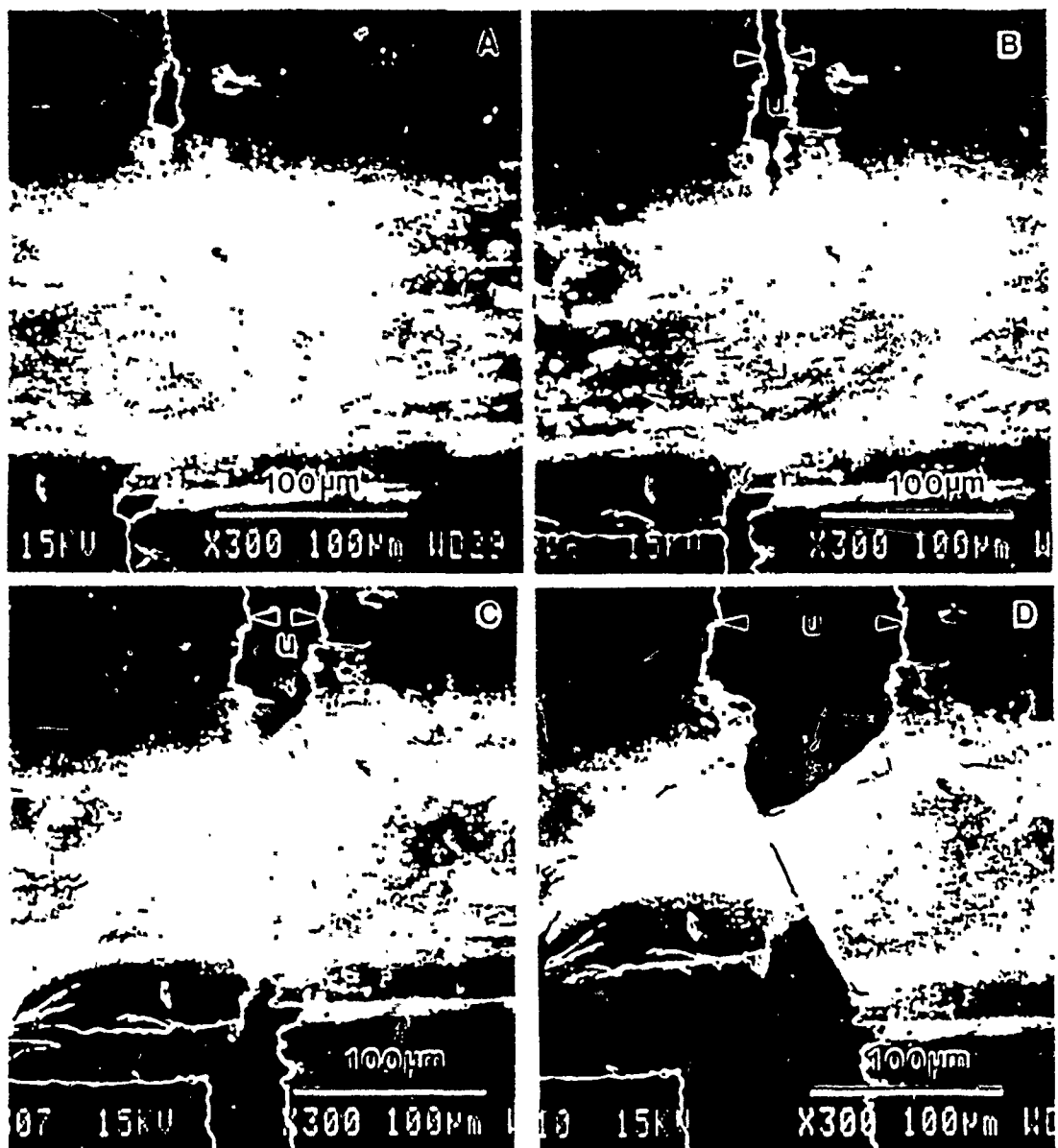
Figure 9 -- The deformation and fracture history of the sandwiched TiNb foil.

It is useful to compare the behavior of the sandwich specimens with the uniaxial tensile characteristics of the TiNb. This requires an appropriately normalized tensile displacement parameter. Since the flow localizes rapidly in this alloy, a sensible choice is the net plastic displacement divided by the appropriate tensile specimen half-thickness, or $u' = (l - l_0)/a_0$, where l_0 is the initial gauge length. A representative tensile test $s(u')$ curve is shown as the dashed line in Figure 8a. The $s(u')_{max}$ for the tensile curve was about 1, u'^* about 1.7 and χ about 1.2. The normalized fracture displacements were similar in the two cases.

A typical $s(u')$ curve for the Nb foil is shown as the solid line in Figure 8b. The corresponding micrographs are shown in Figure 10. Continuous debonding took place up to a d' of about 5 at u' of about 0.1 (Point A/Figure 10a). There was a broad region of maximum stress with a $s(u')$ of about 1.7 from u' of about 0.1 to 0.5; the latter displacement marked the onset of diffuse necking (Point B/Figure 10b). Continued deformation resulted in a nearly linearly decrease in stress out to fracture at u'^* of about 1.75 (Points C and D/Figure 10c and d), yielding a χ of about 2.3. The debond length did not increase significantly in the region from u' of about 0.1 to 1.7. The interface toughness, expressed in terms of the energy release rate, was measured in four point bending at about 45 J/m^2 (20).

Since deformation in Nb was characterized by diffuse necking, a different normalization is needed to compare the sandwich behavior to results of uniaxial tensile tests. In this case, it is reasonable to equate d' with a tensile gauge length, thus $u' = \varepsilon d'$, where ε is the engineering strain. Tensile test results based on this normalization are shown as the dashed line in Figure 10 taking d' to be 5. The $s(u')_{max}$ and u'^* were similar for the tensile tests and sandwich foils. This suggests that deformation and fracture in the Nb foil was largely controlled by the uniaxial tensile properties and the debond length. However, for the broad peak stress region for the tensile tests was shifted to significantly higher displacements. This behavior could indicate that the simple displacement normalization used is not appropriate due to an effect of the sandwich/crack geometry on perturbing the macroscopic deformation patterns. For example, lower necking strains may result from the evolved history of constraint in the sandwich specimens.

While there were general similarities between the behavior of the sandwiched foil specimens and the pancake particles in the alloys, a notable difference was that the particles on average experienced a smaller amount of debonding. The variations in debonding behavior between the particles and foils may be associated with the fact that, unlike the sandwiches (See Figures 9 and 10), the particles are more rigidly restrained from any lateral motion along the crack plane. Further, residual stress effects may be different for embedded particles compared to sandwiched foils.

Discussion

Figure 11 summarizes the effects of debonding on the various toughening parameters. The particles are represented as filled symbols and foils as open symbols; the Nb data are shown as circles and the TiNb data as squares. The data points shown in Figure 11 with large debond lengths were taken from a parallel research effort by Deve et. al. on the effect of Al$_2$O$_3$ and Y$_2$O$_3$ coatings on debonding (20).

The Critical Displacement Parameter, u'^*

TiAl-Nb. Figure 11a shows the variation of u'^* with d'. In the case of Nb foils, u'^* increased roughly in proportion to the debond length. To model this behavior we simply assumed that the u'^* was proportional to the debond length times the total tensile elongation (ε_t). The predictions shown as the solid line were in good agreement with the measured u'^* for the foils except at the largest debond length. In part, this deviation can be explained by noting that the displacement contributions beyond the point of uniform strain (ε_u) are not expected to scale strongly with the debond length. Substituting ε_u for ε_t provides a better estimate for d' of about 25 as shown by the plus (+) symbol in Figure 11a.
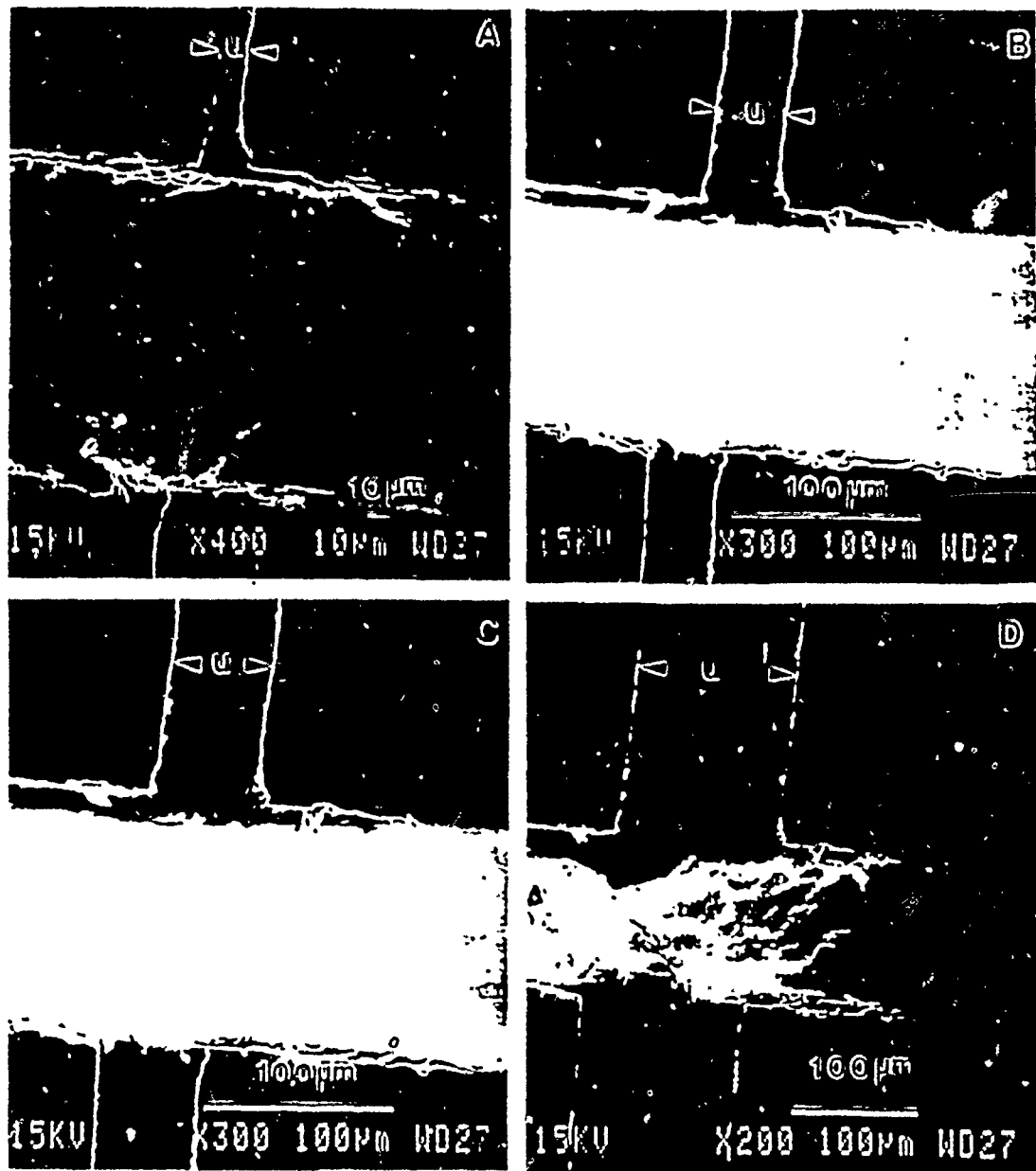
Figure 10 -- The deformation and fracture history of the sandwiched Nb foil.

The u'* for the Nb particles, with a nominal d' of about 2, also deviates from the simple model, which unphysically predicts that the critical displacement approaches 0 as the debond length approaches 0. Of course, there is a finite minimum u'* even without debonding. Assuming volume conservation and ignoring stress-state effects after crack blunting, an estimate of the upper bound of the minimum u'* can be approximately related to the tensile reduction in area (RA) and the initial displacement during the crack blunting, u'_b, as $u'* \approx u'_b/(1-RA)$. The u'_b was estimated from the dislocation pile-up model proposed by Ashby (6), assuming a constraint factor of 3 during blunting; thus $u'_b \approx 60\sigma_0/E$ where E is the elastic modulus. Taking a nominal value of σ_0/E of 1.3×10^{-3}, a minimum u'* of 1.6 is consistent with a RA of about 0.95. While the RA was difficult to precisely characterize in Nb due to the highly ductile fracture mode, this value is within the range estimated from uniaxial tests of flat tensile specimens.
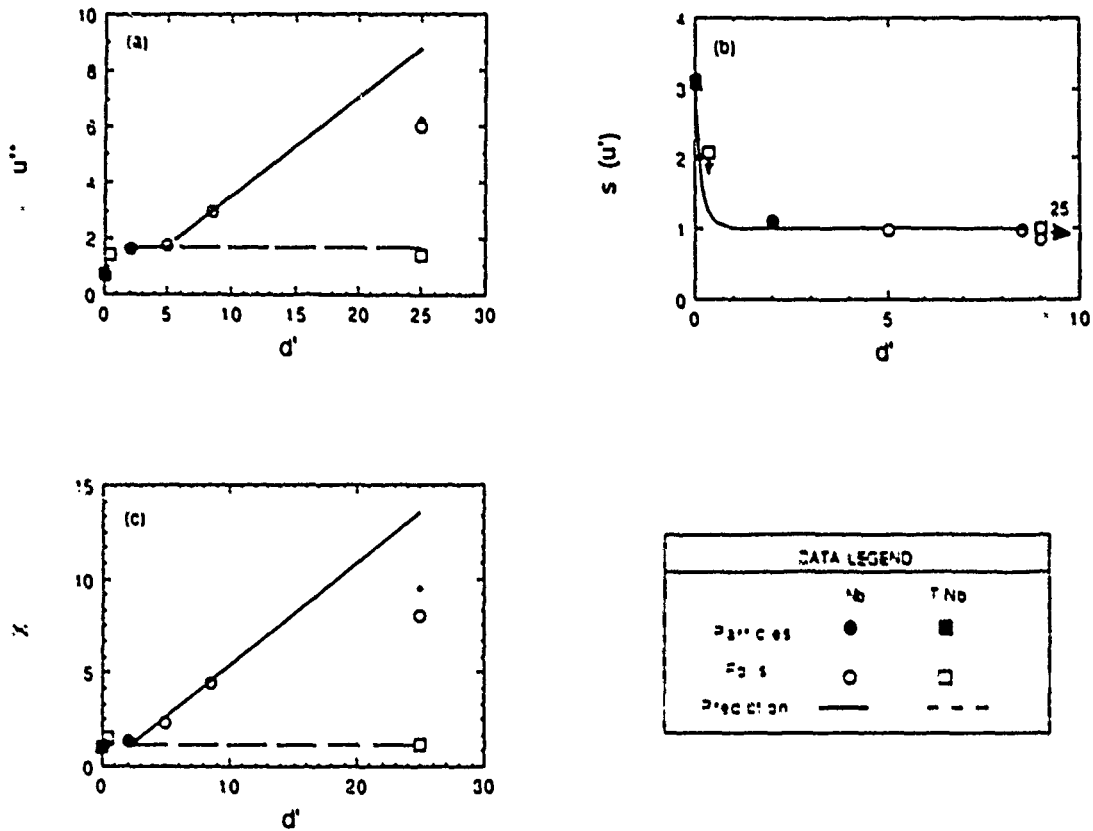

Figure 11 -- The effect of the normalized debonding length, d', on a) the critical normalized displacement, u'*; b) the effective constraint factor, $s_t(u')_{max}$; and c) the work of fracture, χ. The circles represent Nb and the squares represent TiNb; and the solid symbols are for the particles and open symbols are for the foils. The origin of the solid and dashed lines are described in the text.

<u>TiAl-TiNb</u>. For the particles, the u'* for TiNb was about 0.7 for a d' of 0. This is consistent with the simple treatment of the no debonding condition described above, yielding a predicted u'* of 0.66, using the measured RA of 0.8 and a nominal σ_o/E of 2.2×10^{-3}. The nominal debond length for the foil was determined by reducing the observed debond length of about 1.5 by a factor of 4 to 0.38, since the separation occurred only on one side of the crack and on one side of the foil; the corresponding u'* was 1.4. At the large debond lengths u'* was about 2. The average of 1.7±0.3 was consistent with the limiting value determined from the tensile tests (Figure 8b) as shown by the dashed line.

<u>The Maximum Constraint Parameter, $s_t(u')_{max}$</u>

<u>TiAl-Nb and TiAl-TiNb</u>. The maximum particle stress is dictated by a combination of constraint and strain hardening effects. In order to remove the effect of strain hardening when evaluating the effect of debonding on constraint, the particle and foil stress data was analyzed in terms of the maximum stress divided by the ultimate tensile stress, σ_{uts}, or $s_t(u')_{max}$ ($=\sigma(u')/\sigma_{uts}$). The $s_t(u')_{max}$ as a function of d' is shown in Figure 11b. The solid curve was based on Ashby's model of constrained deformation as a function of the debond length (6). The experimental results were consistent with the rapid drop-off in constraint with debonding length predicted by simple models. Note the TiNb point at a nominal d' of 0.38 falls somewhat above the predicted curve. Somewhat better agreement is observed if using the actual $s_t(u')$ at the point where the crack is observed (Point B in Figure 8b) as shown by an arrow in Figure 11b.

<u>The Work of Fracture Parameter, χ</u>

<u>TiAl-Nb</u>. Figure 11c shows the relationship between χ and the debond length. In the case of Nb, χ increased systematically with d'. The solid line is a prediction assuming the Nb behaves like a uniaxial tensile specimen with a normalized gauge length of d', thus,

$$\chi = d' \int_0^{\varepsilon_t} \sigma(\varepsilon)/\sigma_o \, d\varepsilon \qquad (1)$$

where $\sigma(\varepsilon)/\sigma_0$ is the normalized uniaxial stress-strain curve. The simple model predictions were consistent with χ measured for both the particles and foils except at the largest debond length. This difference was again probably due to overestimating the displacement contribution beyond the ultimate stress, in the necking region. Integrating the stress-strain curve only up to ε_u rather than ε_t, shown as the plus (+) symbol in Figure 11c, gave better agreement with the χ for the foil with d' of about 25.

<u>TiAl-TiNb</u>. Figure 11c shows that the magnitude of χ does not vary significantly for case of TiNb particles and foils, ranging from about 1.1 to 1.5. The scatter around the average of 1.3±0.2 is much less than the uncertainties in the measured values and close to the equivalent χ of 1.2 found from the tensile test as shown by the dashed line.

<u>Implications</u>

These results nicely illustrate the need to consider the combined effects of the ductile phase, interface and matrix properties in evaluating toughening potential. For niobium, with brittle reaction layer phases (e.g σ, and δ), some debonding was unavoidable. However, since χ scaled with d, extensive debonding may be desirable in many applications. For a given debond length, χ was controlled by the uniaxial stress-strain behavior of niobium. In contrast, for TiNb particles and uncoated foils the predominant reaction layer α_2 phase was tougher, resulting in minimal debonding. In this case, χ is not significantly influenced by debonding although there were more significant differences in the constraint (increased) and maximum displacement (decreased) for particles that remain attached to the matrix. The behavior of TiNb was due to the rapid formation of a localized neck associated with coarse slip

Of course, steady state toughening is proportional to the strength levels of the ductile phase as well as χ. In particular, the lower value of χ in composites containing TiNb versus Nb particles was more than offset by the higher strength of the former alloy. Ductile phases with both high strength and high strain hardening exponents would provide the maximum toughening potential, and would further benefit from debonding. Indeed, the combination of high uniaxial ultimate tensile strength, strain hardening exponent and uniform elongation along with a moderately brittle reaction layer would be a good guide for identifying promising toughening phases.

However, as noted in the introduction, the initial slope of the resistance curve, or the tearing modulus, T_R, may often be a more important engineering property than steady-state toughness. Optimizing T_R generally requires maximizing constraint, hence, minimizing the debonding. Thus, an idealized composite design might be aimed at achieving progressive debonding of phases with good uniaxial tensile properties and which maintain significant ductility under triaxial stress states. An alternate approach approach could be to use mixtures of bonding and debonding phases. Moreover, extensive debonding may be required to increase the energy absorption capacity of materials as measured in, for example, Charpy impact tests. Because of the limited volume of materials deforming in the vicinity of sharp cracks, a significant increase in the fracture toughness does not mean that the blunt notch energy absorption capacity will increase in a like manner. In principle, the blunt notch energy absorption can be increased by debonding if this leads to a sufficient increase in the volume of deformed ductile phase. Note, however, that the effects of ductile phases on the displacement capacity of a ductile phase reinforced composite is minimal with or without debonding.

Summary and Conclusions

The results of this study on Nb and TiNb reinforced γ-TiAL alloys can can be summarized as follows.

Microstructures and Basic Deformation and Debonding Processes

a) The reaction zone phases and phase substructures observed in powder processed alloys are generally consistent with data in the literature.

b) There is evidence of high temperature deformation recovery processes producing a fine dislocation cell structure in Nb particles. The fine subgrain size may increase the strength of the alloys relative to the undeformed and annealed condition. The outer regions of β-TiNb particles are converted to a mixture of ordered B_2 and α_2 phases during processing.

c) Deformation in TiNb particles occurs by formation of extensive rafted dislocation pile-ups in narrow, coarsely distributed slip bands; while some cross slip and tangling occurs at high strains, neither cell structures nor twinning are observed.

d) The dominant reaction layer phase in alloys containing TiNb particles is α_2 which has a considerable amount of ductility associated with dislocation slip. For Nb particles the reaction zone phases include σ and δ and possibly T_2 and α_2 phases which are brittle and do not twin or slip.

e) The γ-matrix region near the crack faces and reaction zone shows evidence of a considerable amount of deformation by both twinning and slip. Interface cracks appear to be nucleated at the points where twin boundaries intersect the σ but not the α_2 reaction layer.

f) For the Nb particles, debonding occurs between the brittle σ-phase and the γ-matrix. Debonding is highly variable and dependent on crack-particle/foil geometry effects. Debonding may also be influenced by geometric constraints and residual stresses. Debonding is generally minimal for TiNb particles. Limited debonding is observed between the α_2-phase and matrix, and cracking is sometimes observed in the adjoining matrix.

g) Macroscopically, Nb particles and foils deform by homogeneous slip and fail in a highly ductile manner after the formation of a diffuse necks or shear bands. Debonding is established at small strains. In contrast, the TiNb particles deform by coarse slip which propagates large distances in the particles away from the crack faces. Fracture occurs by localized necking and cracking involving the coalescence and intersection of intense primary and secondary shear bands.

Toughening Mechanisms and Relations

a) The steady-state toughening potential for a ductile phase reinforcement depends on the combination of properties of the ductile phase itself, the interface/reaction layer region and the matrix.

b) Considerable toughening is produced by strong and reasonably ductile TiNb phases even in the absence of significant debonding and low uniform strains.

c) Toughening from the TiNb particles occurs under conditions of maximum constraint and minimum ductility, yielding a χ of about 1.

d) Extensive debonding and conditions of minimum constraint does not result in a significant increase in steady-state toughness from TiNb phases. This behavior is due to the coarse slip, limited uniform ductility and localized necking of the alloy.

e) More modest toughening is achieved from the lower strength, higher ductility Nb particles and foils.

f) With d' of about 2, toughening from Nb particles is achieved under conditions of minimum constraint, yielding a χ of about 1.3.

g) The χ for Nb foils increases with the debond length. This is due to the large uniform strain in Nb followed by failure after the formation of a diffuse neck. Assuming an appropriate aspect ratios, enhanced debonding in the particles would be expected to produce similar increases in toughness.

h) For a given debond length, the steady-state toughening, constraint and critical displacement parameters can be crudely predicted using simple models and uniaxial tensile data.

i) In addition to particle bridging contributions, considerable additional toughening can result from deflection and branching. Crack deflection and branching are influenced by the combination of particle, matrix and reaction zone properties and the crack-particle interaction geometry.

Generalizations

a) Toughening could be enhanced further by using ductile phases with higher strength, strain hardening exponents and uniform ductility than TiNb.

b) Debonding and thicker particles would also increase the steady-state toughness from such ductile phases, and debonding may be required for optimizing energy absorption capacity.

c) Debonding generally decreases the the tearing modulus, which may not be desirable for some applications.

d) It might be possible to optimize an alloy by designing for controlled progressive debonding or by using mixtures of bonding and debonding phases.

Acknowledgements

References

1. J. Bowling and G. W. Groves, I. Mater. Sci, 14 (1979) 443.

2. L.S. Sigl et. al., Acta Metall., 36 (1988) 945.

3. A.J. Pysic, I.A. Aksay and M. Sankaya, Ceramic Microstructures, Materials Science Research, 21 (eds, J.A. Pask and A.G. Evans, 1986) 45.

4. C.K. Elliott et. al. High Temperature, MRS Symposium Proceedings on High, Temperature High Performance Composites, 120, (eds. Lemke et. al. 1988) 95.

5. E. Aigeltinger et. al., Microstructure Proprty Relations in Ductile Phase Toughened Gamma-TiAl Alloys, Proceedings of the ASM Symposium on Intermetallic Materials, (Los Angeles, CA March 21 - 23, 1989) to be published.

6. M. F. Ashby, F. J. Blunt and M. Bannister, Acta Metall, 37 (1989) 1847.

7. H. Tada, P.C. Paris and G.R. Irwin, The Stress Analysis of Cracks Handbook, Del Research, St. Louis, MO, 1985.

8. F. Zok and C. L. Hom, Large Scale Bridging in Brittle Matrix Composites, to be published.

9. T. J. Jewett et. al, Experimental Determination of the Ti-Nb-Al Phase Diagram at 1200°C, MRS Symposium Proceedings on High Temperature Ordered Intermetallic Alloys, 133, (eds. C.T. Liu et . al. 1988) 95.

10. H. C. Cao et. al., A Test Procedure for Characterizing the Toughening of Brittle Intermetallics By Ductile Reinforcements, Acta Metall (in press).

11. A.V. Narlikar, A.V. and D. Dew-Hughes, I. Mater. Sci, 1, 317 (1966).

12. C. Baker, I. Mater. Sci, 5, (1970) 40.

13. M.J. Marcinkowski, in: Electron Microscopy and Strength of Crystals, eds, G. Thomas and J. Washburn (Interscience Publishers, New York 1963) 333.

14. H. Lipsitt, D. Shechtman and A. Scharfrik, Met Trans A, 11A (1980) 1369.

15. S. M. L. Sastry and H. A. Lipsitt, Met Trans A, 8A (1977) 1543.

16. S. Hanada, M. Ozeki and O. Izumi, Met Trans A, 16A (1985) 789.

17. D. Schechtman et. al., Met. Trans. A, 5A (1974) 1373.

18. R. Strychor, J. C. Williams and W. A. Soffa, Met. Trans.A, 19A (1988) 225.

19. O. N. Andreyev, Russian Met. 1, (1970) 127.

20. H. Dève, A.G. Evans and R. Mehrabian, to be presented at MRS Symposium on Tailored Interfaces in Composite Materials, November 27-29, 1989, Boston Mass.